X International conference

# Plasma Physics
and
# Plasma Technology

## Contributed papers




**Minsk, Belarus**
**September 12 – 16, 2022**

**B.I. Stepanov Institute of Physics**
**National Academy of Sciences of Belarus**

The National Academy of Sciences of Belarus
B.I. Stepanov Institute of Physics of the National Academy of Sciences of Belarus
Joint Institute for High Temperatures of the Russian Academy of Sciences

# X International Conference

# PLASMA PHYSICS AND PLASMA TECHNOLOGY

# (PPPT-10)

Minsk, Belarus
September 12 – 16, 2022

**CONTRIBUTED PAPERS**

Minsk
«Kovcheg»
2022

UDC 533.3(082)

EDITORS:
N.V. Tarasenko, A.A. Nevar, N.N. Tarasenka, M.S. Usachonak

**Proceedings of the X International Conference «PLASMA PHYSICS AND PLASMA TECHNOLOGY» (PPPT-10): September 12-16, 2022, Minsk, Belarus / Edited by N.V. Tarasenko, A.A. Nevar, N.N. Tarasenka, M.S. Usachonak - Minsk : Kovcheg, 2022. – 520p.**

The reports in these Contributed Papers are presented by the individual authors. The views expressed are their own and do not necessarily represent the views of the Publishers or Sponsors. Whilst every effort has been made to ensure the accuracy of the information contained in this book, the Publisher or Sponsors cannot be held liable for any errors or omissions however caused.

*All rights reserved.*
*No part of this publication may be reproduced, stored in a retrieval system, in any form or by any means, electronic, mechanical, photocopying, recording, or otherwise, without the prior permission of the copying owner*

**ISBN 978-985-884-193-5**

© B.I. Stepanov Institute of Physics,
National Academy of Sciences of Belarus, 2022
© Registration, "Kovcheg LTD", 2022

# IN MEMORY OF VICTOR S. BURAKOV



The 10th International conference on Plasma Physics and Plasma Technology is dedicated to the memory of Victor S. Burakov.

Professor, Academician V.S. Burakov was one of the founders of the PPPT conferences and was standing at the origin of the plasma research field in Belarus. He was an inspiring scientist and leading plasma researcher who made seminal contributions to the fields of plasma physics. Victor Burakov's name is uniquely identified with the plasma spectroscopy and its application in analytics and diagnostics.

The first scientific works of Burakov V.S. were devoted to the development of atomic spectral analysis and its implementation at Belarusian enterprises. The results of this work were summarized by him in the book "Practical handbook on spectral analysis" (co-author - Professor A.A. Yankovsky), published in Belarus (1960) and England (1964).

Later, the scientific interests of Prof. Burakov concentrated on plasma spectroscopy, laser physics, and scientific instrumentation. In 1987 he created his research laboratory working on the directions of plasma diagnostics, and laser spectroscopy. He developed methods for laser diagnostics of plasma, studied the patterns of interaction of laser radiation with plasma and nonlinear optical phenomena in it, developed methods for controlling the characteristics of laser radiation using plasma. Prof. Burakov supervised the creation of the first excimer laser in Belarus, created a lidar system based on it for monitoring the state of the atmosphere. Under his supervision, the diagnostic and analytical possibilities of selective laser spectroscopy including laser-induced fluorescence and intracavity laser spectroscopy were considered, and samples of highly sensitive spectrometers were created.

Among the methods of selective laser spectroscopy, an important role belongs to the laser-induced fluorescence of atoms and molecules, which allows obtaining a detailed information about the density and temperature of various plasma components with high sensitivity and spatial-temporal resolution. The works of Prof. Burakov and

his students made a significant contribution to the development of this method towards the diagnostics of non-equilibrium and non-stationary plasmas, as well as to the studies on the features of selective excitation and resonance fluorescence under the conditions of collisional and chemical interactions of atoms and molecules in plasma.

The developed methods were successfully used for diagnostics of low-temperature gas discharge, laser ablation, and high-temperature tokamak plasma. Together with the Russian colleagues, an important cycle of works on the application of the resonance fluorescence method for determining the parameters of high-temperature plasma in tokamak installations was performed. Prof. V.S. Burakov participated in the creation of specialized diagnostic complexes for laser-fluorescence monitoring of the plasma state in tokamak facilities. The information obtained about the processes in the near-wall plasma of a tokamak under conditions of interaction of powerful energy flows with walls turned out to be extremely important for the further development of research in the field of controlled thermonuclear fusion.

V.S. Burakov research career involved several more breakthrough achievements: such as plasma-activated synthesis of nanomaterials and laser-induced breakdown spectroscopy (LIBS). He took an active part in the development of a new topical field of modern physics - a synthesis of nanosized particles and structures in the processes of laser ablation and electric discharges in liquid media. Among the most important developments of liquid phase plasma synthesis of nanoparticles are a gas-liquid interfacial discharge and a plasma-laser reactor based on the electrical discharge inside the solution for synthesis of metallic, oxide and composite nanoparticles with controllable parameters. In LIBS, he contributed to the development of new express approaches for composition analysis of materials, that subsequently found applications in analysis of environmental samples, archaeological finds, works of art, including calibration-free approach which does not require reference samples.

He gladly shared his vast knowledge with his colleagues and students, leading by example but letting others show the way when ready, remaining dedicated and never passing-up a chance to lend a hand, if required. Standing at the origin of well established plasma school in Belarus, he was a mentor and supervisor of a number of PhD students, that became skilled researches themselves. To Academician Victor S. Burakov, the best traits of a scientist were inherent: purposefulness, principledness and benevolence, constant search for promising directions of research, intuition based on a wide range of knowledge and detailed consideration of the needs of practice.

His legacy stays alive in his research works: V.S. Burakov is the author of more than 700 journal papers, scientific reports and patents in the fields of plasma spectroscopy, plasma diagnostics and plasma technologies. The influence of his research lives on: his ideas and proposed approaches are being actively developed in the works of his students, while the developed methods of diagnostics are actively applied in industry. As a co-organizer of PPPT conferences, he greatly contributed to its expansion and growing success over the years following its inception. Plasma research field in Belarus would not be where it is now without his contribution.

**CONFERENCE ORGANIZERS:**

The National Academy of Sciences of Belarus
B.I. Stepanov Institute of Physics of the National Academy of Sciences of Belarus
Joint Institute for High Temperatures of the Russian Academy of Sciences

**CO-ORGANIZERS:**

A.V. Luikov Heat and Mass Transfer Institute of NAS of Belarus
Al-Farabi Kazakh National University
Scientific Council of the Russian Academy of Sciences on Low-Temperature Plasma Physics
Scientific-Technical Association «Optics and Lasers»
The Belarusian Physical Society

**SPONSORED BY:**

The National Academy of Sciences of Belarus
Belarusian Republican Foundation for Fundamental Research
SOL instruments Ltd.

**Chairmen:** N.V. Tarasenko (Belarus)
O.F. Petrov (Russia)

**Vice-chairmen:** A.N. Chumakov (Belarus)
L.V. Simonchik (Belarus)

**Scientific secretary:** A.A. Nevar

## Advisory Committee

S.Ya. Kilin (Belarus), M.V. Bogdanovich (Belarus), S.V. Gaponenko (Belarus), T.S. Ramazanov (Kazakhstan)

## International Program Committee

V.M. Astashynski (Belarus), Yu.S. Akishev (Russia), V.I. Arkhipenko (Belarus), I.I. Filatova (Belarus), I.S. Nikonchuk (Belarus), A.S. Smetannikov (Belarus), I.P. Smyaglikov (Belarus), A. Hamdan (Canada), Ravi Soni (India), M. Trtica (Serbia), M.M. Vasiliev (Russia), I. Rafatov (Turkey), F. Krcma (Czech Republic), V.V. Uglov (Belarus)

## Local Organizing Committee

M.I. Nedel'ko, V.A. Lyushkevich, N.A. Bosak, S.V. Goncharik, A.A. Kirillov, V.G. Kornev, V.V. Kouhar, V.V. Lychkovski, A.O. Radomtsev, D.V. Shabrov, N.N.Tarasenka, N.V. Tomkovich, M.S. Usachonak, N.V. Varapaj

# CONTENTS


## 1. FUNDAMENTAL PHYSICAL PROCESSES AND PHENOMENA IN PLASMAS

DYNAMICS OF SINGLE PARTICLES IN A DC GLOW DISCHARGE UNDER THE ACTION OF LASER RADIATION 3
A.S. Svetlov, E.A. Kononov, O.F.Petrov, M.M.Vasiliev

EXPERIMENTAL VERIFICATION OF A NONLOCAL MODEL IN THE DISCHARGE IN CROSSED FIELDS AND THE SHORT DISCHARGE IN HELIUM 4
A. Platonov, E. Prokhorova, A. Slyshov

MICRODYNAMICS AND THERMODYNAMICS OF NONLINEAR WAVES IN DUSTY PLASMA 8
F.M. Trukhachev, M.M. Vasiliev, O.F. Petrov

ETCHING KINETICS OF QUARTZ IN A MICROWAVE HYDROGEN PLASMA 10
V. Yurov, V. Ralchenko, D. Sovyk, A. Altakhov, A. Bolshakov, I. Fedorova, E. Zavedeev, F. Popovich

STUDY OF SELF-ORGANIZATION OF NEAR-ELECTRODE CURRENT STRUCTURES IN ATMOSPHERIC PRESSURE GLOW DISCHARGES IN HELIUM 11
I. Rafatov, G. Islamov, C. Yesil

CONTROLLING OF CHARACTERISTICS OF A PLASMA ASYMMETRIC DIPOLE ANTENNA 15
N. Bogachev, M. Usachonak, S. Andreev

## 2. ELECTRICAL DISCHARGES AND OTHER PLASMA SOURCES, NOVEL PLASMA GENERATION APPROACHES

ON THE STABILITY OF DIFFUSE ATTACHMENT ON THE HOT CATHODE OF VACUUM ARC 21
V.P. Polishchuk, R.A. Usmanov, A.D. Melnikov, I.M. Yartsev

NUMERICAL SIMULATION OF LIGHT-EROSION PLASMA DYNAMIC MPC-DISCHARGES 25
V.V. Kuzenov, N.V. Batrak, N.G. Kopaleishvili

SMALL-SIZE PLASMA PULSED FREQUENCY THRUSTER 29
P. Morozov, R. Emlin, I. Punanov, Ye. Shcherbakov, L. Yashnov

NUMERICAL SIMULATION OF THE FLOW OF AN ELECTRICALLY CHARGED DUSTY MEDIUM WITH ONE-DIMENSIONAL GEOMETRY 34
D. Tukmakov

ELECTRIC DISCHARGES OF DIRECT AND ALTERNATING CURRENT IN A GAS-LIQUID FLOW AT ATMOSPHERIC PRESSURE 38
F.M. Gaysin, A.A. Khafizov, R.I. Valiev, L.N. Bagautdinova, Az.F. Gaysin, Al.F. Gaysin

PLASMA STUDIES AT GASDYNAMIC ION SOURCE FOR MULTIPURPOSE OPERATION (GISMO) 42
R.L. Lapin, I.V. Izotov, A.F. Bokhanov, S.V. Golubev, E.M. Kiseleva, S.S. Vybin, A.V. Polyakov and V.A. Skalyga

A NEW TYPE OF MICROWAVE NON-THERMAL ATMOSPHERIC PRESSURE PLASMA SOURCE 46
V.Tikhonov, S. Gorbatov, I. Ivanov, A. Tikhonov

MICROWAVE COMPLEX FOR OBTAINING LOW-TEMPERATURE PLASMA AT ATMOSPHERIC PRESSURE 50
I. Ivanov, S. Gorbatov, A. Tikhonov, V. Tikhonov

ANALYSIS OF PARAMETERS OF COAXIAL DIELECTRIC BARRIER DISCHARGE IN CARBON DIOXIDE FLOW AT ATMOSPHERIC PRESSURE 54
I. Rafatov

NONSTATIONARY SLOW IONIZATION WAVES IN LONG DISCHARGE TUBES AT LOW GAS PRESSURE 58
A. Shishpanov, P. Bazhin, V. Zaletov

LOW-VOLTAGE HIGH-CURRENT PULSED MAGNETRON DISCHARGE AS A SOURCE OF DENSE METAL-FREE PLASMA 62
A.V. Kaziev, D.V. Kolodko, N.P. Orlov, V.A. Tumarkin

**3. ATMOSPHERIC PRESSURE PLASMAS, PLASMA IN AND IN CONTACT WITH LIQUID, PLASMA-LIQUID INTERACTIONS**

DECOMPOSITION OF CO2 IN A MICROWAVE DISCHARGE IN LIQUID HYDROCARBONS 67
Yu. A. Lebedev, T.S. Batukaev, G.V. Krashevskaya, I.V. Bilera

SYNTHESIS AND PHOTOVOLTAIC APPLICATION OF MIXED TUNGSTEN-MOLYBDENUM AND TUNGSTEN-TITANIUM OXIDES NANOPARTICLES OBTAINED USING PULSED UNDERWATER PLASMA 71
N. Sirotkin, A. Khlyustova, V. Titov

LIQUID ANODE METHOD AS A METHOD FOR THE FORMATION OF SPHERICAL METAL PARTICLES 75
YU.S. Baryshnikov, R.O. Kurakin, K.V. Tverdokhlebov, A.V. Chikiryaka, S.A. Poniaev

DIRECT OXIDATION OF BENZENE TO PHENOL IN LOWTEMPERATURE BAARRIER DISACHARGE PLASMA: INFLUENCE OF REACTOR TEMPERTURE 79
A. Leshchik, S. Kudryashov

THE POSSIBILITY OF USING A GAS DISCHARGE WITH A LIQUID ELECTROLYTE CATHODE TO CREATE A STEAM-WATER PLASMA FLOW 83
G. Tazmeev, B. Timerkaev, Kh. Tazmeev

RESEARCH CHARACTERISTICS OF PLASMA JET GENERATED BY COAXIAL DIELECTRIC BARRIER DISCHARGE AT ATMOSPHERIC PRESSURE 87
A. Aksiuchyts, D. Kotov, K. Logunov, A. Osipov

ELECTRICAL DISCHARGE INITIATED CHEMISTRY IN PREBIOTIC ATMOSPHERES 91
F. Krčma, S. Chudják, N. Fojtíková, L. Moravský, Š. Matejčík

ZERO-DIMENSIONAL SIMULATION OF A MICROWAVE DISCHARGE IN A MIXTURE OF ETHANOL WITH WATER 95
Yu.Lebedev, A.Tatarinov, A.Titov, I.Epstein

APOKAMP AND PROSPECTS OF ITS APPLICATION IN BIOMEDICINE 99
V. Panarin, V. Skakun, D. Pechenitsin, D. Schitz

**4. NON-IDEAL AND DUSTY PLASMAS, EXTREME PLASMA REGIMES, FUSION AND ASTROPHYSICAL PLASMAS, COLLECTIVE AND NONLINEAR PHENOMENA**

THE NATURE OF ABNORMAL PARTICLE HEATING IN THE PLASMA DUST STRUCTURES 105
S. I. Mol'kov, A.S. Shtykov

COLLECTIVE EFFECTS IN AN ACTIVE COLLOIDAL SYSTEM OF COMPLEX COMPOSITION UNDER THE ACTION OF LASER RADIATION 108
R.V. Senoshenko, E.A. Kononov, M.M. Vasiliev and O.F. Petrov

SELF-ORGANIZATION OF A LASER-IRRADIATED MONOLAYER OF ACTIVE PARTICLES MODIFIED IN AN RF DISCHARGE PLASMA 110
E.A. Kononov, M.M. Vasiliev, O.F. Petrov

COSMIC DUST, ELECTRICAL PHENOMENA AND WEATHER ON EARTH 112
A. Kostrov

ULTRACOLD MULTIMODAL DUSTY PLASMA IN DC GLOW DISCHARGE 116
R. Boltnev, E. Kononov, F. Trukhachev, M. Vasiliev, O. Petrov

EXPERIMENTAL STUDY OF KINETIC HEATING OF DUST PARTICLES IN A GAS DISCHARGE 120
E.A. Sametov, E.A. Lisin, E.A. Kononov, M.M. Vasiliev, O.F. Petrov

ROTATION MECHANISMS OF DUST CLUSTERS IN STRATIFIED DC DISCHARGES UNDER THE MAGNETIC FIELD ACTION 124
L. Dyachkov, E. Dzlieva, V. Karasev, L. Novikov, S. Pavlov

NEW RESULTS FROM DUSTY PLASMA EXPERIMENTS AT THE "PLASMA KRISTALL - 4" LABORATORY ON BOARD THE INTERNATIONAL SPACE STATION. 128
A. Lipaev, A. Zobnin, R. Syrovatka, A. Usachev, A. Khrapak, O. Petrov, M. Thoma

VOLUME DUST STRUCTURES IN A PLASMA WITH MAGNETIZED IONS 132
V.Yu. Karasev, E.S. Dzlieva, S.I. Pavlov, L.A. Novikov, S.A. Tarasov, D.V. Yanicin, O. E. Bashkircev

FRACTAL ANALYSIS OF THE SURFACE OF MELAMINEFORMALDEHYDE DUST PARTICLES 136
A. Gorbenko, V. Polischuk, E. Dzlieva, S. Pavlov, V. Karasev

FRACTAL DIMENSION OF EXTENSIVE SYSTEMS OF JANUS AND METAL-COVERED GRAINS IN COLLOIDAL PLASMAS 140
X.G. Koss, E.A. Kononov, I.I. Lisina, M.M. Vasiliev and O.F. Petrov

DYNAMIC EFFECTS IN DUSTY CLUSTERS IN A MAGNETIC FIELD 142
S. Pavlov, E. Dzlieva, L. Novikov, V. Karasev

ACTIVE BROWNIAN PARTICLE IN A PLASMA 146
E.A. Lisin, O.S. Vaulina, I.I. Lisina, O.F. Petrov

CALCULATIONS OF THE EQUATION OF STATE AND ELECTRONIC TRANSPORT COEFFICIENTS OF LOW-TEMPERATURE BISMUTH PLASMA 149
E. M. Apfelbaum

STRONGLY COUPLED COULOMB SYSTEMS OF BROWNIAN GRAINS AT TEMPERATURE OF SUPERFLUID HELIUM 153
O.F. Petrov, R.E. Boltnev and M.M. Vasiliev

SELECTION OF DUST PARTICLES IN INERT GASES WITH DIFFERENT IONIZATION POTENTIALS 155
E.S. Dzlieva, M.S. Golubev, L.A. Novikov, S.I. Pavlov, M.A. Gasilov, V.Yu. Karasev

**5. LASER-PLASMA INTERACTIONS WITH MATERIALS, LASER ABLATION, MODIFICATION OF MATERIALS, SPUTTERING AND DEPOSITION**

INFLUENCE OF LASER CRATER TEMPERATURE ON MATERIAL ABLATION AND INTENSITY OF SPECTRAL LINES OF EROSIVE PLASMA TORCH 161
K. Znosko

MORPHOLOGY OF THE SURFACE OF NATURAL LAMB LEATHER AFTER TANNIDE TANNING AND LASER EXPOSURE 165
A. Anisovich, T. Kodirov, U. Khudanov, M. Markevich, V. Zhuravleva

THE PLM-M STEADY-STATE PLASMA LINEAR FACILITY FOR FULL-SCALE TESTING OF THERMONUCLEAR REACTOR MATERIALS 169
V. Tran, V. Budaev, S. Fedorovich, D. Kavyrshin, A. Karpov, K. Rogozin, A. Konkov, V. Kvaskov

LIBS HYDROGEN DETECTION: SIGNIFICANCE IN FUSION TECHNOLOGY 173
M. Trtica, J. Savovic, M. Kuzmanovic, D. Rankovic

ULTRA-SHORT LASER PULSE PROCESSING OF Ti-BASED THIN METALLIC FILMS 177
B. Gaković, S.I. Kudryashov, P.A. Danilov, D. Milovanović, A.A. Ionin

THE SPATIOTEMPORAL VALIDATION OF LOCAL THERMODYNAMIC EQUILIBRIUM DURING THE ANALYSIS OF A ZnAlCu ALLOY BY THE LIBS TECHNIQUE 181
N. Lellouche, S. Messaoud Aberkane, K. Yahiaoui, A. Kellou

ENHANCED PROTON ACCELERATION FROM AN ULTRATHIN TARGET IRRADIATED BY LASER PULSE 185
M.Turki, D. Bennaceur Doumaz

SHIELDING OF THE TARGET DURING LASER-PLASMA TREATING OF METALS IN ELECTRIC FIELD 189
A.Yu. Ivanov, A.L. Sitkevich, S.V. Vasiliev

CRYSTALLINE STRUCTURE CHANGES IN METALS AFTER THEIR LASER TREATING IN DIFFERENT CONDITIONS 193
A.Yu. Ivanov, E.A. Karpovich, A L Sitkevich, N.G. Valko, S.V. Vasiliev

SELECTION OF SPECTRAL VARIABLES FOR MULTIVARIATE CALIBRATION ON C, Mn, Si, Cr, Ni AND Cu IN LOW ALLOY STEELS CHARACTERIZATION BY LIBS METHODS 197
M.V. Belkov, D.A. Borisevich, K.Yu. Catsalap, M.A. Khodasevich

PLASMA-ASSISTED SYNTHESIS OF HYBRID AND DOPED SILICONBASED NANOSTRUCTURES 201
N.N. Tarasenka, V.G. Kornev, A.A. Kuchmizhak

PLASMA FORMATION AT YTTRIUM VANADATE (YVO4) TARGET EXPOSED TO TWO-PULSE BICHROMATIC LASER RADIATION IN THE AIR 205
N.A. Bosak, A.N. Chumakov, A.A. Ivanov, V.V. Kiris, E.M. Dyatlova, A.A. Shevchenok, A.V. Buka

DISTRIBUTION OF ELEMENTS IN HIGH-ENTROPY CoCrFeNi AND NbTaTiV ALLOYS IRRADIATED WITH LOW-ENERGY Kr IONS 209
V.V. Uglov, N.A. Stepanjuk, I.V. Safronov, S.V. Zlotski, I.A. Ivanov, A.E. Ryskulov, A.E. Kurakhmedov, A.L. Kozlovskiy, M.V. Zdorovets, K. Jin

MICROSTRUCTURE AND PHASE STATE OF SILICON CARBIDE IRRADIATED WITH HELIUM IONS 213
V.V. Uglov, V.M. Kholad, P.S. Grinchuk, M.V. Kiyashko, I.A. Ivanov, A.L. Kozlovskiy, M.V. Zdorovets

EFFECT OF IRRADIATION WITH KRYPTON IONS ON THE STRUCTURAL-PHASE STATE OF A MULTICOMPONENT SOLID SOLUTION BASED ON V-Nb-Ta-Ti 217
V.V. Uglov, M.M. Belov, S.V. Zlotsky, I.A. Ivanov, A.E. Ryskulov, A.E. Kurakhmedov, A.L. Kozlovskiy, M.V. Zdorovets, K. Jin

BK-110 GLASS DESTRUCTION UNDER COMBINED LASER IRADIATION AT WAVELENGTHS OF 355 AND 532 NM 221
A.N. Chumakov, V.V. Lychkousky

THE ROLE OF LASER-INDUCED PLASMA IN A LIQUID FOR THE FORMATION OF NANOSIZED PARTICLES 225
N. Tarasenka, A. Butsen, V. Kornev, A. Radomtsev, N. Tarasenko

CONTROLLING OF MATERIALS ABLATION AND PLASMA FORMATION UNDER BICHROMATIC LASER EXPOSURE IN AIR 229
A.N. Chumakov, V.V. Lychkousky, N.A. Bosak

RADIATION RESISTANCE OF AMORPHOUS ZIRCONIUM ALLOYS AFTER IRRADIATION WITH HELIUM IONS 233
V.V. Uglov, S.V. Zlotski, V.A. Goroshko, A.N. Suchkov

**6. PLASMA DIAGNOSTICS AND MODELING**

ELECTRON PARAMETERS AND ABSOLUTE GLOW INTENSITIES IN A DISCHARGE SUPPORTED BY A HOLLOW CATHODE IN MIXTURES OF HELIUM AND WATER VAPOR 239
S.N. Andreev, A.V. Bernatskiy, I. Draganov, I.V. Kochetov, V.N. Ochkin

SPECIFIC FEATURES OF PROBE MEASUREMENTS OF EEDF NEAR THE ANODE 243
S.N. Andreev, A.V. Bernatskiy, N.A. Dyatko, I.V. Kochetov, V.N. Ochkin

TIME-DEPENDENCE OF THE ELECTRON ENERGY DISTRIBUTION FUNCTION IN THE He-Xe AFTERGLOW 247
G.M. Grigorian, A. V. Demyanov, N.A. Dyatko, I.V. Kochetov

EMISSION OF CHALCOGENS IN THE DIELECTRIC BARRIER DISCHARGE 251
S. Avtaeva, A. Heneral

THE USE OF AB-INITIO GENERATED PSEUDO POTENTIAL FOR COMPUTATION OF OPTICAL PROPERTIES IN DENSE PLASMA IN CUT-OFF COULOMB POTENTIAL, HELIUM CASE 255
N.M. Sakan, Z.J. Simić, V.A. Srećković

PLASMA DENSITY SENSOR ON MICRO- AND NANOSATELLITES 259
A. Galka, A. Kostrov, M. Malyshev, I. Vershinin

AMPLITUDE-TIME DYNAMICS OF RADIATION OF LASEREMISSION PLASMA OF METALS FORMED BY DUAL NANOSECOND PULSES 263
N. Kuryan, S. Anufrik, K. Znosko

MATHEMATICAL MODELING OF PARTICLE FLUX FORMATION PROCESSES IN A REACTIVE ION-PLASMA ETCHING SYSTEM AT LOW PRESSURES 267
A.V. Abramov, E.A. Pankratova

LASER-INDUCED PLASMAS OF DIFFERENT ORGANIC MATRICES 271
N. Sushkov, N. Kurian, S. Zaytsev, N. Lobus, A. Kéri, Á. Bélteki, G. Galbács, T. Labutin

MODELING OF HIGH PRESSURE SHORT-ARC XENON DISCHARGE WITH A THORIATED CATHODE 273
N. Timofeev, V. Sukhomlinov, G. Zissis, I. Mukharaeva, D. Mikhaylov, A. Mustafaev, B. Makhsudov, V. Borodina

COMPARISON OF DOUBLE PULSED REGIMES OF LASER PLASMA EXCITATION IN AIR AND INERT GASES 277
V. Kiris, K. Catsalap, M. Belkov

SIMULATION OF CHARGED PARTICLES MOTION IN THE CATHODE-FALL REGION OF AN ABNORMAL GLOW DISCHARGE IN CROSSED E×H FIELD 281
V. Shekelevski, D. Kotov

CHARACTERISTICS OF A CYLINDRICAL PLASMA ANTENNA SYSTEM AND ITS ANALYSIS 285
A. Astafiev, A. Chirtsov, A. Lesiv, A. Altmark

RADIATION PATTERN OF A SYSTEM CONSISTING OF A SHORT LINEAR ANTENNA AND AN EXTENDED PLASMA JET 289
A. Astafiev, A. Chirtsov, A. Lesiv, A. Altmark

OPTOGALVANIC OSCILLATIONS IN HOLLOW CATHODE LAMP 293
M. S.A. Eldakli, S.S. Ivković and B.M. Obradović

STUDIES OF ANALYTICAL CAPABILITIES OF LASER INDUCED BREAKDOWN SPECTROSCOPY FOR DETERMINATION OF SULFUR CONTENT IN OIL PRODUCTS 297
A. Nevar, M. Nedelko, N. Tarasenko

**7. PLASMA APPLICATIONS AND ADVANCED PLASMA TECHNOLOGIES**

ENERGY DISSIPATION IN ARC DISCHARGE OCCURRING AFTER THE FUSE EXPLOSION 303
A.A. Kozlov, A.V. Shurupov, A.V. Kozlov, V.P. Polishchuk, M.A. Shurupov

PLASMA INDUCED MODIFICATION OF ZnO-BASED PHOTOCATALYSTS DOPED WITH PLASMONIC NANOPARTICLES 307
N.A. Savastenko, A.A. Shcherbovich, A.V. Miadzvetski, V.A. Lyushkevich, I.I. Filatova, S.A. Maskevich

THE EFFECT OF DBD PLASMA ON THE MORPHOLOGY OF Ag NANOPARTICLES USED IN PHOTOCATALYSIS 311
N.A. Savastenko, A.A. Shcherbovich, V.A. Lyushkevich, I.I. Filatova, S.A. Maskevich

ENHANCEMENT OF THE PHOTOCATALITYC EFFICIENCY OF NANOSTRUCTURED MATERIALS VIA PLASMA TREATMENT 315
N.A. Savastenko, A.A. Shcherbovich, V.A. Lyushkevich, I.I. Filatova, S.A. Maskevich

UNIFORMITY OF ION FLUX IN A LASER PLASMA SOURCE FOR DEPOSITION OF NANOFILMS 319
V.K. Goncharov, M.V.Puzyrev, N.I.Shulgan

COMPOSITION AND STRUCTURE OF NANOPARTICLES SYNTHESIZED IN THE PLASMA OF AN ELECTRIC EXPLOSION OF METALS IN DISTILLED WATER 323
K.F. Znosko, V.V. Tarkovsky

PHOTOCATALYTIC AND STRUCTURAL PROPERTIES OF NANOSTRUCTURED TITANIUM DIOXIDE OBTAINED BY HYDROTHERMAL METHOD 327
A.V. Miadzvetski, N.A. Savastenko, S.A. Maskevich, I.I. Filatova, M.T. Gabdullin, T.S. Ramasanov, Kh.A. Abdullin, Zh.K. Kalkozova

DEPOSITION OF TiSiCN NANOCOMPOSITE COATINGS IN HOLLOW CATHODE ARC DISCHARGE WITH ACTIVE ANODE 331
A. Menshakov, Yu. Bruhanova

DEPOSITION OF MICRO- AND NANOCRYSTALLINE DIAMOND COATINGS ON CARBIDE CUTTERS OF SMALL DIAMETER IN MW PLASMA 335
E. Ashkinazi, V. Sedov, M. Shevchenko, D. Vinogradov, E. Matasova, A. Khomich, R. Khmelnitsky, V. Ralchenko

STUDY OF THE EFFECT OF PLASMA MODIFICATION OF A UHMWPE THREAD ON THE PHYSICAL AND MECHANICAL PROPERTIES OF POLYETHYLENE COMPOSITE 339
I.Sh. Abdullin, I.K. Nekrasov, A.V. Kormakov, A.S. Krainov, E.F. Kharchenko

EFFECT OF ION-PLASMA NITRIDING AND ELECTROLYTEPLASMA POLISHING ON THE HARDNESS AND CORROSION RESISTANCE OF HIGH-CHROME STEELS 342
V.S. Kaplenko, S.I. Bahayeu, D.V. Zhuk, I.L. Pobol, I.P. Smyaglikov

EFFECT OF PLASMA ELECTROLYTIC PRETREATMENT ON A ROUGHNESS AND COLORING UNIFORMITY OF THE OXIDE FILMS ON TITANIUM AND ITS ALLOYS 346
S.I. Bahayeu, I.P. Smyaglikov

BEAM-PLASMA REACTORS FOR FUNCTIONAL GRADIENT MATERIALS PRODUCTION 350
T. Vasilieva

HYBRID-TYPE PLASMA CHEMICAL REACTORS: DEVELOPMENTS FOR NATURAL BIOPOLYMERS PROCESSING 354
T. Vasilieva, M. Vasiliev

TEMPERATURE EFFECTS UNDER PROCESSING OF NUCLEAR POWER PLANT CONSTRUCTIONS BY ION-PLASMA DEACTIVATION TECHNOLOGY 358
A. Petrovskaya, A. Kladkov, S. Surov, A. Tsyganov

SEM X-RAY MICROANALYSIS STUDIES OF THE NUCLEAR CONSTRUCTION MODEL SAMPLES PROCESSED BY ION-PLASMA DEACTIVATION TECHNOLOGY 362
A. Petrovskaya, A. Kladkov, S. Surov, A. Tsyganov

STUDY OF PLASMA PARAMETERS IN COPPER/GRAPHENE NANOCOMPOSITE NUCLEATION ZONE IN EROSION PLASMA JETS 366
D.I. Kavyrshin, M.B. Shavelkina, V.F. Chinnov, A.S. Myazin

BEAM-PLASMA SYSTEMS FOR “GREEN” TECHNOLOGIES: MULTIFUNCTIONAL EXPERIMENTAL COMPLEX FOR R&D 370
M. Vasiliev, T. Vasilieva

SPATIALLY RESOLVED LIBS AND XRF FOR ENVIRONMENTAL MONITORING IN AQUATIC ECOSYSTEMS 374
N. Sushkov, N. Kurian, S. Anuchin, S. Zaytsev, T. Labutin

CO-PRECIPITATION FROM SOLUTIONS OF IRON, NICKEL, COBALT NITRATES UNDER THE ACTION OF A GLOW DISCHARGE 378
K.V. Smirnova, P.A. Ivanova, D.A. Shutov, A.N. Ivanov, V.V. Rybkin

MICROPLASMA PROCESSES DURING HIGH-VOLTAGE ELECTRIC PULSE CONSOLIDATION OF REFRACTORY METAL CARBIDES POWDERS 382
E. Grigoryev, O. Kuznechik, A. Chumakov, I. Nikonchuk, E. Strizhakov, S. Nescoromniy, S. Ageev

BEHAVIOR OF SF6 IN THE PLASMA MEDIUM OF AN ELECTRON BEAM 386
S. Sosnovskiy

INVESTIGATION OF THE INTERACTION OF ULTRATHIN $MOS_2$ FILMS WITH H2, O2, AND N2 PLASMA 390
D.E. Melezhenko, D.V. Lopaev, A.I. Zotovich, E.N. Voronina

A REAGENT-FREE METHOD FOR MODIFYING CHITOSAN 394
A. Khlyustova, N. Sirotkin, I. Naumova, V. Titov

PLASMA-LIQUID TREATMENT OF THE SURFACE OF METAL PRODUCTS 398
Al. Gaisin, D.N. Mirkhanov, S.Yu. Petryakov

PLASMA-LIQUID PRODUCTION OF METAL POWDER FOR 3D PRINTING APPLICATIONS 402
Al. Gaisin, R. Kayumov, A. Kuputdinova

RESEARCH OF AIR IONS DISTRIBUTION GENERATED BY DIELECTRIC BARRIER DISCHARGE PLASMA 406
Y.V. Zaparozhchanka, A.V. Aksyuchits, D.A. Kotov, A.N. Osipov

INCREASE THE GLASS SURFACE HYDROPHILICITY BY TREATMENT IN PLASMA AT ATMOSPHERIC PRESSURE 410
D.A. Kotov, A.V. Aksyuchits, Y.V. Zaparozhchanka, K.K. Zheliaznova

INVESTIGATION OF ZIGZAG WIRES LAYOUT IN EXPLODING WIRE ARRAY 414
S. Anishchenko, A. Gurinovich, E. Gurnevich, D. Leonenko, A. Rouba

RESEARCH OF MAGNETIC FIELD AND GAS DISTRIBUTION INFLUENCE ON PLASMA GENERATION AND THIN DIAMOND-LIKE FILM UNIFORMITY 418
N. Leonovich, D. Kotov, P. Tovt, A. Zanko

THERMOSENSITIVE PROPERTIES OF VANADIUM OXIDE FILMS DEPOSITED BY PULSED DC REACTIVE MAGNETRON SPUTTERING 422
A. Zanka, D. Kotov, N. Leonovich, V. Kolos, N. Kovalchuk

PLASMA TREATMENT AND SYNTHESIS OF POWDERS FOR ADDITIVE MANUFACTURING 426
A.Kh.Gilmutdinov, K.Yu.Nagulin, I.V. Tsivilskiy

PLASMOCHEMICAL RECOVERY OF POWDER MATERIALS FOR ADDITIVE MANUFACTURING 430
A.Kh.Gilmutdinov, K.Yu.Nagulin, A.A.Terentiev

ELECTROLYTE-PLASMA POST-TREATMENT OF THE SURFACE OF ADDITIVE MANUFACTURING PRODUCTS 434
A.Kh.Gilmutdinov, K.Yu. Nagulin, A.A.Terentiev

THE ROLE OF MONOLAYERS THICKNESSES RATIO FOR OXIDATION RESISTANCE OF AlN/$SiN_X$ MAGNETRON SPUTTERED COATINGS 438
I.A. Saladukhin, G. Abadias, V.V. Uglov, S.V. Zlotski

PROSPECTS FOR THE USE OF LASERS FOR THE FORMATION OF CONFIGURABLE PLASMA ANTENNAS 442
N.G. Gusein-Zade, S.Y. Kazantsev, S.V. Podlesnikh, A.A. Smolsky, P.A. Titovets

MAGNETRON DEPOSITION OF W-COATINGS WITH IN D-HE MIXTURE 446
M.M. Kharkov, D.V. Kolodko, G.S. Lomonosov, M.S. Kukushkina, A.V. Kaziev

PLASMA CHEMICAL PRODUCTION OF WATER-SOLUBLE CHITOSAN AND TESTING OF ITS BIOLOGICAL ACTIVITY 449
V. Titov, I. Naumova, A. Khlyustova, N. Sirotkin

APPLICATION OF COLD PLASMA AND HIGH FREQUENCY ELECTROMAGNETIC FIELDS FOR TREATMENT OF LONGSTEMMED FLAX SEEDS 453
V.A. Lyushkevich, I.I. Filatova, S.V. Goncharik, N.V. Pushkina, N.M. Leschinskaya

PLASMOCHEMICAL MODIFICATION OF NONWOVEN POLYPROPYLENE MATERIALS TO INCREASE ANTIBACTERIAL AND FILTRATION PROPERTIES 457
K. Avdeeva, A. Mikhalko, N. Dudchik, V. Agabekov, A. Rogachev

PREPARATION AND PARAMETERS ADJUSTING OF NANOPARTICLE SUSPENSIONS FOR A WORKING MEDIUM OF A LASER MICROENGINE 460
V.V. Kiris, A.N. Chumakov, M.I. Nedelko, N.N. Tarasenka, A.A. Nevar, N.V.Tarasenko

PROPERTIES OF BIOGENIC METAL NANOPARTICLES PREPARED BY PLASMA ASSISTED ELECTROCHEMISTRY 464
N. Tarasenka, A. Nevar, V. Kornev, M. Nedelko, N. Tarasenko

PLASMA REACTOR FOR INVESTIGATION OF BIOMASS HIGH TEMPERATURE GASIFICAION 468
A. Liavonchyk, I. Khvedchyn, V. Sauchyn

ATMOSPHERIC PRESSURE PLASMA-ASSISTED FABRICATION OF IRON OXIDE NANOSTRUCTURES 472
A.A. Nevar, M.I. Nedelko, A.O. Radomtsev, E.V. Beletskii, N.V. Tarasenko

THE MECHANISM OF SINGLE-FREQUENCY HIGH POWER MICROWAVE GENERATION BY RELATIVISTIC VIRTUAL CATHODE OSCILLATORS 476
P. Molchanov, A. Rouba

INVESTIGATION OF THE EFFECTIVENESS OF THE INTERACTION OF PLASMA BEAMS WITH A MAGNETIZED TARGET 480
N.V. Batrak, M.V. Kutyrev, N.G. Kopaleishvili

BACTERICIDAL COMPONENTS OF AIR PLASMA JETS DIAGNOSTICS USING ABSORPTION IR AND UV SPECTROSCOPY 484
A.V. Kazak, A.A. Kirillov, L.V. Simonchik, M.M. Kuraica, B.M. Obradovich, G.B. Sretenovich

CONVERSION OF CO2-CH4 MIXTURE IN DIRECT CURRENT NONSELF-SUSTAINED GLOW DISCHARGE AT ATMOSPHERIC PRESSURE 488
A.V. Kazak, A.A. Kirillov, L.V. Simonchik, M.U. Tomkavich

FEATURES OF DIELECTRIC BARRIER DISCHARGE IN MILLIMETER RANGE AIR DISCHARGE GAP 492
V. Parashchuk, V. Lyushkevich, S. Goncharik, I. Filatova

**AUTHOR INDEX** 496

# 1. FUNDAMENTAL PHYSICAL PROCESSES AND PHENOMENA IN PLASMAS

# DYNAMICS OF SINGLE PARTICLES IN A DC GLOW DISCHARGE UNDER THE ACTION OF LASER RADIATION

A.S. Svetlov[1,2], E.A. Kononov[1,2], O.F.Petrov[1,2], M.M.Vasiliev[1,2]

[1]Moscow Institute of Physics and Technology, Institutskiy Pereulok 9, Dolgoprudny 141701, Russia
[2]Joint Institute for High Temperatures of the Russian Academy of Sciences, Izhorskaya 13 Bldg 2, Moscow 125412, Russia

Active Brownian motion is of great interest to physicists. In work [1], the following definition of an active particle is given: “Differently from passive Brownian particles, active particles, also known as self-propelled Brownian particles or micro-swimmers and nano-swimmers, are capable of taking up energy from their environment and converting it into directed motion”.

The results of an experimental study dynamics of a single particles with different types of surface under the action of laser radiation of various powers in a dc glow discharge are presented. The study was conducted on Janus, copper coated and uncoated melamine formaldehyde particles. A single particle was injected into a stratified direct current glow discharge where, as a result of the balance of electric force and gravity, its levitation was observed.

To study dynamics the particles were exposed to laser radiation of various powers. The movement of particles was recorded using a high-speed video camera. As a result of processing the obtained experimental video data, the coordinates were obtained for each moment in time, the kinetic energies were determined at various values of the laser radiation power density, and the graphs of the root-mean-square displacement versus time were plotted.

As a result of the analysis of the graphs of the rms displacement of the particle and the dependence of the kinetic energy on the power density of the laser radiation, it was concluded that a change in the power of the acting laser beam leads to a change in the nature of the motion of a single Janus and coated particles in a dc glow discharge. We have experimentally observed active Brownian motion of a single Janus and copper coated particles, caused by the action of a thermophoretic force [2], at various intensities of laser radiation.

## References

1. **Bechinger C. and Leonardo R.D. and Löwen H. and Reichhardt C. and Volpe Giorgio and Volpe Giovanni.** Active Brownian Particles in Complex and Crowded Environments. Rev Mod Phys. 88, 045006 (2016)

2. **Ebbens S.J. and Howse J.R.** In pursuit of propulsion at the nanoscale, 2010, Soft Matter, №6 p.726–38

# EXPERIMENTAL VERIFICATION OF A NONLOCAL MODEL IN THE DISCHARGE IN CROSSED FIELDS AND THE SHORT DISCHARGE IN HELIUM

A. Platonov, E. Prokhorova, A. Slyshov

Petrozavodsk State University, Lenin Str., 33, 185910, Petrozavodsk, Republic of Karelia, Russia, e-mail: prokhorova@petrsu.ru

The paper the results of a study of a short glow discharge of various configurations (with classical geometry and with coaxial cylindrical electrodes) in helium from the point of view of nonlocal electron kinetics are presented.

A short glow discharge was created in a cylindrical discharge tube. The measurements were carried out at discharge current (5-20) mA and gas pressure (0.1-15) Torr. At pressures less than 0.3 Torr, only negative glow (NG) and Faraday's dark space (FDS) are present in the discharge. A potential well is observed, with a minimum near the cathode and extending to the anode. The electron distribution functions (EDF) in a potential well are Maxwellian (Fig. 1(d)). This is due to the nonlocal character of gas ionization by electrons that have gained their energy in the cathode layer.

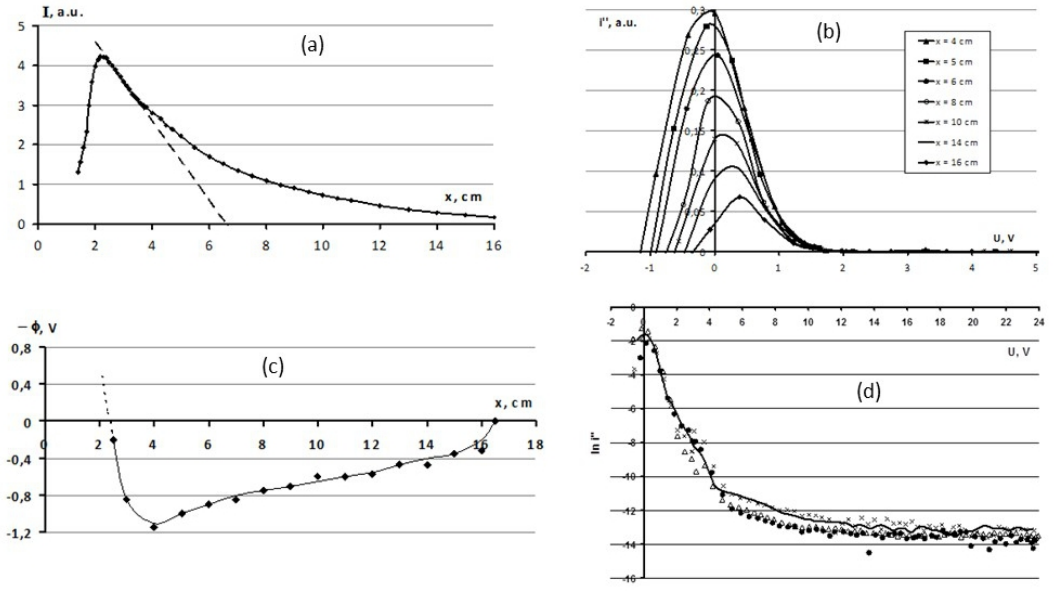



Fig. 1. (a) is the axial distribution of the luminescence intensity, (b) is the second derivatives of the probe current on the discharge axis, (c) is the axial distribution of the space potential, (d) is the logarithm of the second derivative. X is the distance to the cathode.

Depending on the value of the pL parameter, two main scenarios should be expected in glow discharges [1, 2]:

a) At low pressures, when the length of the interelectrode gap is $L < d + \lambda_F$ ($\lambda_F$ is the characteristic scale of the decrease in plasma density in FDS) and the nonlocal ionization is significant throughout the discharge gap, the section of the reverse field with a potential well for electrons extends up to the anode.

In this case, the sign of the anode drop is negative, inhibiting electrons [1]. Most of the electrons are trapped in this well, and the total potential drop is small (~1-2 eV), since it is determined by the relatively low (< 1 eV) temperature of the trapped electrons. The estimation of the position of the characteristic point $x_m$ (the minimum of the potential well) in this case gives $x_m = (L - d)/2$ in wide tubes ($R > L$) and $x_m \approx d + R$ at $R < L$ [1].

б) With an increase in the length of the discharge gap or pressure (parameter pL), the path of fast electrons becomes less than the length of the discharge gap ($L > d + \lambda_F$) and at $\lambda_F < R$, the maximum concentration point is located closer to the boundary of the layer $x_m \approx d + \lambda_F$. Since the plasma concentration decreases rapidly (on the R scale), then further to the anode, the diffusion component of the electron current can no longer provide a condition for maintaining the discharge current density. Therefore, we should expect or 1) the formation of the second field reversal point at $x_2 \approx x_m + R$, after which the direct field is restored in the plasma and the growth of its own ionization by plasma electrons [1]. In this transition region, the electric field is spatially non-uniform and grows to its value in the discharge column (if the length of the interelectrode gap allows); or 2) or a monotone profile of the space potential.

Figures 1(a), 1(c) show axial distributions of discharge parameters in helium at a pressure p = 0.3 Torr and a discharge current I = 5 mA (U = −970 V). Under these conditions, both the energy relaxation lengths $\lambda_\varepsilon$ and the path length of electrons with an energy equal to the cathode incidence are large, so that the case with a single point of the sign of the electric field should be realized. As can be seen from Fig. 1(c), a potential well with a minimum at $x_m \approx 4$ cm and a depth of about 1 eV is observed on the plasma potential profile. This point corresponds to the position of the maximum concentration (Fig. 1(b)). At a distance of less than 2.5 cm near the cathode (in the cathode layer), the voltage relative to the grounded anode varies from – 970 V at the cathode to + 0.2 V at a distance of 2.5 cm from the cathode. The thickness of the cathode layer d, determined by the maximum glow (Fig. 1(a)) is 2.2 cm. This thickness corresponds to the estimate from the potential distribution over the extreme position of the probe, at which a noticeable electric current was recorded. The extrapolation of the glow decay (dotted line in Fig. 1(a)) corresponds to the position of the boundary between NG and FPS at about 6.5 cm from the cathode.

A discharge in crossed electric and magnetic fields was created in a discharge tube with coaxial electrodes. The distance between the electrodes is 25 mm, the length of the electrodes is 90 mm. Discharge current 50 mA, pressure 0.5 Torr, discharge voltage 300 V, magnetic field 15 mTl. A discharge of this type is a discharge in which there is no positive column, and the relaxation length of the electron energy $\lambda_\varepsilon$ exceeds the size of the discharge gap. In this case, there is a region NG in the discharge where the plasma density has a maximum and the direction of the electric field changes [3].

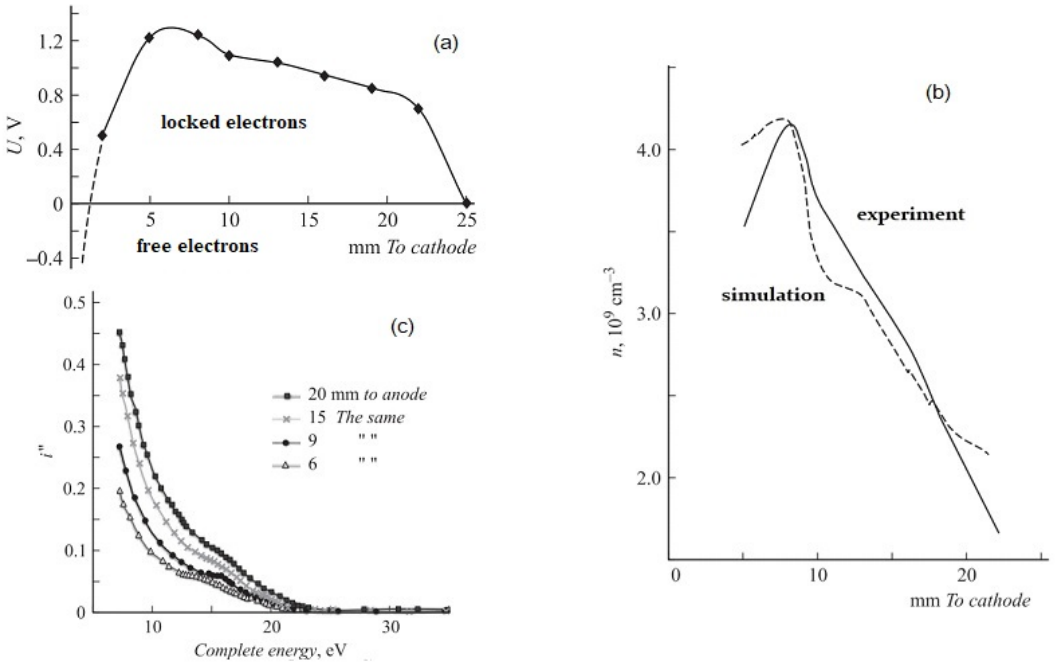



Fig. 2. (a) is the radial distribution of the space potential, (b) is the radial distribution of the electron concentration, (c) is the distribution function of free electrons

A potential well with a depth of 1-1.5 V is observed on the potential profile (Fig. 2(a)). The electric field strength in the center of the discharge gap is very small. This indicates the plasma nature of the discharge in this area. The potential drop in this plasma part of the discharge did not exceed 1-2 V, so that the cathode drop practically coincided with the full voltage on the discharge and was localized in a space of about 1-2 mm. The significant magnitude of the voltage drop in the cathode region allows us to consider the discharge under study as a kind of glow discharge. The concentration of trapped electrons has a maximum near the boundary between NG and FDS. The decrease in the electron concentration in the direction of the anode occurs approximately exponentially. Since the plasma concentration in the plasma part of the NG and in the FDS is

caused mainly by electrons trapped in a potential well, it is described by the Boltzmann equation (Fig. 2(b)).

The features of EDF are an excess of electrons with an energy of about 15 eV and its depletion at energies exceeding 20 eV (Fig. 2(c)). The first is explained by the appearance of electrons during the formation of molecular ions when two metastable atoms collide. The second is formed due to the excitation of the lower levels of helium atoms. Both of these processes occur with the participation of metastable helium atoms He($2^3$S). The processes of conversion from atoms in the ($2^1$S) state and direct excitation of neutral helium atoms by an electron shock lead to the appearance of helium atoms in the ($2^3$S) state.

For both types of discharges, it is established that all electrons can be divided into three groups. The first of them includes fast electrons, which have kinetic energies much higher than the first excitation potential (19.8 eV for helium). These electrons are emitted by the cathode or are born in the cathode drop region. They are responsible for ionization and excitation processes, as well as for the electron current in the layer and the adjacent plasma region. The electron density in plasma is mainly determined by locked electrons, which do not contribute to the current. The electron current in the NG part and in the FDS is determined by free electrons, with energies less than the first excitation potential. Since the cathode potential drop, which determines the energy of fast electrons born at the cathode or in the bulk charge layer, is much higher than the first excitation potential (which is the energy scale for intermediate electrons), and it, in turn, is much higher than the room temperature, then this separation of electrons into three groups is sufficiently clear.

## References

1. **Kudryavcev A.A., Smirnov A.S., Tsendin L.D.** Fizika tleyushego razryada [rus]. SPb: Lan' (2010).
2. **Kudryavcev A.A., Nisimov S.U., Prokhorova E.I., Slyshov A.G.** Technical Physics Letters, 37, 9 (2011) 838–841.
3. **Platonov A.A., Slyshov A.G., Tsendin L.D., Wagner S.D.** Technical Physics, 51, 7 (2006) 841-845.

# MICRODYNAMICS AND THERMODYNAMICS OF NONLINEAR WAVES IN DUSTY PLASMA

F.M. Trukhachev [1,2,3], M.M. Vasiliev[1,2], O.F. Petrov[1,2]

[1]Joint Institute for High Temperatures, Russian Academy of Sciences, Izhorskaya str.13/2, Moscow, 125412, Russia
[2]Moscow Institute of Physics and Technology, Dolgoprudnyi, Moscow region, 141701, Russia
[3] Belarusian-Russian University, Mira Ave, 43, 212000, Mogilev, Belarus.

Properties of the dust-acoustic waves are analyzed on the basis of hydrodynamic model as well as single-particle approximation. Significant differences between dissipative and conservative cases are discussed. The heat dissipation processes that determine the entropy production of are studied.

The concept of dissipative structure is a new field in the physics of nonlinear waves [1]. For example, *dissipative solitons* are considered to be strongly nonlinear wave existing in thermodynamically open systems [1],[2]. The "*dissipative soliton*" concept continues the "classical soliton" concept to non-conservative environment. On the other hand, the wave processes in plasma is one of the forms of self-organization processes [1]. Research of dissipative solitons is connected with researches in such areas as nonlinear optics, laser physics, biology, etc. [3],[4]-[8]. It is important to note, that plasma dissipative soliton physics is a relatively young field of science. Some theoretical models of the plasma dissipative solitons are presented in [9]-[13] (for ion-, electron-, dust-acoustic waves) and [14],[15] (for Langmuir waves). It is important to note, that there are no an acoustic models [9]-[13] considers the nonlinear plasma waves in terms of self-organization phenomena because of a absence of the forces compensating for dissipative forces. We note that the known experimental works [16],[17] contain a description of only dissipative solitons with artificial excitation. However, it should be expected that in the presence of energy sources in the cloak, waves of different nature should be excited [18], including solitons [19]-[23].

A suitable environment for studying the properties of dissipative solitons is dusty plasma and dust-acoustic instability. Indeed, the frequencies of dust-acoustic waves lie in a favorable range of 1–100 Hz [18]. On the other hand, the dynamics of dust particles can be studied using relatively inexpensive equipment. Finally, dusty discharge plasma can be considered a dynamically open system. Dissipation is associated with collisions and charge exchange, and electric fields and currents can be considered as energy pumping.

In this wake, the thermodynamic and microdynamic properties of the nonlinear dust-acoustic waves are analyzed. The influence of dissipative processes on the properties of dust-acoustic waves is discussed. The production of heat by waves moving through the plasma is estimated.

## References


[1] N. Akhmediev and A. Ankiewicz *Dissipative solitons. Lecture Notes in Physics* (Springer, Berlin, Heidelberg, 2005).
[2] N. Akhmediev, A. Ankiewicz, J-M. Soto-Crespo and P. Grelu, International Journal of Bifurcation and Chaos, **19**, 2621 (2009).
[3] M.C. Cross and P.C. Hohenberg, Rev. Mod. Phys. 65, 851 (1993).
[4] S. K. Turitsyn, N. N. Rosanov, I. A. Yarutkina, A. E. Bednyakova, S. V. Fedorov, O. V. Shtyrina, M. P. Fedoruk, Phys.-Usp. **59**, 642 (2016).
[5] V. Skarka, D. V. Timotijević, N. B. Aleksić, J. Opt. A: Pure Appl. Opt. **10**, 075102, (2008).
[6] D. Mao, B. Q. Jiang, W. D. Zhang, J. L. Zhao, Laser Phys. **24**, 105103 (2014).
[7] S. Lin, J. Yu, W. Li, Laser Phys. **29**, 025106, (2019).
[8] S. Y. Choi, H. Jeong, B. H. Hong, F. Rotermund, Dong-II Yeom, Laser Phys. Lett. **11**, 015101, (2014).
[9] S. Ghosh, A. Adak and M. Khan, Phys. Plasmas **21**, 012303 (2014).
[10] S. Khan, A. Rahman, F. Hadi, A. Zeb and M.Z. Khan, Contributions to Plasma Physics **57,** 223 (2017).-
[11] E.K. El-Shewy and A.A. El-Rahman, Phys. Scr. **93**, 115202 (2018).
[12] M. Farooq, A. Mushtaq and J. Qasim, Contrib. Plasma Phys. (published online). (2018) https://doi.org/10.1002/ctpp.201800055.
[13] S.A. Shan, Astrophys. Space Sci. **364**, 36 (2019).
[14] N.R. Pereira and L. Stenflo, Phys. Fluids. **20**, 1733 (1977).
[15] S. Sultana, R. Schlickeiser, I.S. Elkamash and I. Kourakis, Phys. Rev. E **98**, 033207 (2018).
[16] R. Heidemann, S. Zhdanov, R. Sütterlin, H.M. Thomas and G.E. Morfill, Phys. Rev. Lett. **102**, 135002 (2009).
[17] D. Samsonov, A. V. Ivlev, R. A. Quinn, G. Morfill and S. Zhdanov, Phys. Rev. Lett. **88**, 095004 (2002).
[18] P.K Shukla and A.A Mamun, *Introduction to Dusty Plasma Physics* (Institute of Physics Publishing, Bristol, UK, 2002).
[19] R.V. Reddy and G.S. Lakhina, Planet. Space Sci. 39, 1343 (1991).
[20] S. Bounds, R.F. Pfaff, S.F. Knowlton, F.S. Mozer, M.A. Temerin and C.A. Kletzing, J. Geophys. Res. 104, 28709 (1999).
[21] R. Trines, R. Bingham, M.W. Dunlop, A. Vaivads, J.A. Davies, J.T. Mendonça, L.O. Silva and P.K. Shukla, Phys. Rev. Lett. **99**, 205006 (2007).
[22] J. Shi, M. N.S. Qureshi, K. Torkar, M. Dunlop, Zh. Liu and T.L. Zhang, Ann. Geophys. **26**, 1431 (2008).
[23] F.M. Trukhachev, M. M. Vasiliev, O. F. Petrov and E.V. Vasilieva, Phys. Rev. E **100**, 063202 (2019).

# ETCHING KINETICS OF QUARTZ IN A MICROWAVE HYDROGEN PLASMA

V. Yurov[1], V. Ralchenko[1], D. Sovyk[1], A. Altakhov[1], A. Bolshakov[1], I. Fedorova[1], E. Zavedeev[1], F. Popovich[1,2]

[1] Prokhorov General Physics Institute of the Russian Academy of Sciences; Vavilov str. 38, Moscow 119991, Russia; altakhov@gmail.com
[2] Institute of Radio Engineering and Electronics of the Russian Academy of Sciences; pl. Vvedenskogo 1, Fryazino 141190, Russia

Silicon dioxide reacts with hydrogen and hydrogen-oxygen plasma in many processes [1]. However, etching kinetics of these molecular systems at relatively high temperatures (>500$^{o}$C) are still not thoroughly investigated. We have investigated etching of quartz in microwave plasma (MW) in pure hydrogen and in a mixture of hydrogen with the addition of oxygen (0.9% vol.) within the temperature range of 950-1200$^{o}$C. We used MW chemical vapor deposition system "Ardis" operated at 2.45 GHz. The absorbed MW power density we kept constant and the gas pressure we varied in range of 30-60 Torr. Etching rates of silica plates transparent in the UV range (KU-1 in Russia which is the analog of the quartz glass brand HPFS 7980 "Corning") we measured *in situ* using a home-made low-coherence interferometer and the samples temperature we measured by a "SensorTherm M322" pyrometer. Activation energy of silicon dioxide reduction (1) and oxidation (2) reactions was calculated.

$$SiO_2(s) + 4H_2(g) = SiH_4(g) + 2H_2O(g) \quad (1)$$
$$SiH_4(g) + O_2(g) = SiO_2(s) + 2H_2(g) \quad (2)$$

We investigated the presence of respective radicals (OH, $SiH_x$) and atoms (H, Si, O) in the gas phase by means of optical emission spectroscopy in the near-UV and the visible ranges. The silica roughness $R_a$ was controlled using optical profilometer "NewView 5000" (ZYGO).

**Acknowledgements**. This work was supported by the Russian Science Foundation, grant No. 21-12-00403.

## References

1. **Yurov V.Yu., Bolshakov A.P., Altakhov A.S. et al.** Vacuum, 199 (2022) 110939.

# STUDY OF SELF-ORGANIZATION OF NEAR-ELECTRODE CURRENT STRUCTURES IN ATMOSPHERIC PRESSURE GLOW DISCHARGES IN HELIUM

I. Rafatov[1], G. Islamov[1], C. Yesil[1]

[1]METU, Department of Physics, Dumlupinar Blv. 1, 06800 Çankaya, Ankara, TÜRKİYE
rafatov@metu.edu.tr

The work deals with the study of current structures emerging in near-electrode regions of direct current glow discharges at atmospheric pressure in helium. Although these structures are interesting in themselves as fundamental physical phenomena, they can affect the stability of discharges, leading to fluctuations in their parameters. The aim is a comprehensive numerical study of the self-organization of these structures and the mechanisms of their formation.

## 1. Gas discharge model

The equations of the gas discharge model include the particle balance equations for the plasma species

$$\frac{\partial n_k}{\partial t} + \nabla \cdot \mathbf{\Gamma}_k = S_k, \tag{1}$$

where the particle flux densities are defined by the drift-diffusion approximation

$$\mathbf{\Gamma}_k = sgn(q_k)\mu_k n_k \mathbf{E} - D_k \nabla n_k, \tag{2}$$

and Poisson equation for the electrostatic field

$$\epsilon_0 \nabla \cdot \mathbf{E} = \sum_k q_k n_k, \qquad \mathbf{E} = -\nabla \varphi. \tag{3}$$

In these equations, $n$ and $q$ indicate the particle number density and charge, $\varphi$ and $\mathbf{E}$ stand for the electric potential and field, $\mu$ and $D$ are the mobility and diffusion coefficients, $S$ represents the rate of production and destruction of particles, and subscript $k$ denotes the sort of species.

The model also includes the electron energy equation

$$\frac{\partial n_\varepsilon}{\partial t} + \nabla \cdot \mathbf{\Gamma}_\varepsilon = -e\mathbf{\Gamma}_e \cdot \mathbf{E} - \frac{3}{2}\frac{m_e}{m_g}\nu_{ea} n_e k_B (T_e - T_g) - \sum_j \Delta E_j R_j, \tag{4}$$

where $n_\varepsilon = n_e \bar{\varepsilon}$ is the electron energy density, $\bar{\varepsilon} = \frac{3}{2} k_B T_e$ is the mean electron energy, and $\mathbf{\Gamma}_\varepsilon$ is the electron energy flux density,

$$\mathbf{\Gamma}_\varepsilon = -D_\varepsilon \nabla n_\varepsilon - \mu_\varepsilon \mathbf{E} n_\varepsilon. \quad (5)$$

The electron energy transport coefficients are related to the electron transport coefficients via $D_\varepsilon = 5/3 D_e$ and $\mu_\varepsilon = 5/3 \mu_e$. In the electron energy equation, $\nu_{ea}$ is the electron-atomic elastic collision frequency, $R_j$ denotes the reaction rate of the $j$th reaction, $\Delta E_j$ is the corresponding energy loss (or gain), $m$ and $T$ stand for the particle mass and the kinetic temperature, respectively.

The source terms in continuity equation (1) are determined by plasma-chemical reactions occurring in the bulk of the discharge,

$$S_k = \sum_i R_i - \sum_j R'_j, \quad (6)$$

where $R_i$ and $R'_j$ represent the creation and destruction rates in $i$ th and $j$ th reactions.

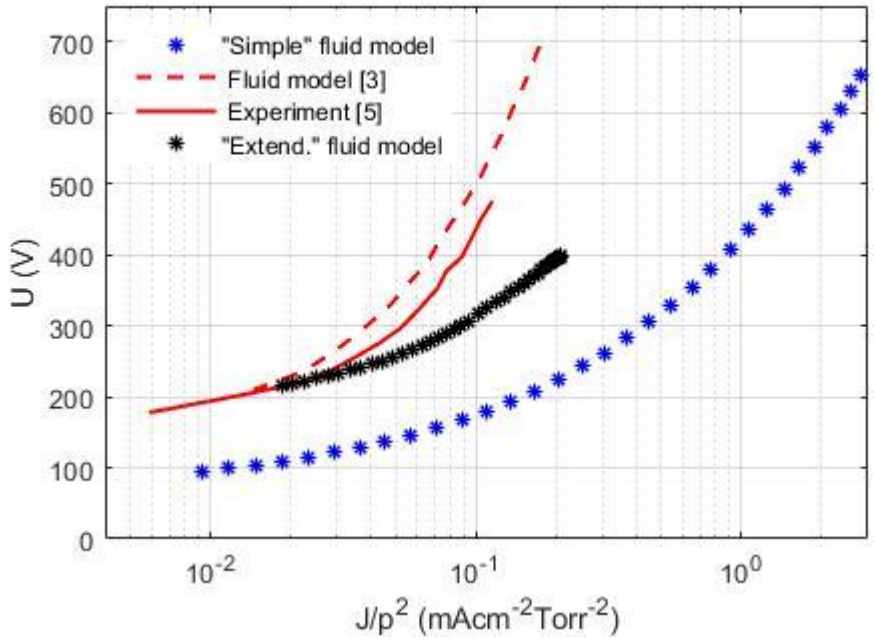



Fig. 1. Current-voltage characteristics of the discharge in helium. $p = 1$ torr, $d = 3$ cm.

The models is completed by definition of the transport coefficients for heavy particles and the boundary conditions. Calculations are carried out for the dc gas discharge in Helium. Six species, namely, electrons, $He^+$ and $He_2^+$ ions, excited $He(2^3S)$ atoms and $He_2(a^3\Sigma_u^+)$ molecules, and $He$ atoms in ground state are taken into consideration.

This model is referred to as "extended" fluid model in the following. Within

this model, electron transport (mobility and diffusion) coefficients as well as the rates of the electron induced reaction are determined as functions of the mean electron energy, from the solution of the corresponding electron Boltzmann equation [1]. In the present calculations, we assumed Maxwellian eedf.

## 2. "Simple" fluid model

Within the "simple" fluid model (see, e.g., Ref. [3]), only two plasma components, namely, electrons and $He^+$ ions, are taken into consideration. The mobility and diffusion coefficients follow the Einstein relation $D/\mu = k_B T/e$. Townsend formula is used to determine the ionization rate, calculated as a function of the reduced electric field, $\alpha = A\,p\,exp(-Bp/|E|)$, where $p$ is the background gas pressure [4].

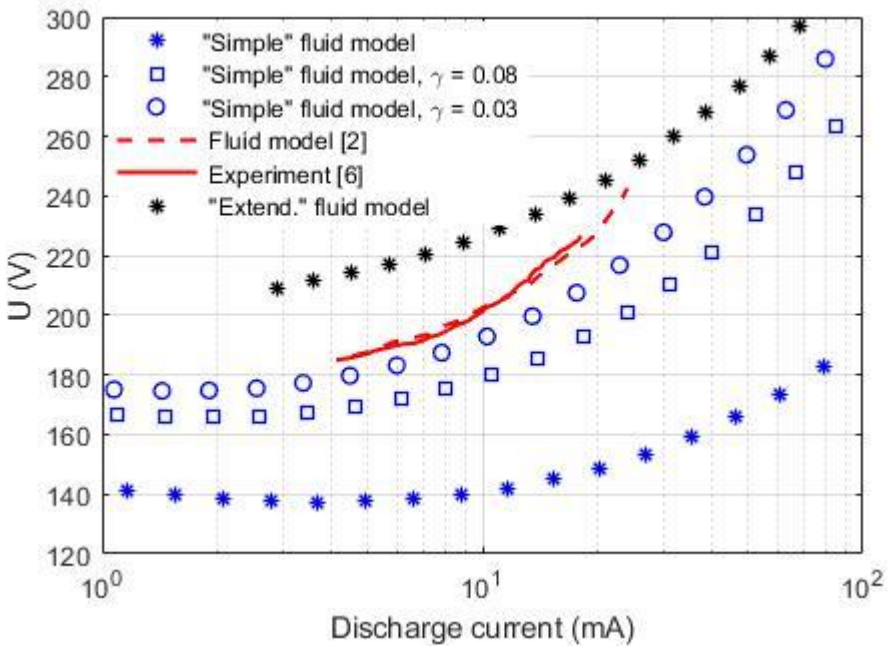



Fig. 2. Current-voltage characteristics of the discharge in helium. $p = 760$ torr, $d = 200$ $\mu$m.

## 3. Verification of the model

Computation of CVCs is carried out for the discharge in Helium at low and high (atmospheric) pressures. At low pressure, the parameter regime from [3, 5] is taken as reference. The input parameters are pressure $p = 1$ torr, discharge gap $d =$

3 cm, the secondary emission coefficient $\gamma = 0.16$. At atmospheric pressure, the parameter regime of experimental [6] and numerical [2] studies is used. In this case, pressure $p = 760$ torr, the discharge gap width $d = 200$ $\mu$m, $\gamma = 0.1$. In both cases, the equation for gas temperature is not taken into account, thereby, the ion temperature is defined to be equal to the background gas temperature, $T_i = T_g = 0.025$ eV.

The results (see figure 1) demonstrate that CVCs computed from the present "extended" fluid model and from [3] are in better agreement with the experimental data [5] compared to the "simple" fluid model. Note that the current density from the "simple" fluid model for any value of voltage is about ten times higher than the realistic value of the current, and, therefore, the "simple" fluid model cannot adequately describe the discharge properties at low pressures. The performance of the present “extended” fluid model can be improved if, instead of the Maxwellian eedf, the realistic eedf computed from the corresponding electron Boltzmann equation is used for the electron kinetic coefficients.

Figure 2 shows that CVC derived from "extended" fluid model again leads to a better agreement with the experiment [2, 6]. As can be observed from this figure, the secondary electron emission coefficient $\gamma$ can be used as a fitting parameter [3]. The present "extended" fluid model can be significantly improved by taking into account gas heating.

**Acknowledgements.** This work was supported by research Grant No 221N363 from the Scientific and Technical Research Council of Turkey (TUBITAK).

## References

1. **Hagelaar, G. J. M., and Pitchford, L. C.** Plasma sources science and technology, 14, (2005) 722.
2. **Wang, Q., Ning, W., Dai, D., Zhang, Y., and Ouyang, J.** Journal of Physics D: Applied Physics, 52, (2019) 205201.
3. **Donkó, Z., Hartmann, P., and Kutasi, K.** Plasma Sources Science and Technology, 15, (2006) 178.
4. **Raizer, Y. P.** Gas discharge physics (Vol. 1, p. 52). Berlin: Springer (1991).
5. **Hartmann, P., Kutasi, K., and Donkó, Z.** Proc. 27th ICPIG (Eindhoven, The Netherlands, 17–22 July 2005).
6. **Wang, Q., Koleva, I., Donnelly, V. M., and Economou, D. J.** Journal of Physics D: Applied Physics, 38 (2005) 1690.

# CONTROLLING OF CHARACTERISTICS OF A PLASMA ASYMMETRIC DIPOLE ANTENNA

N. Bogachev[1], M. Usachonak[2], S. Andreev[1]

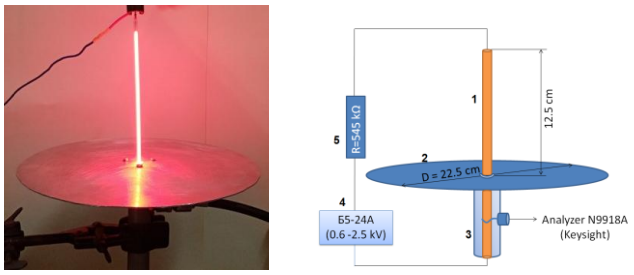
[1]Prokhorov General Physics Institute of the Russian Academy of Sciences, 119991, 38 Vavilova street, Moscow, Russia, bgniknik@yandex.ru
[2] B.I. Stepanov Institute of Physics of the National Academy of Sciences of Belarus, 220072, 68-2 Nezavisimosti avenue, Minsk, Republic of Belarus

Plasma asymmetric dipole antenna (PADA) from a gas discharge tube is one of the most frequently studied types of plasma antennas. The characteristics of plasma asymmetric dipole antennas and their functionality are determined by the PADA tubes used (type of gas or gas mixture, pressure, etc.), the method of plasma creating (RF or microwave discharge, low frequency discharge, direct current), the method of supplying an information signal (directly from a coaxial cable, through a coaxial resonator, capacitive or inductive applicator) [1-6]. A distinctive feature of plasma antennas is the possibility of electrical adjustment of its parameters [7], and as shown in [8, 9], low and atmospheric pressure plasma can act as an effective control element of high-speed microwave devices operating at high microwave power levels. Thus, the purpose of this work was to reveal the dependence of the plasma antenna matching on the electron density in the plasma.

In the work, a plasma asymmetric dipole antenna was studied. The photo and diagram of antenna are shown in Fig. 1. The antenna under study consisted of a gas-discharge lamp GSh-5 *(1),* a metal disk *(2)* and a coaxial resonator *(3)* with a coaxial connector for inputting microwave radiation, used to feed the signal to the antenna (see Fig. 1). The GSh-5 lamp *(1)* is a quartz tube with an outer diameter of 3.8 mm and an inner diameter of 3 mm, filled with neon at a pressure of ~70 Torr. The metal disc is made of a sheet of duralumin 2 mm thick, has a diameter of 22.5 cm and a central hole a diameter of 6 mm.for placing the lamp with. The GSh-5 lamp was connected to the B5-24A *(4)* power source through the ballast resistance R = 545 ohm *(5)* . By changing the voltage not B5-24A in the range from 0 to 2.5 kV, the discharge current was changed from 0 to 5 mA. The length of the plasma column protruding above the surface of the metal screen *(2)* was 12.5 cm and did not change during the experiment.

The measurement of the VSWR of the created plasma asymmetric dipole antenna was carried out using a portable analyzer N9918A (Keysight Technologies) in the frequency range of 1–3 GHz (averaging over 8 measurements) for various electron densities in the plasma column. The output power level of the microwave radiation of the analyzer was -15 dBm. Previously, the analyzer with the coaxial cable necessary for connecting the antenna was calibrated using a set of calibration standards NKMM-11 " Micran ". Density $n_e$ and collision frequency $\nu$ of electrons in

the plasma column were determined by the resonator method using a 10 cm microwave resonator previously calibrated with dielectric rods of known permittivity (see Table I ). The obtained values are in agreement with the estimates of the electron density for the discharge in this lamp at tens of milliamps presented in [7].

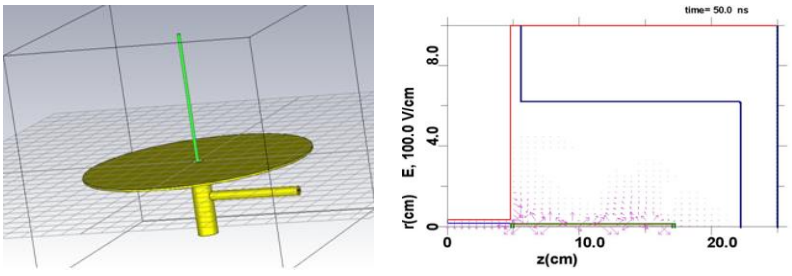



*a)* *b)*

Fig. 1. Plasma asymmetric dipole antenna: photo (a) and diagram of the experimental stand (b).

Table 1. Plasma parameters in the gas discharge tube GSh-5.

| **No.** | **Experimental data** | | |
|---|---|---|---|
| | ***I*, *mA*** | ***ν*, $\times 10^{10}$ $s^{-1}$** | **$\langle n_e \rangle$, $\times 10^{10}$ $cm^{-3}$** |
| 1 | 0.5 | 5.7 | 7.0 |
| 2 | 1 | 7.8 | 12.5 |
| 3 | 2 | 8.5 | 26.0 |
| 4 | 3 | 10.9 | 30.3 |
| 5 | 4 | 15.5 | 418.4 |
| 6 | 5 | 17.0 | 558.4 |

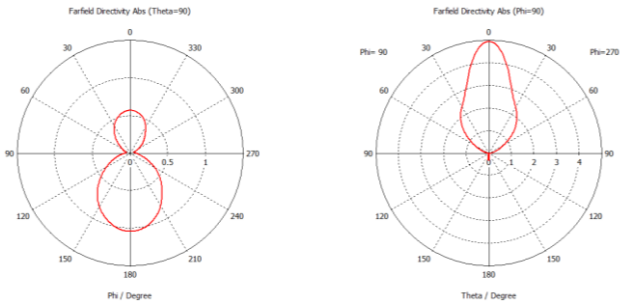



*a)* *b)*

Fig. 2. Images of numerical models of the plasma antenna in Comsol Multiphysics (a) and KARAT code (b).

Numerical simulation was carried out using the Comsol Multiphysics program and the KARAT code. Images of the constructed models are shown in Fig. 2. In

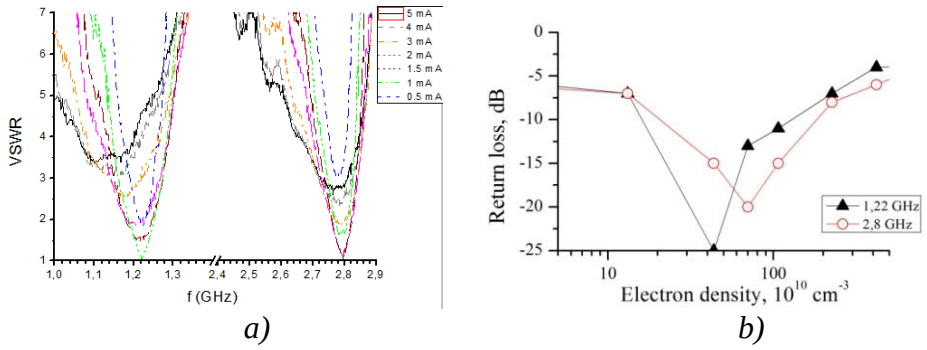
Comsol Multiphysics, a 3D model of the antenna with a coaxial resonator was made (Fig. 2 (a)) and the radiation patterns for the antenna were obtained (Fig. 3). In the KARAT code, a 2.5D axisymmetric model was built with PIC plasma (Fig. 2(b)) to calculate the current distribution and particle density inside the discharge tube.




*a)* *b)*

Fig. 3. Numerical simulation result: radiation pattern of the plasma asymmetric dipole antenna for plasma density 5.58 $\cdot 10^{12}$ $cm^{-3}$ in E-plane (a) and H-plane (b)

The results of measurements of the VSWR of the created plasma asymmetric dipole antenna are shown in Fig 4 (a). In the absence of a plasma column in the GSh-5 lamp, the VSWR of the created antenna in the entire studied frequency range was more than 5. The presence of plasma creates conditions for the formation of antenna radiation. As can be seen, this antenna has two frequency ranges in which the VSWR can be brought to an acceptable level by changing the electron density in the plasma column. For the 1.19-1.25 -GHz band, the best VSWR of 1.01 is achieved at 1.22 GHz with a discharge current of 1 mA, and for the 2.75-2.82 GHz band, the VSWR reaches 1.05 at 2.8 GHz with discharge current 1.5 mA. It should be noted that at the indicated discharge currents, the volume-averaged electron density exceeds the critical density for the minimum frequency of the studied frequency range ($n_c$ = 1.24 $\cdot 10^{10}$ $cm^{-3}$ for 1 GHz) by more than an order of magnitude.




*a)* *b)*

Fig. 4. Experimental results of plasma antenna studies: the VSWR with a change in the discharge current (a) and the dependence of the return loss of the on the electron density (b).

For often 1.22 and 2.80 GHz, the dependence of the return loss during antenna radiation (S11) on the plasma concentration in the GSh-5 tube was studied (Fig. 4,

(b)). The minimum return loss levels for 1.22 and 2.8 GHz were -25 dB and 20 dB, respectively (see Fig. 4, (b)). Without the presence of plasma, the corresponding levels were 2 dB and -3 dB. When the output power of the microwave radiation of the analyzer changed from -45 dBm to 3 dBm , no change in the VSWR of this antenna was detected with a discharge current of the GSh-5 lamp of 1.5 mA.

Thus, at a collision frequency of $\sim 8 \cdot 10^{10}$ s $^{-1}$ and an average electron density of $\sim 5 \cdot 10^{11}$ cm $^{-3}$ in the plasma column, this plasma antenna can be used as a dual-band antenna with the possibility of electrical switching between radiation ranges due to a change in density electrons in the plasma part of the antenna is only 1.5 times.

It should be noted that the resonances in the frequency ranges are quite narrow, which is associated with the small diameter of the gas discharge tube and, as a consequence, the small diameter of the dipole.

As a result of determining the VSWR of the created antenna, the dependence of the VSWR on the electron density in the plasma column of the antenna was revealed, and it was shown that the best VSWR values of 1.01 and 1.05 are achieved for frequencies of 1.22 and 2.8 GHz at a discharge current of 1.0 and 1.5 mA, respectively. The return loss level is -25 dB and 20 dB. Thus, at a collision frequency of $\sim 8 \cdot 10^{10}$ s $^{-1}$ and an average electron density of $\sim 5 \cdot 10^{11}$ cm $^{-3}$ in the plasma column, this plasma antenna can be used as a dual-band antenna with the possibility of electrical switching between radiation ranges by changing the density electrons in the plasma part of the antenna is only 1.5 times.

**Acknowledgements**.

The study was financially supported by RFBR grants No. 20-58-04019 and BRFFR grants No. T21RM-120.

## References

1. **Chung M. et al.** TENCON 2007-2007 IEEE Region 10 Conference, (2007) 1-4.
2. **Bonde S., Ghiye V., Dhande A.** 4-th ICCSNT, (2014) 16-19.
3. **Zali H.M. et al.** 2012 International Symposium on Telecommunication Technologies, (2012), 52-55.
4. **Halili N.A. et al.** 2012 International Symposium on Telecommunication Technologies, (2012), 56-59.
5. **Kumar R., Bora D.** Plasma Science and Technology, 12 (2010), 592.
6. **Zhao J**. et al. AIP Advances, 5 (2015), 127114.
7. **Bogachev N.N., Gusein-Zade N.G., Nefedov V.I.** Plasma Physics Reports, 45(2019), 372-375.
8. **Babitski V.S. et al**. Journal of Applied Physics, 122 (2017), 083302.
9. **Babitski V.S. et al.** Journal of Physics: Conference Series, 1393 (2019), 012072.

# 2. ELECTRICAL DISCHARGES AND OTHER PLASMA SOURCES, NOVEL PLASMA GENERATION APPROACHES

# ON THE STABILITY OF DIFFUSE ATTACHMENT ON THE HOT CATHODE OF VACUUM ARC

Polishchuk V.P., Usmanov R.A., Melnikov A.D., Yartsev I.M.

Joint Institute for High Temperatures of the Russian Academy of Sciences
125412, Izhorskaya 13 Bd. 2, Moscow, Russia, usmanov.r@ihed.ras.ru

Vacuum arcs (VA) are interesting for a number of applications, since they generate high-speed plasma flows of the electrode material. On cold cathodes, the current attachment of the VA has the form of moving microspots (MS), from which an intense ejection of microparticles occurs. Such particles in principle impedes usage of plasma jets in technology. At a sufficiently high temperature of the cathode a stationary diffuse cathode attachment (DCA) of the arc current can exist on it, which is characterized by the absence of microparticles and chaotic voltage pulsations [1, 2]. To date, a discharge with DCA has been obtained on a number of metal cathodes (Cr, Gd, Pb, etc. [2]). Plasma mass separation of spent nuclear fuel [3] requires a discharge with DCA on uranium dioxide. We are testing the elements of this technology on a model substance - cerium dioxide ($CeO_2$), which properties, as a cathode material, is close to $UO_2$. The purpose of this work is to identify the conditions under which the arc mode with the DCA goes into the mode with the MS.

The experiments were carried out in a vacuum chamber at a pressure of less than 10 mPa. A $CeO_2$ cylindrical pellet of 13 mm in diameter and 10 mm high was placed in a heat-insulated molybdenum crucible with an inner diameter of 19 mm. An electron-beam heater (EBH) with a power of up to 1.5 kW was installed under the crucible, which made it possible to change the temperature of the crucible at a fixed VA current. The anode was a molybdenum foil disk of 0.5 mm thick, located at a distance of 30 mm from the cathode. A hole 15 mm in diameter was made in the center of the anode.

The diagnostic system included measurement of the VA current $I$ and the discharge voltage $V_a$, EBH power and the crucible side surface temperature $T_c$. The difference between the temperature $T_c$ that was measured by the pyrometer and the average temperature of the $CeO_2$ surface did not exceed 3%. The discharge was filmed simultaneously by two video cameras — laterally and from above through the hole in the anode. In previous experiments the energy of ions and the ion composition of the plasma jet flowing through the hole in the anode were measured. $Ce^+$, $Ce^{++}$, $CeO^+$, and $Mo^+$ ions were found in the jet; their typical energy was ~10 eV.

The discharge was initiated after application of voltage pulse from a rectifier (~0.4 kV) between the anode and the cathode heated by the EBH. Despite the fact that $CeO_2$ is a dielectric at temperatures up to 0.5 kK, after

heating close to ~2 kK its electrical conductivity increases [4] and the cathode become able to conduct the arc current. During the burning of the arc and $CeO_2$ evaporation the material condensed on the walls of the crucible outlet. Also, an intense condensation of vapor was observed on the anode surface.

The experiment discussed below was carried out at arc currents $I$=40–90 A and temperature $T_c$= 2.1–2.45 kK. The discharge was ignited at a temperature $T_c$=2.26 kK, when the thermionic emission current density $J_{em}$ is ~8 A/cm$^2$, and the density of saturated vapor of $CeO_2$ is $4\times10^{15}$ cm$^{-3}$. At such a vapor density, the maximum density of the ion current on the cathode [2] is approximately half that of $J_{em}$. The physical properties of $CeO_2$ are taken from the reference [4].

During VA burning, regimes with current contraction at both electrodes could exist. Such regimes usually were observed with a decrease in the cathode temperature at a fixed current (a decrease in the EBH power) or a stepwise increase of current.

The current contraction at the anode had the form of a stationary attachment of ~1 cm in size. In this case, chaotic pulsations of the voltage $V_a$ with a relative amplitude of ~5% were observed. This contraction was more pronounced in comparison with the discharge on metal cathodes. Apparently, this happened due to the deposition of an oxide film on the anode surface, which has limited electric conductivity.

The current contraction at the cathode was expressed in the appearance of moving MS. First, they appeared at the moment of arc initiation on the lateral surface of the $CeO_2$ pellet, then they moved to oxide condensate near the crucible outlet. Up to five MS of 0.1–0.3 mm in size could exist simultaneously, and the speed of their movement could reach ~5 cm/s. MS were observed for ~3 s, during this time, the voltage $V_a$ decreased from 27 to 15 V ($I$= 64 A).

For the next ~$10^2$ s, the discharge existed in the gap between the crucible wall and the comparatively cold $CeO_2$ pellet. The transverse size of the pellet decreased with the rate of ~$10^{-2}$ mm/s. For ~30 s, current contraction was observed at the anode, when the voltage $V_a$ reached ~25 V. The extinction of contraction was accompanied by a sharp decrease in voltage to ~11 V. In this experiment the contraction on the anode was yet observed in four modes when the current and arc voltage ranged respectively from 54 to 90 A and 11 to 13 V.

The significant decrease in the arc voltage caused the reduction in the crucible temperature from 2.33 to 2.31 kK. In ~50 s after extinction of the contraction on the anode, MS appeared on the cathode (Fig. 1). The transition to this mode was accompanied by a decrease in the voltage $V_a$ by ~10%. Chaotic voltage pulsations were absent in this case. Several MS could form oval or drawn structures ~1 mm in size. Their movement speed was noticeably lower (~1 cm/s), and the “lifetime” (0.3-0.5 s) was noticeably longer than that of the MS appeared at the moment of VA initiation. MS existed for ~150 s; after

increasing the temperature $T_c$ to 2.39 kK, they disappeared. Ragged edges on the crucible outlet in Fig. 1 are the condensate of $CeO_2$

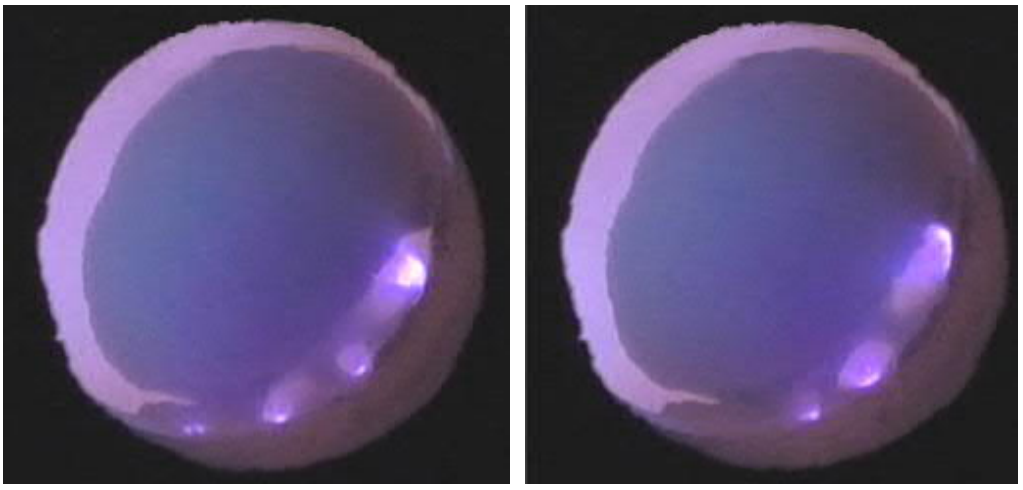
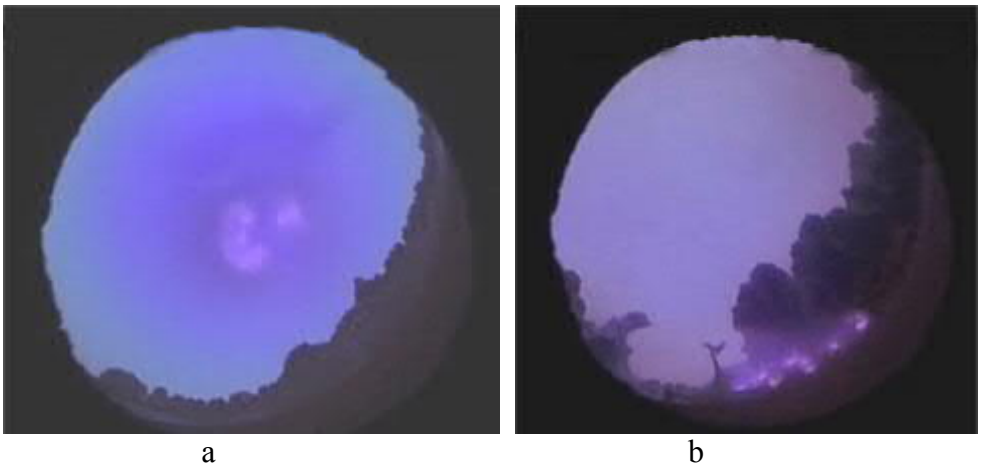


Fig.1. Two frames of the cathode image with interval of 0.15 s: $I$=64 A, $V_a$=10.5 V, $T_c$ = 2.31 kK

The destruction of the dark fragment in the center of Fig. 1 looked like melting. The size of this fragment decreased at a rate of $10^{-2}$ to ~0.5 mm/s, the speed was maximum when MS existed on its surface. Apparently, the cathode completely melted 770 s after the initiation of the arc. The melting point of cerium oxides, depending on their stoichiometric composition, varies in the range from 2.08 to 2.57 kK (at a pressure of 0.1 MPa) [5].

Subsequently, MS could move over the surface of the melt (Fig. 2a) or $CeO_2$ condensate near the crucible outlet (Fig. 2b). MS appeared on the condensate surface immediately after the current was increased from 64 to 90 A. Unlike MS on the condensate surface, they were somewhat larger on the melt surface, and their "lifetime" could reach ~3 s. Apparently, this change in the characteristics of MS was associated with an increase in the electrical conductivity of the oxide with increasing temperature. The number of MS increased with the increase of the current. The new MS usually appeared as a result of fission of existing ones, or were formed at the "molybdenum-oxide" boundary.

In VA with DCA on metal cathodes, MS could be observed only at the moment of arc initiation, if the cathode temperature was insufficient to provide the necessary thermionic emission current or to provide the essential density of the plasma-forming vapor [2]. When using EBH for preliminary heating of metal cathodes, the duration of modes with MS usually did not exceed ~1 s.



a b

Fig. 2. The cathode surface: a - $I$=64 A, $V_a$=11.4 V, $T_c$= 2.35 kK;
b - $I$=90 A, $V_a$=11.3 V, $T_c$= 2.31 kK;

The characteristics of the MS in the described discharge and in VA with cold cathodes are significantly different. First of all, it concerns their lifetime and movement speed. In the modes with MS, there were no chaotic voltage pulsations typical for VA on cold cathodes [6]. The appearance of MS on $CeO_2$ cathode has practically no effect either on the picture of the cathode glow or on the voltage $V_a$. Apparently, this means that the fraction of the VA current passing through the MS was relatively small. According to estimates, the cathode in the described experiment operated at the limit of its thermionic emission capability, so that even a relatively small decrease in its temperature caused instability of the DCA.

**Acknowledgments**. The study was supported by Russian Science Foundation (No. 21-72-00077), https://rscf.ru/en/project/21-72-00077/.

## References

1. **Vasin A.I., Dorodnov A.M., and Petrosov V.A.** Pis'ma Zh. Tech. Fiz., 5 (1979) 1499-1504.
2. **Polishchuk V.P., Usmanov R.A., Melnikov A.D. and other,** High Temp., 58 (2020) 476-494.
3. **Amirov R. Kh., Vorona N.A., Gavrikov A.V. and other**, Plasma Phys. Rep., 41 (2015) 808–813.
4. **Samsonov G.V.** The Oxide Handbook. New York: IFI/Plenum (1973)
5. **Zinkevich M., Djurovic D., and Aldinger F.** Solid State Ionics, 177 (2006) 989-1001.
6. **Anders S., Anders A**. IEEE Trans. Plasma Sci., 19 (1991) 20-24.

# NUMERICAL SIMULATION OF LIGHT-EROSION PLASMA DYNAMIC MPC-DISCHARGES

V.V. Kuzenov[1,2,3], N.V. Batrak[1], N.G. Kopaleishvili[1]

[1]Bauman Moscow State Technical University (BMSTU), 2-nd Baumanskaya, 5, 1, Moscow, 105005, Russia, svryzhkov@bmstu.ru
[2]Ishlinsky Institute for Problems in Mechanics RAS (IPMech), prosp. Vernadskogo, 101, block 1, Moscow, 117526, Russia, kuzenov@ipmnet.ru
[3]Dukhov All-Russian Research Institute of Automatics (VNIIA), Suschevskaya 22, Moscow, 127055, Russia, vik.kuzenov@gmail.com

A physico-mathematical model of magnetoplasma compressor (MPC) is presented. Electrotechnical characteristics and power modes of MPC discharges in gases are considered. Radiation-plasma dynamic structures and spectral-brightness characteristics of MPC-discharges are given. Three different types of quasistationary spatial distributions of plasma parameters are calculated for different heating modes (ohmic, transient and plasma dynamic). The generation and behavior of a plasma jet created on the basis of a plasma dynamic discharge of a magnetoplasma compressor has been studied.

## Introduction.

Radiation processes play an important role in the energy balance of plasma MPC discharges /1-10/. The energy of radiation emerging from the shock wave boundary of the plasma can account for a significant fraction of the energy supplied to the plasma. The integral radiative efficiency (the ratio of the radiation energy $E_{изΣ}$ in the entire spectral range of the gas transparency band at the time $t$ to the energy supplied to the plasma) significantly depends on the mode of energy supply to the plasma load i.e., on the mode parameter $A_m$. Fig. 1 shows the calculated data (signs Δ, +, ...) and approximation dependences of the integrally radiative efficiency of the discharge at the time $t_m$ of the first current maximum on the regime parameter $A_m$.

It should be noted that the dependence of the radiative efficiency on $A_m$ cannot be approximated by a single function, since the curves $\eta_{\Sigma m}(A_m)$ for different storage capacitances are stratified. This circumstance can be explained by the fact that for low-capacitance MPC discharges ($C = 28,6$ мкФ), characterized by a pulsed-periodic mode of energy input into the plasma, the processes occurring in the second and subsequent half-periods of the discharge current play a significant role in the total light yield of radiation. However, the qualitative course of the dependences $\eta_{\Sigma m}(A_m)$ in both cases is similar and

testifies that there is a region of optimal radiation modes of MPC discharges in gases, when $\eta_{\Sigma m}(A_m)$ is maximal. This region falling within the range of regime parameter changes $A_m = 0,4 \div 0,8$ i.e., in the transition regime, in which the storage energy is dissipated into the plasma as a result of the joint action of joule and plasma dynamic heating, and the kinetic energy level is generally insignificant. It is important to note that the type of gas (Ar or air in these calculations) quite weakly affects the integral radiative efficiency of the discharge and the position of the region of extreme values $A_m$. The decrease of $\eta_{\Sigma m}(A_m)$ in the plasma dynamic regime $A_m > 0,8$ is caused both by a significant increase in the fraction of kinetic energy of the moving flux and by a significant excess of the temperature of the radiating regions of the discharge plasma over the effective transparency temperature of the surrounding gas $T_{эф} \approx I_1/3$ (where $I_1$ is the first ionization potential of gas atoms) and, accordingly, by a significant shift of the spectrum of the generated radiation relative to the transparency band of the gas medium.

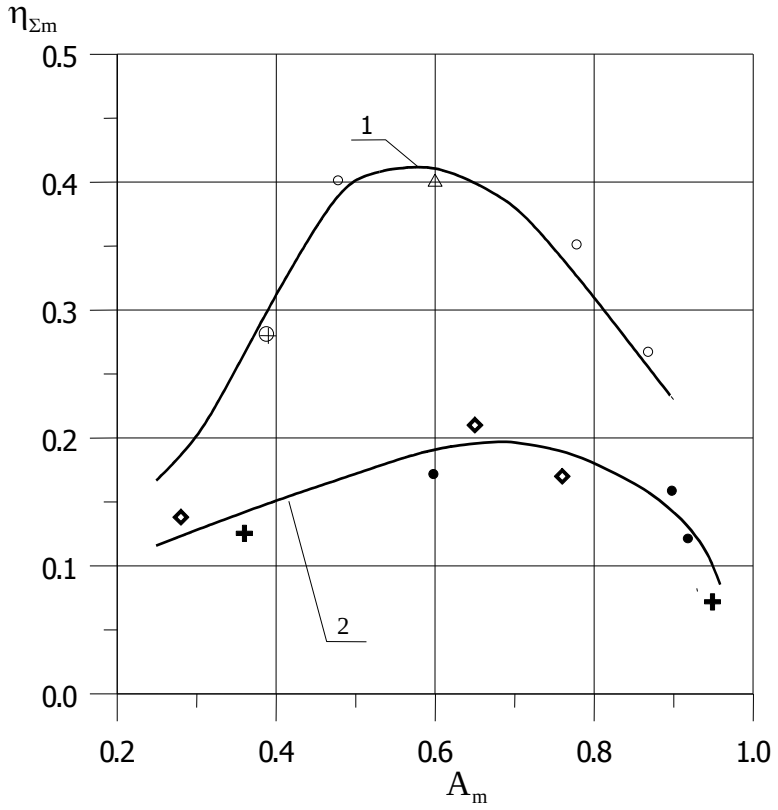



Fig. 1. Dependences of the spectral integral radiative efficiency $\eta_{\Sigma m}$ MPC discharge with storage capacity $C = 750$ мкФ (1) and $C = 28,6$ мкФ (2) on the parameter $A_m$

The growth of $\eta_{\Sigma m}$ when increasing the parameter $A_m$ in the region corresponding to the ohmic mode $A_m < 0,4$, is associated with an increase in the temperature and density of the emitting region of the light-erosion plasma. Assuming that in this case, all the energy supplied to the plasma is spent on increasing the internal energy of the plasma ($\varepsilon_{вн}$ : $T_{п0}$ ) in the temperature region $T_{п0} < T_{эф} \approx I_l/3$, the light efficiency of the discharge depends on $T_{п0}$ and $\rho_{п0}$ approximately as $\eta_{\Sigma m}$ : $\rho_{п0}^2 T_{п0} t_m$ .

**Testing of numerical methods.**

In Refs. /11-13/ the results of test calculations of the gas dynamic part of the one-dimensional equation system on the example of solving the one-dimensional problem of shock wave propagation in a pipe with initial conditions $\rho_1 = 1,\ p_1 = 1,\ V_1 = 0$ and $\rho_2 = 0,125,\ p_2 = 0,1,\ V_2 = 0$ are given. The calculations relied on $\gamma = 1,4$ and $\Delta x = 0,01$. The paper notes the high accuracy of the results obtained using the modified Glimm method and the Godunov-Kolgan method.

The gas-dynamic part of the two-dimensional equations was tested on the problem of a strong explosion without backpressure. The calculation results were compared with the analytical solution /14/. The dimensionless initial parameters of the ideal gas in the calculations were as follows: $\rho = 1$, p=1000, u=v=0 . The calculations were performed in a cylindrical coordinate system on two-dimensional grids sized $50 \times 50$, $100 \times 100$ and $120 \times 120$. The initial region of the explosion occupied $4 \times 4$ cells. It follows from the calculations that the width of the contact rupture and shock wave blur area: $2\Delta x$, the amplitude of the density, pressure fluctuations behind the stationary shock wave $< 1\%$ , which is quite acceptable in the calculations.

As a two-dimensional test of the radiation-magnetic part of the system, the problem

$$\sum_{\alpha=1}^{2} (a_\alpha(x_1, x_2) y_{\bar{x}_\alpha})_{x_\alpha} - d(x_1, x_2) y = -f(x_1, x_2),$$

$$y = 0 \ - \text{at the boundary of the calculation domain } G,$$

defined on a uniform grid $h_1 = h_2 = h = 1/N$ in the unit square. We choose the coefficients $a_1(x_1,\ x_2)$ and $a_2(x_1,\ x_2)$ as follows:

$$a_1(x_1,\ x_2) = 1 + c_0 \left[ (x_1 - 0,5)^2 + (x_2 - 0,5)^2 \right],$$

$$a_2(x_1,\ x_2) = 1 + c_0 \left[ 0,5 - (x_1 - 0,5)^2 - (x_2 - 0,5)^2 \right].$$

where $c_0$ is a constant.

The right part of $f$ is chosen from the condition that the function $y=(1-x_1)x_1(1-x_2)x_2$ is an exact solution of the mentioned difference problem. Initial conditions for the modified alternating-triangular method and the difference scheme, were set as $y(t=0,\ x_1,\ x_2)=0$. When solving the problems of radiation magnetic gas dynamics, one often has to face a situation when the coefficients of difference schemes change strongly in the considered region. Therefore, the test calculations were performed for a number of values of the parameter $\omega=c_2/c_1$, where $c_2$ and $c_1$ are the maximum and minimum values of the coefficients $a_1(x_1,\ x_2)$ and $a_2(x_1,\ x_2)$. This change of the parameter $\omega\in[4,\ 600]$ was achieved by varying the constant $c_0$. The performed calculations showed that the number of iterations in the modified alternating-triangular method for the indicated variants $\omega$ depending on the number of nodes $N=[50,\ 100,\ 120]$ for the accuracy $10^{-4}$ is the value $60$, which is also quite acceptable in calculations of high-current pulsed electric discharge systems.

**References**


1. **Astashynski V.M., Dzahnidze H.M., Kostyukevich E.A., Kuzmitski A.M., Shoronov P.N., Shymanski V.I. and Uglov V.V.** High Temp. Material Processes, 24 (2020) 99–107.
2. **Kuzenov V.V., Ryzhkov S.V., Gavrilova A.Yu. and Skorokhod E.P.** High Temperature Material Processes, 18 (2014) 119–130.
3. **Nosov K.V., Pavlov A.V., Protasov Y.Y., Telekh V.D. and Tshepanuk T.S.** J. of Phys.: Conf. Ser., 1115 (2018) 032011.
4. **Kuzenov V.V. and Ryzhkov S.V.** Computational Thermal Sci, 13 (2021) 45
5. **Khramtsov P. P., Penyazkov O. G., Vasetskii V. A., Grishchenko V. M., Makhnach A. I. and Shikh I. A.** Journal of Engineering Physics and Thermophysics, 88 (2015) 1154–1162.
6. **Kuzenov V.V., Ryzhkov S.V. and Frolko P.A.** JPCS, 830 (2017) 012049.
7. **Garkusha I.E., Chebotarev V.V., Herashchenko S.S., Makhlaj V.A., Kulik N.V., et al.** Nuclear Fusion, 57 (2017) 116011.
8. **Kuzenov V.V. and Ryzhkov S.V.** Symmetry, 13 (2021) 927.
9. **Kuzenov V.V. and Ryzhkov S.V.** Physica Scripta, 96 (2021) 125613.
10. **Kuzenov V.V., Ryzhkov S.V.** Russian J Nonlinear Dynamics 15 (2019) 543.
11. **Grishin Yu.M., Kozlov N.P. and Kuzenov V.V.** Computational Mathematics and Mathematical Physics, 34 (1994) 1489–1491.
12. **Kuzenov V.V. and Ryzhkov S.V.** Physics of Plasmas 26 (2019) 092704.
13. **Kuzenov V.V., Ryzhkov S.V. and Varaksin, A.Yu**. Applied Sciences, 12 (2022) 3610.
14. **Sedov L.I.** Methods of similarity and dimension in mechanics. M.: Nauka, 1977.

# SMALL-SIZE PLASMA PULSED FREQUENCY THRUSTER

P. Morozov[1], R. Emlin[2], I. Punanov[2], Ye Shcherbakov[2], L. Yashnov[3]

[1]IEP UB RAS, 106 Amundsen street, Ekaterinburg Russia, pav99369565@yandex.ru
[2]IEP UB RAS, 106 Amundsen street, Ekaterinburg Russia
[3]NIIMash, 624740, N.Salda, 72 Stroiteley str.

One of the main problems of the development of propulsion systems (PS) of orbit orientation and correction of the rapidly developing class of various small-sized space vehicles with mass from 1-5 кг till tens of kilograms is creation of light electroreactive thrusters (ERT) with mass of the order of 0.3-0.5 kg [1], which uses high-speed plasma beam generation at pulsed electric discharge over the surface of dielectric materials. Concomitant task to reduce propellant inventory requires development and improvement of constructions, in which the highest flow velocity of the working substances is achieved while maintaining low power consumption per one discharge of the order of tenths of joule. The required level of thrust can be achieved when the discharge frequency increases till (100-500 Hz) [2].

The simplest design of the discharge gap has pulsed plasma ERT with high-voltage surface flashover of solid dielectrics in vacuum, and in the last years work is carried out on the use of a liquid working substances in these systems [3, 4]. The presence of one tank comprising the entire volume of liquid used allows to more efficiently distribute the consumption of its stock among correction thrusters in different directions

One of the ways to optimize the proposed option with a decrease in unit discharge energy to tenths of joule is the use of magnetic converter (high-voltage transformer in inductive storage mode) and a ballast small-sized capacitor of several nanofarads. The currents developed in such a scheme reach a value of the order of 1-3 kA and can ensure sufficient flow of the working substance and obtain the required level of thrust impulse.

In [5] a layout of a small-sized ERT powered by a discharge circuit from a 20 kV pulse transformer is described. It has been shown that under these conditions the developed thrust depends on the energy stored in the condenser, and output characteristics are given when the capacitor 600 pF is installed in the discharge circuit. Discharges developed upon a surface of ferroelectric ceramics of capacitor type KVI-3. The obtained results showed that in the proposed scheme, when varying the condenser capacity, optimal mode can be achieved when matching the charging voltage and the length of the discharge gap depending on the composition of the ferroelectric ceramic substrate used.

In the presented work, measurements were carried out and dependencies of thrust developed by the model of the ERT were obtained during the discharge of

various capacitors (700-8000 pF). They charged from a high-voltage pulse transformer with an output energy of the order of 100 mJ and an output voltage of 6-10 kV. A ceramic substrate BaTiO3 was used for applying a liquid propellant. Fig. 1 shows a photograph of the layout of discharge chamber with a dielectric liquid supply unit and a pulse high-voltage transformer for charging a capacitor forming a high-current discharge.

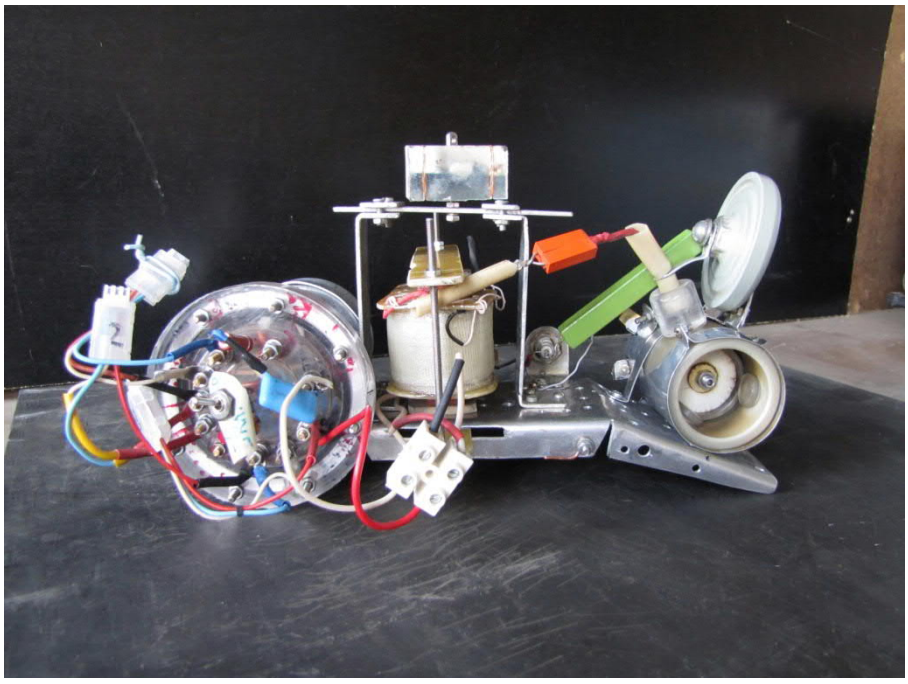


Fig. 1. The platform with transformer, thrust model and power supply and controlling unit

To measure the thrust impulse, the thrust model was located on the suspended platform of the torsion balance in a 0.160 $m^3$ vacuum chamber. A series of discharges is started when an optical signal is sent through the transparent window of the vacuum chamber. The circuit of generation of frequency and number in the sequence of discharge pulses and supply battery is located in a sealed cylinder on the same platform. The value of recoil pulse $p$ is calculated from the measurement of amplitude of oscillation angle of the torsion pendulum with known moment of inertia $J$,

$$p = \frac{2\pi J}{Td}\Delta\varphi_a$$

Where $T$ – period, $d$ distance from thrust model center to suspender axis, $\Delta\varphi_a$ - amplitude oscillation variation.

At Fig. 2 the typical waveforms of voltage pulses at electrodes and current

at discharge circuit through the sample in vacuum using capacitor 4700 pF are presented.

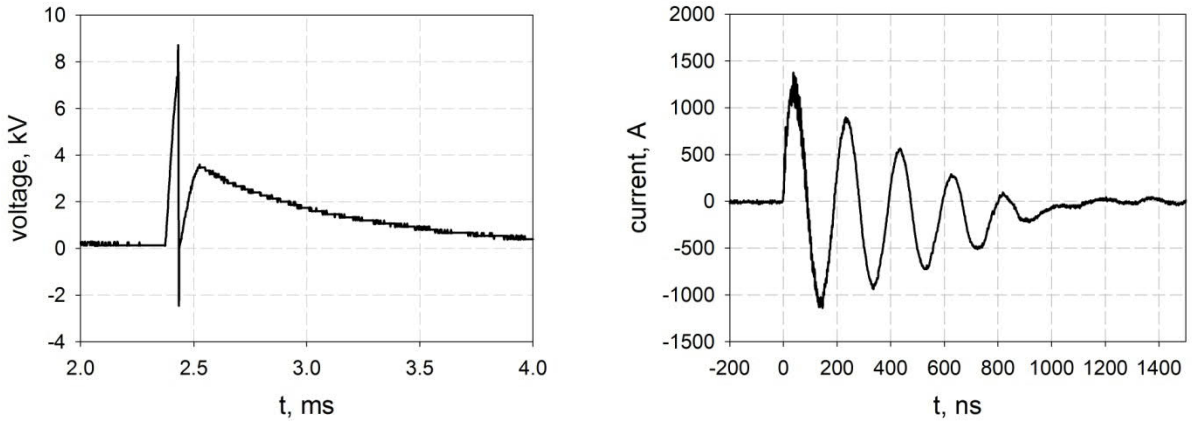



Fig. 2. Waveforms of capacitor voltage (right) and discharge current (left)

Pulse voltage was set within the order of 6-10 kV, the capacitor are charged during 40-50 μs, and discharge begin in self-breakdown mode. It is seen from the waveform that the form of current through the sample has the form of 3-5 damping oscillations with a period of 200 ns and an initial amplitude of 1-2 kA. Measurement of the total energy stored in the capacitor gives a value close to 60 mJ. The period of current oscillations is determined mainly by the constructive inductance of the discharge circuit. Fig. 3 shows a photo of the current channels glow picture (when starting) for a series of 400 discharges in one second

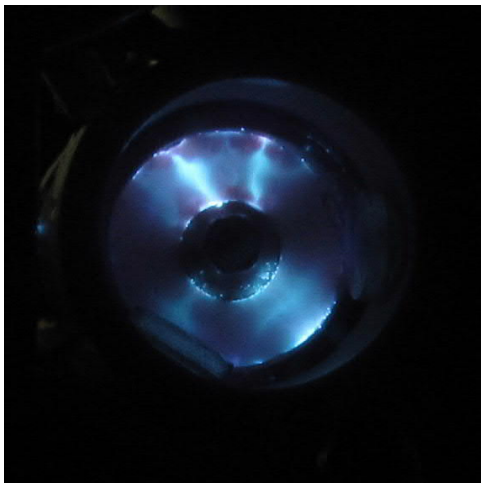


Fig. 3. The discharge glow

In the course of the tests, the return pulses of this model thruster was measured in vacuum with 3300 pF and 4700 pF storage capacitors using two

working substances: a) politetrafluoroethylen (FP-4) and b) castor oil applied on a substrate – ferroelectric ceramics based on BaTiO3. The tests of the generator part with the working substances FP-4 were carried out to determine the maximum electrical operating parameters under vacuum conditions by the output voltage (amplitude, duration of discharge and energy in pulse). Table shows the energy stored in the capacitor when it is charged from a high-voltage pulse developed by a pulse transformer with an amorphous iron core. Reduced values of stored energy for condensers of small capacity are associated with rapid achievement of amplitude voltage of high-voltage pulse.

Table

| C, pF | 680 | 1 200 | 1 600 | 1 800 | 2 100 | 4 000 | 4 700 |
|---|---|---|---|---|---|---|---|
| E, mJ | 44 | 65 | 77 | 79 | 84 | 100 | 102 |

Measurements of trust at discharges by a thin layer of castor oil applied to a substrate made of FP-4 show a significant decrease in it with a decrease in the capacity of the condenser used, which corresponds to a strong dependence of it on the discharge current value even at close values of the energy stored in the capacitor (Fig. 4). Besides, when measured on castor oil with an increase in current from 1 kA to 1.5 kA, the thrust increased from 55 to 67 μN·s. This indicates the need to determine the optimal discharge current with changes in the amount of energy transmitted by the pulse transformer.

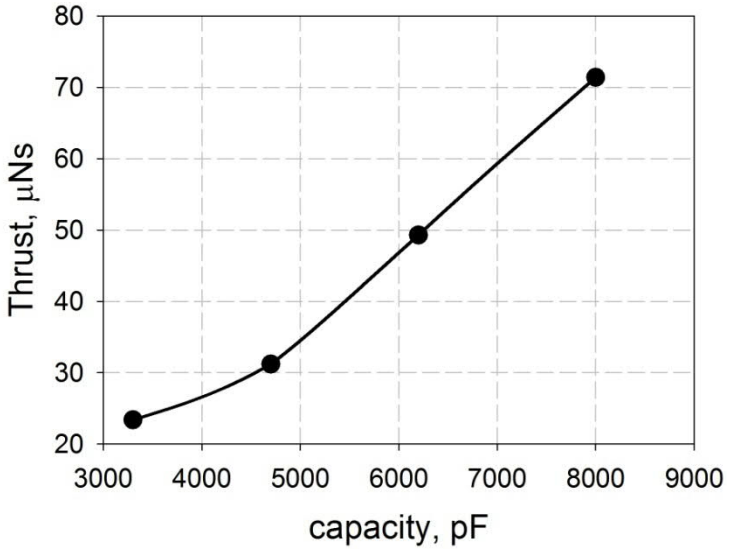



Fig. 4. Dependence thrust from capacitance.

Measurements were also made of the dependence of the thrust pulse developed by the model on the length of the discharge gap. For castor oil

breakdown on ferroelectric ceramic substrate (BaTiO3) with increase of interelectrode gap width from 4 to 8 mm, traction increased from 44 to 55 μN·s for a series of 400 discharges with the same discharge current amplitude. This is due to an increase in the mass consumption of the working substance converted into plasma during elongation of the breakdown channels. These dependencies we have obtained indicate significant possibilities in the proposed discharge circuit for optimizing the breakdown process and achieving a high value of specific thrust per unit of energy stored in the discharge circuit. The values of the plasma beam recoil pulse obtained in our measurements are now 60-67 μN·s, which in terms of one discharge gives 150-170 nN·s /discharge and 1.6 μN·s /J, and can be improved in the process of further studies. One way to increase traction is to raise the voltage applied to the discharge gap electrodes, while increasing the distance between them when using an external discharge igniter, and to increase the current amplitude by a decrease in the inductance of the discharge circuit.

## References

1. **Levchenko I., Bazaka K., Dink Y., et al.** Space micropropulsion for Cubesats and small satellites: from proximate targets to furthermost frontiers, Applied physics review 5, 011104 (2018), DOI: 10.1063/1.5007734.
2. **Potabachniy L., Emlin R., Kazankin F., Yashnov L., Morozov P.** 50 watt pulsed plasma thruster system, Proceedings of IX International conference Plasma physics and plasma technology, Minsk, Belarus, September 17 – 21, 2018, pp. 445 – 448.
3. **Ling Liang W., Schonherr T., Koizumi H.** Characteristics of a non-volatile liquid propellant in liquid-fed ablative pulsed plasma thrusters, J. Appl. Phys. **121**, 073301 (2017); DOI: 10.1063/1.4975349.
4. **Szelecka A., Kurzyna J., Danilko D., Barral S.** Liquid micro pulsed plasma thruster, NUKLEONIKA 2015; 60(2): 257-261, DOI: 10.1515/nuka-2015-0057.
5. **Buldashev S.A. et al.** Thrust characteristics of compact high-voltage pulsed plasma thruster utilizing liquid propellant, J. Phys.: Conf. Ser. 2064 012114.

# NUMERICAL SIMULATION OF THE FLOW OF AN ELECTRICALLY CHARGED DUSTY MEDIUM WITH ONE-DIMENSIONAL GEOMETRY

D. Tukmakov[1]

[1]Kazan Scientific Center of Russian Academy of Sciences, 2/31 Lobachevsky Str., Kazan, 420111, RF , E-mail: tukmakovda@imm.knc.ru

Studies of the dynamics of inhomogeneous media are applicable in many areas [1-10]. Including in plasma physics [3]. The heterogeneity of the studied media is one of the elements of scientific novelty in modern studies of hydrodynamics. As a branch of physics, hydrodynamics has a significant reliance on mathematical mods - methods of mathematical physics. In [3], the dynamics of monodisperse quartz particles in plasma is numerically modeled. In [5], electrohydrodynamic processes in the atmosphere are mathematically described taking into account the inhomogeneous structure of clouds. To study processes involving heterogeneous effects, it is necessary to use various branches of science [11]. The results presented in this study are theoretical in nature and allow bringing together such physical and mechanical concepts as viscosity, compressibility of the medium, intercomponent interaction and electric field.

## 2. Mathematical model

The dynamics of the carrier medium is described by the one-dimensional Navier-Stokes equation. The right-hand sides of the equations contain the terms responsible for the intercomponent momentum exchange $-F(u,u_1)$ and intercomponent heat transfer $-Q(T,T_1)$ [1,2,4, 6-10]:

$$\frac{\partial \rho}{\partial t}+\frac{\partial \rho u}{\partial x}=0 \tag{1}$$

$$\frac{\partial(\rho\ u\ )}{\partial t}+\frac{\partial}{\partial x}\left(\rho\ u^2+p-\tau\right)=-F+\alpha\frac{\partial p}{\partial x} \tag{2}$$

$$\frac{\partial(e\ )}{\partial t}+\frac{\partial}{\partial x}\left(\left[e\ +p-\tau\right]u\ -\lambda\frac{\partial T}{\partial x}\right)=-Q-\left|F\right|\left(u\ -u_1\right)+\alpha\frac{\partial\left(pu\right)}{\partial x} \tag{3}$$

$$\frac{\partial \rho_1}{\partial t}+\frac{\partial\left(\rho_1 u_1\right)}{\partial x}=0 \tag{4}$$

$$\frac{\partial\left(\rho_1 u_1\right)}{\partial t}+\frac{\partial}{\partial x}\left(\rho_1 u_1^2\right)=F-F_C-g\rho_1-\alpha\frac{\partial\ p}{\partial x} \tag{5}$$

$$\frac{\partial\left(e_1\right)}{\partial t}+\frac{\partial}{\partial x}\left(e_1 u_1\right)=Q \tag{6}$$

$$\frac{\partial^2 \varphi}{\partial x^2} = \rho_1 q_0 \qquad (7)$$

Equation (1) is the gas mass continuity equation, equation (2) is the Navier-Stokes equation describing the continuity of the viscous gas momentum, equation (3) is the gas energy conservation equation. Equation (4) is the equation of continuity of the "average density"–$\rho_1$ of the carrier medium. The average density is the product of the physical density of the material, a constant –$\rho_{10}$=const and the volumetric content of the dispersed component $\alpha = \alpha(x,t)$, which is a function of space and time variables. Equation (5) is the equation of continuity of the momentum of the dispersed phase, equation (6) is the equation of conservation of the energy of the dispersed component. Equation (5) takes into account both the intercomponent momentum exchange –$F$, and the Coulomb force acting on particles –$F_C$, as well as the gravitational settling of particles, the term: -$\rho_1 g$. Equation (7) is the Poisson equation describing the electric field created both by the electric charge of dispersed particles and by external electric potentials. Intercomponent momentum exchange $F$ involves several forces: $F=F_{AR}+F_A+F_{AM}$; where $F_{AR}$ is the force of aerodynamic drag (8), $F_A$ is the dynamic force of Archimedes (9), $F_{AM}$ is the force of added masses (10) [1]:

$$F_{AR} = \frac{3\alpha}{4d} C_{di} \rho \, |u - u_1|(u - u_1) \qquad (8)$$

$$F_A = \alpha\rho \left( \frac{\partial u}{\partial t} + u \frac{\partial u}{\partial x} \right) \qquad (9)$$

$$F_{AM} = 0.5\alpha\rho \left( \frac{\partial u}{\partial t} + u \frac{\partial u}{\partial x} - \frac{\partial u_1}{\partial t} - u_1 \frac{\partial u_1}{\partial x} \right) \qquad 10)$$

$$Q = 6\alpha Nu_1 \lambda (T - T_1)/d^2 \qquad (12)$$

$$Nu_1 = 2\exp(-M_1) + 0.459 Re_1^{0.55} Pr^{0.33}, C_d = C_d^0 \eta(\alpha)\psi(M_1),$$

$$C_d = \frac{24}{Re_1} + \frac{4}{Re_1^{0.5}} + 0.4, \ \psi(M_1) = 1 + exp\left( \frac{-0.427}{M_1^{0.63}} \right), \eta(\alpha) = (1-\alpha)^{-2.5},$$

$$M_1 = |u - u_1| / c_0 \ , \ Re_1 = \rho |u - u_1| d / \mu \ , \ Pr = \gamma \ C_p \mu / \lambda \ , \ \tau = \frac{4}{3} \mu \frac{\partial u}{\partial x}$$

The drag coefficient of a single particle $C_d$ is calculated taking into account the compressibility of the medium (factor $\psi$) corrected for multiplicity of particles (factor $\eta$) ($C_d$ is the drag coefficient of a single spherical particle). $Nu_1$ is the relative Nuselt number, $Re_1$ and $M_1$ are the relative Reynolds and Mach numbers, $\tau(u)$ –function of viscous gas stresses. The electric field is described in the following way [11]:

$$div\boldsymbol{E} = \frac{\rho_e}{\varepsilon\varepsilon_0},\ \boldsymbol{E} = -\bar{\nabla}\varphi,\ \Delta^2\varphi = -\frac{\rho_e}{\varepsilon\varepsilon_0},\ \rho_e = \alpha\rho_{10}\cdot q_0 = \rho_1\cdot q_0,\ \varepsilon_0 = \frac{10^{-9}}{36\pi}F/m \quad (13)$$

where $q_0$ is the specific charge per unit mass of the solid fraction, φ is the electric field potential. $E$ is the electric field strength, ε is the relative dielectric constant of air, $\varepsilon_0$ is the absolute dielectric constant of air. The Coulomb force acting on the particles of the dispersed component of the gas suspension is determined by formula (14):

$$F_C = -\rho_1\frac{\partial\varphi}{\partial x} \quad (14)$$

The equations of the mathematical model (1)-(14) were supplemented with boundary conditions. The velocities of the mixture components at the boundaries of the computational domain were set equal to zero. For the rest of the dynamic functions, the homogeneous Neumann boundary conditions were set. For the electric field potential, values were set at opposite ends of the computational domain:

$$u(t,1)=0, u_1(t,1)=0,\ u(t,N)=0, u_1(t,N)=0,\ \rho(t,1)=\rho(t,2),$$
$$\rho_1(t,1)=\rho_1(t,2), \rho(t,N)=\rho(t,N-1), \rho_1(t,N)=\rho_1(t,N-1),$$
$$e(t,1)=e(t,2), e_1(t,1)=e_1(t,2),\ e(t,N)=e(t,N-1), e_1(t,N)=e_1(t,N-1),$$
$$p(t,1)=p(t,2), p(t,N-1)=p(t,N),\ \varphi(1,t)=\varphi_1, \varphi(N,t)=\varphi_2$$

## 3. Solution methods

Let us consider the application of the algorithm of the explicit McCormack method using the example of a scalar nonlinear partial differential equation (15) [12]. The Poisson equation for the potential of the electric field was solved by the finite difference method - the method of establishment applied on the gas-dynamic computational grid. The scheme of the establishment method is as follows [13]. To overcome some of the shortcomings of the numerical method used, a nonlinear grid correction algorithm was used, which will reduce the local maxima and increase the local minima of the grid function [14]. The correction algorithm was performed sequentially along all nodes. Let us consider an algorithm for correcting the solution using the example of the function $f$. If the conditions are met $\left(\delta f_{i-1/2}\cdot\delta f_{i+1/2}\right)<0$ or $\left(\delta f_{i+1/2}\cdot\delta f_{i+3/2}\right)<0$ then the algorithm of the correction scheme is applied to the function f in the $i$-th node: $\tilde{f}_i = f_i + \kappa\left(\delta f_{i+1/2} - \delta f_{i-1/2}\right)$. The subscript indicates the mesh node number.

The notation is used here:

$$\delta f_{i-1/2} = f_i - f_{i-1},\ \delta f_{i+1/2} = f_{i+1} - f_i,\ \delta f_{i+3/2} = f_{i+2} - f_{i+1}$$

Otherwise: $\tilde{f}_i = f_i$, $\tilde{f}_i$ is the value of the function at the i-th node after the transition to the $(n + 1)$ -th time layer according to the McCormack scheme, κ is the correction factor. The numerical solution of the equations of the mathematical model described here is implemented as a computer program in the Fortran programming language.

**Acknowledgements**. The work was carried out within the framework of the state task of the Federal Research Center of the Kazan Scientific Center of the Russian Academy of Sciences.

## References

1. **Nigmatullin R. I.** Fundamentals of the Mechanics of Heterogeneous Media. Moscow: Nauka (1978)
2. **Kutushev A. G.** Mathematical simulation of wave processes in aero dispersed and powdered media. St. Petersburg: Nedra (2003)
3. **Grishin Y. M., Miao L.** High Temperature, 39 (2020) 1-11.
4. **Tukmakov A. L.** Journal of Engineering Physics and Thermophysics, 87 (2014) 38-47.
5. **Sinkevich O. A.** High Temperature 54 (2016) 775-781.
6. **Tukmakov A. L., Tukmakov D.A.** High Temperature. 55 (2017) 509-512
7. **Tukmakov A. L., Tukmakov D.A.** Journal of Engineering Physics and Thermophysics, 91 (2018) 1141-1147
8. **Tukmakov D. A., Ahunov A. A.** 2020 News of the Saratov university. New series. Series: Physics, 20 (2020) 183-192.
9. **Tukmakov D. A. Ahunov A. A.** Chebyshevskii collection, 21 (2020) 257-269.
10. **Tukmakov D. A.** Mathematical Notes of NEFU 27 (2020) 99-109
11. **Salyanov F. A.** Fundamentals of low-temperature plasma physics, plasma devices and technologies. Moscow: Nauka (1997)
12. **Fletcher C. A.** Computation Techniques for Fluid Dynamics. Berlin: Springer-Verlang (1988)
13. **Muzafarov I. F., Utyuzhnikov S. V.** Journal of Computational Mechanics, 5 (1993) 74-83
14. **Krylov V.I., Bobkov V. V., Monastyrnyj P. I.** Computational Methods Part 2. Moscow: Nauka (1977)

# ELECTRIC DISCHARGES OF DIRECT AND ALTERNATING CURRENT IN A GAS-LIQUID FLOW AT ATMOSPHERIC PRESSURE

Gaysin F.M.[1], Khafizov A.A.[2], Valiev R.I.[2], Bagautdinova L.N.[1], Gaysin Az.F.[3], Gaysin Al.F.[1]

[1]Kazan National Research Technical University named after A.N.Tupolev - KAI, Russia, 420111, Kazan, Marx St.10, lilup@bk.ru, FMGaysin@kai.ru
[2]Kazan Federal University - Naberezhnye Chelny Institute, Russia, 423812, Naberezhnye Chelny, 68/19, almazok75@yandex.ru, rivaliev87@mail.ru
[3]Kazan State Power Engineering University, Russia, 420066, Kazan, st. Krasnoselskaya, 51, FMGaysin@kai.ru

Currently, gas-liquid mixtures with a bubble structure are of great scientific and practical interest [1-6]. This is due to the fact that multiphase and including two-phase flows are the main medium in devices for natural and waste water treatment [2-4]. The study of anomalies and features of discharge flow in tubes [5-6], as well as the study of gas-hydrodynamics of vapor-air discharges with liquid electrodes give interesting scientific results.

The aim of the study is to study a gas-liquid mixture with a bubble structure and micro-discharges. In this case, the solid phase is water, and the dispersed phase is air. As a result of experimental studies, graphs of the voltage-current dependence are constructed.

The experimental setup allows you to generate a discharge of direct and alternating current. In all experiments, a dielectric tube with an inner diameter of 10 mm was used, the tube arrangement is horizontal, the shape is U-shaped. To supply the potential, steel electrodes were used, which were immersed at both ends of the tube. The interelectrode distance was the distance between these electrodes. The experimental setup (fig. 1) for the study of DC electrical discharges in a gas-liquid medium consists of a discharge chamber, a DC power supply (4), a universal analog-to-digital converter Sensor-CASSY (5) and a computer (6). The discharge chamber includes two drip funnels (1 and 2) connected by a dielectric tube (3) with a diameter of 10 mm and mounted on two tripods. Copper wires (7) with a diameter of 1.5 mm are immersed in the upper open parts of the funnels to supply potential. The interelectrode distance in these experiments was set to l=50, 100 and 150 mm. The experimental setup is designed to study an electric discharge in the range of parameters Up = 0.3 – 3000 V, currents I = 0.01- 10 A, je = 25 A / $cm^2$, interelectrode distances l = 0.1 – 150 mm.

The experimental setup allows you to generate a DC and AC discharge. In all experiments, a dielectric tube with an internal diameter of 10 mm was used, the tube arrangement is horizontal, and the shape is U-shaped. To supply the potential,

steel electrodes were used, which were immersed at both ends of the tube. The interelectrode distance was the distance between these electrodes.

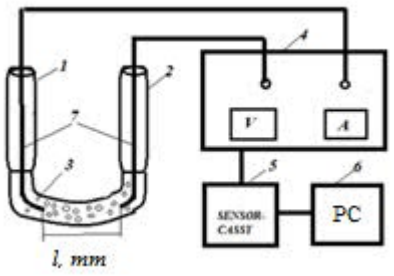
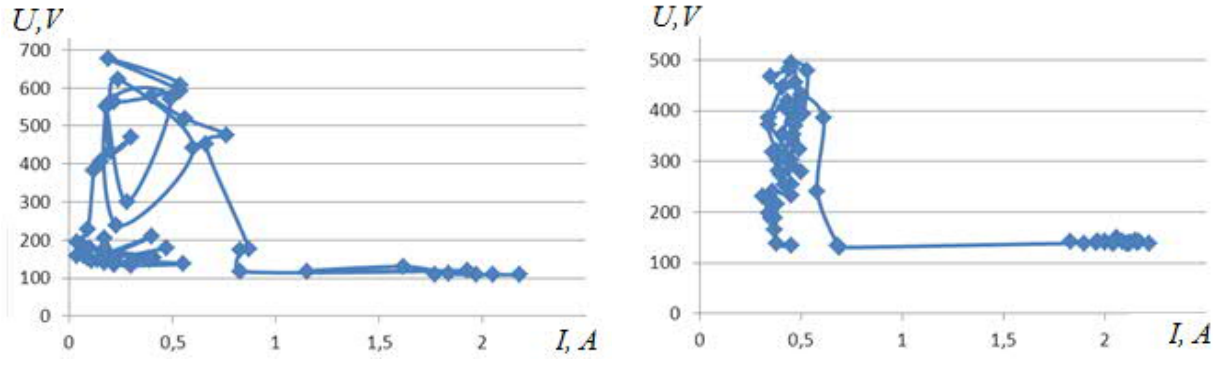



Fig.1. Experimental setup

Fig. 2 shows the voltage-current characteristics of the DC discharge in the tube for various interelectrode distances. In all experiments, the discharge occurred only at the cathode. A 10% solution of sodium chloride in distilled water was used as the electrolyte. As can be seen from Fig. 2, the voltage characteristics are high-voltage anomalous. The value of the micro discharge voltage in the bubbles varies randomly in the range of current forces from 0 to 0.5 A.

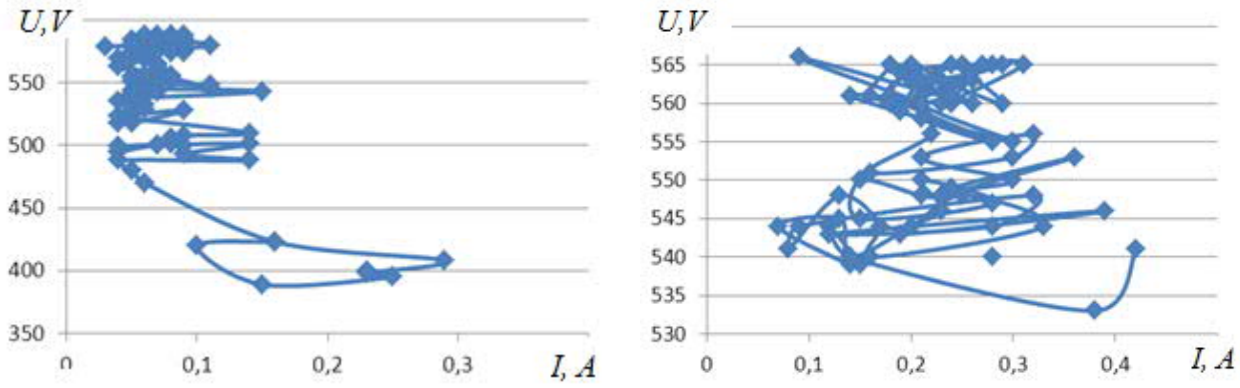
As can be seen from Fig. 2a, in the current range from 0 to 0.55 A, the voltage of micro-discharges in the bubbles behaves randomly and varies from 150 to 700 V. The growth of the current from 0.55 to 2.25 A is explained by the process of electrolysis. At an interelectrode distance of 50 mm (Fig. 2b) in the current range from 0 to 0.5 A, the voltage increases and reaches a maximum, and then drops sharply. The current change in the range from 1 A to 2.25 A is characterized by the electrolysis current. Here, the tension is almost constant. With the growth of the interelectrode distance from l=50 mm to 100 mm, the nature of the dependence U=f(I) practically does not change. However, the value of the maximum voltage decreases by ΔU=200 V as the interelectrode distance increases from 50 mm to 100 mm. In addition, it should be noted that the width of the spread of micro-discharges over the current is narrowing. Thus, for l=50 mm, the current spread is ΔI=1 A, for l=100 mm, ΔI=0.25 A.




a b

Figure 2-Voltage characteristic of a DC electric discharge with 10% sodium chloride solution at: a-l=50 mm, b-l=100 mm

For comparison, similar experiments were performed with a 1 % solution of copper sulfate in distilled water (Fig. 3). The Interelectrode distance varied from 25 mm to 150 mm. The experiment showed that at l= 100 and l= 150 mm, the discharge did not occur and only the process of electrolysis was observed. The lack of discharge can be explained by the low concentration of the solution and the lack of breakdown. At l=50 mm (Fig. 3b), the discharge began to burn at the cathode. Before the discharge occurred, a black mass was formed on the cathode. This is due to the fact that during the electrolysis process, the electrolyte solution is purified. With a decrease in the interelectrode distance at l=25 mm (Fig.3a), the discharge occurred at the anode. In this case, coagulation of the structure in the electrolyte was also observed. This structure has the color of a black mass. Apparently, the process of electrolysis is also going on near the anode. The analysis of Fig. 3 shows that at l=25 mm and 50 mm, the voltage characteristics have similar dependencies, as for 10% sodium chloride solution.




a b

Figure 3-Voltage characteristic of a DC electric discharge with 1 % copper sulfate solution at:
a-l=25 mm, b-l=50 mm

Figure 4 shows the volt-ampere characteristic of the AC discharge for a 10 % solution of sodium chloride in distilled water at l=50 mm.

As seen in Fig.4 the nature of the volt-ampere characteristics is preserved. In the range of current strength I=0.05-0.3 A in the case of alternating current, the discharge voltage increases significantly in comparison with the DC discharge (Fig. 2).

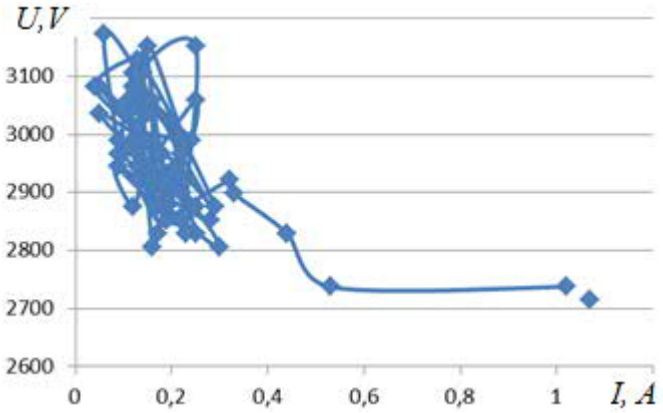



Figure 4-Voltage characteristic of an AC electric discharge with 10% sodium chloride solution at l=50 mm

Based on the analysis of data on video recording of the discharge, it was possible to establish the mechanism of ignition of an electric discharge of direct and alternating current in a gas-liquid environment at atmospheric pressure. After switching on the power supply, the electrolysis process begins first. In this case the formation of bubbles occurs in the upper part of a horizontally located dielectric tube in the gap between the electrodes. The size of the bubbles ranges from 0.1 mm to 6 mm, the shape from almost round to oval. The movement of the bubbles goes from the center of the tube towards the electrodes. Before the discharge is ignited, the size of the bubbles increases to 12 mm in length and 6 mm in width. That bubble divides and before the discharge is ignited, the bubbles are violently mixed. After the breakdown, a volumetric multi-channel discharge is observed in the porous medium of micro-bubbles.

## References

1. V.E. Fortov, E.E. Son, M.-E.H. Isakaev, A.V. Karpukhin. Patent 2516307, 2012.
2. V.A. Panov, Y.M. Kulikov, E.E. Son. Patent No. 134921, 2013.
3. S.N. Dolgoborodova. Fundamental Research, No. 12, 2014.
4. E.E. Son, I.F. Suvorov, S.V. Kaurov, A.F. Gaisin, G.T. Samitova, T.L. Solovyova, A.S. Yudin, T.V. Rokhletsova. Thermophysics of high temperatures. 52 (2014) 4.
5. V.A. Panov, L.M. Vasilyak, S.P. Vetchinin, V.Ya. Pecherkin, E.E. Son. Applied physics. (2016) 1.
6. Al. Gaisin, N. Kashapov, G. Akhatova and A. Gaisina. Journal of Physics: Conference Series. 1328 (2019) 1.

# PLASMA STUDIES AT GASDYNAMIC ION SOURCE FOR MULTIPURPOSE OPERATION (GISMO)

R. L. Lapin, I. V. Izotov, A. F. Bokhanov, S. V. Golubev, E. M. Kiseleva, S. S. Vybin, A. V. Polyakov and V. A. Skalyga

Federal Research Center Institute of Applied Physics of the Russian Academy of Sciences (IAP RAS)

**Introduction.** High-current pulsed ECR (electron cyclotron resonance) ion source with powerful plasma heating by millimeter wave gyrotron radiation (37.5 or 75 GHz / 100 kW) in an open magnetic trap with was designed and has operated as an experimental facility SMIS-37 in IAP RAS (Nizhny Novgorod, Russia) for more than 20 years. The proton beams with the current of 500 mA and normalized RMS emittance below 0.1 $\pi$·mm·mrad were obtained and the possibility of getting the current density of 800 mA/cm$^2$ was shown (with an extraction voltage less than 50 kV) [1 and links within].

The key feature of such approach is a reaching of plasma density of $10^{13}$ - $10^{14}$ cm$^{-3}$ and electron temperature near 100 eV, and thus a realization of so-called quasigasdynamic regime of plasma confinement. It is characterized by the plasma lifetime defined as ion escape from the trap (with effective length $L$ and mirror ratio $R$) with ion-sound velocity $V_s$ through magnetic mirrors [2]:

$\tau = LR/(2V_s)$. So it is possible to obtain plasma fluxes with record densities at the level of 10 A/cm$^2$ due to small plasma lifetime (tens us) and high density.

Achieved results indicate the high prospects of the transition from pulsed to CW (continuous wave) regime of quasigasdynamic ECR ion source operation. A multiplicity of goals in fundamental and applied (such as boron neutron capture therapy) research can be solved with the obtaining of high-current (~100 mA) ion beams in CW regime. The first results of plasma studies at high-current CW ECR ion source based on powerful ECR plasma heating in an open magnetic trap with millimeter wave gyrotron radiation (28 GHz / 10 kW) as an experimental facility Gasdynamic Ion Source for Multipurpose Operation (GISMO) are discussed.

**Experimental facility.** GISMO experimental facility is based on a 28 GHz / 10 kW CW gyrotron [3] manufactured by IAP RAS. This microwave

generator radiation ignites and sustains the ECR discharge plasma in the fully permanent magnetic system consisting of consecutive two traps: a simple mirror trap with 12 cm length and a cusp. The magnetic field strength is about 1.5 T at magnetic mirrors and is nearly 0.25 T at the trap center, so the mirror ratio is $R = B_{max}/B_{min} = 6$.

The experimental scheme of GISMO facility is presented in Fig. 1. The input gyrotron electromagnetic radiation (circular waveguide TE02 mode) converts to the Gaussian beam and passes through the 15 cm air gap, playing the role of a DC-break. Then the radiation converts into the circular waveguide TE11 mode and focuses to the plasma with the use of special microwave-to-plasma coupling system. Assuming the lack of plasma microwave reflection, one can estimate overall transmission efficiency as about 95%. The water-cooled plasma chamber with the inner diameter of 32 mm is used.

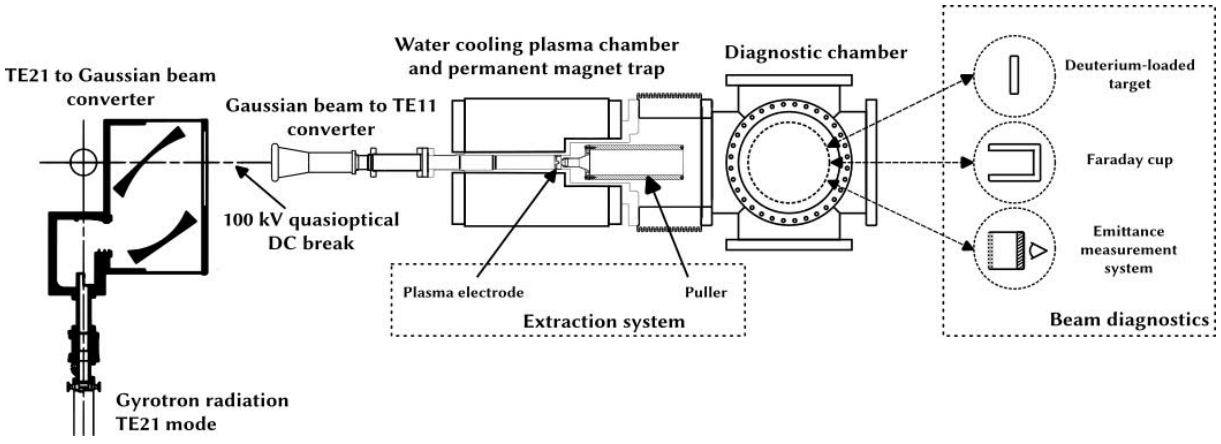



Fig. 1. GISMO experimental facility

The two-electrode extraction system is used for beam formation with the help of a bipolar high voltage source. The set of extracted beam analysis systems is available for installation into the diagnostic chamber. The different Faraday cups can be used for extracted beam current measurement, and the “pepper-pot” method was implemented for the measurement of the beam emittance. It is possible to set a special target there for the experimental investigation of the neutron source based on ECR discharge plasma. Moreover, the magnetostatic analyzer and some extra beam diagnostics systems can connect to the chamber flange opposite the microwave beam inlet.

The current article is focused on three of many various CW ECR source applications: proton source, negative hydrogen ions source, and CW ECR discharge as a part of the neutron source.

**ECR discharge as a proton source.** The proton beams with a current of ~100 mA with a duration of 10 ms and a repetition rate of up to 10 pulse/s have recently obtained at GISMO facility. It had been shown with the use of "pepper-pot" method that the normalized 4 rms-emittance does not exceed $2\pi \cdot$mm$\cdot$mrad for both electrodes of the beam formation system in the extraction voltage range from 41 to 48 kV [4].

A new approach to the extraction system for both pulsed and CW ECR sources had been proposed [5] and experimentally proved for SMIS-37 [6]. The use of an inhomogeneous accelerating field allows improving the ion beam formation efficiency significantly. The increase of electric field magnitude is achieved by changing the shape of the electrodes only, without increasing the accelerating voltage and decreasing the interelectrode distance. The use of a new electrode geometry allows increasing the electrodes' lifetime and to form high-quality ion beams with a current density of more than 1A/cm$^2$.

**Negative hydrogen ion source based on ECR discharge.** The two main applications for negative hydrogen ion sources are the cyclotrons, where they are needed for charge exchange injection, and the magnetic fusion projects as a part of a neutral injector [7]. The negative hydrogen ion current density of 80 mA/cm$^2$ has obtained at pulsed ECR facility SMIS-37 earlier [8].

$H^-$ ions are produced volumetrically via dissociative electron attachment (DEA) through high vibrational hydrogen molecule states when the peak of the DEA cross-section corresponds to the electron energy of several eV, while the optimal electron energy for high vibrational molecular excitation equals 30 – 100 eV. Therefore, there should have been two electron fractions with different temperatures, what had been implemented with the use of a perforated conducting plate placed between the magnetic traps. It prevented further microwave radiation propagation, which helped to keep so-called cold electrons together with the cusp as a natural high-energy electron filter.

The system parameters were optimized and the maximum current density $j$ = 41 mA/cm$^2$ was obtained together with clarification of $H^-$ generation area.

**Neutron generator based on ECR discharge.** Neutron sources are widely used in fundamental research and are suitable for various applications, such as neutronography, boron neutron capture therapy (BNCT), etc. However, there is

a need for an increase in the existing neutron generators' intensity according to BNCT requirements [9]. The prospects of the compact neutron generator based on ECR discharge sustained by gyrotron radiation had been shown in the pulsed regime [10].

In this approach, neutrons were produced as a result of D-D fusion in a deuterium-loaded target bombarded by a focused high-current deuterium ion beam. A high neutron yield ($10^8$ n/s per 1 mA $D^+$ beam current) was obtained with a deuterium beam energy of 100 keV. It's worth noticing that such neutron flux could be obtained in case of sharp ion beam focusing into 1 mm spot and creating so a «point-like» source which is also suitable for neutron tomography [11].

The prospects for the neutron generator functionality based on the CW ECR discharge were shown, and the optimal extraction system parameters were determined, which make it possible to form a deuterium ions beam with a current of more than 500 mA. Further magnetic system modernization was proposed, and the CW cooled neutron-forming target is under development.

**Acknowledgments.** The work was carried out with the support of RSF grant #21-12-00297.

## References

1. **Skalyga V. et al** Rev. Sci. Instrum., 87 (2016) 02A716.
2. **Skalyga, V. et al** Rev. Sci. Instrum., 77 (3) (2006) 03A325.
3. **Litvak A. G., Denisov G. G., and Glyavin M. Y.** IEEE J. Microw., 1 (1) (2021), 260–268.
4. **Барабин С.В. и др.** Письма в ЖЭТФ, 10 (2021) 7.
5. **Vybin S. S., Izotov I. V., Skalyga V. A.** Plasma Sources Sci. Technol., 29 (2020) 11LT02.
6. **Vybin S. S. et al** Plasma Sources Sci. Technol., 30 (2021) 125008.
7. **Bacal M., Sasao M., and Wada M.** J. Appl. Phys., 129 (2021) 221101.
8. **Lapin R. L. et al** JINST, 13 (2018) C12007.
9. **Dymova, M. A. et al** Cancer Commun, 40 (2020) 406–421.
10. **Skalyga, V. et al** J. Appl. Phys., 118 (2015) 093301.
11. **Golubev, S. V. et al** JINST, 16 (2021) T02008.

# A NEW TYPE OF MICROWAVE NON-THERMAL ATMOSPHERIC PRESSURE PLASMA SOURCE

V.Tikhonov[1], S. Gorbatov[1], I. Ivanov[1], A. Tikhonov[1]

[1] Russian Institute of Radiology and Agroecology, Kiev highway 109th km, Obninsk, Kaluga region, 249032, Russian Federation, E-mail: v.n.tihonov@yandex.ru

The unique applications of Non-Thermal Atmospheric pressure Plasmas (NTAP) are associated with its enormous potential for low-temperature plasma chemistry and for treating heat-sensitive materials, including polymers and biological tissues [1, 2]. A new type of microwave source of NTAP, presented earlier by the authors [3, 4], has both the characteristics of a dielectric barrier discharge (in terms of the configuration and low gas temperature) and an ability to form a "clean" plasma jet like a classical microwave plasma torch. The microwave discharge is excited in a dielectric tube passing across the waveguide, perpendicular to the electric field strength vector **E**. In this configuration, two wide walls of the waveguide can be considered as an electrode system of two flat parallel electrodes located in parallel to the axis of the discharge tube, which walls play the role of a dielectric barrier. Such a configuration of a microwave NTAP source can be implemented on the basis of waveguide concentrators of the electromagnetic field strength in three ways - a resonant console, a broadband pass-through or with a three-decibel H-plane waveguide bridge.

Figure 1 shows a general view of a microwave NTAP source in a resonant console configuration (on the left) and a diagram of its connection to a microwave generator (on the right). Such a plasma source itself is quite simple to manufacture, but requires the use of an expensive circulator to protect the magnetron from the reflected wave.

A less budgetary and very simple through-pass non-resonant NTAP source (Fig. 2) does not require a circulator for its operation, since the microwave generator **G** is always loaded to a matched load **L** here. However, the conditions for initiating and maintaining the discharge deteriorate here, and the small size of the plasma leads to the fact that the efficiency of the deposition of microwave power passing through the waveguide into the discharge is very low, as a result, a significant part of it is lost in the matched load.

The main idea of the third variant of the NTAP source configuration is to replace the circulator used in the console configuration (Fig. 1) with a three-decibel waveguide bridge in the H-plane, which has a connection through a narrow wall (Fig. 3).

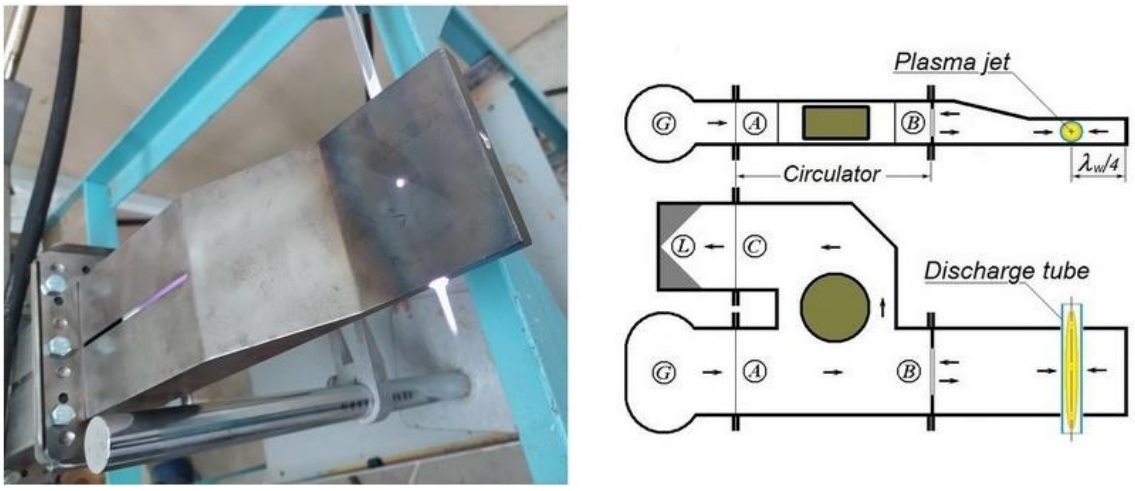



Fig. 1. A microwave NTAP source in a resonant console configuration

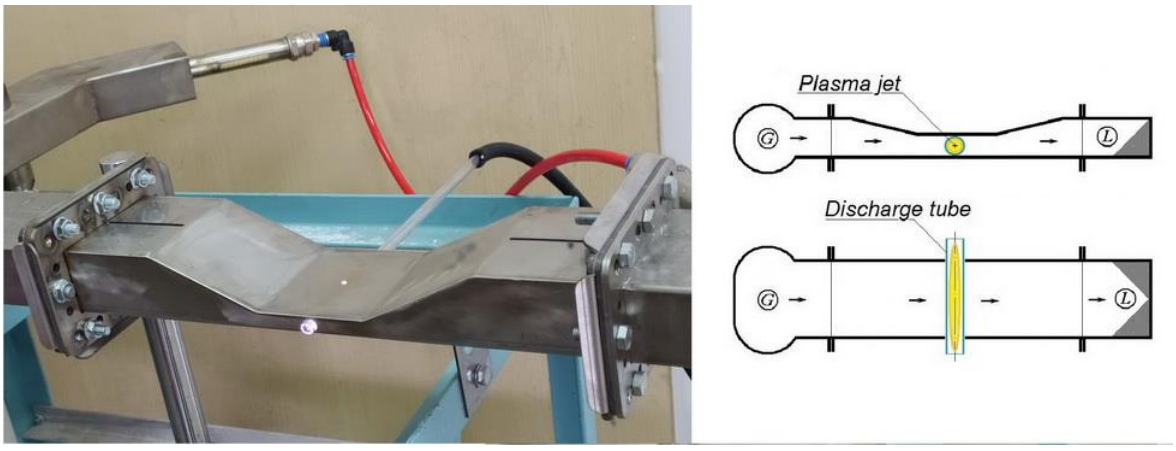



Fig. 2. A simple through-pass non-resonant NTAP source

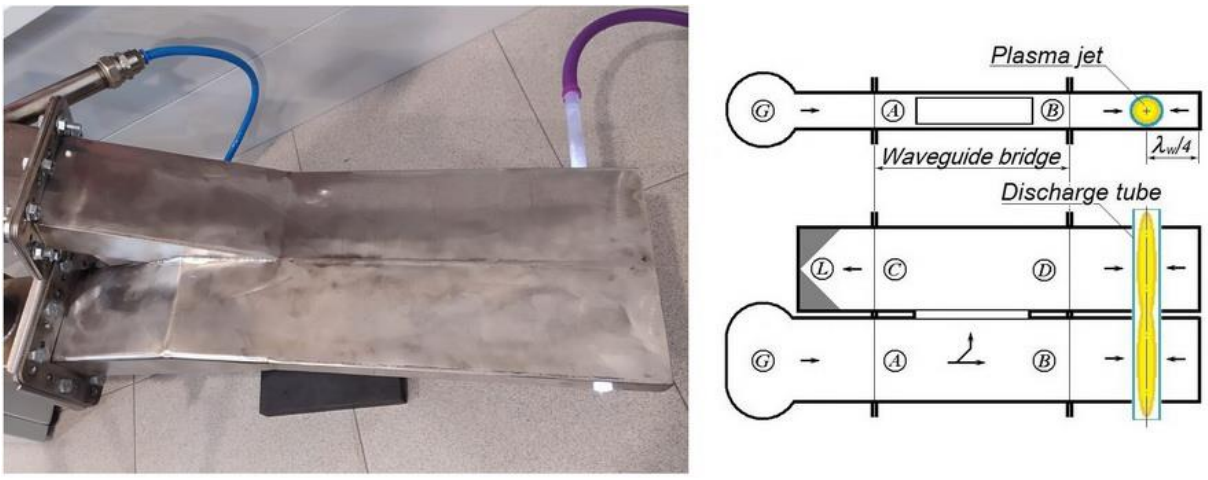



Fig. 3. A microwave NTAP source based on a three-decibel waveguide H-bridge

A three-decibel waveguide bridge unique property is that if both output arms of such a bridge are loaded on any arbitrary but identical loads, then all the power reflected from them will go to the fourth, "untied" arm **C** of the bridge. By connecting the matched load **L** to the untied arm **C**, we will save the microwave generator **G** from troubles, even in the case of very significant reflections. The constructive solution of such a source is somewhat more complicated than the previous two, but there is no need to use a circulator.

It is important to note that in the presented sample of the microwave NTAP source, the height of the waveguides in the discharge formation zone is 20 mm compared to 8 and 10 mm in the E-concentrators described above (Fig. 1, 2). Therefore, the cross-sectional area of the discharge tube and the formed plasma jet can be increased fourfold. In addition, the power supplied to the H-bridge and introduced into the microwave discharge can also be significantly increased.

The dynamics and structure of the microwave discharge were investigated by the method of high-speed video recording. The discharge radiation was recorded by the *Phantom Miro M110* camera with a shooting frequency of up to $10^5$ frames per second. The discharge inside the tube consists of wide luminous channels moving along the gas flow at speeds of about 50-100 m/s (for gas flow rates up to 40 l/min). The channels have the form of vertical discharges-columns splitting into filaments at the upper and lower ends, which form a tree-like structure near the walls in the upper and lower parts of the tube and end on the surface of the tube with a lot of bright micro spots (Fig. 4).

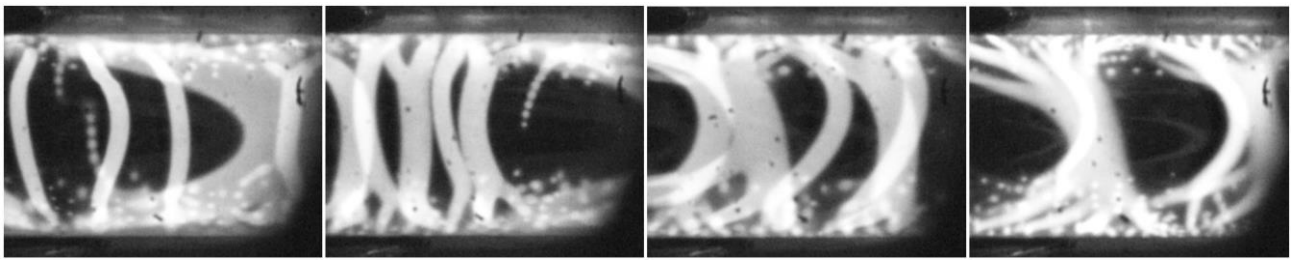


Fig. 4. Typical frames from high-speed video shooting in the middle of the discharge tube

Thermocouple and thermal imaging measurements of the temperature profiles of the argon plasma jet formed behind the outlet of the dielectric tube were carried out, as well as measurements and analysis of its emission spectra were carried out. At an argon flow rate of 10 and 20 l/min, the length of the visible (luminous) part of the plasma jet was about 26 and 21 mm (Fig. 5), and the temperature of the plasma jet along the central axis of the discharge tube at a distance of 20 mm from the waveguide wall was 290 and 200 degrees Celsius, respectively.

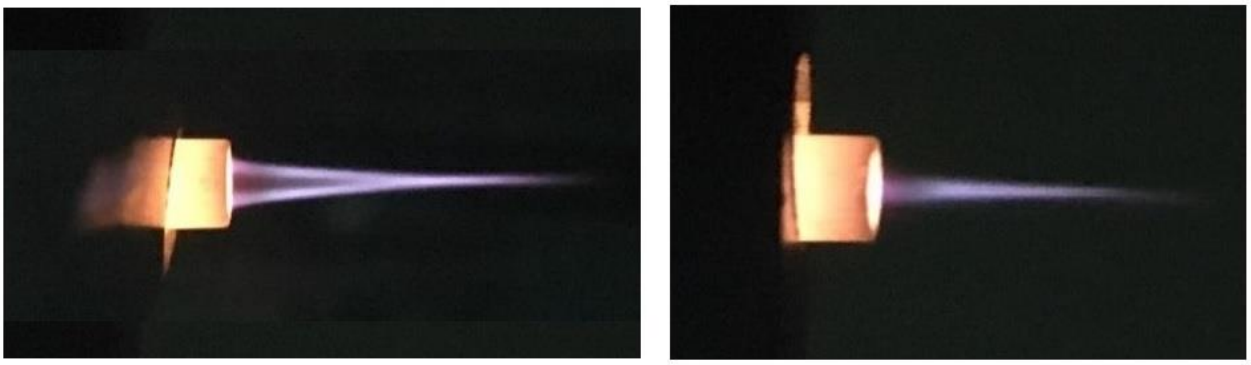


Fig. 5. Argon plasma jet at the outlet of the ceramic discharge tube

An analysis of the atomic lines of excited Argon in the emission spectra obtained in different zones of the discharge channel made it possible to estimate the electron temperature in the plasma jet, which was about 0.4÷0.5 eV.

**Acknowledgements**. This work was supported by the Russian Foundation for Basic Research (project No. 20-08-00894).

## References

1. **Vijay Nehra, Ashok Kumar, H.K. Dwivedi** Atmospheric Non-Thermal Plasma Sources // International Journal of Engineering (2008) Volume (2): Issue (1), pp. 53-68.
2. **N.N.Misra, Oliver Schlüter, P.J.Cullen** Cold plasma in food and agriculture: fundamentals and applications. London, United Kingdom: Academic Press, 2016.
3. **V.N. Tikhonov, I.A. Ivanov. and A.V. Tikhonov** A new type of nonthermal atmospheric pressure plasma source // J. Phys.: Conf. Ser. 1393 (2019) 012062 doi:10.1088/1742-6596/1393/1/012062
4. **V. N. Tikhonov, S. A. Gorbatov, I. A. Ivanov, A. V. Tikhonov** A new type of non-thermal atmospheric pressure plasma source based on a waveguide bridge // J. Phys.: Conf. Ser. 2064 (2021) 012131 doi:10.1088/1742-6596/2064/1/012131

# MICROWAVE COMPLEX FOR OBTAINING LOW-TEMPERATURE PLASMA AT ATMOSPHERIC PRESSURE

I. Ivanov[1], S. Gorbatov[1], A.Tikhonov[1], V. Tikhonov[1]

[1] Russian Institute of Radiology and Agroecology, Kiev highway 109th km, Obninsk, Kaluga region, 249032, Russian Federation, E-mail: ivanov.i.an@mail.ru

Today, in the promising, rapidly developing fields of science, industry, medicine and agriculture, there is an acute need for simple, reliable and inexpensive sources of low-temperature plasma. They are needed both for R&D on new materials and technologies, and for the intensification and modernization of already used "classical" technological processes.

Traditional plasma generators, such as electric arc, high-frequency and microwave plasma torches produce plasma with operating temperatures from several thousand to tens of thousands of degrees. According to the classification of physicists, such plasma refers to low-temperature plasma, as opposed to high-temperature, "hot" plasma used in fusion work, where the temperature is measured in millions of degrees. This division is due to the importance of using high-temperature plasma in solving the global problem of controlled thermonuclear fusion [1].

Over the past two decades, the scientific and technical community has made significant efforts to develop, maintain and use the so-called atmospheric non-thermal plasma (ANTP) in which ions and neutral components remain near room temperature [2]. This allows the use of such non-thermal plasma for low-temperature plasma chemistry and for the processing of heat-sensitive materials, including polymers and biological tissues [3]. The unique properties of ANTP - a strong thermodynamic non-equilibrium nature, low gas temperature, the presence of chemically active radicals, high selectivity provide a huge potential for use the “cold” plasma sources in a wide range of applications.

The purpose of this work is to present the universal hardware complex, designed to generate both traditional low-temperature plasma and two types of ANTP for both laboratory and industrial applications. The core of the complex is a low-budget the 2.45 GHz magnetron microwave oscillator with a high-voltage power unit built on the magnetrons, transformers and capacitors used in microwave ovens for domestic and industrial use [4]. The output power of the microwave generator can be changed discretely from 0.5 to 3 kW.

Figure 1 shows a schematic diagram and a general view of components and blocks of one of the many possible options for completing the hardware complex [5]. In the presented package the complex included: the microwave generator with high voltage power supply, the set of replaceable elements of the waveguide path, the water load, the 50 Ω cable assembly and ANTP applicator.

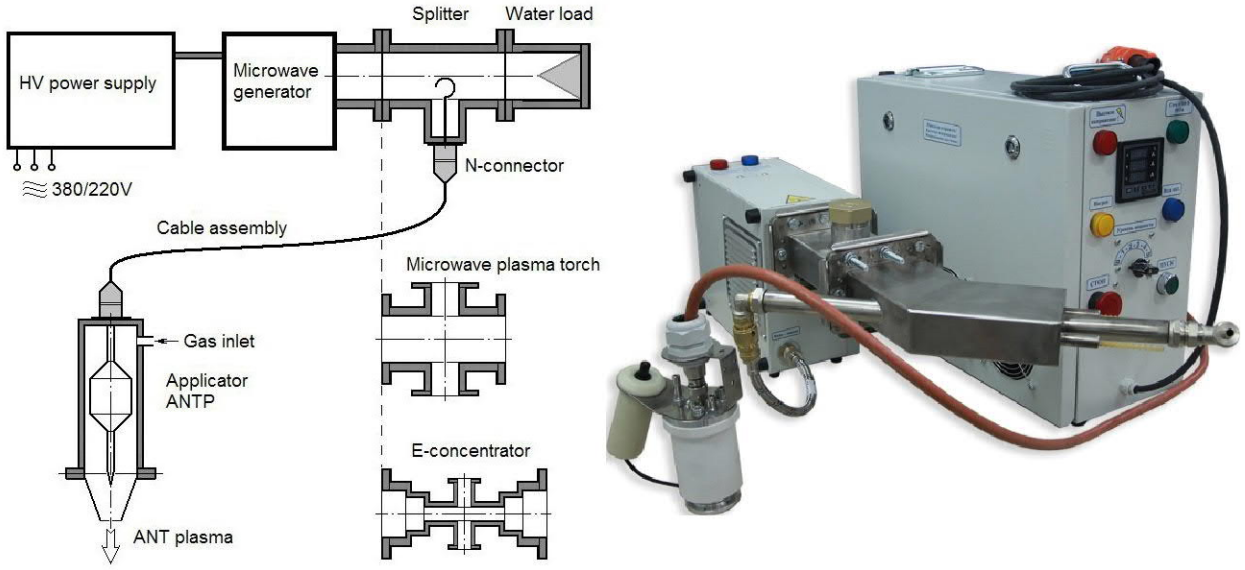



Fig. 1. Schematic diagram of components and blocks, as well as a general view of the hardware complex

The main elements of the waveguide system with a cross section of 90x45 mm are made of non-magnetic stainless steel with flange sizes according to the WR-340 standard. The waveguide path is usually loaded onto a finite broadband water load, and between the output of the microwave generator and the load, elements of the waveguide path from the following set can be placed.

**The microwave plasmatron** of classical configuration on the main type $\mathbf{H_{01}}$ oscillations in the waveguide, built on the basis of standard threaded stainless steel and brass fittings for metal pipes [5] (Fig. 2). Water cooling of the shielding pipe or the entire section of the waveguide creates opportunities for the implementation of long-term technological processes.



Fig. 2. A simple microwave plasmatrons on the standard threaded brass fittings

**The inductive-type splitter** is a coupling loop located on a narrow wall of the waveguide. The design of the coupler allows to change the communication value by rotating the loop plane, which is loaded on the N-type coaxial connector. It is possible to combine in one node the coupler and the microwave plasma torch (Figure 3, left).

**The E-field concentrator** can be made of a stepped design or with a smooth change in the waveguide cross section - to increase the electric field strength in the area where the microwave plasma torch is located (Figure 3, right). The narrowing of the waveguide can be symmetrical or one-sided.

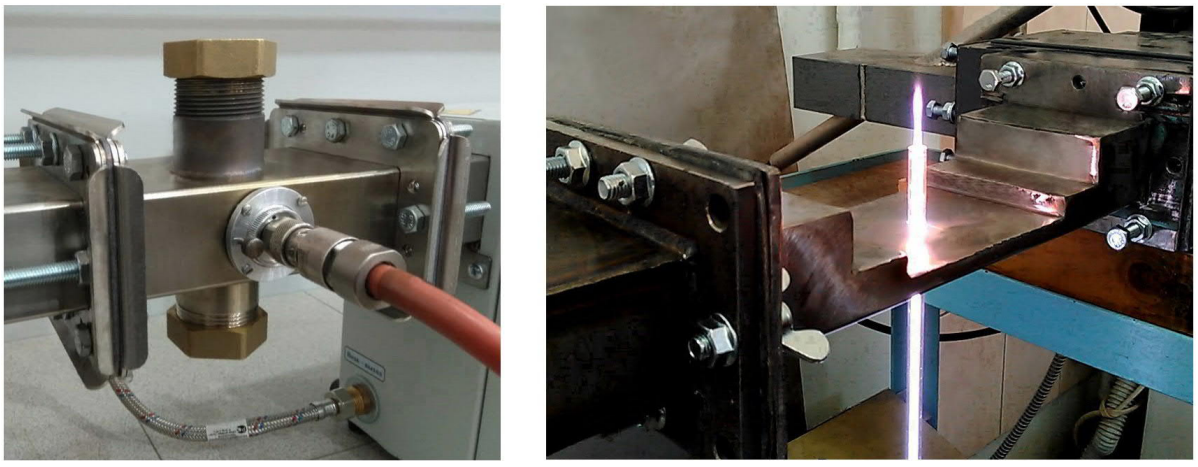


Fig. 3. The inductive-type splitter and the E-field concentrator

One of kind of the **ANTP applicator** design is shown in Figure 4, left. The plasma reactor vessel and air cooling radiator made of aluminum alloy. The protective body of the applicator is made of Teflon. N-type cable connector located on the applicator cover. There is also the supply pipe for working gas (argon) and two hose connectors forced air cooling system of the reactor.

Figure 4 on the right shows another type of **ANTP source**. The basis of its design is a rigid waveguide-coaxial junction, which significantly reduces the mobility of the source, but greatly simplifies the design and reduces its cost. The matched waveguide load connected to it on the right is also shown here.

In addition to those described above, the following elements of the waveguide path can also be used: a microwave plasma torch based on a three-decibel bridge, an NTAP source using a microwave barrier discharge in three configurations [6], as well as a number of others. To expand the technical and technological capabilities, the hardware complex can be additionally equipped with a microwave circulator, a contactless waveguide short-circuiting plunger and strip directional couplers to measure the incident and reflected waves.

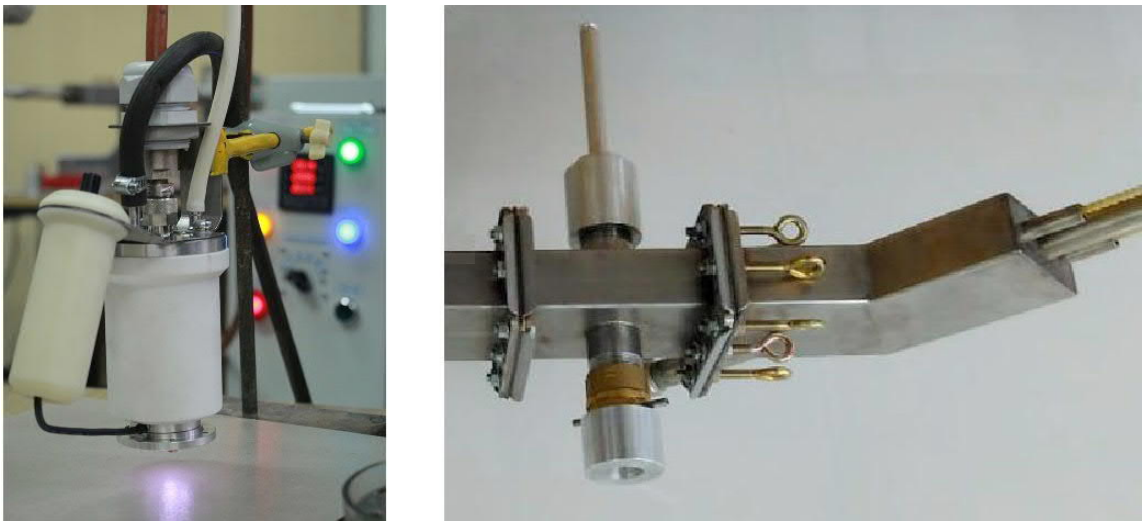


Fig. 4. Two types of ANTP applicators

**Acknowledgements**. This work was supported by the Russian Foundation for Basic Research (project No. 20-08-00894).

## References

1. Encyclopaedia of Low-Temperature Plasma. Entrance Volume, Book 2. Ed. by **V.E.Fortov**. (Moscow: MAIK Nauka/Interperiodika, 2000) [Russian]
2. **Vijay Nehra, Ashok Kumar, H.K.Dwivedi** Atmospheric Non-Thermal Plasma Sources // Int. Journal of Engineering (2008) Volume (2): Issue (1), pp. 53-68.
3. **N.N.Misra, Oliver Schlüter, P.J.Cullen** Cold plasma in food and agriculture: fundamentals and applications. London, United Kingdom: Academic Press, 2016.
4. **V.Tikhonov, I.Ivanov, A.Kryukov, A.Tikhonov** 2015 J. Prikl. Fiz., **5** pp. 102-106 [Russian]
5. **I.Ivanov, V.Tikhonov and A.Tikhonov** Microwave complex for obtaining low-temperature plasma at atmospheric pressure // J. Phys.: Conf. Ser. **1393** (2019) 012042, doi:10.1088/1742-6596/1393/1/012042
6. **V.Tikhonov, S.Gorbatov, I.Ivanov, A.Tikhonov** A new type of non-thermal atmospheric pressure plasma source based on a waveguide bridge // J. Phys.: Conf. Ser. **2064** (2021) 012131 doi:10.1088/1742-6596/2064/1/012131

# ANALYSIS OF PARAMETERS OF COAXIAL DIELECTRIC BARRIER DISCHARGE IN CARBON DIOXIDE FLOW AT ATMOSPHERIC PRESSURE

I. Rafatov

METU, Department of Physics, Dumlupinar Blv. 1, 06800 Çankaya, Ankara, TÜRKİYE
rafatov@metu.edu.tr

The work deals with the numerical simulations of atmospheric pressure DBD sustained in carbon dioxide in coaxial discharge cell. The aim is to gain a deeper understanding of the mechanisms underlying the DBD-assisted carbon dioxide conversion. The effect of various operating conditions on the discharge characteristics is studied for wide ranges of parameters such as the amplitude and frequency of the applied voltage, the gas temperature, and different configurations of the discharge cell.

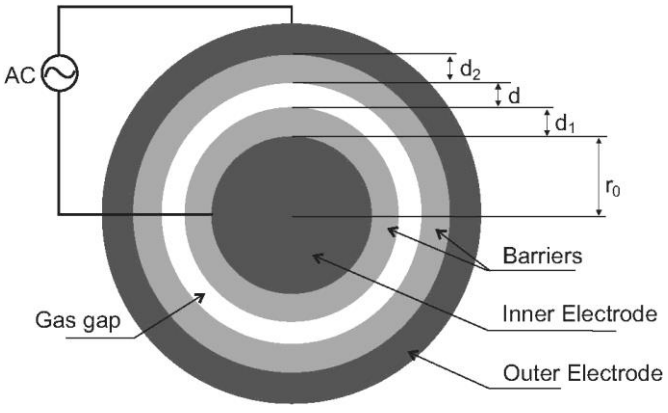



Fig. 1. Schematic description of coaxial DBD tube.

## 1. Gas discharge model

The gas discharge model includes equations for the electron number and energy densities

$$\frac{\partial n_{\mathrm{e}}}{\partial t} + \nabla \cdot \mathbf{\Gamma}_{\mathrm{e}} = S_{\mathrm{e}} \tag{1}$$

and

$$\frac{\partial n_{\epsilon}}{\partial t} + \nabla \cdot \mathbf{\Gamma}_{\epsilon} = \mathbf{J}_{\mathrm{e}} \cdot \mathbf{E} - Q_{el} - \sum_j \Delta E_j R_j, \tag{2}$$

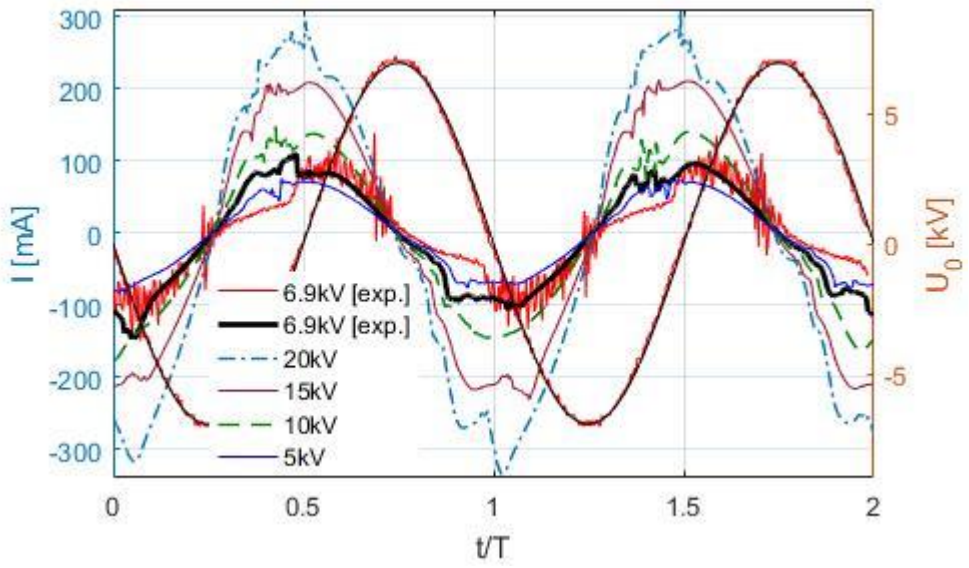



Fig. 2. Discharge current and voltage wave forms.
$p = 1$ atm, $d = 1.9$ mm, $\varepsilon_r = 4$, $f = 106$ kHz.

the transport equations for the heavy species (neutrals and ions)

$$\rho \frac{\partial w_k}{\partial t} = \nabla \cdot \mathbf{j}_k + S_k, \tag{3}$$

the energy balance equation for the background gas

$$\rho c_p \frac{\partial T_\mathrm{g}}{\partial t} - \nabla \cdot \left(k \nabla T_\mathrm{g}\right) = \mathbf{J}_\mathrm{i} \cdot \mathbf{E} + Q_{el}, \tag{4}$$

and the Poisson equation for the electrostatic field

$$-\epsilon_0 \nabla^2 \varphi = \sum_k q_k n_k. \tag{5}$$

In these equations, $\varphi$ and $\mathbf{E} = -\nabla\varphi$ are the electric potential and field, $n_k$ is the particle number density, the subscript $k$ defines the type of species, $q_k$ is the charge number for species $k$. The electron number and energy flux densities are expressed by the drift-diffusion approximation as

$$\mathbf{\Gamma}_\mathrm{e} = -\mu_\mathrm{e} n_\mathrm{e} E - D_\mathrm{e} \nabla n_\mathrm{e} \tag{6}$$

and

$$\mathbf{\Gamma}_\epsilon = -\mu_\epsilon n_\epsilon E - D_\epsilon \nabla n_\epsilon, \tag{7}$$

respectively, where the mobility and diffusion coefficients are related via $D_\epsilon = 5/3 D_\mathrm{e}$ and $\mu_\epsilon = 5/3 \mu_\mathrm{e}$ [1].

In the electron energy equation (2), $n_\epsilon = n_e \bar{\varepsilon}$ denotes the electron energy

density, $\bar{\varepsilon} = 3/2\, T_\mathrm{e}$ is the mean electron energy, $\mathbf{J}_\mathrm{e} = -e\mathbf{\Gamma}_\mathrm{e}$ is the electron current density, $Q_\mathrm{el} = 1.5 m_\mathrm{e}/m_\mathrm{g} \nu_{ea} n_\mathrm{e}(T_\mathrm{e} - T_\mathrm{g})$ accounts for the loss of electron energy in elastic collisions, $\nu_{ea}$ is the frequency of the electron-atomic elastic collisions, $R_j$ is the rate of the $j$th reaction and $\Delta E_j$ is the corresponding energy loss (or gain), $m$ is the particle mass, and $T$ is the kinetic temperature.

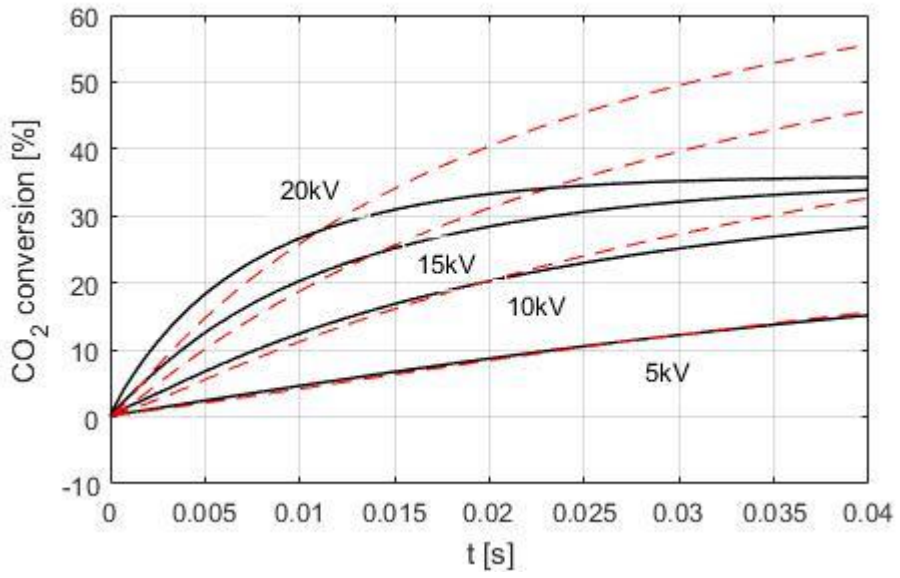



Fig. 3. $CO_2$ conversion rate (average over the discharge gap). Solid and dash-dot lines correspond to models with and without taking account of gas heating. $p = 1$ atm, $d = 1.9$ mm, $\varepsilon_r = 4$, $f = 100$ kHz.

In the transport equations (3), $w_k$ denotes the mass fraction of the $k$th species, $\rho$ is the density of the mixture, which is defined by the ideal gas law, $\rho = pM_n/RT_\mathrm{g}$, where $R$ is the universal gas constant. The diffusive flux vector $\mathbf{j}_k$ is defined as $\mathbf{j}_k = \rho w_k \mathbf{V}_k$, where the diffusion velocity $\mathbf{V}_k$ is expressed by the Fick's law. In the energy equation for the background gas (4), $c_p$ denotes the specific heat at constant pressure, $k$ is the thermal conductivity, and $\mathbf{J}_\mathrm{i} = e\mathbf{\Gamma}_\mathrm{i}$ is the total ion current density.

The rate expressions $S_k = \sum_i R_i - \sum_j R'_j$ are defined by the gain $R_i$ and loss $R'_j$ of particles in $i$th and $j$th reactions. These rates are proportional to the constants of the corresponding reactions and the densities of the species involved in these reactions. The rate constants of the electron induced reactions as well as the electron mobility and diffusion coefficients are computed as functions of the mean electron energy, obtained by convolving the corresponding collision cross sections with

EEDF, obtained from solution of the corresponding electron Boltzmann equation [1].

The models is completed by definition of the transport coefficients for heavy particles and the boundary conditions.

## 2. Plasma composition

The plasma-chemical model basically follows that from our previous work and also [2]. This model takes into account a reduced set of reactions dominating the $CO_2$ conversion. The plasma includes the electrons, the three types of ions, namely, the positive ions $CO_2^+$ and the negative ions $O_2^-$ and $O^-$, and the five types of neutral species, namely, $CO_2$, CO, O, $O_2$, and $O_3$. Within this model, vibrationally and electronically excited levels of the molecules, which contribution in DBD plasmas is of minor importance [2], are ignored. The reactions responsible for $CO_2$ splitting are electron impact dissociation and electron dissociative attachment.

## 3. Parameter regime

The discharge is ignited in a discharge cell of coaxial geometry, consisting of two quartz tubes of different diameters, inserted into each other. Pressure of the $CO_2$ gas is specified as atmospheric, $p = 760$ Torr. The radius of the inner electrode, widths of the inner and outer dielectric layers, and the gas gap width are defined as follows (see Fig. 1): $r_0 = 4$ mm, $d_1 = d_2 = 1$ mm, and $d = 1.9$ mm. The discharge tube lengths and correspondingly the inner electrode length of 30 cm, while the external electrode (wrapped around the outer discharge tube) is of the length $h = 3.7$ cm. The dielectric constant is set equal $\varepsilon_r = 4$. The frequency is varied over the range from 20 to 120 kHz, and the applied voltage amplitudes from 1 to 20 kV.

**Acknowledgements.** This work was supported by research Grant No 3191899 from the Scientific and Technical Research Council of Turkey (TUBITAK).

## References

1. **Hagelaar, G.J.M. and Pitchford, L.C.** Plasma Sources Science and Technology, 14, (2005) 722.
2. **Robby, Aerts, R., Somers, W., and Bogaerts, A.** ChemSusChem, 8, (2015) 702–716.

# NONSTATIONARY SLOW IONIZATION WAVES IN LONG DISCHARGE TUBES AT LOW GAS PRESSURE

A. Shishpanov, P. Bazhin, V. Zaletov

Saint Petersburg State University, 198504 Saint Petersburg, Peterhof, Ul'yanovskaya str.3
sispanov@mail.ru

Electrical gas breakdown at low pressure in discharge gaps with the length significantly exceeding the size of the electrodes, proceeds through the passage of an ionization wave (IW) [1]. IW is a high intensity electric field area localized in space where intense ionization and excitation of gas particles occur. This area corresponds to a solitary electric field wave and a potential front. IW appears near a high-voltage electrode (HVE) and propagates toward the external field potential lowering, which results in gas ionization in those discharge chamber areas where the initial external field was not sufficient for this to happen. The waves are classified into slow waves ($v_w$~$10^5$-$10^8$ cm/s) and fast waves - FIW ($v_w$> $10^9$ cm/s). Most of the research that have been performed so far focus on stationary waves ($v_w$=const), and most frequently this property is attributed to FIWs. However, in breakdown experiments, nonstationary waves are also observed, but these are less studied.

The decrease of the wave velocity is due to spatial attenuation of its field amplitude. For the first time this effect was observed by Winn for FIW [2], and it was him who gave an explanation of the phenomenon. On IW propagation, a plasma channel remaining behind the front connects it with the HVE. As a result, the potential at the front is lower than the HVE potential by the value of the voltage drop across the channel. Since the channel length increases with time, the front potential amplitude also decreases. For slow IW appearing at glow discharge ignition in long tubes, the attenuation is almost unstudied. This paper presents the results of experiments on the study of the above waves attenuation in long sealed tubes ($L$ = 40-80 cm, diameter: 1.5 cm) containing neon at pressures 0.6 - 30 Torr. An attempt was made to experimentally identify general patterns of this wave motion at a fixed HVE ($U_0$) voltage.

The IW was excited by applying rectangular voltage pulses of positive polarity to one of the discharge tube electrodes, while another electrode was not connected to the circuit. Under such conditions, only one ionization wave propagating from the anode was formed. Pulses were applied at a frequency 1 Hz, and the amplitudes thereof varied from the breakdown threshold up to 3.5 kV. The discharge tube was placed in a grounded cylindrical foil screen with a diameter of 6 cm. The dependences of the distance from the HVE was measured for the following parameters: the potential amplitude at the IW front ($\varphi_w$), the current

flowing from the front to the HVE, the time of IW travel, and the instantaneous velocity ($v_w$). The potential was measured by a calibrated capacitive voltage divider [3] that was placed into the screen split and could move freely above the tube surface over its entire length. The current was recorded by a shunt connected between the screen and its grounding point. Another capacitive divider installed near the HVE, was used to measure the time of the IW passage over a given tube section. The wave motion time was measured by time shifting of signals from both dividers. A separate experiment was carried out with both sensors positioned at a fixed distance and displaced along the tube; this resulted in obtaining the instantaneous IW velocity as a function of distance to the HVE.

Fig. 1 shows the *x*-*t* diagrams of attenuated IW, while Fig. 2 presents an example of $v_w(x)$ and $\varphi_w(x)$ dependencies. It can be seen from the graphs that the drop in velocity leading to *x*-*t* diagram curvature, is due to the decrease of the front potential and consequently also of the field strength. And precisely combination of these processes represents the IW attenuation.

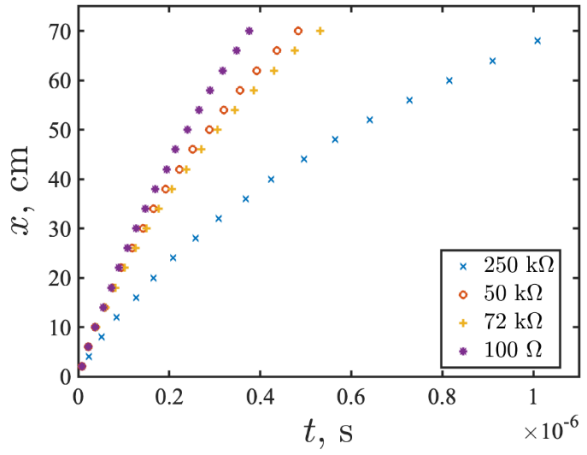



Fig.1. *X*-*t* diagrams of slow IW obtained with different limiting resistances in HVE circuit. Neon 3 Torr, $U_0 = 3$ kV

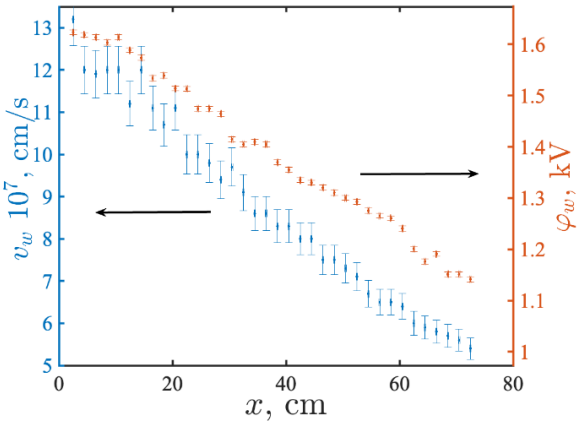



Fig.2. Dynamics of IW potential amplitude and instantaneous velocity along the discharge tube. Neon 3 Torr, $U_0 = 2$ kV, $R_b = 1$ kOhm.

The analysis has shown that *x*-*t* diagrams of non-stationary IW in our conditions yield power law with an index close to 2/3. Fig. 3 shows the diagrams linearization examples for different pressures and a single voltage, illustrating the power law. It has been found that the IW attenuation is enlarged both by an increase in pressure and by a limiting resistance in the HVE circuit (Fig. 1 and Fig. 3).

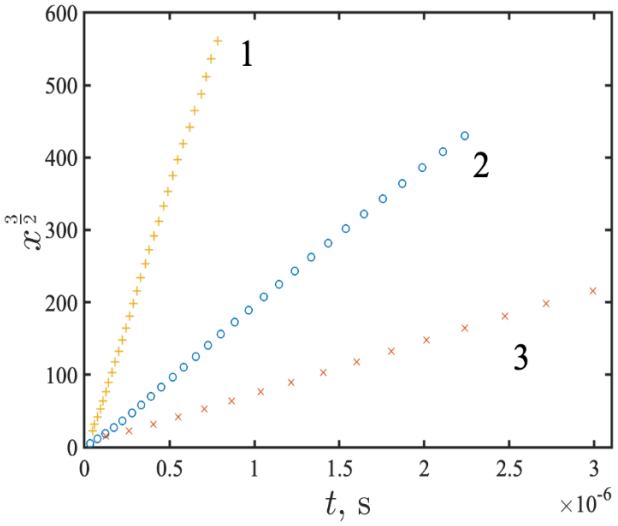



Fig.3. Examples of *x-t* diagrams linearization by a power law with index 2/3 at different neon pressures. (1) – 3 Topp, (2) – 10 Topp, (3) – 30 Topp. $U_0$ = 2 кВ.

The last result is related to the IW current limitation in the phase of its propagation. From the results of fig.2 it also follows that the wave velocity decreases almost linearly with the potential at its front.

The combination of these facts makes it possible to establish the law of IW motion based on the dimension theory. We shall take into account that to produce ionization, the wave consumes a certain energy, which must be replenished from an external source per unit time during which the front is displaced. Then the front movement does not depend on the voltage and current separately, but on their product, i.e. on the supplied electrical power, as well as on gas pressure. As a result, the law of wave motion can be formulated as:

$$x(t) = A\left(\frac{P_w}{p\tau}\right)^{\frac{1}{3}} t^{\frac{2}{3}} \qquad (1)$$

where $P_w$ is the power supplied to the front, $p$ is the gas pressure, $\tau$ is the characteristic time of potential establishment at the point, $A$ is a dimensionless constant. One of the (1) consequences is the similarity relation between power and pressure, as well as a certain relationship between the power and the IW motion time.

Fig. 4a and fig. 4b show the results of verifying the correlation (1) by measuring the dependence of IW time of movement in the given tube section on the input power at different pressures. In Fig. 4a, a fixed time is marked with a dotted vertical line, the points of the line intersection with the graphs are: 30 Torr - 179 W, 10 Torr - 60 W, 3 Torr - 15 W, which confirms the similarity relation $P_w/p$ within the low power measurement errors. The exception is the pressure of 0.6 Torr, which corresponds to the IW minimum attenuation and the maximum of its velocity. It is well known [4] that at the same voltage pulse amplitude, $v_w$ depends nonmonotonically on the gas pressure. There is a pressure at which the IW propagation velocity reaches its maximum. Fig.4b shows an approximately quadratic decrease in the wave motion time with an input power increase, as predicted by formula (1). However, in the pressure region to the left of the velocity

maximum (≈ 1 Torr), the obtained law is violated, in particular, here: $P_w \sim t^{-3}$. It is worth to note that expression (1) obtained from dimensional considerations can only be considered as an approximate result. However, the obtained law of motion makes it possible to compare waves under different conditions and indicates the presence of a similarity complex, which includes power, pressure, and time of charging of the tube wall unit length. The latter value is introduced into the formula for equalizing the dimensions, and it presumably should take into account the fact of the IW front interaction with the tube wall.

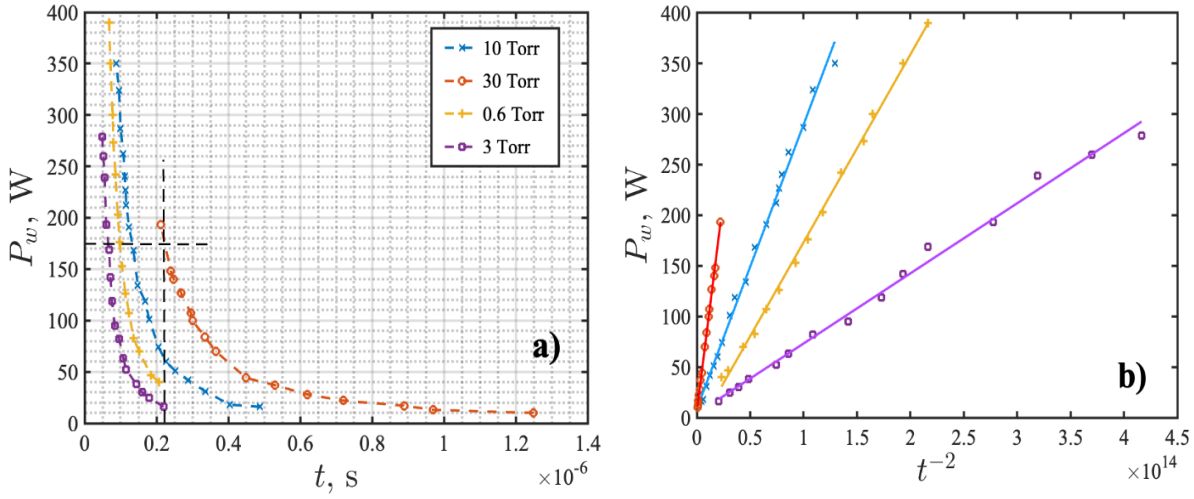



Fig.4. Dependences of the power supplied to the front on the time of IW arrival at the point $x_0$ = 14 cm from HVE and on the inverse square of this time demonstrating verification of the formula (1).

**References**


1. **Ionikh Yu. Z**. Plasma Physics Reports, 46 (2020) 1015-1044.
2. **Winn W.P.** Journal of Applied Physics, 38 (1967) 783.
3. **Klochko A.V., Starikovskaya S.M., Xiong Z., Kushner M.J.** J. Phys. D: Appl. Phys. 47 (2014) 365202.
4. **Vasilyak L. M., Kostuchenko S.V., Kudryavtsev N.N., Filugin I.V.** Physics – Uspehi (Advances in Physical Sciences), 164 No3 (1994) 263 - 286.

# LOW-VOLTAGE HIGH-CURRENT PULSED MAGNETRON DISCHARGE AS A SOURCE OF DENSE METAL-FREE PLASMA

A.V. Kaziev[1], D.V. Kolodko[1,2], N.P. Orlov[1], V.A. Tumarkin[1]

[1]National Research Nuclear University MEPhI (Moscow Engineering Physics Institute), 31 Kashirskoe sh., 115409 Moscow, Russia, kaziev@plasma.mephi.ru
[2]Kotelnikov Institute of Radioengineering and Electronics RAS, Fryazino Branch, 1 Vvedenskogo str., 141190 Fryazino, Russia

Today, a lot of practical applications demand utilizing efficient sources of highly ionized metal-free plasmas. One of the ways to produce such plasmas is to use high-power pulsed magnetron discharges. However, since they are usually considered for sputtering and thin film deposition processes [1], less attention is drawn to the low-voltage regimes of operation [2–5], which could potentially be suitable for production of metal-free plasmas with high ionization degree.

Here, the operation of millisecond-scale pulsed low-voltage (50–100 V) magnetron discharge in hydrogen was examined. The maximum pulse power was around 80 kW. Plasma parameters were monitored with an electric probe, while the plasma composition was evaluated by an optical emission spectrometer. Experimental setup scheme is shown in Fig. 1.

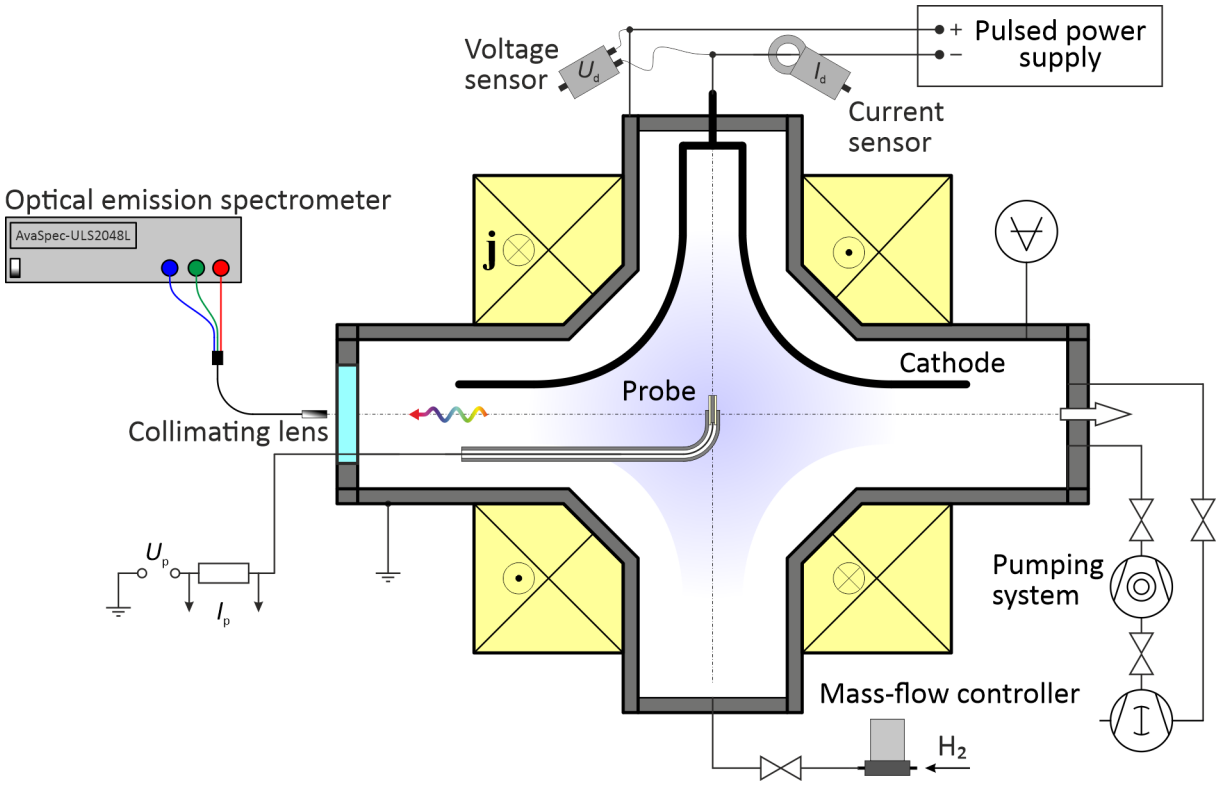



Fig. 1. Experimental setup scheme

The low-voltage discharge modes can be completely diffuse, however as a rule they exhibit transition into arc after several or tens of milliseconds. The arcing is preceded by an intermediate diffuse-constricted mode. The corresponding discharge plasma images are shown in Fig. 2.

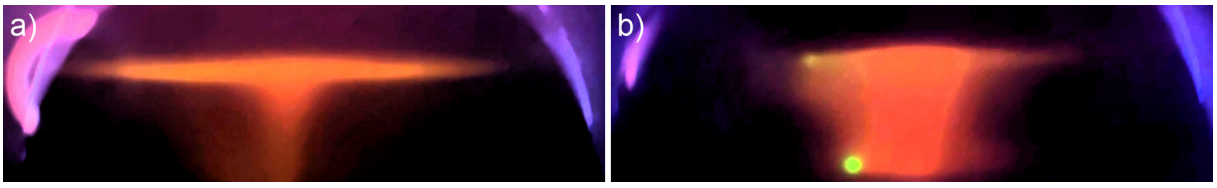



Fig. 2. Side images of the discharge taken with an optical filter: a) diffuse mode; b) transient diffuse-constricted mode before arcing

The optical emission spectra of a constricted arc in hydrogen is shown in Fig. 3. The integration time was 1.05 ms.

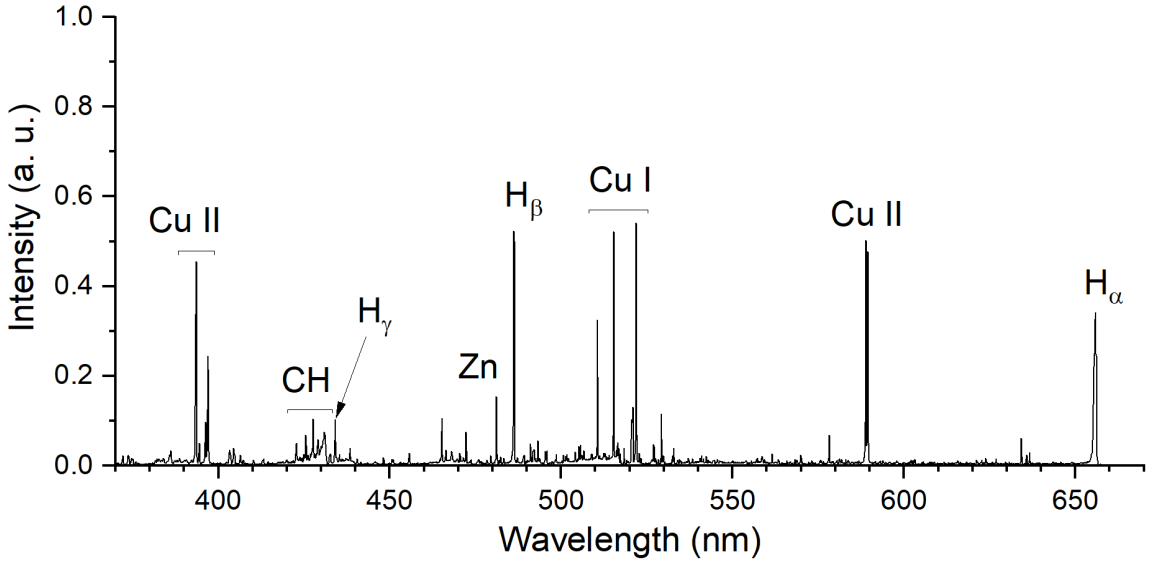



Fig. 3. Optical spectrum of a constricted arc

Because of high pulsed power (tens of kW) concentrated in small spots, such arcs inflict visible damage to the cathode surface, and their optical emission spectra contain strong metal lines.

The optical emission spectra recorded in diffuse non-sputtering mode is shown in Fig. 4. Unlike the spectrum of an arc, this one only contains lines that correspond to hydrogen working gas (except traces of CH, which are probably due to decomposition of uncooled polymer insulator materials). This is in accord with the results previously obtained for lower power values and/or for other gas mixtures [2, 3].

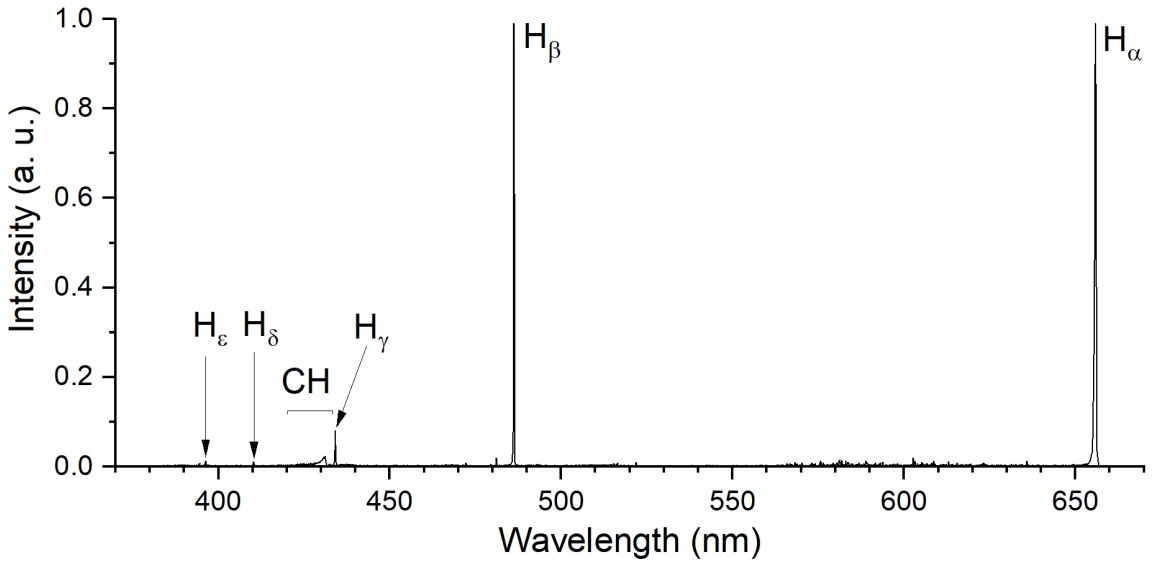



Fig. 4. Optical spectrum of a low-voltage non-sputtering diffuse discharge

The maximum measured plasma density of a high-current pulsed magnetron discharge in hydrogen was $1.8\times10^{20}$ $cm^{-3}$ at an average discharge current of 1200 A. The current per probe was 0.9 A. The degree of ionization in this case was about 20%.

The results indicate that the non-sputtering magnetron discharge can be considered as a prospective source of metal-free plasma. On the other hand, the physical mechanisms of millisecond-scale sustaining of the diffuse plasma in discussed conditions are not well understood and require further investigation.

**Acknowledgements.** The work was supported by the Russian Federation President grant no. MK-4445.2022.4.

## References

1. **Gudmundsson J.T., Brenning N., Lundin D., Helmersson U.** J. Vac. Sci. Technol. A, 30 (2012) 030801.
2. **Khodachenko G.V., Mozgrin D.V., Fetisov I.K., Stepanova T.V.** Plasma Phys. Rep., 38 (2012) 71.
3. **Kaziev A.V.** Vacuum, 158 (2018) 191.
4. **Sommerer T.J., Aceto S.C., Trotter J.F. et al.** J. Phys. D: Appl. Phys., 52 (2019) 435202
5. **Smith D.J., Sommerer T.J., Lawler J.E., Hitchon W.N.G.** J. Phys. D: Appl. Phys., 54 (2021) 295201

# 3. ATMOSPHERIC PRESSURE PLASMAS, PLASMA IN AND IN CONTACT WITH LIQUID, PLASMA-LIQUID INTERACTIONS

# DECOMPOSITION OF $CO_2$ IN A MICROWAVE DISCHARGE IN LIQUID HYDROCARBONS

Yu. A. Lebedev[1], T.S. Batukaev[1], G.V. Krashevskaya[2], I.V. Bilera[1]

[1]Institute of Petrochemical Synthesis named after. A.V. Topchiev RAS, Leninsky prospect 29, 119991, Moscow, Russia, E-mail: batukaev@ips.ac.ru
[2]National Nuclear University "MEPhI", Kashirskoe highway 31, 115409, Moscow, Russia.

In recent years, much attention has been paid to the problem of global warming. One part of this problem is related to $CO_2$ emissions into the Earth's atmosphere. $CO_2$ emissions resulting from the combustion of fossil fuels (coal, natural gas and oil) in energy and transport have a negative impact on human life.

Currently, many studies are being carried out on energy-efficient $CO_2$ conversion technologies, such as thermal catalysis, electrocatalysis, photocatalysis, bioelectrocatalysis, etc. Among them, a special place is occupied by the method of plasma-chemical decomposition of $CO_2$ using a weakly ionized low-temperature plasma of gas discharges and hybrid methods with the simultaneous use of plasma and catalytic/photocatalytic materials.

Various types of gaseous electrical discharges are used to decompose $CO_2$: direct current discharges, HF, microwave discharges, barrier discharge. There is practically no information about such processes implemented in a microwave discharge in liquid hydrocarbons [1]. At the same time, this discharge has a number of advantages in relation to the $CO_2$ decomposition process. First, the discharge is surrounded by a liquid with a temperature not exceeding the boiling point of the liquid whose vapor enters the discharge. This ensures a high rate of quenching of the products (in the case of $CO_2$ decomposition, this is important to suppress the reverse reaction leading to the formation of $CO_2$). Second, it is known that the addition of hydrogen and methane to a discharge with $CO_2$ leads to the removal of the formed oxygen and to an increase in the degree of decomposition of $CO_2$ [2]. These products are produced in microwave discharges in liquid hydrocarbons [1]. All this arouses interest in experiments on the decomposition of $CO_2$ in a microwave discharge in liquid hydrocarbons.

The measurements were carried out using Nefras C2 80/120 petroleum solvent as a liquid medium. Petroleum solvent Nefras C2 80/120 is a mixture of light hydrocarbons with a boiling point of 33 to 205 ° C. This solvent can be considered as a representative of non-polar liquid alkanes ($C_nH_{2n+2}$). Our previous study showed that the emission spectra and composition of the main gaseous products in Nefras are the same as for other non-polar hydrocarbons [1]. One of the products of discharge in hydrocarbons is a solid carbon-containing

phase, which absorb microwave radiation, reduces its transparency and limits the duration of the long-term existence of the discharge.

To suppress the soot formation process, experiments were carried out with argon bubbling through a channel in the antenna. In the experiments, the argon flow was mixed with $CO_2$. The gas mixture flow rate was constant and equal to 0.6 l/min, the $CO_2$ concentration in the mixture was 10 and 5%.

At the outlet of the reactor, the flow rates of the products were determined using a flow meter. The content of $CO_2$ in the initial mixture, as well as the composition of the main gas products of the discharge at the reactor outlet, were determined by chromatographic analysis.

The degree of decomposition of $CO_2$ α(%) is determined by the formula:

$$\alpha(\%) = \left(1 - \frac{Q_{out}^{CO_2}}{Q_{in}^{CO_2}}\right), \quad (1)$$

where $Q_{in}^{CO_2}$ and $Q_{out}^{CO_2}$ are the flow rates of $CO_2$ [ml/min] at the inlet and outlet of the reactor.

Chromatographic analysis of the products at the outlet of the reactor showed that the main products of the gas phase are $H_2$, $C_2H_2$, $C_2H_4$, $CH_4$, $CO_2$, CO. No oxygen was found in the products.

Figures 1 and 2 show the dependence of the degree of $CO_2$ decomposition on the incident microwave power and the dependence of the $H_2$ volumetric flow rate at the reactor outlet on the incident power for different initial concentrations of $CO_2$ in the mixture. It can be seen that the degree of $CO_2$ decomposition increases with an increase in the incident microwave power and with a decrease in the $CO_2$ concentration at the reactor inlet. It can also be seen that the rate of $H_2$ formation increases as the concentration of $CO_2$ in the mixture at the reactor inlet decreases. Together with the absence of oxygen in the gas mixture at the reactor outlet, this can be explained by the consumption of hydrogen formed in the discharge in reactions with oxygen formed during the decomposition of $CO_2$. This agrees with the results of [2].

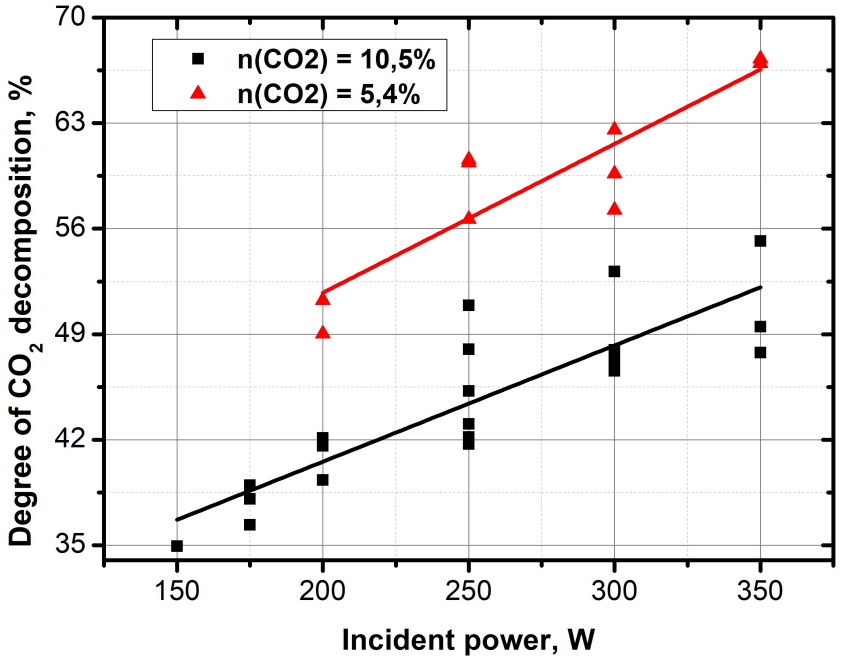



Fig. 1. Dependence of the degree of $CO_2$ decomposition on the incident microwave power at different initial concentrations of $CO_2$ in the mixture

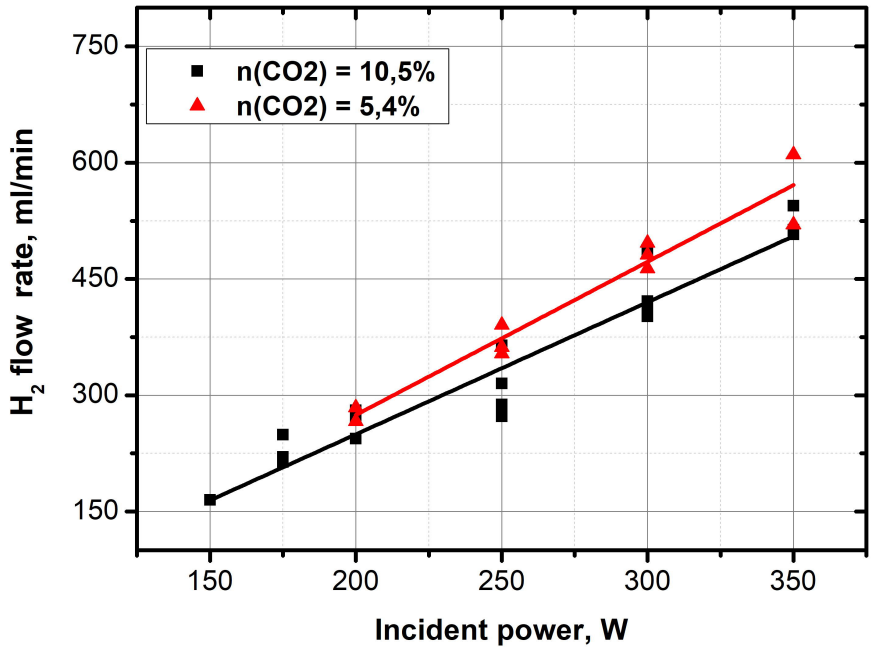



Fig. 2. Dependence of the $H_2$ flow rate at the reactor outlet on the falling power at different initial concentrations of $CO_2$ in the mixture

As a result of a chromatographic study of gas products at the outlet of the reactor with a microwave discharge in liquid Nefras during $CO_2$ bubbling, it was shown that the degree of $CO_2$ decomposition reaches 70%. The first experiments showed the perspective of using this method for the decomposition of $CO_2$.

**Acknowledgements.** The work was carried out within the framework of research under the grant of the Russian Science Foundation No. 17-73-30046.

## References

1. **Lebedev Yu. A.** Microwave Discharges in Liquid Hydrocarbons: Physical and Chemical Characterization, 13 (2021) 1678.
2. **R. Aerts, R. Snoeckx, A. Bogaerts.** In Situ Chemical Trapping of Oxygen in the Splitting of Carbon Dioxide by Plasma, 11 (2014) 985.

# SYNTHESIS AND PHOTOVOLTAIC APPLICATION OF MIXED TUNGSTEN-MOLYBDENUM AND TUNGSTEN-TITANIUM OXIDES NANOPARTICLES OBTAINED USING PULSED UNDERWATER PLASMA

N. Sirotkin[1], A. Khlyustova[1], V. Titov[1]

[1]G. A. Krestov Institute of Solution Chemistry, Academicheskaja, str., 1, Ivanovo, Russia 153045, e-mail: alexsad8@yandex.ru

With the development of science and technology, the living standards of human beings continue to improve, and the demand for energy is also greatly increased. In order to solve this problem, looking for efficient solar energy conversion materials to manufacture high-performance solar panels has become the focus of today's research. In recent years, due to the low cost, easy manufacturing and environmental friendliness of dye-sensitized solar cells (DSSC), many researches have been conducted on them [1]. Mesoporous $TiO_2$ has been successfully used as an electron transport material in DSSC. In addition to the common $TiO_2$ photoanode, other metal oxides such as $Nb_2O_5$, $MoO_3$ and $WO_3$ are also used as photoanode mesoporous layers [2]. Molybdenum oxide and tungsten oxide are good candidates for replacing $TiO_2$ due to their favorable optical and electrical properties. To change the electronic properties of pure metal oxides, doping can be used or heterostructures can be created. At present, a branch of research is based on the research of molybdenum-tungsten oxide or titanium-tungsten oxide composite materials. The mixed nanocomposite material composed of titanium and molybdenum oxide was synthesized uses low temperature by underwater discharge plasma [3]. Mo and Ti electrodes are used as oxide sources. TEM analysis indicated the presence of a heterostructure. The use of low-temperature underwater plasma is a promising method for the reagent-free synthesis of bimetal oxide composite materials. In the synthesis of nanoparticles using underwater plasma the control over the composition can be achieved by an appropriate choice of electrode materials and discharge polarity.

In this work we prepare mixed nanostructures based on tungsten, molybdenum and titanium oxides by pulsed underwater plasma. The change of discharge polarity will make it possible to obtain composite materials with different compositions. After that, we manufacture DSSC based on mixed bimetallic oxides nanoparticles.

The experiment was carried out in a plasma cell with a fixed solution volume of 200 mL and a flat optical quartz window. In the experiment, 1 mm diameter tungsten, molybdenum and titanium rods were used as electrodes. Metal rods (W-Mo or W-Ti) are placed in a ceramic tube in pairs. The non-

isolated length of the electrode is 2.5 mm. The electrodes were immerse in distilled water at a distance of 3 mm. The underwater DC plasma was igniting between the electrodes in the water. The details of the experiment are described in our previous work [3]. Four series of experiments were carried out (Table 1). We use a self-made power supply DC with an output voltage of up to 10 kV and a ballast resistance of 0.5 kOhm to stimulate the discharge. The average discharge current value is 0.25 A. The spectrum of the aqueous suspension was analyzed by a spectrophotometer SF-56. Dynamic Light Scattering (DLS) is used to monitor particle diameter and measure the electrophoretic mobility of nanoparticles, and then convert the obtained value into zeta potential. The phase composition of obtained bimetallic oxide nanoparticles was analyzed by X-ray diffraction. The surface morphology of mixed oxides nanoparticles was obtained with the scanning electron microscopy (SEM) and transmission electron microscopy (TEM). The chemical composition was obtained with X-ray energy dispersive spectroscopy. The characteristics of dye-sensitized solar cells were measured in the air using a fiber-optic illuminator OV-12 (LLC Lomo, Russia) equipped with a 150 W visible and near UV lamp allowing measurements under illumination 15 mW/cm$^2$. The volt-current characteristics were recorded using a potentiostat P-20X. For the investigation of the photovoltaic properties of obtained bimetallic oxide nanoparticles the dye-sensitized solar cells were fabricated.

The synthesis of nanoparticles of mixed oxide nanoparticles takes place in the plasma of an underwater discharge. The discharge plasma causes the temperature of the electrode tip to locally increase to thousands of degrees Celsius. As a result, the metal electrode evaporates. Depending on the polarity of the electrode, the surface will be bombarded by positive ions or electrons from the plasma zone, which have the energy to atomize the electrode material. The atomized metal enters the plasma zone where the metal atoms are converted in an active form. The atoms interact with OH particles to form oxides. Further the processes of agglomeration occur for the synthesized nanoparticles.

The EDS analysis showed oxygen, tungsten, molybdenum and titanium signals only for all samples. But the percentage between the elements depends on the electrodes configuration used. The sputtering rates of the anode are always higher than the sputtering rates of the cathode in all cases. The total yield of oxide nanoparticles is about 0.5 g/h. The tungsten content in the sample is more than 70% when using a W rod as the anode. The ratios W:Mo or W:Ti are close to 1:1 when molybdenum or titanium rods used as the anodes. The phase and crystal structure of the obtained mixed oxide nanoparticles were examined by X-ray diffraction (XRD) analysis. The peaks γ-monoclinic $WO_3$ were recorded on the diffraction patterns. The characteristic diffraction line corresponds to the monoclinic $MoO_2$ phase was recorded on the XRD pattern of

Sample 1. The Sample 2 contains a mixture of molybdenum oxides according to the XRD analysis results. The XRD patterns of Samples 3 and 4 contain lines associated to titanium dioxide. It should be noted the presence of peaks related to the two polymorphic phases of an atase and rutile.

Molybdenum, tungsten and titanium oxides are the n-type semiconductors with polycrystalline nature. The band gap values were obtained from the absorption spectra of aqueous suspensions containing nanoparticles. The smallest values of the band gap are typical for Sample 2 containing non-stoichiometric molybdenum oxide (Table 1). The band gap values are lower than for pure tungsten oxide (3.11) or non-stoichiometric molybdenum oxide (3.31 eV). Low values of the band gap are characteristic of mixed oxide particles and can prove the presence of heterostructures [4]. In the case of mixed oxides of tungsten and molybdenum, the particle size does not exceed 150 nm (Table 1). The particle size distribution of the mixed particles of tungsten and titanium dioxide is bimodal, and the maximum value is around 65 nm and 160-180 nm. The zeta potential of the obtained tungsten-molybdenum mixed oxide nanoparticles is about -27 mV. The zeta potential of the tungsten-titanium composite oxide particles is about -15mV, which indicates the ability of nanoparticles to agglomerate. Figure 2 shows the SEM image of the sample. For samples 1, 2, and 3, the particles with a size of 140-170 nm have the form of spheres. The image shows agglomeration of the powder, but the particle size seems to be in the same order of magnitude as the DLS result. For Sample 4, the particles are plate-shaped with spherical inclusions. The large spherical particles correspond to pure tungsten oxide. The SEM analysis data confirmed the bimodal distribution of particles found in Samples 3 and 4. High-magnification TEM images show that the particles are composed of crystallites of different oxides and the presence of heterostructures can be clearly detected.

The photovoltaic parameters of DSSCs prepared by photoanode prepared from different nanoparticle samples obtained from underwater plasma are summarized in Table 2. It can be clearly seen that the DSSC made from Sample 2 containing mixed tungsten oxide and molybdenum oxide nanoparticles shows the best performance. The reasons for this advantage are higher short-circuit current ($J_{SC}$) and good electronic properties. The DSSC fabricated with Sample 2 showed higher open-circuit voltage ($V_{OC}$), indicating better performance of the cell in terms of electron transport and fill factor (FF) improvement. In this way, pure tungsten oxide has suitable electron transport properties, and electron lifetime and recombination are affected due to the presence of surface defects. On the other hand, titanium oxide and molybdenum oxide with lower charge transport and better dye absorption may be effective. Therefore, the combination of these materials will significantly improve the performance of DSSCs including power conversion efficiency (PCE).

Table 1. The characteristics of aqueous suspensions of nanoparticles.

| | Experimental conditions | $E_g^{dir}$, eV | $E_g^{indir}$, eV | Average diameter, nm | Zeta potential, mV |
|---|---|---|---|---|---|
| Sample 1 | W-anode Mo-cathode | 3.54 | 3.93 | 142 | -26.6 |
| Sample 2 | W-cathode Mo-anode | 2.97 | 3.30 | 118 | -27.9 |
| Sample 3 | W-anode Ti-cathode | 3.82 | 3.89 | 62/194 | -14.8 |
| Sample 4 | W-cathode Ti-anode | 2.99 | 3.79 | 68/148 | -16.3 |

Table 2. The photovoltaic characteristics of DSSCs based on different bimetallic oxides nanoparticles

| | $V_{OC}$, V | $J_{SC}$, mA cm$^{-2}$ | $P_{max}$, mW | FF | PCE, % |
|---|---|---|---|---|---|
| Sample 1 | 0.641±0.008 | 1.51±0.12 | 0.42±0.05 | 0.73±0.03 | 1.42 |
| Sample 2 | 0.595±0.012 | 4.82±0.18 | 1.23±0.08 | 0.51±0.02 | 4.11 |
| Sample 3 | 0.598±0.011 | 1.66±0.09 | 0.51±0.06 | 0.42±0.02 | 1.75 |
| Sample 4 | 0.567±0.009 | 3.89±0.13 | 0.93±0.07 | 0.55±0.03 | 3.12 |

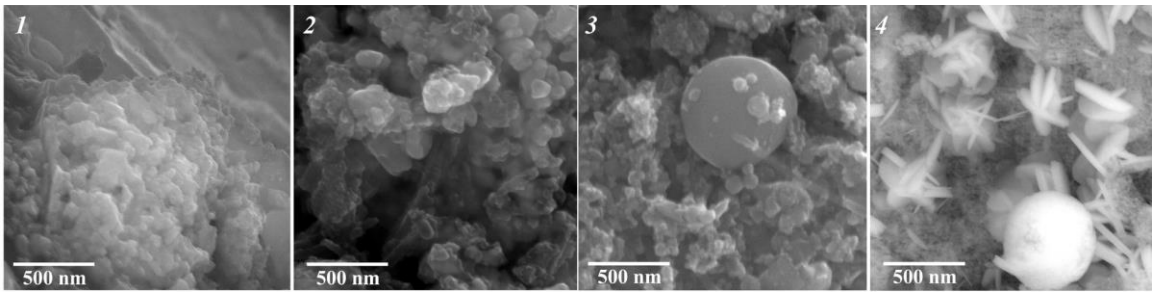



Fig. 1. SEM images of nanoparticles.

**Acknowledgements**. This work is supported by the Russian Science Foundation under grant 21-73-00034. The authors thank Dr. N. Fomina for performing the XRD analysis and SEM analysis.

## References

1. **Marimuthu T., Anandhan N., Thangamuthu R.,** J. Mater. Sci., 53 (2018) 12441.
2. **Zheng H., Tachibana Y., Kalantar-Zadeh K.**, Langmuir, 26 (2010) 19148-19152.
3. **Khlyustova A., Sirotkin N., Titov V., Agafonov A.,** J. Alloys Comp. 858 (2021) 157664.
4. **Khan A. Q., Yuan S., Niu S., Zheng L., Li W., Zeng H.**, Optics Exp., 25 (2017) A539.

# LIQUID ANODE METHOD AS A METHOD FOR THE FORMATION OF SPHERICAL METAL PARTICLES

YU.S. Baryshnikov[1], R.O. Kurakin, K.V. Tverdokhlebov, A.V. Chikiryaka, S.A. Poniaev

[1]Ioffe Institute, Saint-Petersburg, Russia, iulianbaryshnikov@yandex.ru

Currently, there are various methods for obtaining spherical metal particles [1]. The difference between different methods are in the field of technology needs, where one method of obtaining is more preferable than another depending on the chosen metal, the possibility of obtaining strictly specified ranges of the geometric dimensions of the sphere, energy costs, and in general manufacturability. In our study, in addition to the well-known method of electrical exploding wire method (EWM), we will consider the use of a liquid anode (LA) as a method for obtaining spherical particles. In the two methods under consideration, the main difference is the difference in the discharge currents, for example, with EWM, the discharge current was tens of kiloamperes at a discharge voltage of kilovolts (current density up to $10^8$ A/m$^2$); and for LA method electrical parameters are smaller (current density up to $10^3$ A/m$^2$), but in both cases spherical particles were obtained. In this work, we studied the production of particles on different metals: stainless steel, iron, zirconium, galvanized iron, titanium, tungsten, nickel-chromium, copper, tin [2]. It is worth noting that the liquid anode method is structurally close to such a method as the liquid cathode method, which is characterized by a higher discharge energy (electrical parameters of the described liquid cathode method [3]: 300-1000V, 100-500A).

The commonality of the processes of the presented EWM and LA methods is that they arise due to the passage of current, the scattering of metal droplets and their rapid cooling in the environment (Fig. 1, Fig. 2).



Fig.1. The process of droplet scattering in the EWM method.

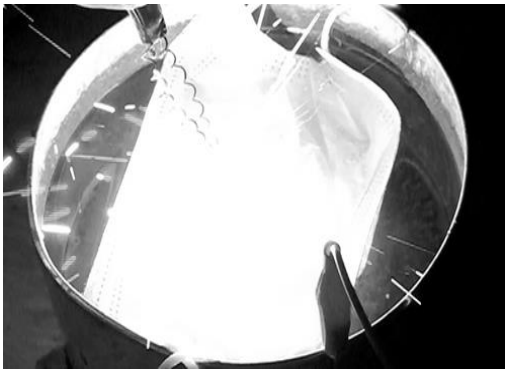


Fig.2. The process of droplet scattering with the LA method.

The difference, in addition to a significant difference in current density ($10^8$A/m$^2$ versus $10^3$ A/m$^2$ according to the maximum value), also consisted in the experimental design, with EWM (Fig. 5), the conductor was placed between two brass rods, which were the electrodes of a high-voltage battery, anda pulsed current was passed through it (Fig. 3, Fig. 4).

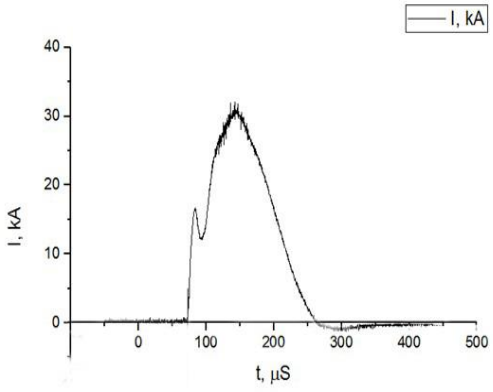



Fig.3. Discharge parameters during EWM, current.

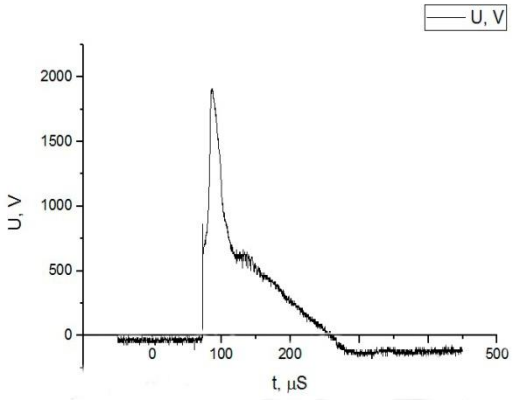



Fig.4. Discharge parameters during EWM, voltage.

In the LA method, the cathode wire was periodically lowered with its sharp end into the liquid anode (conductive container with a solution of water and sodium chloride) until the formation of metal scattering from the electrode (Fig. 6).

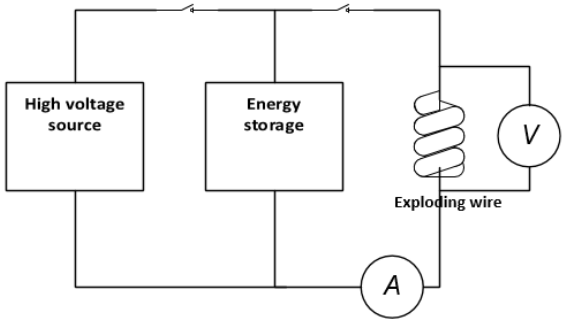



Fig.5. Scheme of the device with EWM.

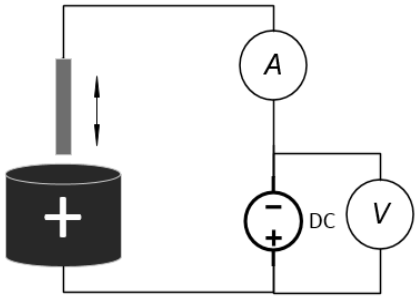



Fig.6. Scheme of the device with LA.

In these processes, particles of an ideal spherical shape were mainly obtained. But with EWM, more particles of non-ideal shape (with chips and deviations from sphericity) were obtained comparing with particles obtained by LA method. Figs. 7 and 8 show the results of experiments with a galvanized iron conductor with a diameter of 0.8 mm, with EWM and LA, images were obtained using a Phenom ProX scanning electron microscope. The main diameter of the obtained spherical particles in both cases is 15-150 microns.

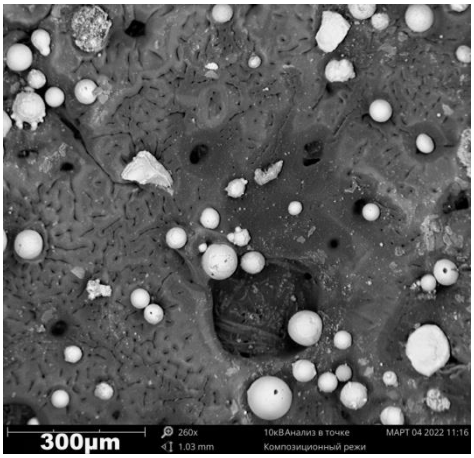



Fig.7. EWM spherical particles, galvanized iron.

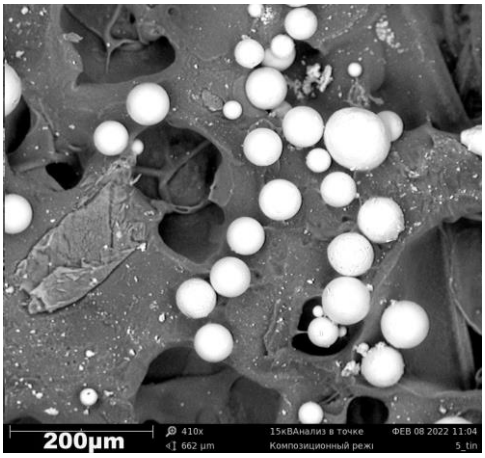



Fig.8. Spherical particles obtained by LA, galvanized iron.

The chemical composition of the particles was in the case of iron oxide, Table 1 and 2 show the chemical composition measured by Phenom ProX scanning microscope.

Tab. 1. Chemical composition of a spherical particle during EWM

| Element Symbol | Atomic Conc. | Weight Conc. |
|---|---|---|
| O | 80.16 | 54.29 |
| Fe | 19.20 | 45.38 |

Tab. 2. Chemical composition of a spherical particle in LA

| Element Symbol | Atomic Conc. | Weight Conc. |
|---|---|---|
| O | 57.50 | 27.93 |
| Fe | 42.50 | 72.07 |

For copper, the results for sphericity with EWM and LA turned out to be different. In the case of EWM, they were obtained in an approximately spherical shape; for LA, the shape of particle sphericity was generally not observed, Fig. 9-10. Images of powder particles were obtained on an Altami MET 5 optical microscope with an Altami USB 3150R6 1/2CMOS camera, followed by processing in Altami Studio 3.5 software.

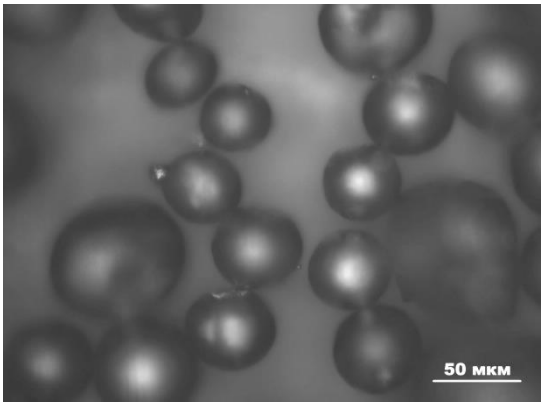



Fig.9. Particles obtained by EWM, copper.

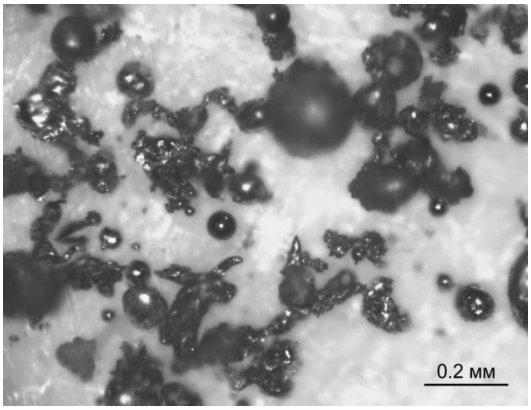



Fig.10. Particles obtained with LA, copper.

## CONCLUSION

From the point of view of practical implementation, the LA method seems to be simpler, not only in comparison with the EWM, but also with other currently existing methods for obtaining spherical particles. The LA method is less energy-intensive than the liquid cathode method, because in the LA method positive ions fly onto the wire-electrode. The resulting range of spherical particles of 15-150 μm with LA is of interest for additive technologies, as well as other technologies. As part of experiments with the LA method, it was shown that it can be used to obtain spherical particles from various materials, such as iron, stainless steel, titanium, while for tungsten and copper materials, the results are currently unsatisfactory due to the presence of a large number of non-spherical particles.

## References

1. **Rodionov A. I., Efimochkin I. Yu., Buyakina A. A., Letnikov M. N.** Spheroidization of metal powders (review) // Aviation materials and technologies. 2016 No. 1 P. 60–64
2. **Baryshnikov Yu.S.** et al Sfereoziciya metallicheskih chasticz s pomoshh`yu zhidkogo anoda // Innovacionny`e materialy` i texnologii : materialy` Mezhdunar. nauch.-texn. konf. molody`x ucheny`x, g. Minsk, 23–24 marta 2022 g. – Minsk : BGTU, 2022 S. 98-101 (In Russian)
3. **Kashapov R. N.** et al 2021 J. Phys.: Conf. Ser. 1923 012025 https://doi.org/10.1088/1742-6596/1923/1/012025

# DIRECT OXIDATION OF BENZENE TO PHENOL IN LOW-TEMPERATURE BAARRIER DISACHARGE PLASMA: INFLUENCE OF REACTOR TEMPERTURE

A. Leshchik[1], S. Kudryashov[1]

[1]Institute of Petroleum Chemistry, Siberian Branch of the Russian Academy of Sciences, Tomsk, Russia, E-mail: ms.leshchzchik7@gmail.com

Phenol is one of the product of large-volume organic chemical industry. In Russia the production of phenol increased to 238000 t/y in 2020 [1]. The main method of phenol production is the oxidation of cumene to cumene hydroperoxide which is enabled at temperature of 130 °C in the presence of liquid catalyst following the decomposition into acetone and phenol in equimolar amount [2]. This method has commercial problem which results from a market necessity for acetone and phenol.

There are another industrial methods for obtaining phenol but they also have some shortcomings (low benzene conversion, high concentration of by-products, difficult process) [3].

Nowadays it is desirable to obtain chemicals by more efficient and environmentally methods. Thus there is a great demand to develop commercially available processes and to elaborate novel procedures of obtaining basic substances, which answer requirements of “green” chemistry.

There is in particular promising direct oxidation of benzene to phenol by means of selective catalytic methods and plasma-chemical manners in non-thermal discharge plasmas, for instance dielectric barrier discharge (BD), as well [4].

In this communication we provide some experimental results on the direct one-stage oxidation of benzene to phenol in the barrier discharge plasma-chemical reactor carried out under some temperatures in 20-40 °C region.

The discharge is excited between the coaxial electrodes being fabricated from borosilicate glass “Pyrex”. High voltage pulses with ~10 kV peak amplitude and 400 Hz pulse repetition frequency is applied to the high voltage electrode. Active discharge power is equal to 1.8 W. The temperature of plasma reactor walls is changed from 10 to 40 °C. Volumetric flow rates are 60 mL/min for air and 0.3 mL/min for benzene. Residence time of the initial mixture in the reactor is 10.5 s.

Oxidation of benzene by air in BD results in a formation of a mixture which composed of liquid substances (87 %wt) and polymer-liked components. Polymer-liked components are composed as a non-soluble in benzene particles which are deposit on the walls of the product container.

Liquid products of the process of the oxidation of benzene in BD is

examined using the gas chromatography (HP 6890). A chemical structure of the polymer-liked components is confirmed by NMR (Bruker AVANCE AV300), IR (Nicolet 5700), UV/Vis(UVIKON 943), and element (Vario EL Cube) analysis

Surface and size of depositing particles are investigated by electronic microscope (Quanta 200 3D). A weight of dried polymer-like components is measured by digital lab analytical balance (Sartorius RC 210P).

Conversion of benzene is calculated by the formula:

$$X=M_{prod}/M\times 100\%, \quad (1)$$

Where $M_{prod}$ is the mass of reaction products in mg, $M$ is the mass of the initial benzene in mg.

The content of reaction products in the final product mixture is counted by the expression:

$$S=M_i/M_{prod}\times 100\%, \quad (2)$$

Where $M_i$ is the mass of the $i$-th product of the reaction in mg, $M_{prod}$ is the mass of reaction products in mg.

Energy consumption for the transformation of initial benzene is determined by the formula:

$$P=(W\times t)/M_{prod}, \quad (3)$$

Where $W$ is the active discharge power in W, $t$ is the time of experiment duration in s.

Procedure of the assumption of the discharge parameters and account of active discharge power are described in [5] in detail.

Accordingly the analysis of the reaction product mixture it is established that the main components of the liquid part of the reaction mixture are largely phenol and some dihydric phenols (pyrocatechol, hydroquinone).

The selectivity of formation of phenol is reached 77.3 %wt.. Selectivity of dihydric phenols, mainly hydroquinone, does not exceed 3.4 %wt.

When insoluble particles precipitate on the reactor walls they make into the deposit which arrangement is composed of spherical grains with a diameter 1-5μm. Its molecular structure is examined to contain phenolic and carbonyl functional groups as well as phenoquinone and polyhydroquinone in its configuration.

In the indicated temperature region the conversion of benzene increases from 0.4 to 0.5 %wt which corresponds to energy consumption for benzene of 30 and 25 kW·hr/kg.

At the lowest temperature the content of dihydric phenols is larger than one at the highest temperature (Fig. 1).

In particularly the content of hydroquinone at 40 °C has increased four times comparatively the temperature of 10 °C.

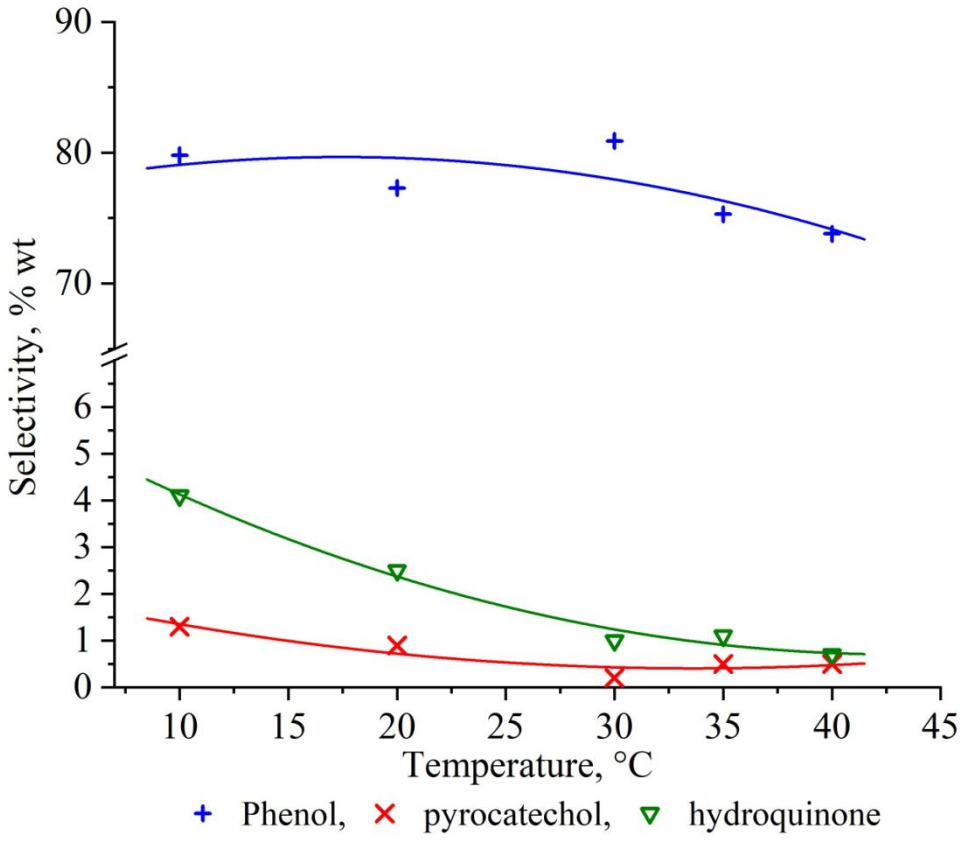



Fig.1. The effect of reactor temperature on selectivity for main products of the oxidation of benzene by air in BD

The analysis of the obtained results of the oxidation of benzene by air in BD and the information in literature on transformations of organic compounds in the BD plasma allow us to suggest a probable process reaction mechanism. The formation of phenol we suppose to occur as a result of the addition of atomic oxygen, forming by electron impact in BD, to the double bond of the molecule of benzene.

Reached results demonstrate an advisability of employing the temperature for controlling the process, and also show a feasibility of elaboration of novel environmentally friendly processes for phenol production from benzene using non-thermal plasmas of various discharges, for example BD.

**Acknowledgements.** The work was funded by the Ministry of Science and Higher Education of the Russian Federation, project no. FWRN-2021-0003.

## References

1. Phenol market in Russia. URL: https://alto-group.ru/otchot/rossija/445-rynok-fenola-tekushhaya-situaciya-i-prognoz-2015-2019-gg.html.
2. **Ascenzi D., Franceschi P., Guella G., Tosi P.** The Journal of Physical

Chemistry. A., 110 (2006) 7841–7847.
3. **Koshel G.N., Kurganova E.A., Frolov A.S., Rybina G.V., Lebedeva N.V., Kabanova V.S.,** Neftegaz, 2 (2022) 20–23.
4. **Kudryashov S.V., Rybov A.Yu., Sirotkina E.E., Shchegoleva G.S.** High Energy Chemistry, 34 (2000) 145–148.

# THE POSSIBILITY OF USING A GAS DISCHARGE WITH A LIQUID ELECTROLYTE CATHODE TO CREATE A STEAM-WATER PLASMA FLOW

G. Tazmeev[1], B. Timerkaev[2], Kh. Tazmeev[1]

[1]Kazan Federal University, Naberezhnye Chelny Institute, 68/19, prospekt Mira, Naberezhnye Chelny, 423812, Russia. gktazmeev@kpfu.ru
[2]Kazan National Research Technical University named after A. N. Tupolev. 10, K. Marx Street, Kazan, 420111, Russia.

Gas discharges with liquid electrolyte electrodes have great potential for practical applications. They are promising for use in water disinfection technologies, synthesis of various functional materials, plasma activation of liquid reagents, and other areas of industrial activity. In high-current regimes, a significant amount of matter enters the plasma column from the liquid cathode. The discharge burns in a vapor-gas medium. It becomes possible to create a plasma flow that is acceptable for energy-intensive technologies. For example, the work [1] shows the acceptability of a gas discharge with a liquid electrolyte cathode for processing waste polymer materials. However, methods for generating powerful plasma flows in gas discharges with liquid electrolyte electrodes are still far from perfect. There are questions related to the choice of electrolyte, the design of the plasma generator, the introduction of reagents into the plasma, etc.

To the choice of electrolyte.

With prolonged discharge burning, the aqueous solution used as a liquid electrolyte cathode decreases. The aqueous solution is partially spent on the formation of the plasma flow. An additional amount of aqueous solution is required. In this case, it is desirable to keep the electrophysical parameters of the solution unchanged. If they remain unchanged, then there is no need to adjust the discharge current, and the electric power of the discharge device will not change.

In the simplest version, distilled water can be added instead of a solution. This option has been tested experimentally. The essence of the experiments was as follows. In the hydraulic system, the volume of the aqueous solution was kept constant ($V_s$ = const). Distilled water was added continuously. After adding a certain amount of water, a sample was taken and the specific electrical conductivity of the aqueous solution σ was measured.

Figure 1 shows the results obtained for various aqueous solutions. They are prepared with the same concentrations. Relative values are plotted along the axes. Horizontally - the ratio of the amount of distilled water to the total volume of the aqueous solution. On the vertical - the ratio of electrical conductivity to its

initial value. This ratio varies for different electrolytes in different ways. For some it decreases, and for others it increases. In the case of an aqueous solution of sodium chloride, it changes insignificantly. On the basis of this, an aqueous solution of sodium chloride was chosen as the electrolyte.

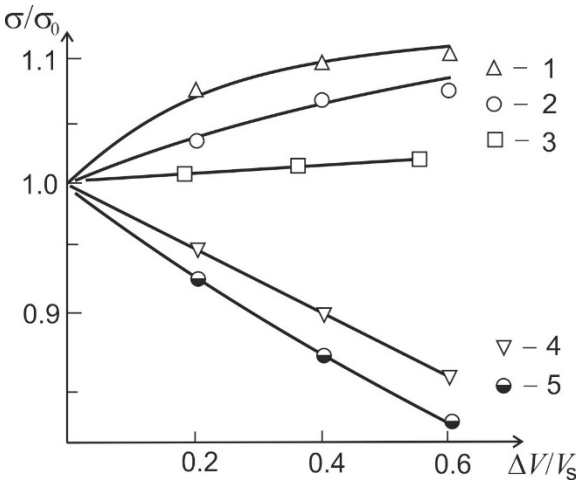



Fig. 1. Changes in electrical conductivity of aqueous solutions. 1 – 0.1M $Na_2SO_4$; 2 – 0.1M KCl; 3 – 0.1M NaCl; 4 – 0.1M NaOH; 5 – 0.1M KOH.

The choice of concentration of the aqueous solution.

The current-voltage characteristics of the discharge (I–V curve) turned out to be increasing (fig. 2). Moreover, the steepness varied depending on the electrolyte concentration. The lower the concentration, the steeper the I–V curve. From a practical point of view, this I-V curve is a very good discharge property, as the combustion stability increases and there is no need for a ballast resistor in the power supply circuit. Accordingly, energy losses are reduced.

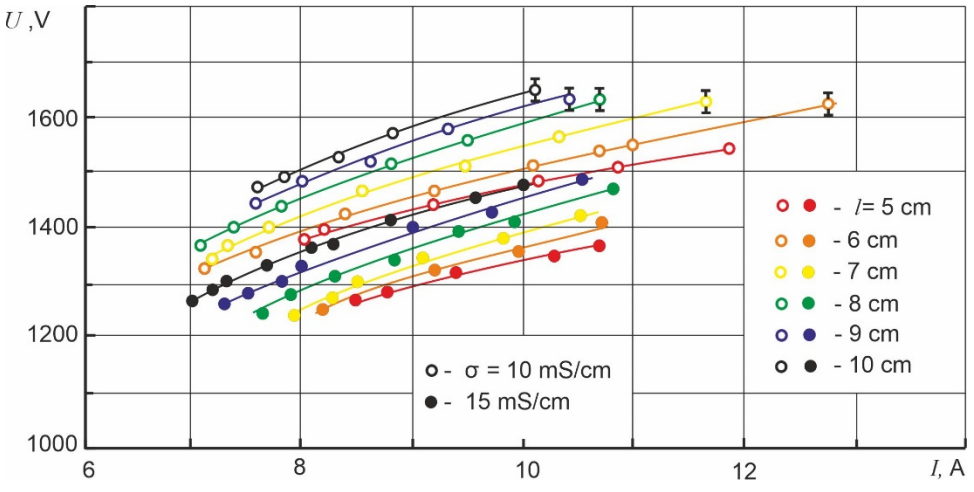



Fig. 2. Current-voltage characteristics.

Experiments have shown that the discharge burns steadily at concentrations at which $\sigma < 20$ mS/cm.

In the case of using aqueous solutions with low concentrations, the discharge switched to the combustion mode with contracted channels. When such channels appeared, the current increased sharply. Again there was a need for a ballast resistor. It was experimentally found that for operation without resistor, the concentration of an aqueous solution of sodium chloride should be in the range of 0.05 to 0.2 mol/l.

To the orientation of the plasma flow in space.

In the classical version, the liquid cathode is located at the bottom and the solid anode is installed above the cathode. The discharge between the cathode and the anode burns in the vertical direction. The plasma flow goes up from the liquid cathode. This configuration of the discharge makes it difficult to form a plasma flow in other directions. Technical solutions are required that allow the formation of a different discharge geometry. In this work, the problem is solved by using a porous insert on the cathode. On fig. 3 shows instantaneous photographs of plasma streams going in different directions from the cathode.

The photos were taken using a high-speed video camera VIDEOSCAN-401. Exposure 0.2 ms. The discharge current is 8 A. The distance between electrodes is 6 cm.

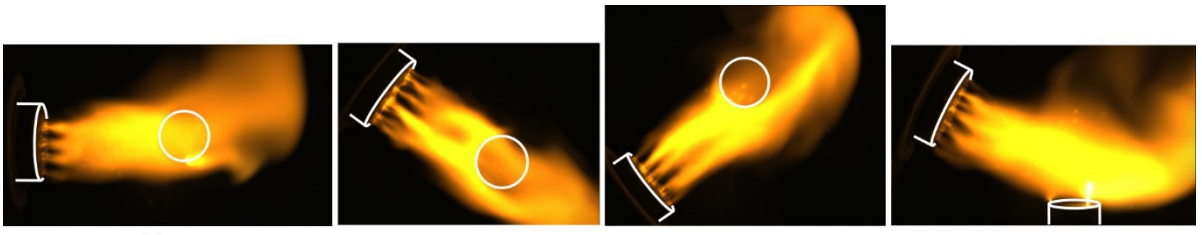



Fig. 3. Plasma flows horizontally (a), at an angle downward (b), at an angle upwards (c) and downward on the anode end (d). White lines indicate the contours of the cathode unit and the metal anode.

The porous insert was made of a refractory material. The anode was a copper rod with a diameter of 25 mm. He was cooled by water.

Electric power was supplied from a rectifier with an output voltage of 1700 V. The current was controlled by a step change in the ballast resistor. The flow of the electrolyte through the porous insert in the current range of 7–12 A was 5–8 ml/s.

To heat losses.

A feature of a gas discharge with a liquid electrolyte cathode is that the heat loss through the cathode unit depends on the flow rate of the electrolyte flowing through it. Regulation of the electrolyte flow allowed the reduction of heat losses through the electrodes to relatively small values (fig. 4). Total heat losses through the electrodes did not exceed 30% of the power consumption.

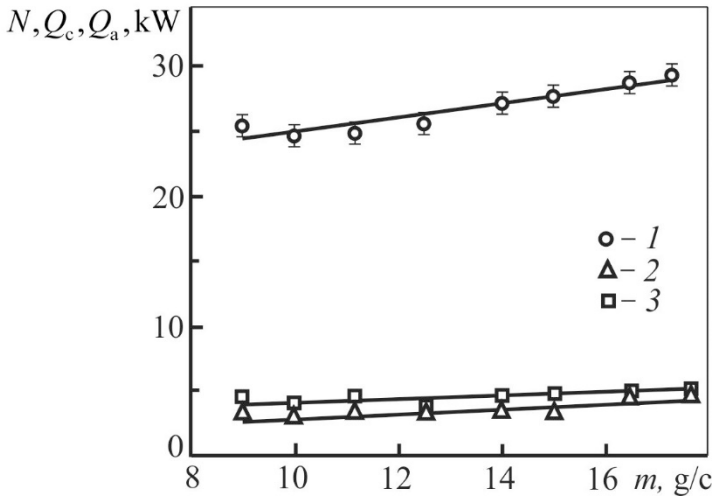



Fig. 4. Powers of the plasma generator ($N$) and heat losses through the electrodes ($Q_c$ and $Q_a$) as a function of the electrolyte mass flow rate ($m$). σ = 11 mS/cm. *1* – $N$; *2* - $Q_k$; *3* - $Q_a$.

Conclusions.

The most suitable electrolyte for long-term combustion of a gas discharge is an aqueous solution of sodium chloride. Its concentration should be in the range of 0.05 to 0.2 mol/l. Using a porous insert on the cathode, one can obtain plasma flows in different directions in space.

**Acknowledgments.** This work is supported by the Russian Federation President's grant for the state support of young Russian scientists - МК-111.2022.1.2

## References

1. **Friedland S.V., Tazmeev A.K., Miftakhov M.N.** Vestnik Kazanskogo tekhnologicheskogo universiteta. 2006. № 6. С. 10-15.

# RESEARCH CHARACTERISTICS OF PLASMA JET GENERATED BY COAXIAL DIELECTRIC BARRIER DISCHARGE AT ATMOSPHERIC PRESSURE

A. Aksiuchyts, D. Kotov, K. Logunov, A. Osipov

Belarusian State University of Informatics and Radioelectronics, 6 Petrusya Brovki str. Minsk, Belarus, kotov@bsuir.by

Recently, plasma methods for surface modification (including its activation) have attracted great attention. Atmospheric pressure plasma treatment technology allows to achieve a high level of disinfection and processing of food products, medical instruments, living biological tissue, can be used in a treatment of various types of skin diseases, etc. The object placed in plasma have the temperature close to room temperature during treatment. Therefore, the plasma does not damage the treated surfaces. Plasma processing is a new interdisciplinary area of research, including physics, chemistry, biology and medicine. The ability to control the parameters of atmospheric plasma generation provides a wide range of applications with low power consumption and low processing costs. [1]

In this work, we research temperature of samples placed in a plasma flow [2], length of plasma jet, dependence change the contact angle with distance of sample from the end of the discharge system, and optical radiation spectrum of the atmospheric discharge plasma.

To measure the object temperature was used a Bosch CIS C Professional thermal detector with a measurement range from -40 to 1000 °C. The measurement was carried out until the temperature became constant. We used a two-channel spectrometer SOL Instruments S150-2 to research a plasma composition from its optical emission spectrum (OES). The length of the plasma jet was determined visually, using a measuring scale, since it can give an enough understanding of the discharge properties.

During an experiment was determined effect of changing a gas flow rate and input voltage on the length of the plasma jet and the temperature of the treated samples surface.

During the experimental research (Figure 1(a)) the flow rate of argon $Q_{Ar}$ varied from 85 to 380 l/h at input voltages 14 V. At the gas flow rate more than 160 l/h, the growth rate of the plasma jet length slowed down. The increase plasma jet length with the addition of a gas flow can be explained by an increase in the gas dynamic velocity.

In the graph shown in Figure 1(b), the gas flow rate $Q_{Ar}$ was fixed at around 227 l/h, and the input voltage varied in the range from 11.3 to 21.7 V. The grow in the jet length with an increase in the input voltage on the primary winding of

a high-voltage transformer can be explained by an increment in the degree of

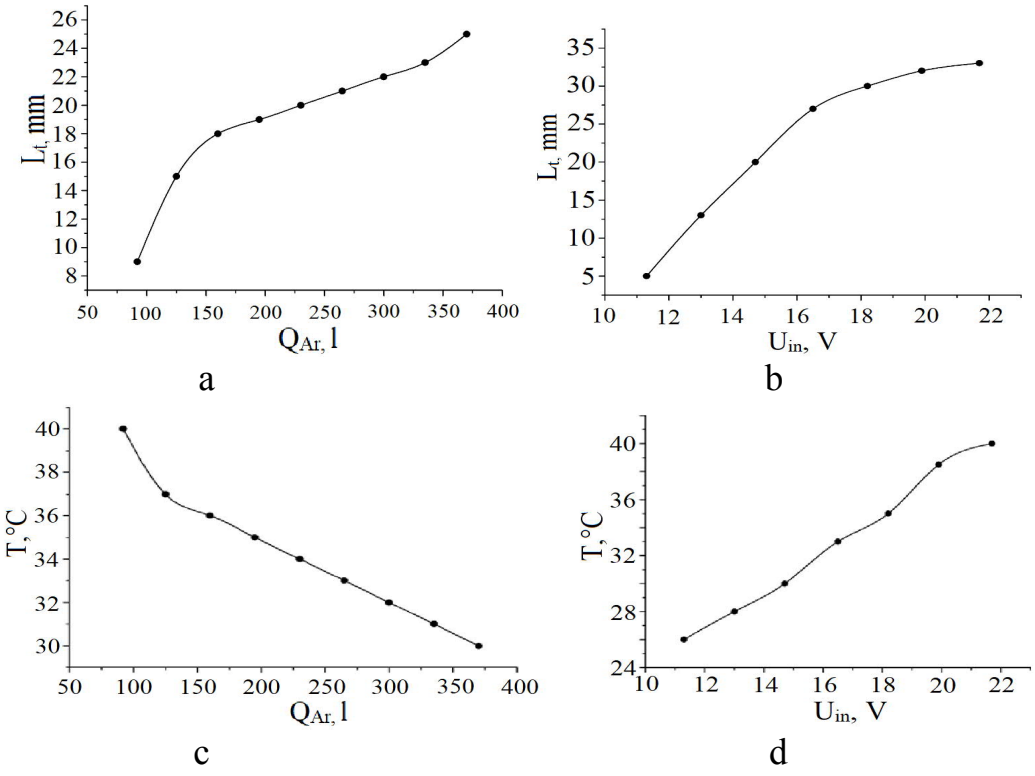



Fig. 1. Dependences of the jet length (a, b) and the surfaces sample temperature (c, d), of the input voltage (b, d) and the gas flow rate (a, c)

argon ionization. Thus, at input voltages above 14 V it is possible to obtain a plasma jet with a length more than 20 mm.

When research the influence of the working gas flow rate on the surface temperature of the processed samples (Figure 1(c)), the $Q_{Ar}$ value varied from 85 to 370 l/h. With an increase in argon consumption, there is an energy dissipation excited and charged particles because of gas flow divergence, and, as a result, a decrease in sample temperature.

In the case of the plasma jet temperature dependence on the input voltage on the primary winding of a high-voltage transformer (Figure 1(d)), can observe a lineari grow of the curve over the entire input voltage range (from 11.3 to 21.7 V). This dependence of the temperature increase can be explained by a proportional increase in the degree of gas ionization.

Research the composition of atmospheric discharge plasma along the jet (Fig. 2) was carried out in the wavelength range from 200 to 1000 nm with a spectral resolution of 0.1 nm. The measured emission spectra of the plasma show the presence of hydroxyl radicals OH (309 nm), excited argon atoms (696.54 nm, 763.51 nm, 826.45 nm), oxygen ions (673.8 nm), atomic oxygen

(715 nm), molecular nitrogen (337.1-380.4 nm) [3, 4].

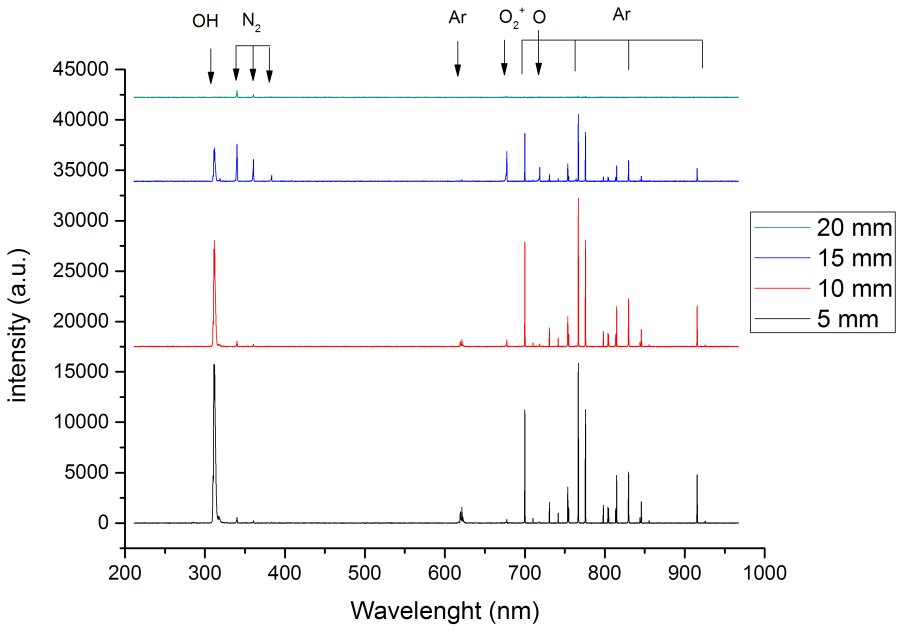



Fig. 2. Optical radiation spectrum of the plasma jet at atmospheric pressure

With distance from the gas-discharge tube, the argon lines intensity decreases and reaches the lowest values at the visual edge of the torch. A similar dependence is observed for radiation intensity OH radicals, which can be explained by the presumed presence of water vapor in argon, which decompose in plasma to form OH radicals. On the contrary, the intensity of molecular nitrogen, oxygen atoms and ions increases, reaching the highest intensity at a distance of 15 mm from the tube. At a distance of 20 mm, which corresponds to the visual length of the torch, there is a significant decrease in all emission bands. Atmospheric air acts as a source of nitrogen and oxygen, a plasma jet transfers atoms to an excited state, which we fixed on emission spectra. Oxygen formations observed in plasma, such as OH, O, $O_2^+$, are highly reactive due to the presence of unpaired valence shell electrons.

In the graph shown in Fig. 3 of the dependence of the contact angle on the distance to the end of the gas discharge tube, the smallest contact angle is achieved at a distance of 10-15 mm, this range corresponds to the high intensity of the OH, O, $O_2^+$ elements that interact with the treated surface and increase its wettability. The contact angle in this range reaches up to 14-15°. When the sample is removed from the tube by more than 15 mm, it leads to an increase in the contact angle to the initial values and was 38°.

As a result of experimental studies, it was found that an increase in the flow rate of the working gas (argon) from 85 to 375 l/h leads to a decrease in the temperature of the treated sample surface to 26 ° C, and an increase in the visual

length of the jet to 32 mm. The surface temperature of the sample placed in plasma

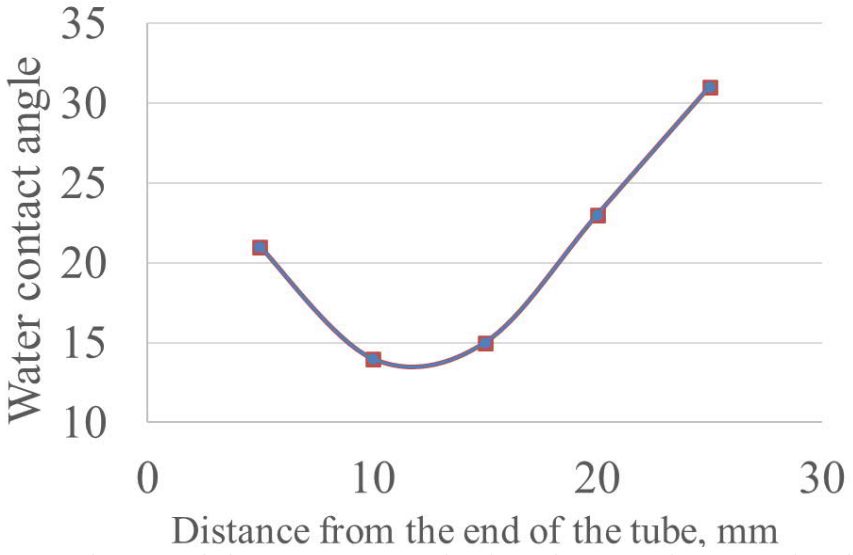



Fig. 3. Dependence of the contact angle the glass surface on the distance from the end of the discharge system

at atmospheric pressure can be set from 41°C to 26°C, allowing surface treatment of mineral and biological samples. The greatest wettability of the glass surface is achieved when the sample is placed in the central region of the plasma jet length. At a distance of 10-15 mm from the end of the discharge system, due to the high intensity of the OH, O, $O_2^+$ elements that interact with the treated surface and increase its wettability.

**References**

1. **H. Ayan.** Heating Effect of Dielectric Barrier Discharges for Direct Medical Treatment, IEEE Transactions on Plasma Science, 2009. – Vol. 37: p. 113-120.
2. **Kotov D., Krivenchuk D., Osipov A., Patseev S., Aksiuchyts A, Ponomarenko G. and Kulchitsky V.** Cold Atmospheric Plasma Treatment of Medical Devices. *Journal Scientific and Technical Research*, 22, Iss3, pp 16745-16749.
3. **Bibhuti Bhusan Sahu, Su Bong Jin, Jeon Geon Han.** Development and characterization of a multielectrode cold atmospheric pressure DBD plasma jet aiming plasma application, The Royal Society of Chemistry 2017. DOI: 10.1039/c6ja00419a.
4. **Zaplotnik, R.; Primc, G.;Vesel, A.** Optical Emission Spectroscopy as a Diagnostic Tool for Characterization of Atmospheric Plasma Jets. *Appl. Sci.* **2021**, *11*, 2275. https://doi.org/10.3390/app11052275.

# ELECTRICAL DISCHARGE INITIATED CHEMISTRY IN PREBIOTIC ATMOSPHERES

F. Krčma[1], S. Chudják[1], N. Fojtíková[1], L. Moravský[2], Š. Matejčík[2]

[1]Faculty of Chemistry, Brno University of Technology, Purkyňova 118, 612 00 Brno, Czech Republic, krcma@fch.vut.cz
[2]Faculty of Mathematics, Physics and Informatics, Comenius University Bratislava, Mlynská dolina F2, 84248 Bratislava, Slovakia

The chemical processes initiated by electrical discharges in prebiotic atmospheres became a hot topic during the last decade because of extensive discovering of exo-planets. Exoplanets or extrasolar planets data are not so detailed, so the best currently studied exo-Earth systems Titan and Mars [1]. Titan atmosphere is composed mainly from nitrogen and methane at low temperature of about 94 K and pressure about 1.5 atmospheres at its surface [2] and the composition od Mars atmosphere is carbon dioxide and nitrogen at temperature about 210 K and pressure 600-1000 Pa [3].

The majority of studies were carried out in the Titan's atmosphere up to now because there are many in situ available data and its atmosphere seems to be very similar as Earth's before life creation [4, 5]. Besides the exo-planetary atmospheric processes initiated by UV and VUV radiation and particles fluxes coming from the space, the electrical discharge phenomena can play an important role in the planetary atmosphere chemistry [5]. Lightning on Earth is a highly complex phenomenon involving physical processes on various spatial and temporal scales [4, 6, 7] starting from electron avalanches and resulting in the formation of hot, conducting lightning leaders. The early stages of lightning discharges are formed by streamers, thin and short duration ionized plasma channels. Lightning was confirmed in more planetary atmospheres [4, 8]. While the occurrence of lightning on Venus is still a controversial question [9, 10], there are clear evidences of lightning in the atmospheres of the gas giants like Jupiter, Saturn and Uranus [10-12]. Lightning is also believed to take place at Neptune [10, 13]. Thus, we can suppose that electrical discharge phenomena can at least partially contribute to the overall chemical processes also in the Titan's atmosphere [7, 14]. However, their direct evidence was not confirmed, yet.

The planetary scale processes can be simulated by laboratory experiments using various discharges: corona and DBD conditions are similar as the St. Elmo's fire, spark and arc relates to lightning, and corona and glow discharge conditions are similar to conditions in aurora borealis [5, 7]. There could be also transient luminous event (TLE) which belongs to a group of short-lived electrical-breakdown phenomena that occur above the altitudes of normal lightning and storm clouds. TLE event was also observed in Jupiter's upper

atmosphere [15]. Upper-atmospheric lightning is believed to be electrically induced forms of luminous plasma [15, 16]. Nearly all laboratory studies of Titan atmosphere discharge initiated processes up now were carried out at ambient temperatures and pressure that are not fully reflecting real Titan surface conditions [7, 14].

The first part of the presented study focuses on the simulation of the atmosphere of Titan, the second largest moon of the solar system. Thus, the most common composition of the gaseous mixture was methane (1-4 Sccm) in 200 Sccm of nitrogen. Measurements with trace amounts of oxygen and carbon dioxide were also performed. In addition to the composition of the gas mixture, the experiments also varied the value of the electrical power delivered from 2 W - 12 W. The measurements were carried out at laboratory temperature but also at liquid nitrogen temperature, which made the experiment much closer to the real conditions on Titan where the surface temperature is only 94 K.

The discharge itself was characterized by optical emission spectrometry, confirming the presence of active nitrogen species and radicals arising from methane. In addition, the first negative and nitrogen second positive systems as well as the violet CN radical system were identified in the measured spectra. The intensities of the selected spectral systems were studied under selected conditions, i.e. different gas mixture composition and power. From the nitrogen second positive system, the rotational temperature was determined to be approximately 2300-2400 K. The vibrational temperature was also determined from this system depending on the concentration of the gas mixture composition from 3100-3400 K. Next, the vibrational temperature was calculated from the nitrogen first negative system, but it decreased slightly with methane concentration and increased with power in the interval from 3950-4350 K. The vibrational temperature obtained for the violet spectral CN system had a very similar dependence, with values ranging from 5900-7700 K.

A number of aliphatic hydrocarbons, some aromatic hydrocarbons and also amino or cyano compounds were detected at laboratory as liquid nitrogen temperatures using a proton ionization mass spectrometer with time-of-flight analyzer (PTR-TOF). The highest molecular weights at laboratory temperature were up to 150 g·mol-1 with hydrogen cyanide, acetylene or acetonitrile being the most abundant compounds. In experiments closer to real conditions, temperature proved to be extremely important. In measurements at liquid nitrogen temperature, nearly 200 different substances up to a molecular weight of 500 g·mol-1 were identified. Even in low temperature measurements, acetonitrile or diacetylene were the dominant substances, but hydrogen cyanide was not as abundant as at ambient temperature. Furthermore, a small amount of oxygen was also used in the measurements and under these conditions formamide or acetone, were among the significant detected substances.

Formamide was probably also formed in liquid and crystalline state in the experiments, which was also measured by FTIR. In both laboratory and low-temperature measurements, it was confirmed that with increasing methane concentration, higher molecular weight substances were formed and lower number of simple substances were formed, which were probably consumed for more complex substances. The same dependence was observed with increasing power delivered to the system.

The discharge exhaust gas was also analyzed using ion mobility spectrometry. The most important gas detected was ammonia, followed by propane-2-ol, ethanol and most likely diethylamine.

The last set of measurements in Titan simulated atmosphere was FTIR measurements, which are in agreement with the PTR-TOF results. The basic discharge spectrum is the methane structure and the spectrum shows intense bands belonging to both aliphatic hydrocarbons (3050-2800 $cm^{-1}$) and aromatic compounds (benzene at 1506 $cm^{-1}$), bands belonging to nitrogen substituted hydrocarbons (1350-1600 $cm^{-1}$ and 3200-3400 $cm^{-1}$, respectively) were identified too. The spectrum further contains peaks of HCN (713 $cm^{-1}$) and C2H2 (729 $cm^{-1}$) from which graphs of methane concentration dependence have been obtained. Comparing the overall spectra at different methane concentrations, it can be seen that much of the methane passes through the reactor into the detector unreacted. However, this proportion of unreacted methane decreases significantly with increasing power supplied to the system.

The substances detected in this work are in good agreement with the available literature and also with substances detected in Titan's atmosphere by the Cassini interplanetary probe with the Huygens module. An important detected substance is also formamide, which is considered to be an ideal precursor of prebiotic synthesis.

The second set of experiments was carried out in the atmosphere simulating conditions on Mars at atmospheric pressure and ambient temperature. Mars' atmosphere is composed mostly of carbon dioxide, which makes up more than 90 % of Mars' atmosphere, rest are various traces. A DC glow discharge was generated in flowing regime in a specially designed stainless steel reactor was generated at atmospheric pressure at a $CO_2$ flow of 135 Sccm at discharge current of 20, 25, 30, 35 and 40 mA. Besides pure CO2, nitrogen, hydrogen and methane at flow rates of 1, 2, 3, 4 and 5 Sccm were added. The discharge formed products were in situ analyzed using a PTR-TOF, optical emission spectrometry was used for plasma diagnostics.

Mainly simple aliphatic hydrocarbons, alcohols, aldehydes, and ketones were detected. With increasing flow rates of the individual gases, more complex aromatic compounds with higher molecular weights were formed. There is clear evidence that concentrations are strongly dependent on admixture kinds and its

concentration. Among others, some molecules that are considered as the direct life precursors (like formamide that can be thermally transferred to uracyl) were determined in non-negligible concentrations.

The presented results showed PTR-TOF mass spectrometry as a powerful tool for the studying of discharge exhaust gas. Huge number of different organic molecules was identified in all gas mixtures and some of them are known as real life precursors.

## References


1. **Brennan P.** PlanetQuest. NASA: The search for life. (2019). http://planetquest.jpl.nasa.gov/.
2. **Kammer J.A., et al.** Planetary and Space Science, 88 (2013) 86-92.
3. **McFadden L.A.A., Weissman P.R., Johnson T.V.** Encyclopedia of the solar system. 2nd ed. Amsterdam: Academic Press. (2007).
4. **Johnson R.E., Tucker O.J., Volkov A.N.** Icarus. 271 (2016) 202-206.
5. **Kammer J.A., et al.** Planetary and Space Science. 88 (2013) 86-92.
6. **Hőrst S. M.** Journal of Geophysical Research: Planets. 122 (2017) 432-482.
7. **Hendrix A.R, Yung Y.L.** Journal of Astrobiology & Outreach. 5 (2017) 1000157.
8. **Gilliam A.E., Lerman A.** Icarus. 275 (2016) 252-258.
9. **Moinelo C., et al.** Icarus. 277 (2016) 395-400.
10. **Zarka P., et al.** Planetary and Space Science. 52 (2004) 1435-1447.
11. **Dyudina U., et al.** Icarus. 172 (2004) 24-36.
12 **Konovalenko A.A., et al.** Icarus. 224 (2013) 14-23.
13 **Gibbard S.G., et al.** Icarus. 139 (1999) 227-234.
14 **Aplin K.L., Fischer G.** Weather. 72 (2017) 46-50.
15 **Giles R.S. et al.** Journal of Geophysical Research: Planets. 125 (2020) 006659.
16 **Sosnin E.A. et al.** Physics-Uspekhi. 64 (2021) 191-210.

# ZERO-DIMENSIONAL SIMULATION OF A MICROWAVE DISCHARGE IN A MIXTURE OF ETHANOL WITH WATER

Yu.Lebedev, A.Tatarinov, A.Titov, I.Epstein

TIPS RAS, 119991 Moscow, Leninsky pr., 29, atat@ips.ac.ru

In recent decades, discharges in liquids and in contact with liquids have attracted much attention from researchers. In particular, discharges in a mixture of ethanol and water are used to produce hydrogen. Various types of electrical discharges are used, but microwave discharges are the least studied. This work continues our series of works on modeling a microwave discharge in liquids and is devoted to the study of kinetic processes in a gas mixture of an ethanol-water.

The concentrations of decomposition products and the temperature of the gas inside a bubble filled with microwave plasma for a mixture of water and ethanol vapors and their decomposition products are calculated. The bubble is surrounded by a boiling mixture of water and ethanol, $T_0$ = 320 K. The pressure inside the bubble is constant, equal to one tenth of an atmosphere (corresponds to the experimental conditions [1-2]). The bubble is located at the end of the cylindrical microwave antenna. The specific power $P$ absorbed by a discharge from a microwave source ($f$ = 2.45 GHz) is a given parameter. The initial mass fractions of water and ethanol vapors are also set. The initial temperature of the gas mixture inside the bubble is 320 K. The San Diego Mechanism (SDM) reaction set [3] is used to describe thermal processes. In addition, reactions with charged particles are added. We considered direct ionization, dissociation, attachment, detachment and electron-ion recombination.

The model contains balance equations for the mass fractions of neutral and charged gaseous plasma components $W_i$, the Boltzmann equation for free plasma electrons, the equation for the average microwave field in a small volume filled with plasma, and the heat conduction equation for the gas temperature.

The heat conduction equation is written as:

$$V_r \rho \sum_{i=1}^{N} \left(\frac{w_i}{M_i} C_{p,i}\right) \frac{dT}{dt} = Q + V_r (P - \sum_l Q_{ek}\, r_k) - Q_{cond} \quad (1)$$

Here $T$ is the gas temperature, $V_r$ is the volume of the plasma bubble. $C_{p,i}$ is the heat capacity of each component, $Q$ is the heat released or absorbed in chemical reactions, $r_k$ is the rate of the $k$-th chemical reaction. The second term on the right side of equation (1) describes the energy of the microwave field used to heat the gas, $Q_{ek}$ is taken into account for reactions occurring under electron impact. For $Q_{ek}$ the expression $eu_kN_A$ is used, where $e$ is the electron charge, $u_k$ is the threshold of the $k$-th reaction, $N_A$ is the Avogadro number. The third term on the right side of equation (1) $Q_{cond}$ describes the energy loss due to heat conduction. The magnitude of the microwave field in the plasma is

calculated from the relationship: $E = \sqrt{P\sigma^{-1}}$ under the condition that the value of $P$ is constant in time. Here $\sigma$ is the electronic conductivity of the plasma. To determine the electron energy distribution function (EEDF), the Boltzmann equation written in the two-term approximation is used. The reaction rates constants of electronic processes are calculated using a set of corresponding reactions cross sections and EEDF and, as a result, obtained as functions of the values of the reduced field *E/N*. To simplify the calculations, the EEDF was calculated for the mixture composition $H_2$ – 66 vol. %, CO - 34 vol. % given in [1]. In this work, the EEDF was calculated using the BOLSIG+ program.

Comparison of the results of zero-dimensional calculation with experimental data [1, 2] is a rather difficult task. It should be noted right away that comparison with the experimental results shows that the stationary composition of the products obtained from kinetic calculations and the results of thermodynamic calculations do not agree with the experimental data. This may mean that the bubble detaches from the antenna faster than the time to reach the stationary state. Let us assume that the experimental data on the component composition correspond to the composition of the products in the bubble at the moment of its detachment from the antenna. This may mean that the bubble detaches from the antenna at times shorter than the time to reach the stationary state. Let us assume that the experimental data on decomposition products correspond to the decomposition of products in the bubble at the moment of its detachment from the antenna. To determine the moment of separation, we used the data of [1], in which it was noted that the maximum diameter of a plasma formation is about 1 cm. We also assume that plasma ignition corresponds to the moment when the diameter of the expanding boiling bubble becomes of the order of the diameter of the cylindrical end of the antenna. The justification for this assumption is our calculations of the structure of the microwave field at the end of a cylindrical antenna [4]. In this case, the maximum field is concentrated near the edge of the antenna, and it is there that gas breakdown occurs. In the present work, the antenna diameter corresponded to the experiment and was equal to 4 mm [2]. Therefore, the initial bubble volume in our calculation is determined by the size of the antenna. From the condition of conservation of the mass of the mixture, knowing the initial and final diameter of the bubble, we found the bubble separation time. It is at this point in time that a comparison is made with experimental data. According to the results of calculations, the time of separation of the bubble from the antenna for all regimes is in the range of 0.1÷0.6 ms. We understand that the algorithm used by us for linking the results of calculations with experimental data is not quite correct and is based on a number of assumptions. For a more accurate correlation between the calculated and experimental results, at least a one-dimensional model is required.

The concentration of each of the main hydrocarbons we received

(acetylene, methane and ethylene) does not exceed 10 vol. %. Their concentrations do not change with increasing power. The concentration of acetylene increases with an increase of the initial fraction of ethanol. This is confirmed by experiment. The main products for all regimes are hydrogen and CO in an approximate ratio of 2:1. Their concentrations weakly depend on the input power and the initial composition of the mixture (Fig. 1-2).

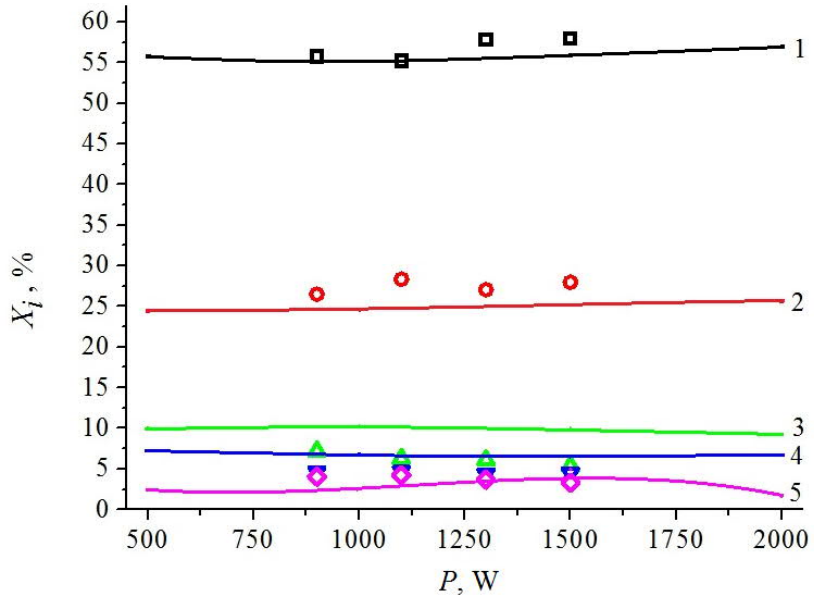



Fig.1. Dependences of molar fractions of the gas products in experiments (symbols) and calculations (lines) on the absorbed power. □, 1 – hydrogen; ○, 2 – CO; Δ, 3 - $C_2H_2$; ∇, 4 - $CH_4$; ◊, 5 - $C_2H_4$. Initial concentration of ethanol is 50 vol %.

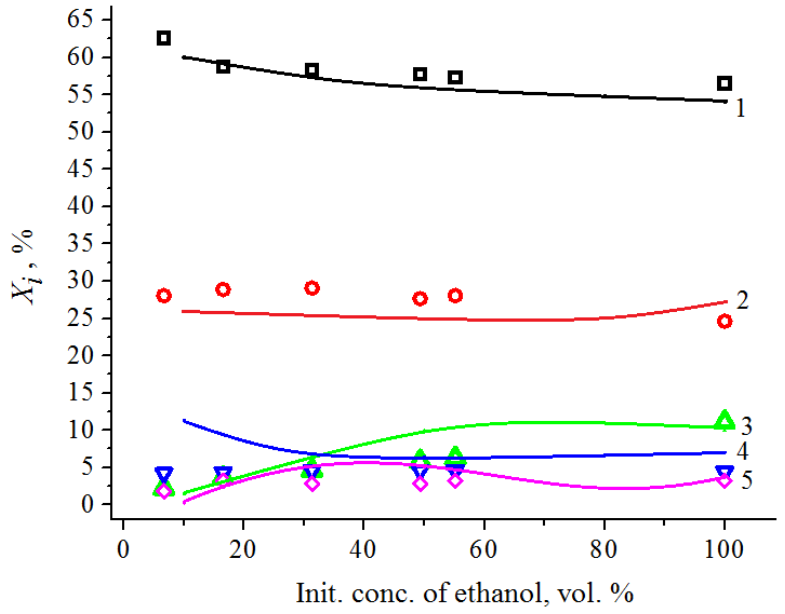



Fig.2. Dependences of molar fractions of the gas products in experiments (symbols) and calculations (lines) on the initial concentration of ethanol. □, 1 – hydrogen;○, 2 – CO; Δ, 3 - $C_2H_2$; ∇, 4 - $CH_4$; ◊, 5 - $C_2H_4$. Absorbed power is $P$ = 1500 W.

The rates of reactions with charged particles and the rates of reactions between neutral particles were compared. Our calculations have shown that the electronic and ionic processes are important at the initial times, when the gas temperature is close to the boiling point of the initial mixture and thermal processes do not occur. At these times, due to processes with charged particles, radicals are formed, the presence of which then ensures the occurrence of processes with neutral particles. At times longer than $10^{-4}$-$10^{-3}$s, processes with charged particles also have an effect, since at these times a maximum of the reduced field is observed and their velocities are comparable in magnitude with the velocities of thermal processes.

**Acknowledgements**. The work has been carried out within the framework of the state task of the Institute of Petrochemical Synthesis of the Russian Academy of Sciences with the partial support of the Russian Foundation for Basic Research, grant no. 21-52-53012.

## References

1. **Sun Bin, Zhao Xiaotong, Xin Yanbin, Zhu, Xiaomei.** Int. J. Hydr. Energy. 42 (2017), 24047.
2. **Liu Jing-Lin, Zhu Tong Hui, Sun Bing**. Int. J. Hydr. Energy, 47(2022), 12841.
3. https://web.eng.ucsd.edu/mae/groups/combustion/mechanism.html UC San Diego Combustion Research Group, San Diego Mechanism
4. **Lebedev Yu.A., Tatarinov A.V., and Epshtein I.L.** High Temperature, 49( 2011), 775

# APOKAMP AND PROSPECTS OF ITS APPLICATION IN BIOMEDICINE

V. Panarin[1], V. Skakun[1], D. Pechenitsin[1], D. Schitz[2]

[1]Institute of High Current Electronics SB RAS, ave. Akademichesky 2/3, Tomsk, Russian Federation
[2]Immanuel Kant Baltic Federal University, Nevsky str. 14, Kaliningrad, Russian Federation, DSchitz@kantiana.ru

The formation of a jet of cold plasma in atmospheric air that goes beyond the electrode system is a very difficult task, since electrons in the resulting gas-discharge plasma quickly transfer energy to the molecular components of air. The extinguishing process is also provided by the presence of electronegative gases in air, e.g., oxygen. Increasing in the voltage at the electrodes leads to a breakdown of an interelectrode gap and the formation of a spark discharge or arc.

Relatively recently [1], a jet of cold plasma has been obtained using atmospheric air as a working gas. When a high-voltage short-pulse voltage was applied, an arc discharge was ignited between two pointed metal electrodes. A plasma jet up to 6 cm long was formed from the surface of the arc discharge (Fig. 1). This type of plasma was called "*apokamp*" (from Greek «off» and «bend»).

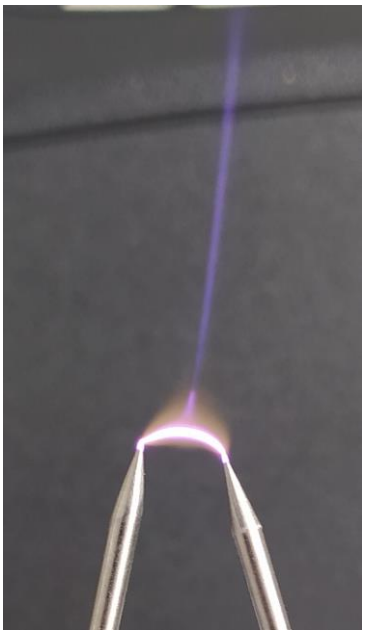


Fig. 1. Formation of the apokamp between two pointed electrodes

The discharge was powered by voltage pulses with duration of 1.2 μs, frequency of 50 kHz and amplitude of 12.5 kV. The circuit diagram of high voltage transformer and electrode system connection for generating of the apokamp is shown in Fig. 2.

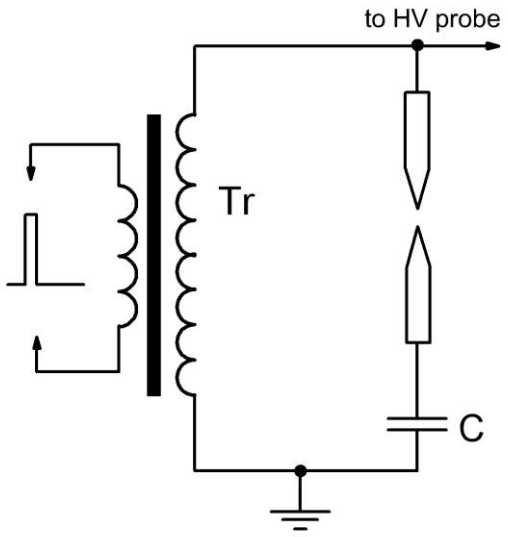



Fig. 2. Transformer and electrode system connection.

When positive polarity pulses were applied to one of the electrodes and the second electrode was connected through a capacitor *C* to ground, an arc surrounded by a volumetric diffuse discharge occurred in the discharge gap (Fig. 1). With further increasing of pulse amplitude, the plasma jet (apokamp) up to 6 cm long was radially formed from the volume of the diffuse discharge. When polarity of the pulses was changed and/or the capacitor *C* was replaced with a resistor, only an arc discharge was observed in the interelectrode gap, a diffuse discharge on its surface and the apokamp were absent.

Duration of positive pulses and frequency of their repetition also influenced efficiency of apokamp formation. So, at increasing of pulse duration up to 2 μs or decreasing of frequency up to 40 kHz the length of the apokamp reduced by half all other conditions being equal. Increasing of pulse frequency provided a multiple increase of the consumed power of the arc discharge and its heating, which led to increasing of intensity of convective flows and instability of the apokamp operation: multichanneling, branching, disorderly moving.

Distribution of gas temperature of the apokamp has been investigated. The coldest part of the discharge is at the end of the jet (1 – white color, see Fig. 3) and has temperature of +109°C. The hottest area (8 – blue color) is located on the surface of the arc, where the temperature reaches +1342±170°C. Temperature distribution in the layers of the apokamp has been measured by an

isolated thermocouple and by processing of a photo of a Canon PowerShot SX60 HS camera. This technique of measurements is described in details in [2].

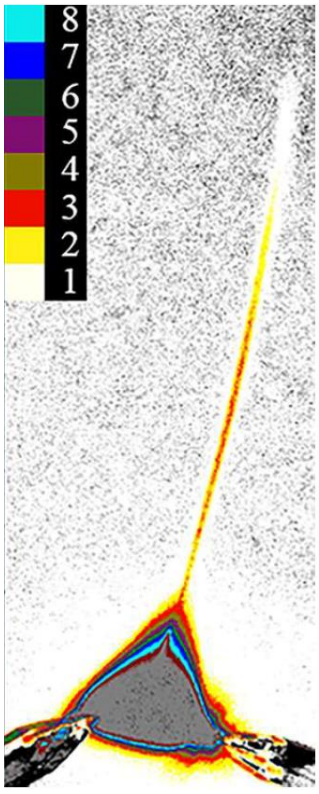



Fig. 3. Temperature destribution of the apokamp discharge.

Currently, cold gas-discharge plasma is successfully used in biomedicine. Based on treatment by plasma or its radiation, devices have been developed that have an anti-diaphoretic or hemostatic effect. Besides tissue regeneration and suppression of neoplasms can also be stimulated with plasma use.

Direct and long-term effects on the human or animal body are possible at a non-thermal plasma jet generating only, where the plasma gas temperature should not exceed +42°C. Devices capable of generating non-thermal plasma jets are mass-produced and successfully used, e.g., in surgery [3] (healing of septic wounds, regeneration of skin), in dermatology [4] (treatment of acne, chronic ulcers, dermatitis, seborrhea, keratosis, etc.) and in cosmetology [5]. There are also well-known works where non-thermal plasma is used to stimulate plant growth and increase seed germination [6]. In all devices capable of a non-thermal plasma jet generating, a discharge is formed in an inert gas stream or in a gas mixture based on an inert gas.

The application of the apokamp in biomedicine is possible if at least two conditions are met:

1. generated plasma should be non-thermal, because the effect of a gas flow with temperature of more than +42°C will cause not only pain, but also protein denaturation and tissue necrosis;

2. an electrode system of the apokamp must be electrically safe, i.e. leakage of high-voltage from the electrode system to a treated surface must be excluded.

The development of a device that generates non-thermal plasma in the form of the apokamp will eliminate need for using an inert gas as a working gas, which will reduce the cost of physiotherapy procedures.

Further theoretical investigation of the apokamp phenomenon and experimental study of new electrode systems capable of generating the apokamp with improved plasma characteristics will allow in the near future creating new efficient and safe equipment for its varied application in biomedicine.

**Acknowledgements**. The studies have been carried out in the framework of the State Task for IHCE SB RAS, the project #FWRM-2021-0014 and the project #FZ-2020-0003 "The study of new materials and methods for plasma and phototherapy of cancer, dermatitis and suppurative complications" financed by the Ministry of Science and Education of the Russian Federation.

## References

1. **Sosnin E.A., Skakun V.S, Panarin V.A., Pechenitsin D.S., Tarasenko V.F and Baksht E.Kh.** JETP Letters, 103 (2016) 761–764.
2. **Andreev M.V., Kuznetsov V.S., Skakun V.S., Sosnin E.A., Panarin V.A. and Tarasenko V.F.** Applied Physics, 6 (2016) 32-36 (in russian).
3. **Lloyd G., Friedman G., Jafri S., Schultz G., Fridman A. and Harding K.** Plasma Process. Polym, 7 (2010) 194–211.
4. **Bernhardt T., Semmler M.L., Schäfer M., Bekeschus S., Emmert S. and Boeckmann L.** Oxidative Medicine and Cellular Longevity, 4 (2019)1-10.
5. **Shemshuk M.I., Korotky V.N., Serov D.N., Kochetkov M.A., Stenko A.G. and Korotky N.G.** Bulletin of RSMU, 2 (2018) 57-62.
6. **Dubinov A.E., Lazarenko E.R. and Selemir V.D.** IEEE Trans. Plasma Sci., 28 (2000) 180–183.

# 4. NON-IDEAL AND DUSTY PLASMAS, EXTREME PLASMA REGIMES, FUSION AND ASTROPHYSICAL PLASMAS, COLLECTIVE AND NONLINEAR PHENOMENA

# THE NATURE OF ABNORMAL PARTICLE HEATING IN THE PLASMA DUST STRUCTURES

S. I. MOL'KOV [1], A. S. SHTYKOV [2]

Petrozavodsk State University, Petrozavodsk, Russia

Dusty plasma is an example of an open non-equilibrium system in which the process of self-organization occurs and dissipative dust-plasma structures (DPS) are formed [1]. Massive dust particles effectively lose their kinetic energy due to collisions with neutral atoms with frequency $\nu_{da}$, so it is assumed that they are in equilibrium with the atomic component and their temperature $T_d$ is equal to the atom temperature $T_a$ (~300 K=0.026 eV). In the experiment, the temperature of the dust component reaches significant values ~ $10^3$ $T_a$.

In a discharge tube filled with working gas He, Ne, or Ar under various pressures and discharge currents, a glow discharge plasma was induced and a DPS was formed with a dust component of particles of various materials ($Al_2O_3$, Zn) of several radius $a$ and masses $m_d$ [2]. The velocity, temperatures of dust particles, distances between them $r_d$ and plasma parameters were determined. The velocity distribution corresponds to an anisotropic normal distribution with an effective temperature $T_d$ related to the chaotic velocity of the dust component $v_d$ : $m_d v_d^2 / 2 = 3T_d / 2$ .

The table presents the calculated and experimental results for DPS: Ne – $Al_2O_3$ at various pressures and discharge current i = 0.6 mA which are necessary to substantiate the proposed conclusion.

According to our data, heating cannot be related to stochastic fluctuations of the particle charge [3] (see lines 2 and 3 of the table). To establish the mechanism of heating of dust particles to temperatures at about a few tens of eV, it is necessary to consider the particle motion equation:

$$m_d \frac{d\mathbf{u}}{dt} = eZ_d \mathbf{E} - m_d \nu_{da} \mathbf{u} + \mathbf{f}_r \,, \qquad (1)$$

where $eZ_d$ – the charge of a dust particle; $\mathbf{u}$ – the instantaneous velocity of the particle; $\mathbf{f}_r$ – the random Langevin force. Multiplying equation (1) by $\mathbf{u}$ and averaging over an ensemble of dust particles within a unit volume, we obtain: :

$$n_d \frac{d}{dt} \frac{m_d \langle u^2 \rangle}{2} = \langle \mathbf{j_d E} \rangle - 2\nu_{da} n_d \frac{m_d \langle u^2 \rangle}{2} + n_d \langle \mathbf{u f_r} \rangle , \qquad (2)$$

where the last term, due to the lack of correlation between $f_r$ and $u$, after averaging is replaced by zero: $n_d = r_d^{-3}$ – the concentration of dust particles; $\mathbf{j}_d$ $\mathbf{j}_d$ – the current density of dust particles; $\mathbf{E}$ – the local electric field strength near

the particle; $\langle \mathbf{j_d E} \rangle = W_d$ $\mathbf{j}_d$ – the density the power released in the discharge and used to heat dust particles under the condition of averaging not only over the ensemble, but also over time, since the values $\mathbf{j}_d$ and $\mathbf{E}$ fluctuate near average values. Taking into account that $\langle u^2 \rangle = v_d{}^2 = 3T_d/m_d$ and solving this equation with the initial condition $T_d = T_a$, we obtain the time dependence for the temperature of dust particles:

$$T_d = T_a exp\{-2v_{da}t\} + \frac{W_d}{3n_d v_{da} k}\left(1 - exp\{-2v_{da}t\}\right). \quad (3)$$

The dust component heats up in a characteristic time $\tau \approx (2v_{da})^{-1}$ to a temperature determined by the factor $W_d/3n_d v_{da}k$. The value of $W_d$ can be determined from experimentally measured temperatures: $W_d$~$10^{-11}$W/cm$^3$, which is much less than the power density dissipated in the discharge ($10^{-5}$ W/cm$^3$).

The current density of dust particles $j_d$ is due to elementary currents $eZ_d v_d / r_d$ near the node of the crystal lattice. The value of the lattice field strength can be estimated using the frequency of electrostatic oscillations $\omega_E$.

For particles of various materials and sizes in the Ne discharge, we obtain the elasticity coefficient $\alpha = \omega_E^2 m_d \sim (8 \pm 2)10^{-8}$ kg/cm$^2$. Then the field strength is $E_r = \alpha r / e|Z_d|$ and the potential $\varphi = -\int E_r dr = \alpha r^2 / 2e|Z_d|$ at a distance $r$.

The charge of a particle is determined by the balance of the fluxes of ions and electrons in the plasma, taking into account the emission processes on the surface [4]: $|Z_d| = 4\pi\varepsilon_0 a T_e \eta_W(\tau)/e^2$, where $\eta_W$ – the dimensionless potential of the particle,which depends on the normalized electron temperature $\tau = T_e/T_a$.

Calculation $Z_d$ taking into account the uncertainty of the properties of the particle surface for DPS Ne – $Al_2O_3$ at various pressures gives $|Z_d| = (3 \pm 0.6)10^4$. If $p$ = 0.3Torr parameter the non-ideal of the system is $\Gamma = (eZ_d)^2 / r_d T_d$ ~100 and the melting of the lower part of the DPS was visually observed. With increasing pressure, melting stops, $\Gamma \geq 106$.

Assuming the thermodynamic equilibrium of the dust component and using the theorem on the uniform distribution of kinetic energy over degrees of freedom, we obtain:

$$e|Z_d|\langle\varphi\rangle = \alpha\langle r^2\rangle/2 = 3kT_d/2 \text{ or } r_c = \sqrt{\langle r^2\rangle} = \sqrt{3kT_d/\alpha}. \quad (4)$$

The value $r_c$ characterizes mean-squared displacement of a particle from the equilibrium position in a conditional crystal lattice.

| | | | | |
|---|---|---|---|---|
| $p$ , Torr. | 0.3 | 0.6 | 0.9 | |
| $T_d$,$10^3$ K | 940 | 590 | 300 | $T_d = 3m_d v_d^2 / k$ |
| $T_d$, $10^3$ K | 270 | 193 | 155 | Calculation [2] |
| $W_d$ ,$10^{-11}$Wcm$^{-3}$ | 2.28 | 1.03 | 0.41 | $W_d = 3n_d \nu_{da} kT_d$ . |
| $\Gamma$ (estimated) | ~100 | ~120 | ~180 | $\Gamma = (eZ_d)^2 / r_d T_d$ |
| $r_c$, μm | 22.0 | 17.5 | 12.5 | $r_c = \sqrt{3kT_d / \alpha}$ . |
| $E_d$, V cm$^{-1.}$ | 3.67 | 2.92 | 2.09 | $E_d = \alpha r_c^2 / e\lvert Z_d \rvert$ |
| $j_d$ $10^{-11}$, А см$^{-2}$ | 0.62 | 0.35 | 0.196 | $j_d = W_d / E_d$ |
| $r_c / r_d$ | 0.14 | 0.08 | 0.045 | Lindemann criterion [5] |

According to Lindemann's crystal melting criterion [5] $r_c / r_d \geq 0.15$ which is close to our results $r_c / r_d = 0.14$ .

Thus, the heating source of dust particles is only partially related to their charge fluctuation induced by discrete charging current [3]. This dust particle in lattice site loses the equilibrium position due to the random collisions with gas atoms and because of the force action of the nearest dust particles in constant Brownian motion. The potential energy upon displacement from the lattice site increases by an average of $\alpha r_c^2/2$, which is converted into kinetic energy of directed motion $3kT_d/2$.

**References**

1**. Fortov V. E., Khrapak A. G., Khrapak S. A**., et al., Dusty plasmas, Physic s-Uspekhi. 47 (5) (2004) 447–492.

2. **Morfill G. E., Thomas H.**, Plasma crystal, J. Vacuum Sci. & Technol. A. 14 (2) (1996) 490–495.

3**. Shtykov A. S.** The measuring of the kinetic characteristics values of dusty plasma using the high-speed video camera, Proceedings of Petrozavodsk State University. (6 (151)) (2015) 121–123 (in Russian).

4. **Mol'kov S. I., Savin V. N.** Mechanisms of dust grain charging in plasma with allowance for electron emission processes, Plasma Physics Reports. 43 (2) (2017) 202–212.

5. **Vaulina O. S., Petrov O. F., Fortov V. E**. et al., Pylevaya plazma: eksperiment i teoriya [Dusty plasmas: Experiment and theory], Fizmatlit, Moscow, 2009 (in Russian).

# COLLECTIVE EFFECTS IN AN ACTIVE COLLOIDAL SYSTEM OF COMPLEX COMPOSITION UNDER THE ACTION OF LASER RADIATION

Senoshenko R.V.[1], Kononov E.A.[2], Vasiliev M.M.[2] and Petrov O.F.[2]

[1]Joint Institute for High Temperatures of the Russian Academy of Sciences, Izhorskaya 13 Bldg 2, Moscow 125412, Russia, senoshenko@mail.ru
[2]Joint Institute for High Temperatures of the Russian Academy of Sciences, Izhorskaya 13 Bldg 2, Moscow 125412, Russia; Moscow Institute of Physics and Technology, Institutskiy Pereulok 9, Dolgoprudny 141701, Russia, GADvin@yandex.ru (E.A.K), mixxy@mail.ru (M.M.V.), ofpetrov@ihed.ras.ru (O.F.P.)

Active colloidal systems are a special form of soft matter, which is a dispersed medium (plasma, gas or liquid) containing tiny dispersed active particles (droplets) able to move autonomously [1]. Active colloidal systems can be both colloidal plasma containing levitating charged microparticles and active emulsions, which are stabilized structures of surface-charged microdroplets stable to coalescence. The mechanisms of activity and self-organization of microobject collectives as in colloidal plasma and in liquid media have similar character - their analysis will make it possible to understand some similar mechanisms in natural systems.

The results of an experimental study of collective effects in a colloidal system, which is a quasi-two-dimensional structure of monodispersed microdroplets of emulsion of complex composition, under the laser radiation are presented. The emulsion was a dispersion of vaseline oil with an aqueous suspension of magnetite in water with a stabilizer. Microdroplets of a complex emulsion are generated using microfluidics technology.

An analysis of video recording of changes in the quasi-two-dimensional structure of emulsion microdroplets as a result of laser radiation exposure to an originally stationary system is presented. Observation of the colloidal system was carried out using a stereomicroscope and recorded with a high-speed video camera. The experimentally observed motion of microdroplets of the emulsion of complex composition resulting from the motion of intra-droplet inclusions. When metal inclusions absorbed laser radiation, a thermophoretic force was generated, driving the inclusions into motion, which, in turn, microdroplets were driven by the transmission of an undamped impulse. As a result of microdroplet motion, the order in the quasi-two-dimensional structure was disturbed and the colloidal system was broken.

The coordinates of the emulsion droplet centers for each moment of time were determined, and their trajectories were constructed and analyzed. Instantaneous velocities and accelerations, mean square displacement of moving

microdroplets, diffusion coefficients, kinetic and total energy of their motion were measured and analyzed. Probability density distributions of velocities of microdroplets on both axes were constructed.

It has been experimentally found that the motion of microdroplets of complex composition in the structure is active [2], including their motion in the superdiffusion mode is observed. Thus, the observation of collective effects in the colloidal system when exposed to laser radiation became possible due to the active properties of emulsion microdroplets containing absorbing metal inclusions.

**Acknowledgements.** The research was supported by Russian Science Foundation (project № 20-12-00372).

## References

1. **Xia H. and Xu B. and Zhang H. and Zhang L. and Liu X.** Materials Letters, 66 (2012) 29–32.
2. **Bechinger C. and Di Leonardo R. and Löwen H. and Reichhardt C. and Volpe G.** Review of Modern Physics, 88(4) (2016) 045006.

# SELF-ORGANIZATION OF A LASER-IRRADIATED MONOLAYER OF ACTIVE PARTICLES MODIFIED IN AN RF DISCHARGE PLASMA

E.A. Kononov[1], M.M. Vasiliev[2], O.F. Petrov[2]

[1]Joint Institute for High Temperatures of the Russian Academy of Sciences, Izhorskaya 13 Bldg 2, Moscow 125412, Russia; Moscow Institute of Physics and Technology, Institutskiy Pereulok 9, Dolgoprudny 141701, Russia, GADvin@yandex.ru
[2]Joint Institute for High Temperatures of the Russian Academy of Sciences, Izhorskaya 13 Bldg 2, Moscow 125412, Russia; Moscow Institute of Physics and Technology, Institutskiy Pereulok 9, Dolgoprudny 141701, Russia, mixxy@mail.ru (M.M.V.), ofpetrov@ihed.ras.ru (O.F.P.)

One example of thermodynamically open, dissipative systems often found in the surrounding world - in space, in technological processes - is plasma containing levitating charged microparticles [1]. A plasma in which the formation of levitating Coulomb structures is possible is called colloidal. Coulomb structures can be formed from different particles that differ in shape, composition, and have different properties, which makes it possible to observe a wide range of effects. Particles in plasma can be both passive and active Brownian, capable of autonomously converting the available energy of the environment (chemical, electromagnetic, thermal, etc.) into its own mechanical motion. A change in the state of Coulomb systems formed from passive Brownian particles is possible only by varying the parameters of their environment (changing the parameters of the gas discharge). At the same time, a change in the state of systems of active Brownian particles is possible as a result of a change in the kinetic temperature of the particles as a result of an external action (laser radiation) at constant parameters of the medium.

The action of such an active medium as plasma can lead to the development of unique properties by macroparticles. As a result, their behavior in the Coulomb system can change dramatically: passive Brownian particles can become active. As a result, such structures can exhibit active properties, as well as the ability to self-organize under external influences.

The results of an experimental study of the laser-induced self-organization of a monolayer levitating in the plasma of a capacitive radio-frequency discharge as a result of modification of the macroparticles that form it are presented. The results of the analysis of the average kinetic energy and the pair correlation function of the modified macroparticles in the Coulomb structure are presented, and estimates of the coupling parameter of the colloidal system are carried out [2]. A decrease in the degree of ordering of the colloidal structure and an increase in the kinetic energy of the Coulomb particles in it were observed experimentally with increasing laser radiation power.

The results of the analysis of particle modification are presented, namely, changes in the composition and structure of the surface of polymer particles during their exposure to plasma in a quasi-two-dimensional structure [3]. It was experimentally shown that exposure of polymeric particles to the Coulomb system leads to deposition of metals on their surface - a metallic island film is formed on the surface of the particles.

The results of the analysis of trajectories, root-mean-square displacement and persistence length of modified particles moving in a monolayer are presented for various values of the power of the acting laser radiation [4]. It was found experimentally that when exposed to laser radiation, particles with a modified surface begin to exhibit properties characteristic of active Brownian particles. The movement of macroparticles is affected by a significant photophoretic force resulting from the effective absorption of laser radiation by the metal film on the surface of the modified particles.

Thus, modification of the surface of particles in plasma, forming a Coulomb structure, can lead to a change of state and the emergence of the phenomenon of self-organization of such a system.

**Acknowledgements**. This work was supported by Russian Science Foundation (project No. 20-12-00372).

## References

1. **Fortov V.E. and Morfill G.E.** Complex and Dusty Plasmas: From Laboratory to Space, 1st ed. Boca Raton, USA: CRC Press (2009).
2. **Kononov, E.A., Vasiliev, M.M. and Petrov O.F.** Journal of Experimental and Theoretical Physics, 153 (2018) 721–725.
3. **Kononov E.A., Vasiliev M.M., Vasilieva E.V. and Petrov O.F.** Nanomaterials 11(11) (2021) 2931.
4. **Vasiliev M.M., Kononov E.A., Arkar K. and Petrov O.F.** Journal of Physics: Conference Series 1556 (2020) 012074.

# COSMIC DUST, ELECTRICAL PHENOMENA AND WEATHER ON EARTH

A. Kostrov

Federal research center Institute of Applied Physics of the Russian Academy of Sciences,
46 Ul'yanov Street, Nizhny Novgorod, 603950, Russia
kstr@ipfran.ru

Our planet Earth is surrounded by cosmic dust, which is continuously deposited on the surface and actively affects the physical processes on our planet.

Cosmic dust is considered to be particles of solid matter ranging in size from fractions to several microns. According to various data, and more recently from satellite measurements, from 100 to 300 thousand tons of dust per day falls on the Earth's surface. Interstellar particles have refractory cores. These are silicates, graphite, silicon, iron, etc. [1]. Dust in space plasma, both in the Solar System and outside, is negatively charged. This is due to the higher mobility of electrons than ions. A stationary negative charge of a material body (a grain of dust) in a plasma creates a self-consistent electric field that repels some electrons and attracts ions. Such a system is open, i.e. the charge of the body is not shielded according to the exponential dependence, but has a power-law asymptotic to ensure the flow of ions to the surface of the body. Negatively charged dust freely penetrates through the Earth's magnetic field and charges its surface. The stationary charge of the Earth is achieved due to the current of positive ions from the ionosphere («clear weather» current), with an average density of $(2\text{-}4)\cdot10^{-12}$ A/m$^2$, which corresponds to the total current to the Earth's surface $I_0\sim1700$ A. It is known that the average stationary electric field near the surface is about E~140 V/m. Such a field is created by a negative charge $Q\sim5\cdot10^5$ C. If the Earth did not maintain a negative charge, then the «clear weather» current would compensate for it in 8-10 minutes.

Using the average dust flow to the Earth and the value of the «clear weather» current, it was found that the average size of dust particles is $r\sim4\cdot10^{-7}$ m, the mass is $m\sim5\cdot10^{-17}$ kg, and the charge is $q\sim10^{-16}$ C.

Negatively charged dust particles reach the troposphere at altitudes of 2-8 km, where they act as water condensation centers. Condensation activity on negatively charged centers is several orders of magnitude higher than on positive ones [2]. Negative water drops are concentrated near the bottom of the cloud, and the positive charge, determined by the «clear weather» current, is located on top. Thus, a dipole character of cloud charging is created.

The proposed model of the Earth's global electrical circuit (for more details, see [3]) combines electrical processes in the atmosphere, ionosphere,

and space. The openness of the system is determined on average by the stationary flow of dust and ions from space, and this maintains the constant potential of the planet.

Particles of cosmic charged dust participate in the formation of clouds, are condensation cores, and fall to the Earth as precipitation - rain, snow, hail, i.e. the water cycle on Earth is driven by cosmic dust.

The discharge of the bottom of a thundercloud in the form of lightning leads to the appearance of a potential difference between the top of the cloud and the ionosphere, and in this case, upper lightning (sprites) occurs.

Long-term observations indicate that, against the background of a stationary dust flow, at times inhomogeneous ones arise, associated with the motion of the Earth in outer space.

An analysis of daily ozone maps in the Earth's atmosphere made it possible to link local non-stationary ozone disturbances at altitudes of 20–25 km with spatiotemporal fluctuations in the cosmic dust flux. This dust reaches the Earth's surface in 10-13 days with a Stokes velocity of about $2 \cdot 10^{-2}$ m/s and causes a change in the weather, usually cooling, in areas over which a local change in ozone density was observed.

Figure 1 shows a map of ozone distribution in the Northern Hemisphere on February 20, 2022 [4]. Let us consider the European part of Russia, where an area with a high ozone content arose at that time. After 12 days, i.e. on March 4, the air temperature in many cities under the area with disturbed ozone decreased sharply [5]. This result indicates that cosmic dust, moving towards the Earth's surface with a Stokes velocity $V=2 \cdot 10^{-2}$ m/s, entrains cold air from above due to viscous friction. Depending on air temperature in the stratosphere, dust flows can lead to a decrease in ozone content. Such an example is shown in Figure 2. Note that a tornado was observed on the edge of the ozone disturbance region in Michigan on May 21, 2022.

Every year our planet gets in the wake of various comets, such as the Quadrantid comet on January 1-6, the Hominid in mid-December, and the Perseid in late August. Dust from a swarm of the first two comets reaches the Earth and usually causes Christmas (January 6-7) and Epiphany (since January 19) frosts. Figure 3 shows the air temperature in January in Russia (left) and America (right).

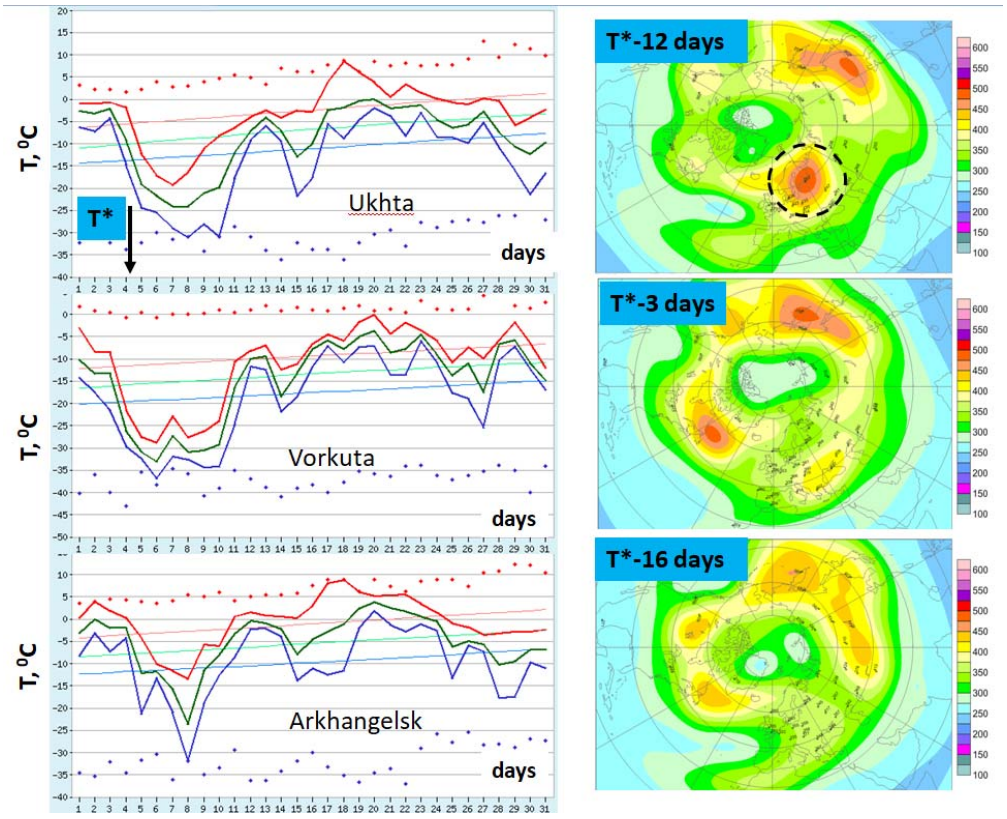



Fig. 1. Air temperature in March 2022 (left) and ozone distribution in the northern hemisphere (right)

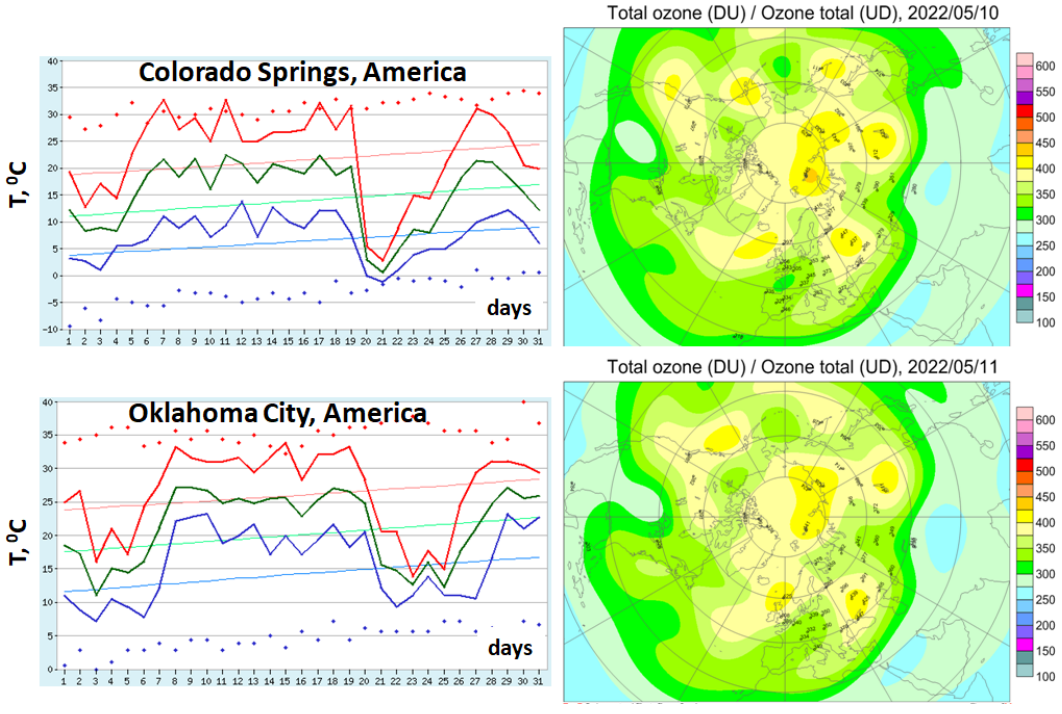



Fig. 2. Air temperature in May 2022 (left) and ozone distribution in the northern hemisphere (right)

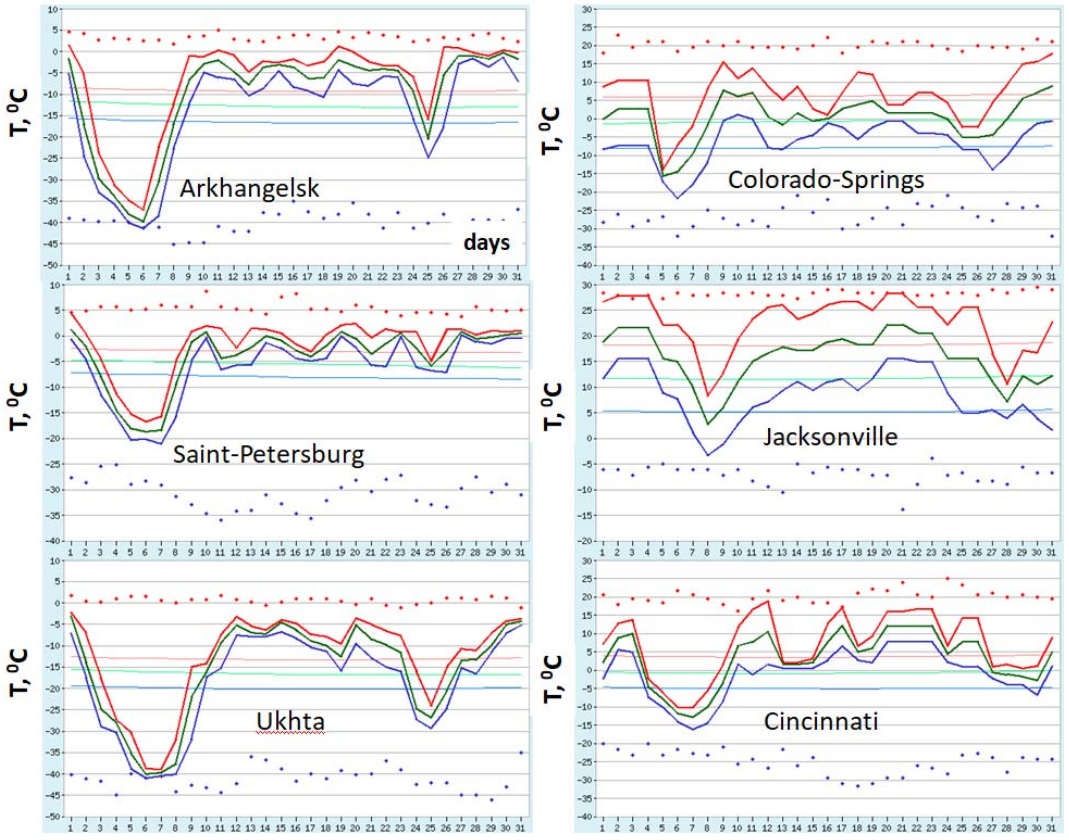



Fig. 3. Air temperature in January 2017 in Russia (left) and America (right)

The observed correlation of ozone perturbation in the Earth's stratosphere makes it possible to predict a significant change in the weather in 10-13 days - cooling, storms, tornadoes in local areas of our planet.

## References

1. **Mathis J.S., Rumpl W., Nordsieck K.H.** Astr. J. V. 217, № 2 (1977), 425-433.
2. **Rusanov A.I.** Dokl. Akad. Nauk SSSR. V. 238, № 4 (1978), 831-834.
3. **Kostrov A.V.** Plasma Physics Reports. V. 46, № 4 (2020), 443–451.
4. https://exp-studies.tor.ec.gc.ca
5. http://pogodaiklimat.ru/monitor.php

# ULTRACOLD MULTIMODAL DUSTY PLASMA IN DC GLOW DISCHARGE

R. Boltnev[1,2,3], E. Kononov[1,3], F. Trukhachev[1,3], M. Vasiliev[1,3], O. Petrov[1,3]

[1]Joint Institute for High Temperatures, Russian Academy of Sciences, Izhorskaya str.13/2, Moscow, 125412, Russia
[2]Branch of N. N. Semenov Federal Research Center for Chemical Physics, Russian Academy of Sciences, pr. acad. Semenova 1/10, Chernogolovka, Moscow region, 142432, Russia
[3]Moscow Institute of Physics and Technology, Dolgoprudnyi, Moscow region, 141701, Russia

We present the results of experimental studies of ultracold multimodal dusty plasma in a positive column of the DC glow discharge. A multimodal complex plasma consisting of a spheroidal dusty structure consisting of polydisperse $CeO_2$ particles superimposed with a cloud of nanoclusters and solid helical filaments was observed and studied at the temperatures below 2 K and pressure ≈ 4÷6 Pa. Geometry of the experiment is shown in Fig. 1. The experimental setup is described in detail elsewhere [1,2,3].

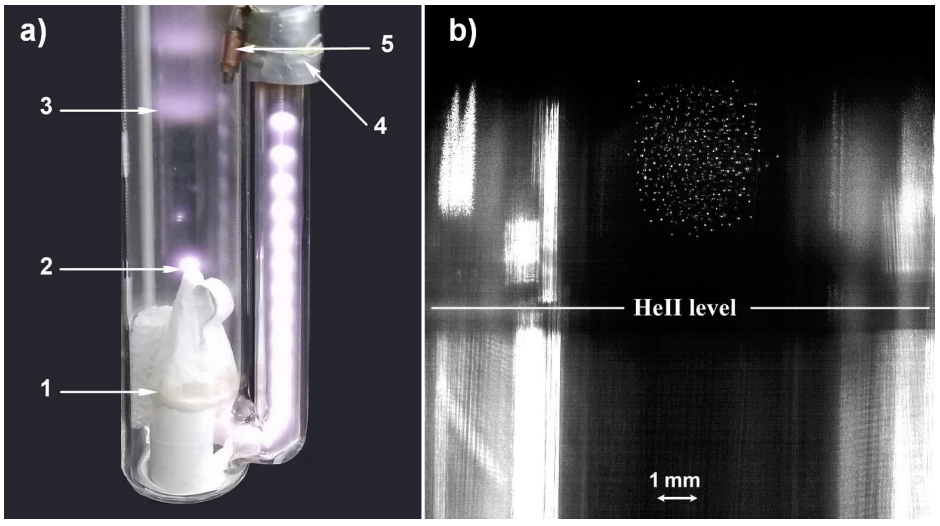



Fig. 1. The DC glow discharge, strata and dusty plasma structure: a) bottom part of the glass discharge tube: 1 – clay insert; 2- area of intense ion-electron recombination; 3 – the lowest stratum; 4 – insulated cathode; 5 – thermometer attached to the tube wall; b) dusty plasma structure in the DC discharge (at 1.69 K, 5 Pa, 3200 V and 50 μA). The level of superfluid helium (He-II) around the discharge tube is marked by white line.

Polydisperse dusty particles were introduced into the discharge region by an injector located in the upper section of the discharge tube. The injected particles

fell into the positive column of the discharge, where they were charged and trapped in ionization regions (strata). The dusty plasma structures formed in the lowest stratum of the positive column were monitored and studied (Fig. 2a). The structure sizes varied within the range from 2 to 5 mm and its height was usually larger than its diameter. The liquid-like structures consisted of randomly moving particles of $CeO_2$. The mean interparticle distance was equal to 170–200 $\mu$m.
The cloud of nanoparticles (with the sizes ~ 10 nm) appeared in the field of view approximately 1000 s after ignition of the glow discharge and was observed due to light scattering on non-linear waves (Figures 2b, 2c), the collective oscillating motion of the nanoparticles [4,5]. The cloud of nanoclusters spread over a broader area ($d \approx 1$ cm) than the dusty plasma structure diameter.

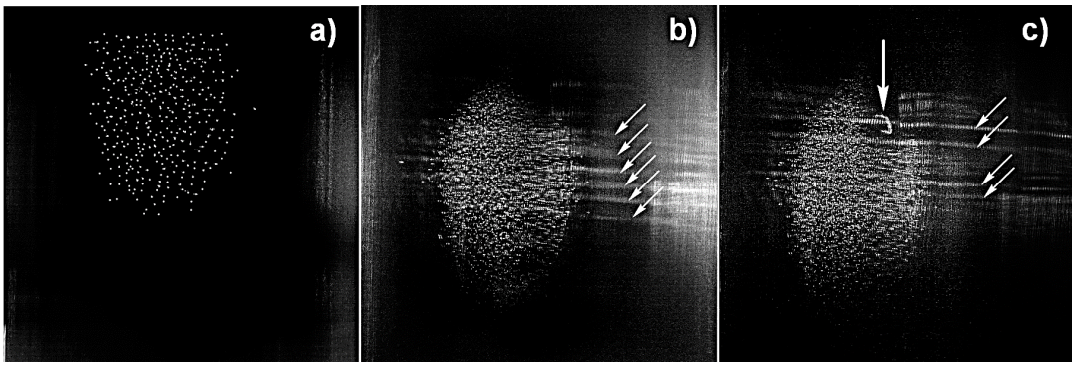



Fig. 2. Multimodal dusty plasma within the temperature range from 1.63 up to 2 K: a) dusty plasma structure formed with $CeO_2$ particles at T = 1.63 K; b) dusty plasma structure and waves (white arrows) in a cloud of polymer nanoparticles, T = 2.0 K; c) dusty plasma structure, a cloud of polymer nanoparticles, and solid filament (big vertical arrow) at T = 2 K.

Separate solid filaments started to enter and leave the field of view soon after the appearance of the cloud. Such a filament is marked with a thick vertical arrow in Fig. 2c. The filaments were solid helical bands with the widths from 12 to 22 μm and the thickness 2–5 μm. SEM micrographs of a filament with the length of 5 mm are given in Fig. 3. Micrographs with different optical magnifications show the filament structure (Figures 3a, 3b) and the nanoclusters on the filament surface (Figures 3c, 3d). The height of nanocluster attached to the filament surface is shown with the black arrow. The cluster diameters were distributed within the range from 10 to 80 nm. The nanoclusters were aggregated in cold helium gas from products of polymeric clay cone decomposition. The cone performed the function of formation of radially symmetric electron flow over the discharge tube. More polarizable products of the cone decomposition were attracted by inhomogeneous electric fields in the vicinity of the cellulose fibers

protruding above the cone surface. These fibers served as templates for self-assembling of filaments.

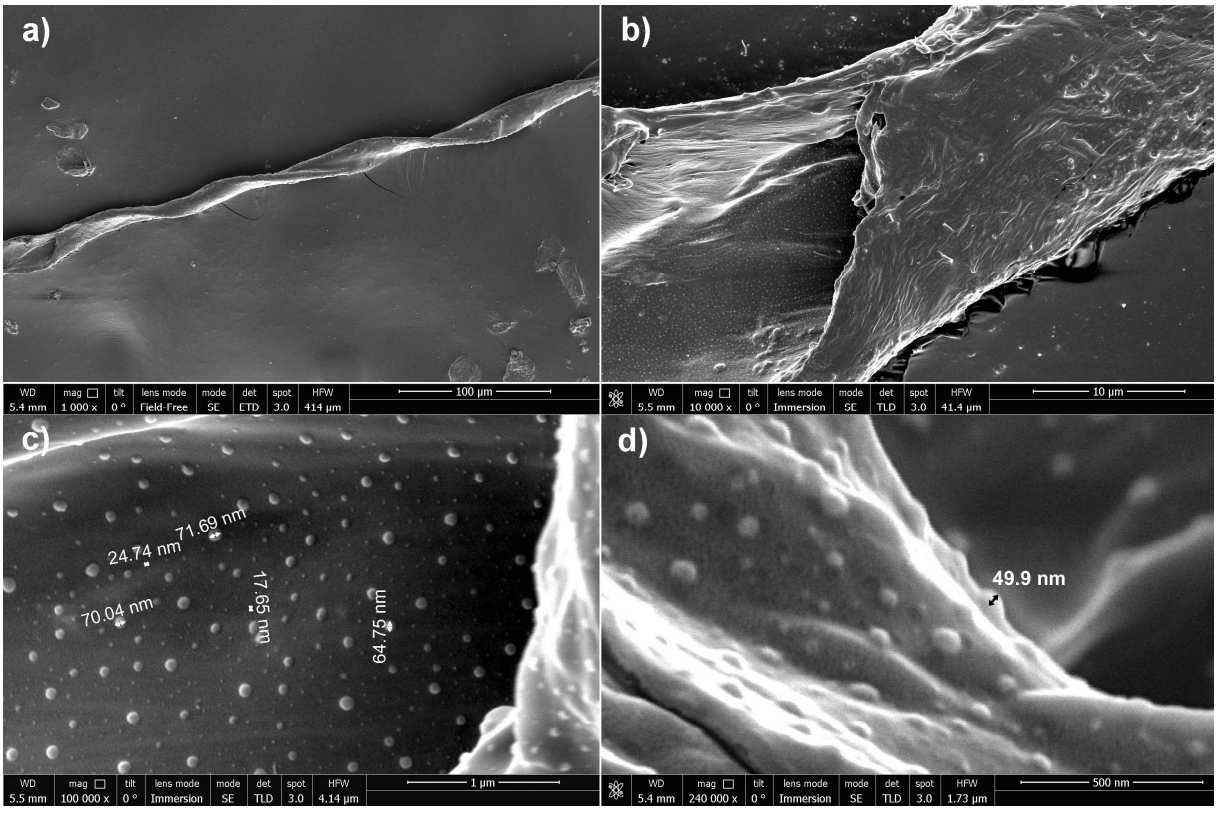



Fig. 3. SEM micrographs of a helical filament and its surface made at different magnifications: a) x1000; b) x10000; c) x100000; d) x240000.

The main discharge and multimodal dusty plasma parameters were estimated on the basis of knowledge of the particle (nanoclusters, dust grains, and filaments grown) sizes and dust-acoustic wave analysis. In particular, the temperature and density of ions, as well as the Debye radius, were determined (Tables 1 and 2). It was shown that the ion temperature exceeds the temperature of the neutral gas. The drift characteristics of all plasma fractions were also estimated.

Table 1. DC glow discharge parameters

| | | | |
|---|---|---|---|
| Gas pressure | ≈ 5 Pa | Discharge current | ~ $10^{-5}$ A |
| Gas temperature | ≈ 2 K | Electron concentration | ~ $10^{7}$ cm$^{-3}$ |
| Gas concentration | $2 \cdot 10^{17}$ cm$^{-3}$ | Electron temperature | ~ $10^{4}$ K |
| Electric field strength | ≈ 20 V/cm | Electron Debye length | ≈ 2200 μm |
| Ion temperature | ≈ 45 K | Ion Debye length | ≈ 30 μm |
| Ion concentration | ~ $10^{8}$ cm$^{-3}$ | Ion free path | ≈ 5.5 μm |

Table 2. Multimodal dusty plasma parameters

| | | | |
|---|---|---|---|
| Diameter of dust particles | 1-6 μm | Diameter of nanoclusters | 10-80 nm |
| Charge of dust particles | ≈ 500e | Charge of nanoclusters | ~ e |
| Concentration of dust particles | ~ $10^5$ $cm^{-3}$ | Nanocluster concentration | ~ $10^7$ $cm^{-3}$ |
| Charge of filaments | ~ $10^6$e/mm | Mass of filaments | ~ $10^{-7}$g/mm |

The total flow of cone material decomposed was estimated so high as ~ 100 ng/s at the DC discharge power < 0.1 W. The synthesis rates for nanoclusters and filaments were found as ~ 10 ng/s and ~ 1 ng/s, correspondingly, in ultracold dusty plasma at T ≤ 1 K. The higher efficiency of cone decomposition at the lowest temperatures allows us to suggest that the main cause of the decomposition is the damage of polymeric molecules by low energy electrons [6,7], neither the ion sputtering nor ion etching requiring ions with rather high energies ~ keV.

**Acknowledgements**. The work was supported by the Russian Science Foundation (Grant # 19-12-00354).

**References**

1. **Boltnev R.E., Vasiliev M.M., and Petrov O.F.** Instrum. and Exp. Tech. 61, (2018) 626–629
2. **Boltnev R.E., Vasiliev M.M., Kononov E.A., and Petrov O.F** Sci. Rep. 9 (2019) 3261.
3. **Boltnev R.E., Trukhachev F.M., Vasiliev M.M., Kononov E.A., and Petrov O.F.** Plasma Sources Sci. Technol. 29 (2020) 085004.
4. **Boltnev R.E., Vasiliev M.M., Kononov E.A., and Petrov O.F.** J. Exp. Theor. Phys. 126 (2018) 561–565.
5. **Trukhachev F.M., Boltnev R.E., Vasiliev M.M., and Petrov O.F.** Molecules 27 (2022) 227.
6. **Baccarelli I., Bald I., Gianturco F.A., Illenberger E., Kopyra J.** Phys. Reports 508 (2011) 1-44.
7. **Gao Y., Zheng Y., Sanche L.** Int. J. Mol. Sci. 22, (2021) 7879.

# EXPERIMENTAL STUDY OF KINETIC HEATING OF DUST PARTICLES IN A GAS DISCHARGE

E.A. Sametov[1,2], E.A. Lisin[1,2], E.A. Kononov[1,2], M.M. Vasiliev[1,2], O.F. Petrov[1,2]

[1]Joint Institute for High Temperatures of the Russian Academy of Sciences, Izhorskaya 13 Bldg 2, Moscow 125412, Russia
[2]Moscow Institute of Physics and Technology, Institutskiy Pereulok 9, Dolgoprudny, Moscow Region 141701, Russia

One of the experimentally observed features of laboratory dusty plasma is the high kinetic energy of microparticles compared to the temperatures of the neutral, ionic, and electronic subsystems. This phenomenon is called "anomalous heating" of dust particles. The main mechanisms of “anomalous heating” of dust are usually associated with various temporal and spatial changes in their charges, caused, for example, by the random nature of ion and electron currents that charge dust particles, or by the stochastic motion of dust in the volume of a spatially inhomogeneous plasma. Since the charge of a dust particle is determined by the local parameters of the plasma in its vicinity, the power of the energy pumping sources, and, accordingly, the "kinetic temperature" of the particles can vary significantly in space. The sources of non-uniform heating of the system of particles can also be the non-uniform distribution of the temperature of the surrounding gas, laser radiation used for diagnostics, the occurrence of chemical reactions, etc.

These mechanisms of heating the dust component are considered for systems with reciprocal interparticle interaction. These models do not explain some features of the redistribution of thermal energy in the observed dust structures, such as, for example, an increase in the kinetic temperature of microparticles in the direction of the ion flow and a nonequilibrium distribution of thermal energy between degrees of freedom. A nonreciprocal type of interaction between dust particles can take place in a plasma with an ion flow (due to the effect of ion focusing), as well as due to the forces of shading by neutrals for particles with different surface temperatures. It should be noted here that, in contrast to reciprocal interaction, for non-reciprocal there is a so-called “violation” of the interaction symmetry. Such a formal non-fulfilment of Newton's third law can arise, for example, when a subsystem of particles in a medium is considered, while the medium itself is taken into account indirectly - through the potential of interparticle interaction, dissipative forces, and also as a source of kinetic energy of particles. In [1], the mechanism of kinetic heating of particles and the redistribution of their kinetic energy for disperse systems of different nature due to the work of effective forces of interparticle interaction was theoretically described.

The average effective kinetic temperature attributable to the ξ-th degree of freedom of one particle in a system of particles with violation of the symmetry of the effective interparticle interaction can be written as

$$T_{\text{eff}}^{(\xi)} = T^{(\xi)} + \delta T^{(\xi)}, \quad (1)$$

where $T^{(\xi)}$ is the effective temperature quantifying the intensity of translational noise (heat source) acting on a solitary microparticle (in the absence of influence from the neighboring particle); $\delta T^{(\xi)} = 2\delta K^{(\xi)}$, and $\delta K^{(\xi)}$ – additional kinetic energy that the particle acquires due to the work of nonreciprocal interparticle forces. The relative change in temperature due to additional pumping of energy into the system is determined by the following relation [1]:

$$\frac{\delta T^{(\xi)}}{T^{(\xi)}} = \frac{\left(f_{21}^{(\xi)} - f_{12}^{(\xi)}\right)^2}{\left(f_{21}^{(\xi)} + f_{12}^{(\xi)}\right)^2 + 2\nu^2\left(f_{21}^{(\xi)} + f_{12}^{(\xi)} + f_1^{(\xi)} + f_2^{(\xi)}\right)}, \quad (2)$$

where $f_{ij}^{(\xi)}$ is the stiffness of the ξ-component of the specific force $\mathbf{F}_{ij}/M$ acting on the $j$-th particle with mass $M$ from the $i$-th one, $f_j^{(\xi)}$ is the stiffness of the ξ-component of the specific confining force $\mathbf{F}/M$ acting on the $j$-th particle from the stratum, and $\nu$ is the friction coefficient of the particles in the medium. Within the framework of this model, in order to determine the amount of additionally pumped energy, it is sufficient to measure the correlator of particle velocities, since [2]

$$\delta T^{(\xi)} = M\langle V_1^{(x)} V_2^{(x)}\rangle, \quad (3)$$

where angle brackets mean time averaging.

In order to study the mechanism of kinetic heating of dust particles in a gas-discharge plasma, the results of experiments with a solitary particle and with a pair of particles were analyzed. The experiment was carried out in a direct current gas discharge plasma at a pressure of 0.015 Torr and various discharge current strengths (from 0.75 mA to 2.05 mA) with monodisperse polystyrene particles with a diameter of 4.6 μm. The data were analyzed using a new experimental method [3] based on the analysis of the spectral density of random processes. Fitting experimental data with analytical functions [3] allows us to obtain the stiffness of the forces acting on the particles, the particle friction coefficient and the temperatures quantifying the translational noise intensity (thermal source) in the gas discharge. This method does not require any external disturbances and a special design of the experimental setup, preliminary measurements of external fields and assumptions about the type of interaction.

The experiment was carried out in two stages. At the first stage, for each of the selected values of the discharge current, the trajectory of a solitary microparticle was obtained. The probability density function of particle velocities PDF(V) and the spectrum of particle oscillations allow us to

determine the stiffness of the confining force acting on the particle from the stratum, the friction coefficient of the particle and effective kinetic temperature of the stochastic motion of a particle, which for a solitary particle coincides with the temperature quantifying the intensity of translational noise acting on the particle in the gas-discharge.

At the second stage, two new particles were thrown in and aligned vertically along the axis of the gas discharge tube. The trajectories of two interacting particles were obtained for the same values of the current strength that were previously established for a solitary particle. Further analysis of the trajectories gives us information on the forces acting on the particles, their friction coefficients, effective kinetic temperatures and velocity correlations, and the temperatures quantifying the intensity of translational noises.

Figure 1 shows the temperatures quantifying the translational noise acting on the particles, obtained as a result of fitting the spectral densities with analytical functions. It turns out that the mean intensity of translational noise acting on a particle in the two-particle system is up to 1.5 times higher than the noise intensity for the solitary particle with the same mass and at the same gas discharge parameters. This can be explained by an increase in the translational noise intensity of the lower particle associated with a change in its charge due to the influence of the ionic wake of the upper particle. Comparison of the stiffness of the confining forces acting on the solitary particles and on the pair shows that the charge of the lower particle in a pair is 25-30 percent less than the charge of a solitary particle of the same mass, while the charges of the upper particle and the solitary are practically the same, taking into account measurement errors.

Figure 1 also shows the mean effective kinetic temperatures measured with PDF(V). It turns out that the mean effective kinetic temperature (per particle) $T_{\text{eff}}^{(x)}$ in the particle pair is ~ 5 times higher than the kinetic temperature of the solitary particle $T_0^{(x)}$ (with the same mass and at the same gas discharge parameters). Consequently, the work of the effective forces of interparticle interaction can be considered the dominant mechanism for heating microparticles in chain structures in a gas discharge.

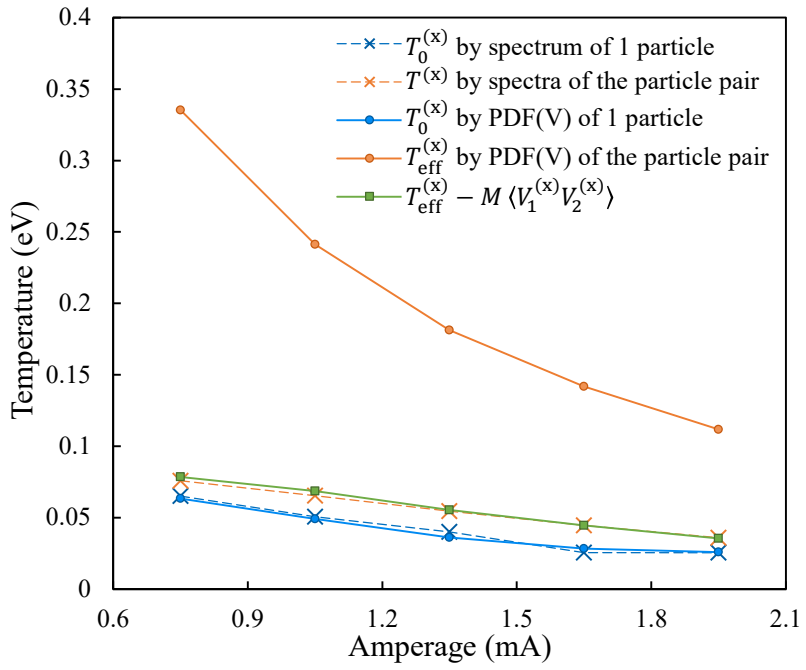



Fig. 1. Effective kinetic temperatures (marked with circles ●), measured with PDF(V), and the temperatures quantifying the mean intensity of translational noise (×), obtained with spectral analysis, for a solitary particle (blue) and two non-reciprocally interacting particles (orange) depending on the strength of the discharge current. Subtraction of $M\langle V_1^{(x)} V_2^{(x)}\rangle$ from $T_{eff}^{(x)}$ is shown in green squares.

Thus, the previously developed model of the kinetic heating of a system of two interacting particles was experimentally tested using a new spectral method. It was shown that the dominant mechanism of heating of dust particles in the plasma of a gas discharge with an ion flow is indeed the work of the effective forces of interparticle interaction.

**Acknowledgements**. This work was supported by the Russian Science Foundation under grant № 19-12-00354.

## References

1. **Vaulina O.S., Lisina I.I. and Lisin E.A.** Energy exchange in systems of particles with nonreciprocal interaction. J. Exp. Theor. Phys. 121, 717-726 (2015).
2. **Lisina I.I., Lisin E.A., Vaulina O.S. and Petrov O.F.** Self-confined particle pairs in complex plasmas. Phys. Rev. E 95, 013202 (2017).
3. **Lisin, E.A., Petrov, O.F., Sametov, E.A. et al.** Experimental study of the nonreciprocal effective interactions between microparticles in an anisotropic plasma. Sci. Rep/ 10, 13653 (2020).

# ROTATION MECHANISMS OF DUST CLUSTERS IN STRATIFIED DC DISCHARGES UNDER THE MAGNETIC FIELD ACTION

L. Dyachkov[1], E. Dzlieva[2], V. Karasev[2], L. Novikov[2], S. Pavlov[2]

[1]Joint Institute for High Temperatures of RAS, Izhorskaya st. 13, bld. 2, 125412, Moscow, Russia, dyachk@mail.ru
[2]Saint-Petersburg State University, Universitetskaya nab. 7/9, 199034, Saint-Petersburg, Russia, plasmadust@yandex.ru

For more than 20 years, research has been carried out on the influence of a magnetic field on dusty structures in plasma [1]. In particular, such an influence is of interest as a way to control dust particles in various technological processes. Most of the research has been done in HF discharges [2, 3], but there are also many studies of dust structures in stratified DC discharges (for example [4] and references there). Stratification of DC discharge is necessary, since the stable position of dust particles is possible only in an inhomogeneous electric field with $\nabla E$ directed downward. One of the most interesting effects of the action of a magnetic field on a dust structure is its rotation with a change in the rotation direction when the field increases [5]. Rotation inversion means that the rotation mechanism has changed. In low fields ($B \sim 0.01$ T), the rotation is counterclockwise if viewed in the direction **B** (in this case, we set the rotation angular velocity to be negative, $\Omega < 0$). With an increase in the field, the rotation angular velocity first grows linearly in absolute value, then slows down and approaches zero; with a further field increase, the rotation direction changes ($\Omega > 0$). Rotation inversion is associated with a change in the main rotation mechanism [6, 7]. The dependence $\Omega(B)$ for $B < 1$ T, obtained in our experiment [4], is shown in Fig. 1. The irregularity of $\Omega(B)$ at $B = 0.15$–$0.5$ T is due to the appearance of current-convective instability. At $B \sim 1$ T, after the loss of part of the particles by the dust structure, the discharge stabilizes.

The main mechanism of dust structure rotation at $B \sim 0.01$ T is ion drag [8]. The ions rotate as a result of their drift in crossed radial ambipolar electric and axial magnetic fields, as well as the radial ion pressure gradient. The main mechanism that prevails at $B > 0.1$ T is the neutral gas drag force. The gas rotation occurs under the influence of eddy currents **j** arising in striations in the presence of axial gradient of electron temperature $T_e$ and radial gradient of electron density $n_e$ [9]:

$$b_e \nabla n_e \times \nabla T_e = -\mathrm{curl}\,\mathbf{j}, \qquad (1)$$

where $b_e$ is the electron mobility. In an axial magnetic field, the Ampere force acting on the radial component of the eddy currents causes the gas to rotate and equilibrated by the gas viscosity:

$$\eta \frac{\partial^2 \mathbf{u}_\varphi}{\partial r^2} + \mathbf{j} \times \mathbf{B} = 0, \tag{2}$$

where $\eta$ is the gas-dynamic viscosity. The direction of the eddy current changes along the striation length because of direction $\nabla T_e$ changes, the rotation direction also changes. However, in the striation head, where there is a region of dust particle stable equilibrium, the rotation is clockwise ($\Omega > 0$).

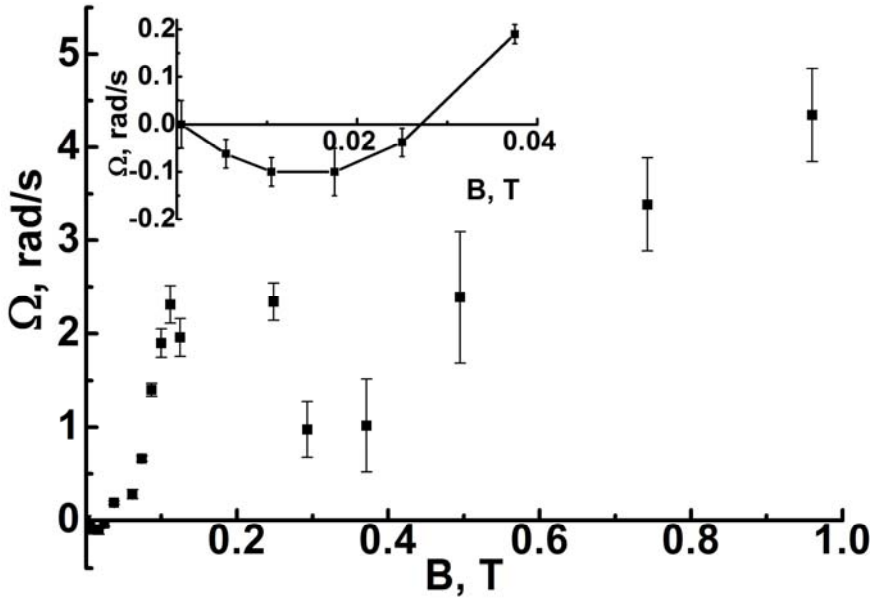



Fig. 1. Dependence of the angular velocity of a dust structure on the axial magnetic field in neon at $p$ = 0.6 Torr, $I$ = 1.4 mA.

In [10] we measured $\Omega(B)$ at $B$ = 1.1–2.2 T and proposed an analytical model for calculating $\Omega(B)$ based on the concepts of eddy currents. The $T_e$ and $n_e$ distributions in the model were approximated by a superposition of the constant and oscillating components. The ratio of the amplitude of the oscillating component to the constant one in the $T_e$ and $n_e$ distributions, according to the numerical calculation [11], should be about 0.5. The results of measurements (symbols) and calculation (dashed curves) from [10] are shown in Fig. 2. The parameters $k_T$ and $k_n$ show the ratio of the amplitude of the oscillating component to the constant one for $T_e$ and $n_e$ correspondingly. The calculation with reduced values of $k_T$ and $k_n$ to 0.4 showed better agreement with experiment than with 0.5. The contribution of ion drag in [10] was not taken into account in the calculation, since it was assumed to be insignificant. Obviously, its role in comparison with the neutral gas drag contribution at $B > 1$ T is not great however it may also be of some interest. In this communication, we present the results of calculations taking into account the ion drag contribution.

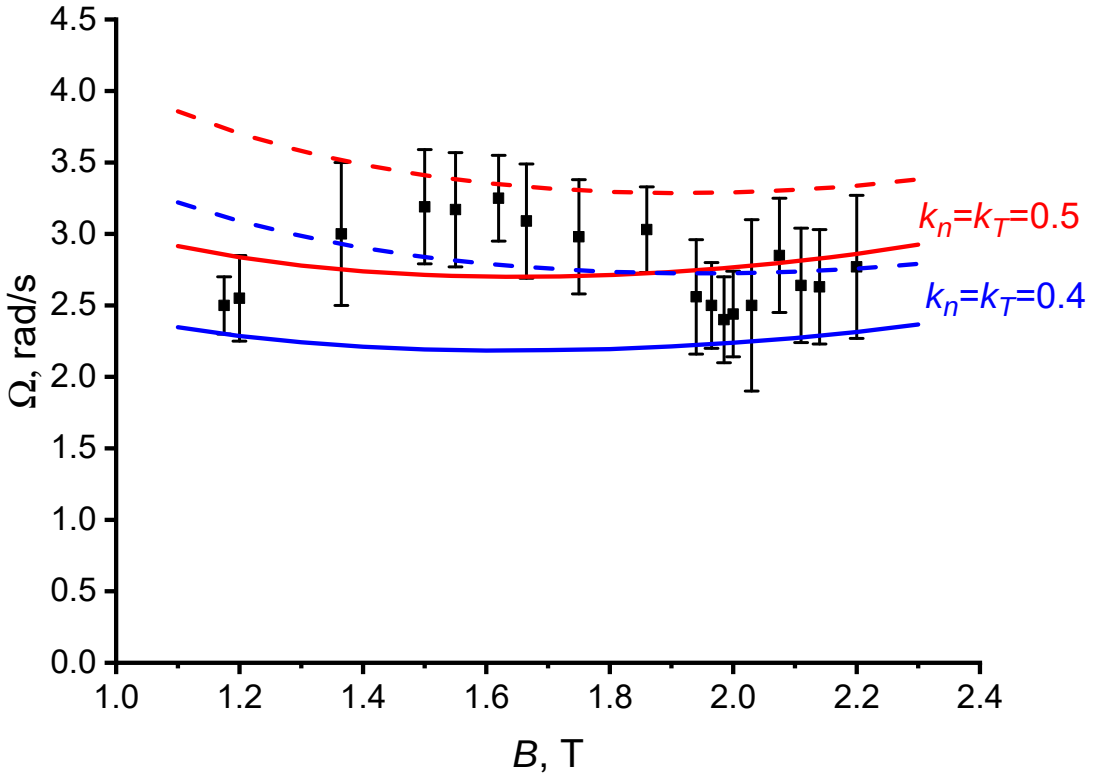



Fig. 2. Dependence of the angular velocity of the dust structure in a striation of a glow discharge on the magnetic field in neon at $p$ = 0.66 Torr and $I$ = 1.5 mA. Experimental data are given by black squares, curves show the calculation results obtained with allowance for ion drag (solid curves) and without it (dashed curves); red (upper) curves correspond to $k_T = k_n = 0.5$, blue (lower) curves correspond to $k_T = k_n = 0.4$.

The equation for calculating the contribution of ion drag, which is also valid for high magnetic fields ($B \sim 1$ T and more), was obtained in [12]:

$$\Omega_{id} \cong -\frac{2.9 n_{i0}(z)}{R^2 n_a} \frac{T_i z_d^2 \tau^3(z) \nu_{ea} \omega_{iB}}{m_i \nu_{ea} (\nu_{ia}^2 + 4\omega_{iB}^2) + 2 m_e \nu_{ia} (\nu_{ea}^2 + \omega_{eB}^2)}, \qquad (3)$$

where $R$ = 0.95 cm is the discharge tube radius, $n_a$ is the atom number density, $n_{i0}(z)$ is the ion number density near the discharge tube axis, $z$ is the axis coordinate of the dust particle in the striation ($z$ = 0 correspond to the $T_e$ maximum), $z_d = |Z_d| e^2 / a T_e$ is the dimensionless charge of the dust particle ($eZ_d$ is the dust particle charge), $\tau(z) = T_e(z)/T_i$ is electron to ion temperature ratio, $m_{i(e)}$ is the ion (electron) mass, $\nu_{e(i)a}$ is the frequency of electron (ion) collisions with atoms and $\omega_{e(i)B}$ is the electron (ion) cyclotron frequency. In experimental conditions [10] $n_a = 2.1\times10^{16}$ cm$^{-3}$, $n_{i0}(0) = 6.6\times10^{8}$ cm$^{-3}$, $\tau(0) \approx 10^2$, $z_d = 2.7$. The position of a dust particle in the striation $z$ is determined from the balance of the forces acting on it in the vertical direction: the electric field, gravity and ion drag forces.

The solid curves in Fig. 2 correspond to the results of calculations taking into account the contribution of ion drag (3). The role of this mechanism is secondary, however even at $B > 1$ T it affects the rotation velocity of dust particles. When it is taken into account, the values $k_T = k_e = 0.5$ lead to better agreement of the calculation with experiment than $k_T = k_e = 0.4$. Moreover, the slope of the theoretical curves with allowance for ion drag is in better agreement with the experimental data (on average) than without it.

**Acknowledgements**. This work was supported by the Russian Science Foundation (grant No. 22-12-00002) in the part of experiment and by the Ministry of Science and Higher Education of the Russian Federation (state assignment No. 075-01056-22-00) in the part of theoretical calculations.

## References

1. **Fortov V.E. and Morfill G.E.** Complex and Dusty Plasmas: From Laboratory to Space. New York: Taylor and Francis (2010).
2. **Melzer A., Kruger H., Schutt S. and Mulsow M.** Phys. Plasmas, 26 (2019) 093702.
3. **Choudhary M., Bergert R., Mitich S. and Thoma M.H.** Phys. Plasmas, 27 (2020) 063701.
4. **Dzlieva E.S,, D'yachkov L.G., Novikov L.A., Pavlov S.I. and Karasev V.Y.** Europhys. Lett., 123 (2018) 15001.
5. **Karasev V.Yu., Dzlieva E.S., Ivanov A.Yu. and Eikhval'd A.I.** Phys. Rev. E, 17 (2006) 066403.
6. **Nedospasov A.V.** Phys. Rev. E, 79 (2009) 036401.
7. **Vasiliev M.M., D'yachkov L.G., Antipov S.N., Huijink R., Petrov O.F. and Fortov V.E.** Europhys. Lett., 93 (2011) 15001.
8. **Golant V.E., Zhilinskii A.P. and Sakharov S.A.** Fundamentals of Plasma Physics. New York: Wiley (1980).
9. **Nedospasov A.V.** Europhys. Lett., 103 (2013) 25001.
10. **Dzlieva E.S., D'yachkov L.G., Novikov L.A., Pavlov S.I. and Karasev V.Y.** Plasma Sources Sci. Technol., 29 (2020) 085020.
11. **Sukhinin G.I. and Fedoseev A.V.** High Temperature, 44 (2006) 157–165.
12. **Dzlieva E.S., D'yachkov L.G., Novikov L.A., Pavlov S.I. and Karasev V.Y.** Plasma Sources Sci. Technol., 28 (2019) 085020.

# NEW RESULTS FROM DUSTY PLASMA EXPERIMENTS AT THE "PLASMA KRISTALL - 4" LABORATORY ON BOARD THE INTERNATIONAL SPACE STATION.

A. Lipaev[1], A. Zobnin[1], R. Syrovatka[1], A. Usachev[1],
A. Khrapak[1], O. Petrov[1], M. Thoma[2]

[1]Institute for High Temperatures, Russian Academy of Sciences, Izhorskaya 13/19, 125412 Moscow, Russia, usachev@ihed.ras.ru
[2]I. Physikalisches Institut, Justus-Liebig-Universit¨at Gießen, Heinrich-Buff-Ring 16, 35392 Gießen, Germany, Markus.H.Thoma@exp1.physik.uni-giessen.de

Laboratory dusty plasma is a "usual" gas discharge plasma with an admixture of micrometer size dust particles – microparticles. Due to plasma fluxes the microparticles are quickly charged up to $10^3$ – $10^4$ of the elementary electron charges and begin to interact with each other and with plasma fields and fluxes. They play an important role in the plasma charge balance, i.e. the microparticle component becomes an immanent part of the plasma. From this point of view, the laboratory dusty plasma is called complex plasma. Due to the large microparticle charges the coupling parameter $\Gamma$ for the dust subsystem can achieve hundreds of units, which makes it a very interesting physical object as an example of classical strongly coupled many-body system. In addition, the microparticles can be easily recorded by a video camera with high spatial and temporal resolution, which provides a unique opportunity to investigate it at the most fundamental kinetic level.

To avoid the stress of gravity on dust particles microgravity conditions are needed. The most suitable conditions for systematic experimental investigations are on board the International Space Station (ISS). For this purpose the joint Russian-European space experiment "Plasma Kristall - 4" (PK-4) was developed by Joint Institute for High Temperatures of Russian Academy of Sciences (Moscow, Russia) and Max-Planck Institute fur Extraterrestrische Physik (Garching, Germany) [1]. PK-4 was delivered to the ISS and operated there since 2015 in the European Laboratory Module "Columbus" (Fig. 1, left) based on a PK-4 Specific Agreement between Roscosmos and European Space Agency (ESA). The scientific program of the investigations is developed by the international PK-4 Facility Science Team (FST). The program of experiments includes the following tasks: microscopic properties of dusty plasma (processes of charging and discharging of dust particles, forces acting on particles, interaction between particles, their growth and agglomeration), structural properties of dusty plasma (self-organization of nonequilibrium dissipative systems), types of crystal lattices, wave properties of dusty plasma (self-excited and induced dust-plasma waves, dispersion relation of plasma-dust waves,

solitons and “dark” solitons, shock waves, Mach cones), new types of plasma-

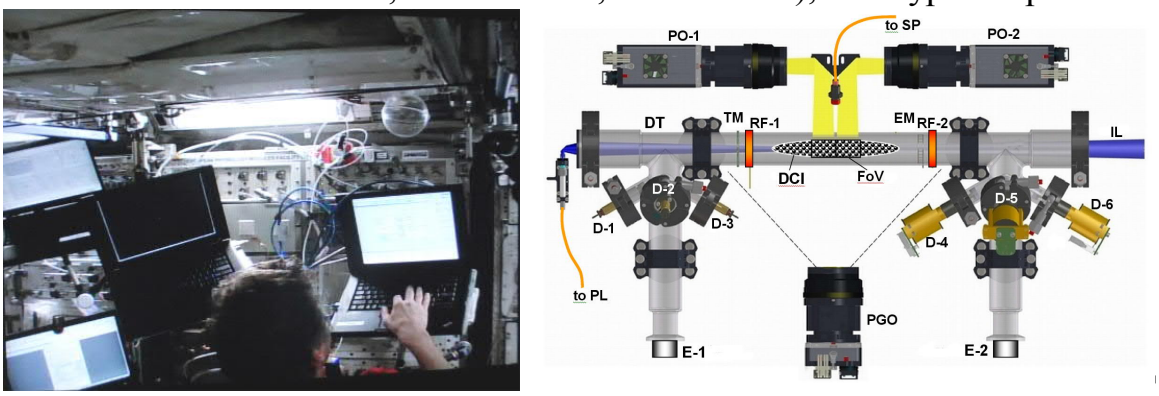



Fig. 1. Cosmonaut Gennady Padalka performs space experiments on the PK-4 setup in the Columbus module of the ISS during 1st experimental series in June 2015 (left). Scheme of the PK-4 discharge tube and equipment (right). Abbreviations please see text.

dust instabilities, mesoscopic physics, hydrodynamics of strongly non-ideal plasma-dust liquid (viscosity, turbulence), etc.

The scheme of the PK-4 discharge chamber is presented in Fig. 1 (right) [1]. The direct current (DC) gas discharge takes place in a П-shape glass tube of 3 cm inner diameter and of 85 cm total length between two cylindrical electrodes E-1 and E-2 at its ends. The discharge gases are neon or argon at a pressure between 10 Pa and 250 Pa. The discharge current can be set from 0.5 to 3 mA. To control the dust cloud position the discharge polarity can be switched with adjustable frequency (50 – 5000 Hz) and duty cycle. Six dust dispensers D-1 – D-6 can inject into the discharge plasma monodisperse spherical plastic microparticles of 1.31, 2.64, 3.38, 6.68 and 10.4 μm diameters. After their injection, the microparticles are transported by the axial electric field to the experimental central part of the tube and stopped there using the symmetrical polarity switching (DC-PS) mode forming a stable dust cloud (DCl). The microparticles are illuminated by a laser sheet (IL) and are recorded by two particle observation (PO) video cameras. A third plasma glow observation (PGO) video camera records the plasma glow in three spectral ranges separately: 585 and 703 nm (Ne spectral lines) and broad range 400 – 800 nm. An OceanOptics USB2000+ mini spectrometer can register plasma emission spectra in the spectral rage of 350 – 1000 nm with a spectral resolution of 1.5 nm to control the discharge regime.

During an experiment, the dust cloud is usually located in the center of the discharge tube and is subjected to external influences of various nature, such as powerful laser beam (PL), thermal manipulator (TM), two radio frequency inductive coils (RF-1) and (RF-2), electrical manipulator (EM), axial electric field and gas flow. The action of all these manipulators can be programmed and performed during an experiment, operators (cosmonaut or scientist) can

manually change any parameter. An interpretation of the obtained results is carried out on the basis of data of probe and spectral diagnostics of dusty plasma in the laboratory and the kinetic model of a positive column with a dust cloud of arbitrary shape [2].

Already in the first PK-4 space experiment conducted by cosmonaut Gennady Padalka in July 2015, a previously unknown phenomenon was discovered - the transverse instability of an extended plasma-dust cloud in a homogeneous positive column (Fig. 1 (left)), [3]. Oscillations were excited due to an ionization instability and the oscillation frequency was about 22 Hz.

An interesting structural feature of the dusty-plasma cloud in the positive column with a switchable polarity is the formation of a string liquid in an initially anisotropic structure, characterized by a bulk liquid order with the inclusion of dust chains called solid-like strings (Fig. 2) [4]. The direction of the

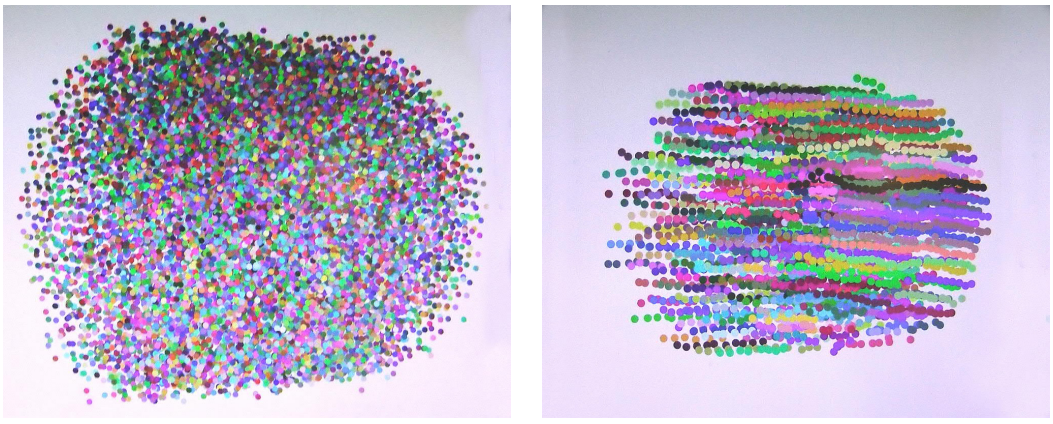


Fig. 2. Formation of a string liquid in the discharge chamber of the PK-4 setup: left – 3D dust structure immediately after the microparticle injection. Right - 3 minutes after the injection. Image size is about 15 mm.

strings corresponds to the direction of the axial electric field. Individual strings were identified and their size spectrum calculated. Interest in the string-liquid state of dusty plasma arose after the discovery of its electrorheological state, when, under the influence of an external electric field, it can drastically change its structure and viscosity. This opens up opportunities for other experiments. In particular, we find a slowing of dust acoustic waves and hypothesize that the additional attractive interaction leads to slower wave speeds than in complex plasmas with purely repulsive potentials [5]. Experiments are underway to measure the viscosity of the string fluid [6].

Recently, an attraction between negatively charged micron-sized plastic particles 3.4 μm of diameter and the formation of boundary-free dust clusters were observed in the bulk of a low-pressure DC-RF combined discharge plasma. The existence of such attractive forces was originally predicted by V. Tsytovich [4]. As a rule, usually all dust structures exist in electrostatic traps, which

prevent its expansion due to Coulomb repulsion of negatively charged microparticles. To prevent that, a high density discharge plasma is needed. Then the plasma fluxes can exceed the Coulomb repulsion. Unfortunately, high density plasma fluxes push the microparticles to the chamber walls. A compromise can be found in a dynamic regime – a dust acoustic wave has been compressed by a high power RF-discharge and the boundary-free clusters up to 0.5 mm in diameter were formed in wave crests (Fig. 3, right).

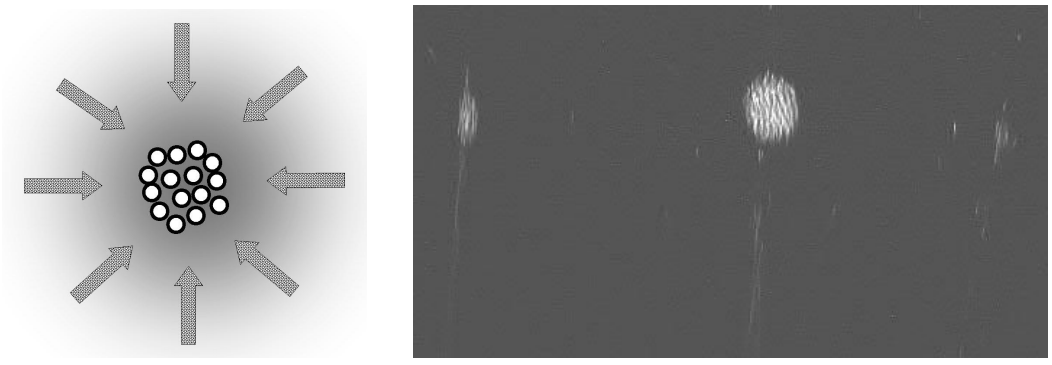


Fig. 3. Dust cluster is compressed by plasma fluxes (left)..
Experimental observation of a boundary-free cluster (right).

The obtained data can be used in different fundamental and practical applications.

**Acknowledgements.** All authors greatly acknowledge the joint ESA-Roscosmos "Plasmakristall-4" experiment on board the International Space Station. A. Lipaev, R. Syrovatka, A. Usachev and A. Khrapak were supported by the Russian Science Foundation Grant No.20-12-00365 and participated in the preparation and execution the space experiments on board the ISS. M. Thoma is supported by the German Aerospace Agency (DLR) under grant number 50WM2044.

## References

1. **Pustylnik M.Y. *et al.*** Review of Scientific Instruments, **87** (2016) 093505.
2. **Zobnin A.V., Usachev A.D., Petrov O.F., Fortov V.E., Thoma M.H., and Fink M.A**. Physics of Plasmas, **25 (2018)** 033702.
3. **Zobnin A.V., Usachev A.D., Lipaev A.M. *et al.*** Journal of Physics: Conference Series, **774** (2016) 012174.
4. **Pustylnik M.Y. *et al.*** Physical Review Research, 2 (2020) 033314.
5. **Schwabe M. *et al.*** New Journal of Physics, **22** (2020) 083079.
6. **Nosenko V. *et al.*** Physical Review Research, 2 (2020) 033404.

# VOLUME DUST STRUCTURES IN A PLASMA WITH MAGNETIZED IONS

V.Yu. Karasev, E.S. Dzlieva, S.I. Pavlov, L.A. Novikov,
S.A. Tarasov, D.V. Yanicin, O. E. Bashkircev

Saint Petersburg State University, 199034, Universitetskaya nab., 7/9,
St. Petersburg, Russia
Emails: plasmadust@yandex.ru, v.karasev@spbu.ru

Abstract. A dusty plasma was created in the experiment in the form of 3D dusty structures in a strong magnetic field. Dust traps with bulk dusty plasma are organized under conditions of dc discharge under the action of a longitudinal magnetic field. In the lightest inert gases in a magnetic field of 2 T, not only electrons, but also ions are magnetized. The electron cyclotron radius is comparable to the size of a dust particle, and the ion radius is comparable to the Debye screening length.

Volumetric dusty plasma structures are very attractive objects compared to two-dimensional monolayers due to the large opportunities for study, ranging from crystal packing and ordering to the impact on them of directed plasma flows in an anisotropic plasma medium, as well as charging and dynamics. The magnetic field is one of the types of external influences imposed on dusty plasma for its study, it has been actively used in recent years.

The purpose of this work is to describe experiments performed with dust traps in a glow discharge capable of holding bulk dust structures when a strong magnetic field is applied. The studies in dust traps in standing striations in a homogeneous and inhomogeneous magnetic field, as well as in the region of narrowing of the current channel (inside the dielectric discharge insert) are presented in more detail. In these traps, it turned out to be possible to keep dusty plasma in a magnetic field in the range up to 2 T.

The most used and studied dust trap is the *standing stratum*. In the case of a homogeneous magnetic field, the stratum can be kept at the center of the single magnetic coil. If discharge instabilities do not develop in a magnetic field, then a dust structure can form in a magnetic field of 2 T and higher. In [1] and [2], dusty plasma was studied separately in the range of magnetic induction up to 1 T and from 1 to 2 T. The geometric shape of the structure depends on the shape of the stratum and changes in a magnetic field. As the magnetic induction increases, the discharge parameters change. First of all, the ambipolar and diffusion coefficient and the ambipolar field change (when magnetization is

reached $\omega_e\tau_e\omega_i\tau_i = 1$). At B=0.1 T and p=0.7 torr in Ne the discharge already begins to contract radially and the length of the stratum increases. As a consequence, the dust structure itself in the stratum is radially compressed and elongated; some of its parameters are given in Table 1.

Tab. 1. Variation of structure parameters in a stratum in a magnetic field. $D_r$ is the radial size, H is the longitudinal size, N is the number of particles in the cross section.

| | 0 | 1 T | 2 T |
|---|---|---|---|
| $D_r$ | 5 mm | 1 mm | 1 m |
| H | 0.2 cm | 1 cm | 5 cm |
| N | 400 | 20 | 10 |

The second dust trap which turned out to be stable in a strong magnetic field, is the region of *narrowing of the discharge current channel*. This volume trap was discovered in [3] in a discharge insert 4 mm wide, elongated to 1 cm. In the absence of a magnetic field as well as in a field up to 0.02 T, the dust structure in it has the size of a tube section and is a small flat cluster. In a magnetic field of about 0.1 T, it undergoes a sharp radial compression and a decrease in the radial interparticle distance to 0.1 mm, followed by longitudinal elongation. For example in a field B=1 T (in Ne at the pressure p=0.4 Torr), its length is about 0.5 cm. Further radial compression as well as a decrease in the radial interparticle distance in a magnetic field above 0.1 T are not observed, see Table 2. This dust trap is very attractive for use in a magnetic field due to its great stability. For example, in the area of development of instability in the stratum at 0.3-0.4 T with partial loss of dust particles, only a radial displacement of the dust structure is observed in this trap on a scale of no more than one interparticle distance.

Tab. 2. Changes in the structure parameters in the region of narrowing of the current channel in a magnetic field. Designations correspond to Table1.

| | 0 T | 1 T | 2 T |
|---|---|---|---|
| $D_r$ | 3 mm | 1 mm | 1 mm |
| H | 3 mm | 5 mm | 5 mm |
| N | 200 | 50 | 50 |

The third volumetric dust trap, which turned out to be stable in a magnetic field, appears in *the region of a strong and sharply inhomogeneous magnetic field*; it was discovered in [4]. Probably, if the standing stratum is located close

to the face end of the magnetic coil, then it is significantly deformed in an inhomogeneous magnetic field. The shape of the observed "plasmoid" inside the coil (field B decreases from the center to the face end, from 2 T to 0.6 T) is significantly elongated. For example, in Ne at p=0.6 Torr, it exceeds 10 cm. In this case, dust chains of approximately the same length are formed above the end face of the magnetic coil. This area is characterized by the maximum longitudinal magnetic field gradient B/L=0.2 T/cm.

In addition to those listed above, there are volumetric dust traps in the glow discharge above the bottom wall of the chamber and in the region of the low-voltage arc, but when a strong magnetic field was applied, they did not give stable dust structures.

The discussed dust traps in a magnetic field differ significantly in their dynamics. In discharge and power plants in a magnetic field the plasma often comes into rotation. Let us formulate the difference between the rotation mechanisms and the dependence of the angular velocity on the magnetic induction in the discussed volume traps.

In the standing stratum in the strong magnetic field the rotation of the dust structure is associated with the rotation of the gas (different in direction in different phases of the stratum - at different heights) due to the action of the electron eddy current. Rotation mechanisms, separately for different ranges of magnetic induction, are presented in detail in [1,2]. Two features of the dust structure in this dust trap are: the rotation speed, on the order of 1 rad/s, which is limited by the viscosity of the gas; and the large longitudinal angular velocity gradient, up to 8 rad/(s*cm). The latter is possibly associated with a feature of the geometry of the bulk structure - the maximum elongation of the striation with the approach of dust structures to the region of the striation phase with the opposite direction of gas rotation.

In the region of the narrowing of the current channel, the ion drag mechanism operates at an increased plasma (ion) density. Even in the magnetic field of 0.01 T, the rotation rate exceeds any other experimental observations in both glow and RF discharges, from 15 rad/s. In the magnetic field above 1 T at a discharge current of 3 mA, the rotation speed reaches a record value of 100 rad/s, which was detected by high-speed video recording. The distribution of the rotation velocity along the longitudinal coordinate shows the almost complete absence of its gradient. This is radically different from the rotational dynamics in a standing stratum. For the trap used, the rotation mechanism is described in detail in [3].

For the trap in a nonuniform magnetic field, the rotation model has been developed so far for small structures located near the end face of the solenoid, when the shape of the striation is not yet disturbed [4]. Its features are the

simultaneous action of several rotation mechanisms. The position of the structure, its geometry, as well as the inhomogeneity of rotation strongly depend on the inhomogeneity of the magnetic field; detailed “maps” are given in [4] - the magnetic field, the radial and longitudinal coordinates of the section, and the speed of its rotation. The rotation speed is about 5 rad/s, its maximum gradient is in the area of maximum field inhomogeneity 10 rad/(s*cm).

The following features were found in the studied volumetric dust traps in a strong magnetic field. In the standing stratum, the largest elongation of the structure and the largest longitudinal gradient of the angular velocity are observed. In the region of the current channel narrowing, the elongation of the structure is not large and the longitudinal velocity gradient is completely absent, but the absolute value of the rotation velocity is record high. In an inhomogeneous magnetic field, the elongation of the structure is maximum, and the rotation rate depends significantly on the position of the cross section of the structure and the magnitude of the inhomogeneity of the magnetic field. Detailed descriptions of the discovered characteristics of dusty plasma are contained in the cited literature. The most interesting dynamical effects in a magnetic field begin to manifest themselves when the conditions under which the ions become magnetized are approached.

**Acknowledgements**. This work was supported by the RSF (grant No 22-12-00002).

## References

1. **Dzlieva E. S., D’yachkov L. G., Novikov L. A., Pavlov S. I. Karasev V. Y.** EPL. 123 (2018) 15001
2. **Dzlieva E.S., Dyachkov L.G., Novikov L.A., Pavlov S.I. , Karasev V. Yu.** Plasma Sources Science and Technology**.** 29 (2020) 085020.
3. **Dzlieva E.S., Dyachkov L.G., Novikov L.A., Pavlov S.I. , Karasev V. Yu.** Plasma Sources Science and Technology**.** 28 (2019) 085020.
4. **Dzlieva E.S., Dyachkov L.G., Novikov L.A., Pavlov S.I., Karasev V.Yu** Molecules. 26. (2021) 3788.

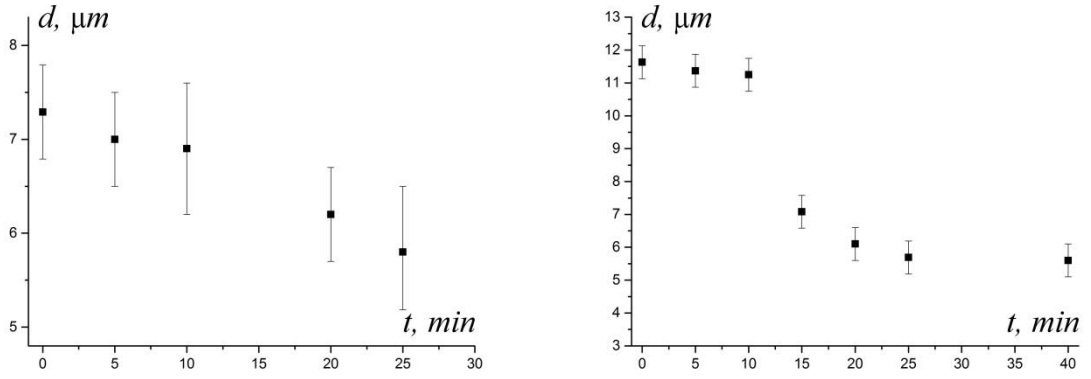
# FRACTAL ANALYSIS OF THE SURFACE OF MELAMINE-FORMALDEHYDE DUST PARTICLES

A. Gorbenko[1], V. Polischuk[2], E. Dzlieva[1], S.Pavlov[1], V.Karasev[1]

[1]Saint-Petersburg State University, Russia, 199034, St.Petersburg, Universitetskaya nab., 7-9, a.gorbenko@spbu.ru
[2]Admiral Makarov State University of Maritime and Inland Shipping, Russia, St.Petersburg, Dvinskaya str., 5/7

Plasma treatment is now widely used for modifying polymer surfaces properties such as adhesion, friction, penetrability, wettability and biocompatibility [1-2]. The possibility of "trapping" polymer microparticles in the vertical part of a gas-discharge tube in a non-uniform electric field of a glow discharge opens new perspectives in this area. The authors of [3-5] obtained data on the modification of calibrated spherical particles of melamine-formaldehyde (MFR) with a diameter of $7.3 \pm 0.4$ μm in neon plasma (Ne, $p = 40$ Pa, $i = 2.5$ mA, exposure time from 5 to 25 min). The experimental technique is described in detail in [4]. Particles were injected into the vertical discharge region from a container located inside the discharge tube. Almost instantaneously, the particles acquired a significant negative charge. In a non-uniform stratum field for charged particles there were areas where the Coulomb force can balance the force of gravity. Particles "hang" in plasma-dust traps and can be in them for a long time under the influence of plasma. When you turn off the discharge, particles fall on a collecting platform, which was then removed from the discharge tube. Extracted particles were examined by electron microscopy (SEM method). The obtained 2D Tiff images of various scales were analysed using software: Smart tiff - for measuring the particle diameter, Gwyddion - for studying the properties of the surface. The roughness $R_a$, which was defined as the absolute deviation of all points of the profile from the midline, averaged over the length of the estimate, was chosen as a parameter for evaluating the properties of the surface.

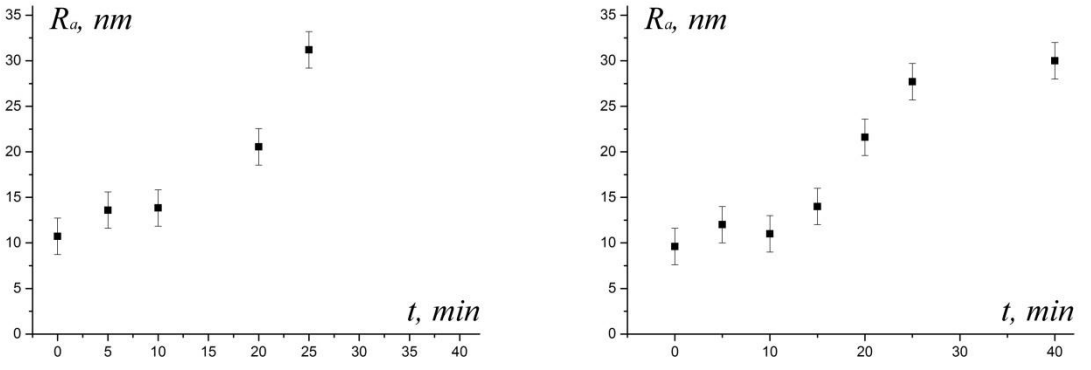
Subsequently, the authors of [6] managed to modify microparticles of larger diameter ($11.6 \pm 0.4$ μm) in the same discharge tube (Ne, $p = 25$ Pa, $i = 2.1$ mA, exposure time from 5 to 40 min). In experiments with MFR particles of two sizes, the following results were obtained: 1) particles under the influence of plasma decrease in size, maintaining a spherical shape (Fig. 1); 2) the surface of the particles changes its properties, which is manifested in a change in the roughness $R_a$ depending on the residence time in the plasma (Fig. 2).




a) b)

Fig. 1. The change in the diameter of MFR microparticles: a) the diameter of the original particles is 7.3 ± 0.4 μm, Ne, p = 40 Pa, i = 2.5 mA, exposure time from 5 to 25 min; b) the diameter of the original particles is 11.6 ± 0.4 μm, Ne, p = 25 Pa, i = 2.1 mA, exposure time from 5 to 40 min.

The construction of a model of processes under the influence of which MFR particles are modified in the glow discharge plasma requires an assessment of the rough surface area. Fractal analysis methods allow making such estimates. Many randomly rough surfaces belong to the class of random objects that exhibit the properties of affine self-similarity and are treated as affine-like statistical fractals. The fractal analysis of such surfaces makes it possible to obtain the value of the parameter Df, which acts as a power factor in estimating the area of a rough surface.




a) b)

Fig. 2. The change in surface roughness $R_a$ of MFR microparticles: a) the diameter of the original particles is 7.3 ± 0.4 μm, Ne, p = 40 Pa, i = 2.5 mA, exposure time from 5 to 25 min; b) the diameter of the original particles is 11.6 ± 0.4 μm, Ne, p = 25 Pa, i = 2.1 mA, exposure time from 5 to 40 min.

The estimation of the parameter $D_f$ by the cube counting method is carried out as follows. In the image obtained by the SEM method, an area of optimal size is chosen (in our case, this is a square of 400x400 px), a cubic lattice with a lattice constant *l* is superimposed on the surface expanded in z. On the z-axis of the surface image, a gray gradation from 0 to 255 is plotted. Initially, *l* is set to 200 px, resulting in a grid of 2 × 2 × 2 = 8 cubes. Then N (*l*) is the number of all cubes containing at least one pixel of the image. The lattice constant *l* at each step is halved and the process repeats until *l* becomes equal to the distance between two adjacent pixels. The slope of the graph of logN(*l*) from log1/*l* directly gives the fractal dimension $D_f$. The cube counting algorithm is built into the Gwyddion software.

An estimate of the $D_f$ value for the surface of particles of two sizes (original and plasma treated) gives values of 2.4 to 2.8. This result shows that the calculation of the surface area of particles when modelling processes in the dusty plasma without taking into account its topology can lead to significant errors. Table 1 shows the values of the parameter $D_f$ for the original particles and the particles plasma treated for 20 minutes, which were used in the experiments; the surface area of the sphere, calculated as $4\pi r^2$ (S), and the microparticle surface area taking into account its topology (S`).

| | **d, μm** | **$D_f$** | **S, μm$^2$** | **S`, μm$^2$** |
|---|---|---|---|---|
| Original particles | 7.3 | 2.71 | 170 | 8600 |
| Exposure time 20 min | 6.6 | 2.63 | 140 | 3000 |
| | **d, μm** | **$D_f$** | **S, μm$^2$** | **S`, μm$^2$** |
| Original particles | 11.6 | 2.74 | 420 | 15300 |
| Exposure time 20 min | 6.1 | 2.52 | 120 | 1500 |

Table 1. The surface area of the particle, calculated as $4\pi r^2$ (S), the calculation of the surface area taking into account the surface topology (S`).

**Acknowledgements**. This work was supported by the Russian Science Foundation (RSF) (grant № 22-12-00002).

## References

1. **Yasuda H.** Plasma Polymerization. Academic, Orlando, Florida, (1985).
2. **Hisham M.** Abourayana and Denis P. Dowling, Plasma Processing for Tailoring the Surface Properties of Polymers. IntechOpen, London, (2015)
3. **Ermolenko M.A., Dzlieva E.S., Karasev V.Yu., Pavlov S.I., Polishchuk V.A., and Gorbenko A.P.** Tech. Phys. Lett., 41 (2015) 1199.
4. **Karasev V.Yu., Polishchuk V.A., Gorbenko A.P., Dzlieva E.C., Ermolenko M.A., and Makar M.M.,** Phys. Solid State, 58 (2016) 104.

5. **Karasev V.Yu., Dzlieva E.S., Gorbenko A.P., Mashek I.Ch., Polishchuk V.A., and Mironova I.I.,** Tech. Phys., 62 (2017) 496.
6. **Karasev V.Yu., Dzlieva E.S., Pavlov S.I., Matvievskaya O.V., Polischuk V.A., Ermolenko M.A., Eikhval'd A.I., Gorbenko A.P.,** Contr. Plasma Phys., (2019) e201800145.

# FRACTAL DIMENSION OF EXTENSIVE SYSTEMS OF JANUS AND METAL-COVERED GRAINS IN COLLOIDAL PLASMAS

X. G. Koss, E. A. Kononov, I. I. Lisina, M. M. Vasiliev and O. F. Petrov

[1]Joint Institute for High Temperatures of the Russian Academy of Sciences, 125412, Izhorskaya st. 13 Bd.2, Moscow, Russia, Xeniya.Koss@gmail.com
[2]Moscow Institute of Physics and Technology, 141701, Institutskiy per., 9, Dolgoprudny, Moscow Region, Russia

Recently, the problems considering the dynamics of so-called active Brownian, or self-propelled, particles, become more and more essential. These particles possess the unique property to convert external energy into the kinetic energy of their motion [1]. The nature of these particles may be various: colloid grains in buffer media, protozoa and bacteria, chemically activated particles and even mechanical objects [1]. Active Brownian particles and structures made of them, thanks to their ability to transform energy, have some exceptional properties and features which are interesting both for the fundamental science and for the practical tasks – in biology, medicine, engineering [1].

The entropy and other instruments used in the framework of physics of dissipative systems are universal, and they can be successfully applied to study the evolution of active Brownian systems. In this work we use the approach proposed in [2] – the calculation of the mean first-passage time (MFPT) dynamic entropy. With this approach, one can describe the motion of each separate (active or passive) Brownian particle with the help of several parameters (such as the fractal dimension of its trajectory and the size of the localization area), compare the different regimes of motion with each other.

We have analyzed the experimental data on the motion of active Brownian micrograins in RF-discharge plasmas. Two types of microparticles were considered: 1) plastic grains fully covered with metal; 2) Janus particles with a thin metal cap. The trajectories of separate grains were obtained, pair correlation functions of the structures were plotted. We have studied the dependencies of the MFPT dynamic entropy on the coarsening parameter, the fractal dimension of the system on its mean kinetic temperature $\Delta_f(T)$, the mean localization area of the grain on its mean kinetic temperature. The curve plotting the dependence $\Delta_f(T)$ for metal-covered particles has two special points $T_1$ and $T_2$ (Fig. 1). The point $T_1 \sim 30$ eV seems to correspond to the dynamic phase transition from the more ordered state to the less ordered ("crystal-liquid" transition). On the figures plotting the trajectories of all the particles in the structure, after passing this point the trajectories of the separate particles become indistinguishable. Further, for the range of temperatures 30-100 eV the fractal dimension of trajectories changes slightly and is close to 1.5 — the value of the fractal dimension of

trajectories of active Brownian clusters at high temperatures [3]. For $T > T_2 \sim 120$ eV $\Delta_f(T)$ of metal-covered particles experiences a jump. This jump demonstrates the transition to the state when the particle begins to "feel" the trap, and its trajectory covers the plane denser. Based on the obtained results, we conclude that the character of motion of our active Brownian systems changes as the power of illuminating laser (and therefore the mean kinetic temperature of the grains) increases. We have revealed two critical points for metal-covered particles.

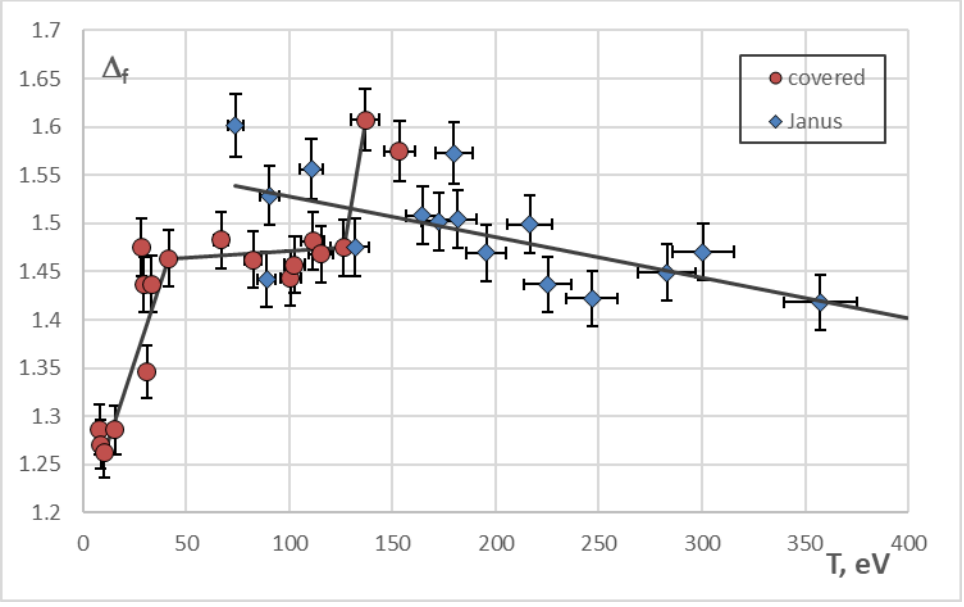



Fig. 1. The dependence of mean fractal dimension of the trajectories for ○ — metal-covered and ◊ — particles on their mean kinetic temperature.

For the Janus particles, we have observed the monotonous growth of the mean localization area and the decrease of the mean fractal dimension of their trajectories with increasing kinetic temperature T. That is the evidence that the motion of Janus particles becomes less chaotic and more directed as the system warms up.

## References

1. **Bechinger, C.; Di Leonardo, D.; Löwen, H.; Reichhardt, C.; Volpe, G.; Volpe, G.** Rev. Mod. Phys., 88 (2016), 045006.
2. **Allegrini, P.; Douglas, J.F.; Glotzer, S.C.** PRE 60 (1999), 5714.
3. **Koss, X.G.; Petrov, O.F.; Statsenko, K.B.; Vasiliev, M.M.** EPL 124 (2018), 45001.

# DYNAMIC EFFECTS IN DUSTY CLUSTERS IN A MAGNETIC FIELD

S. Pavlov, E. Dzlieva, L. Novikov, V. Karasev

Saint Petersburg State University, 199034, Universitetskaya emb., 7/9, St. Petersburg, Russia, and E-mail: s.i.pavlov@spbu.ru

**Introduction.** Threshold and critical phenomena are of great interest in physics because they are associated with a change in the properties of the medium in which the system under study is located. In dusty plasma [2] and in a number of other systems representing "soft matter" [2-4], as well as in plasma itself [5], threshold and nonlinear phenomena are the subject of research. Their examples are fluxes of the dust component [6], own rotation (demonstration of paramagnetic properties) of dust particles [7-8]. Of particular interest for the study of this phenomenon may be a dust system with a variable countable number of particles, when a change in the number of particles one at a time (at the kinetic level) changes the state and dynamics of the entire system (macroparameters).

Dust clusters with a small countable and a significant number of particles were created in [9–13]. They are characterized by the order in which shells of certain configurations are filled. For this purpose, exposure is applied, for example, by a laser beam, which can set in motion individual shells and excite certain vibrational modes [9–10]. In the present study, a magnetic field is used as an influence, capable of causing, due to the ion drag force, rotation (azimuth movement), which is not affected by other forces.

The influence of the number of dust particles on the dust structure and its dynamics found in [13, 14] is still not unambiguously understood, and the experimental data differ significantly. In the presented study, the study of the influence of number of particles on the dynamics of rotation (the threshold for its appearance and the velocity trend) was chosen as the basis. It was found that the number of particles in the cross section of the cluster perpendicular to the magnetic induction is not an unambiguous parameter for the occurrence of threshold rotation. The paper also contains detailed information about the parameters that affect the value of the untwisting threshold: the size of dust particles, the discharge current, the pressure and type of the plasma-forming gas, and the magnetic field.

**Experiment**. The study was carried out in the stratum of glow discharge: Plasma-dust structures were created in the glow discharge stratum in a vertically oriented discharge tube. The first stratum from the dielectric insert (stabilizing the discharge) was chosen for observation. Neon was used as a plasma-forming gas at the pressure range from 0.3 to 1 Torr. The discharge current was varied in

the range from 1.6 to 2.2 mA. Polydisperse particles of lithium niobate with an average size of 4 μm and a density of $4.6*10^3$ kg/m$^3$, hollow microspheres of borosilicate glass with a size of 10 μm and a density of about $0,4\text{-}0,9*10^3$ kg/m$^3$ and calibrated particles of melamine-formaldehyde with a size of 4 μm and a density of $1.5*10^3$ kg/m$^3$ were used as the dust component.

By gently shaking the container with dust particles, it was possible to inject a countable number of particles into the discharge, thereby making it possible to create clusters or structures with the required number of particles in a horizontal section. Dust particles were illuminated with a laser knife formed by a semiconductor laser module with a wavelength of 650 nm and a power of 40 mW and a cylindrical lens. The observation was made through the upper end window. The magnetic field was created by a system of magnetic coils in such a way that the magnetic induction vector coincided with the discharge axis. Video recording was carried out using a camera with long focal length lens, with a frequency of 25 fps (Fig. 1).

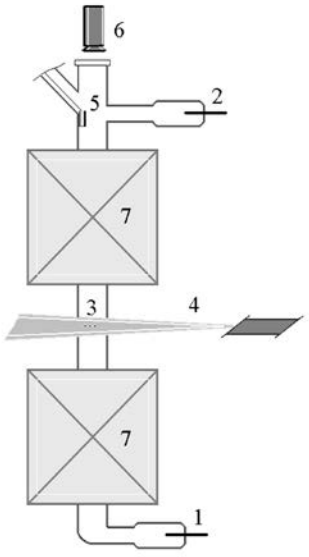



Fig. 1. Layout of the experimental setup: (1) cathode, (2) anode, (3) dusty structure, (4) laser illumination, (5) container with particles, (6) video camera, and (7) magnetic coils.

**Results**.

The following results were obtained:

1. For “small” (2 μm) particles, a rotation threshold appears for a cluster consisting of 3 particles, while the rotation of the structure begins immediately with an increase in the magnetic field (Fig. 2).

2. For “small” (1 μm) particles, the rotation threshold appears for a cluster consisting of both 6 and 10 particles.

3. For large particles (10 μm) at a current of 2.0 mA, there is no threshold,

and there is no difference between the dependences of the angular velocity of rotation on the magnetic field for 3 and 10 particles.

4. The existence of a threshold magnetic field (at which rotation of the dust formation occurs) from the discharge current is found. Under the chosen conditions, at a current of 1.6 mA, rotation occurs at a magnetic field of the order of 50 G, and an increase in current to 2.2 mA leads to the absence of a rotation threshold.

5. The gas pressure affects the threshold magnetic field: with increasing pressure, there is a threshold for the occurrence of rotation.

6. On the dependence of the angular velocity of rotation of the dust formation on the number of particles, peaks were found when there are 7 particles in the horizontal section and in the region of 19 particles in the horizontal section, i.e. full 1 or 2 hexagonal shells.

7. There is a threshold for the onset of rotation for "average" particles (4 mkm): for a cluster of 3 particles, rotation begins after 50 G, while for a cluster of 10 particles at a lower magnetic field (10 G).

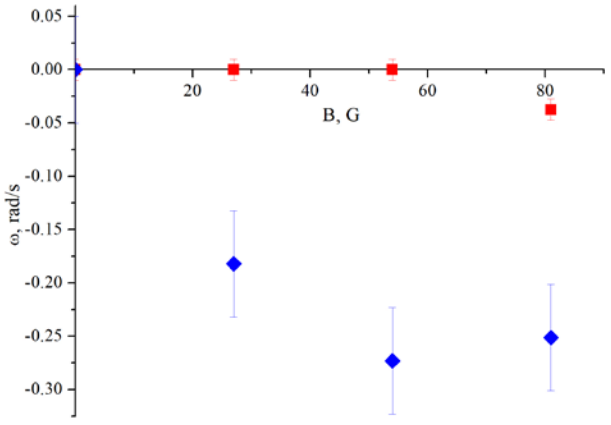



Fig. 2. Dependence of the angular velocity of rotation on magnetic induction. Conditions: Ne, p=0.3 Torr, $LiNiO_3$, I=2.2 mA, ■- 3 particles per cross-section, ♦- 30 particles per cross-section.

**Conclusion.** On the basis of the experiment, it is possible to give a qualitative explanation of the unwinding. The reasons for the threshold are a compromise between the driving force: ion drag (depends on discharge current i, magnetic field induction B and depends weakly on gas pressure P) and the force that prevents directional movement (friction force) and "coupling" in the structure. There is no static friction force. The “coupling” depends on the number of particles and the charge density (size) of the particles. The unwinding phase (the start of rotation) passes through the development of intense oscillations in the azimuth direction. For example, one particle starts azimuthal rotation, but the

rest stand still and the directed motion of the first particle "dissipates" through the repulsion and rearrangement of the others. And only if the azimuthal flux of ions (i, B) is large, or the dust cluster is rigidly bound, the rotation of the cluster as a whole begins with ω=const, so the unwinding threshold, in addition to B, also depends on i, P, d and the type of gas.

**Acknowledgements**. This work was supported by the Russian Science Foundation (grant No 22-12-00002).

## References

1. **Fortov V.E. and Morfill G.E.** Complex and Dusty Plasmas: From Laboratory to Space. New York: Taylor and Francis (2010).
2. **Romanov V.P.** Soros educational journal, 7 № 1 (2001) (in russian).
3. **Zakhlevnykh A.N., Makarov D.V.** Liquid crystals and their practical use, № 2 (32). (2010) C. 58-66 (in russian).
4. **Nedospasov A.V.** Phys. Rev. E, 79 (2009) 036401.
5. **F. Chen** Introduction to Plasma Physics and Controlled Fusion. Plenum press New York & London (1983).
6. **Gavrikov A.V., Goranskaya D.N., Ivanov A.S., Petrov O.F., Timirkhanov R.A., Vorona N.A., Fortov V.E.** J. Plasma Phys., 76. No. 3–4 (2010) 579.
7. **Sato N., Uchida G., Kaneko T., Shimizu S. and Iizuka S.** Phys. Plasmas, 8 (2001) 1786-90
8. **Karasev V.Yu., Dzlieva E.S., Eikhval'd A.I., Ermolenko M.A, Golubev M.S., Ivanov A.Yu.** Phys. Rev. E., 79 (2009) 026406.
9. **Juan W.-T. et al.** Phys. Rev. E., 58 (1998) R6947.
10. **Klindworth M. et al.** Phys. Rev. B., 61 (2000) 8404.
11. **Cheung F., Samarian Al., James B.** New Jour. Phys., 5 (2003) 75.1-15.
12. **Bonitz M., Horing N. and Ludwig P.** Introduction to Complex Plasma. Berlin: Springer (2010).
13. **Sato N.** AIP Conf. Proc, 649 (2002) 66-73.
14. **Konopka U., Samsonov D., Ivlev A .V., Goree J., Steinberg V. and Morfill G. E.** Phys. Rev. E, 61 (2000) 1890-8.

# ACTIVE BROWNIAN PARTICLE IN A PLASMA

E. A. Lisin, O. S. Vaulina, I. I. Lisina, O. F. Petrov

Joint Institute for High Temperatures, Izhorskaya 13 Bd 2, Moscow 125412, Russia

A colloidal plasma is a nontrivial instance of soft condensed matter [1]. Under certain conditions, the colloidal plasma becomes a thermodynamically open, non-Hamiltonian system that can exhibit the properties of active matter [2–5]. Active matter is a state of condensed matter, which represents an ensemble of active Brownian nano- or microparticles in a dissipative medium. Such particles autonomously convert the available (chemical, electromagnetic, thermal, etc.) energy of the environment into their own directed mechanical motion. Many examples of active matter are of biological origin; however, a significant part of the current experimental and theoretical research is devoted to artificial systems. A striking example of a synthetic active particle is the Janus particle. It is a bifunctional particle the two parts of which differ in chemical composition and as a result have different surface and/or volume properties. The interaction of the Janus particle with the environment generates a driving force that causes the particle to move itself. In a colloidal plasma, suitable conditions can be implemented for non-uniformly light-absorbing Janus particles driven by thermophoretic forces [3-5]. Depending on their shape and surface inhomogeneity such particles have either random or looped trajectories combining hot Brownian, spinning and circling motion. In the simplest case, the dynamics of a perfect spherical Janus particle represents a combination of translational Brownian motion and propulsive motion coupled with random rotation.

It is convenient to use the Ornstein-Uhlenbeck process as an approximated treatment of evolution of a driving (propulsion) force acting on a self-propelled particle [6, 7]. Consider the one-dimensional motion of a particle of mass $M$ and charge $Q$ in a homogeneous medium under the influence of two independent random forces of different nature: the time-correlated driving force $R$; and the Langevin force $L$ which is the source of stochastic (thermal) motion with the temperature $T$, i.e. Brownian motion due to collisions with atoms/molecules of the surrounding media. We also include in our model a harmonic trap with a characteristic frequency $\omega_0=(Q\beta/M)^{1/2}$, where $\beta$ is the gradient of the external linear electric field $E$. The velocity $V$ and the displacement $x$ of such a particle can be found from the Langevin equation:

$$M\frac{dV}{dt}=-M\nu_{\rm fr}V-M\omega_0^2x+R+L,$$

where $\nu_{\rm fr}$ is the friction coefficient of the particle. In a local thermodynamic equilibrium, $\langle RL\rangle = 0$. Here and further $\langle\ldots\rangle$ denotes the result of averaging. The

autocorrelation function for the Langevin force is $\langle L(0)L(t)\rangle = 2T\,M\nu_{\rm fr}\delta(t)$, where $\delta(t)$ is a delta function that describes a delta-correlated Gaussian process. The evolution of the force $R$ is described by the Ornstein-Uhlenbeck process:

$$\frac{dR}{dt} = -\omega R + \vartheta,$$

where $\vartheta$ is a random number with $\langle\vartheta\rangle=0$ and $\langle\vartheta(0)\vartheta(t)\rangle = 2\langle R^2\rangle\omega\delta(t)$ which describes a delta-correlated Gaussian process, and $\omega$ is the characteristic frequency of this process.

If $\omega_0 < \nu_{\rm fr}/2$, the mean-square displacement of the particle is described as follows:

$$\left\langle x^2(t)\right\rangle = \left\langle x_T^2(t)\right\rangle + \left\langle x_R^2(t)\right\rangle,$$

$$\left\langle x_T^2(t)\right\rangle = \frac{2T}{M\omega_0{}^2}\left[1 - e^{-\nu_{\rm fr}t/2}\left(\mathrm{ch}(\nu_{\rm fr}t\psi) + \frac{\mathrm{sh}(\nu_{\rm fr}t\psi)}{2\psi}\right)\right],$$

$$\left\langle x_R^2(t)\right\rangle = \frac{2\delta V^2}{\omega_{\rm c}{}^2}\left\{1 - \frac{1}{b}\left[(\omega_0{}^2 - \omega_{\rm c}{}^2)e^{-\omega t} + e^{-\nu_{\rm fr}t/2}\left(\begin{array}{l}\mathrm{ch}(\nu_{\rm fr}t\psi)\{\omega_{\rm c}{}^2 + \omega(\omega - \nu_{\rm fr})\} + \\ + \dfrac{\mathrm{sh}(\nu_{\rm fr}t\psi)}{\nu_{\rm fr}\psi}\{\omega_{\rm c}{}^2(\dfrac{\nu_{\rm fr}}{2} - \omega) + \omega\dfrac{\nu_{\rm fr}}{2}(\omega + \dfrac{2\omega_0{}^2}{\nu_{\rm fr}} - \nu_{\rm fr})\}\end{array}\right)\right]\right\},$$

where

$$\delta V^2 = \frac{\left\langle R^2\right\rangle}{M^2\nu_{\rm fr}\left[\nu_{\rm fr} + \omega + \omega_0^2/\omega\right]},$$

and $\psi = (1 - 4(\omega_0/\nu_{\rm fr})^2)^{1/2}/2$, $b = (a_1 - \omega)(a_2 - \omega)$, $a_1 = -\nu_{\rm fr}/2 + \nu_{\rm fr}\psi$, $a_2 = -\nu_{\rm fr}/2 - \nu_{\rm fr}\psi$, $\omega_{\rm c}{}^2 = \omega\,\omega_0{}^2/(\nu_{\rm fr} + \omega)$. If $\omega_0 > \nu_{\rm fr}/2$, the value of $\psi$ is given by $\psi = (4(\omega_0/\nu_{\rm fr})^2 - 1)^{1/2}/2$, and the functions *ch* and *sh* should be replaced by *cos* and *sin*, respectively.

The characteristic frequency $\omega$ is the rotational diffusion coefficient. The ratio of the rotational diffusion coefficient to the friction coefficient depends on the parameters of the medium and the particle as follows [8]

$$\frac{\omega}{\nu_{\rm fr}} = \frac{\rho T}{36\pi a\eta^2}$$

where $a$ is the particle radius and $\rho$ is the average particle density and the coefficient of dynamic viscosity can be calculated using the Epstein formula [8, 9]. At low gas pressures, the $\omega/\nu_{\rm fr}$ ratio is proportional to $P^{-2}$ and $a^{-3}$. For example, $\omega/\nu_{\rm fr} \sim 10$ for a particle with $a$=10 $\mu$m at a pressure of 1 Pa, and $\omega/\nu_{\rm fr} \sim 0.1$ for $a$=10 $\mu$m and $P$=10 Pa. Thus, laboratory experiments with self-propelled particles in a weakly ionized gas discharge plasma have great potential for studying active Brownian motion since they enable to control the $\omega/\nu_{\rm fr}$ ratio over a wide range.

If intensity of rotational fluctuations is small, $\omega/\nu_{fr}$ <1 or ~1, the equations obtained above for the mean-square displacement of a spherical Janus particle in a trap are valid. However, when $\omega/\nu_{fr} \gg 1$, it is necessary to take into account the rotational inertia of the particle [10]. In the latter case, if $\omega_0$=0, then $\delta V^2$ should be replaced by $\delta V^2\sqrt{1+5J\omega^2/3T}$, where $J$ is the particle moment of inertia [10].

**Acknowledgements**. This work was supported by the Russian Science Foundation under grant №22-22-00899.

## References

1. **Ivlev A., Morfill G., Lowen H., Royall C.P.** Complex plasmas and colloidal dispersions: Particle-resolved studies of classical liquids and solids. World Scientific Publishing Company (2012).
2. **Bechinger C., Di Leonardo R., Löwen H., Reichhardt C., Volpe G., Volpe G.** Rev. Mod. Phys., 88 (2016) 045006.
3. **Nosenko V., Luoni F., Kaouk A., Rubin-Zuzic M., Thomas H.** Phys. Rev. Res., 2 (2020) 033226.
4. **Arkar K., Vasiliev M. M., Petrov O. F., Kononov E. A. and Trukhachev F. M.** Molecules, 26 (2021) 561.
5. **Koss X.G., Kononov E.A., Lisina I.I., Vasiliev M.M., Petrov O.F.** Molecules, 27 (2022) 1614.
6. **Caprini L. and Marconi U.M.-B.** J. Chem. Phys., 154 (2021) 024902.
7. **Nguyen G.P., Wittmann R. and Löwen H.** Journal of Physics: Condensed Matter, 34 (2021) 035101.
8. **Lisin E.A., Vaulina O.S., Lisina I.I. and Petrov O.F.** Phys. Chem. Chem. Phys., 23 (2021) 16248.
9. **Epstein P.S.** Physical Review, 23 (1924) 710.
10. **Lisin E.A., Vaulina O.S., Lisina I.I. and Petrov O.F.** Phys. Chem. Chem. Phys., 24 (2022) 14150-14158

# CALCULATIONS OF THE EQUATION OF STATE AND ELECTRONIC TRANSPORT COEFFICIENTS OF LOW-TEMPERATURE BISMUTH PLASMA

E. M. Apfelbaum[1]

[1]Joint Institute for High Temperature of Russian Academy of Sciences, Izhorskaya 13 bldg. 2, Moscow 125412, Russia, apfel_e@mail.ru

The thermophysical properties of any substance play an important role in many applied and fundamental tasks [1]. Thus, their calculations and measurements continue for more than a century for various substances within different area of the phase diagram. Here we will consider among these properties the thermodynamical ones and the electronic transport coefficients - the electrical conductivity, thermal conductivity and thermal power. The metals have been also intensively studied and presently there exist reliable equations of states and models for the transport coefficients, which can be safely used in various macroscopic (hydrodynamics) problems [2]. However, so benign situation for metals concerns only the areas with relatively low $T$ - namely the solid and liquid states. (Below $T$ is the temperature, $V$ is the volume, $\rho$ is the mass density, $P$ is the pressure, $U$ is the internal energy, $C_V$ is the heat capacity at constant volume.) At elevated $T$ it is the problem in the experiments to create the corresponding equilibrium (or local equilibrium) state even without any other measurements. Such a situation is usual at $T >$ 2-5 kK for various metals. There are also some intrinsic obstacles in the theory and calculations [1]. Thus, the low temperature plasma for metals, which is located at $T \sim$ 10 - 100 kK, was less studied in comparison with analogous plasmas for gases up to now.

However, during recent 20 years there have been developed new experimental and calculations techniques, which can solve this problem, see for example [3-8]. Thus, presently we have appropriate information for different metals, including Al, Fe, Ni, Cu etc. But there are still some elements that have not been studied yet in this concern. Bismuth (Bi) is among them.

Bismuth has a relatively low melting temperature $T_m$ = 544.7 K, so there is even more information for this element in the liquid state up to $T \sim$ 2 kK, than for other mentioned above metals, which have higher $T_m$. Moreover, the estimates of the critical point parameters for Bi are less scattered than for many other metals [9]. However, at higher $T$, the number of data for the considered properties of Bi is drastically lessened. Of course, there are the results of shock-wave measurements, which started 60 years ago and continue nowadays [10-12]. The measurements are supported by the most advanced calculations techniques [4-8]. But all these investigations concerns only the region of relatively high $\rho$,

namely $\rho \sim \rho_n$, $\rho_n$ = 10.05 g/cm$^3$ - is Bi density under ambient conditions. The lowest density reached in shock - wave measurements [11] (without measurements of $T$) was $\rho \sim \rho_n/3$. As a result, at $\rho < \rho_n/3$ and $T$ higher than ~ 10 kK there have not been any published data on the considered properties for Bi up to now. Thus, the aim of present study is to fill up this gap. We should also note that at $T$ > 100 kK the influence of radiation can be important, so we limit our consideration by the range 10-100 kK and $\rho < \rho_n/3$.

Previously, we have developed a model of calculation of the considered thermophysical properties for the low temperature plasma containing neutral component. This model was successfully applied to a number of metals [13,14]. Thus, it is reasonable to apply it to Bi plasma as well. It has been recently done and some obtained results can be found in our article [15]. The detailed description of the model is presented in our previous publications [13-15]. So here we give only its main features and present some new results. The model is based on the so-called chemical approach [1]. Within it the plasma is considered as a mixture of positive ions of various charges, electrons and neutral atoms. The free energy of the mixture can be written as a sum of an ideal part and different contributions due to the interactions:

$$F(N_0, N_1, ..., N_s, N_e, V, T) = F_{id} + F_{Ch-Ch} + F_{N-Ch} + F_{N-N} \quad (1)$$

The free energy $F$ in eq. (1) depends on $V$, $T$ and the particle numbers of different components, i. e. $N_0$, $N_1$,… $N_s$, $N_e$. Below index "*0*" refers to the atoms, indices *1,…,s* denote the positive ions, index "e" is kept for the electrons. In our calculations we have included the ions up to $s$=5. In (1) $F_{id}$ is the free energy of an ideal gas, which also includes the interior partition function of atoms and ions. The latter values are calculated according to Planck-Larkin convention [1, 13-15]. The subscript *Ch-Ch* (charge-charge) denotes the contribution due to the charged particles interactions (electrons and ions), *N-Ch* (neutral- charge) - due to the charged particles and the atoms, *N - N* –due to the atom-atom interaction. For *Ch-Ch* term we have used the expression, obtained in [16]. In [16] corresponding contributions to $P$ and $U$ are presented as well. The neutral-charge and neutral-neutral contributions can be described within the second virial coefficient approximation, see [13-15]. The expression (1) should be minimized with respect to $N_0$, $N_1$,… $N_s$, $N_e$. It gives the system of equation known as the acing mass law. The solution of the latter is the composition of the mixture under study. For known composition $F$ can be obtained by eq. (1), while $P$, $U$ etc. are expressed as the derivatives of $F$ [1]. Corresponding formulas are presented in [1,13-15]. To calculate the transport coefficient (conductivity $\sigma$, thermal conductivity $\kappa$ and thermal power $S_t$) we have used the relaxation time approximation (RTA). (see [13-15] and references therein). RTA gives the following expression for the coefficients under study:

$$\sigma = -\frac{2|e|^2\sqrt{2m_e}}{3\pi^2\hbar^3} I_{3/2},\ \ \kappa = \frac{2\sqrt{2m_e}}{3\pi^2\hbar^3 T}\left(-I_{7/2} + \frac{(I_{5/2})^2}{I_{3/2}}\right),$$

$$S_t = \frac{1}{|e|T}\left(\mu_e - \frac{I_{5/2}}{I_{3/2}}\right),\ S_t^* = S_t - \frac{1}{|e|}\frac{\partial \mu_e}{\partial T} \qquad (2)$$

$$I_s = \int_0^\infty \varepsilon^s \tau(\varepsilon)\frac{\partial f_0}{\partial \varepsilon} d\varepsilon,\quad f_0 = \frac{1}{\exp\left(\frac{\varepsilon-\mu}{k_B T}\right)+1},\quad \frac{1}{\tau(\varepsilon)} = \sum_{l=0,\ldots,s} n_l A_{l-e}^m(\varepsilon)\sqrt{\frac{2\varepsilon}{m_e}}$$

In (2) $A_{l-e}^m(\varepsilon)$ is the momentum cross-section of electrons on heavy particles (atoms and positive ions), $\varepsilon$ is the free electron energy, $f_0$ is the Fermi–Dirac distribution function, $m_e$, $e$, $\hbar$, $k_B$ are the fundamental constants, $\tau$ is the relaxation time. For *e-i* scattering the generalized Rutherford formula was used for $A_{l-e}^m(\varepsilon)$, while for e-*a* corresponding cross-section presented in [17]. Eq. (2) supposes that the electrons are scattered by the heavy particles only. The correction due to electron-electron collisions is introduced by means of an additional factor, i. e. for conductivity, for instance, $\sigma \to \gamma_{ee}\sigma$. The most advanced expression for $\gamma_{ee}$ is deduced in [18]. There are two possible expression for $S_t$ as one can see in (2). $S_t^*$ includes the inhomogeneity due to the chemical potential of electrons $\mu_e$ and it will be used below.

The results of calculations of $P$, $U$ and σ at isotherms $T$ = 10-100 kK have already been presented in [15]. So here we complement these data by the new results for $C_v$ $\kappa$, $S_t^*$ and the Lorenz number $L$, presented in Figs 1-4. The latter are $L = \kappa/(\sigma T)$ and it is constant in the solid state, while it should be changed in any partially ionized plasma with neutrals [1,19]. These changes are shown in Fig. 4 for Bi plasma, where the normalized value $L_1 = L(e/k_B)^2$ is presented at $T$=10 kK.

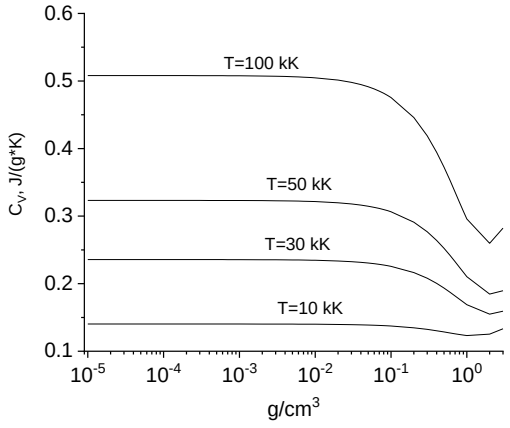



Fig. 1. Heat capacity of Bi plasma at various $T$

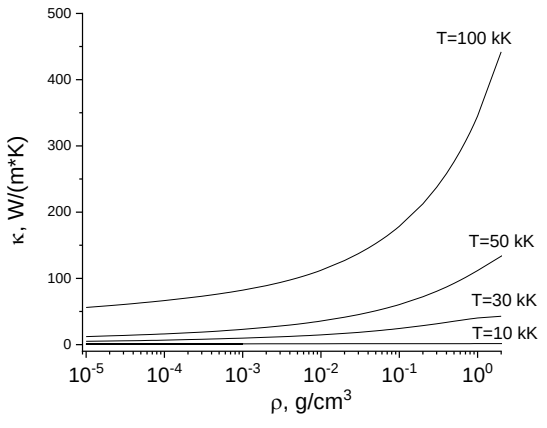



Fig. 2. Thermal conductivity of Bi plasma at various $T$.

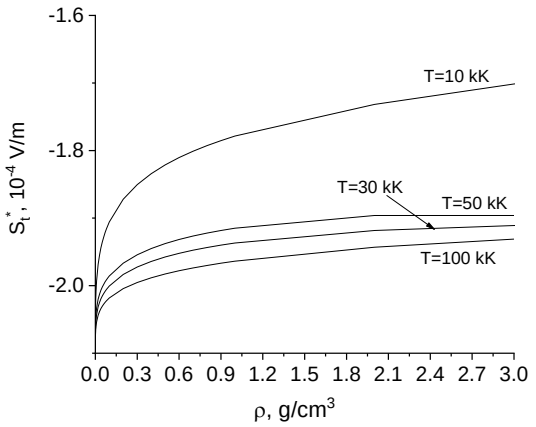



Fig. 3. Thermal power of Bi plasma at various $T$

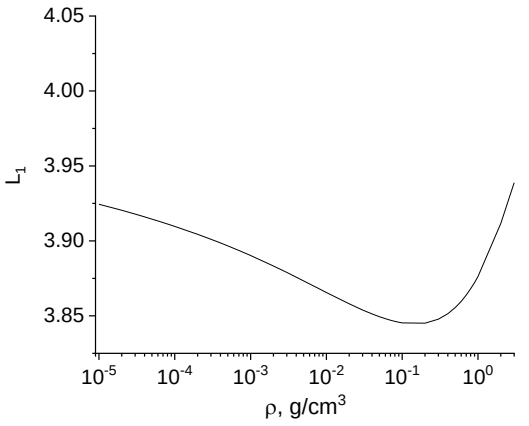



Fig. 4. Lorenz number of Bi plasma at $T$=10 kK.

**Acknowledgements**. The work is supported by the grant of Russian Science Foundation № 20-21-00093.

## References

1. **Fortov V. E., Yakubov I. T.** The Physics of Non-Ideal Plasmas. Singapore: World Scientific Publishing (2000).
2. **Su C., Liu Y. et. al.** Physica B. 524, (2017) 154-162.
3. **DaSilva A. W., Vunni G. B.** Phys. Rev. E, 83 (2011) 037402.
4. **Clerouin J., Noiret P. et. al.** Phys. Plasmas, 19 (2012) 082702.
5. **Grabowski P. E., Hansen S. B. et. al.** HEDP, 37 (2020) 100905.
6. **Militzer B. et. al.** Phys. Rev. E, 103 (2021) 013203.
7. **Minakov D. V. et.al.** Phys. Rev. Bm 103 (2021) 184204.
8. **Kondratyev A. M. et.al.** J. Phys.: Condens. Matter. 34 (2022) 195601.
9. **Apfelbaum E. M.** Teplofiz. Vys. Temp, 59 (2021) 597-513. (*in Russian*)
10. **Al'tshuler L. V. et al.** Sov. Phys. JETP, 24 (1958) 614-619.
11. **Glushak B. L. et al.** Sov. Phys. JETP, V.69 (1989) P.729-749.
12. **Fortov V. E., Lomonosov I. V.** Physics- Uspekhi, 57 (2014) 219-233.
13. **Apfelbaum E. M.** Phys. Plasma, 27 (2020) 042706.
14. **Apfelbaum E. M.** Contrib. Plasma Phys., 61 (2021) e202100063.
15. **Apfelbaum E. M.** Plasma Physics Reports, 48 (2012) (to be published).
16. **Potekhin A. Y. et al.** Phys. Rev. E, 79 (2009) 016411.
17. **Predojević P. et al** Phys. Rev. A, 101. (2020) 032704.
18. **Reinholz H. et al.** Phys. Rev. E, 91 (2015) 043105.
19. **Apfelbaum E. M.** High Temp. 56 (2018) 609-612.

# STRONGLY COUPLED COULOMB SYSTEMS OF BROWNIAN GRAINS AT TEMPERATURE OF SUPERFLUID HELIUM

Oleg F. Petrov[1], Roman E. Boltnev[1] and Mikhail M. Vasiliev[1]

[1] Joint Institute for High Temperatures, Russian Academy of Sciences, Moscow, 125412 Russia (email: ofpetrov@ihed.ras.ru)

The observation of processes in nature and social phenomena shows that many complex structures, consisting of a large number of interacting subsystems, under certain conditions have the ability to self-organize and evolve. The structures are called dissipative, provided that the scattering of energy coming from outside provides a stationary ordered structure with an entropy less than the equilibrium one. The dissipative structures are capable of self-organization and evolution while increasing the flow of entropy into the environment [1, 2].

In recent years, active Brownian motion has attracted great interest in biology, physics, sociology, material science, and epidemiology. While passive Brownian grains are in thermal equilibrium with their environment, active Brownian grains are able to absorb energy from their environment and turn it into their kinetic energy that displaces them from thermodynamic equilibrium [3]. Thus, the systems of active Brownian grains can be considered as open systems, and the structures of grains themselves are systems far from thermodynamic equilibrium.

Active Brownian grains can be charged particles suspended in plasma or levitated in a cryogenic liquid (cryogenic colloid), the kinetic motion of which is induced by laser radiation. In this case, the state of grains is maintained by the free energy of radiation.

We provide experimental evidence for the active Brownian motion and evolution of structures driven by quantum effects for micron-sized grains levitating in superfluid helium. One of the fundamental problems here is the role of quantum phenomena in the evolution of macroscopic objects [4].

The active Brownian motion of grains was induced by quantum turbulence during the absorption of laser irradiation by grains. The intensity of Brownian motion associated with quantum vortices increased by 6-7 orders of magnitude compared to the values from the Einstein formula. We observed the grain structures in a state far from thermodynamic equilibrium and their evolution to more complex organized structures with lower entropy due to the quantum mechanism of exceedingly high entropy loss in superfluid helium.

**Acknowledgements**. The work was carried out under the support of the Russian Science Foundation (Project # 20-12-00372).

**References**

1. **Prigogine I., Nicolis G. and Babloyantz A.** Thermodynamics of evolution. Physics Today, 25 (11) (1972) 23-28.
2. **Ebeling W. and Feistel R.** Physics of self-organization and evolution. Wiley-VCH, Berlin (2011).
3. **Bechinger C., et al.** Active particles in complex and crowded environments. Rev. Mod. Phys., 88 (2016) 045006.
4. **Petrov O.F., Boltnev R.E. and Vasiliev M.M.** Experimental evolution of active Brownian grains driven by quantum effects in superfluid helium. Sci. Rep., 12 (2022) 6085.

# SELECTION OF DUST PARTICLES IN INERT GASES WITH DIFFERENT IONIZATION POTENTIALS

E.S. Dzlieva, M.S. Golubev, L.A. Novikov, S.I. Pavlov, M.A. Gasilov, V.Yu. Karasev

Saint Petersburg State University, 199034, Universitetskaya nab., 7/9, St. Petersburg, Russia
E-mails: plasmadust@yandex.ru, maksider@ya.ru

Dust particles are selected according to certain parameters in plasma traps in dusty plasma [1-3] during the self-organization process. The study of the particle selection process can be carried out experimentally either by using a wide range of dust particles, or by varying the parameters of dust traps, for example, by changing the plasma-forming gas. In the latter case, both the electron temperature (average energy) and the confining electric field change simultaneously.

In this work, we experimentally study the selection of the parameters of dust particles levitating in a stratum in a glow discharge in the inert gases: helium and xenon. Statistics of captured particles is collected, the average particle size and the shape are determined. A comparison of the extracted particles in terms of size and discharge parameters has been carried out. The results obtained make it possible to choose the conditions under which the parameters of the dust trap can be controlled and the "plasma filter" can be tuned to select the special particle size.

The method for extracting dust particles from a dust-plasma trap is described in detail in the works [4, 5] and consists in the following. The discharge tube, oriented vertically with the anode upward, has a horizontal section in its lower part. The cathode is located at one end; the other side serves for the movement and operation of the device collecting dust particles. The device consists of a movable carriage, driven by an external magnet. A plate that collects particles is located on the carriage. Its type (dielectric/conductor, transparent/opaque, etc.) depends on the type of microscope used, where the plate for determining the particle size is placed.

From the point of view of setting up the experiment, the greatest difficulty lies in the choice of discharge conditions for pressure and current, under which it is required to compare the results. It was decided to accept the conditions under which the selection of particles was previously studied in neon and krypton: pressure 0.3 Torr, discharge current 1.5 mA.

The experiment was carried out as follows. A discharge in helium or in xenon was ignited in the prepared discharge tube. Polydisperse quartz powder (the size of particles was up to 25 μm and a density of 2.5 g /cm$^3$) was injected

from above. The carriage moved under the stratum above the horizontal section of the tube. When the discharge was turned off, the particles fell onto the collecting surface. Further, the carriage with the collection of particles was removed from the discharge tube through a wide vacuum port on the horizontal section of the tube. The collected particles were photographed through an optical microscope. An example of a photograph of particles extracted from a discharge in helium is shown in Fig. 1.

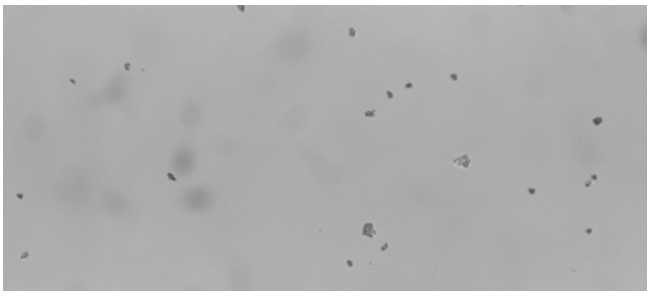


Fig. 1. Image of particles collected after levitation in a stratum in He. Conditions: P = 0.33 Torr, i = 1.5 mA. The horizontal size of the photograph is 0.75 mm.

The average particle sizes in a two-dimensional projection were determined from the obtained photographic images of the collected particles; and histograms of the distribution of particles by the average size were constructed. The distributions for the dust trap in helium and in xenon are shown in Fig. 2. Under the used experimental conditions, the average particle size $d_{eff}$ collected in helium is 6.3 μm, for particles in xenon, about 3.0 μm.

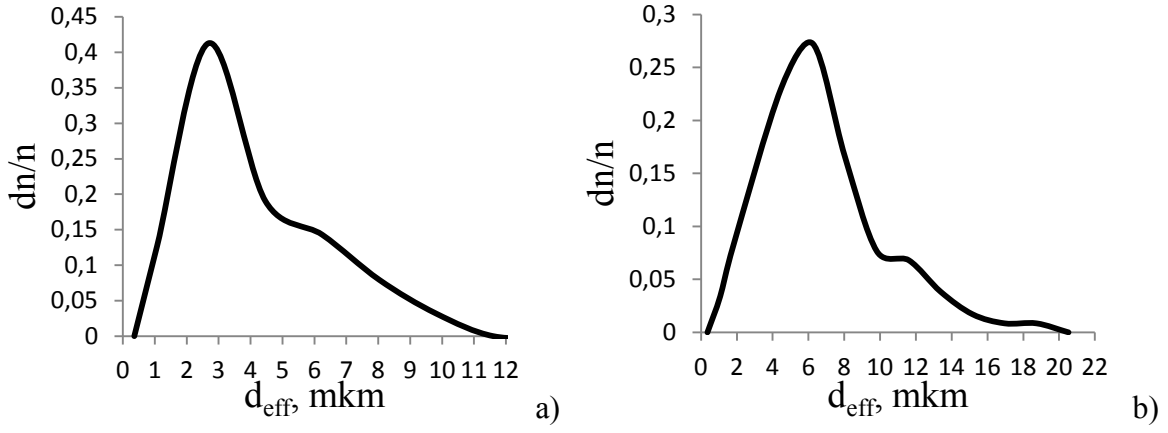



Fig. 2. The average size distribution of particles collected after levitation in a stratum in Xe (a) and He (b). Conditions: P = 0.33 Torr, i = 1.5 mA.

In [5], in studies performed earlier under similar conditions (current and pressure) it was found that plasma retains dust particles of various sizes in a glow discharge in neon and krypton. Based on the distributions in work, the

average sizes of particles levitating in stratum in two gases were determined. In neon, the average size is 5.8 microns; in krypton 4.3 μm. Comparing the data from [5] and this work, we plotted the dependence of the average particle size on the value of the ionization potential of the plasma-forming gas, fig.3.

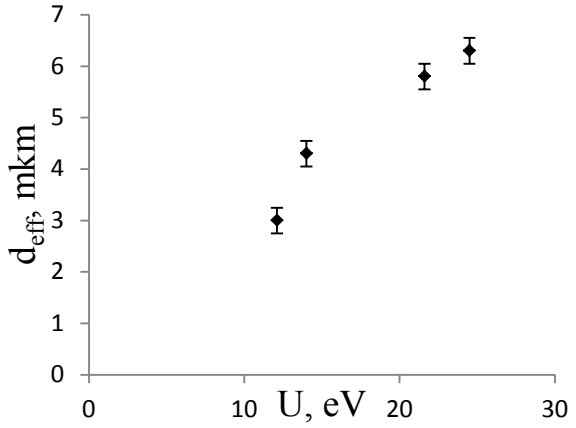



Fig. 3. Dependence of the size of the collected particles on the value of the ionization potential of the atoms of the plasma-forming gas. Conditions: P = 0.33 Torr, i = 1.5 mA.

Fig. 3 shows an unambiguous dependence of the size of the trapped particles on the mass/ionization potential of the working gas. The size of the particles is determined by the balance of forces, which depend not only on the mass of the particles, but also on the conditions in the discharge. First of all, in a low-temperature plasma, the potential of an atom determines the magnitude of the electric field and the electron temperature, which determines the potential and charge of a dust particle. To interpret the dependence of the particle size on the type of gas, one can compare the balance of forces for the two most different gases: He and Xe.

To compare the sizes of particles in different gases in the simplest case, you can use the simplest condition of particle levitation:

$$mg = qE \qquad (1)$$

Assuming the particle shape is closed to spherical, we assume m ~ $a^3$, where $a$ is the radius of the particle. The confining field is determined from the potential drop between the electrodes. The particle charge $q$ is estimated through the charge number $Z_d$ and the ratio of the temperatures of electrons and ions. The data required for an elementary assessment are taken from [1, 2, 6, 7, 8].

Since the data from the literature on the charge of particles, on the electron temperature, as well as experimentally chosen conditions may differ, the most accurate estimate can be made for the ratio of sizes and parameters (particles and discharge) in different gases. The ratio obtained from the levitation equation for helium and xenon is:

$$\left(\frac{a_{He}}{a_{Xe}}\right)^2 = \frac{Z_{He}}{Z_{Xe}} \frac{T_e^{He}}{T_e^{Xe}} \frac{E_{He}}{E_{Xe}} \quad (2)$$

According to the performed estimates, $a_{\mathrm{He}}/a_{\mathrm{Xe}}$ lies in the range 2.1 – 3.0, which fits into the experimental comparison of the average sizes of the obtained distributions.

The performed study shows the possibility of obtaining samples of selection of dust particles in very different inert gases under similar conditions. Elementary estimates show the agreement of size, electron temperature (average energy) and levitation conditions. The study that has begun can be continued by varying the gas mixture with the control of the electron temperature in the process of sampling particles.

**Acknowledgements.** This work was supported by the RSF (grant No 22-22-00154).

## References

1. **Fortov V.E. and Morfill G.E.** Complex and Dusty Plasmas: From Laboratory to Space. CRC Press Taylor & Francis Group: New York, NY, USA (2010).
2. **Fortov V.E., Khrapak A.G., Khrapak S.A., Molotkov V.I., Petrov O.F.** Phys. Usp. 47 (2004) 447.
3. **Tsytovich V.N, Morfill G.E., Vladimirov S.V. Thomas H.M.** Elementary Physics of Complex Plasmas. New York: Springer (2008).
4. **Dzlieva E.S., Ermolenko M.A., Karasev V.Yu.** Tech. Phys. 57 (2012) 145.
5. **Karasev V.Yu, Dzlieva E.S, Eikhval'd A.I., Ermolenko M A, Golubev M.S., Ivanov A.Yu.** Phys. Rev.E 79 (2009) 026406.
6. **Nekuchaev V.O., Kudryavtsev A.A., Golubovskii Yu.B., Tsendin L.D., Porokhova I.A.** Kinetics of Electrons in a Non-Equilibrium Gas-Discharge Plasma. St. Petersburg: SPbSU Publishing House (2004).
7. **Golubovskii Yu.B., Karasev V.Yu, Kartasheva A.A.** Plasma Sources Science and Technology 26 (2017) 115003.
8. **Kartasheva A.A, Golubovskii Yu.B, Karasev V.Yu.** J. Phys.: Conf. Ser. 1556 (2020) 012079.

# 5. LASER-PLASMA INTERACTIONS WITH MATERIALS, LASER ABLATION, MODIFICATION OF MATERIALS, SPUTTERING AND DEPOSITION

# INFLUENCE OF LASER CRATER TEMPERATURE ON MATERIAL ABLATION AND INTENSITY OF SPECTRAL LINES OF EROSIVE PLASMA TORCH

K. Znosko

State University of Grodno, Ozheshko Street 22, 230023, Grodno, Belarus,
znosko@rambler.ru

Laser ablation is the removal of matter by powerful laser radiation. It is widely used in science and production. Laser ablation is being developed in two directions. The first is the removal of the substance to give the object the desired shape [1-3]. The second is the use of the removed dispersed mass of the substance [3-9]. In works [10-12] it is shown that use of double laser pulses considerably increases efficiency of laser ablation, in comparison with use of single pulses. In [4, 6, 13, 15], an increase in the radiation intensity of laser-emission plasma was shown when dual laser pulses were used. Various mechanisms have been proposed to explain these effects. In [14-16], it was shown that the high temperature of the erosion crater formed by the first laser pulse significantly increases the ablation efficiency.

The aim of the present work is to investigate the effect of the erosion crater temperature on the laser ablation rate and the intensity of the spectral lines of the laser-emission plasma.

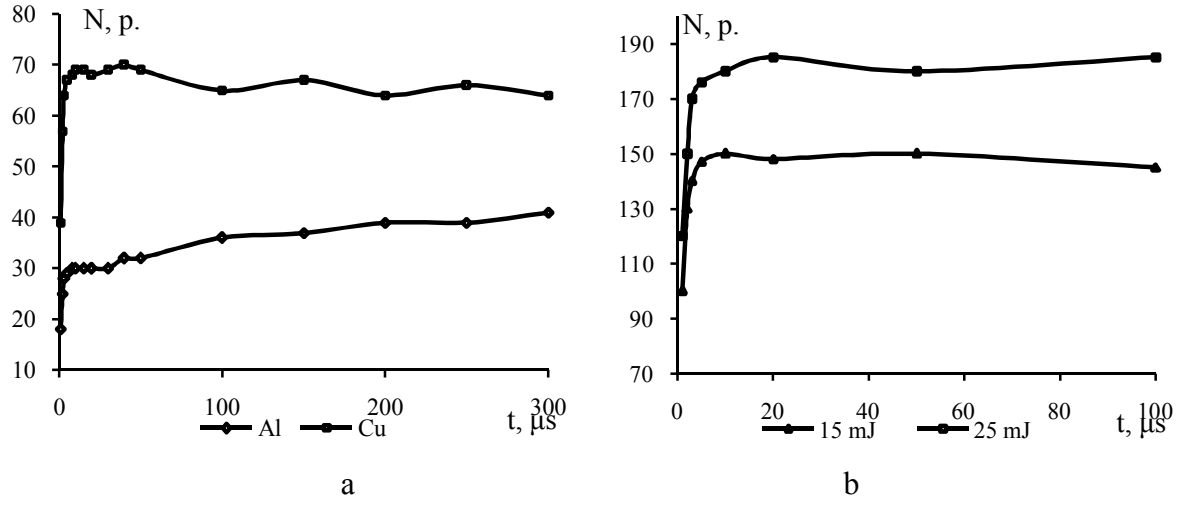
The studies were carried out on the experimental setup described in detail in [11-13]. A YAG:$Nd^{3+}$ laser with a pulse duration of ~15 ns at half-height was used. The laser could generate both single and double pulses. The delay of the second pulse relative to the first pulse could vary from 1 μs to 300 μs.

Experiments were carried out on laser penetration of holes in aluminum, copper and stainless steel plates (12X18H9TJI). Single pulses with an energy of 25 mJ were used. For the breakdown of holes in aluminum, copper, and stainless steel plates, ~200, ~500, and ~1000 pulses were required.

Figure 1 shows the dependences of the number of twin laser pulses required to break through a hole in the same plates on the value of the inter-pulse interval. The minimum number of twin laser pulses required for hole penetration was observed at the value of the inter-pulse interval equal to ~1 μs. For hole penetration in aluminum, copper, and stainless steel plates, ~20, ~40, and ~120 pulse pairs were required, respectively. These experiments confirm that the efficiency of laser ablation with twin pulses is significantly higher than single-pulse ablation.

The increase in laser ablation efficiency is due to the high temperature of the crater after the first pulse. The shorter the time interval between pulses, the higher the crater temperature. The action of laser radiation of the second pulse

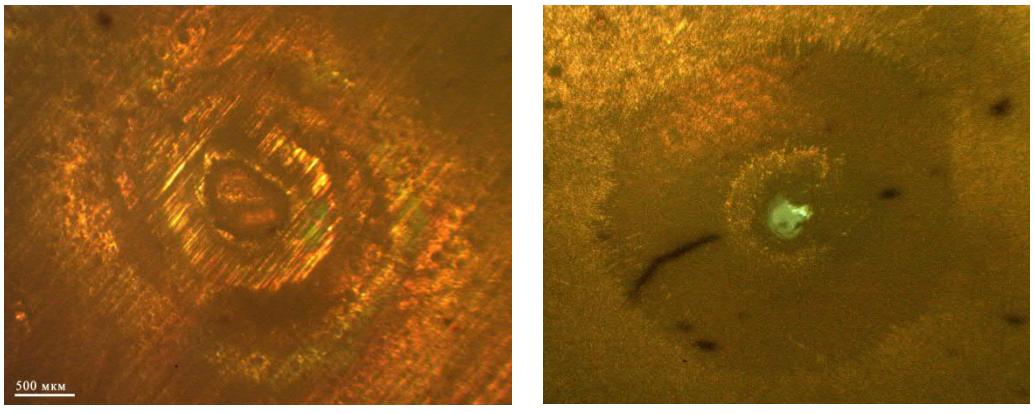
on the hot surface leads to an increase in the portion of ablated substance. This is due to the reduction of energy expenditure for its heating of the crater. Most of the energy of the second laser pulse goes to melting, evaporation and ionization, which ultimately leads to an increase in ablation efficiency. The high temperature of the crater compensates the energy expenditure for its heating. This mechanism is confirmed by the experiments described in [15].




a b

Fig. 1. Dependences of the number of double pulses, for the hole breakdown in Al with Cu plate (a) and stainless steel plate (b)

Figure 2 shows photographs of a laser crater on a copper plate (a) and a punched hole in stainless steel (b). They were taken in reflected light at 25× magnification. The dimensions of the microscopy area are 3.8 mm × 3.2 mm. It can be seen that the crater and hole surround an area of annealed metal. Ring-shaped whitewashing colors are observed. This suggests that the areas surrounding the crater were exposed to high temperatures.




a b

Fig. 2. Picture of the laser crater on the copper plate (a) and the hole in the stainless steel plate (b)

We can also see the presence of a weak berm surrounding the crater. It is formed by molten metal. This suggests that the removal of matter from the crater occurs both by evaporation and by displacement of the melt by the pressure of the vapors themselves.

Experiments on laser ablation of Ni-Cr alloy heated to high temperature were carried out. The object of the study was Ni-Cr alloy containing 80% Ni and 20% Cr. It was heated by passing an electric current through it. The target temperature was measured using an optical temperature meter IT-3CM.

Figure 3 shows the dependences of the spectral line intensities of Ni atoms on the temperature during one- and two-pulse plasma formation. Up to 500°C the alloy temperature has practically no effect on the line intensity. Beginning from 500°C the growth of the line intensities is observed. For single-pulse plasma formation, the maximum intensity of the spectral lines falls at 950°C, and for two-pulse - at 750°C. The intensity of Ni spectral lines increased by ~3 times for the one-pulse mode and >3 times for the two-pulse mode. A similar situation is observed in the dependences of the intensity of the spectral lines of chromium atoms on the temperature. The estimate of the crater temperature after exposure of the Ni-Cr alloy to the first laser pulse is 600-900°C. It is the higher, the smaller the inter-pulse interval is.

Figure 4 shows the dependence of the two-pulse laser ablation rate on the temperature of the Ni-Cr alloy. It can be seen that at temperatures >1000°C the ablation rate increased >3.5 times. At high temperatures (temperatures close to the melting point), the removal of material from the erosion crater by microdroplets increases significantly. This is indicated by the presence of a berm surrounding the crater.

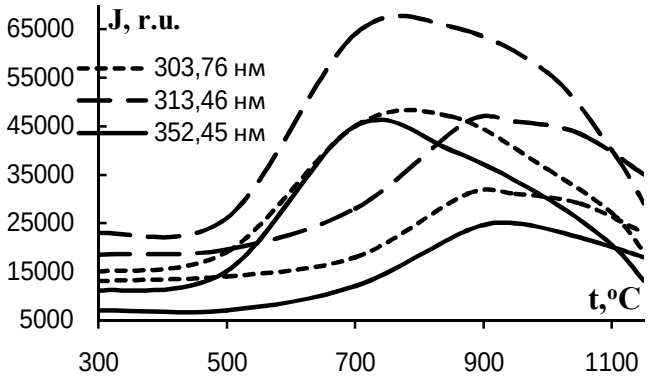



Fig. 3. - Dependences of Ni atoms line intensity on temperature

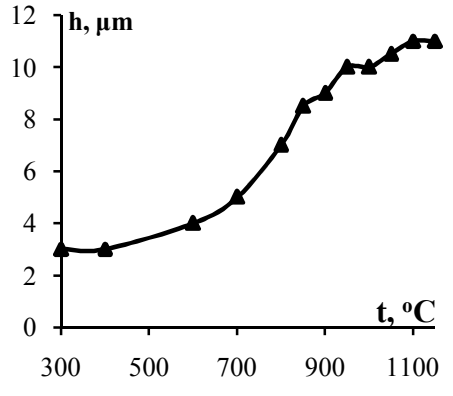



Fig. 4. Ablation rate dependence on temperature

Thus, the temperature of the laser crater significantly affects the ablation of the material and the intensity of the spectral lines of the erosive plasma torch. The growth of material ablation and the intensity of spectral lines, with a two-

pulse laser action on the object, is due to the high temperature of the crater after the first laser pulse. The temperature of the crater in 1 μs after the action of the laser pulse is estimated at 600-900$^{o}$C.

The work was performed within the framework of the research task 1.5 NIR 6 "Photonics and Electronics for Innovation" subprogram "Photonics and its Applications".

## References

1. **Sobol E.N.** Phase Transformations and Ablation in Laser-Treated solids. Michigan: Wiley (1995).
2. **Miller J.C.** Laser Ablation: Principles and Applications. Berlin: Springer (1994).
3. **Zazhogin A.P. and Fadayan A.R.** Vestnik BSU. Series 1. Physics. Mathematics and Informatics, No. 3 (2008) 15–18.
4. **Kremers D. and Radiemski L.** Laser-Induced Breakdown Spectroscopy. Moscow: Technosphera, (2009).
5. **Popov A.M., Labutin T.A. and Zorov N.B.** Vesnik of Moscow University, Series 2. Chemistry, 50 (2009) 453-467.
6. **Anufrik S.S., Kurian N.N., Znosko K.F. and Belkov M.V.** Journal of Applied Spectroscopy, 85 (2018) 285-292.
7. **Anufrik S.S., Kurian N.N., Zhukova I.I., Znosko K.F. and Belkov M.V.** Journal of Applied Spectroscopy, 83 (2016) 724-730.
8. **Tarasenko N.V. and Butsen' A.V.** Quantum Electronics, 40 (2010) 986-1003.
9. **Goncharov V.K., Kozadaev K.V. and Shchegrikovich D.V.** Journal of Engineering Physics, 84 (2011) 723–728.
10. **Pershin S.M.** Quantum Electronics, 39 (2009) 63-67.
11. **Znosko K.F.** Vesnik of Yanka Kupala State University of Grodno. Series 2. Mat..Phys..Inform.,Computer Technol. and Contr., 10 No.3 (2020) 100-113.
12. **Znosko K.F.** Vesnik of Yanka Kupala State University of Grodno. Series 2. Mat..Phys..Inform.,Computer Technol. and Contr., 10 No.2 (2020) 103-115.
13. **Znosko K.F. and Leshchyk S.D.** Vesnik of Yanka Kupala State University of Grodno. Series 6. Engineering Science, 11, No. 1 (2021) 45-58.
14. **Veiko V.P., Libenson M.N., Chervyakov G.G. and Yakovlev E.B.** The interaction of laser radiation with matter. Power optics. Moscow: Fizmatlit (2008).
15. **Corsi M.** [et al.] Spectrochimica Acta, Part B. 59 (2004) 723-735.
16. **Znosko K.F.** Vesnik of Yanka Kupala State University of Grodno. Series 2. Mat..Phys..Inform.,Computer Technol. and Contr., 11, No.1, (2021) 94-106.

# MORPHOLOGY OF THE SURFACE OF NATURAL LAMB LEATHER AFTER TANNIDE TANNING AND LASER EXPOSURE

A. Anisovich[1], T. Kodirov[4], U. Khudanov[4], M. Markevich[2], V. Zhuravleva[3]

[1]Institute of Applied Physics of the National Academy of Sciences of Belarus, st. Academic 16, 220072, Minsk, Belarus
[2]Physical-Technical Institute of the National Academy of Sciences of Belarus, st. Kuprevich, 10, 220141, Minsk, Belarus, a.chaplanov@gmail.com
[3]Military Academy of the Republic of Belarus, Independence Ave. 220, 2200057, Minsk, Belarus
[4]Tashkent Institute of Textile and Light Industry, 100100, Tashkent, Republic of Uzbekistan

Introduction. An important process in obtaining high-quality leather is the tanning process. In the process of tanning, there is a change in the properties of the dermis of the skin (tanned semi-finished product).

Often tanning is carried out with compounds of trivalent chromium, which makes it possible to obtain high quality leathers that have good thermal resistance.

Recently, much attention has been paid to environmental problems in the world, in particular, environmental problems of leather production. The environment is harmed by chromium salts, there are problems in wastewater treatment, it is almost impossible to purify water from chromium compounds to the required parameters. In addition, with intensive mining of chromium compounds, chromium reserves on the planet are decreasing, which can lead to an increase in the price of chrome tanning agent. Therefore, scientific research is being carried out on the production of chrome-free leathers as an alternative to chrome tanning. In particular, methods of tannin tanning (vegetable tanning agents) are being developed.

This direction is very promising. The skin of this treatment absorbs moisture better and retains it for a long time. Due to the absence of plasticized coatings on the surface of the skin, shoes made of such leather maintain the microclimate and temperature conditions well.

This skin is well stretched and molded. However, tannin tanning also has disadvantages. Vegetable tanned leather is porous, dents, more expensive to manufacture, and dries out and hardens when exposed to hot and dry climates for long periods of time.

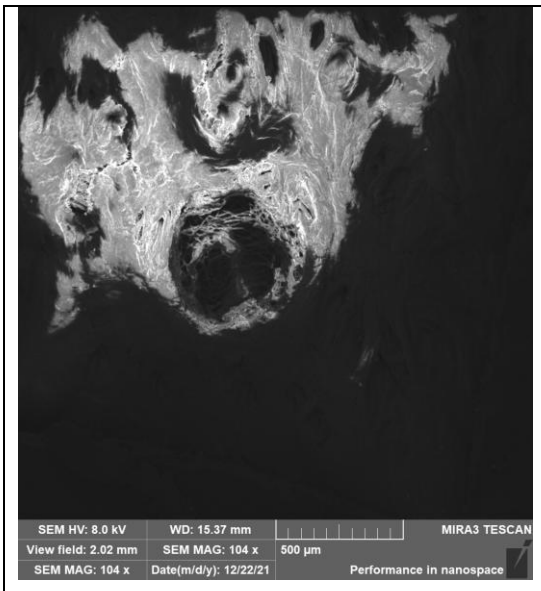
The purpose of this work is to study the morphology of tannin tanned lamb skin after laser exposure.

Main part. To process natural leather samples, laser treatment was used in the dual pulse mode. We used an LS-2134D yttrium aluminum garnet laser (LOTIS, Belarus) with a wavelength of 1064 nm, generating in a two-pulse

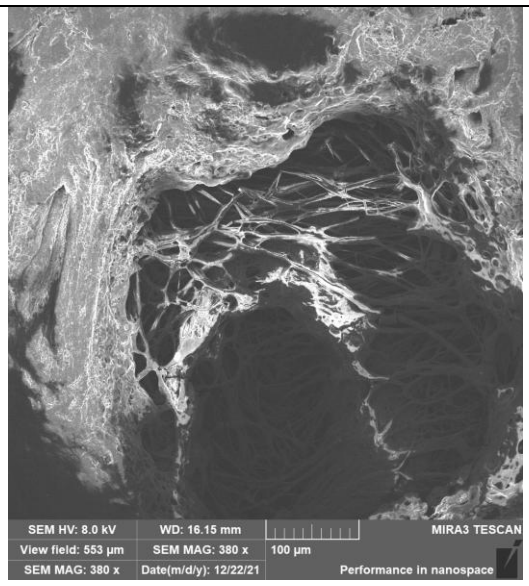
mode (the pulses are separated by a time interval of 3 μs; the pulse duration is 10 ns [1–3]. The input energy was determined by the exposure time and ranged from 1 to 200 J. Under these processing modes, both leather polishing and its perforation can occur.Undyed lamb skin waste (manufactured in Uzbekistan) was used in the research.Samples of the semi-finished leather product were treated with laser radiation from the front side.

The study of the chemical composition of the skin was carried out using a scanning electron microscope MIRA-3 (Czech Republic) with a system of microanalyzers from Oxford Instruments (Great Britain). The device allows you to simultaneously study the morphology of the surface of the material, determine the distribution of chemical elements of the sample under study, and also obtain an image of the object in a wide range of magnifications.

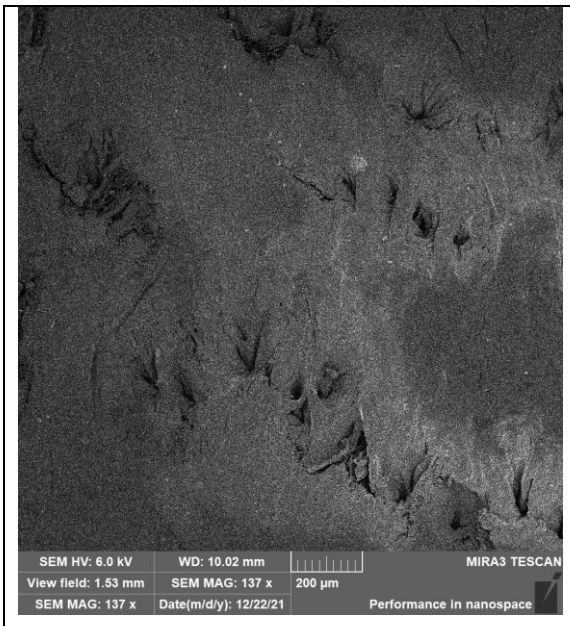
The ablation plasma formed as a result of substance evaporation under the action of the first pulse creates a region with an increased temperature and a reduced particle density in the surface layer, which leads to a more complete use of the energy of the second pulse for laser ablation. As a result of exposure to laser radiation with the surface of the skin, its polishing is observed. Figure 1 shows the results of the interaction at various input energies.



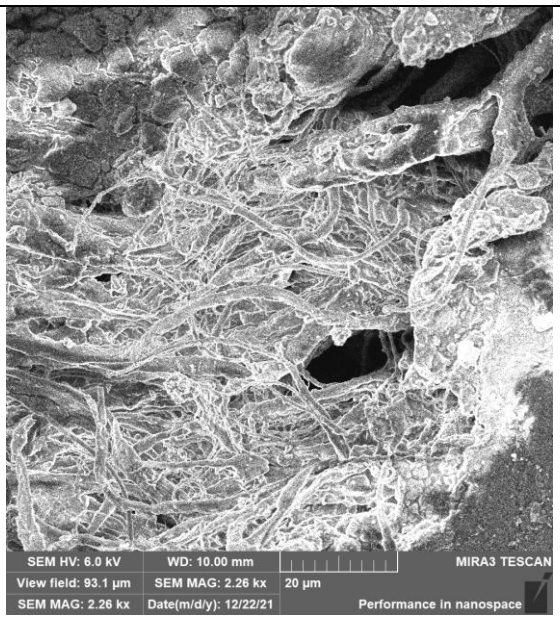

a)




b)




c)

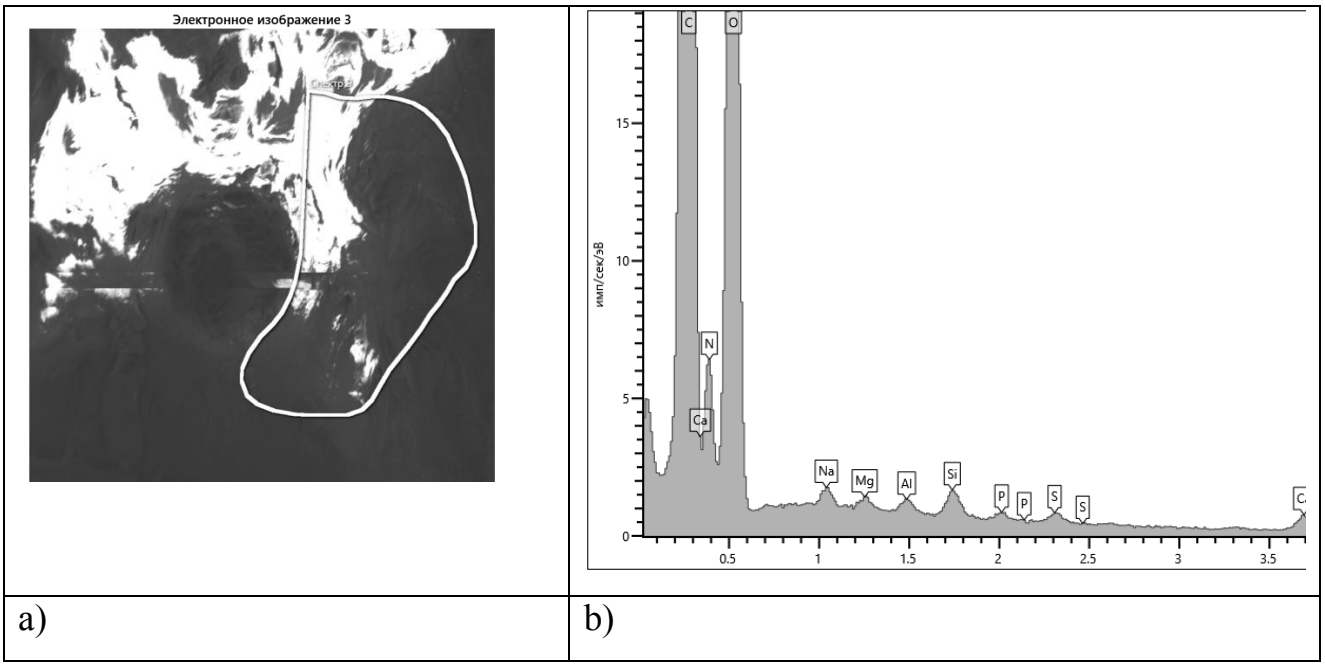



d)

Fig. 1. Morphology of the surface of the front side of the skin after laser exposure: a), b) input energy 10 J, c), d) input energy 20 J (at various magnifications).

The images clearly show individual collagen fibers 1-2 μm thick, the connections of these collagen fibers form bundles of fibers 5-10 μm thick, intertwining in different directions and forming a complex dermal tissue. Holes from hair bags ranging in size from 20 to 150 microns are found. It follows from Figure 1 that skin resurfacing occurs, however, due to the more porous structure of the skin (Fig. 1a,b) after tannin tanning, skin resurfacing is less effective [1,2].

Figure 2 shows the elemental composition of natural lamb leather after tannin tanning (no chromium).




a) b)

Fig. 2 - elemental analysis of the skin: a) analysis area, b) elemental composition

Findings. For the first time, the surface morphology of natural lamb leather was studied after tannin tanning and laser exposure in a two-pulse mode (pulses separated by a time interval of 3 μs, pulse duration 10 ns) with a wavelength of 1064 nm in a wide range of input energies (1J-200J). The modes of laser processing in the ablation mode are determined. The possibility of changing the structure of natural skin due to defibration of the dermis and conformational changes is shown.

## References

1. **A.Yu Toshev, M.I. Markevich, T.J. Kodirov, V.I. Zhuravleva** Revista de Pielarie Incaltaminte, 20 (2020) 5-10.
2. **Kodirov T.J., Markevich M.I., Malyshko A.N., Zhuravleva V.I., Sodikov N.A**. International Journal of Resent Technology and Engineering, (2020) 4880-4884.
3. **Anisovich A.G., Kodirov T.Zh., Khudanov U.O., Markevich M.I., Zhuravleva V.L.** Electronics+, (2022) 55-58.

# THE PLM-M STEADY-STATE PLASMA LINEAR FACILITY FOR FULL-SCALE TESTING OF THERMONUCLEAR REACTOR MATERIALS

V. Tran[1], V. Budaev[1,2], S. Fedorovich[1],
D. Kavyrshin[1,3], A. Karpov[1,2], K. Rogozin[1], A. Konkov[1], V. Kvaskov[1]

[1]National Research University "MPEI", Moscow, Russia.
[2]National Research Center "Kurchatov Institute", Moscow, Russia.
[3]Joint Institute for High Temperatures of the Russian Academy of Sciences (JIHT RAS), Moscow, Russia.

The PLM-M steady-state plasma linear multi-cusp facility was built for the purpose of full-scale testing of materials, mock-ups and prototypes of the wall and divertor of future thermonuclear reactors. In the PLM-M, experiments were carried out with the combined effect of a powerful stationary plasma, pupulsed arc, and laser load on the surface of the thermonuclear reactor materials, including tungsten mock-ups of the divertor tiles and lithium capillary-porous system (CPS).

The magnetic system of the PLM-M setup consists of a solenoid coil and an eight-pole system of permanent magnets, creating a multi-cusp configuration. (an analogue of the well-known scheme with longitudinal "Ioffe's Sticks". To achieve a pressure of less than $1.10^6$ Torr, the discharge chamber is evacuated by turbomolecular high-vacuum and fore-vacuum oil-free pumps.

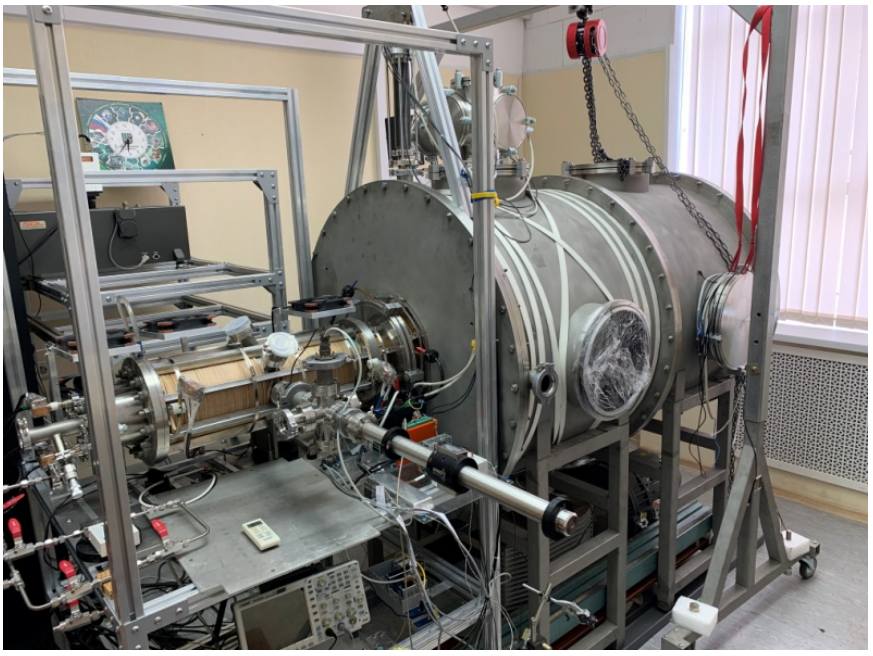


Fig. 1. The PLM-M steady-state plasma linear multi-cusp facility

A tantalum cathode was used to form a plasma discharge in the PLM-M facility. The cylindrical anode with an inner hole of 35 mm is made of copper and mounted on a steel ring that provides heat removal to the water-cooled chamber. Plasma heating is carried out due to the process of stepwise ionization by electron impact of atoms of the plasma-forming gas. The electron current density required for the stepwise ionization process is achieved due to electron thermal emission from the cathode. The cathode heating power is up to 2 kW. The cathode emission current reaches up to 30 A. An important feature of the discharge is plasma generation near the axis of the plasma chamber, which makes it possible to minimize plasma losses, reduce thermal loads on the chamber walls, and use sources in a stationary mode.

To simulate the loads at the level of ELMs in a large reactor-sized tokamak, a system based on a high-power laser complex with a pulsed Nd:YAG laser model LQ529A with a radiation wavelength of 1064 nm and a pulse energy of 500 mJ and an arc generation system based on a Marx generator was built.

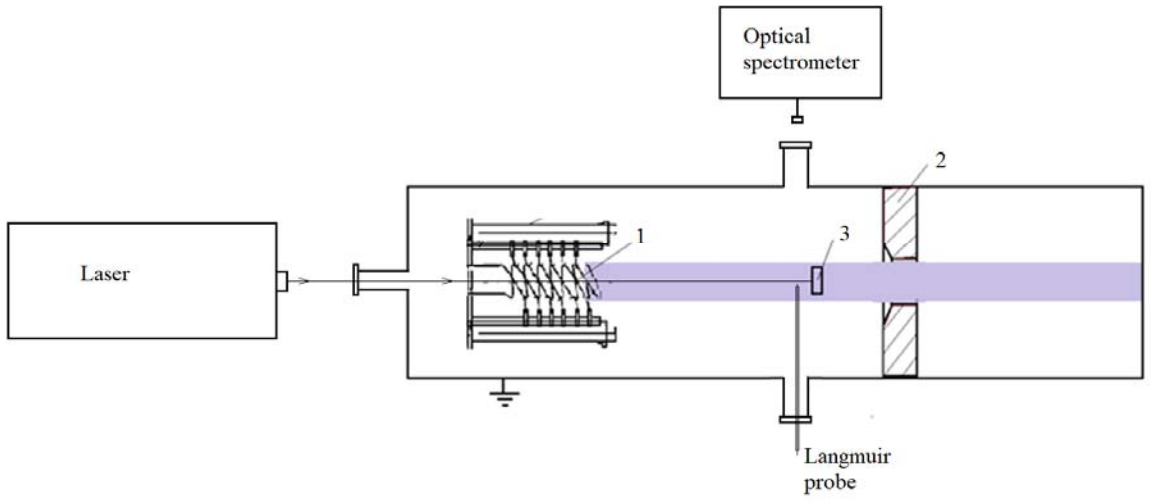



Fig. 2 - Scheme of the experiment in the PLM-M with a powerful laser

Table 1 - Parameters achieved in the PLM-M installation

| Parameter | |
|---|---|
| Vaccum chamber/plasma cord diameter, cm | 16/3.5 |
| Magnetic field on the axis, T | 0.02 |
| Magnetic field at cusps, T | up to 0.2 |
| Electron density, $m^{-3}$ | $5*10^{18}$ |
| Electron temperature, eV | 1 - 10 |
| Plasma thermal load on the target surfaces, $MW/m^2$ | up to 5 |
| Stationary plasma discharge up to 500 minutes | |
| Working gas - helium, argon | |

In order to increase the plasma parameters in the PLM-M facility, a section for ICR plasma heating at a frequency of 13.56 MHz using a helicon antenna was developed and manufactured. The maximum input power is 5 kW. The design of the helicon antenna is proposed to provide a stationary mode of operation.

The near-surface plasma diagnostic system includes an optical spectrometer and a Langmuir probe.

As part of the work in the PLM-M facility, methods for intensive cooling of the modules of the heat-shielding lining of the divertor and the first wall of the thermonuclear reactor during stationary operation were developed.

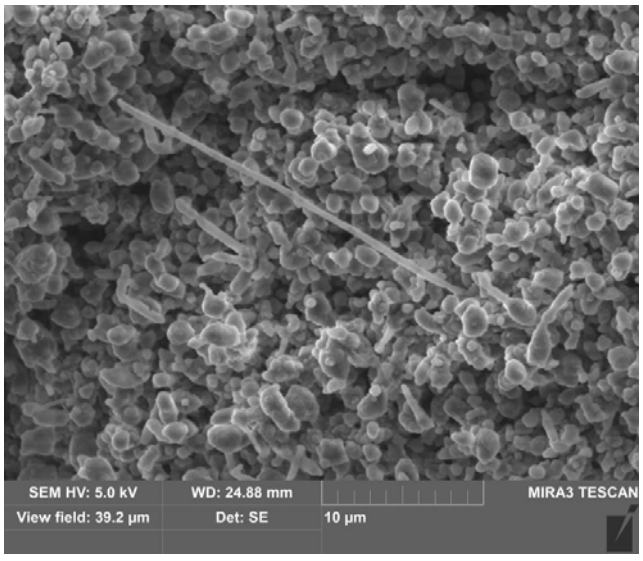



Fig. 3. SEM images of the surface of a lithium capillary-porous system in the zone of high-power laser loads.

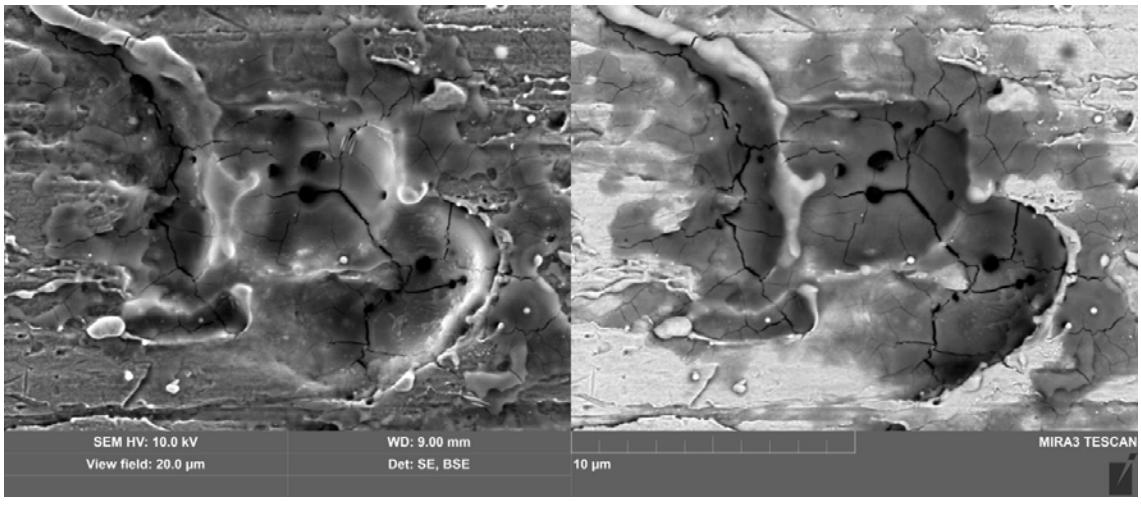



Fig. 4. SEM images of a crater from an arc process on the surface of a tungsten mock-up

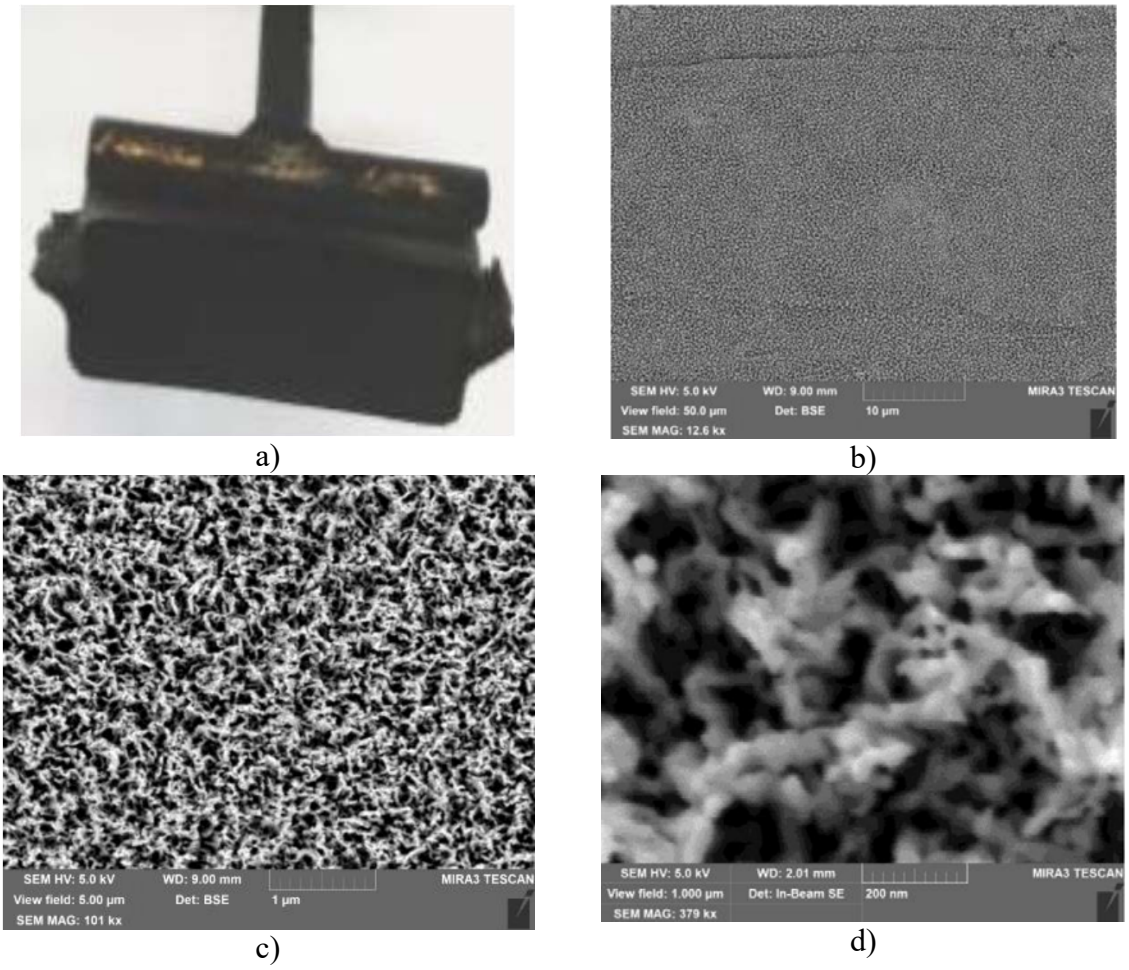



Fig. 5. ITER tungsten module - (a) photo in visible light. (b)-(d) SEM micrographs of the nanostructured tungsten surface of "fuzz" type, irradiated with the PLM-M plasma

Experiments are planned to achieve the "detached" mode, an analogue of the closed divertor of the tokamak reactor. The PLM-M facility has no analogues in Russia, it is planned to bring the parameters to the design parameters, similar to the most powerful facility in the world MAGNUM-PSI (European Union).

**Acknowledgements**. The spectroscopic study was supported by the RSF grant 21-79-10281, test of materials on the PLM device was supported by the project No. 223 EOTP-UTP 774/158-D SC "Rosatom" PI "Science and Innovations".

## References

1. **V. P. Budaev** et al 2019 J. Phys.: Conf. Ser. 1383 012016.
2. **V. P. Budaev** et al 2019 Phys. Atom. Nuclei 82, 1281–1291.
3. **V. P. Budaev** et al 2021 Fusion Engineering and Design, 167, 112335.

# LIBS HYDROGEN DETECTION: SIGNIFICANCE IN FUSION TECHNOLOGY

M. Trtica[1], J. Savovic[1], M. Kuzmanovic[2], D. Rankovic[2]

[1]University of Belgrade, VINCA Institute of Nuclear Sciences - National Institute of the Republic of Serbia, Mike Petrovica Alasa 12-14, 11001 Belgrade, Serbia
(etrtica@vinca.rs; lelas@vinca.rs)
[2]Faculty of Physical Chemistry, University of Belgrade, Studetski trg 12-16, 11158, Belgrade, 118, PAC 105305, Serbia
(miroslav@ffh.bg.ac.rs; ranko@ffh.bg.ac.rs)

Nowadays, developing sensitive methods for hydrogen detection in nuclear (fusion and fission) technology is of great interest and challenge [1,2]. Focusing on a fusion reactor, detecting hydrogen in the plasma-facing wall and reactor structural materials is particularly important. The fusion reactor is a unique and complex system posing high demands regarding material properties, which should also have a low affinity to hydrogen isotopes. Reactor-relevant materials, among others, include tungsten, beryllium, and W-Be alloys used for plasma-facing components, and 316L stainless steel and ODS (oxide dispersion strengthened) steel used as a structural materials. The permeation and retention of hydrogen isotopes in these materials can cause degradation and drastically reduce their lifetime. Typical effects of hydrogen presence in materials of fusion reactors can be the appearance of cracking, swelling, blisters, and other unfavorable phenomena, Fig. 1.

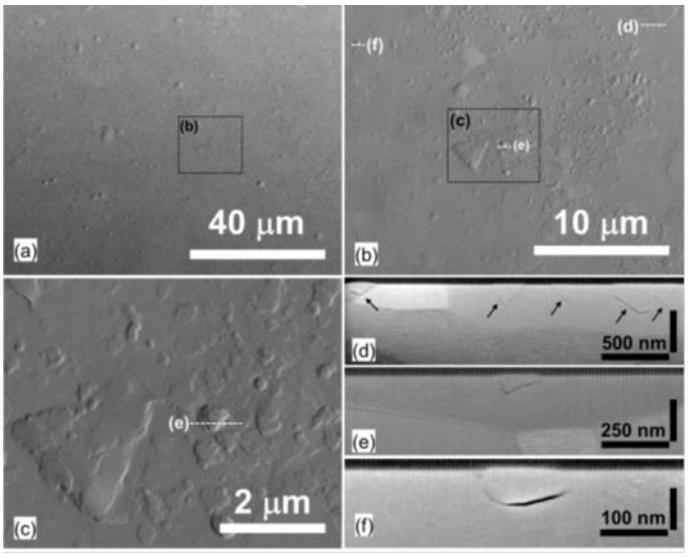



Fig. 1. (a-f) Morphology of W samples exposed to low-flux D-plasma [3]

In this context, hydrogen detection is of high importance. Among several methods available for hydrogen detection in metals, such as thermal desorption spectroscopy, nuclear methods (e.g., nuclear reaction analysis), mass spectrometry, glow discharge optical emission spectroscopy, the laser-induced breakdown spectroscopy (LIBS) is highly promising. LIBS ensures highly sensitive, fast, and reliable analysis, including the possibility for in-situ/stand-off detection [4].

At the VINCA Institute, the LIBS method was applied for hydrogen detection in polymer - polymethyl methacrylate (PMMA; $(C_5O_2H_8)n$) samples. The polymer was chosen for two reasons. Firstly PMMA served as a test target simulating hydrogen-bearing reactor material. Secondly, fundamental research on laser-polymer interaction is significant because, in the inertial fusion DT concept, the fuel is situated in a capsule where the outer layer is a plastic-ablator. Generally, the primary intention of the VINCA experiments was to demonstrate the feasibility of laser-induced breakdown spectroscopy to detect hydrogen in the solids. LIBS experimental setup based on pulsed TEA $CO_2$ laser (Fig. 2) was described elsewhere [1,5], but for the sake of completeness, it will be briefly mentioned here. The specific pulse shape of the employed TEA $CO_2$ laser consists of a gain-switched spike followed by a slowly decaying tail (inset in Fig. 2). The FWHM of the spike was about 100 ns, while the tail duration was ~2 μs. Approximately 35% of the total irradiated laser energy is stored in the initial spike. The intensity of the focused laser beam was of the order of tens MW/cm$^2$. For such low intensity, the plasma over the polymer surface could be induced only in the presence of a metal sub-target. The experiments were conducted in a vacuum using high-quality steel as a sub-target. A typical view of the bluish plasma is depicted in the inset of Fig. 2. LIBS signal was detected using a CCD detector, and the spectra were recorded using time-integrated, spatially resolved optical emission measurements [1,5].

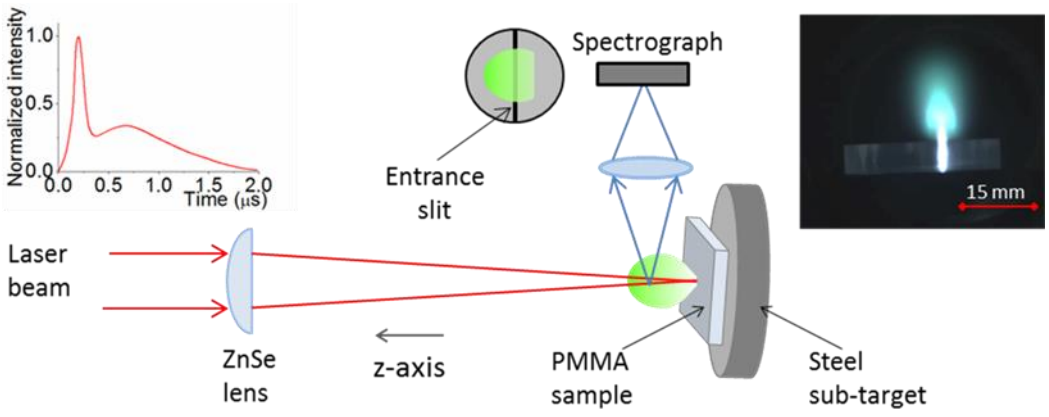



Fig. 2. (a) Schematic illustration of PMMA irradiation by $CO_2$ laser - LIBS experiment (insets - $CO_2$ laser pulse shape and view of the plasma)

A series of complex phenomena were involved in plasma generation and propagation. A simplified description includes two main processes: (i) absorption of laser radiation by sub-target, causing its ablation, vaporization, and plasma generation; (ii) propagation of the plasma along a previously created PMMA channel, causing PMMA heating, vaporization, and decomposition. In the case of IR radiation, the main decomposition mechanism of PMMA is thermal. As the laser wavelength decreases from the IR to the UV, thermal decomposition becomes less important than photochemical mechanisms.

The plasma emission consisted of the spectral lines of the PMMA constitutive elements (hydrogen, carbon, and oxygen), Fig. 3 (a,b), and a band spectra of small molecular species created in the plasma, such as $C_2$ and CN (Fig. 4). For all atomic species, the highest emission intensity was recorded in the vicinity of the PMMA surface.

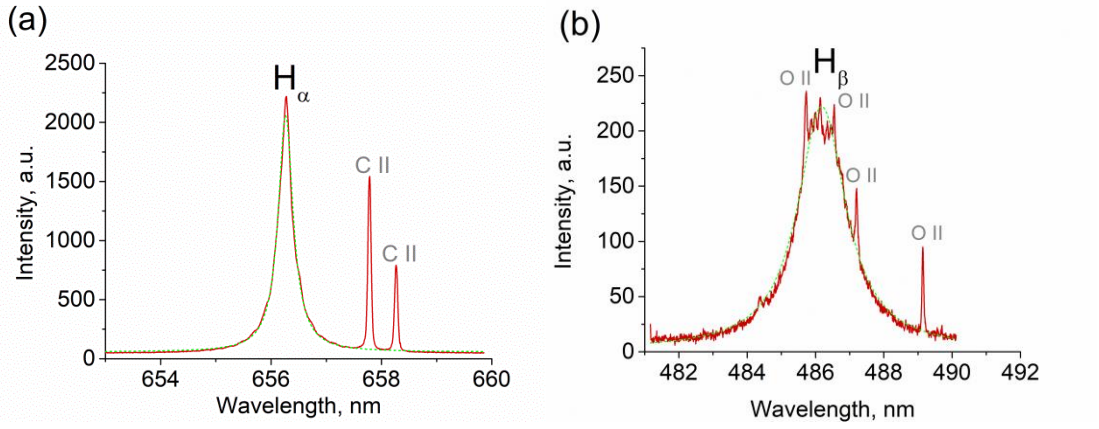



Fig. 3. LIBS spectra acquired from a plasma slice 2 mm above the PMMA-steel sub-target system: (a) $H_\alpha$ 656.27 nm line and (b) $H_\beta$ 486.13 nm line.

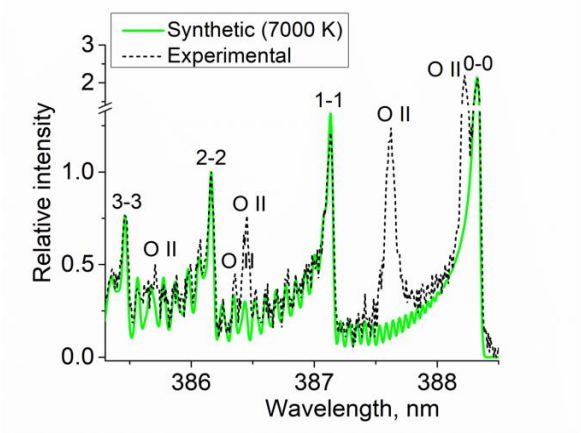



Fig. 4. LIBS spectra of CN-band emission acquired from a plasma slice 2 mm above the PMMA-steel sub-target system. The spectra were recorded at 0.1 mbar of air.

The plasma parameters, electron number density ($N_e$), and ionization temperature ($T$) were estimated to characterize the excitation conditions in the laser-induced plasma. The electron density was inferred from the Stark broadened $H_\alpha$ and $H_\beta$ line widths recorded from a plasma slice 2 mm above the PMMA surface. The estimated value of $N_e$ was 1.6 x $10^{16}$ $cm^{-3}$. The FWHM of both hydrogen lines decreased with increasing distance from the PMMA surface. The ionization temperature was determined from the measured intensity ratio of carbon ionic and atomic line pair (C II 250.9 nm/C I 247.9 nm) and previously obtained $N_e$. Depending on the distance from the PMMA surface, the temperature varied from 16500 K to 13600 K. Apart from atomic lines of H, C, and O, intensive molecular emission could be observed in the plasma. The formation of CN molecules in laser plasmas requires a reaction of atomic C or molecular $C_2$ with atmospheric nitrogen [6]. Figure 4 shows LIBS spectra of the CN violet system recorded at 0.1 mbar air pressure. By comparing the experimental and simulated CN emission spectra, the vibrational temperature of 7000 K was estimated. In vacuum conditions, strong molecular emission of the $C_2$ Swan band system was also registered.

**Acknowledgements**. The research was sponsored by: (i) International Atomic Energy Agency (IAEA) through contract no. 24076, "Contemporary and New IF Structural-First Wall Materials: Conditions of High Thermal and Electromagnetic Fluxes"; (ii) The Ministry of Education and Technological Development of the Republic Serbia through project no. 451-03-68/2022-14/200017.

## References

1. **Trtica M., Kuzmanovic M., Savovic J., Rankovic D.** Applied Surface Science 572 (2022) 151424 (8pp).
2. **Taylor C.N.** Journal of Nuclear Materials 558 (2022) 153396 (8pp).
3. **Gao L., Manhard A., Jacob W., von Toussaint U., Balden M. and Schmid K.** Nuclear Fusion 59 (2019) 056023 (8pp).
4. **Van der Meiden H.J., et al.** Nuclear Fusion 61 (2021) 125001 (14pp).
5. **Savovic J., Stoiljkovic M., Kuzmanovic M., Momcilovic M., Ciganovic J., Rankovic D., Zivkovic S., Trtica M.** Spectrochimica Acta Part B 118 (2016) 127-136.
6. **Dong M., George Chan C.-Y., Mao X., Gonzalez J.J., Lua J., Russo R.E.** Spectrochimica Acta Part B 100 (2014) 62-69.

# ULTRA-SHORT LASER PULSE PROCESSING OF Ti-BASED THIN METALLIC FILMS

B. Gaković[1], S.I. Kudryashov[2], P.A. Danilov[2], D. Milovanović[3], A.A. Ionin[2]

[1]Vinča Institute of Nuclear Sciences, University of Belgrade, Serbia, biljagak@vin.bg.ac.rs
[2]Lebedev Physical Institute, Russian Academy of Sciences, Moscow, Russia
[3] Institute of General and Physical Chemistry, Belgrade, Serbia

**Abstract.** In this work we show the results of our study of Ti-based nanolayer modification by ultrashort laser pulses (ULPs) irradiation. Multilayer thin films (MLTFs) are widely applicable in contemporary nanotechnology. Direct processing of MLTFs, with ULPs, is an extremely precise and fast technique. ULPs can be used for removing complete MLTF from the substrate, or layer/layers from its surface, known as selective ablation. Selective ablation was achieved only at well-defined values of ULP and MLTFs.

**Introduction.** Multilayer metallic thin-film (MLTF) structures, consisting of alternating layers, combined with Ti and some other metals, are broadly applicable in modern technology including microelectronics, biotechnology, solar power engineering, etc. [1, 2]. Direct laser processing conducted with ULPs represents an accurate and fast technique because of the non-contact, well-controlled, and precise processing and modification of the surface. The ULP irradiation (pulse duration from dozens fs to 10 ps) of metallic surface can be used for the single-step processing, without photo masks and a special environment. The most important part in our investigation concerns selective ablation of the one metallic layer or a few of them form the MLTFs. This kind of ablation, characteristic for ULP processing is also known as spallation, was achieved on Ti-Al and Ni-Ti nanolayer [3, 4, 5].

## Experimental.

The MLTFs were deposited on Si substrate by PVD technique. The samples were: five bilayers of (Al/Ti) (227 nm thick, with 27 nm of Ti on the surface), and five bilayers of (Ni/Ti) (100 nm thick, with 10 nm of Ni on the surface). ULP irradiation was done in the air using an experimental setup with a Yb-fiber laser [5]. Single pulse and multy pulse irradiation was completed at wavelength of 515 nm, pulse duration of 220 fs. The pulse energy was gradually changed from 0.02 to 1.3 μJ. In the case of Gaussian spatial beam profile, from values of pulse energy $E_p$ and beam radius w (at which the beam intensity has fallen to $1/e^2$ of its peak), it is easy to calculate laser fluence as $F = 2E_p/(\pi w^2)$.

The values of applied pulse energies were chosen in the intervals at which surface ablation was registered and continued until the entire NLTF was removed. Surface morphology and composition of the irradiated surface was monitored by a JEOL 7001F scanning electron microscope (SEM), equipped with energy-dispersive x-ray (EDX) spectroscopy. The sample surfaces were examined in 2D and 3D modes by optical profilometry.

## Results and Discussion

Fs laser irradiation of metals proceed through multiple steps - as absorption of photon energy including photo excitation of electrons, energy transfer from electrons to the lattice, melting and thermal expansion, damage of the surface without or with ablation, and in some cases photomechanical spallation, and thermal relaxation. It was shown that there is a "window" of the laser pulse energy/fluence at which specific selective ablation–photomechanical spallation- is registered. Spallation brings about the irradiated region of the surface having a characteristic crater with a flat centre and a sharp edge. Theoretical explanations and examples of photomechanical spallation can be found in the paper 6. In the conducted experiment with the single fs laser pulses and the MLTFs we estimated laser pulse energy/fluence that caused selective ablation/spallation of the first nano-layer and a part of the bottom ones.

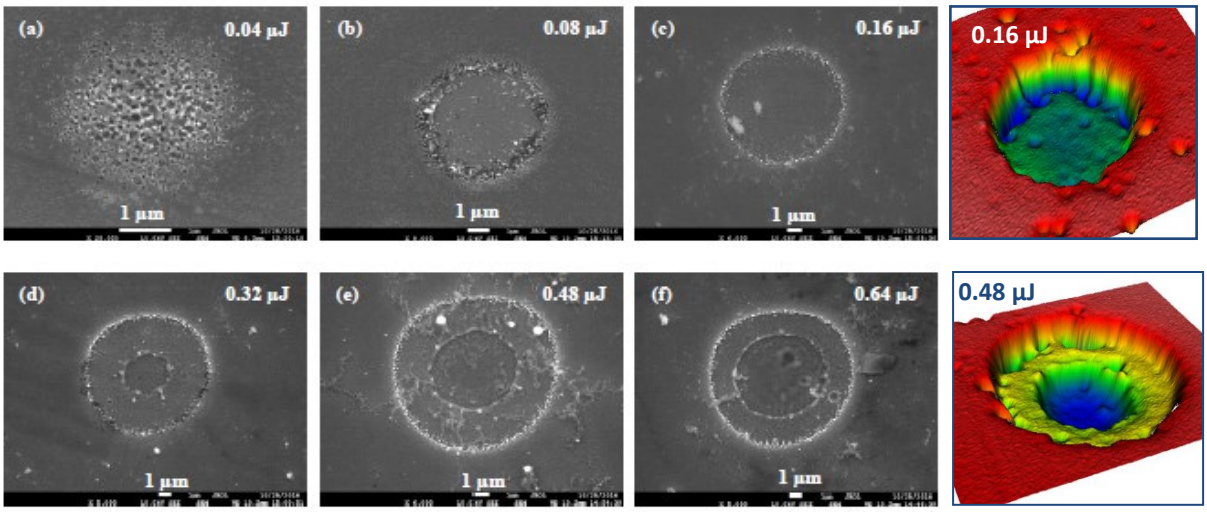



Fig. 1. Top-view SEM images and 3D profilometry of Ti(Al/Ti) after single pulse irradiation with different pulse energies. The one-step selective ablation can be seen at single pulse energy of 0.08 and 0.16 μJ, two-step ablation at 0.32, 0.48 and 64 μJ.

The effects of single pulse irradiation of Ti(Al/Ti) and (Ni/Ti) using different pulse energies, is presented on Fig.1., and Fig.2. Surface modiffication was monitored by SEM, while 3D analyses was done by profilometry. For applied

laser pulse irradiation, the minimal pulse energy that can modify the thin film surface- damage tresholds- were found and were less than 0.04 μJ for both MLTFs [5]. Irradiations with pulse energy of 0.08 μJ produced on both MLTFs clearly visible ablated regions with flat botoms clear edges, the so-called single-step ablation. Much sharper edge was in the case of (Ni/Ti) (Fig.2.). As the pulse energy increased, SEM and proflometry revealed a new type of surface morphology the two-step ablation. That is visible for pulse energies of 0.32 μJ in the case of Ti(Al/Ti), and 0.16 μJ in the case of (Ni/Ti) (Fig.1., and Fig.2.). Additional increase of pulse energy, coaused multy-step and total ablation of MLTFs from the Si substrate.

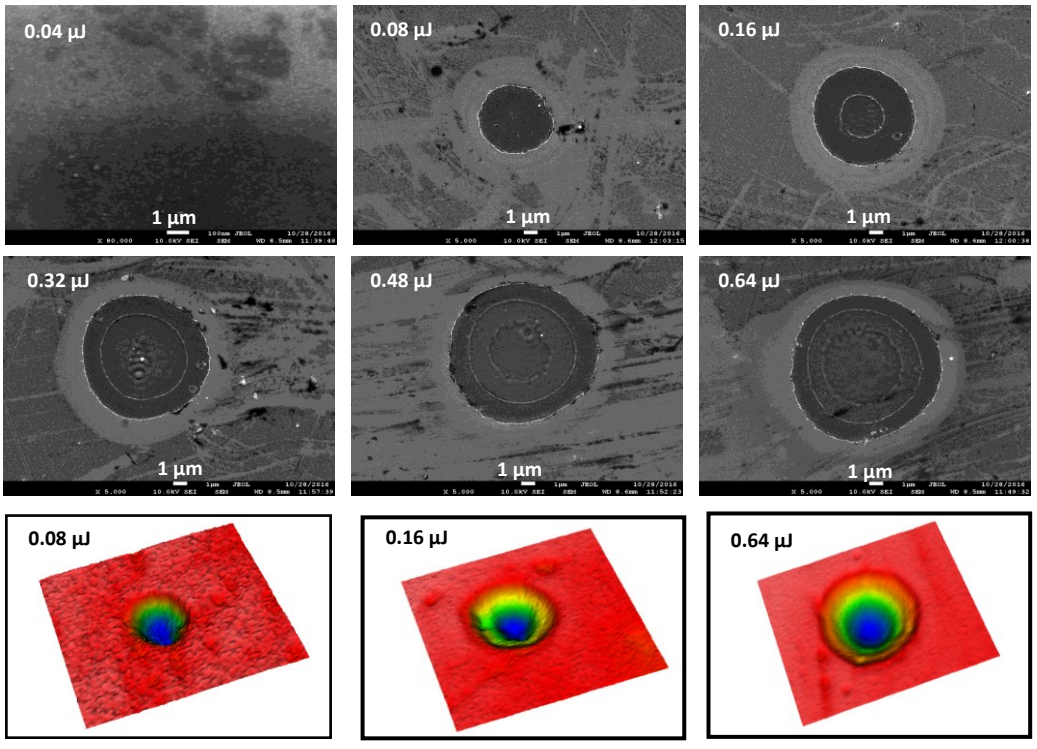



Fig. 2. Top-view SEM images and 3D profilometry of (Ni/Ti) after single pulse irradiation with different pulse energies. The one-step selective ablation can be seen at single pulse energy of 0.08 μJ, two-step ablation at 0.16 and 0.32 μJ, and multi-step ablation at 0.48 and 0.64 μJ.

The 3D profilometry is usefull for space visualization of ablated areas, while the 2D profilometry profiles, are helpful for measuring of the steps hight. It was proved that for both MLTFs the one-step ablation got nearly the same hights as the first layers thickness. Fig.3. is ilustration of morphological and compositional analysis of the single pulse surface damage and single-step selective ablation of the Ti(Al/Ti) thin film [5].

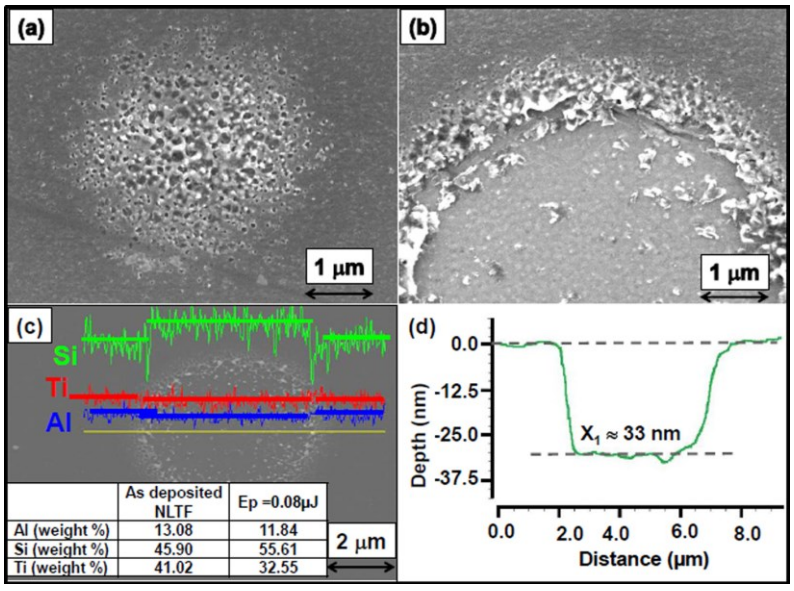



Fig. 3. Top-view SEM images of Ti(Al/Ti). The sub-threshold exfoliated damaged spot at $F_0$=0.08 J/cm$^2$ (a) and single-step crater at $F_0$ = 0.16 J/cm$^2$ (b), the colored EDX elemental (Si, Ti, Al) profiles across the crater and the table (c), and the 2D crater profile (d) [5].

## Conclusion.

The single-shot ULP femtosecond laser ablation of Ti(Al/Ti) and (Ni/Ti) MLTFs on silicon substrates demonstrated selective energy/fluence-dependent removal of its distinct single- and multi-layer sets at lower fluences and then rather continuous removal at higher fluences. The selective rupture at the different Ti/Al and Ni/Ti interfaces was related to tensile-stress and interface facilitated explosive boiling at the interfaces with the corresponding energy deposition in the MLTF provided by the "cascaded" heat conduction in the poorly conducting Ti and Ni and highly conducting Al layers [5].

**Acknowledgements.** This work was supported by STSM Grant given to B.Gaković by Cost Action CA17126-TUMIEE to visit Lebedev Physical Institute, Moscow, Russia, and by the Government of the Russian Federation (Grant No.074-U01) through ITMO Visiting Professorship Program (for S. I Kudryashov), the Presidium of Russian Academy of sciences, and the Russian Foundation for Basic research (Grant No. 16-32-00880).

**References**

1. **N.M. Bulgakova** et al, J. Laser Micro Nanoeng. 2 (2007) 76.
2. **B. Gaković,** et al., Journal of Applied Physics 122 (2017) 223106.
3. **B. Gaković,** et al., Applied Optics 60 (2021) H12-H19.
4. **B. Gaković**, et al., European Physical Journal D 75 (2021) 288.
5. **S.I. Kudryashov, B.** Applied Physics Letters, 112 (2018) 023103.
6. **Chengping Wu, Leonid V. Zhigilei**, Appl. Phys. A 114 (2014) 11.

# THE SPATIOTEMPORAL VALIDATION OF LOCAL THERMODYNAMIC EQUILIBRIUM DURING THE ANALYSIS OF A ZnAlCu ALLOY BY THE LIBS TECHNIQUE

N. Lellouche[1], S. Messaoud Aberkane[2], K. Yahiaoui[2], A. Kellou[1]

[1]Laboratoire électronique quantique, faculté de physique, Université des Sciences et de la Technologie Houari Boumediene USTHB. BP 32 El-Alia, Bab Ezzouar, Alger 16111, Algérie
lellouchenoora@gmail.com / hamidkellou@yahoo.fr
[2]Centre de Développement des Technologies Avancées, Division Milieux Ionisés & Laser, Cité du 20 Août 1956, Baba Hassen, BP 17 Alger, Algérie
smessaoud@cdta.dz / kyahiaoui@cdta.dz

## Abstract

The estimation of the plasma parameters such as temperature T, electron number density $n_e$, and the total number density N for the calibration free laser induced breakdown spectroscopy (CF-LIBS) is strictly connected to the concept of local thermodynamic equilibrium (LTE). For a plasma to be in LTE, the McWhirter criterion and two other conditions which take into account the transient and heterogeneous nature of the laser induced plasma (LIP) must be verified. The LIP was created by the interaction of a zinc-based alloy with a powerful Nd: YAG laser operating at its fundamental wavelength of 1064 nm. The plasma spectral radiation was collected and spectroscopically studied in order to extract valuable information about the material composition.

## 1. Introduction

LIBS is an analytical elemental analysis technique that can be used to detect and characterize materials. It uses the LIP as the emitting source.

The LIP is generated when a high power pulsed laser is focused on the target (liquid, solid, gas...). The emitted light from the plasma is used for the determination of elemental composition of the sample using either the calibration curve method or the CF-LIBS method. In order to imply this latter, the plasma has to be in local thermodynamic equilibrium (LTE). For this condition to be fulfilled we used different criteria that take into account the transient and heterogeneous nature of the LIP.

## 1. Experimental set up

A schematic representation of the experimental setup is shown in Fig. 1. A Q-switched Nd:YAG laser at a wavelength $\lambda$ = 1064 nm, was focused onto a ZnAlCu based alloy placed in air to form the LIP. LIP emission is collected and focused on the entrance of an optical fiber and sent to an Echelle spectrometer

array equipped with an ICCD camera for the detection, which is connected to a PC that is used for the analysis of the spectral signal.

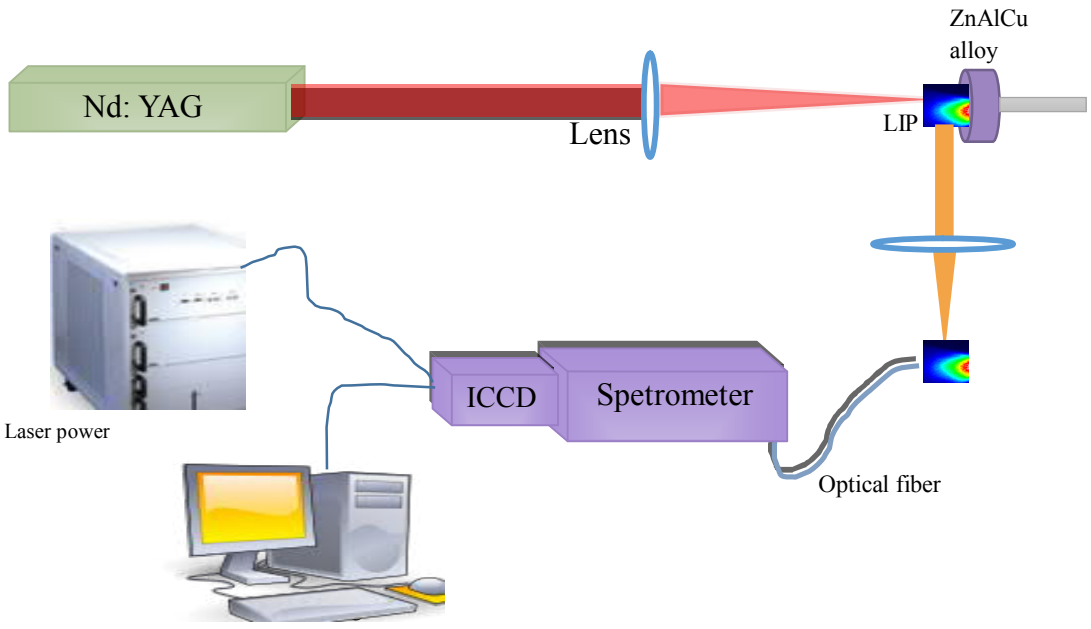



Fig. 1. Schematic diagram of the experimental setup

At a fixed gate width of 500 ns, the spatially and temporally resolved plasma was collected by varying the delay time from 0.8-12 μs and the collecting position on the plasma plume along the propagation axis from 0 to 3 mm.

## 2. Results and discussion

The collected emission spectra were characterized by various atomic and ionic transitions of Zn, Al and Cu identified using NIST and Kurucz databases.
In this study, we focused our interest on the spectroscopic evolution of Zn atomic and ionic lines, the major element in the alloy.

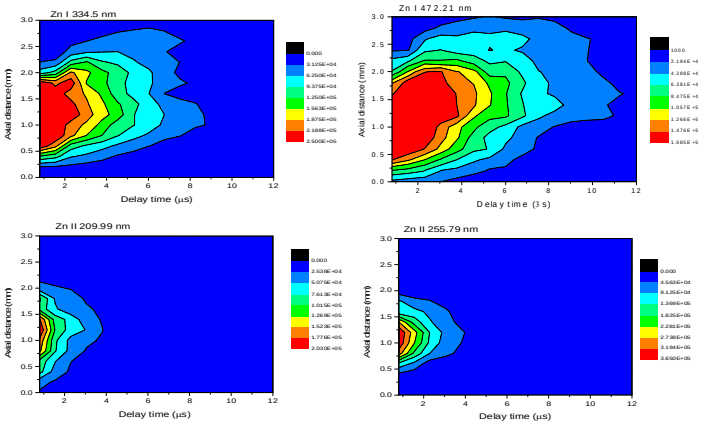



Fig. 2. The Spatiotemporal evolution of the Zn atomic and ionic spectral lines.

Fig. 2 shows the spatiotemporal evolution of the Zn atomic and ionic lines. As we can observe, the intensity of ionic emission lines decrease significantly at early time compared to atomic lines and this is due to recombination mechanisms.

For LIP, which considered as a transient and heterogeneous plasma, the LTE is warranted using the McWhirter criterion [1] given by:

$$N_e(cm^{-3}) \geq 1.6 \,.\, 10^{12} T^{\frac{1}{2}} (\Delta E_{nm})^3 \qquad (1)$$

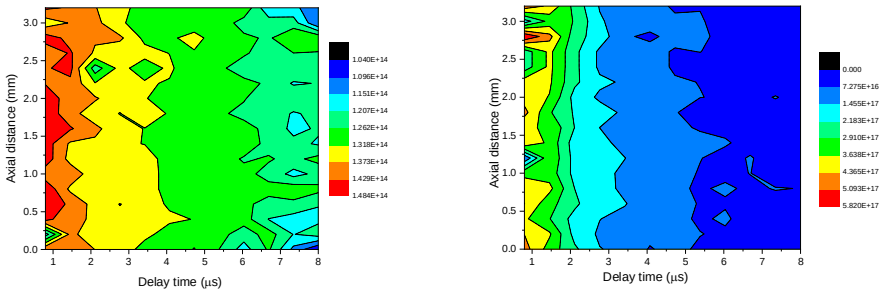
And two other conditions, the first one takes into account the transient behavior of LIP. For this condition to be validated, the temporal variation of thermodynamic parameters should be slower than the relaxation time ($\tau_{rel}$ ) [2]; this can be expressed as:

$$\frac{T_e(t+\tau_{rel}\ )-T_e(t)}{T_e(t)} \ll 1 \ \ and \ \ \frac{N_e(t+\tau_{rel}\ )-N_e(t)}{N_e(t)} \ll 1 \qquad (2)$$

The second criterion takes into account the heterogeneous nature of LIP. It requires that the variation length of the plasma temperature and electron number density should be larger than the diffusion length (λ) [2]. This is given by the following inequalities:

$$\frac{T_e(x+\lambda)-T_e(x)}{T_e(x)} \ll 1 \ \ and \ \ \frac{N_e(x+\lambda)-N_e(x)}{N_e(x)} \ll 1 \qquad (3)$$

When comparing the figures (a) and (b) in Fig. 3, we notice that the electron number density measured in our experiment is nearly three orders of magnitude bigger than the minimum electron number density given by the McWhirter criterion, thus validating the first condition for the existence of LTE.




(a) The Mcwhirter limit (b) Electron number density

Fig. 3. Comparison between the measured $N_e$ and the minimum $N_e$ given by the McWhirter criterion.

From Fig. 4, we can see that the relaxation time is of the order of $4x10^{-9}$ s, which is shorter than the decay time which is of the order of $1.4x10^{-6}$ s thus confirming the existence of LTE in a transient LIP.

As it is shown in Fig. 5 , the diffusion length is of the order of $10^{-5}$ cm, which is shorter than the length of the plasma plume (the emissive plasma length is approximately 0.25 cm) thus confirming the existence of LTE in an inhomogeneous plasma.

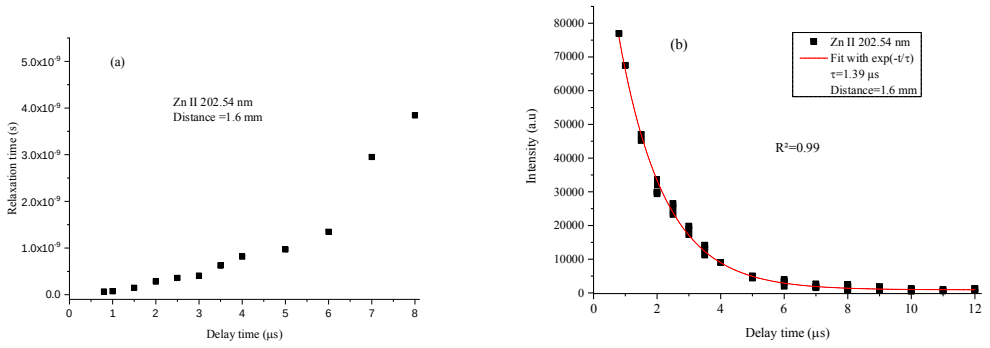



Fig. 4. A comparison between the relaxation time (a) and the decay time (b), for the validation of LTE under the transient nature of LIP.

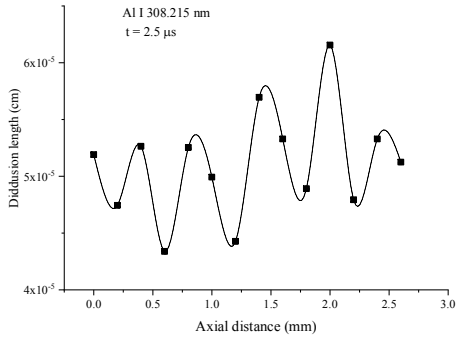



Fig. 5. The variation of the diffusion length as a function of axial distance

## 3. Conclusion

In this work, we studied the spatiotemporal evolution of the Zn atomic and ionic spectral lines, and we have validated the LTE condition for LIP generated by the interaction of a Nd:YAG laser with a ZnAlCu based alloy.

## References

1. Fujimoto, Takashi, and R. W. P. McWhirter. "Validity criteria for local thermodynamic equilibrium in plasma spectroscopy." *Physical Review A* 42.11 (1990): 6588.
2. Cristoforetti, Gabriele, et al. "Local thermodynamic equilibrium in Laser induced breakdown spectroscopy: beyond the McWhirter criterion." *Spectrochimica Acta Part B: Atomic Spectroscopy* 65.1 (2010): 86-95.

# ENHANCED PROTON ACCELERATION FROM AN ULTRATHIN TARGET IRRADIATED BY LASER PULSE

M.Turki[1], D. Bennaceur Doumaz[2]

[1]Radiation Physics Department, Faculty of Physics, USTHB, BP 32 Bab Ezzouar, 16111, Algiers, Algeria, mturki@usthb.dz
[2]Centre de développement des technologies avancées (CDTA), Cité ‹20 Août 1956, Baba Hassen ‹16081 Algiers, Algeria, ddoumaz@gmail.com

## Introduction

Acceleration of charged particles by ultra-intense short laser pulses with high brightness, short duration, and low emittance has been widely explored in recent decades because of its prospective application in many areas, such as medical therapy [1], materials processing [2], particle radiography [3], and high energy density physics [4] and so on. To obtain high quality and high energy ion beams, different acceleration mechanisms are described. Among these mechanisms, the most widely investigated in proton acceleration is target normal sheath acceleration (TNSA) scheme [5]. This latter proceeds via the build-up of TV $m^{-1}$ electrostatic fields at the rear side of a thin target foil, produced by hotter electrons generated at the laser-irradiated side of the target, typically via the oscillating $j \times B$ heating of linearly polarized light.

The energy spectrum of the accelerated protons could be controlled by appropriately choosing the laser and target parameters, such as laser energy, intensity, prepulse contrast, polarization, target thickness with its density and structure [6]. The use of ultrathin target offers optimal conditions for accelerating protons to high energies from laser-matter interaction in the framework of the TNSA mechanism.

In this work, by performing two-dimensional Particle-In-Cell (PIC) simulations, we will demonstrate how the proton energy is increasing with low atomic number Z targets by examining the proton energy spectra of different materials by varying the target thickness.

## PIC simulations set-up

PIC simulations, using a pulse laser with an amplitude of $a_0$=10 and a duration of 30 fs, are performed to determine how the energy of protons varies with the composition and the target thickness. We use the open source PIC code EPOCH [7] developed by the University of Warwick (UK) to carry out the simulations employing a simulation box of size $L_x \times L_y$ = 80 μm×30 μm, from

0 µm to 80 µm in the x direction and between ± 15 µm in the y direction with square cells of 10nm, it yields 1800 × 1000 cells in the simulation box. We introduced 64 electrons, 64 ions, and 100 protons by cell.

We assumed a laser pulse with a field amplitude $a_0 = eE_0/m_e\omega c = 10$ corresponding to an intensity $I = 2\times 10^{20}\ W/cm^2$, with a wavelength $\lambda_L = 0.8$ µm. It has a pulse duration of 30 fs, and a spot size of 5 µm. $E_0$ is the initial laser electric field amplitude, $e$ is the electron charge, $m_e$ is the electron mass, $\omega$ is the laser frequency, and $c$ is the light speed. The laser is linearly polarized and the boundaries are chosen open, in order to minimize the reflection effect.

We considered a target with fully ionized atoms, of different materials, namely, He, C, and Al. A contaminant proton layer of 20 nm thickness is assumed on the backside of the target. The different material ions and electrons densities are resumed in Table 1.

| Material | He | C | Al |
|---|---|---|---|
| **Z** | 2 | 6 | 13 |
| **$\rho$ (g.cm$^{-3}$)** | 0,178x10$^{-3}$ | 2 | 2.7 |
| **M (a.u)** | 4.00 | 12.01 | 26.98 |
| **$n_i$ ($10^{22}$ cm$^{-3}$)** | 2.68x10$^{-3}$ | 10.02 | 6.02 |
| **$n_e$ ($10^{22}$ cm$^{-3}$)** | 5.36x10$^{-3}$ | 60.12 | 78.26 |

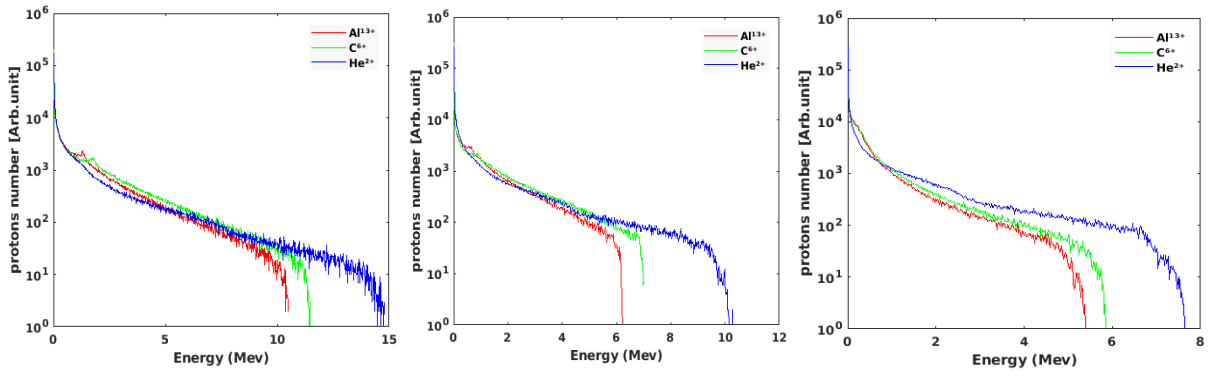
Table1: Volumetric mass density ρ, ion mass M, ion density $n_i$ and electron density $n_e$ of the materials.

## Results and discussion

The effects of foil thickness and target composition on proton acceleration were studied using different materials (He, C, and Al) of varying thicknesses (50, 200 and 500 nm). The proton energy spectra obtained for different foil thicknesses and compositions is plotted in Figure 1. We observed a significant enhancement of maximum proton energy with helium target which is about a factor of 1.5 compared to the Al and C for 50 nm thick target, this energy becomes smaller with thicker targets (200 and 500 nm).

This can be understood as follows. The TNSA sheath electric field formed at target rear surface created by the energetic electrons escaping from the rear surface is responsible for proton acceleration. These electrons are generated at the target front surface and propagate through the target with typical divergence

angles [8]. The electric field is directly proportional to the square of the electron density. This latter itself is inversely proportional to the product of target thickness and divergent angle tangent [9]. The scattering angle is known to increase with the atomic number Z when the electrons are propagating through the target. Consequently, for thick targets and high Z, the density of hot electrons is decreasing, which consequently results in reduction of sheath field and hence the maximum proton energy.




(a) (b) (c)

Fig. 1. The proton energy spectra from He, C, and Al for different target thicknesses (a) 50 nm, (b) 200 nm, (c) 500 nm.

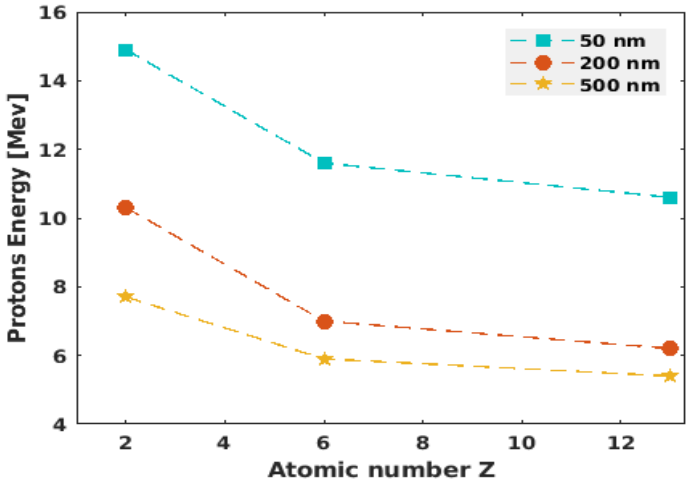



Fig. 2. The proton energy as a function of atomic number Z for different thicknesses.

In addition, the high intensity interaction process is largely governed by the material mass, in consequence the helium ions are predicted to move $\sqrt{m_{Al}/m_{He}} \approx 2.59$ times and $\sqrt{m_C/m_{He}} \approx 1.73$ times faster than aluminum and carbon. As a result, helium may decompose earlier (the fast electrons are produced earlier) than C and Al. This may explain the observed results in the

figure 2, when the proton energy is increasing with low atomic number Z of target. The maximum proton energy is then obtained with helium target with the smallest thickness.

## Conclusion

It is found that materials of low Z are more favorable for enhancing proton energy with thin targets (≈ 50 nm) instead of commonly used elements (C, Al) usually used for proton acceleration in TNSA mechanism.

## References

1. **Bulanov S.S., Brantov A., Bychenkov V.Y., Chvykov V., Kalinchenko G., Matsuoka T., Rousseau P., Reed S., Yanovsky V., Krushelnick K., Litzenberg D.W. and Maksimchuk A.**, Med. Phys. 35 (2008) 1770-1776.
2. **Zhu X.P., Ding L., Zhang Q., Isakova Yu., Bondarenko Y., Pushkarev A.I. and Lei M.K.**, Laser and Particle Beams, 3 (2017) 587–596.
3. **Borghesi M., Campbell D.H., Schiavi A., Haines M.G., Willi O., Mackinnon A. J., Patel P., Gizzi L. A., Galimberti M., Clarke R. J., Pegoraro F., Ruhl H. and Bulanov S. V.,** Plasma Phys. 9 (2002) 2214-2220.
4. **Sharkov B.Yu., Hoffmann D.H.H., Golubev A.A., Zhao Y**., Matter and Radiation at Extremes, 1 (2016) 28-47.
5. **Wilks S.C., Langdon A.B., Cowan T. E., Roth M., Singh M., Hatchett S., Key M.H., Pennington D., MacKinnon A. and Snavely R. A.**, Plasma Phys. 8 (2001) 542-549.
6. **Badziak J**, IOP Conf. Series: Journal of Physics: Conf. Series, 959 (2018) 012001.
7. **Arber T.D., Bennett K., Brady C.S., Lawrence-Douglas A., Ramsay M.G., Sircombe N.J., Gillies P., Evans R.G., Schmitz H., Bell A.R. and Ridgers C.P.**, Plasma Physics and Controlled Fusion 57, (2015) 113001.
8. **Tayyab M., Bagchi S., Ramakrishna B., Mandal T., Upadhyay A., Ramis R., A. Chakera J., Naik, P. A. and Gupta P. D.**, Physical Review E 90 (2014) 023103.
9. **Tatomirescu E.D.** Laser-plasma acceleration at ultra-high intensity numerical modeling. PhD thesis, Bordeaux University, France (2019).

# SHIELDING OF THE TARGET DURING LASER-PLASMA TREATING OF METALS IN ELECTRIC FIELD

A.Yu.Ivanov, A L Sitkevich, S.V.Vasiliev

Grodno State University, Ozheshko 22, 230023 Grodno, Belarus.
e-mail: ion_ne@mail.ru

In the publication [1] was shown that under the action of laser radiation with the mean radiation flux density ~ $10^6$ W/cm$^2$ at the surface of some metals (Cu, Al, Sn, Pb, In) in the external electric field with different polarity and the strength up to $10^6$ V/m the mean size of the target substance droplets carried out of the irradiated zone decreases by several times with increasing external electric field strength in spite of short duration of electric field existence. The aim of the present work is to study the influence of electric fields of different strength (from 0 to $10^6$ V/m) on the spatial and temporal evolution of the laser plasma arising under the action of millisecond laser pulses at the surface of metals and to explain the mentioned effect.

To treat a metal sample we used operating in the free oscillation regime GOR-100M laser (wavelength $\lambda$ = 0.694 μm, pulse duration ~1.2 ms). Its radiation with the help of the focusing system was directed through the hole in the first electrode onto the target serving as the second electrode. Diameter of the hole was equal to 1 cm. The electric voltage applied to the electrodes varied from -25 kV to + 25 kV in different experiments. The optical stop allowed us to form on the surface of irradiated target the radiation spot with sharp edges. Its diameter in the course of experiments was varied from 1 to 2 mm. Energy of the laser pulse varied from 10 to 60 J. High-speed holographic cinematography method was used to study the temporal and spatial evolution of the plasma plume near the sample treated by laser radiation. The target was placed in one of the arms of a Mach – Zehnder interferometer. Interferometer was illumined with the radiation of operating in the free oscillation regime ruby laser. With the help of the collimator we obtained a parallel light beam of the probing radiation with the diameter up to 3 cm. Such size of the observation field allowed to observe the plasma cloud development. The interferometer was conjugated by the high-speed recording camera SFR-1M, in which the plane of the film was attended with the meridian section of the treating the sample laser beam by means of the objective. This apparatus allowed us to record the time-resolved holograms of the focused image of the laser plasma plume. Separate holographic stills had temporal resolution 0.8 μs (the single still exposure time) and the spatial resolution in the object field ~ 50 μm.

After laser treating of the target many small droplets appear on its surface of irradiated target independently either positive or negative potential was applied

to the electrode. For instance, after treating a spot of led target with the diameter of 2 mm by laser pulse with energy 20 J and using electric field having strength $10^6$ V $cm^{-1}$ one observed ejection of droplets with the mean size less than ~ 0.1 mm. The maximal size of the droplets was 0.4 mm. The droplets were observed up to the distance of 2 cm from the crater centre. It is essential that without external electric field the mean size of the droplets was ~ 0.4 mm, and droplets were seen at the distance up to 1 cm from the crater centre.

The interferograms reconstructed from the holograms recorded with means of high-speed holographic cinematography that despite a considerable temporal increase of the plasma formation size the mean concentration of electrons in the plume remains practically stable and slightly grows.

Presence of an external electric field weakly affects the concentration of electrons in the laser plasma plume. Maximal transverse size of the plasma plume for negative voltage on the led sample was 2 cm. In the absence of the external electric field maximal transverse size of the plasma plume was 1.5 cm. After reaching the second electrode in 56 – 72 μs plasma plume practically does not grow in the transverse dimension.

At the first stage of the laser plume development dynamics of plasma formation, in principle, do not differ from those observed in the absence of the external electric field. The metal of the irradiated target melts and evaporates. As a result of local erosion plasma formation the plasma plume with a material dispersed liquid-drop phase begins to form [2, 3]. Note, that the bulk evaporation is promoted by the gases, diluted in the metal and by the spatiotemporal non-uniformity of the laser radiation [2]. Bulk evaporation is typical for all metals used in our experiments if they were treated by laser radiation with flux density $10^6 – 10^7$ W/$cm^2$ [3]. Obviously, the presence of the external electric field affects (increases or decreases depending on the direction of the field strength vector) the velocity of motion of the plasma front and causes some distortion of the plasma cloud shape.

It is material that even when the plasma front reaches the second electrode, its velocity not only does not decrease (which is typical for late stages of the laser plasma plume evolution [4]), but even increases. This effect was observed in the presence of the external electric field of any orientation. Already was mentioned that this phenomenon can be explained by the permanent and material increase of the mass of the metal carried out during laser treating of the irradiated sample as well by the secondary ionization of plasma by laser radiation. The maximal expansion velocity of the plasma plume front was 350 m $s^{-1}$ for the negative voltage at the target (*3*), 310 m $s^{-1}$ without external electric field and 270 m $s^{-1}$ for the positive voltage applied to the electrode (3).

It is essential that the mentioned differences (at the considered parameters of laser radiation) are observed only at the initial stage of the laser plume

development, because after the steam-plasma cloud reaches the electrode an electric breakdown (short-circuit) occurs, and the external field in the interelectrode gap disappears.

The inerferograms presented at figure 1 show that electric breakdown leads to the spasmodic increase of electron density of plasma. In the hole of the second electrode forms a plasma bubble where the interference fringes are not separated. This means that refraction in the plasma bubble differs not les then $10^{-3}$ from the initial (non-varied) air. In our case it can be only if electron density in this area is not less $10^{20}$ $cm^{-3}$, and this means full ionization of plasma in the plume. This leads to the effective absorption of laser radiation by plasma torch and to the shielding of the target.

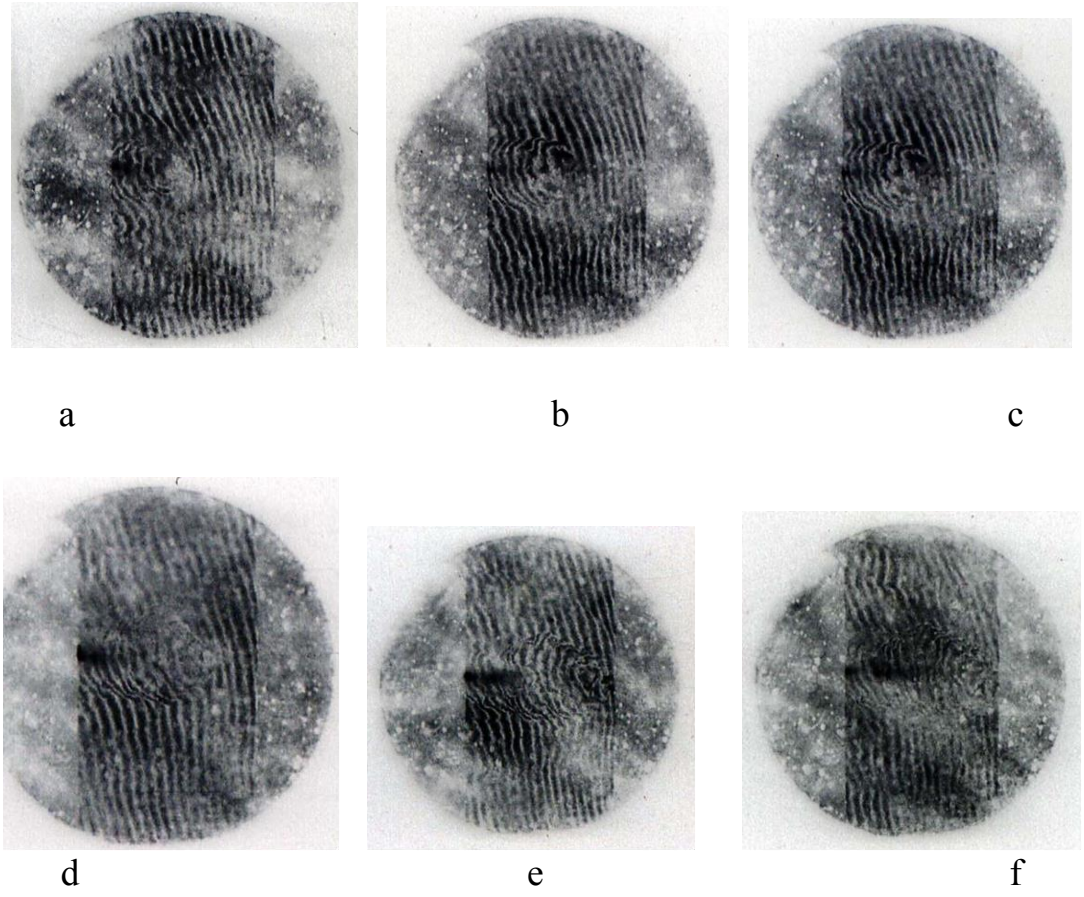



**Figure 1.** Interferograms of laser plasma plumes after electric breakdown at the positive target potential. Interferograms were obtained 90 (a), 150 (b), 270 (c), 360 (d), 450 (e), 510 (f) μs after start of laser treating of led sample.

The interferograms show also that the plasma bubble moves supersonically from the second electrode toward the laser beam direction. This means a light-detonation wave generation that is typical for such value of electron density. It is

to be mentioned that not only electron density but plasma temperature in the light-detonation wave increases in several times verses to the temperature in the plasma cloud near the irradiated target.

In consequence of shielding droplets generation happens only during electric field existence. This explains decrease by several times of the characteristic size of the target substance droplets in spite of short duration of electric field existence.

**Conclusion**

The studies performed have shown that evolution of plasma plume generation on the surface of metal (Cu, Al, Sn, Pb, In) irradiated by laser beam with the mean radiation flux density $\sim 10^6$ W cm$^{-2}$ in the external electric field with different polarity and field strength from 0 to $10^6$ V m$^{-1}$ was experimentally investigated.

It is shown that the mean size of metal droplets carried out from the irradiated zone of target becomes materially (in several times) smaller when of the external electric field strength amplitude grow, independently to its polarity. It is also shown that the change in the evolution of parameters plasma plume formed on the surface of metals (Cu, Al, Sn, Pb, In) treated by laser radiation at early stages is quantitative rather than qualitative.

The mentioned differences (at the considered parameters of laser radiation) are observed only at the initial stage of the laser plume development, because after the steam-plasma cloud reaches the electrode an electric breakdown (short-circuit) occurs, and the external field in the interelectrode gap disappears. Electric breakdown leads to the spasmodic increase of electron density and temperature of plasma and to effective absorption of laser radiation by plasma torch (shielding of the target). In consequence of shielding droplets generation happens only during electric field existence. This explains decrease by several times of the characteristic size of the target substance droplets in spite of short duration of electric field existence.

**References**

1 Ivanov A Yu, A.V. Kapytski A V, Vasiliev S V Materials Physics and Mechanics. 41, 97 – 102 (2019).

2 Goncharov V K, Kontsovoy V L, Puzyrev M V *Inzhenerno- JIzicheskii zhurnal,* 66, 662 – 667 (1994) [Journal of Engineering Physics and Thermophysics*,* **66,** 588 – 593 (1994)].

3 Goncharov V K, Kontsovoy V L, Puzyrev M V *Kvantovaya Elektron.,* 22, 249 – 254 (1995). [Sov. J. Quantum Elelctron., 25, 232 – 237 (1995)].

4 Barikhin B A, Ivanov A Yu, Nedolugov V I Kvantovaya Elektron., 17, 1477 – 1480 (1990) [Sov. J. Quantum Electron., 20, 1386 – 1389 (1990)].

# CRYSTALLINE STRUCTURE CHANGES IN METALS AFTER THEIR LASER TREATING IN DIFFERENT CONDITIONS

A.Yu.Ivanov, E.A.Karpovich, A L Sitkevich, N.G.Valko, S.V.Vasiliev

Grodno State University, Ozheshko 22, 230023 Grodno, Belarus.
e-mail: ion_ne@mail.ru

The aim of this work is to study the changes and relaxation of the structure of a number of metals exposed to laser radiation (LR) with a flux density of $10^4$ - $10^5$ W/cm$^2$, as well as explanation of the detected structural changes.

As a source of laser radiation (LR) was used GOR-100 M ruby laser with a wavelength of $\lambda$ = 0.694 μm operating in the free-running mode (pulse duration $\tau \sim 1.2$ ms). Passing through the focusing system LR was sent to the sample which made it possible to construct the image of the aperture on the surface of the sample 3 as a spot with sharp edges (the diameter was varied in during experiments from 1 to 2 mm), which, in turn, ensured a change in the radiation flux density q from $10^4$ to $10^6$ W/cm$^2$.

The DRON-2.0 X-ray diffractometer was used to determine the structural changes in metal samples (solid polycrystalline), in equilibrium with a cubic face-centered crystal lattice, before and after exposure to laser radiation. The Kα line from a tube with a copper anticathode filtered by a nickel standard filter at a wavelength of 154.050 pm was used in the diffractometer.

Calculation of temperature changes after action on the target of each pick of free oscillation pulse was also fulfilled.

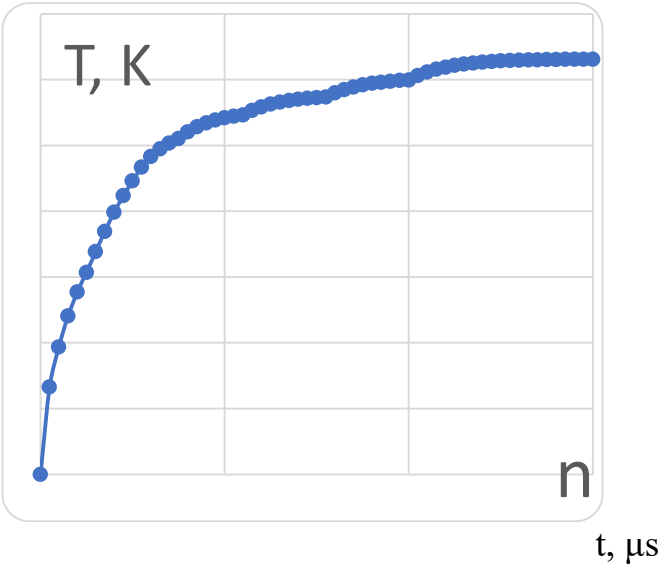
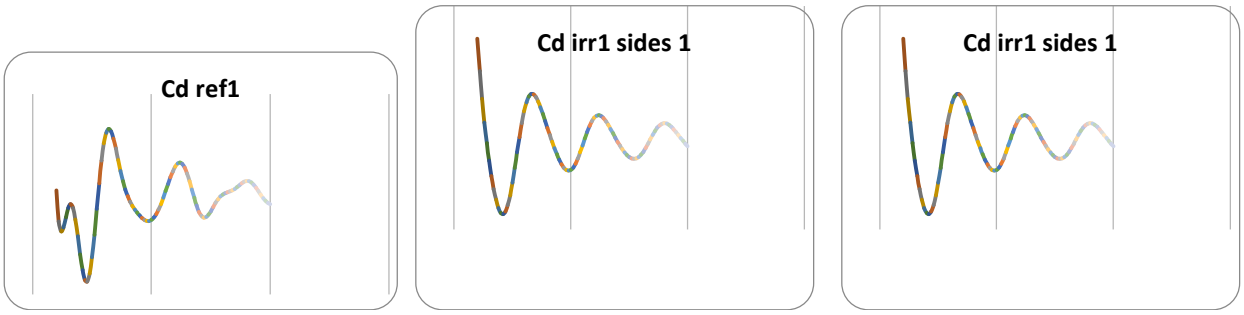



Figure 1 Calculated temporal dependence of temperature of titanium surface irradiated by laser pulse with a flux density of $10^5$ W/cm$^2$.

Let's now consider the effects of laser radiation on cadmium samples. Figure 2 represents correlation functions P (u) [1] for cadmium samples (a) – before irradiation, degree of crystalline is 63,49%; (b) – after laser irradiation of one side of a sample, degree of crystalline is 84,35%; (c) – after laser irradiation of one both sides of a sample, degree of crystalline is 86,84%.




a b c

Figure 2– Correlation functions P (u) for cadmium samples (a) – before irradiation, (b) – after laser irradiation of one side of a sample, (c) – after laser irradiation of both sides of a sample.

Table 1 – Parameters of the correlation functions of a cadmium sample before and afte rlaser irradiation with q ~ $10^5$W/cm$^2$.

| | | **Ev** | min | max | Δ | σ |
|---|---|---|---|---|---|---|
| **Cd ref** | **a** | 2,967 | 2,951 | 2,974 | 0,024 | 0,007381 |
| | **c** | 5,586 | 5,472 | 5,627 | 0,155 | 0,044975 |
| **Cd irr 1 sides** | **a** | 2,959 | 2,946 | 2,968 | 0,021 | 0,009531 |
| | **c** | 5,578 | 5,526 | 5,625 | 0,099 | 0,03164 |
| **Cd irr2 sides** | **a** | 2,920 | 2,803 | 3,078 | 0,275 | 0,101995615 |
| | **c** | 5,459 | 5,154 | 5,638 | 0,484 | 0,197518 |

Number of cells changed the crystal structure after laser irradiation of one side of a sample is 64%, after laser irradiation of one both sides of a sample – 67%.

Let's now consider the effects of laser radiation on titanium samples. Typically, titanium can crystallize in two crystalline structures: α – Ti and β – Ti. When it crystallizes at low temperatures (room temperature), an α – Ti hexagonal close packed (HCP) structure is formed. While if it crystallizes at high temperatures, a body-centered cubic (BCC) β – Ti structure is formed. Complete transformation of the crystal structure from one to another occurs at a temperature of 882 ± 2 ° C.

Consider the effect of laser radiation on an α – Ti sample. Figure 4 shows the X-ray diffraction patterns of the samples before and after its processing, from which it

can be seen that after laser processing there is a change in the intensity of the reflexes, their position and profiles. For example, reflex 103 practically disappeared.

Each intensity maximum in the X-ray diffraction pattern is an n-order reflection from a series of planes (hkl) with an interplanar distance dhkl corresponding to the slip angles. According to the Hull chart, for determining the X-ray patterns of crystals with a hexagonal compact structure, we determine hkl.

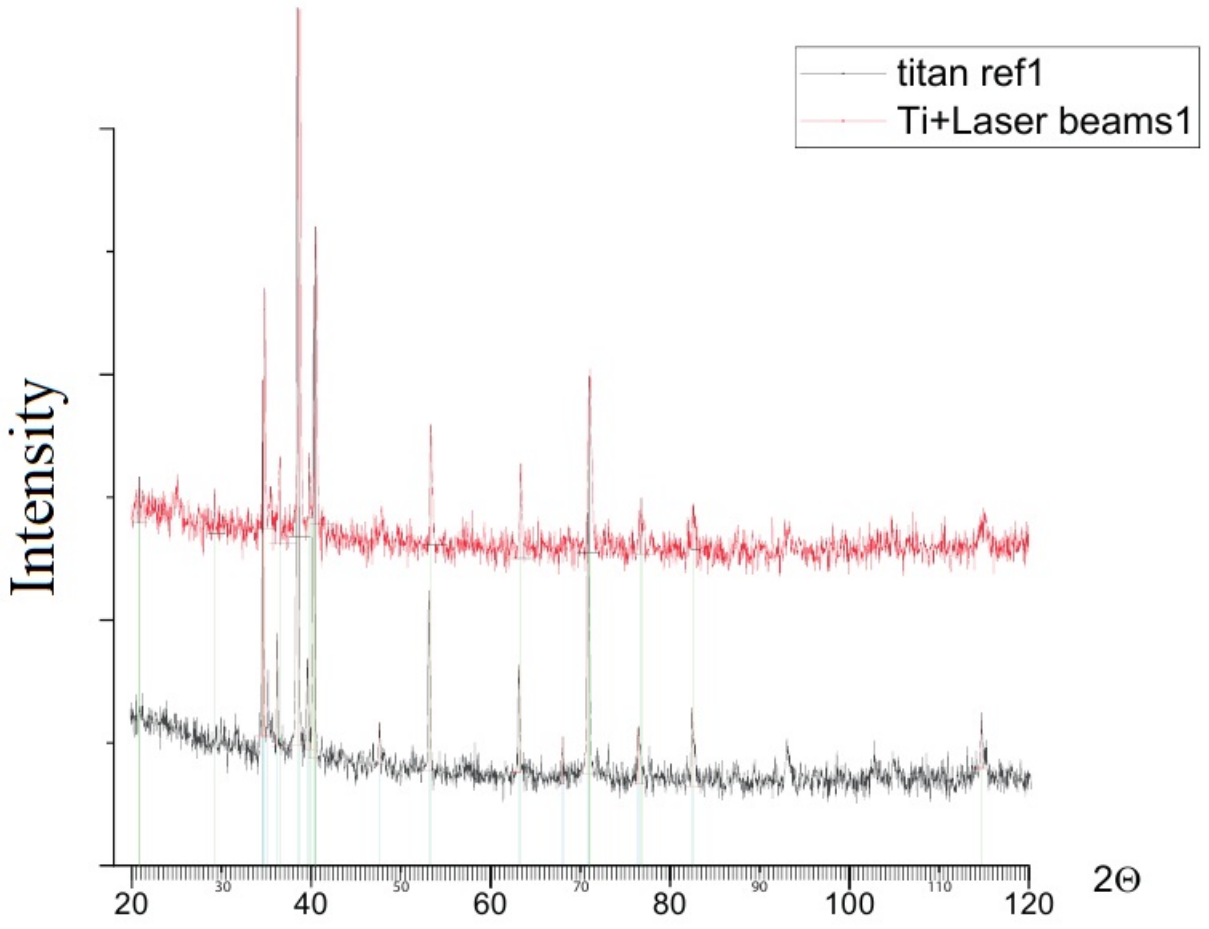



Figure 3 – X-ray patterns of α – Ti before (lower) and after (upper) laser treatment.

Degree of crystalline is in reference sample 36,13%, after laser irradiation of one side of a sample 38,91%, after laser irradiation of one both sides of a sample 47,63%.

To clarify the indication of reflexes, it is necessary to compare the experimental (hkl) exp and theoretical (hkl) theoretical indices of the plane.

The next step is to determine the experimental parameters of the cell.

From table 3 it follows that the distribution of the parameters of the unit cells before and after laser irradiation is quite different from each other.

For the titanium samples treated by laser radiation with the flux density of radiation q ~ $5 \cdot 10^4$ W $cm^{-2}$ splitting of correlation function maxima was not observed. However, the width of X-ray difractograms was essentially changed.This effect testifies the considerable growth of crystalline grid defects concentration in the irradiated zone.

Micro-hardness of titanium samples in the irradiated zones also considerably increased. The calculations show that after treating of titanium sample by laser radiation with the flux density q ~ $5 \cdot 10^5$ W $cm^{-2}$ number of crystalline elementary cells were subjected to the transformation from the cubic side-centered to the distorted (having a form of parallelepiped, different from the cub) can reach 50 %.

Table 2 – Comparison of X-ray diffraction patterns of α – Ti before (1) and after (2) irradiation: average, smallest (min) and largest (max), theoretical values of the cell parameters which determined by all reflexes (in $\mathring{A}$), $\sigma_{11}$ - standard deviation of the parameters (in $\mathring{A}$)

| | | The average | min | max | $\sigma_{11}$ | Theory |
|---|---|---|---|---|---|---|
| a | 1 | 2,708 | 2,546 | 2,992 | 0,18 | 2,937 |
| | 2 | 2,518 | 2,364 | 2,577 | 0,09 | |
| c | 1 | 4,747 | 4,660 | 4,956 | 0,12 | 4,582 |
| | 2 | 4,660 | 4,421 | 4,923 | 0,21 | |

## III. CONCLUSIONS

The investigations showed that under the action of laser radiation on the surface of metal samples, their crystal structure changes in the irradiated zone from cubic face-centered to distorted (having a parallelepiped shape different from the cube).

## REFERENCES

1 Vasiliev S.V. Change in the crystalline structure of metals under the influence of laser radiation / S.V. Vasiliev, A.Yu. Ivanov, V.A. Liopo // Engineering Physics Journal. - 2007. - T. 80, No. 5. - S. 12 - 18.

# SELECTION OF SPECTRAL VARIABLES FOR MULTIVARIATE CALIBRATION ON C, Mn, Si, Cr, Ni AND Cu IN LOW ALLOY STEELS CHARACTERIZATION BY LIBS METHODS

M.V. Belkov, D.A. Borisevich, K.Yu. Catsalap, M.A. Khodasevich

B.I.Stepanov Institute of Physics, National Academy of Sciences of Belarus,
Minsk, Nezavisimosti Ave., 68-2, e-mail: k.catsalap@dragon.bas-net.by

Laser induced breakdown spectroscopy (LIBS) is a widely demanded optical method for chemical analysis. Other modern technologies, such as X-ray fluorescence analysis and mass spectrometry, typically correspond to laboratory-based analytical techniques. Small-sized LIBS devices have common advantages in practical operation, such as simple sample preparation or even its absence, real-time measurement of a complete set of chemical elements and the possibility of remote sensing. Therefore, LIBS is considered as the most promising technology for real-time chemical analysis in metallurgy, mining industry, cement production, food products, etc. Steel plays a special role in heavy industry. The main element of steels is iron. Special properties of steels are given by technological impurities and additives, such as manganese, silicon, chromium, nickel, copper and others. In VIS and UV spectral regions the analytical emission lines of these elements are superposed and their use for calibration of the concentration of elements in steels becomes difficult. In this case methods of multivariate analysis are preferable [1, 2].

Previously, we used the partial least squares method to calibrate the concentrations of C, Mn, Si, Cr, Ni and Cu using low-resolution emission spectra (190–440 nm, resolution 0.4 nm, step along the spectrum 0.1 nm). The experimental setup and measurement conditions are given in [3]. Reference samples of low-alloy steels UG0d-UG7d, UG9d (Russia) and 51/1-58/1, 72-76, 101-103, 110-125 (Poland) were used for calibration. From 31 to 39 steels with non-repeating values of the calibrated concentrations were divided to training dataset by Kennard-Stone algorithm [4] and test dataset. The developed multivariate models based on partial least squares (PLS) method [5] are characterized by root-mean-square error (RMSE) of 0.06 % for C (in the range of not more than 0.8 %), 0.12 % for Mn (2.0 %), 0.09 % for Si (1.2 %), 0.13 % for Cr (1.0 %), 0.07 % for Ni (0.8 %) and 0.08 % for Cu (0.5 %).

The error values show the effectiveness of this approach applied to the calibration of the chemical composition of low-alloy steels using the LIBS method. Multivariate data analysis handles with latent variables hidden in matrix of spectral information. These non-physical variables reflect only essential information extracted from multicollinear broadband spectra. The classical one- or low-variate approach handles with spectral variables with clear physical

meaning. The classical and multivariate approaches are fundamentally different in terms of the use of spectral information. As numerous studies show (for example [6]), the best results can be obtained with a compromise approach with optimization of the spectrum range and selection of spectral variables. It can reduce the data redundancy and prevent the overestimation of multivariate models.

Three methods of spectral variables selection are used for improving the calibration accuracy: method of ranking spectral variables (RSV) by their correlation coefficient with the value of the calibrated parameter [7], a successive projection algorithm (SPA) [8] and an original modification of the method of searching combination moving windows for partial least squares model (scmwiPLS) [9].

In RSV method all spectral variables are ranked in order of decreasing correlation coefficient with the calibrated concentration. Then one spectral variable with minimal correlation is removed at each step and a multivariate model is developed using PLS with optimizing number of latent variables. The selected spectral variables are determined by the minimum value of RMSE in the test dataset. The use of RSV method is not effective in our case. RMSE have not changed for Cr and Cu, decreased by 0.02 % for C and Si and by 0.03 % for Mn and Ni. Figure 1 shows the dependence of the RMSE for calibration of C in the test dataset on the number of removed spectral variables for RSV and calibration for the best PLS+RSV model for the selected 757 spectral variables out of 3630.

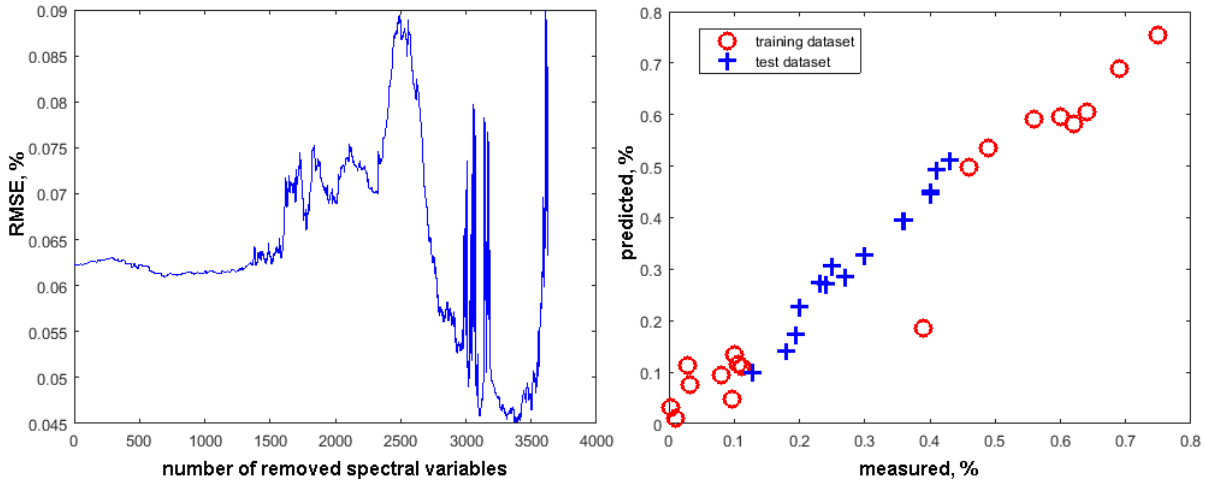



Fig. 1. RMSE for calibration of C vs number of removed spectral variables and the best calibration for PLS+RSV model

The first stage of SPA is to construct for each spectral variable an ordered sequence of the remaining variables in the order of maximum projection into the

space perpendicular to the space of the already selected variables. At the second stage PLS models are constructed using an increasing set of elements of each sequence with the choice of the optimal number of latent variables. At the third stage, the best multivariate model is determined by the minimum value of RMSE. The results showed that the RMSE of the PLS+SPA calibration models decreased compared to the PLS+RSV for Si (by 0.02 %), Mn, Cr and Cu (by 0.01 %), but increased for C (by 0.01 %). For Ni the RMSE value has not changed.

The scmwiPLS method does not operate with individual spectral variables, but with spectral intervals of a certain width – windows. The first stage of scmwiPLS determining the optimal number of *n* latent variables and developing the broadband multivariate PLS model is shown in Figure 2.

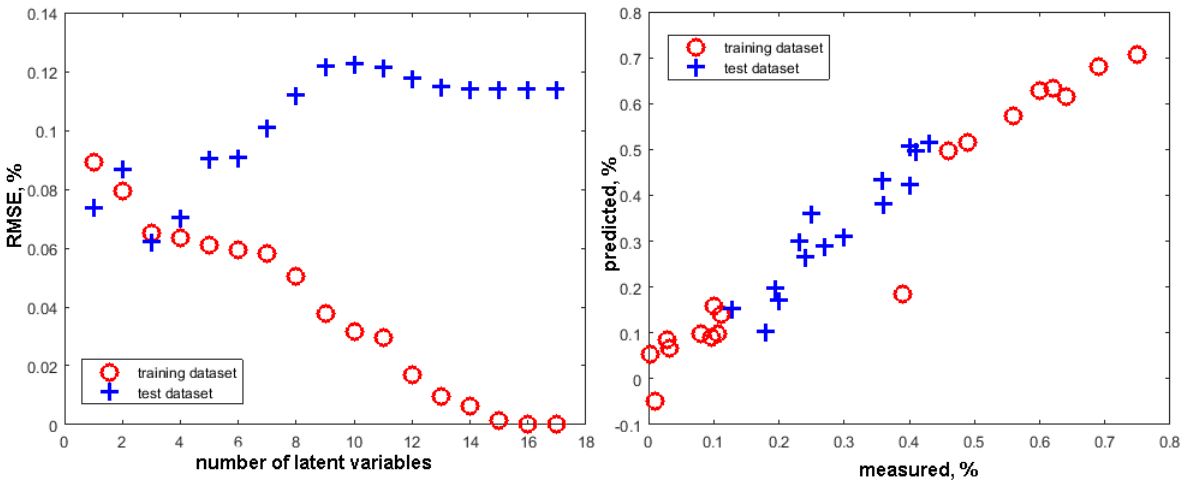



Fig. 2. RMSE for calibration of C vs number of latent variables and the best calibration for wideband PLS model

At the second stage, the width of spectral windows is fixed by *n*+1 spectral variables. This condition minimizes the width of the window while maintaining the possibility of selecting latent variables even in one window. Next, the first window is shifted by one spectral variable per step and a multivariate model is developed using the PLS method at each step. The optimal position of this window is determined by the minimum value of RMSE and fixed. The procedure is repeated with the second spectral window. In this case, the simulation is carried out by combining the spectral variables belonging to the fixed first window and moving second window. Each subsequent window adds *n*+1 spectral variable to the model until all measured variables are taken into account in the calibration. The third stage consists in choosing the scmwiPLS model with the minimum RMSE value depending on the number of windows and the spectral variables corresponding to this model. Figure 3 shows the dependence of the RMSE for calibration of C on the number of spectral

windows and calibration for the best scmwiPLS model for the selected 208 spectral variables out of 3630.

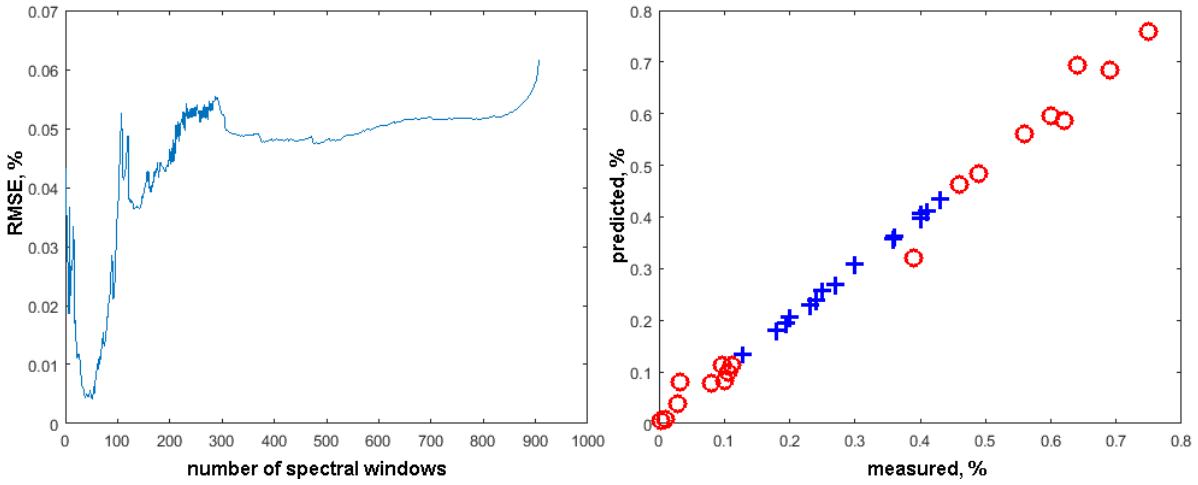



Fig. 3. RMSE for calibration of C vs number of spectral windows and the best calibration for scmwiPLS model

The scmwiPLS model is the best and quantitative for C (RMSE = 0,004 %, the residual prediction deviation (RPD) in the test dataset is 23,4 in the concentration range from 0,13 to 0,43 %), for Mn (0,04 % and 5,2 in the range of 0,47–1,15 %), for Si (0,003 % and 20,7 in the range of 0,15–0,33%), for Cr (0,04 % and 3,1 in the range of 0,09–0,43 %) and for Ni (0,01 % and 4,8 in the range of 0,05–0,25 %). Calibration model is considered quantitative if RPD exceeds 3. For Cu in the concentration range of 0,06–0,26 %, scmwiPLS model is qualitative only (RMSE = 0,04 % and RPD = 1,4).

It can be concluded that the use of scmwiPLS as the spectral variable selection method for LIBS data improves the quality of multivariate calibration models for concentrations of technological impurities and additives in low alloy steels.

## References

1. **Wang Z. [et al.].** Trends in Analytical Chemistry, 143 (2021) 116385-1–21.
2. **Zhang Y. [et al.].** Spectrochimica Acta Part B, 166 (2020) 105802-1–9.
3. **Belkov M. [et al].** Journal of Applied Spectroscopy, 88 (2021) 970–974.
4. **Kennard R.W., Stone L.A.** Technometrics, 11 1969. – V. 11. – P. 137–148.
5. **Geladi P., Kowalski B.** Analytica Chimica Acta, 186 (1986) l–17.
6. **Guezenoc J. [et al.].** Spectrochimica Acta Part B, 152 (2019) 6–13.
7. **Xiaobo Z. [et al.].** Analytica Chimica Acta, 667 (2010) 14–32.
8. **Soares S.F.C. [et al.].** Trends in Analytical Chemistry, 42 (2013) 84–98.
9. **Khodasevich M., Aseev V.** Optics and Spectroscopy, 124 (2018) 748–752.

# PLASMA-ASSISTED SYNTHESIS OF HYBRID AND DOPED SILICON-BASED NANOSTRUCTURES

N.N. Tarasenka[1], V.G. Kornev[1], A.A. Kuchmizhak[2]

[1] B.I. Stepanov Institute of Physics of National Academy of Sciences of Belarus, 220072 Belarus, Minsk, Nezalezhnasti Ave. 68-2
[2] Institute of Automation and Control Processes of FEB RAS, RUSSIA

Application of plasma- and laser induced processes for the synthesis of novel nanomaterials has recently become a hot topic in science and technology. The recent advances in this emerging field has resulted in the development of novel plasma excitation regimes and schemes that enable controllable formation of nanoparticles (NPs) of pre-determined size, structure and composition. Among these methods, plasma generation in liquids has multiple advantages for applications in nanotechnology, such as simplicity, scalability, environmental safety, operation under atmospheric pressure as well as non-equilibrium chemistry of the processes [1]. In liquids, plasma can be ignited using electrical breakdown or laser radiation, giving rise to several schemes of NPs generation, most widely used of them being electrical discharge in liquids, atmospheric pressure glow discharge in contact with liquid as well as laser ablation process. Further development of plasma-assisted formation of NPs is related to novel approaches towards the formation of composite and hybrid nanostructures, alloyed and hybrid NPs. In this work, several approaches based on laser ablation and electrical discharge in liquids were developed for the formation of hybrid and doped silicon-based NPs.

Si NPs are known to be biocompatible nanomaterials that exhibit size and surface tailorable optical properties. Due to their efficient light absorption in the UV and near-IR regions, Si NPs are promising for a row of applications, namely solar energy converters, optical materials, sensors and contrast agents, among others. The size and structure of these materials influence their optical, chemical and physical properties. Therefore, by combining Si nanostructures with plasmonic NPs or by their doping with Ge or Sn, the optical properties can be tuned thus playing an important role in their future-generation applications.

To prepare silicon NPs, several synthesis schemes based on laser ablation and electrical discharge in a liquid were proposed and implemented (Fig. 1). Silicon NPs with different particle sizes have different resonant absorption wavelengths in the range from the ultraviolet region to the near IR region; therefore, the influence of the main parameters of the laser-plasma NPs synthesis was studied and the optimal conditions were identified that make it possible to obtain NPs of the required size and structure, as well as having broadband absorption of radiation in the range from UV to IR. In a laser ablation

experiment, it has been found that laser focusing conditions are among the crucial parameters influencing the NPs size and morphology. The experiments were carried out by focusing the radiation of a fundamental harmonic of a Nd:YAG laser on a bulk Si target in ethanol with the following parameters: wavelength 1064 nm, repetition rate 10 Hz, pulse duration 10 ns, laser radiation power density on the target surface in the range $10^8$ -$10^9$ W/cm$^2$, ablated spot size 200 μm. The experiments were carried out in ethanol to reduce the effect of oxidation processes on the composition of NPs. As can be concluded from the comparison of TEM images in Fig. 1d and e, change of a target configuration that allowed a decrease of a liquid layer thickness above the Si target, results in an increase of the resulting NPs size. The results the NPs morphology studies prepared in two configurations: when the target is located vertically (a) and horizontally (b) are shown in Fig 1.

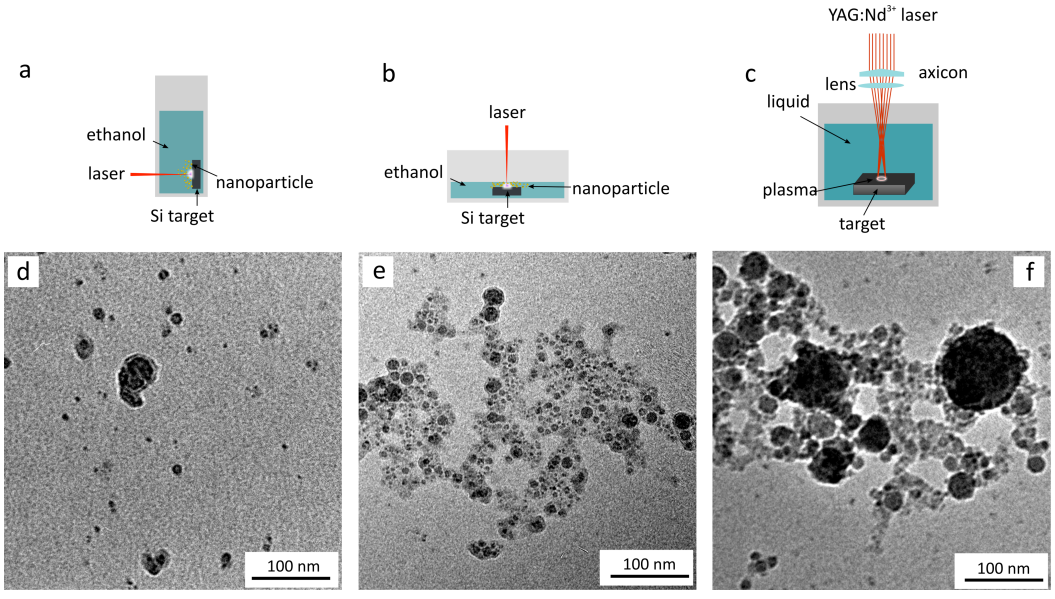



Fig. 1. Synthesis and morphology of silicon NPs prepared by laser ablation of Si target in ethanol: *a, b* and *c* show schematic images of the experimental configurations used for ablation. Figures *d, e* and *f* show the corresponding TEM images of NPs obtained using configurations *a, b* and *c*, respectively

When prepared in a scheme 1a, the particles formed during laser ablation in ethanol had an average size of 6 nm and a cubic crystal structure. Despite the particle size being mainly in the range of 1-10 nm, larger particles (30-40 nm) were also observed in the TEM images. In a scheme shown in Fig. 1b, with a liquid layer thickness above the target of 1–2 mm, the distribution of the resulting NPs becomes narrower, while the average size of the formed NPs increases up to 20–30 nm. This effect can be explained by the confinement of a

bubble propagation that changes the NPs formation conditions and therefore their structure and morphology [2].

The size of NPs can be further tuned by using the scheme presented in Fig. 1c, in which the laser radiation of the same Nd:YAG laser is focused into the annular beam by using an axicon. This approach allows formation of so-called plasma compression layer (stagnation layer) along its symmetry axis perpendicular to the target surface in which plasma propagation slows down in the collision plane, while its kinetic energy is converted into excitation energy [3]. As a result, a plasma jet is formed on the plasma propagation axis [4]. The resulting plasma expands both in the radial and axial directions resulting in the formation of an explosive wave with a non-spherically symmetric shock wave having a bubble shape on the axis. This approach enabled to increase the average size of the obtained NPs. As can be concluded from the Fig. 1f, which shows the TEM image of the NPs obtained by laser ablation of crystalline silicon in ethanol with an annular laser beam, the formed NPs have a spherical shape and a size in the range of 6–108 nm. In this case, the average particle size is 18.5 nm.

This approach was further extended towards synthesis of hybrid silicon NPs with plasmonic metal NPs. Due to variation of the optical properties that are dependent on the composition and morphology of the resulting nanocomposite, such nanostructures are promising for application in solar energy converters. In this case, metal NPs, having the increased absorption cross sections due to the excitation of localized surface plasmon resonances, contribute to the localization of heat around the NPs. To form the hybrid NPs, a sequential scheme was developed, that implemented preparation of Au and Ag NPs by laser ablation of corresponding targets in acetone, mixing of Ag and Au NPs colloids and subsequent laser ablation of Si target in this mixed colloid using annular profile. To increase the ablation efficiency, the radiation of the second harmonic of the YAG:$Nd^{3+}$ laser was used, which allowed increasing the absorption of radiation by the target. Using this approach, Si-Ag-Au NPs with a wide absorption spectrum from the UV to IR region were obtained, as can be concluded from Fig. 2.

The ablation of gold and silver targets in acetone resulted in the formation of NPs of the corresponding metals. This was evidenced by the observation of the plasmon absorption band at 423 nm, corresponding to silver NPs and at 520 nm, which is typical to gold NPs. In this case, the bands are quite wide, that may indicate a wide particle size distribution. After ablation of a silicon target in the mixture of Ag and Au colloids, the absorption increases in the region of 300–1000 nm, which may indicate the formation of Si–Ag–Au nanohybrids. The observed broadband absorption is promising for application in nanofluids for photothermal light conversion.

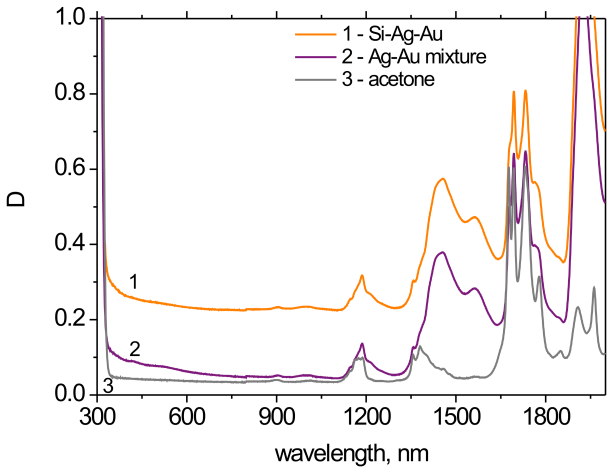



Fig. 2. Optical absorption spectra of a Ag-Au colloids mixture prepared by laser ablation in acetone (2), and a colloid synthesized by laser ablation of a pressed Si target using an annular laser beam (1) in this mixture. The absorption spectrum of acetone (3) is presented for comparison

In conclusion, it has been shown that laser-plasma methods can be applied for fabrication of silicon NPs as well as hybrid Si NPs decorated with metal NPs. Variation of focusing conditions and laser parameters allows selective tuning of the NPs size in the range 5-100 nm. A number of synthesis schemes have been proposed for fabrication of NPs of complex composition, such as Si-Cu, Si-Ag, Si-Ag-Au. An approach based on laser ablation using beam of annular profile allows obtaining Si-Ag-Au nanoparticles with a wide absorption spectrum in the region from UV to IR promising for the photothermal light converters.

**Acknowledgements.** This work was supported by the National Academy of Sciences of Belarus (project Convergence 2.2.05) and by BRFFR (grant number F21RM-105).

**References**

1. **Zhang D., Gökce B., Barcikowski S.** Chem. Rev. 117 (2017) 3990-4103.
2. **Choudhury K., Singh R.K., Kumar P., Ranjan M., Srivastava A., Kumar A.** Nano-Structures & Nano-Objects, 17 (2019) 129-137.
3. **Delaney B., Hayden P., Kelly T.J., Kennedy E.T., Costello J.T.** Spectrochimica Acta B: Atomic Spectroscopy, 193 (2022) 106430.
4. **Valenzuela-Villaseca V., Veloso F., Muñoz-Cordovez G., Favre M., Ruiz H., Wyndham E.** Journal of Physics: Conference Series, 1043 (2018) 012046.

# PLASMA FORMATION AT YTTRIUM VANADATE ($YVO_4$) TARGET EXPOSED TO TWO-PULSE BICHROMATIC LASER RADIATION IN THE AIR

**N.A. Bosak [1], A.N. Chumakov [1], A.A. Ivanov [1], V.V. Kiris [1], E.M. Dyatlova [2], A.A. Shevchenok [3], A.V. Buka [2]**

[1]B.I. Stepanov Institute of Physics, National Academy of Sciences of Belarus, 68-2 Nezavisimosti Ave., 220072, Minsk, Belarus; n.bosak@ifanbel.bas-net.by
[2] Belarusian State Technological University, 13-a Sverdlova str., 220006, Minsk, Belarus
[3] Belarusian State Agrarian Technical University, 99 Nezavisimosti Ave., 220023, Minsk, Belarus

**Introduction**. A high-frequency pulse-periodic laser action on metals in the air with a pulse repetition frequency of more than 5 kHz results in the effective formation of erosion plasma [1, 2]. The transition to a paired laser action at harmonics of an Nd:YAG laser expands the possibilities to control the processes of plasma formation and ablation of various materials [3]. The work is aimed at clarifying the features of plasma formation during irradiation of yttrium vanadate in air by the Nd:YAG laser harmonics, as the optical elements made of this material are widely used in laser technology.

**Experimental setup.** The installation is based on two Nd:YAG lasers generating at wavelengths of 1064 and 532 nm. The LTI-403 laser ($\lambda_1$ = 1064 nm, $E$ = 78 MJ, $\tau$ = 20 ns) showed almost the same values of the pulse duration and energy, as those of the LS-2130 laser ($\lambda_2$ = 532 nm, $E$ = 69 MJ, $\tau$ = 20 ns). The installation enabled a double-pulse impact of laser radiation on yttrium vanadate in the air with an adjustable time interval between laser pulses and a modified sequence order of the pulses with synchronous recording of the near-surface plasma spectra and the spread and glow of the plasma torch. The plasma spectra were recorded with a 7 ms exposure by an SDH – IV spectrometer with a linear CCD detector (TCD 1304 AP, Toshiba), linked to a computer and a synchronization unit of the laser system. The laser pulses and the plasma glow were recorded by a GwINSTEK digital oscilloscope (4 channels, 200 MHz bandwidth). The negative values of the time interval between laser pulses in the figures correspond to the primary action of the short–wave pulse ($\lambda$ = 532 nm), and the positive ones – to the secondary impact of the long-wave pulse ($\lambda$ = 1064 nm). The laser power densities in the experiments were $q_{532}$= $2.7 \cdot 10^9$ W/cm$^2$ and $q_{1064} \leq 3.1 \cdot 10^9$ W/cm$^2$ in the irradiation spot, $d_s \sim 0.4$ mm. The structure of the luminous area of the laser torch and its dependence on the time interval

between laser pulses were studied using a Nikon D3200 camera with a matrix photodetector.

**Experimental results and their analysis.** The conditions for laser irradiation of yttrium vanadate at two wavelengths significantly affect the structure of the emerging near-surface plasma torch (Figure 1, *a–b*). The structure of the plasma torch on the target depends not only on the time interval, but also on the sequence order of the laser pulses with wavelengths of 1064 and 532 nm. When the short-wave ($\lambda$ = 532 nm) radiation pulse is the primary one, a luminous torch with a gap and a bright core is observed near the target surface (Fig. 1, *a*). In the case of the primary action by the long-wave ($\lambda$ = 1064 nm) laser pulse, the continuous torch is observed (Fig. 1, c). Under the simultaneous exposure of the target to both pulses, the torch decreases in the length and a laser spark is ignited in the air (Fig. 1, *b*). The maximum length of the torch, $l_{max}$, reaches 8.6 mm at the time delay of $\Delta t$ = - 13 microseconds, and the minimum torch length, $l_{min}$ = 4.6 mm, is observed at the time delay, $\Delta t$ = 0 microseconds (Fig. 1, *d*).

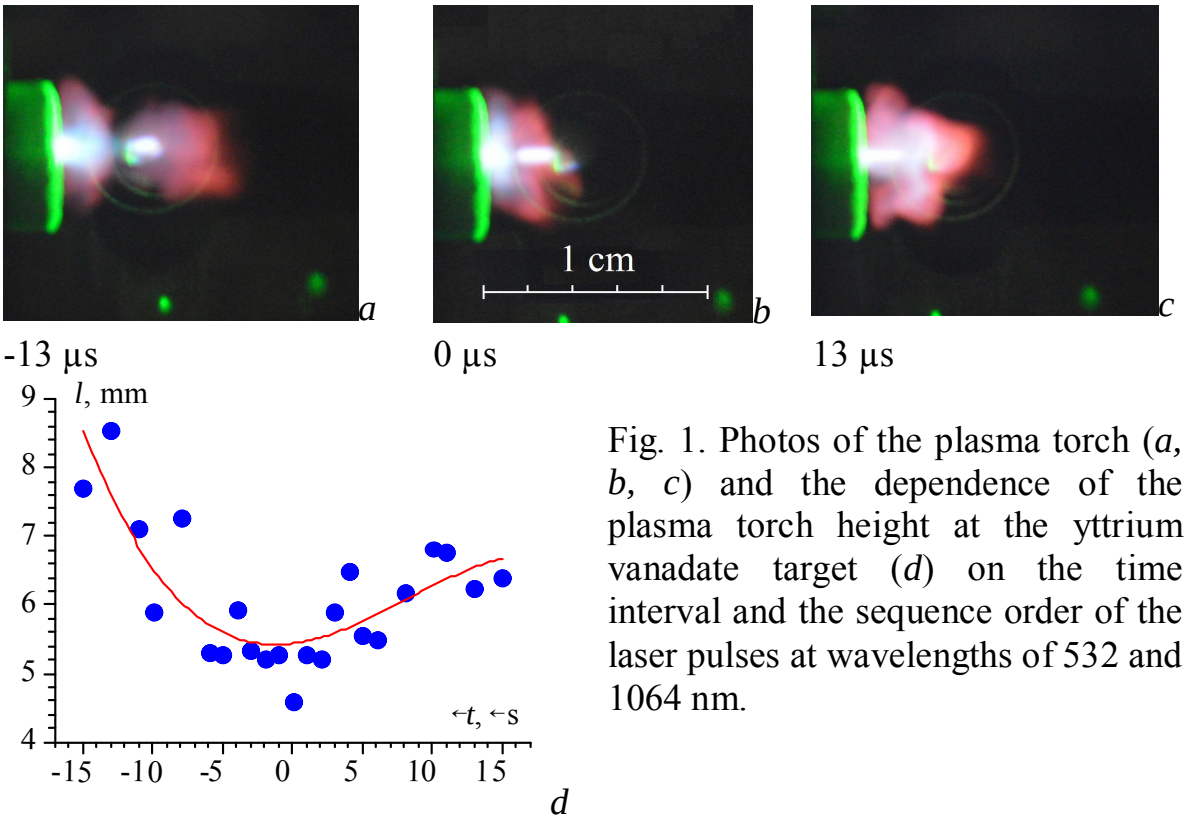



Fig. 1. Photos of the plasma torch (*a*, *b*, *c*) and the dependence of the plasma torch height at the yttrium vanadate target (*d*) on the time interval and the sequence order of the laser pulses at wavelengths of 532 and 1064 nm.

The glowing of the near-surface yttrium vanadate plasma was recorded using an FEU–114 photoelectron multiplier in the spectral region ($\lambda_{max}$ = 0.4 – 0.8 microns). Under a primary exposure by the short-wave laser pulse ($\Delta t$ = -13 µs), the plasma glow is more intense, than after the subsequent long-wave laser pulse action (Fig. 2, *a*). In the reversed sequence order of the pulses, the

most intense plasma glow is also observed under exposure of the target to the short-wave laser pulse. The duration of the decreasing plasma glow is ~ 100 microseconds, which is three orders of magnitude longer than the duration of laser pulses (~ 20 ns). The dependence of the integral plasma glow intensity on the time interval and the sequence order of laser pulses at wavelengths of 532 and 1064 nm is shown in Fig. 2, *b*, reaching its maximum and minimum values at $\Delta t$ = -1 microsecond and $\Delta t$ = 0 microseconds respectively.

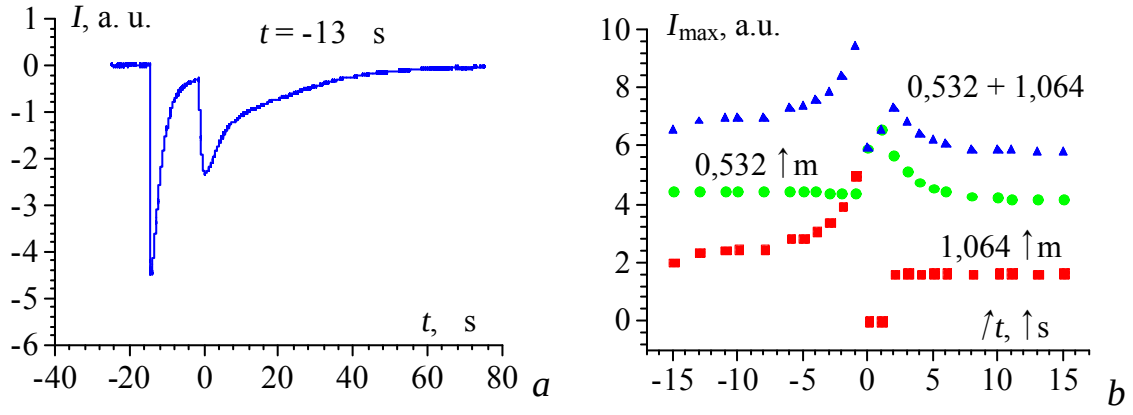



Fig. 2. Oscillograms of the of yttrium vanadate plasma glow at the time interval between laser pulses equal to -13 μs (*a*) and the dependence of the integral glow intensity of the plasma torch on both the time interval and the sequence order of the pulses of the resultant laser radiation at the wavelengths of 532 and 1064 nm (*b*).

The spectra of the near-surface yttrium vanadate laser plasma recorded at different time intervals between the laser pulses indicate a pronounced dependence of the resultant plasma composition on the sequence order of bichromatic laser pulses (Fig. 3, *a*, *b*). The plasma temperature was determined from the Boltzmann graph based on the yttrium ion lines (Y II 317.305 nm, Y II 324.228 nm, Y II 332.788 nm, Y II 336.198 nm) and using the values of transition probabilities, energy, and the degeneracy order of the upper levels for the corresponding transitions from the database [4]. The maximum of the yttrium vanadate plasma temperature (0.93 eV) is achieved when the primary and secondary pulses (at 1064 and 532 nm respectively) start with the pulse-to-pulse interval of $\Delta t$ = 6 microseconds (Fig. 3, *b*). Thus, the plasma parameters significantly depend on the sequence order and the time interval between laser pulses.

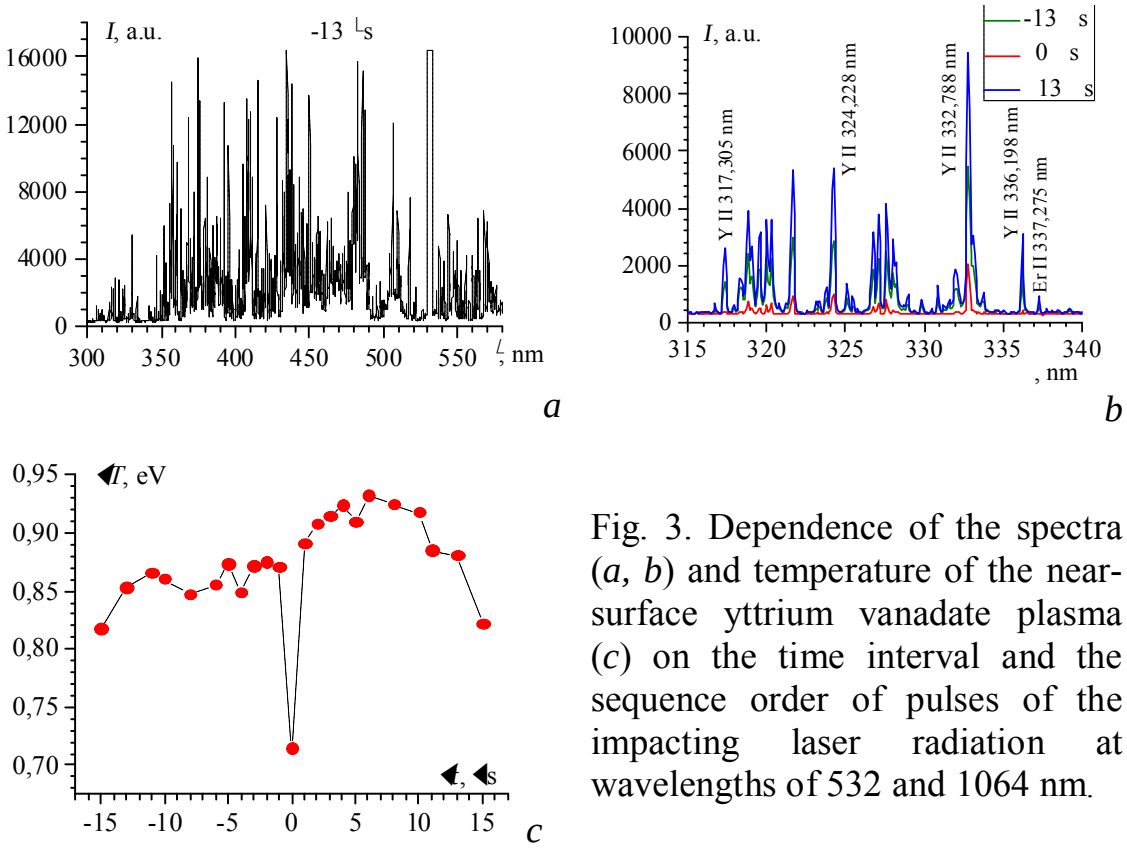



Fig. 3. Dependence of the spectra (*a*, *b*) and temperature of the near-surface yttrium vanadate plasma (*c*) on the time interval and the sequence order of pulses of the impacting laser radiation at wavelengths of 532 and 1064 nm.

**Conclusion.** The two-pulse laser exposure of yttrium vanadate in air at wavelengths of 532 and 1064 nm with a radiation power density of $q \sim 3 \cdot 10^9$ W/cm$^2$ results in the development of near-surface plasma formations, whose structure, composition, and parameters significantly depend on both the pulse-to-pulse time interval and the sequence order of the laser pulses. The maximum temperature reaches $\sim 1 \cdot 10^4$ K, and the glow time is recorded to be within ~ 100 microseconds.

The work was partially supported by the "Photonics and Electronics for Innovation"State Research Program, task 1.5.

**Literature**

1. **Minko L.Ya., Chumakov A.N., Bosak N.A.** // Quantum Electronics. 1990. Vol.17, No. 11, 1480-1484.

2. **Chumakov A.N., Avramenko V.B., Bosak N.A.** // Journal of Applied Spectroscopy. 2012, Vol.79, 287.–279

3. **Chumakov A.N., Bosak N.A., Panina A.V.** // Journal of Applied Spectroscopy. 2017. vol. 84, No. 4, 602.–595

4. https://lweb.cfa.harvard.edu/amp/ampdata/kurucz23/sekur.html

# DISTRIBUTION OF ELEMENTS IN HIGH-ENTROPY CoCrFeNi AND NbTaTiV ALLOYS IRRADIATED WITH LOW-ENERGY Kr IONS

V.V. Uglov[1], N.A. Stepanjuk[1], I.V. Safronov[1], S.V. Zlotski[1], I.A. Ivanov[2,3], A.E. Ryskulov[2], A.E. Kurakhmedov[2], A.L. Kozlovskiy[2,3], M.V. Zdorovets[2,3], K. Jin[4]

[1]Belarusian State University, 4 Nezavisimosty ave., 220030 Minsk, Belarus
[2]Institute of Nuclear Physics, Abylai Khan str., 2/1, 010008 Nur-Sultan, Kazakhstan
[3]L.N. Gumilyov Eurasian National University, Satpayev Str., 2, 010008 Nur-Sultan, Kazakhstan
[4]Beijing Institute of Technology, 5 South Street, Zhongguancun, Haidian District, 100081 Beijing, China

Modern challenges in the fields of nuclear energy are concentrated greatly across the increment of power and efficiency of nuclear facilities by increasing their working temperatures [1–3]. Classical materials, such as steels (including austenitic), nickel and other metal alloys with a binary base, are facing phase transformations and significant degradation of physical and mechanical properties at elevated temperatures, corroding when in contact with liquid coolants and some gases, and swelling under high doses of neutron irradiation [2–3].

One of the most perspective classes of materials for the aims named upper can be high-entropy alloys (HEAs) [1–7]. The vanguard works on the theme of high-entropy alloys belong to Senkov and Kantor [8, 9]. HEAs mostly form single-phased either FCC (transitive 3d-metals) or BCC (refractory metals) distorted crystal lattice with disordered element location, which is the reason of their elevated thermal stability, corrosion and radiation resistance [10].

The cuboid samples with linear dimensions of 5×5×1.5 mm for CoCrFeNi and 6×6×1 mm for NbTaTiV were prepared in Beijing Institute of Technology by arc melting in argon atmosphere from high-purity (>99,97%) constituent metal powders. After casting into copper mould ingots were annealed at 1150 °C for 24 h, cold-rolled till 85% thickness reduction and again annealed at 1150 °C for 72 h. The samples were irradiated in Astana Branch of Institute of Nuclear Physics Institute on DC-60 heavy ion accelerator with $Kr^{14+}$ ions, energy 280 keV, fluence $5\times10^{15}$ $cm^{-2}$. Heavy ion Rutherford backscattering (HIRBS) experiment was performed on the same installation using $^{14}N^{2+}$ ions with energy of 14 MeV.

The HIRBS spectra of non-irradiated and krypton ion irradiated HEAs samples are performed on Fig. 1-2. They show, that in non-irradiated samples of CoCrFeNi and NbTaTiV HEAs takes place relatively uniform elemental depth composition, the results of mathematical simulation are shown on Table 1.

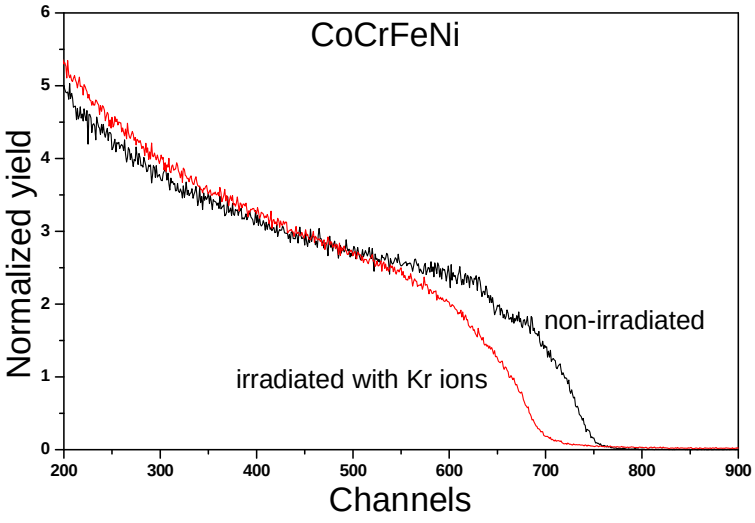



Fig. 1. HIRBS spectra of non-irradiated and irradiated with Kr14, 40 keV CoCrFeNi HEAs

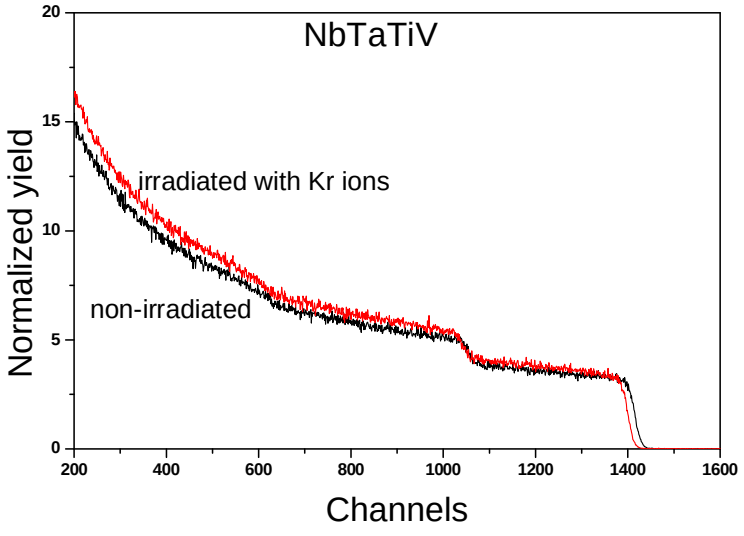



Fig. 2. HIRBS spectra of non-irradiated and irradiated with Kr14, 40 keV NbTaTiV HEAs

In case of NbTaTiV irradiation caused no significant changes in HIRBS spectrum profile. But in CoCrFeNi alloy irradiation with crypton led to rearranging of elements with depth. The plot of elemental composition, obtained from simulation results, is introduced on Fig. 3.

Table 1. Elemental composition of non-irradiated CoCrFeNi and NbTaTiV HEAs samples (HIRBS)

| Composition, at. % | Co | Cr | Fe | Ni | Nb | Ta | Ti | V |
|---|---|---|---|---|---|---|---|---|
| CoCrFeNi | 28,9 | 26,0 | 26,2 | 17,9 | - | - | - | - |
| NbTaTiV | - | - | - | - | 30,0 | 30,0 | 20,4 | 19,6 |

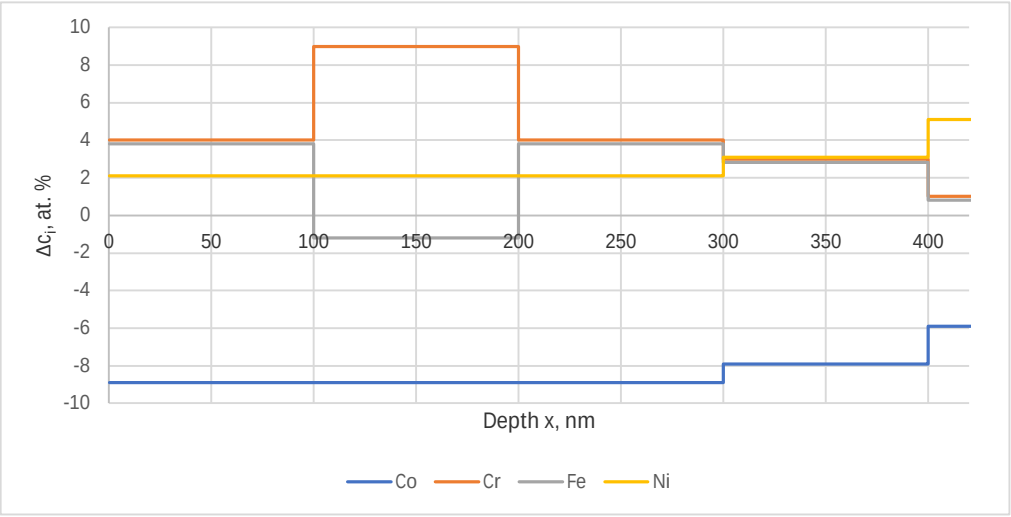



Fig. 3. Depth profile of elements of CoCrFeNi HEA after Kr irradiation

As seen on Fig. 3, irradiation led to decrease of Co concentration on nearly 9 at. % till the depth of 300 nm. All the other element concentration increased. In Cr distribution there is a + 9 at. % maximum on the depth from 100 nm till 200 nm, which fully correlates with -1 at. % minimum of Fe concentration.

Correlative plot of damage dose and implanted Kr concentration, calculated from SRIM data, and dislocation density depth distribution, calculated from XRD spectra with Williamson-Hall uniform deformation model, are represented on Fig. 4. Evidently, takes place some kind of irradiation defect annealing and crystalline size increase in the region near the maximum implanted Kr, where usually situated maximal amount of voids and bubbles. Dislocation density there is decreased on $8\times10^{12}$ $cm^{-2}$ compared with non-irradiated sample. Maximum of

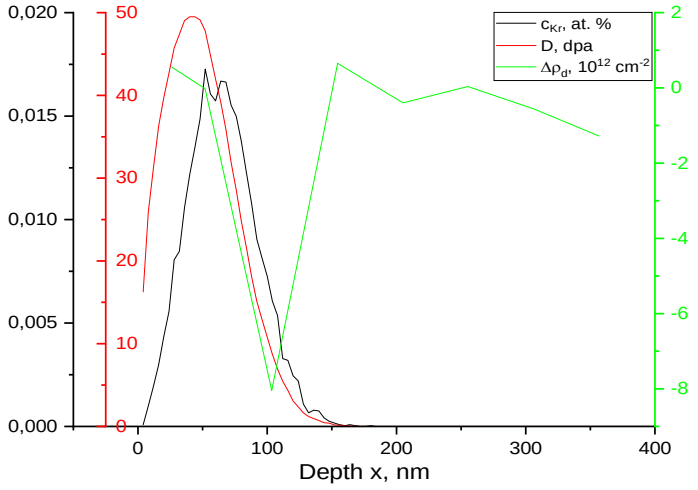



Fig. 4. Depth profile of concentration of implanted Kr, damage dose and dislocation density change after Kr irradiation of CoCrFeNi HEA

chromium and minimum of iron distribution occurs in the region behind the minimum of dislocation density change, which can be the consequence of radiation-induced diffusion and movement of crystalline borders.

Element composition in irradiated region of CoCrFeNi shows redistribution with cobalt depletion and enrichment of chromium and nickel. Iron is depleted mainly in region of dislocation density minimum, where chromium is mostly enriched by irradiation defect annealing. But in NbTaTiV there is no redistribution observed, which tells about better irradiation induced diffusion suppression in BCC-latticed HEA. Probable reason for such behavior can be lack of crystal lattice symmetry in BCC lattice in comparison with FCC lattice and greater atomic radii of Nb and Ta, providing greater crystal lattice distortion of NbTaTiV compared with CoCrFeNi. All these results lead to the hypothesis of better irradiation phase and structural stability of BCC HEAs upon FCC ones in case of ion irradiation with low implanted Kr concentration and higher damage doses, while free vacancies and voids prevail on gas-vacancy complexes and gas bubbles.

**Acknowledgements**. This work was financially supported by State Program of scientific research “Energy and nuclear processes and technologies” (2.1.03.2) and Ministry of Education and Science of the Republic of Kazakhstan Science Committee (grant No. AP14872199).

**References**

1. **Y. F. Ye, Q. Wang, J. Lu, C. T. Liu, Y. Yang** Progress in Materials Science, Materials Today, (2015) 1 – 14.
2. **A. M. Manzoni, U. Glatzel** Encyclopedia of Materials: Metals and Alloys, (2020).
3. **W. Li, D. Xie, D. Li, Y. Zhang, Y. Gao, P.K. Liaw.** Progress in Materials Science, 118 (2021) 100777.
4. **S. Son, S. Kim, J. Kwak, G.H. Gu, D.S. Hwang, Y.T. Kim, H.S. Kim** Materials Letters, 300 (2021) 130130.
5. **P. F. Yu, L. J. Zhang, H. Cheng, H. Zhang, M. Z. Ma, Y.C. Li, G. Li, P.K. Liaw, R.P. Liu** Intermetallics, 70 (2016) 82 – 87.
6. **N.E. Koval, J.I. Juaristi, R.D. Muiño, M. Alducin** Journal of Applied Physics, 127 (2020) 145102.
7. **Y. Zhang, T.T. Zuo, Z. Tang, M.C. Gao, K.A. Dahmen, P.K. Liaw, Z.P. Lu** Progress in Materials Science 6 (2014) 1 – 93.
8. **B. Cantor, I.T.H. Chang, P. Knight, A.J.B. Vincent** Materials Science Eng., 375 (2004) 213-218
9. **O.N. Senkov, J.M. Scott, S.V. Senkova, D.B. Miracle, C.F. Woodward** Journal of Alloys and Compounds, 509 (2011) 6043–6048.
10. **A.S. Rogachev** Metal physics and metal science, 121 (2020) 807 – 841 (in Russian).

# MICROSTRUCTURE AND PHASE STATE OF SILICON CARBIDE IRRADIATED WITH HELIUM IONS

V.V. Uglov[1,*], V.M. Kholad[1,**], P.S. Grinchuk[2], M.V. Kiyashko[2], I.A. Ivanov[3,4], A. L. Kozlovskiy[4], M.V. Zdorovets[3,4]

[1]Belarusian State University, Minsk, Belarus
[2]Institute of Heat and Mass Transfer. Lykov NAS RB, Minsk, Belarus
[3]L.N. Gumilyov Eurasian National University, Nur-sultan, Kazakhstan
[4]Institute of Nuclear Physics, Nur-sultan, Kazakhstan
*Uglov@bsu.by
**valentinakholad@mail.ru

Silicon carbide (SiC) is an important semiconductor material of potential applications for electronic device fabrication and for structural components in fusion energy systems. A fundamental understanding of the accumulation and recovery of irradiation damage in SiC is needed to advance technological applications [1].

The samples were prepared at the Lykov Institute of Heat and Mass Transfer by binding two fractions of SiC powders M5 and M50 (grain size 5 microns and 50 microns, respectively) using a thermoplastic binder based on paraffin P-2 and subsequent silicification at a temperature of 1800° with and a pressure of 0.13 Pa [2].

The samples were irradiated with He ions with an energy of 40 keV at RT at the DC-60 linear heavy ion accelerator (Institute of Nuclear Physics, Nur-Sultan, Kazakhstan). Irradiations with helium ions were carried out with fluences $1\times10^{14}$, $1\times10^{15}$, $1\times10^{16}$, $5\times10^{16}$ and $2\times10^{17}$ $sm^{-2}$.

The structural and phase state of the initial and irradiated silicon carbide samples was studied by X-ray diffraction analysis (XRD), atomic force microscopy (AFM) and scanning electron microscopy (SEM).

The calculation of energy losses was carried out in the SRIM 2013 program. The concentration and dpa for each dose were calculated and their maximum are listed in Table 1. The maximum concentration of helium ions is reached at a depth of 348 nm. As can be seen from Figure 1, the highest energy losses of helium ions occur in a layer about 60 nm thick.

Table 1. SRIM simulation results

| Dose, $cm^{-2}$ | $1\times10^{14}$ | $1\times10^{15}$ | $1\times10^{16}$ | $5\times10^{16}$ | $2\times10^{17}$ |
|---|---|---|---|---|---|
| He, at. % | 0.009 | 0.09 | 0.9 | 5 | 18 |
| dpa | 0.006 | 0.06 | 0.6 | 3 | 12 |

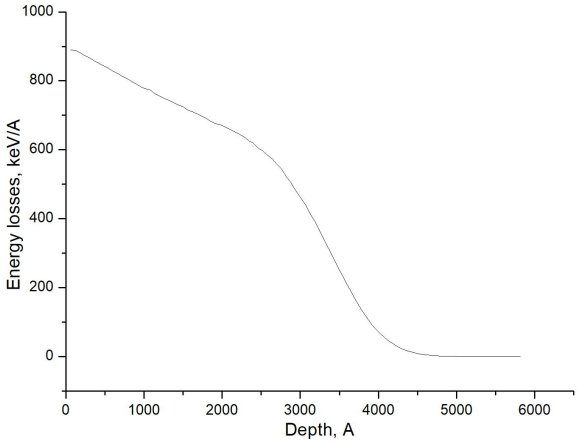



Fig. 1. Energy loses of He ions in SiC samples.

The results of studies of the phase composition showed that the initial samples are a multiphase system: SiC-6H – hexagonal (P63mc) syngony, Si – cubic (Fd-3m) syngony, SiC-15R – trigonal (R3m) syngony, as can be seen from Figure 2. The main phase is SiC-6H (about 80%), the content of the SiC-15R phase is about 20%, Si is less than 5%.

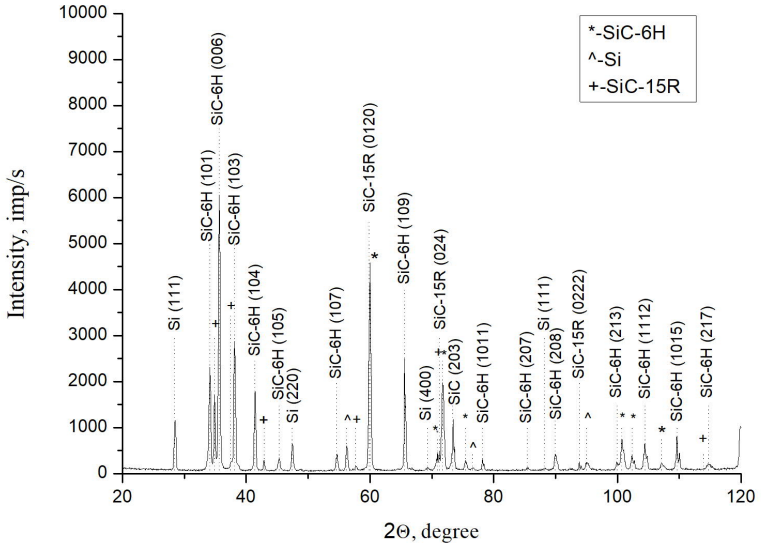



Fig. 2. X-ray diffraction pattern of the initial SiC sample.

Figure 3 shows the dependence of the relative change of the lattice parameter *a* and *c* on the dose. These graphs can be divided into 3 parts. The first part is up to the dose of $1\times10^{16}$ $cm^{-2}$. This site is characterized by the accumulation of helium and defects (interstitial atoms and vacancies), as well as their clustering [3]. The relative change in both parameters in absolute value increases, the difference is in the stresses: compressive stresses in the direction

of parameter *a* and tensile stresses in the direction of parameter *c*. The next part is the dose of $1\times10^{16}$ $cm^{-2}$. In this area, there is a drop in residual strain. This is due to the fact that helium bubbles are formed, which are sinks for defects [4]. Consequently, for both parameters, the relative change drops sharply. And in the third section ($5\times10^{16}$ - $2\times10^{17}$ $cm^{-2}$), deformation increases again. This is due to the growth of bubbles and, consequently, an rise in stresses. It should also be noted an increase in the lattice parameter *a* and a decrease in *c*. Such a change in the crystal lattice occurs as a consequence of irradiation growth. This irradiation effect is characteristic of HCP metals, especially zirconium [5].

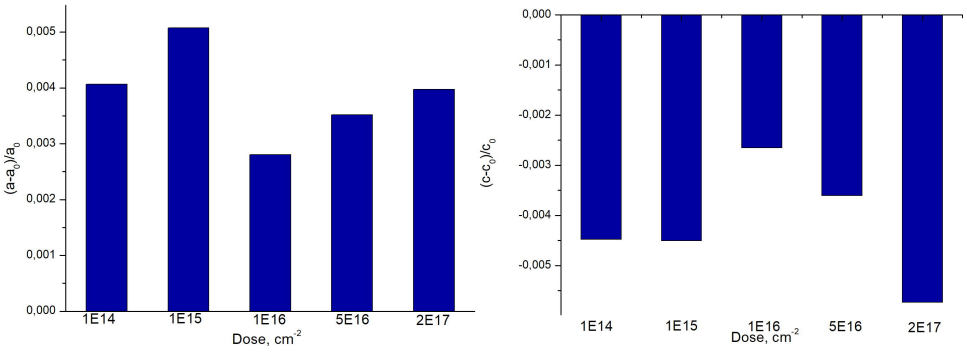



Fig.3. Dependence of relative change of lattice parameters *a* (a) and *c* (b) of 6H-SiC on the radiation dose of SiC samples irradiated with He ions.

Based on the results of AFM, it can be concluded that the roughness increases with increasing dose (fig. 4), which is also confirmed by literature [6]. Also, results demonstrate that implantation with He ion produces bubbles and swelling on the surface at higher doses.

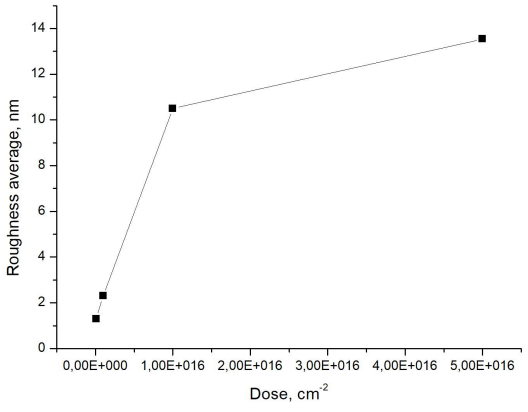



Fig. 4. Atomic force microscopy roughness graph.

Figure 4 shows the SEM images of the initial and irradiated samples. On the initial sample, the elemental contrast makes it possible to identify grains of silicon carbide, and silicon between them (which is related to the technology of

sample preparation). At a dose of $1\times10^{15}$ $cm^{-2}$, a grain structure is observed, but with a further increase in the dose, the amorphization of the near-surface layer occurs, what is confirmed by the literature [7].

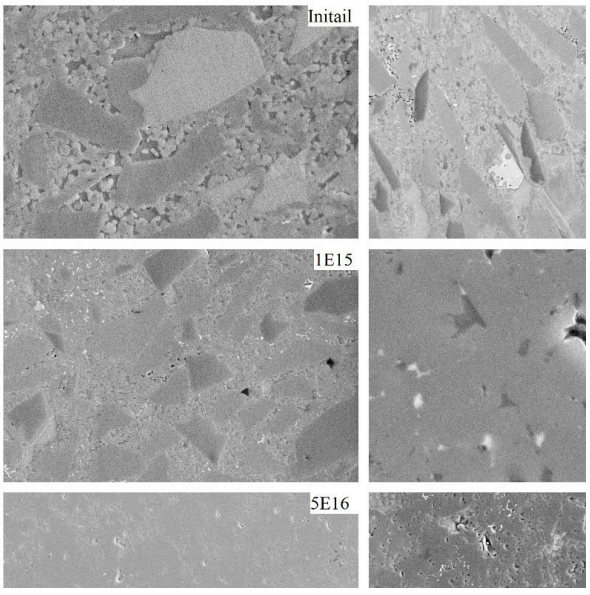



Fig. 5. Results of scanning electron microscopy.

Thus, when SiC is irradiated with helium ions with energy 40 keV, an increase in deformation is observed, but at a dose of $1\times10^{16}$ $cm^{-2}$, stress relaxation occurs, due to which the deformation decreases. The roughness also increases and the near-surface layer is amorphized.

## References

1. **W. Jiang, S. Thevuthasan, W.J. Weber, R. Grötzschel.** Nuclear Instruments and Methods in Physics Research B, 161-163 (2000) 501-504
2. **P.S. Grinchuk, M.V. Kiyashko, H.M. Abuhimd et al**, Journal of the European Ceramic Society, 38 (2018) 4815-4823.
3. **B.S. Li, Y.Y. Du, Z.G. Wanga**, Nuclear Instruments and Methods in Physics Research B, 345 (2015) 53-57.
4. **A. Debelle, J.P. Crocombette, A. Boulle, A. Chartier, T. Jourdan, S. Pellegrino, D. Bachiller-Perea, D. Carpentier, J. Channagiri, T.H. Nguyen, et al**, Physical review materials, 2 (2018) 013604.
5. **Li Yang, Ghoniem Nasr**, Journal of Nuclear Materials, 540 (2020) 152312.
6. **A. Ashraf Ali, J. Kumar, V. Ramakrishnan, K. Asokan,** Materials Letters, 213 (2018) 208-210.
7. **N. Daghbouj, B.S. Li, M. Callisti, H.S. Sen, M. Karlik, T. Polcar**. Acta Materialia. 181 (2019) 160-172.

# EFFECT OF IRRADIATION WITH KRYPTON IONS ON THE STRUCTURAL-PHASE STATE OF A MULTICOMPONENT SOLID SOLUTION BASED ON V-Nb-Ta-Ti

V.V. Uglov[1], M.M. Belov[1], S.V. Zlotsky[1], I.A. Ivanov[2], A.E. Ryskulov[2], A.E. Kurakhmedov[2], A.L. Kozlovskiy[2,3], M.V. Zdorovets[2,3], K. Jin[4]

[1]Belarusian State University, 4 Nezavisimosty ave., 220030 Minsk, Belarus, Uglov@bsu.by
[2]Institute of Nuclear Physics, Abylai Khan str., 2/1, 010008 Nur-Sultan, Kazakhstan
[3]L.N. Gumilyov Eurasian National University, Satpayev Str., 2, 010008 Nur-Sultan, Kazakhstan
[4]Beijing Institute of Technology, 5 South Street, Zhongguancun, Haidian District, 100081 Beijing, China

The development of nuclear power in the world places increased demands on the structural materials used, their production technology and performance control. Under the influence of irradiation, these materials undergo structural-phase transformations, which have a negative effect primarily on mechanical properties. High-entropy alloys (HEA) based on a single-phase solid solution and a large number (more than five) of basic elements in equimolar or almost equimolar ratios are promising for obtaining radiation-resistant materials for nuclear power. It is believed that the maximization of the configuration entropy of the HEA contributes to the formation of a single-phase disordered solid solution instead of the precipitation of complex intermetallic or second phases, as a result of which the alloy has a simple microstructure with improved properties compared to traditional alloys [1-3]. Numerous studies have shown that wind turbines have high elastic limit, fatigue strength, thermal and corrosion resistance, creep resistance, radiation resistance. The properties of these alloys are associated with four main effects: high entropy, large lattice deformation, multi-element composition and delayed diffusion [4-6].

Multi-component solid solutions based on V-Nb-Ta-Ti, specifically V, VNb, VNbTa, VNbTaTi were manufactured at the Beijing Technological University. Samples were synthesized using high purity metals (>99.9%) by arc melting and casting in a copper cell, followed by homogenization. Then vacuum annealing was carried out for 24 hours and 72 hours at a temperature of 1150°C with cold rolling up to 85% reduction in thickness.

The samples were irradiated at a DC-60 heavy ion accelerator located in Nur-Sultan, Kazakhstan. Low-energy $Kr^{14+}$ ions with an energy of 40 keV were chosen as the type of irradiation. The irradiation fluence was $5\times10^{15}$ $cm^{-2}$.

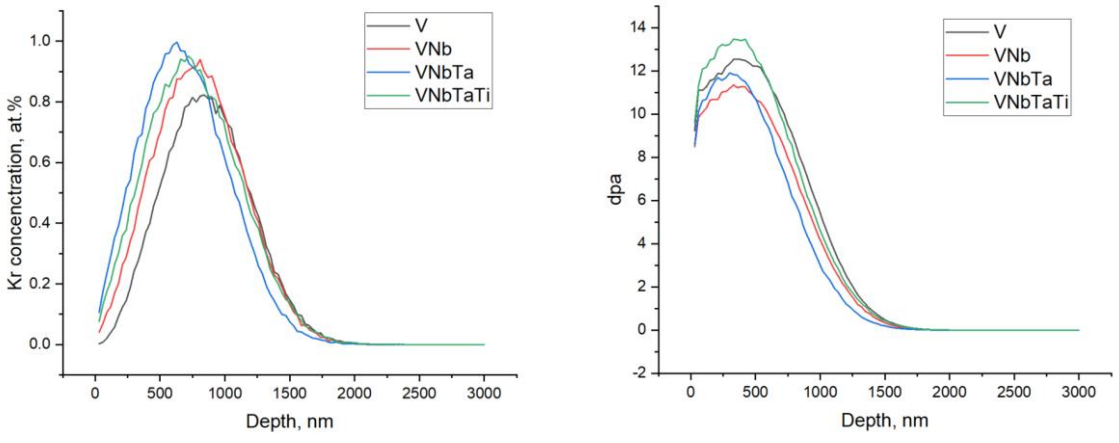
The effect of irradiation on the spatial distribution of elements were carried out by Rutherford backscattering spectroscopy (RBS) and energy-dispersive X-ray analysis (EDX).

The table shows the results of the elemental composition analysis calculated by the EDX and PIXE methods. The equiatomic and homogeneous distribution of elements over the surface was confirmed by the EDX method, and the equiatomic and homogeneous distribution of elements over the depth was confirmed by the PIXE method.

Table 1. Results of the elemental composition in the initial samples of the V-Nb-Ta-Ti system

| Sample | PIXE | | EDX | |
|---|---|---|---|---|
| | Концентрация, ат.% | | | |
| V | V | 100 | V | 100 |
| VNb | V | 50 | V | 49.5 |
| | Nb | 50 | Nb | 50.5 |
| VNbTa | V | 32.0 | V | 33.9 |
| | Nb | 33.0 | Nb | 34.2 |
| | Ta | 35.0 | Ta | 31.9 |
| VNbTaTi | V | 24.5 | V | 23.6 |
| | Nb | 25.5 | Nb | 26.1 |
| | Ta | 26.0 | Ta | 25.9 |
| | Ti | 24.0 | Ti | 24.5 |

The calculation of energy losses was carried out in the SRIM 2013 program using the Kinchin-Pease model [7]. Fig. 1 shows the distribution profiles of implanted $Kr^{14+}$ ions and the results of modeling radiation damage (measured in displacement per atom, dpa). The maximum range of krypton ions was 1800 nm with maximum damage for vanadium at a depth of 160-170 nm, and for VNbTaTi alloy – 120-140 nm. The highest value of the damaging dose is 3.5–6.5 dpa, depending on the samples. The concentration of implanted $He^{2+}$ ions does not exceed 23%.




a b

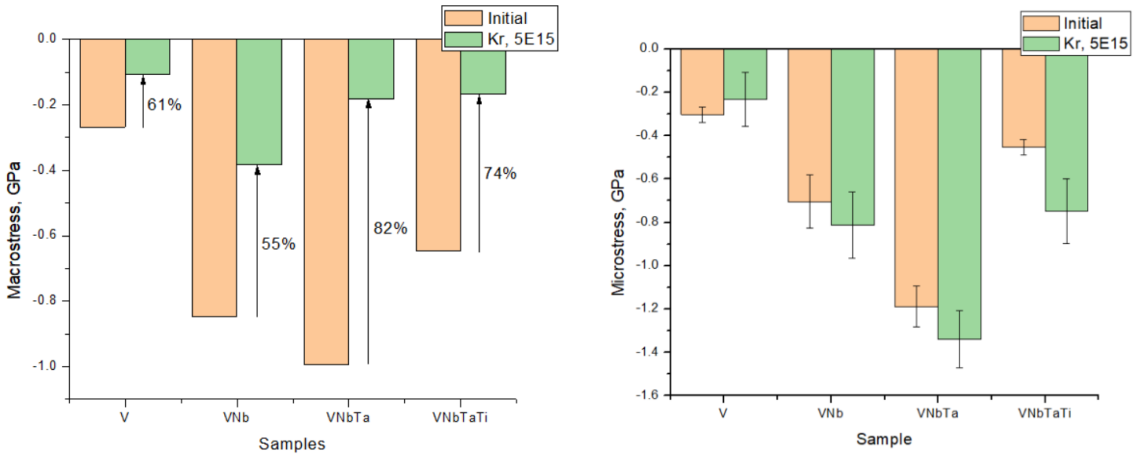
Fig. 1 Profiles of the distribution of implanted $Kr^{14+}$ ion (a) and the damaging dose (b) in samples V, VNb, VNbTa, VNbTaTi by depth

Irradiation does not lead to a significant violation of the equiatomic elements, as evidenced by the results of EDX and PIXE. According to the results of RBS, krypton is observed only in pure vanadium and both its concentration and depth of occurrence coincide with the results of SRIM. Krypton was not detected on the other alloys, possibly due to the low concentration and close atomic numbers of krypton and neobium.

Table 2. Results of the elemental composition in irradiated samples of the V-Nb-Ta-Ti system

| Sample | PIXE | | EDX | |
|---|---|---|---|---|
| | Concentration, ат.% | | | |
| V | 25 нм | V - 100 | V | 100 |
| | 90 нм | V – 99.2 | | |
| | | Kr - 0.8 | | |
| VNb | V | 50 | V | 49.7 |
| | Nb | 50 | Nb | 50.3 |
| VNbTa | V | 29.0 | V | 36.3 |
| | Nb | 35.0 | Nb | 31.2 |
| | Ta | 36.0 | Ta | 32.6 |
| VNbTaTi | V | 21.0 | V | 25.2 |
| | Nb | 29.0 | Nb | 25.4 |
| | Ta | 29.0 | Ta | 24.3 |
| | Ti | 21.0 | Ti | 25.1 |

To quantify the effect of radiation damage on the structure of samples, changes in micro- and macro-stresses relative to non-irradiated samples were calculated.




a b

Fig. 2 Values of macrostress (a) and microstresses depending on the complexity of the composition of the V-Nb-Ta-Ti system for the initial and irradiated samples (b)

There is a decrease in macro stresses as a result of irradiation, which can be

explained by several reasons. Irradiation leads to the formation of a large number of radiation vacancies, which cause the growth of tensile stresses and, possibly, for more complex systems, a decrease is observed due to the saturation of existing dislocations with interstitial atoms. Another reason may be thermal annealing, as a result of which most of the previously existing defects recombine. In contrast, an increase in compressive stresses is observed in microstresses, which may be due to radiation-stimulated diffusion of lighter elements to the boundaries of the coherent scattering region. However, it is not possible to assess which of the elements is more stable at the moment. It is also hard to say with certainty that there is a dependence of stresses on the complexity of the composition.

Irradiation with krypton ions leads to the formation of tensile stresses of the first kind, which may be associated with the formation of a large number of radiation vacancies and saturation of dislocations. There is an increase in microstresses in multicomponent solid solutions, which may be due to the radiation-stimulated diffusion of lighter elements to the boundaries of the coherent scattering region, which leads to an increase in microstresses due to the dimensional factor.

**Acknowledgements**. This work was supported by the Ministry of education of the Republic of Belarus

## References

1. **J.W. Yeh, Y.L. Chen, S.J. Lin, S.K. Chen** Mater. Sci. Forum., 560 (2007) 1–9.
2. **M.-H. Tsai, J.-W. Yeh** Mater. Res. Lett., 2 (2014) 107-123.
3. **Y. Jien-Wei** Ann. Chim. Sci. Mat., 31 (2006) 633-648
4. **D.B. Miracle, O.N. Senkov** Acta Materialia, 122 (2017) 448-511
5. **N. Sellami, A. Debelle, M.W. Ullah et. al.** Curr. Opin. Solid State Mater. Sci., 23 (2019) 107-115
6. **K. Jin, S. Mu, K. An et. al.** Mater. Des., 117 (2017) 185-192
7. **www.srim.org**

# BK-110 GLASS DESTRUCTION UNDER COMBINED LASER IRADIATION AT WAVELENGTHS OF 355 AND 532 NM

A.N. Chumakov, V.V. Lychkousky

Institute of Physics of the National Academy of Sciences of Belarus, Minsk, Nezavisimosti Ave., 68-2; e-mail: a.chumakov@dragon.bas-net.by

**Abstract.** The destruction of BK-110 glass in air under action of single and paired nanosecond pulses of laser radiation with wavelengths of 355 and 532 nm using optical microscopy and photo recording of plasma' plume glow has been experimentally investigated. The influence of time interval between the double pulses of bichromatic laser radiation and their sequence order on the nature of glass destruction and the dynamics of near-surface plasma is established.

## 1. Introduction

Investigation of laser destruction of transparent materials started with appearance of Q-switched lasers [1]. An opinion was formed that in area of "long" (nanoseconds) laser pulses take place variety of destruction caused by absorbing inhomogeneities, while in area of "short" (femtoseconds) pulses it's caused by electron impact or multiphoton ionization [1, 2]. Further detailed investigation has shown that formation of cracks using longer laser pulses caused by thermoelastic stresses of material and is not dependent on the mechanism of absorption, while irradiation by shorter laser pulses, damage to solid body can be caused by ablation or formation of defects without appearance of a crack [3]. Current work is dedicated to features of destruction of optical glass using single and paired nanosecond laser pulses with wavelengths 355 and 532 nm.

## 2. Experimental setup

The experimental setup is created based on two Nd:YAG lasers and synchronization system. It allows to generate paired nanosecond pulses of laser radiation (LR) with wavelengths 355 and 532 nm, time duration 18 and 15 ns respectively, that follow in controlled order and time interval [4]. The focus depth of both beams was ~3 mm. As a target was used 3 mm thick disk of BK-110 glass, majority of which (~75%) consist of $SiO_2$.

For studying of bichromatic irradiation spot diameters were 300 μm for λ=355 nm and 260 μm for λ=532 nm. Laser induced plasma plume near the sample surface registered with CCD camera [5] based on ICX415AL matrix. Exposure of single frame was ~3 ms. For case of combined bichromatic

irradiation, camera was synchronized with second pulse of pair. Emission spectra of surface laser plasma were registered by SL-40-2 spectrometer (exposure time ≈ 7ms) with multielement photoreceiver based on diode array TCD 1304 (Toshiba).

## 3. Results and discussion

Irradiation of BK-110 glass disk in air with 10 pulses of monochromatic LR with wavelengths of 355 and 532 nm, intensities range $q_{355}$ from 0.1 to 2.7 GW/cm$^2$ and $q_{532}$ from 0.32 to 0.94 GW/cm$^2$ leads to differences in material destruction in irradiated area observed on Fig. 1.

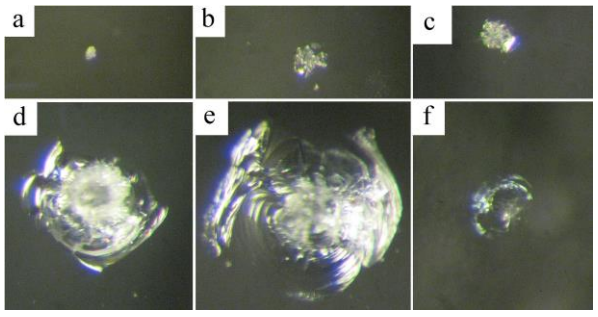



Fig. 1. Photos of craters, formed due to laser irradiation on BK-110 glass in air by LR 355 nm (intensity on sample's surface $q_{355}$ = 0.1 (a); 1.0 (b) and 2.7 (c) GW/cm$^2$) and 532 nm ($q_{532}$ = 0.32 (d); 0.79 (e) and 0.94 GW/cm$^2$ (f, destruction inside sample))

For 335 nm laser irradiation (LI), destruction started with intensities no more than 0.1 GW/cm$^2$ and it looked like a crater on the front side formed by combination of cracks and spalled material. 532 nm LI led to destruction starting with intensities more than 0.32 GW/cm$^2$ that looked like similar crater but on back side of the sample. With intensities more than 0.57 GW/cm$^2$ emission of plasma's plume was observed on both sides, but visible destruction was only present on back side. With LR intensity 0.94 GW/cm$^2$ destruction area shifted inside sample. This could be caused by beam focusing not particularly on sample's surface but on some depth of more optically dense (n ≈ 1.57) medium of glass, which led to stretching of converging beam and shift of focus point toward the back side of the sample.

BK-110 glass material destruction in irradiated area under 10 pairs of bichromatic pulses that follow in different order and time interval between pulses from −40 to +40 μs (negative value corresponds to leading action of LR 355 nm) was studied by mean of optical microscopy (Fig. 2).

Leading action of LR with λ=532 nm caused fairly smooth deepening (paired, due to flaws of laser emitter) surrounded with halo on sample's surface (similar to one observed on Fig.2 d). While leading action of LR λ=355 nm

caused cracked craters with traces of smooth deepening (Fig 2. b). Crater size increased with value of time interval between pulses, gradually covering area irradiated by second pulse. Irradiated areas also were surrounded by visible halo for all regimes of bichromatic irradiation. Absence of cracked craters for leading action of 532 nm LR could be caused by defocusing of second pulse on formed smooth deepening, which served as a lens, overlapping with mismatch of focal points for 355 and 532 nm beams.

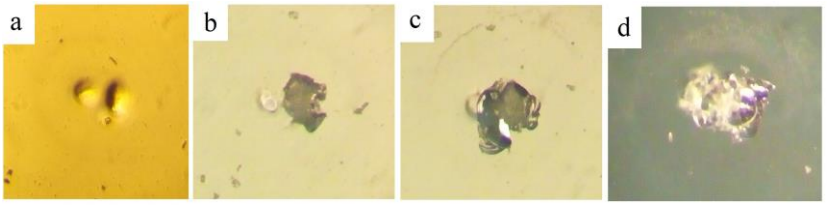



Fig. 2. Images of craters, formed by bichromatic LI on glass (λ = 355 and 532 nm, intensities on sample surface $q_{355}$ = 0.85 GW/cm$^2$ and $q_{532}$ = 1.31 GW/cm$^2$) with different order and time interval in pulses: a – typical look of crater for Δτ > 0 μs; b – Δτ = −1.4 μs; c – Δτ = −20 μs; d – Δτ = −40 μs. (negative value corresponds to leading action of 355 nm LR)

Separate videoframes of plasma's plume glow under mono- and bichromatic LI with wavelengths 355 and 532 nm on glass in air are shown in Fig. 3. For action of monochromatic LR with λ=355 nm plasma's glow looked like a prolonged pillar. On the contrary, action of 532 nm LR led to weaker glow around sample surface. Transition to bichromatic irradiation leads to increased heating of plasma's plume, that gradually weakens as value of time interval between pulses grow, eventually reaching minimum "plateau" for time intervals Δτ more than ~ −25 μs for case of leading action of LR 355 nm and Δτ~ +20 μs for leading action of LR 532 nm.

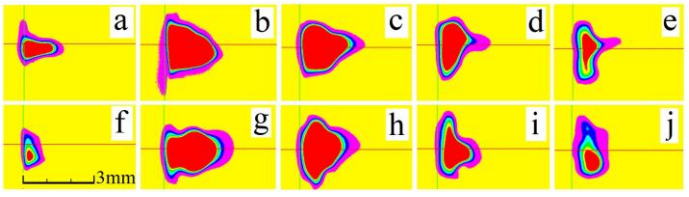



Fig. 3. Plasma plume images for mono- (a, f) and bichromatic (b–e, g–j) LI (355 and 532 nm, intensities on sample surface $q_{355}$=0.85 GW/cm$^2$ and $q_{532}$=1.31 GW/cm$^2$); a – action of LR 355 nm; b–e – combined irradiation with leading action of LR 355 nm and time intervals of pulses Δτ = −5; −10; −20; −30 μs; f – action of LR 532 nm; g–j – combined irradiation with leading action of LR 532 nm and time intervals of pulses Δτ = +5; +10; +20; +30 μs;

Emission spectra of plasma's plume, registered for above regimes of bichromatic irradiation (Fig. 4) show increase of plasma's heating as well. And leading action of λ=355 nm radiation causes stronger heating than leading action

of λ=532 nm with the same values of intervals between pulses. It is also worth noticing presence of double ions spectral lines (Si III 455.3 and Al III 490.4 for example), what indirectly point on high level of plasma's heat.

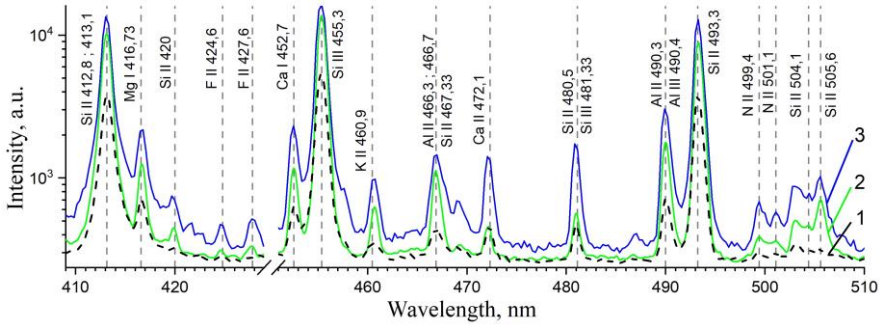



Fig. 4. Spectra of surface plasma for mono- (1) and bichromatic (2, 3) LI on glass in air: 1 – LI (λ = 355 nm); 2 – combined LI (λ = 532 and 355 nm, Δτ = +5 μs); 3 – combined LI (λ = 355 and 532 nm, Δτ = –5 μs). $q_{355}$ = 0.85 GW/cm$^2$ and $q_{532}$ = 1.31 GW/cm$^2$.

## 4. Conclusion

Laser destruction of BK-110 glass under λ = 355 ($q_{355} \leq 2.7$ GW/cm$^2$) and 532 nm ($q_{532} \leq 1$ GW/cm$^2$) monochromatic LI as well as influence of time interval between pulses of bichromatic LI and order in which they follow on formation of laser crates and surface plasma was investigated.

Much lower threshold for sample's face side destruction under λ=355 nm LI (~0.1 GW/cm$^2$) relative to λ=532 nm LI (~0.6 GW/cm$^2$) was established, as well as specific form of material destruction with abundance of cracks for variety of LI regimes (what can be caused by defocusing of beam on sample's surface). Transition to bichromatic LI leads to increase in heating of sample's surface plasma. Destruction intensity raise with formation of cracks is observed for leading action of LR with wavelength 355 nm.

**Acknowledgements.** This work is partially supported by State Program "Convergence-25" (grant NO 2.2.02)

## References

1. **A. Manenkov and A. Prokhorov**, Physics-Uspekhi 179 (1986) 148.
2. **M. Coldunov, A. Manenkov, I. Pokotilo**, Quant. electr. 25 (1998) 277.
3. **M. Coldunov, A. Manenkov, I. Pokotilo**, Quant. electr. 32 (2002) 335.
4. **A. Chumakov, V. Luchkousky, I. Nikonchuk, A. Matsukovich,** J. Tech. Phys. 92 (2022) 36.
5. **I. Nikonchuk, A. Chumakov,** J. Phys.: Conf. Ser. 666 (2016) 012021.

# THE ROLE OF LASER-INDUCED PLASMA IN A LIQUID FOR THE FORMATION OF NANOSIZED PARTICLES

N. Tarasenka[1], A. Butsen[2], V. Kornev[1], A. Radomtsev[1], N. Tarasenko[1]

[1]Institute of Physics of National Academy of Sciences of Belarus,
220072 Belarus, Minsk, Nezalezhnasti Ave. 68-2
[2]Belarusian State Technological University, 220006 Belarus, Minsk, Sverdlova str. 13a.

Pulsed laser ablation in liquids (PLAL) for the production of colloidal nanoparticles (NPs) has been widely studied in recent decades due to a number of promising advantages, including: environmental friendliness, ease of implementation, and possible long-term stability of the produced NPs [1]. Recent studies have demonstrated the importance of the initial plasma stage and cavitation bubble dynamics in the processes leading to the nucleation and formation of NPs in solution [2].

The interaction of high-intensity pulsed laser radiation with a solid-state target in a liquid leads to the formation of a dense plasma with rapidly changing parameters above the target surface. Plasma expands at a supersonic speed, cooling as a result of electron-ion radiative recombination and chemical reactions. In this case, the duration of the emitting stage of the laser-induced plasma is relatively short (as a rule, several hundred nanoseconds). After plasma attenuation, a hemispherical cavitation bubble is formed, consisting of gaseous ablation products and the vapor of the surrounding liquid. Arising after the laser pulse and constantly expanding, the gas bubble reaches its maximum size after several hundred microseconds (depending on the target material and laser pulse energy) and then collapses.

The formation mechanism of NPs after the laser ablation of a solid target in a liquid is still a controversial and remains insufficiently studied. Since the first investigations in this field, two main mechanisms have been discussed. The first relies on the nucleation and growth of ablated matter in the laser plume; the second assumes ejection of droplets from the molten layer in the liquid matrix.

Since laser plasma parameters, such as component concentrations and temperature, directly affect the processes leading to particle synthesis, knowledge of the dynamics of the evolution of the composition of the laser plasma is important for optimizing the conditions for producing nanoparticles by the PLAL. The composition of the laser plasma formed during ablation, in particular, the density of atoms in the gas phase, as well as the plasma temperature, play an important role in the NPs growth. Despite the complex spatiotemporal structure, high density and non-uniformity of laser-induced plasma, the spectroscopic diagnostics of such plasma seems to be very informative but require the high time and space resolved measurements.

In this regard, studies aimed at establishing the features of plasma formation and determining the parameters of laser-induced plasma in liquids, elucidating the

influence of plasma parameters on the nanoparticle growth processes which are the subject of this study, are important and relevant.

In the present work, to determine the parameters of laser plasma in a liquid, we applied a technique based on recording and analyzing the spectra of continuous radiation, which was previously proposed in [2]. Based on the results of spectroscopic diagnostics, the features of the initiation and evolution of laser plasma of a silver target in water in the mode of NPs generation are considered. Using plasma images with temporal and spectral resolution in the transmission region of narrow-band filters, information was obtained on the spatial distributions of plasma parameters at various time delays from the moment of plasma creation.

In the experiments, a YAG:Nd laser (LOTIS TII, model S-2131D) operating at the fundamental harmonic frequency (1064 nm) with a pulse duration of 10 ns and a pulse repetition rate of 10 Hz was used as a source for ablation. The energy of laser pulses could be varied in the range of 20–80 mJ. The laser radiation after the telescope was focused by a quartz condenser onto a target placed in a cell with quartz windows filled with distilled water.

The plasma images were taken through interference filters at wavelengths of 486 and 550 nm, with a full width at half maximum of 10 nm. Plasma images were acquired with time resolution at a gate width of 10 ns. The obtained images qualitatively characterize the structure of the plasma plume, illustrating the features of the spatial distribution of plasma species in it.

The continuous spectrum of plasma radiation is due to two reasons: bremsstrahlung of free electrons in the electric field of positive ions, and radiation when free electrons are captured by positive ions (recombination radiation). Due to the strong (exponential) dependence of radiation intensity on the frequency, free-free radiation makes the greatest contribution only in the low-frequency region of the spectrum. The energy distribution in the visible region of the spectrum at low temperatures is completely determined by the exponential factor $\exp\left(-h\nu / kT_e\right)$, and if this distribution measured in relative units at some fixed point in time when the values $n_e$ and $T_e$ are given then the temperature can be estimated.

Fig. 1a and 1b show, as an example, a map of the intensity distribution of laser plasma emission induced by ablation of a silver target in water, observed with filters of 550 and 486 nm at different delays from the laser pulse. It should be noted that the obtained images have a form characteristic of the laser-induced plasma plume with a pronounced high-density core and peripheral regions.

The distributions of the plasma emission intensity along the laser beam expansion axis are presented in Fig. 1c. The temperature profiles calculated using equation for recombination radiation from [3] along the axial direction, i.e. along the direction of the laser pulse, for two fixed time delays relative to the moment of laser exposure, are shown in Figure 1d. Figure 1d shows that in the first tens of ns the temperature is lower in the inner part of the plasma, while at the expansion front it is more than 30% higher. This feature of the spatial distribution of intensity suggests that where the density is higher (higher intensity), the temperature is

lower, according to the equation of state ($p = nkT$), assuming that the pressure is uniform throughout the plasma volume.

Thus, during laser ablation in water under the conditions of our experiments at the initial stage of plasma formation, the temperature inside the laser plume is lower than in the outer layer. This can be explained by the screening effect of the front of the plasma, which always occurs during ablation with a nanosecond laser, and in the case of a liquid, the effect is more pronounced due to the slower plasma plume expansion.

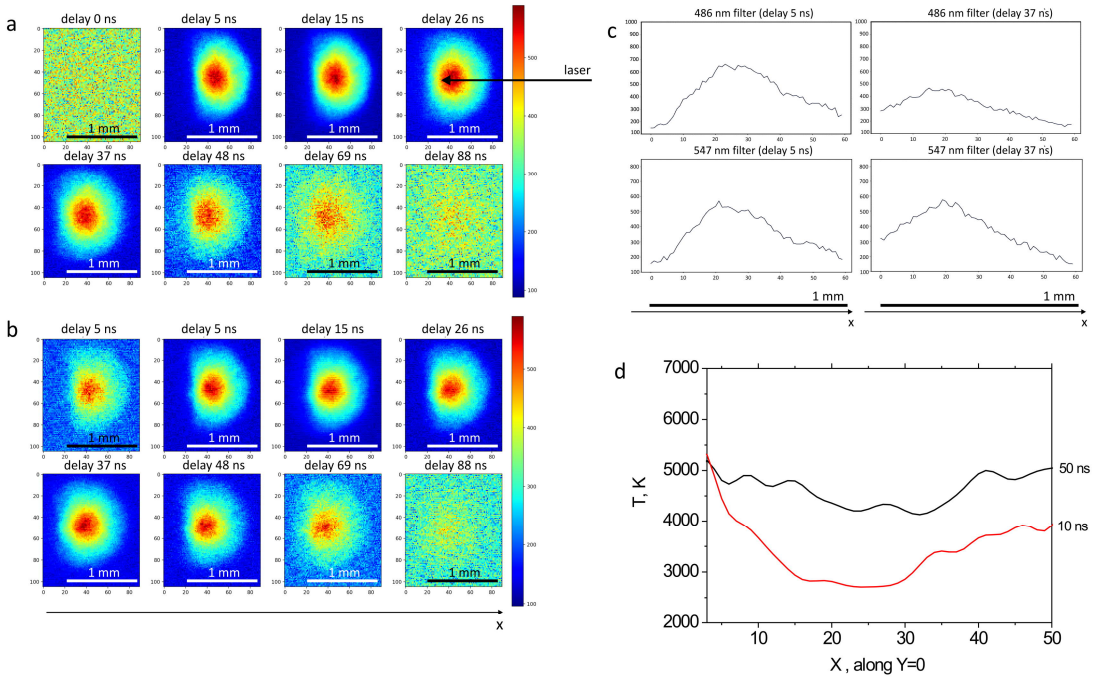



Fig. 1. The map of laser plasma emission intensity at 486 nm (a) and 550 nm (b) with the corresponding axial profiles (c, d), and the axial temperature profile along the direction of the laser beam for two time delays (10 and 50 ns) relative to the laser pulse. Ag target in water, delay times = 10 and 50 ns, gate width = 10 ns.

In conclusion, recording emission images of plasma at different wavelengths (550 and 486 nm), experimental maps of the temperature of laser-induced plasma in water used to generate metal (Ag) nanoparticles were obtained. The results of image processing showed a change in temperature in the range of 3000 and 6000 K over the plasma volume. An analysis of the spatial distribution of temperature and density along the axis of plasma expansion made it possible to identify a hypothetical condensation zone in which NPs can form. The experimental results show the importance of the plasma phase investigations for understanding the mechanisms of NP nucleation and growth during laser ablation in liquid media.

**Acknowledgements.** This work was supported by the National Academy of Sciences of Belarus (project Convergence 2.2.05) and by BRFFR (grant number F21UKRG-009).

## References

1. **Zhang D., Gökce B., Barcikowski S.** Chemical Reviews, 117–5 (2017) 3990–4103.
2. **Dell'Aglio M., Gaudiuso R., De Pascale O., De Giacomo A.** Applied Surface Science, 348 (2015) 4–9.
3. **Зельдович, Я.Б.** Физика ударных волн и низкотемпературных гидродинамических явлений / Я.Б. Зельдович, Ю.П. Райзер. – М.: Наука, 1966.

# CONTROLLING OF MATERIALS ABLATION AND PLASMA FORMATION UNDER BICHROMATIC LASER EXPOSURE IN AIR

Chumakov A.N., Lychkousky V.V., Bosak N.A.

*B.I. Stepanov Institute of Physics of the National Academy of Sciences of Belarus, 220072, Minsk, Belarus*

**Abstract.** The analysis of a number of materials ablation in atmospheric air with formation of near-surface plasma under irradiation by pulsed Nd:YAG laser with radiation wavelengths of 355, 532 and 1064 nm at power density of radiation up to 5 GW/cm$^2$ is given. The increased efficiency of ablative plasma formation and heating under bichromatic irradiation of metals, graphite, silicon and glass at leading action of short-wave nanosecond laser pulses has been established.

## 1. Introduction

The effectiveness of laser ablation of materials in air depends not only on the laser power density but also on the laser pulse repetition frequency. At high repetition frequencies of laser pulses (>5 kHz), the predominant formation of ablative plasma occurs with a multiple increase in pressure on the target surface [1]. In such multi-pulse conditions, the efficiency of laser micro-drilling increases significantly for a number of materials in gases. Even when exposed to two laser pulses separated by a time interval of several microseconds, it is possible to increase the efficiency of laser processing and analysis of materials [2]. The use of combined laser pulses (especially those that differ in wavelength) with an adjustable time interval and sequence order should provide an opportunity to significantly increase the efficiency of ablation of materials and heating of ablative plasma. Two-pulse bichromatic laser treatment provides more degrees of freedom to control the laser ablation process of materials that differ in their thermal and optical characteristics. However, it still remains insufficiently studied.

The aim of this work is to identify new opportunities for effective laser processing of materials in air and control of parameters of near-surface laser plasma using harmonics of Nd:YAG laser radiation.

## 2. Experimental setup

The installation is based on two Nd:YAG lasers (JV ”LOTYS TII“, Minsk) and a synchronization system for generating paired nanosecond laser

pulses with wavelengths of 532 and 1064 nm, as well as 355 and 532 nm with a duration from 15 ns to 20 ns. The sequence order and the time interval between pulses can be adjusted. The diameter of the laser radiation spots on the targets varied from 200 to 350 microns. A more detailed description of experimental facilities and research methods is given in [3–7].

## 3. Results and discussion

The bichromatic irradiation of brass and graphite in air using doubled laser pulses with wavelengths of 532 and 1064 nm at radiation power density of 4 GW/cm$^2$ was investigated in detail [3]. The dependence of near-surface plasma temperature, its electron density and recoil momentum of laser-produced plasma on the time interval between laser pulses and the order of their sequence was revealed (Fig. 1, negative time intervals correspond to pulse sequences in which the 532-nm pulse came first).

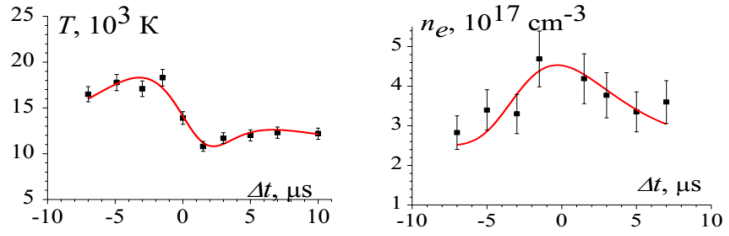



Fig. 1. Dependence of temperature (a) and electron density (b) in the carbon plasma on the time interval between laser pulses 532 and 1064 nm

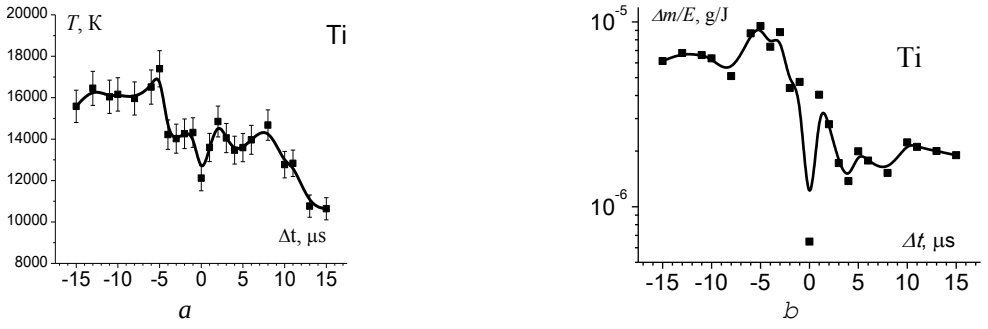



Fig. 2. Dependence of plasma temperature Ti (*a*) and specific mass removal Ti (*b*) on the time interval between laser pulses with power density $q_{532}$ = 2.7 and $q_{1064}$ = 3.1 GW/cm$^2$

It was shown that the optimal conditions for recording the spectra of brass and graphite ablation plasma are provided in the case of outrunning shortwave laser irradiation at $\lambda$ = 532 nm with the time interval between the pulses within 3–6 μs range. As for generation of the recoil momentum, the optimum time interval is 1.5–2 μs. These results are essential for the enhancement of the

sensitivity of laser spectral analysis and of the efficiency of laser plasma microengines.

Similar studies on the bichromatic laser effect on titanium samples in the air were carried out using the installation described above. The modes of laser irradiation of titanium samples used differed somewhat only in the laser radiation power density of 3 GW/cm$^2$. The results obtained for titanium and graphite targets are qualitatively similar. The maximum temperature of the ablative plasma of titanium, as well as the maximum of titanium specific mass removal, is achieved under the advancing action of short-wave radiation (532 nm) with a time interval of 5–7 microseconds (Fig. 2).

The results of pulsed mono- and bichromatic laser radiation action on silicon are summarized in the articles [5–7]. The nonliner dependence of the specific mass removal of silicon is revealed not only on the power density of the impacting laser radiation, but also on the time interval and sequence order of bichromatic laser pulses (Fig.3).

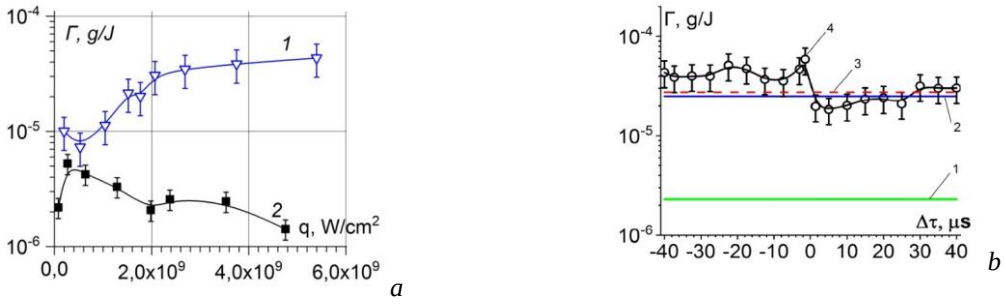



Fig. 3. Dependences of the specific mass removal of silicon: *a* – on the power density of LR with wavelengths of 355 (*1*) and 532 nm (*2*); *b* – on the time interval within bichromatic LR pulses with power density $q_{355}$ = 1.9 and $q_{532}$ = 3.5 GW/cm$^2$ (*1* – $\lambda$ = 532, *2* – $\lambda$ = 355 nm, *3* – estimate of the overall effect of LR at both wavelengths; *4* – irradiation with bichromatic LR pulses).

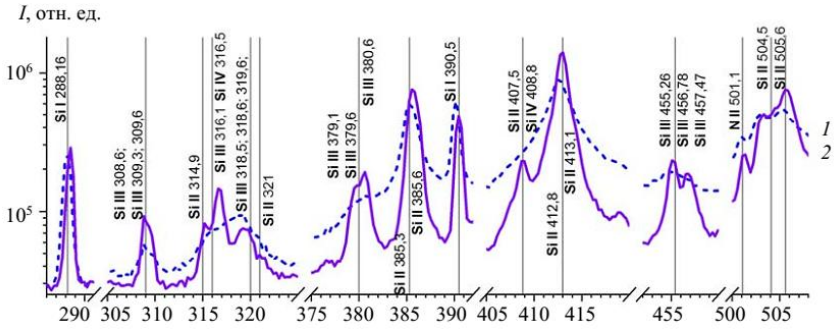



Fig. 4. Spectra of surface plasma induced by monochromatic LR with λ=355 nm and $q_{355}$=4,6 GW/sm2 (1) and by birchromatic LR with $q_{355}$=1,9 GW/sm$^2$ + $q_{532}$=3,5 GW/cm$^2$ (Δτ = –1,4 μs) (2) on silicon sample in air.

Studies have shown an increased efficiency of spectra excitation of ablative

silicon plasma when the target is irradiated in air by bichromatic laser pulses at the advanced effect of short-wave radiation with wavelength of 355 nm (Fig. 4).

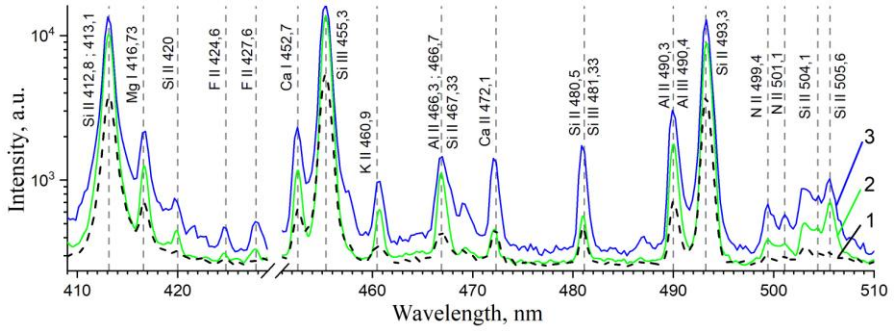



**Figure 5.** Emission spectra of surface plasma for mono - (1) and bichromatic (2, 3) laser action on BK-110 glass in air: 1 – λ = 355 nm; 2 – bichromatic action 532 and 355 nm (Δτ = +5 μs); 3 – bichromatic action 355 and 532 nm (Δτ = –5 μs). $q_{355}$ = 0.85 GW/cm$^2$ and $q_{532}$ = 1.31 GW/cm$^2$.

Bichromatic laser exposure to glass in the air also leads to increased efficiency of ablative plasma excitation under these conditions (Fig. 5).

## Conclusion

The use of bichromatic pulsed laser irradiation of a number of materials in air expands the possibilities of increasing the efficiency of materials ablation and excitation of ablative plasma spectra, which is promising for use in laser technologies for processing and analysis of materials, as well as in laser-plasma micro-motors.

## Acknowledgements

This work is partially supported by state scientific research program of Belarus “Convergence – 2025” under the grant NO 2.2.02.1

## References

1. Min’ko L.Ya., Chumakov A.N. et al., Sov. J. Quant. El., **20** (11), 1990, 1389.
2. A. A. I. Khalil. Laser Phys., **20**, N 1 (2010) 238.
3. Chumakov A.N., Bosak N.A. et al., J. Appl. Spectr., **84** (2017) 620.
4. Chumakov A.N., Bosak N.A. et al., J. Appl. Spectr., **86** (2019) 836.
5. Chumakov A.N. et al., High Temp. Mater. Processes, **18** (4), (2014) 269.
6. Chumakov A.N., Lychkovsky V.V., J. Appl. Spectr., **88** (6), (2021) 1169.
7. Chumakov A.N., Lychkovsky V.V., Nikonchuk I.S., Matsukovich A.C., J. Tech. Phys., **92**(1), (2022) 36.

# RADIATION RESISTANCE OF AMORPHOUS ZIRCONIUM ALLOYS AFTER IRRADIATION WITH HELIUM IONS

V.V. Uglov[1], S.V. Zlotski[1], V.A. Goroshko[1], A.N. Suchkov[2]

[1]Belarusian State University, 4 Nezavisimosty ave., 220030 Minsk, Belarus
[2] National Research Nuclear University MEPhI, 31 Kashirskoye Highway, 115409 Moscow, Russia

Many amorphous alloys have completely different properties compared to crystalline alloys of the same composition. Amorphous alloys can absorb a larger dose of radiation than crystalline alloys, can have better strength characteristics, and can be more resistant to corrosion. This is due to the amorphous structure, which is characterized by the absence of long-range order.

In thermonuclear reactors, the synthesis of deuterium and tritium can occur, one of the products of this reaction is helium. Helium is poorly soluble in metals, so it tends to accumulate inside the material, which can lead to deterioration of its mechanical properties [1, 2]. One of the potential ways to solve this problem can be the use of amorphous alloys, since they, in fact, do not have point defects [3], and, after the atom moves as a result of irradiation, the structure will not actually change. Moreover, after irradiation with helium, the characteristics of amorphous alloys can be improved [4, 5]. Given the resistance of zirconium alloys to blistering, it makes sense to study amorphous zirconium alloys, the purpose of which is to absorb the maximum possible doses of helium ions without significant changes in characteristics or with subsequent improvement in the characteristics of the alloy.

In this paper, we consider two alloys containing a significant part of zirconium: A1 ($Zr_{51.32}Ti_{17.54}Ni_{15.18}Cu_{14.61}In_{1.35}$) and A2 ($Ti_{65.23}Zr_{34.77}$). The samples were obtained by high-speed hardening [6] and are small thin quadrangular metal plates. The molten alloy enters the cooled drum, after which it is rapidly cooled. Due to the high cooling rate, the atoms do not have time to be distributed in an orderly manner, an amorphous structure appears. Due to the temperature gradient, the samples are heterogeneous, that is, there are two sides that differ from each other: matte (adjacent to the drum) and mirror (reverse side). In this work, only the matte side of the samples is considered, since the fastest cooling and, consequently, the solidification of the alloy occurred in this region.

The samples were irradiated with helium ions with an energy of 40 keV and a fluence of $5\times10^{17}$ $cm^{-2}$. After that, the phase composition of the samples before and after irradiation was studied by X-ray diffraction analysis on a Rigaku Ultima IV diffractometer using copper radiation ($\lambda$ = 0.15418 nm). To

study the effect of implanted helium on the near-surface layer, the samples were taken at a small fixed angle of incidence of X-rays (1°). The change in free volume was evaluated, and with the help of the RAD program, plots of the radial distribution for the samples were obtained, from which the short-range order values were found before and after irradiation.

Figures 1 and 2 show X-ray patter of two samples before and after irradiation. X-ray diffraction pattern A before irradiation has two amorphous peaks, indicating that the Al alloy sample is completely amorphous. After irradiation, the sample did not undergo any significant changes; the intensity of the peaks only slightly decreased. On X-ray B before irradiation, there is a large crystalline peak and 3 more smaller ones, two of which are not visible due to the scale, as well as a small amorphous peak. After irradiation, a significant amorphization occurred in the A2 alloy sample, the intensity of the first crystalline peak significantly decreased, therefore, it can already be concluded that there are significant changes in the structure.

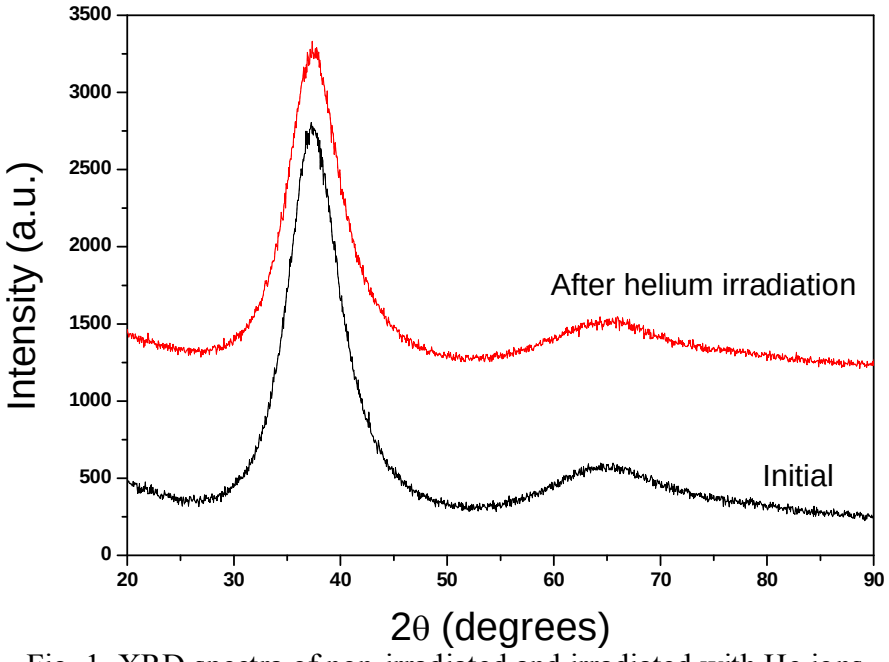



Fig. 1. XRD spectra of non-irradiated and irradiated with He ions $Zr_{51.32}Ti_{17.54}Ni_{15.18}Cu_{14.61}In_{1.35}$ samples

Table 1 shows the values of the change in free volume and short-range order in the samples after irradiation with helium ions. In the sample from alloy A1, there were no significant changes in the free volume and the short-range order did not change. Significant changes in both parameters occurred in the A2 alloy sample.

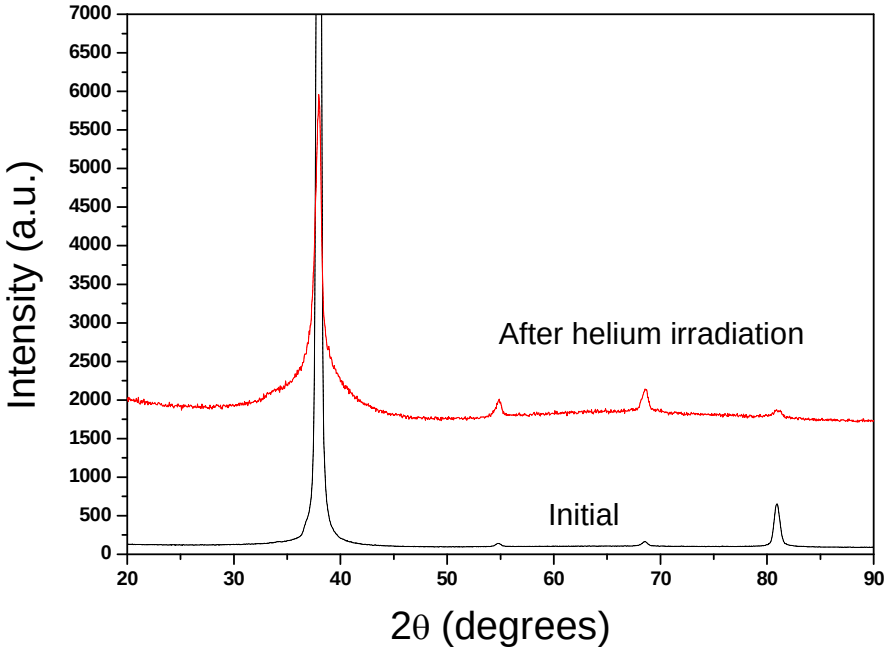



Fig. 2. XRD spectra of non-irradiated and irradiated with He ions $Ti_{65.23}Zr_{34.77}$ samples

Tabl. 1. Changes in the short-range order $\Delta r/r_0$ and changes in the free volume of the first amorphous peak $\Delta V_1/V_0$ and the second amorphous peak $\Delta V_2/V_0$ for samples from A1 and A2 alloys

| Sample | Phase composition | $\Delta r/r_0$,% | $\Delta V_1/V_0$, % | $\Delta V_2/V_0$, % |
|---|---|---|---|---|
| A1 | Amorphous | 0.00 | 0.39 | -0.82 |
| A2 | Amorphous and crystalline | 7.86 | -2.24 | 10.14 |

Based on the results obtained, it can be concluded that amorphous alloys practically do not change after irradiation with helium ions; When amorphous-crystalline alloys are irradiated with helium ions, significant changes occur in the structure of the alloy and, consequently, its mechanical characteristics change. This may be due to the fact that during irradiation, incident particles, interacting with target atoms, knock them out of the crystal lattice nodes, thereby deforming it. In amorphous alloys, after irradiation, the structure actually does not change, since it is not ordered initially, while implanted helium can accumulate in a free volume.

Thus, the considered amorphous zirconium alloy A1 ($Zr_{51.32}Ti_{17.54}Ni_{15.18}Cu_{14.61}In_{1.35}$) remained almost unchanged after irradiation with helium ions with a fluence of $5\times10^{17}$ $cm^{-2}$, which makes it promising for further research or modification.

**References:**

1. **H. Trinkaus, B.N. Singh,** Journal of Nuclear Materials, 323 (2003) 229-242. – Mode of access: https://doi.org/10.1016/j.jnucmat.2003.09.001.
2. **S.-H. Li, J.-T. Li, W.-Z. Han,** Materials, 12 (2019). – Mode of access: https://doi.org/10.3390/ma12071036.
3. **R.E. Baumer, M.J. Demkowicz,** Acta Materialia, 83 (2015) 419-430. – Mode of access: https://doi.org/10.1016/j.actamat.2014.10.020.
4. **J. Carter, E.G. Fu, G. Bassiri, B.M. Dvorak, N. David Theodore, G. Xie, D.A. Lucca, M. Martin, M. Hollander, X. Zhang, L. Shao,** Nuclear Instruments and Methods in Physics Research Section B: Beam Interactions with Materials and Atoms, 267 (2009) 1518-1521. – Mode of access: https://doi.org/10.1016/j.nimb.2009.01.081.
5. **R. Liontas, X.W. Gu, E. Fu, Y. Wang, N. Li, N. Mara, J.R. Greer,** Nano Letters, 14 (2014) 5176-5183. – Mode of access: https://doi.org/10.1021/nl502074d.
6. Amorfnie metally / **Sudzuki K., Xudzimory X., Xasimoto K.** – M.: Metallurgija, 1987. – 38 p (in Russian).

# 6. PLASMA DIAGNOSTICS AND MODELING

# ELECTRON PARAMETERS AND ABSOLUTE GLOW INTENSITIES IN A DISCHARGE SUPPORTED BY A HOLLOW CATHODE IN MIXTURES OF HELIUM AND WATER VAPOR

S.N. Andreev[1], A.V. Bernatskiy[1], I. Draganov[1,2], I.V. Kochetov[1,3], V.N. Ochkin[1]

[1]P.N. Lebedev Physical Institute of the Russian Academy of Sciences, 53 Leninskiy Prospekt, Moscow, 119991, Russia. andreevsn@lebedev.ru, bernatskiyav@lebedev.ru, ochkin@sci.lebedev.ru

[2]Moscow Institute of Physics and Technology (National Research University), 9 Institutskiy per., Dolgoprudny, Moscow Region, 141701, Russia. draganov.i@phystech.edu

[3]SRC RF Troitsk Institute for Innovation and Fusion Research, Troitsk, Moscow, 108840, Russia. kochet@triniti.ru

Due to the problem of studying the near-wall plasma in reactors, the spectral diagnostic technique of discharge plasma in helium with water vapor supported by a hollow cathode is being developed [1–3]. The methods of optical actinometry have been developed, the results of measurements and plasma-chemical simulation have been compared [1, 2]. The measured and calculated concentrations of $H_2O$, $H_2$, $O_2$ molecules, OH radicals, and O, H atoms have been compared. In order, to refine the parameters of the plasma-chemical model, it is advisable to supplement it with a comparison with the measured absolute populations of the electronic levels of helium atoms. For this it is necessary to carry out absolute measurements of the emission intensities of lines of optical transitions from highly excited electronic levels of helium and hydrogen atoms [1, 3], which critically depend on the parameters of plasma electrons: their concentration and the electron energy distribution function. This work is devoted to comparing the absolute intensities measured and calculated in the coronal model approximation under such conditions.

Absolute intensities were measured with preliminary calibration of the optical system [3]. To calculate the absolute intensity of the lines, the electron energy distribution functions (EEDF) and the electron density ($N_e$) were measured. The simplest coronal model was used for calculations: the assumption that the electron levels under consideration are populated only by the direct electron impact mechanism, and the main settlement mechanism is radiative [1]. Knowledge of the excitation cross section of radiating states, can be calculated the absolute intensity of these transitions [1]. Such a procedure, in case of agreement between the calculated and measured intensities, will demonstrate how justified made assumption is and whether these lines can be used for quantitative diagnostic of plasma.

The studies were carried out on the experimental system "Leak" [1-6]. The measurement scheme is shown in Fig. 1.

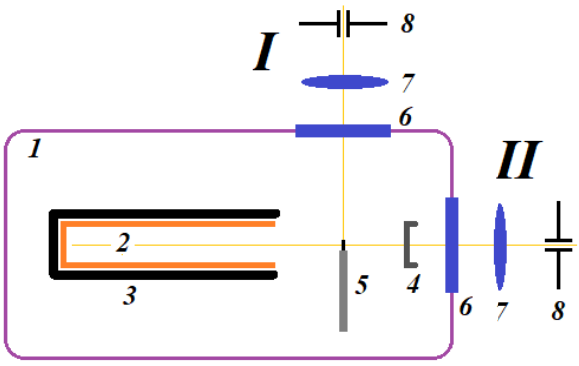



Fig. 1. Measurement scheme: *1* – vacuum chamber; *2* – copper cathode; *3* – Teflon cathode insulator; *4* – grid anode; *5* – probe; *6* - flange with a quartz window; *7* – lens system; *8* – entrance slit of the MDR-204 monochromator.
I – spectral measurements in the area of probes; II – spectral measurements opposite the open side of the cathode

The configuration of the discharge device is represented by a rectangular copper hollow cathode (100×50×10 mm) *2*, which has a Teflon insulator *3* on the outside. The anode *4* is a grid (100×10 mm) with a surface area of 3600 . The distance between the open part of the cathode and the anode is 30 mm.

To measure the EEDF and Ne, the method of a single Langmuir probe was used [1, 4–6]. In recent years, we have developed a new approach [4-6] for the formation of a current-voltage characteristic (CVC) on a single Langmuir probe. The created probe system forms the CVC of the probe circuit when voltage is applied to the probe in the form of a noise signal or a combination of noise and periodic signals [4, 5]. This approach made it possible to achieve a large dynamic range of measurements [4, 5].

It bears mentioning that a feature of probe measurements is the vitiation of the EEDF in the low-energy region [6]. This phenomenon is called the “sink” effect of electrons on the probe [6], and consists in the fact that the process of diffusion of “slow” electrons does not ensure their arrival from the plasma to the region from which they fall on the probe without collisions. In [6] we proposed methods for correcting the measured EEDF, which were used in this work.

A probe made of tungsten wire (diameter 0.1 mm, length 2 mm) with a ceramic insulator was used in the measurements. During the research, the probe was placed in the space between the anode and the cathode at distances of 3, 11, 19 mm from the cathode, with the active part opposite the geometric center of the open side of the cathode. The second reference electrode was the anode.

Spectral measurements were carried out in different regions of the plasma (see Fig. 1): *I* - in the measurement region of each probe; *II* - spectral measurements opposite the open side of the cathode (in the text this area is designated "cathode"). In case *I*, the radiation from the inner part of the hollow cathode did not reach the entrance slit of the monochromator, while in case *II* it did.

The measurements were carried out in $He+H_2O$ mixtures at a He concentration of $5.4\cdot10^{16}$ $cm^{-3}$ and different water vapor concentrations: 0 $cm^{-3}$; $4.1\cdot10^{15}$ $cm^{-3}$; $1.4\cdot10^{16}$ $cm^{-3}$. The discharge current was stabilized at 147 mA in all cases.

An example of measured EEDFs at different concentrations of water molecules, obtained at distance of 3 mm from the cathode, is shown in Fig. 2.

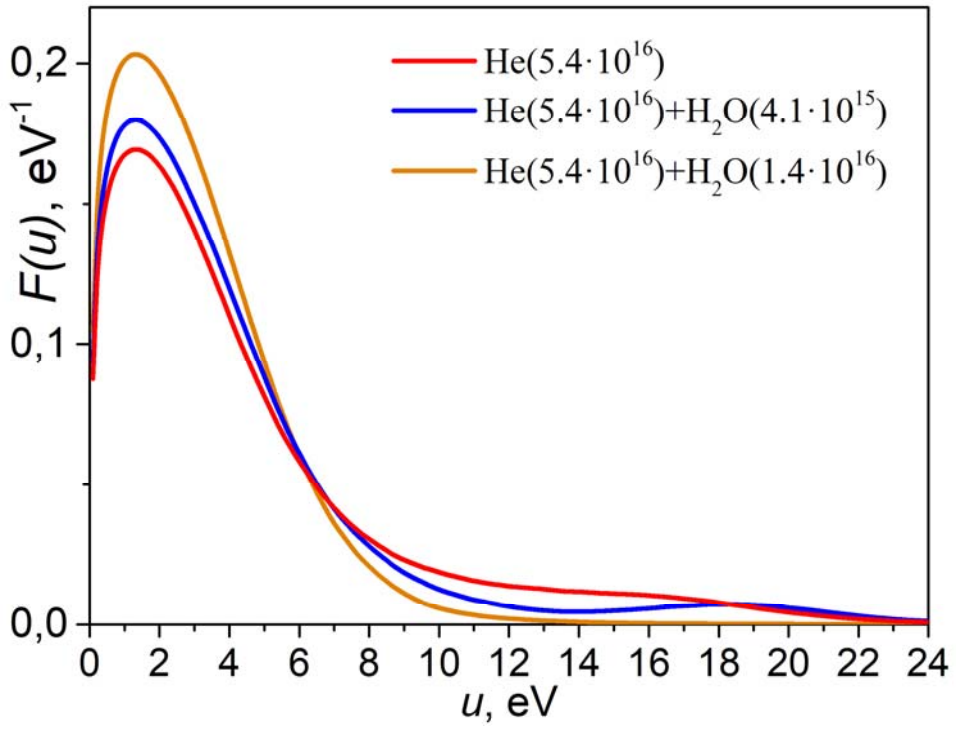



Fig. 2. Measured EEDF (probe 3 mm from the cathode) at different concentrations of water molecules.

A comparison of the measured and calculated absolute intensities of the He atomic transition lines was carried out using the lines 318.77 nm, 381.96 nm, 388.86 nm, 396.47 nm, 402.61 nm, 412.08 nm, 438.79 nm, 447.14 nm, 471.31 nm, 492.19 nm, 501.56 nm, 587.656 nm, 728.13 nm. An example of comparing the measured and calculated absolute intensities in a He mixture ($5.4\cdot10^{16}$ $cm^{-3}$) at a distance of 3 mm from the cathode is shown in Fig. 3.

The measurement results showed that there is no complete agreement between the measured and calculated intensities for all observed lines. However, there are lines with reasonable agreement between calculations and measurements for all mixtures: 388.86 nm, 492.2 nm, 501.6 nm, 587.6 nm, 667.81 nm. These lines seem to be the most perspective for quantitative diagnostic of plasma using the coronal model. It can be seen that the radiating levels of these lines are characterized by lower energies. Mostly this may be due to a more accurate experimental determination of the EEDF in this energy range.

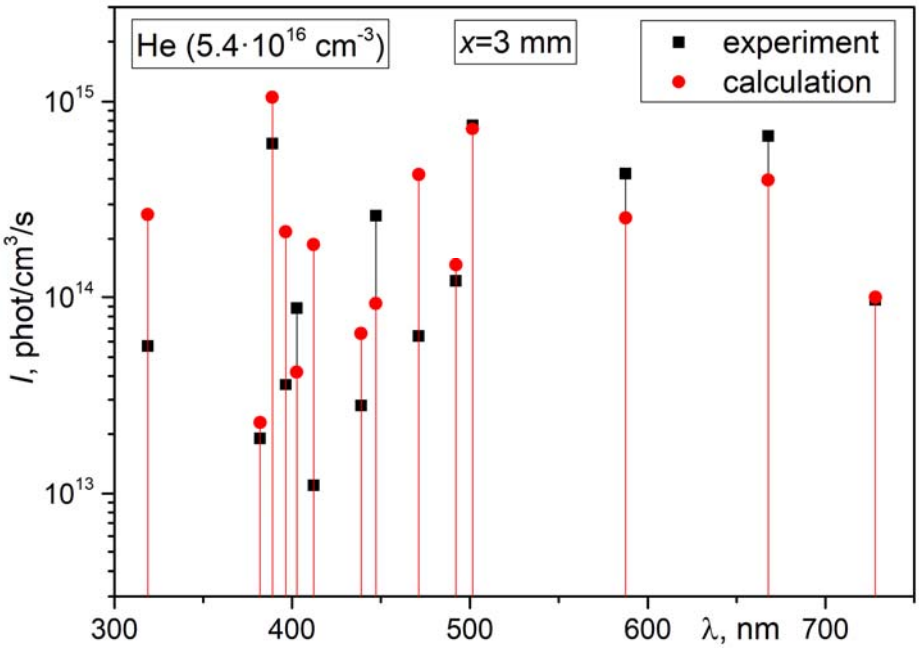



Fig. 3. An example of comparing the measured (experiment) and calculated (calculation) absolute intensities of a mixture of He ($5.4 \cdot 10^{16}$ $cm^{-3}$). The measurements were carried out at a distance of 3 mm from the cathode.

**Acknowledgements**. This work was supported by the Russian Science Foundation Project No. 19-12-00310.

## References

1. **Bernatskiy A.V., Kochetov I.V., Ochkin V.N.** Plasma Physics Reports, 46 (2020) 874 https://doi.org/10.1134/S1063780X20090020
2. **Bernatskiy A.V., Kochetov I.V., Ochkin V.N.** Plasma Sources Science and Technology, 28 (2019) 105002 https://doi.org/10.1088/1361-6595/ab4301
3. **Bernatskiy A.V., Ochkin V.N., Afonin O.N., Antipenkov A.B.** Plasma Physics Reports, 41 (2015) 705 https://doi.org/10.1134/S1063780X15090032
4. **Andreev S.N., Bernatskiy A.V., Ochkin V.N.** Vacuum, 180 (2020) 109616. https://doi.org/10.1016/j.vacuum.2020.109616
5. **Andreev S.N., Bernatskiy A.V., Ochkin V.N.** Plasma Chem. Plasma Process., 41 (2021) 659–672. https://doi.org/10.1007/s11090-020-10137-4
6. **Andreev S.N., Bernatskiy A.V., Dyatko N.A., Kochetov I.V., Ochkin V.N.** Plasma Sources Science and Technology, 30 (2021) 095004. https://doi.org/10.1088/1361-6595/ac1ee2

# SPECIFIC FEATURES OF PROBE MEASUREMENTS OF EEDF NEAR THE ANODE

S.N. Andreev[1], A.V. Bernatskiy[1], N.A. Dyatko[1,2], I.V. Kochetov[1,2], V.N. Ochkin[1]

[1]P.N. Lebedev Physical Institute of the Russian Academy of Sciences, 53 Leninskiy Prospekt, Moscow, 119991, Russia. andreevsn@lebedev.ru, bernatskiyav@lebedev.ru, ochkin@sci.lebedev.ru

[2]SRC RF Troitsk Institute for Innovation and Fusion Research, Troitsk, Moscow, 108840, Russia. dyatko@triniti.ru, kochet@triniti.ru

Measurements of the electron energy distribution function (EEDF) in low-temperature plasma are carried out mainly using probes introduced into the plasma [1]. The applicability of the classical methods for reconstructing the EEDF from the current-voltage characteristics of the probe is associated with the condition that the probe diameter be small compared to the electron mean free path. This condition limits the range of gas pressures at which correct measurements are possible. Qualitatively, the main reason for this limitation is related to the fact that the process of diffusion of slow electrons does not ensure their arrival from the plasma to the region from which they reach the probe without collisions. The distortion of the measured EEDF due to this effect (electron sink effect) manifests itself, first of all, at low electron energies.

For a cylindrical probe, the relationship between the measured EEDF $f_e(u)$ and the unperturbed $f(u)$ far from the probe is given by the expression [1, 2]:

$$f_e(u) = f(u)\left[1 - 2\int_u^\infty \frac{\delta(\varepsilon) f(\varepsilon) d\varepsilon}{\varepsilon f(u)\left[1+(1-\frac{u}{\varepsilon})\delta(\varepsilon)\right]^3}\right], \quad \delta(u) = \frac{3a}{4\lambda(u)} \ln\left(1+\frac{2l}{a+\lambda(u)}\right), \quad (1)$$

where $u$ is the electron energy, $l$ and $a$ are the length and radius of the probe, $\lambda(u) = [N\sigma(u)]^{-1}$ is the electron mean free path, $N$ is the number density of atoms, $\sigma(u)$ is the transport cross section for electron scattering on atoms. The formula for $\delta(u)$ is valid at $l/a >> 1$. Note that, the electron sink effect theory is approximate and several different expressions for $\delta(u)$ have been proposed in the literature.

When measuring the EEDF in the positive column of the glow discharge in the tube, it was found that the form of the distribution function depends on the distance between the probe and the anode [3, 4]. It was found that the smaller this distance, the more significant the EEDF is depleted in low-energy electrons. The reason for the EEDF transformation is the absorption of electrons by the

anode, theoretical studies confirm this conclusion [3, 5-7]. Note that experimental and theoretical studies were carried out under glow discharge conditions in neon. It was shown that the described effect can manifest itself at sufficiently large distances from the anode (several centimeters at a pressure of 1 Torr), i.e. at distances significantly exceeding the thickness of the anode layer.

Thus, during measurements near the anode, the resulting EEDF will be depleted in low-energy electrons due to two effects: natural (proximity to the anode) and instrumental (distortions introduced by the probe). In the present work, the influence of these effects on the shape of the EEDF is analyzed under conditions of a discharge with a hollow cathode in helium.

Figure 1a shows the arrangement of electrodes and probes in the discharge setup. The hollow cathode, made of three interconnected tungsten plates, is insulated with ceramic plates on all sides, except for the one facing the anode. A detailed description of the setup is given in [8, 9]. We note that the cathode-to-anode distance is only 3 cm, and it can be expected that the proximity of the anode will affect the shape of the EEDF in the discharge plasma.

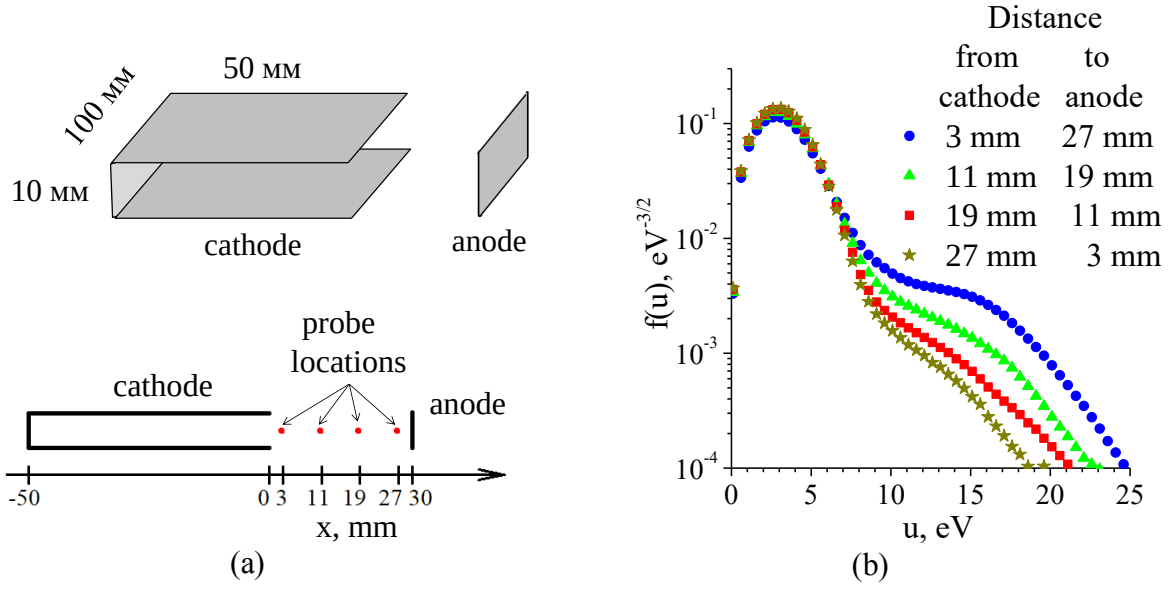



Fig. 1. (a) Schematic of the electrodes system indicating the location of the probes. (b) EEDFs measured at various locations in the cathode-anode gap.

The experiments were carried out in pure helium at a pressure $P$ = 0.75 Torr and a discharge current of 160 mA, the gas temperature was $T \approx 340$ K. The measurements were carried out sequentially using four identical tungsten cylindrical probes with a radius $a$ = 0.05 mm and a length $l$ = 2 mm. In this case, an original technique was used that provides a large dynamic range of measurements [9, 10]. The measured EEDFs are shown in Fig. 1b. As can be seen from the figure, they are depleted in low-energy electrons. The measured value of the electric field strength is $E \approx 1.3$ V/cm, the corresponding value of

the reduced electric field is $E/N \approx 6.1$ Td.

The degree of influence of the above effects on the shape of the EEDF under considered conditions was estimated by comparison with the local distribution function calculated by solving the Boltzmann equation at $E/N = 6.1$ Td. The set of cross sections for the electron scattering from helium atoms was taken from [11].

In Figure 2a, the local $f(u)$ is represented by a solid line, and the dashed line shows the function obtained by taking into account the distortions introduced by the probe, i.e. calculated by formula (1) assuming that the unperturbed function is local one. As can be seen from the Fig. 2a, the distorted distribution function $f_e(u)$ is depleted in low-energy electrons, so that at $u \approx 1.5$ eV the maximum of the function is formed. Note also that at $u = 0$ the value of $f_e$ is approximately two times smaller than the value of the original function.

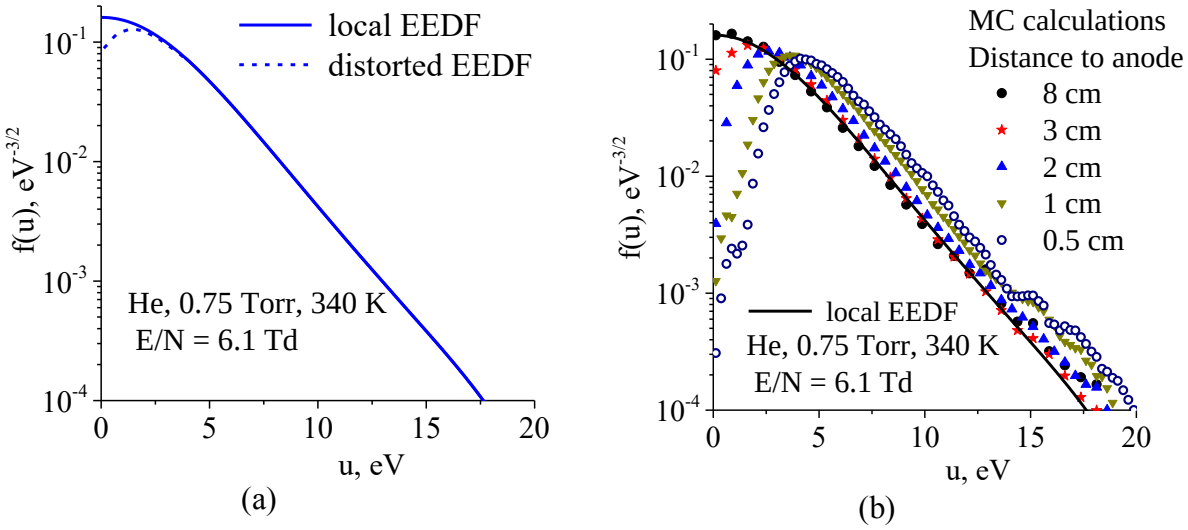



Fig. 2. (a) Comparison of the local EEDF and that distorted due to sink effect.
(b) Comparison of the local EEDF and those calculated at different distances to anode.

The effect of electron absorption by the anode on the shape of the EEDF was studied numerically by simulating the motion of electrons in helium in a uniform electric field by the Monte Carlo technique. The simulation was carried out for conditions ($P$, $T$, $E$) corresponding to the experimental ones. The set of cross sections from [11] was used in the calculations, and the calculation procedure was similar to that described in [12]. The trajectory of each launched electron was traced until it crossed the boundary corresponding to the position of the anode. The anode was located far enough from the electron source, so that an EEDF corresponding to the local distribution function was formed at some distance from the source. Further, when approaching the anode, the calculated EEDF began to be distorted due to the effect of electron absorption by the anode. Results of calculations are shown in Fig. 2b. As can be seen from the

figure, at a distance of 8 cm to the anode, the EEDF is still close to local one. A noticeable difference between the calculated EEDF and the local one is observed at distances of 3 cm to the anode, where the calculated function is depleted in low-energy electrons. When approaching the anode, this effect is enhanced, so that at distances of 1 cm - 0.5 cm, the EEDF has a pronounced maximum in the energy range ~ 4 eV.

Distortions of the EEDF due to the effect of the electron sink on the probe are always present, and the degree of influence of the absorption of electrons by the anode on the form of the EEDF depends on the distance to the anode. A qualitative comparison of the measured (Fig. 1b) and calculated (Fig. 2a-b) EEDFs allows us to conclude that the measured EEDFs are depleted in low-energy electrons due to both considered effects. But at short distances (< 3 cm) to the anode, the depletion is mainly due to the effect of electron absorption by the anode.

**Acknowledgements**. This work was supported by the Russian Science Foundation Project No. 19-12-00310.

## References

1. **Demidov V.I, Koepke M.E, Kurlyandskaya I.P. and Malkov M.A.** Phys. Plasmas, 27 (1987) 020501.
2. **Lukovnikov A.I. and Novgorodov M.Z.** Sov. Phys. Lebedev Inst. Rep., 1 (1971) 27 – 34.
3. **Golubovskii Y.B., Al Hawat S.H.** Sov. Phys.-Tech. Phys., 32 (1987) 25-28.
4. **Djermanova N., Kiss'ovski Zh., Tsankov Ts.** Contrib. Plasma Phys., 46 (2006) 31-321.
5. **Golubovskii Y.B., Al Hawat S.H., Tsendin L.D.** Sov. Phys.-Tech. Phys., 32 (1987) 760-763.
6. **Petrova Ts., Petrov G.M.** Physica Scripta, 61 (2000) 102-111.
7. **Loffhagen D., Sigeneger F. and Winkler R.** J. Phys. D: Appl. Phys., 35 (2002) 1768–1776.
8. **Andreev S.N., Bernatskiy A.V., Dyatko N.A., Kochetov I.V.,Ochkin V.N.** Plasma Sources Sci. Technol., 30 (2021) 095004.
9. **Andreev S.N., Bernatskiy A.V., Ochkin V.N.** Plasma Chem. Plasma Process., 41 (2021) 659–672.
10. **Andreev S.N., Bernatskiy A.V., Ochkin V.N.** Vacuum, 180 (2020) 109616.
11. **Sigeneger F., Dyatko N.A. and Winkler R.** Plasma Chem. Plasma Process., 23 (2003) 103–116.
12. **Dyatko N.A., Kochetov I.V., Ochkin V.N.,** Plasma Sources Sci. Technol., 29 (2020), 125007.

# TIME-DEPENDENCE OF THE ELECTRON ENERGY DISTRIBUTION FUNCTION IN THE He-Xe AFTERGLOW

G. M. Grigorian[1], A. V. Demyanov[2], N. A. Dyatko[2], I. V. Kochetov[2,3]

[1]St. Petersburg State University, 7-9 Universitetskaya Embankment,199034, St. Petersburg, Russia, galgr2@rambler.ru
[2]SRC RF Troitsk Institute for Innovation and Fusion Research, Pushkovykh street 12, 108840, Troitsk, Moscow, Russia, demyanov@triniti.ru, dyatko@triniti.ru, kochet@triniti.ru
[3]P.N. Lebedev Physical Institute of the Russian Academy of Sciences, Leninskiy Prospekt 53, 119991, Moscow, Russia

In this work, experimental and theoretical studies of the electron distribution function (EEDF) in the afterglow plasma of a glow discharge in a mixture of He + 1.5% Xe were carried out. In addition, the population of the lower metastable Xe($1s_5$) level on the tube axis was measured. A molybdenum glass discharge tubes 25 mm in diameter were used in the experiments. Cylindrical electrodes placed in the vertical branches of the tube were made of tantalum. The distance between the electrodes was 40 cm. The measurements were carried out at a pressure $P$ = 0.5–1 Torr. Spectroscopically pure helium and xenon 95 (99.995%) were used as working gases. The gas mixture was pumped through the tube at a speed of 20–30 cm/s.

The experimental setup made it possible to operate both in the DC discharge mode and in the repetitively pulsed mode. In the DC mode, the high-voltage stabilized source provided a voltage of up to 2 kV, and the discharge current could vary in the range $I_d$ = 10–100 mA. In a repetitively pulsed mode, the current pulse repetition frequency was 2–3 kHz, the pulse duration was up to 400 μs, and the trailing edge of the current pulse was ~2 μs.

The emission spectrum of the discharge positive column in the range of 400–900 nm was recorded using a monochromator with a diffraction grating of 1200 lines/mm. The photomultiplier PMT-106 was used as a photodetector. Optical measurements were carried out in the longitudinal direction, along the axis of the horizontal part of the discharge tube. Using a diaphragm, the radiation of the gas discharge plasma from the axial region was selected.

The population of the Xe($1s_5$) level on the tube axis was measured by the optical absorption method [1], namely, the method of two identical sources [2] was used. The Xe($1s_5$) population was determined from the measured absorption of radiation at the $2p_6 - 1s_5$ transition (wavelength 823.39 nm).

The EEDF was measured with the use of Langmuir probe AC technique [3]. The modulation frequency was 67 kHz. A probe 25 μm in diameter and 3 mm long, made of molybdenum wire, was placed on the tube axis at a distance of 20 cm from the cathode. In probe measurements, the grounded cathode was

used as a reference electrode.

Figure 1 shows the EEDFs measured at $t$ = 5, 20 and 30 μs in the afterglow. The normalization of the measured functions is proportional to the electron density. In the experiments, the absolute value of the electron concentration was not obtained, but using the measured EEDFs, it is possible to calculate the relative change in the electron concentration, $n_e$, with time. According to our estimates, $n_e(t=20\ \mu s)/n_e(t=5\ \mu s) \approx 1.35$ and $n_e(t=30\ \mu s)/n_e(t=5\ \mu s) \approx 1.9$

As can be seen, the low-energy part of the EEDF relaxes to room temperature within ≈ 20 μs. The average electron energy, $\langle u \rangle$, calculated from measured EEDFs is equal to 0.327, 0.046 and 0.04 eV at $t$ = 5, 20 and 30 μs, respectively.

The measured temporal variation of the Xe($1s_5$) population is shown in figure 2. One can see that the population decreases insignificantly within 30 μs.

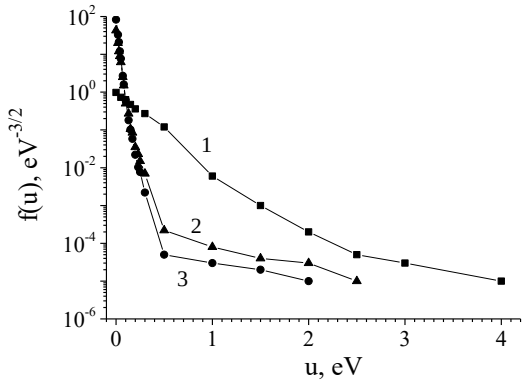



Fig. 1. EEDF measured at different times in the afterglow. $P$ = 1 Torr, $I_d$ = 10 mA. 1- 5, 2 - 20 and 3 - 30 μs.

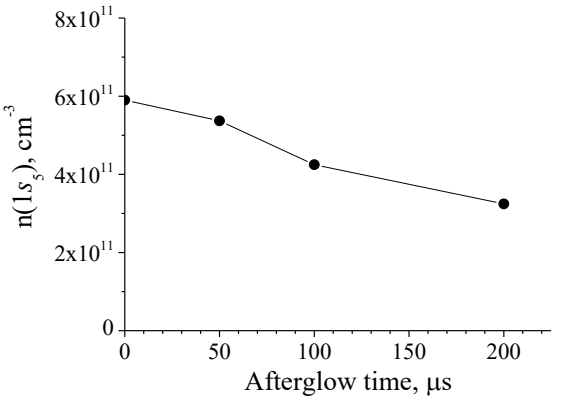



Fig. 2. Xe($1s_5$) population measured in the afterglow. $P$ = 1 Torr, $I_d$ = 10 mA.

The calculation of the EEDF in the afterglow of the discharge in the He+1.5% Xe mixture was carried out by numerically solving the time-dependent Boltzmann equation for the symmetric part of the distribution function. The calculation procedure was as follows. First, the steady-state EEDF was calculated, corresponding to the experimental values of gas pressure and temperature, electric field strength, electron concentration, and population of the lower metastable xenon level. Then, the electric field was assumed to be equal to zero, and the change (relaxation) of the EEDF with time was calculated. The electric field in the discharge plasma at pressure $P$ = 1 Torr and current $I_d$ = 10 mA was estimated to be $E \approx 4.6$ V/cm ($E/N \approx 12.5$ Td, $N$ is the number of atoms per unit volume), the population of Xe($1s_5$) level was taken as $n(1s_5) \approx 6.\cdot 10^{11}$ cm$^{-3}$ (see figure 2), electron concentration (estimated from discharge current and calculated electron drift velocity) was $n_e \approx 10^{10}$ cm$^{-3}$. The following processes

were taken into account in Boltzmann equation: elastic scattering of electrons by atoms, excitation of electronic levels, ionization of atoms by electron impact from the ground state, stepwise ionization from Xe($1s_5$) level, electron-electron collisions, second kind collisions of electrons with excited Xe($1s_5$) atoms. In addition, a term describing the escape of electrons to the tube wall due to ambipolar diffusion process was included in the equation, and a source of electrons with an energy of ~ 4.5 eV, appearing in the chemionization processes $Xe(1s_5)+Xe(1s_5) = Xe^+ + Xe + e$, ($k = 1.9 \cdot 10^{-10}$ $cm^3s^{-1}$ [4]) was specified. The sets of cross sections for electron scattering from atoms were taken from [5–7].

Under discharge conditions, the EEDF was established, at which the equality of the rates of production (ionization of Xe atoms from the ground state, stepwise ionization, chemoionization) and loss (ambipolar diffusion) of electrons was fulfilled. After turning off the electric field, the calculation was carried out under the assumption that the population of Xe($1s_5$) state remains constant at times of ~ 30 μs. This assumption is based on measurements of the population of Xe($1s_5$) state in the afterglow (see figure 2). The EEDFs, the mean electron energy, and the electron concentration calculated under afterglow conditions are shown in figures 3 and 4.

As can be seen from the figure 4, at the very beginning of the afterglow, the electron concentration slightly decreases. This is due to the fact that the rate of electron escape due to ambipolar diffusion is greater than the rate of electron production. Further, with a decrease in the average electron energy, the rate of ambipolar diffusion decreases, and the electron concentration begins to increase due to production of electrons in chemionization processes.

In order to qualitatively compare the experimental and calculated $n_e(t)$ dependences, we assumed that the "experimental" value of the electron concentration at time $t$ = 5 μs is equal to the calculated one. Results of comparison are shown in figure 4. It can be seen that in the experiment, in contrast to the calculation, the electron concentration increases with time.

The calculated values of the average electron energy in the afterglow turn out to be higher than the measured ones (figure 4). The high average energy is due to a source of electrons with energy of 4.5 eV, which appear in chemionization processes. Note that a similar situation was described in [8], where the EEDF was calculated and measured in the afterglow of a glow discharge in neon. The calculated values of the average energy appeared to be much higher than the measured ones, while in the calculations a high average energy was also obtained due to electrons appearing in chemionization processes (with an energy of ~11.5 eV). The authors were unable to explain the significant difference between the experimental and calculated results, but showed that agreement can be achieved if it is assumed that the energy of electrons produced

in chemionization processes is only ~ 0.5 eV. However, such a variation of the electron energy seems to be physically unreasonable.

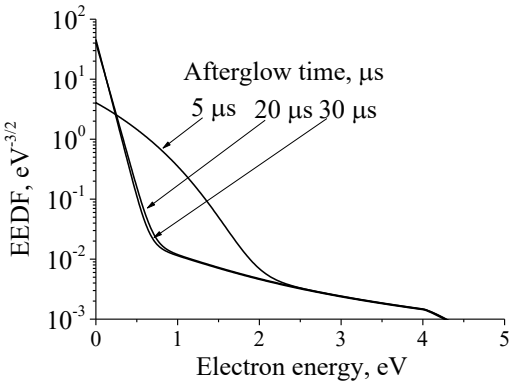



Fig. 3. EEDF calculated at different times in the afterglow.

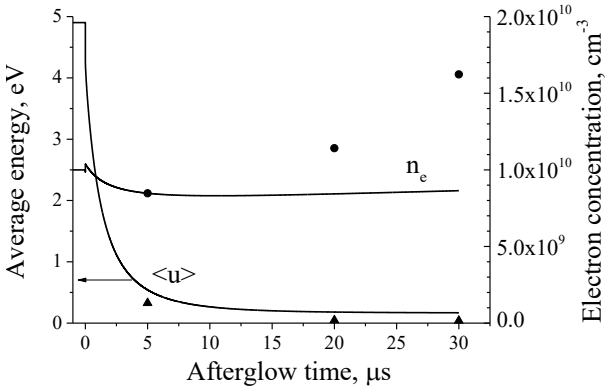



Fig. 4. Calculated (lines) and measured (symbols) average electron energy and electron concentration in the afterglow ($t > 0$).

If the energy of the generated electrons is not reduced, then in order to decrease the average energy in the calculations, it is necessary to reduce the intensity of the electron source due to chemionization processes. This can be done by decreasing the rate constant of the chemionization processes and/or by decreasing the population of the lower metastable Xe($1s_5$) state. The results of such test calculations will be reported at the conference.

**Acknowledgements**. This work was supported by the Russian Foundation for Basic Research, Project No. 20-02-00270.

## References

1. **Grigorian G. M., Demyanov A. V., Dyatko N. A. and Kochetov I. V.** Plasma Physics Reports, 47 (2021) 588–597.
2. **Frish S. E.** (ed) 1970 Spectroscopy of Gas-Discharge Plasmas (Nauka, Leningrad) (in Russian).
3. **Branner G.R., Friar E.M. and Medicus G.** Review of Scientific Instruments, 34 (1963) 231-237.
4. **Kolokolov N. B. and Blagoev A. B.** Physics-Uspekhi, 36 (1993) 152-170.
5. **Sigeneger F., Dyatko N.A. and Winkler R.** Plasma Chem. Plasma Process., 23 (2003) 103-116.
6. **Hayashi** database, www.lxcat.net, retrieved on July 11, 2022.
7. **Hyman H. A.** Phys. Rev A., 20 (1979) 855 – 859.
8. **Bräuer T., Gortchakov S., Loffhagen D., Pfauy S. and Winkler R.** J. Phys. D: Appl. Phys., 30 (1997) 3223 – 3239.

# EMISSION OF CHALCOGENS IN THE DIELECTRIC BARRIER DISCHARGE

S. Avtaeva[1], A. Heneral[2]

[1]Institute of Laser Physics SB RAS, Lavrentieva 15B, Novosibirsk, 630090, Russia, avtaeva_sv@laser.nsc.ru

[2]Institute of Electron Physics, NAS of Ukraine, Universitetska 21, Uzhhorod, 88017, Ukraine, heneral@i.ua

Sources of spontaneous ultraviolet (UV) and visible radiation are rapidly spreading due to the growing interest for their practical application in microelectronics, photochemistry, ecology, agriculture, medicine, and lighting [1, 2]. However, the leading place among the sources of UV radiation is still occupied by mercury-filled lamps [3, 4]. To increase the service life of gas-discharge radiant, it is necessary to develop and study new active media containing less aggressive atoms and molecules. Of course, these radiating media must be efficient in the desirable region of the spectrum. Chalcogens, namely sulfur or selenium, are currently considered as one of the possible options. Discharges in mixtures of noble gases with sulfur vapor make it possible to obtain an emission spectrum close to that of the sun; such a spectrum is due to the emission of sulfur dimers, the band systems of which are approximately at the same distance from each other and merge into a continuous spectrum in the wavelength range of 300–600 nm.

We have already observed the emission of $S_2$ bands in the luminescence of the longitudinal pulse-periodic discharge in mixtures of argon with sulfur vapor [5, 6]. Having developed a 0D model of this discharge, we found that the optimal concentration of sulfur molecules is 0.5%, while their radiation efficiency reaches 1% [6]. Here we present a study of the radiation of a new impulse DBD in mixtures of Ar with chalcogen vapor (sulfur or selenium).

Plasma luminescence based on chalcogen vapors was excited by a pulse-periodic dielectric barrier discharge (DBD) in inert gas argon. The experiments were carried out using the experimental setup, the scheme of which is shown in Figure 1. The choice of the DBD as a method for obtaining low-temperature plasma is because this discharge belongs to low-current discharges and therefore does not cause significant heating of the gas component of the plasma, which important for most practical applications and increases the service life of the discharge device. The presence of a dielectric barrier itself provides a limitation of the amount of electrical energy introduced into the gas discharge during the pump pulse.

High purity (99.999%) sulfur or selenium powder was sprayed onto the inside bottom of the DBD device. The gas-discharge device was evacuated by a

vacuum pump to a residual pressure of 10-1 Pa. Argon was injected from an additional volume. The saturated vapor pressure in the gas-discharge device was set by the temperature of the quartz bulb walls, which was determined by the discharge energy dissipated on the walls and was measured by the Pt-Pt+Rh thermocouple.

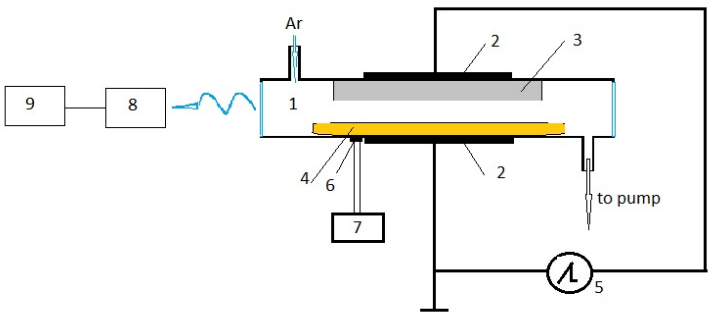



Fig. 1. The experimental setup of the pulse-periodic discharge in argon-chalcogen vapor. 1 – discharge tube, 2 – electrodes, 3 – ceramics, 4 – sulfur (selenium) powder, 5 – impulse power source, 6 – thermocouple, 7 – millivoltmeter, 8 – spectrometer, 9 – computer.

The longitudinal DBD in the gas-discharge device was excited using a thyratron generator with a switch and resonant recharging of the working capacitance. A high-voltage impulse power supply of the discharge provided an impulse voltage of up to 10 kV, a pulse repetition rate from a few Hz to 10 kHz, an average current of up to 1 A, and a maximum output power of up to 2.5 kW.

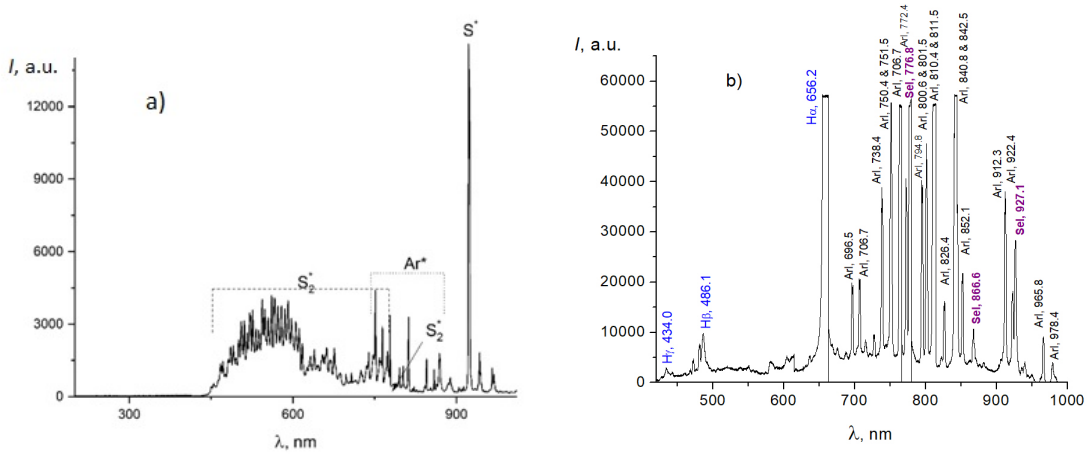



Fig. 2. Typical spectra of the pulse-periodic barrier discharge in mixtures of argon with a) sulfur and b) selenium vapor at $U$= 3 kV, $f$= 5 kHz, $P_{total}$= 300 Torr and $I$= a) 0.08 A, b) 0.1 A.

The radiation was output through quartz windows transmitting up to 85% of the radiation at a wavelength of 200 nm. The spectral characteristics of the

pulse-periodic barrier discharge were recorded using a Solar TII MS 7504i monochromator and a PMT R928 photomultiplier. The spectral resolution in our experiments did not exceed 0.1 nm.

The emission spectrum of the DBD in a mixture of argon with sulfur vapor contains intense bands of $S_2$ sulfur molecules ($B^3\Sigma \rightarrow X^3\Sigma$ transition) in the visible region (Fig. 2a). In the long-wavelength region of the spectrum (700-1000 nm), radiation of argon and sulfur atoms is also observed. The intensity of $S_2$ bands increases almost linearly with increasing frequency of the impulse voltage. An increase in the argon pressure also contributes to an increase in intensity of $S_2$ emission. However, as the pressure increases above 300 Torr, the intensity of the bands of sulfur molecules decreased with increasing pressure.

In the emission spectrum of the DBD in a mixture of argon with selenium vapor lines of atomic hydrogen (Balmer series) are observed in the visible region of the spectrum, indicating the presence of a small amount of water vapor in the mixture (Fig. 2b). In the wavelength range from 696 to 1000 nm, the spectrum contains lines of argon and selenium atoms. The bands of selenium molecules scattered along the spectrum in the wavelength range from 400 to 1000 nm and apparently belong to large $Se_n$ molecules ($n>2$). We did not find a clear presence of selenium dimer bands ($Se_2$) in the spectrum. The intensity of the bands of selenium molecules increases with increasing frequency of the impulse voltage only up to 4 kHz, then saturation of the intensity is observed.

In general, it should be noted that the main part of the discharge radiation in mixtures of argon with sulfur vapor falls on the region from 450 to 800 nm, while the main discharge radiation in mixtures of argon with selenium vapor falls on the region of 700-1000 nm. Therefore, we believe that the discharge in mixtures of argon with sulfur vapor is more promising for creating radiation sources compared to the discharge in mixtures of argon with selenium vapor.

To study processes in the asymmetric pulse-periodic DBD in mixtures of argon with sulfur vapor we developed the 1D fluid model of a DBD in $Ar–S_2$ mixture based on continuity equations for electrons and positive and negative ions under the assumption of a local electric field, balance equations for neutral components, the Poisson's equation, and equation for the external electric circuit. Seven charged species, and nine neutral species coupled via 37 reactions were considered in the model [7]. The discharge was simulated in a 4-mm-long discharge gap between 2-mm glass layer ($\varepsilon=4$) covered the grounded electrode and 5-mm ceramic layer ($\varepsilon=50$) covered the powered electrode. Gas pressure was 100 Torr; $S_2$ content in $Ar\text{-}S_2$ mixture was 0.5%. Source voltage pulse had maximum value of 5-7 kV, rise time of ~40 ns and duration ~100 ns.

Figure 3 shows spatiotemporal behaviors of the mean electron energy and the electron number density in the asymmetric pulse-periodic DBD in the $Ar\text{-}S_2$ mixture. As one can see the power mainly released in first 150-200 ns. During

this time interval the electron number density in the discharge gap fluctuates and reaches almost $1.5\times10^{18}m^{-3}$, after which it falls up to $10^{17}m^{-3}$ and lower. The mean electron energy is maximal in very narrow layers near dielectrics, where it reaches 8–9 eV. Simulations show that during voltage pulse the DBD plasma is electropositive and electron number density is high over the entire discharge gap. After voltage pulse plasma become electronegative due to fast attachment of electrons to sulfur molecules. Modeling showed that the radiative efficiency of $S_2$* molecules in the asymmetric pulse-periodic DBD is several times higher compared with the conventional DBD (<1% [7]) and during voltage pulse it reaches 4%. The radiation of $S_2$ molecules dominates during voltage pulse, and the emission of Ar atoms is prevalent after voltage pulse when power is small. Radiation of other excited species is very small.

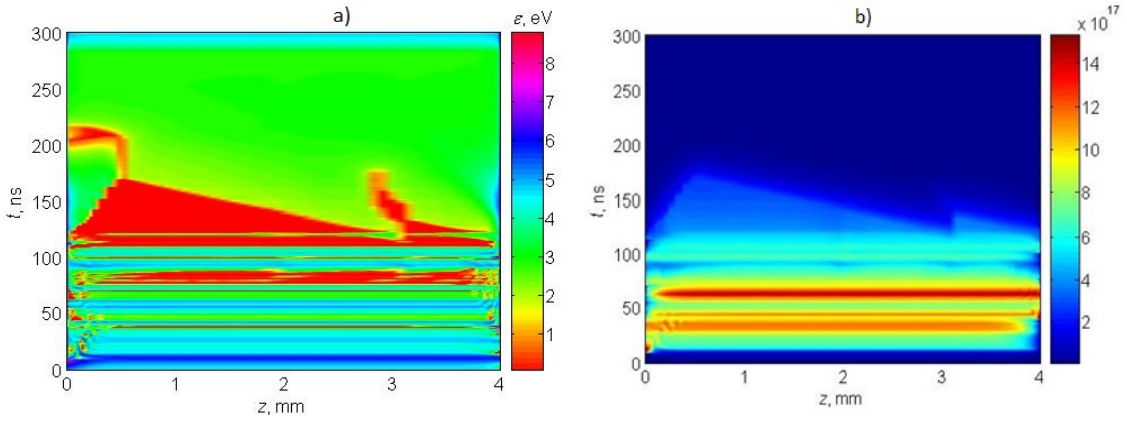



Fig. 3. Spatiotemporal behavior of (a) the mean electron energy and (b) the electron number density (in $m^{-3}$) in the asymmetric pulse-periodic DBD in the Ar-$S_2$ mixture.

**Acknowledgements**. The work was supported by the National Academy of Sciences of Ukraine, scientific project "Physical-chemical processes and emission properties of low-temperature gas-discharge plasma on sulfur, selenium and tellurium vapors" (2020–2022).

## References

1. **Pollak J. et al.** *J. Phys. D: Appl. Phys*. 41 (2008) 135212.
2. **Lerouge S. et al.** *Plasmas and Polymers*. 6 (2001) 175.
3. **Gross U. et al.** *J. Phys. D: Appl. Phys.*, 33 (2000) 1588.
4. **Baeva M., Reiter D.** *PCPP,* 23 (2003) 371.
5. **General A.A. et al.** *J. Appl. Spectrosc.,* 83 (2016) 598.
6. **Avtaeva S.V. and Heneral A.A.** *PCPP*, 40 (2020), 839.
7. **Avtaeva S.** *PCPP*, 41 **(**2021) 1059.

# THE USE OF AB-INITIO GENERATED PSEUDO POTENTIAL FOR COMPUTATION OF OPTICAL PROPERTIES IN DENSE PLASMA IN CUT-OFF COULOMB POTENTIAL, HELIUM CASE

N. M. Sakan[1], Z. J. Simić[2], V. A. Srećković[1]

[1]Institute of Physics, Belgrade University, Pregrevica 118, 11080 Zemun, Belgrade, Serbia
[2]Astronomical Observatory, Volgina 7, 11060 Belgrade, Serbia

The cut-off Coulomb potential was used up until now for the describing dense plasma optical characteristics. The model itself is a fully quantum mechanics model for describing plasma. Usage of numerical calculation methods makes it possible to use more complex pseudo potentials in describing plasma. Up until now the calculated results are used for the describing dense plasma characteristics primary in the case of astrophysical plasma. The step forward was carried out by using a pseudo potential that posses ionic core, in case of Ar atom. Since the Ab-initio potential is mature method for describing solid state characteristics of atoms, the possibility of using them as a basis for the potentials that could be used in describing plasma up to the metal densities has arise. In the presented paper the investigation of the use of the potential for the helium atom is presented.

**Introduction.** Dense plasma is a object of interest in recent years [1]. Up until now the absorption coefficients of hydrogen plasma, were calculated within the frame of cut-off Coulomb potential model, for the wide area of electron densities and temperatures [2-9]. The optical parameters of hydrogen plasma of mid and moderately high non-ideality parameter are described successfully, thus enabling the modeling of optical properties [2,3], [5-9]. Governed by this results a effort has been made to introduce a extension of a model towards the more complex atoms. As a first goal the Ar atom model was used since the ionic core model potential for the Ar I was analyzed in [10]. As it was case with the hydrogen model here, the model potential for Ar is solvable in entire space and within entire energy spectrum, thus the yielded wave function solutions are a combination of a special functions. As it was proven a faster, and no less reliable, method of numerical integration using a Numerov integration is used. It posses a fast convergence and as such is preferred method for introduction of more complex atom and ion model potentials in consideration, the comparison and application is shown in [11]. Further development that is in progress in focused on the application of the pseudopotentials calculated with the help of Opium ab-initio software [12] presented in the Perdew-Burke-Ernzerhof GGA pseudopotential database [13]. As it was presented on PDP 2020 conference [14], the need for more precise potentials for describing complex component

dense plasma is needed. The presented ionic core potential for Ar yielded a good, expected results. The check of applicability of GGA pseudopotentials is done and should be presented on PDP 2022 conference [15].

**Theory.** As it was presented in previous papers, the reduced radial part of Schrodinger equation simplified by the applied transform $P(r)=rR(r)$ is used here

$$\frac{-\hbar^2}{2m}\frac{d^2}{dr^2}P_{nl}(r)+\left[V(r)+\frac{\hbar^2 l(l+1)}{2mr^2}-E_{nl}\right]P_{nl}(r)=0. \qquad (1)$$

The dipole matrix element, $\hat{D}(r;r_0;r_c;n_i l_i;n_f l_f)=\langle n_f l_f|r|n_i l_i\rangle$ is calculated numerically with the usage of Numerov method. The used pseudopotential is presented in Figure 1., it could be seen that the potential goes to constant value in the vicinity of radial axis origin, while on the other end, with enlarging of the radius goes to the other limiting value, the adequate Coulomb potential, in this case ionic core sees charge Z = 2. The plasma influence is described by the cutting-off of the potential or pseudopotential on the cut-off radius $r_c$:

$$U(r)=\begin{cases} U^0+1/r_c & :r\leqslant r_c \\ 0 & :r>r_c \end{cases} \quad \text{where} \quad U^0 \ \texttt{is the adequate potential.}$$

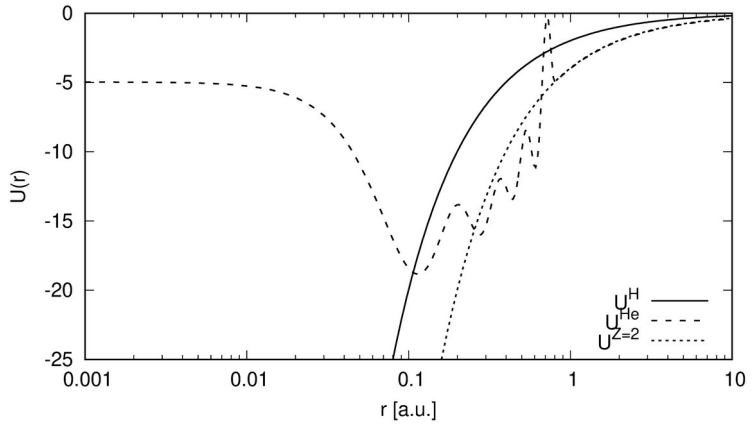



**Figure 1.** The potentials, solid line hydrogen, short dash Coulomb Z=2, short dash He pseudopotential.

**Results and discussion.** The small set of calculated wave function are presented in Figure 2. Based on this wave functions a set od dipole matrix elements are calculated. The check of the quality of describing the He atom and He ion in plasma should be judged upon the comparison of the calculated values of the

transition oscillator strengths with the experimental ones. This is a work in progress.

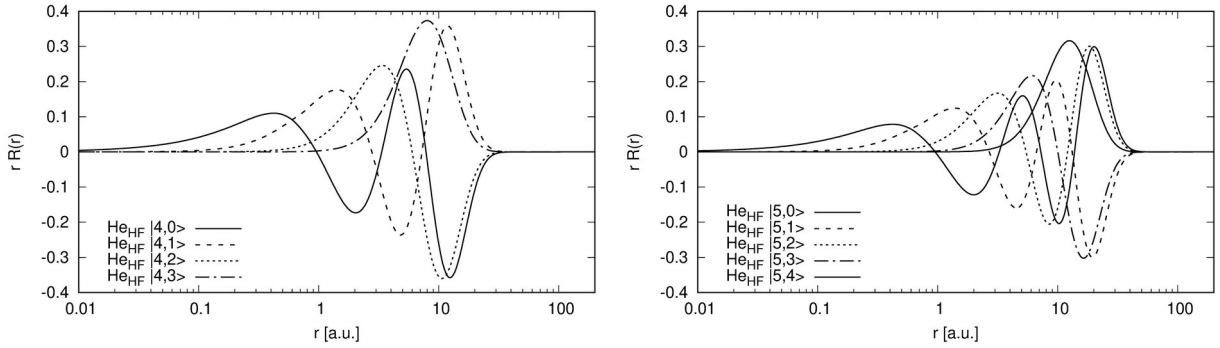



**Figure 2.** The example of some of the realized wave functions calculated with the usage of He pseudopotential from [13].

**Conclusion.** The presented results, as well as research presented in [15] is a step forward towards a describing more complex atoms in plasma as well as mixtures of atoms in plasma. The possibility of calculating pseudopotentials with the help of ab-initio procedures are leading a possibility to describe a complex atoms in plasma as well as complex composition plasmas and steps towards this goal should be made. This kind of approach enables the possibility to consider the core with valence electrons densities functions as a model for entering the molecular dynamics code for simulating a plasma influence. There is a need for further check of dipole matrix elements by the comparison of oscillator strengths with known experimentally observed transitions, and when proven the potential could be used for further research.

**Acknowledgements**. The research was funded by the Ministry of Education, Science and Technological Development of the Republic of Serbia, Contract: **451-03-68/2022-14/200024** and **451-03-68/2022-14/200002**.

## References

1. **Fortov, V.E., Iakubov, I.T.** // The physics of non-ideal plasma / World Scientific, 1999.
2. **Mihajlov, A.A., Sakan, N.M., Srećković, V.A., Vitel, Y.** // Modeling of continuous absorption of electromagnetic radiation in dense partially ionized plasmas. J. Phys. A (2011), 44, 095502.
3. **Mihajlov, A.A., Ignjatović, L.M., Srećković, V.A., Dimitrijevi´c, M.S., Metropoulos, A.** // The non-symmetric ion-atom radiative processes in the stellar, atmospheres, Mon. Not. R. Astron. Soc. 2013, 431, 589–599.
4. **Mihajlov, A.A., Djordjević, D., Popović, M.M., Meyer, T., Luft, M., Kraeft, W.D.** // Determination of the Electrical Conductivity of a Plasma

on the Basis of the Coulomb cut-off Potential Model., Contrib. Plasma Phys., 1989, 29, 441–446.
5. **Ignjatović, L.M., Srećković, V.A., Dimitrijević, M.S.** // The Screening Characteristics of the Dense Astrophysical Plasmas: The Three-Component Systems., Atoms, 2017, 5, 42.
6. **Mihajlov, A.A., Sakan, N.M., Srećković, V.A., Vitel, Y.** // Modeling of the Continuous Absorption of Electromagnetic Radiation in Dense Hydrogen Plasma., Balt. Astron., 2011, 20, 604–608.
7. **Mihajlov, A.A., Srećković, V.A., Sakan, N.M.** // Inverse Bremsstrahlung in Astrophysical Plasmas: The Absorption Coefficients and Gaunt Factors., J. Astrophys. Astron., 2015, 36, 635–642.
8. **Sakan, N.M., Srećković, V.A., Mihajlov, A.A.** // The application of the cut-off Coulomb potential for the calculation of a continuous spectra of dense hydrogen plasma., Mem. S. A. I. Suppl., 2005, 7, 221–224.
9. **Sakan, Nenad M. and Srećković, Vladimir A. and Simić, Zoran J. and Dimitrijević, Milan S.** // The Application of the Cut-Off Coulomb Model Potential for the Calculation of Bound-Bound State Transitions, Atoms, 2018, 6, 1, 4
10. **A. Mihajlov and D. Djordjević and M.M. Popović** // The inner charge defect method as an analog to the quantum defect method, JQSRT, 1980, 47-52, https://doi.org/10.1016/0022-4073(80)90040-0
11. **Nenad M. Sakan, Zoran J. Simić, and Momchil Dechev** // The optical properties of Hydrogen plasma described in the frame of the fully quantum method based on a cut-off Coulomb model potential, 16th ESPM - European Solar Physics Meeting, 6-10 September 2021, online
12. http://opium.sourceforge.net/sci.html
13. https://www.sas.upenn.edu/rappegroup/research/pseudo-potential-gga.html
14. **Sakan N. M. and Simić Z. J.**, The introduction of more complex atoms in a cut-off Coulomb model potential, the Ar I model, PDP 2021.
15. **Sakan Nenad M., Simić Zoran J. and Srećković Vladimir A.**, The pseudo potential usage for calculation of optical properties in case of hydrogen atom in plasma, PDP 2022. (to be presented).

# PLASMA DENSITY SENSOR ON MICRO- AND NANOSATELLITES

A. Galka[1], A. Kostrov[2], M. Malyshev[3], I. Vershinin[4]

[1, 2, 3, 4] Federal research center Institute of Applied Physics of the Russian Academy of Sciences, 46 Ul'yanov Street, Nizhny Novgorod, 603950, Russia
[1]galasnn@ipfran.ru, [2]kstr@ipfran.ru, [3]malyschev@ipfran.ru, [4]i.vershinin@ipfran.ru

The investigation of the non-stationary and inhomogeneous structure of the ionosphere is the most important fundamental problem in space plasma physics. Monitoring of the concentration of ionospheric plasma and its disturbances is extremely important for the functioning of modern technological communication systems, navigation, global positioning, radar, energy, space technology [1], the development of methods for forecasting "space weather" [2], the study of plasma-wave effects accompanied by fluctuations in electron concentration [3].

Taking into account the development of miniaturization technology in the last decade, there has been an explosive growth in the number of launches of micro- and nanosatellites capable of fully solving problems of studying the ionosphere [4]. For the possibility of installing diagnostics on the platform of small and ultra-small spacecraft, important requirements for the developed equipment are small dimensions and weight, low power output, low cost, and the ability to work in continuous mode. Among the traditionally used satellite diagnostics of ionospheric parameters, the Langmuir probe should be singled out. Despite the simplicity of the design, interpretation of the probe readings on small spacecraft is complicated by many factors.

The IAP RAS has developed a new probe technique for studying the concentration of the Earth's ionospheric plasma and its fluctuations in the range of $10^3 - 10^6$ cm$^{-3}$ on board micro- and nanosatellites with an orbit height of about 500 km. The sensor operation is based on the method of a probe with a microwave resonator successfully used to measure the concentration of laboratory plasma, made on a quarter-wave segment of a two-wire line shorted at one end and open at the other end [5]. The excitation of the resonator and the removal of its response is carried out by magnetic coupling loops near the shorted end. The eigenfrequency $f$ of a resonator depends on the dielectric constant of the medium $\varepsilon$ in which it is immersed. Knowing the frequency in plasma $f$ and without plasma $f_0$, one can find $\varepsilon$ and, accordingly, the electron concentration $N_e$. As part of the development of the technique, a laboratory model of the resonator of the plasma density sensor (PDS) was made. Length 40 cm, eigenfrequency 180 MHz, quality factor 220. The resonator is brought out of the transport (folded) state into the working position by means of an axial opening assembly due to a spring mechanism. Figure 1 shows a 3-D model of

the measuring device. The weight of the resonator is not more than 0.2 kg.

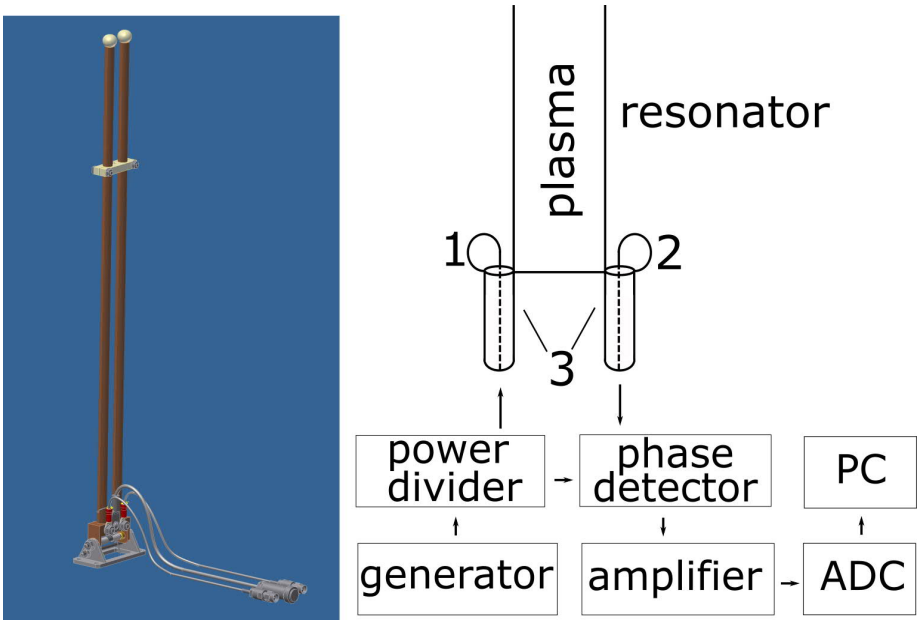



Fig. 1. Left: 3-D model of the plasma parameters sensor resonator with the open end. Right: block diagram of the amplitude-phase method. 1 and 2 - exciting and receiving magnetic loops, 3 - connecting coaxial cables

With the standard method of measuring by the shift of the resonance maximum, it is necessary that the frequency shift exceed the width of the resonance curve determined by the quality factor $Q$. Then, to determine the low plasma density $N_e \sim 10^3$ cm$^{-3}$, a probe with a length of more than 20 m is needed, which is unacceptable on microsatellites.

The paper proposes to use the amplitude-phase method [6], which allows reducing the minimum value $N_e$ by three orders of magnitude without increasing the resonator length. The probe operates at a fixed frequency corresponding to the eigenfrequency of the resonator without plasma, and small frequency shifts are fixed by means of the amplitude-phase characteristics of the resonator. It should be noted that this method was previously successfully tested for determining the pressure of gases in the range from 0.1 Torr to 1 atm [7]. The essence of the method is to measure the phase shift of the signal that has passed through the resonator with plasma. The signal from the generator $U_G$ is divided into two equal ones, one of which is connected to the excitation loop of the resonator by means of a coaxial cable, and the second one is supplied to the phase detector as a reference. The signals from the receiving communication loop $U_0$ and the reference one are mixed at the phase detector that generates an output signal $U$ depending on the phase difference $\Delta\varphi$ between $U_G$ and $U_0$: $U = k \cdot U_0 \cdot \sin(\Delta\varphi)$, where $k$ is the coefficient that takes into account the

attenuation in the connecting wires and the gain of the final low-frequency stage. The phase shift $\Delta\varphi$ was determined by the length of the connecting cables and the plasma concentration $N_e$ in the resonator. An electrodynamic model of the measuring system has been developed for the connection between $\Delta\varphi$ and $N_e$. The amplitude-frequency and phase-frequency characteristics of the resonator were obtained by converting the original distributed system to an equivalent circuit with concentrated parameters. The calibration dependence of the output signal from the sensor $U(N_e)$ was also obtained.

The use of the amplitude-phase method is justified in the case when the total Q-factor of the measuring system does not depend on plasma losses. Estimates show that the main contribution to the Q-factor is made by losses due to the coupling of the resonator with the exciting and receiving communication lines, and the collisional losses in the plasma are negligibly small.

The sensor was tested at the *Ionosphere* plasma stand, designed to simulate electrophysical processes in the ionized shells of the Earth, including plasma tests of space technology samples. The stand is a cylindrical vacuum chamber 1.5 m long and 1.2 m in diameter. The plasma was created by an induction RF discharge in an argon atmosphere at a pressure of $3.5 \cdot 10^{-3}$ Torr in a weak magnetic field. The electron concentration during the breakdown reached a maximum value of the order of $10^{12}$ cm$^{-3}$ and decreased after switching off the source to the background level. All experiments were carried out in a decaying plasma after the source was switched off. The probe was installed in the center of the chamber. The good repeatability of the discharge parameters in a wide range of values allowed to test PDS under conditions as close to ionospheric.

Figure 2 shows the time dependence of the decaying plasma concentration. At times $t > 80$ ms, values $N_e$ in the $10^3 - 10^6$ cm$^{-3}$ range were restored using the amplitude-phase method, and at $t < 80$ ms in the $10^6 - 10^8$ cm$^{-3}$ range, by the classical method - by shifting the maximum of the resonance curve. The total range of measured values was five orders of magnitude. The linear dependence of the decrease in concentration with time on a logarithmic scale corresponded to the unchanged parameters of longitudinal ambipolar diffusion over a wide time interval, which testified to the correctness of the developed method. The minimum plasma concentration was $10^3$ cm$^{-3}$.

The diagnostics will make it possible to study small-scale spatial inhomogeneities of the plasma density up to 8 m in size. The high sensitivity of the PDS will allow us to detect small perturbations in the plasma density of the order of $\delta N_e / N_e \sim 10^{-3}$, associated with wave processes in the ionosphere, in a wide frequency range up to 1 MHz.

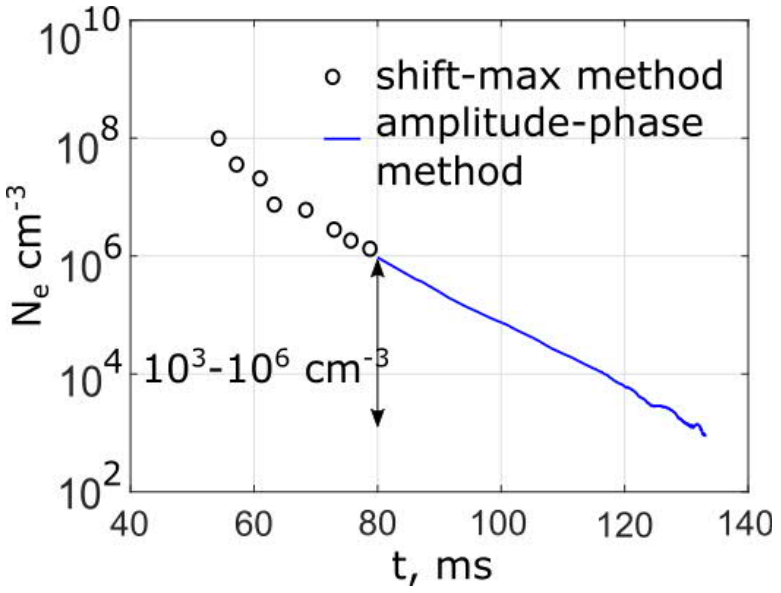



Fig. 2. The test of the plasma parameters sensor at the *Ionosphere* device: the time dependence plasma concentration after turning off the source (t=0). The solid curve is the data obtained by the amplitude-phase method, the discrete - the shift-max method

The results will form the basis for experimental design work on the creation of a set of scientific equipment for the diagnosis.

**Acknowledgements**.

This work was supported by the Russian Science Foundation, Project No. 22-22-20093.

**References**

1. **Petrov A.A., Cherniak I., Krankowski A., Zakharenkova I.** Radio Sci. V. 49, № 8 (2014), 653—662.
2. **Parrot M., Berthelier J.J., Lebreton J.P., Sauvaud J.A., Santolik O., Blecki J.** Physics and Chemistry of the Earth. V. 31, № 4 (2006), 486–495.
3. **Zaboronkova T.M., Kostrov A.V., Kudrin A.V., Tikhonov S.V., Tronin A.V., Shaikin A.I.** JETP.V. 75, № 4 (1992), 625-632.
4. **Petrukovich A.A., Nikiforov O.V.** Rocket-Space Device Engineering and Information Systems. V. 3, № 4 (2016), 22-31.
5. **Stenzel R. L.** Rev. Sci. Instrum. V. 47, № 5 (1976), 603-607.
6. **Galka A.G., Yanin D.V., Kostrov A.V., Priver S.E., Malyshev M.S.** J. Appl. Phys. V. 125, № 12 (2019), 124501.
7. **Yanin D.V., Galka A.G., Kostrov A.V., Priver S.E., Smirnov A.I.** Applied Physics. № 1 (2017), 74-80.

# AMPLITUDE-TIME DYNAMICS OF RADIATION OF LASER-EMISSION PLASMA OF METALS FORMED BY DUAL NANOSECOND PULSES

N. Kuryan, S. Anufrik, K. Znosko

Yanka Kupala State University of Grodno, Ozheshko 22, 230023, Grodno, Belarus
kurian90@mail.ry

Determination of the elemental and chemical composition of a substance is one of the most important components of modern science, technology and industry. One of the promising methods of chemical analysis is the method of laser emission spectral analysis (LIBS) [1].

The use of a two-pulse mode of excitation of the objects under study significantly expanded the analytical capabilities of the LIBS method [2–3]. A significant increase in the intensity of spectral lines was explained by various physical mechanisms. A number of models of the process of substance ablation using various types of lasers have been proposed in the literature [4]. In [5-7], a review of models of the process of interaction of laser radiation with matter is presented, and the main factors affecting the amplification of the analytical signal during two-pulse excitation are indicated.

The aim of this work is to study the influence of the energy of doubled laser pulses and the time delay between them on the radiation of laser emission plasma of metals.

The objects of study were metals: Al, B, Bi, C, Cr, Cu, In, Pb, Ti, Zn. The study of the radiation of laser emission plasma of metals was carried out on a laser emission spectrum analyzer [8].

The radiation of a YAG:$Nd^{3+}$-laser with a pulse duration of ~15 ns was focused onto the samples of the above metals. Under the influence of laser radiation, a laser-emission plasma was formed on the sample under study, the spectral and temporal characteristics of which were recorded.

Figure 1 shows oscillograms of the integral emission of metal laser-emission plasma obtained at a single laser pulse energy of ~21.4 mJ. The duration of laser-emission plasma radiation for all studied metals (at the level of 0.4) is within 200 ns. The exception is Ti. The duration of the radiation of its laser-emission plasma is about 400 ns.

A feature of the presented results is that the durations indicated above characterize the radiation of the front of the laser-emission torch. At this time, the expansion rate of the plasma torch is maximum. The plasma itself is highly nonequilibrium. Its electron temperature is tens of thousands of degrees, and the spectrum is dominated by Planck radiation. The obtained durations of laser-emission plasma radiation correspond to peaks at the pulse front given in [9].

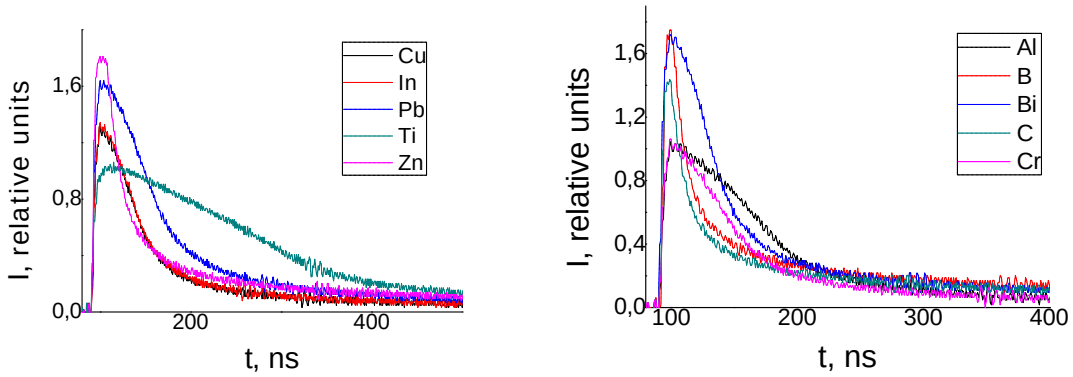



Fig. 1 - Integral glow of laser emission plasma of metals

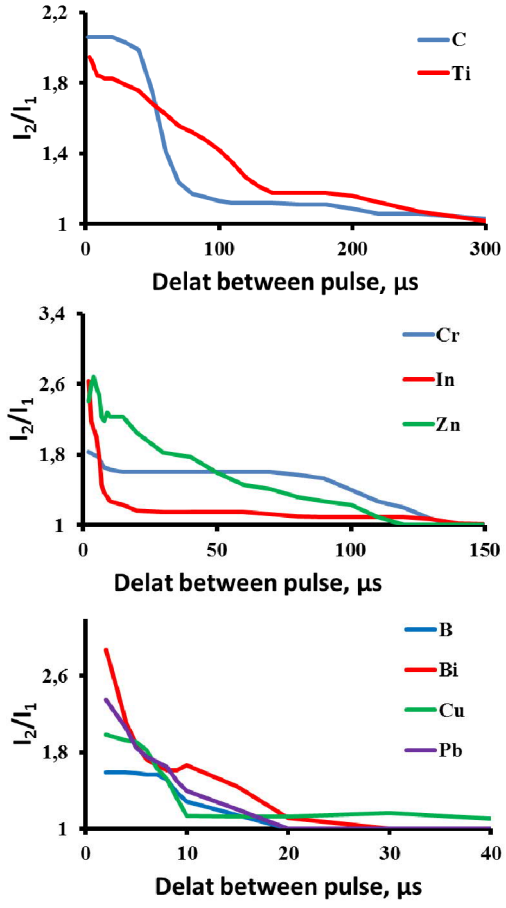



Fig. 2 – Ratio (I2/I1) vs. delay between dual laser pulses

In the case of two-pulse formation of laser-emission plasma, the intensity of its radiation increases significantly [2, 7]. An increase in the intensity of its radiation is provided by an increase in the radiation of the plasma formed by the second laser pulse. This is due to various physical mechanisms. The most significant are: the presence of a high temperature of the erosion crater [10-11] and the interaction of plasma torches formed by paired laser pulses [12].

Figure 2 shows the dependences of the ratio of the radiation intensity of the plasma plume formed by the second laser pulse to the radiation intensity of the plasma plume formed by the first laser pulse ($I_2/I_1$) on the delay between them. The delay values varied from 1 μs to values when $I_2/I_1$~1. It was assumed that at $I_2/I_1$~1, the plasma formed by the first laser pulse had no significant effect on the glow of the plasma formed by the second laser pulse, or these influences were multidirectional and compensated. It was found that $I_2/I_1$~1 for Cr is – 130 μs, Zn - 110 μs, In - 140 μs, C - 300 μs, Ti - 250 μs, B - 1 μs, Bi - 20 μs, Cu - 40 μs, Pb - 15 μs.

Studies were carried out on the effect of the energy of the second laser pulse on the emission intensity of a number of spectral lines of aluminum, with a

two-pulse formation of a laser-emission plasma. Figure 3 shows oscillograms of the emission of the spectral line Al I (393.5 nm) obtained with the energy of the first laser pulse equal to ~10.9 mJ and the energy of the second laser pulse varying in the range of 5.8 – 21.4 mJ. It can be seen that as the energy of the second laser pulse increases, the amplitude and duration of the spectral line caused by the first pulse do not change. The amplitude and duration of the same spectral lines of aluminum due to the second laser pulse increases.

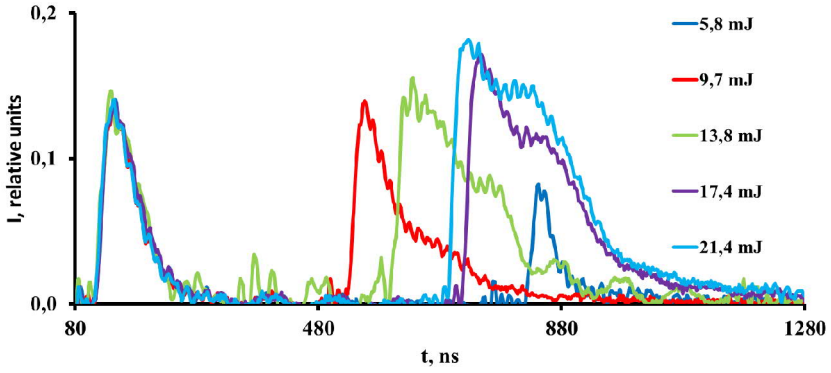



Fig. 3 - Oscillograms of the emission of the spectral line Al I (393.5 nm) at the energy of the first pulse 10.9 mJ

Figure 4 shows oscillograms of the emission spectral line of the Al I (393.5 nm) obtained with the energy of the first laser pulse varying in the range 10.9 – 31.8 mJ and the constant energy of the second laser pulse equal to 10.9 mJ. It can be seen that as the energy of the first laser pulse increases, the amplitude and duration of the spectral line due to the first pulse increase. The amplitude and duration of the spectral line due to the second laser pulse also increase, although its energy does not change. This is due to an increase in the temperature of the crater, after the action of the first laser pulse, with an increase in the energy of the first pulse.

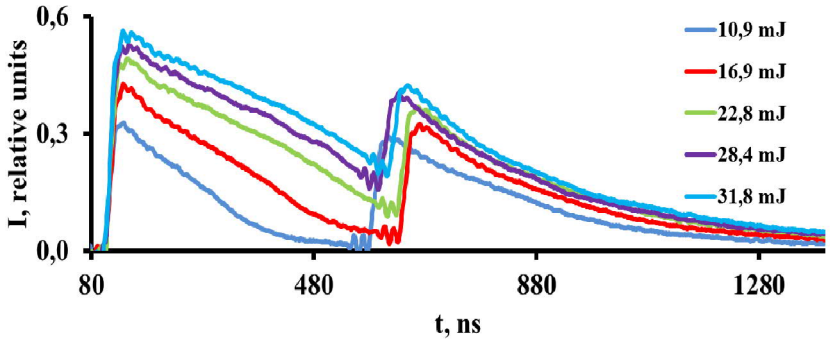



Fig. 4 - Oscillograms of the emission of the Al I spectral line (393.5 nm) at a second pulse energy of 10.9 mJ

Thus, it is shown that the glow of the laser emission plasma of metals (Al, B, Bi, C, Cr, Cu, In, Pb, Ti, Zn) has an individual duration.

## References


1. **Kremers D., Radiemski L.** Laser-spark emission spectroscopy Moscow, Technosphere (2009) 92-115.
2. **Pershin S.M.** Quantum Electronics, 39 (2009) 63-67.
3. **Burakov V.S., Bohonov A.F., Nedelko M.I., Tarasenko N.V**. Quantum Electronics, 12 (2003) 1065-1071.
4. **Ershov-Pavlov E.A., Katsalap K.Yu., Stepanov K.L., Stankevich Yu.A.,** Spectrochim. Acta Part B., 10 (2008) 1024–1037.
5. **Corsi M., Cristoforetti G., Giuffrida M., Hidalgo M., Legnaioli S., Palleschi V., Salvetti A., Tognoni E., Vallebona C.** Spectrochim. Acta, Part B, 59 (2004) 723-735.
6. **Hahn D.W., Omenetto N.** Applied Spectroscopi., 4 (2012) 347–419.
7. .**Anufrik S.S., Kuryan N.N., Znosko K.F.**, **Belkov M.V.** Journal of Applied Spectroscopy, 85 (2018) 285-292.
8. **Anufrik S.S., Znosko K.F., Kuriyan N.N.** Vesnik of Yanka Kupala State University of Grodno. Series 2. Mathematics. Physics. Informatics, Computer Technology and Control, 3 (2015) 83-92.
9. **Kuriyan N.N., Znosko K.F., Grigut V.V.** Vesnik of Yanka Kupala State University of Grodno. Series 2. Mathematics. Physics. Informatics, Computer Technology and Control, 2 (2018) 101-110.
10. **Znosko K.F.** Vesnik of Yanka Kupala State University of Grodno. Series 2. Mat..Phys..Inform.,Computer Technol. and Contr., 1 (2021) 94-106.
11. **Znosko K.F. and Leshchyk S.D.** Vesnik of Yanka Kupala State University of Grodno. Series 6. Engineering Science, 1 (2021) 45-58.
12. **Znosko K.F.** Vesnik of Yanka Kupala State University of Grodno. Series 2. Mat..Phys..Inform.,Computer Technol. and Contr., 2 (2020) 103-115.

# MATHEMATICAL MODELING OF PARTICLE FLUX FORMATION PROCESSES IN A REACTIVE ION-PLASMA ETCHING SYSTEM AT LOW PRESSURES

**A.V. Abramov[1], E. A. Pankratova[2]**

[1]Voronezh state technical University, 394006, 20th anniversary of October, 84,Voronezh, Russia abramovvgasu@yandex.ru
[2]MTRC AF «AFA named after Prof. N.E. Zhukovsky and Yu.A. Gagarin», 394052, Krasnoznamennaya str., 153/4, Voronezh, Russia.

The anisotropy of reactive ion-plasma etching (RIE) is mainly associated with the presence of directed ion bombardment. At the same time, there are practically no reports on the development of methods for increasing the directivity of RIE by controlling the flows of uncharged chemically active particles (ChAP). It is generally assumed that these particles move isotropically in the discharge chamber (DC), which is true in the case of the diffusion mode of their motion. The purpose of the presented work is to show the possibility of influencing the characteristics of ChAP and ion fluxes by changing the DC design under the condition of particle motion in a mode close to free molecular. In this case, ChAP should fall on the etching surface mainly after reflection from the DC walls, the probability of sticking to which ($k_s$) for them is much less than one. On the contrary, positively charged ions should get to the etching surface directly from the places of their formation in the plasma volume. Particle fluxes were calculated for a diode-type DC with a height of L and a radius of R. A rectangular groove of length T, width $l_g$ and depth H such that T >> $l_g$ and H, and L and R >> T served as an element of the surface on which the particles arrived. As an initial condition, it was assumed that the density of the flow reflected from the DC surface, ChAP (γ), is the same for all its points. In this case, the density of the flow ChAP (j) entering an arbitrary point A of the groove surface from the surface DC, provided their diffuse reflection within the solid angle 2π is expressed as

$$j = \frac{\gamma}{2\pi} \iint_S \frac{\cos\alpha}{\rho^2} dS, \qquad (1)$$

where ρ - the distance from point A to the element ΔS, α - the angle between the normal to the surface at this point ($\bar{n}$) and the direction ρ. This formula is valid provided that the linear dimensions of the element ΔS are much smaller than ρ.

*Calculation of ChAP flows*. To find the resulting density of the ChAP flow entering point A, integration was carried out along the part of the DC surface visi-

ble from this point. The calculation of j was performed in cylindrical coordinates separately for the walls of DC ($j_w$) and for the potential electrode ($j_e$). The integral (1) in our conditions was not analytically calculated in general, but was reduced to an elliptic one. Therefore, the construction of graphs was carried out using a computer. Figure 1 shows the distribution of the ChAP flux density over the surface of the electrode with the plate being processed. It can be seen that at R > L there is a maximum in the center and two minima at the edges, and at R < L there is only one minimum in the center of the electrode, due to the receipt of ChAP from the walls of DC.

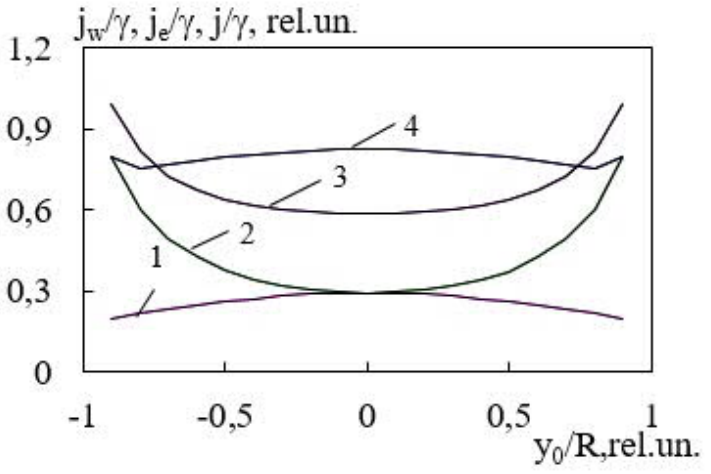



Fig.1. Distribution of the ChAP flux density over the lower electrode. For particles coming from the upper electrode (1), from the walls of DC (2), from the entire surface of DC (3-4) at L/R = 1 (1-3); 0,2 (4).

The density of the flow ChAP going to an arbitrary point of the groove wall ($j_w$) was composed of the densities of the flows coming from the walls DC ($j_{ww}$) and the upper electrode ($j_{we}$). Assuming that the probabilities of ChAP sticking to the bottom and walls of the etching groove are equal, it is possible to express the anisotropy of etching as the ratio of the densities of ChAP flows to these surfaces. This can be achieved if the effect of ion bombardment on the RIE process is minimized, for example, by lowering the HF voltage ($U_{HF}$) on the discharge. If we denote the direction of the ChAP flow through the ratio $j / j_b$ (M), then according to the calculations carried out for a cylindrical DC at $L/R \rightarrow \infty$ the value of $M \rightarrow \pi$. The optimal value of L/R is $3 \div 5$, which makes it possible to obtain $M = 2.5 \div 2.8$. This means that with a free molecular mode of particle motion and an optimal ratio of the height and radius of the cylindrical DC, the anisotropy index of etching in it should be about three. The obtained result is confirmed in practice by etching Si in $SF_6$ plasma at a pressure of 0.133 Pa in DC with a ratio of L/R = 4. When the pressure increases to 1.33 Pa, which leads to an increase in ChAP scattering in the plasma volume, etching becomes isotropic. At

the same time, the free path of ChAP remains in the entire pressure range much larger than the thickness of the ion layer at the grounded electrode and the scattering of ions in it is not significant. Therefore, the change in the anisotropy of etching is not associated with the action of ions.

*Calculation of ion fluxes.* Considering that the ions are accelerated vertically to the surface in the bulk charge layer, it can be assumed that the values of $j_i$ at the plasma-layer and layer-surface boundaries are equal and do not depend on the ratio of the parameters H and $l_g$, i.e. they arrive exclusively at the bottom of the groove. This means that to obtain complete information about the flow of ions going to the treated surface, it is enough to find its distribution over the surface of the electrode. When calculating $j_i$, it was assumed that the ion generation rate ($G_i$) is uniform in plasma volume and, after generation, move isotropically within a solid angle of $4\pi$ without collisions. At the same time, the thickness of the ion layer at the electrode is much less than L. Taking into account these provisions, converting the formula (1), we write down the expression for the density of the ion flux going to the point of the surface

$$j_i = \frac{G_i}{4\pi} \iiint_V \frac{\cos\alpha}{\rho^2} dV . \qquad (2)$$

Turning to cylindrical coordinates, we also get an elliptic integral. Figure 2 shows the dependences characterizing the distribution of ion density across the

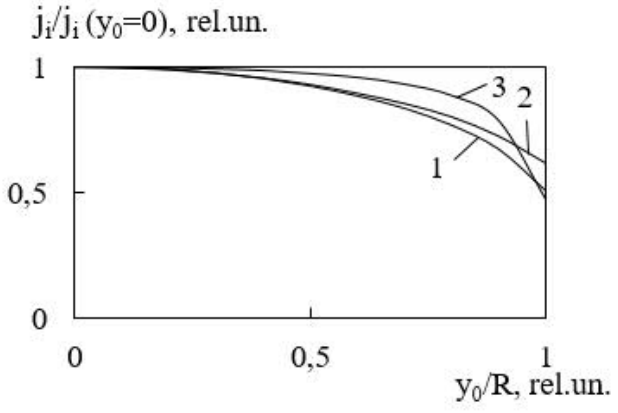



Fig.2. Distribution of the ion flux along the radius of the electrode.
At L/R = 1(1); 10 (2); 0,2 (3).

electrode at different ratios of L and R. As can be seen from these dependencies, a maximum is always observed in the center of the electrode, in contrast to the flow density ChAP. The best uniformity of the ion flux distribution in the central part of the electrode at small values of the L/R ratio, however, the value of $j_i$ is

also small, and the discharge in real DC with such parameters cannot burn at low pressures. Therefore, it is necessary to increase the uniformity of the ion flow by increasing L/R. If $y_0 = 0$ (2) also has an analytical solution from which it follows that $j_i$ changes from 0 to $G_iR/2$ when L/R changes from 0 to ∞. The optimal value of the L/R ratio to obtain a close to the maximum value of $j_i$ for real values of DC parameters lies in the range of 3 ÷ 5.

The results of the mathematical modeling show, for example, that by changing the conditions of reflection of the ChAP from the walls of the DC in its lower part, it is possible to influence the direction of their flow to the treated surface and, accordingly, the anisotropy (A) of the RIE (Fig. 3). In this case, a part of

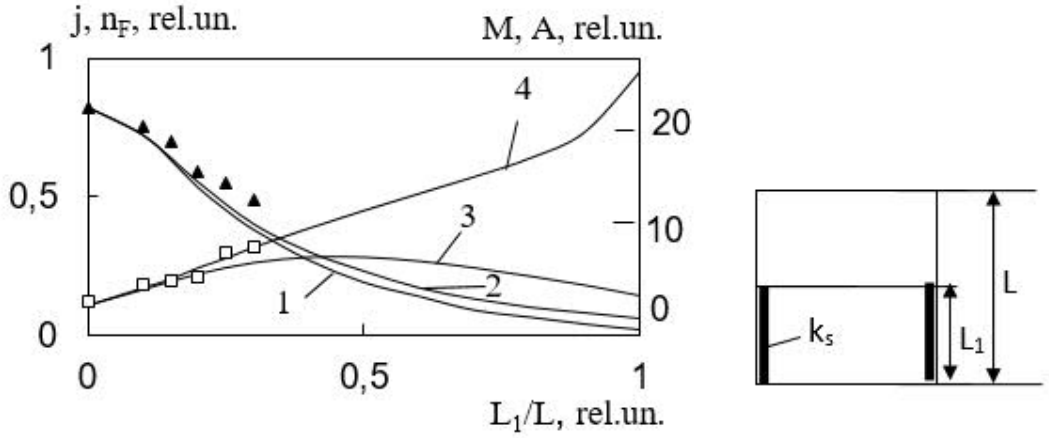



Fig.3. The influence of DC parameters on the density (1,2) and the direction of the ChAP flow (3,4), the concentration F (triangles) and the anisotropy of silicon etching (squares). Calculation at L = 0.25, R = 0.06 m, $k_s$ = 1(1,4), 0,95 (2,3). Experiment in gas -$SF_6$ at P = 6.65·10-2 Pa, G = $3 \cdot 10^{-3}$ $m^3 \cdot Pa \cdot s^{-1}$, $U_{HF}$ = 1 kV.

the surface of the DC with a height of L1 was closed with fluoroplastic rings of 10 mm, on the inner sides of which grooves with a depth of 5 mm and a width of 0.5 mm were drilled with a step of 0.6 mm. The branched surface ensured the effective death of ChAP on it, where ks ≈ 1. This led to a decrease in the concentration of ChAP in the DC. The concentration of F atoms ($n_F$) in the discharge was controlled by actinometry using the KCBУ-23 M spectral computing complex [1]. To increase the uniformity of the ion flow along the electrode, a constant magnetic field can be used, which allows changing the value of the floating potential on the walls of the DC and creating conditions for the reflection of ions from them.

## References

1. **Abramov A.V., Dikarev Y.I., Abramova E.A., Surovtsev I.S.** Journal of Applied Spectroscopy, 2004.V.71. №5. P.715-720.

# LASER-INDUCED PLASMAS OF DIFFERENT ORGANIC MATRICES

N. Sushkov[1], N. Kurian[2], S. Zaytsev[1], N. Lobus[3], A. Kéri[4], Á. Bélteki[4], G. Galbács[4], T. Labutin[1]

[1]Lomonosov Moscow State University, 1 str. 3 Leninskie gory, Moscow 119234, Russia, nikolaisushkov@laser.chem.msu.ru
[2]Yanka Kupala State University of Grodno, 22 Ozheshko ul., Grodno 230023, Belarus
[3]Timiryazev Institute of Plant Physiology, Russian Academy of Sciences, 35 str. 2 Botanicheskaya ul., Moscow 127276, Russia
[4]Department of Inorganic and Analytical Chemistry, Faculty of Science and Informatics, University of Szeged, 7 Dóm tér, Szeged 6720, Hungary

Hydrobiota provides a number of matrices with variable chemical composition and physical properties (from highly mineralised to mostly organic materials). For example, fish scale, bones and fins contain considerable amounts of calcium, whereas muscles and liver contain very little metals [1]. This means that the characteristics of their laser-induced plasmas should be substantially different.

We studied the parameters and temporal evolution of plasmas of different organic samples (fish and aquatic plants from the Neman River, Belarus, and zooplankton samples from the Arctic region and the Black Sea). The 4th harmonic of a Nd:YAG laser ($\lambda$ = 266 nm, $E$ = 21 mJ) was used to excite the plasma, and the spectra were acquired in the time-resolved mode using a gated ICCD-based detector.

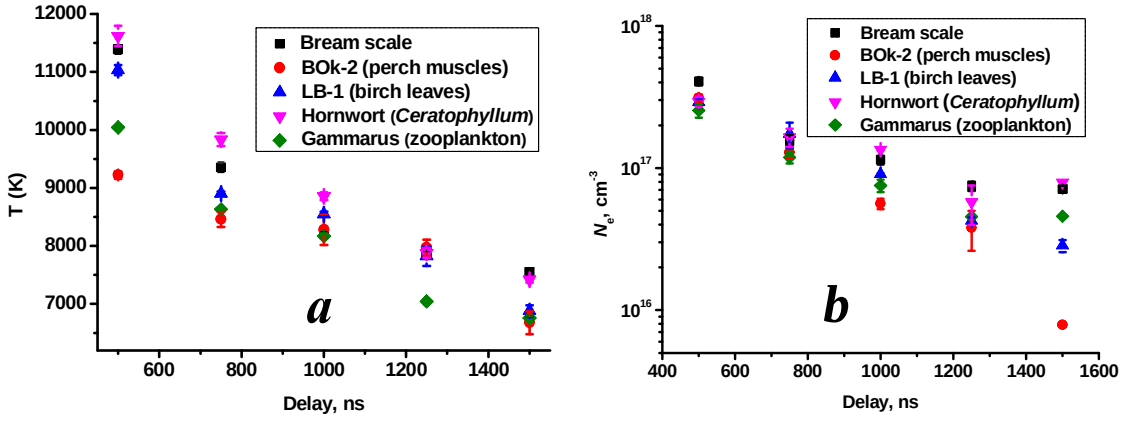



Fig. 1. Plasma parameters as a function of delay after the laser pulse (gate is 10 % of delay):
*a* — temperature, *b* — electron number density (in logarithmic scale).

Fig. 1 shows the results of plasma diagnostics. We assessed the temperature using Saha-Boltzmann plot for Ca I-II lines within the range of 363–374 nm,

and the Stark broadening of $H_\alpha$ line at 656.279 nm was used to calculate $N_e$. The figure shows that the highest $T$ and $N_e$ are observed for highly mineralised hornwort (*Ceratophyllum*) and bream scale samples, whereas CRM BOk-2 (perch muscles) gives the lowest values. The broadest $T$ spread is observed at small delays ($\leq 0.75$ μs); the $N_e$ differences, on the contrary, become more important at relatively large delays (1.25–1.5 μs).

The elemental composition of zooplankton samples was also studied by ICP-MS with laser ablation (LA-ICP-MS). To this end, Applied Spectra J200 Tandem LA-LIBS and Agilent 7700 Series ICP-MS instruments were used. In this fashion, it has become possible to detect elements like uranium or chlorine which are not measurable by laser-induced breakdown spectroscopy, at least in this kind of samples. However, our results for other elements reveal discrepancies between the two techniques.

**Acknowledgements**. The study was funded by the Russian Foundation for Basic Research (project No. 20-53-04036) and the Belarusian Republican Foundation for Fundamental Research (project No. Б21РМ-085). The authors are grateful to D. Palásti, P. Janovszky (University of Szeged), and A. Zakuskin (Moscow State University) for their assistance during the experiments.

## References

1. **Vinogradov A.P.** The elementary chemical composition of marine organisms. New Haven: Sears Foundation for Marine Research, Yale University (2019).

# MODELING OF HIGH PRESSURE SHORT-ARC XENON DISCHARGE WITH A THORIATED CATHODE

N. Timofeev[1], V. Sukhomlinov[1], G. Zissis[2], I. Mukharaeva[1], D. Mikhaylov[1], A. Mustafaev[3], B. Makhsudov[4], V. Borodina[1]

[1]Saint Petersburg State University, Ulianovskaya 3, Petrodvorets, Saint-Petersburg, 198504 Russia (e-mail: niktimof@yandex.ru)
[2]Université de Toulouse, LAPLACE UMR 5213 CNRS-INPT-UT3, 118 route de Narbonne, 31062 Toulouse cedex 9, France (e-mail: zissis@laplace.univ-tlse.fr)
[3]Saint Petersburg Mining University, 2, 21 st. Line, Vasilievsky Island, Saint Petersburg, 199106 Russia (e-mail: alexmustafaev@yandex.ru)
[4]Tajik National University, Rudaki 17, Dushanbe, 734025 Tajik Republic (e-mail: maksudov_barot@mail.ru)

Short-arc xenon discharges at high (ultrahigh) pressure are used as a source of optical radiation when the emission spectrum has to be as close as possible to the solar spectrum and when it is necessary to have high intensity radiation of a point source of light.

The presented study is devoted to the research of a high pressure short-arc xenon discharge, exactly to its modeling with taking into account the evaporation of thorium into the discharge volume. The reason for the presence of thorium atoms in the discharge plasma is thorium-doped tungsten cathodes, which are used in xenon light sources of high and ultrahigh pressure [1, 2].

The base of the present study is experimental data from [3]. The main results are presented in Fig. 1. These results were obtained using a standard xenon lamp with a power of 250 W. It can be seen that the presence of thorium near the cathode (region “I” in the figure) reduces the plasma temperature and ensures prevailing of the thorium ion density over that of xenon, the latter being close to zero in this region. In contrary, the density of xenon ions is the main in the region “II”. The radiation intensity in the visible range of the spectrum has a peak near the cathode and does not correlate with the obtained plasma temperature. This obviously cannot be interpreted if the atomic composition of the discharge is homogeneous (the presence of only xenon atoms in the plasma).

The model is based on the assumption that the plasma is in the local thermodynamic equilibrium [1, 2]. The second assumption is that the plasma contains thorium atoms emitted by the thoriated cathode. The discharge geometry is such that, in our opinion, it is convenient to use the ellipsoidal coordinates (oblong ellipsoid of revolution) [4] for describing spatial distributions of plasma characteristics (see Fig. 2). In this representation we suppose that the cathode surface coincides with some surface $\tau_0$, and the anode surface coincides with $\tau_L$, these surfaces being surely equipotential.

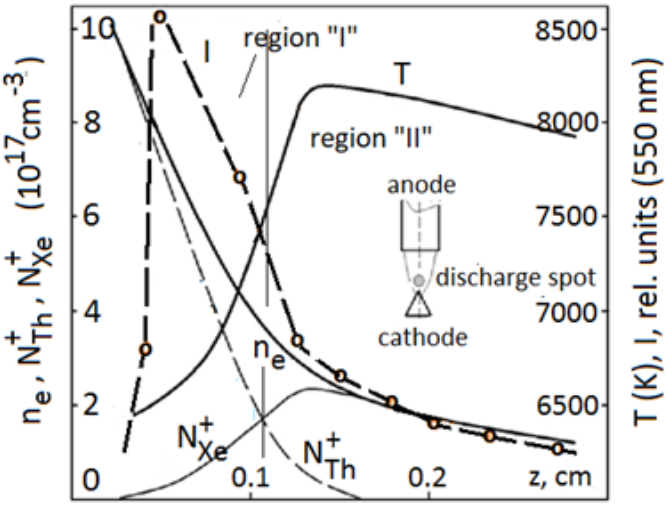



Fig. 1. Longitudinal distributions of plasma temperature $T$, light intensity $I$ at 550 nm, electron density $n_e$, as well as thorium and xenon ion densities in the ultrahigh-pressure short-arc xenon lamp with a power of 250 W [3]; the discharge geometry is shown in the inset. Cold lamp pressure – 20 atm., distance between electrodes – 0.3 cm, discharge current – 14 A.

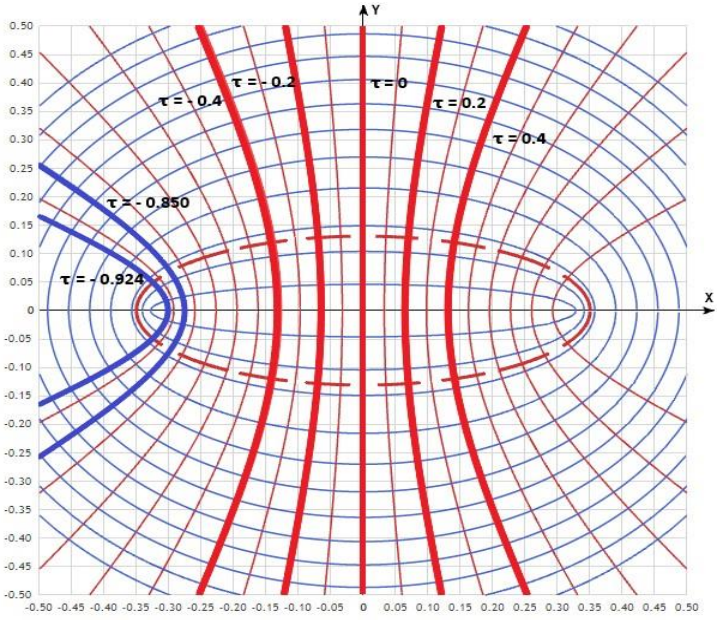



Fig. 2**.** The geometry of the discharge in question in the ellipsoidal coordinate system: thick blue lines on the left with the coordinates $\tau = -0.924, -0.850$ are the cathode surfaces; thick red lines in the center with the coordinates $\tau = -0.4, -0.2, 0, +0.2$, and $+0.4$, are the anode surfaces; a thick dashed line is the outer border of the electric current channel. The Cartesian coordinate grid is also shown in the figure.

To determine plasma characteristics we formulated five equations: two Saha equations for thorium and xenon ions, the power balance equation, the equation for the electric current through the plasma, and the balance equation for

the number of thorium atoms and ions. We use the "initial" concentration of thorium atoms $N_{Th}^{0}$ on the cathode surface as a parameter based on the temperature dependence of saturation pressure of thorium atoms [5].

To show the plasma properties with thorium atoms inside, it is useful to present plasma characteristics in one figure. These data are shown in Fig. 3. One can see that the discharge gap can indeed be divided into two regions: thorium ions are mainly in the region "I", xenon ions in the region "II". The minimum of the plasma temperature is also confirmed.

Another very interesting issue is the influence of electrode surface shape (firstly anode) on plasma characteristics. Primarily, they are defined by the electric field strength $E$ in a discharge gap. Changing the shape of the anode and/or cathode surface necessarily changes the spatial distribution of the electric field in the discharge volume. This obviously affects plasma characteristics.

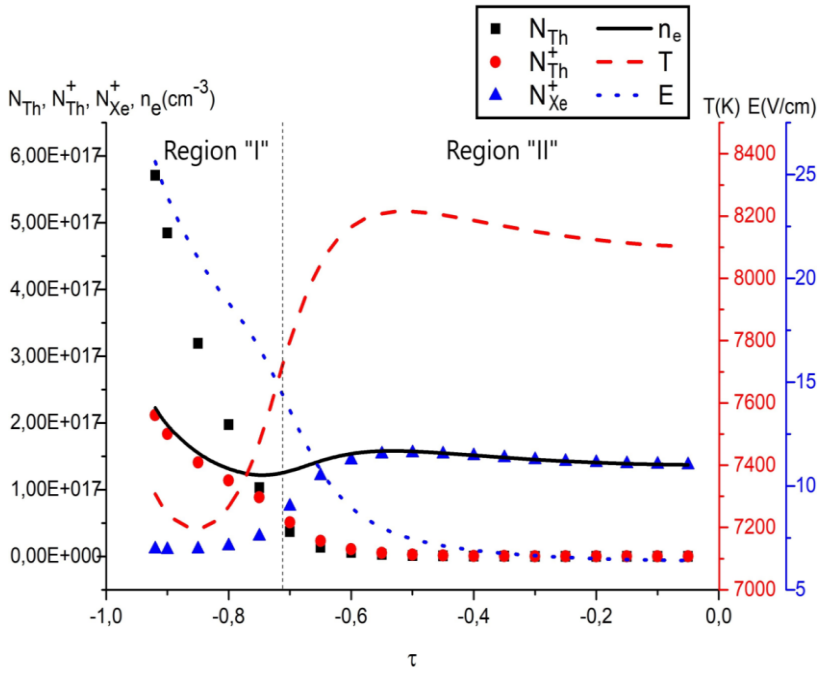



Fig. 3. The plasma temperature $T$, electric field strength $E$, electron density $n_e$, densities of xenon $N_{Xe}^{+}$ and thorium $N_{Th}^{+}$ ions, and concentration of thorium atoms $N_{Th}$ in the discharge.

Fig. 4 shows the plasma temperature $T$ for two shapes of the cathode $\tau_0 = -0.924, -0.850$ and three shapes of the anode $\tau_L = -0.4, 0, +0.4$ (one can see these surfaces in Fig. 3). As shown the shape of the electrodes strongly affects the plasma temperature. The effect of the cathode cone angle is quite expected: the smaller the angle, the higher the temperature due to the higher strength of the electric field on the cathode tip. The shape of the anode surface also strongly affects $T$. One can see that in comparison with the flat anode ($\tau_L = 0$) the concave surface decreases the plasma temperature, while the convex surface increases it.

The difference is large and reaches the order of (2500-3000) K.

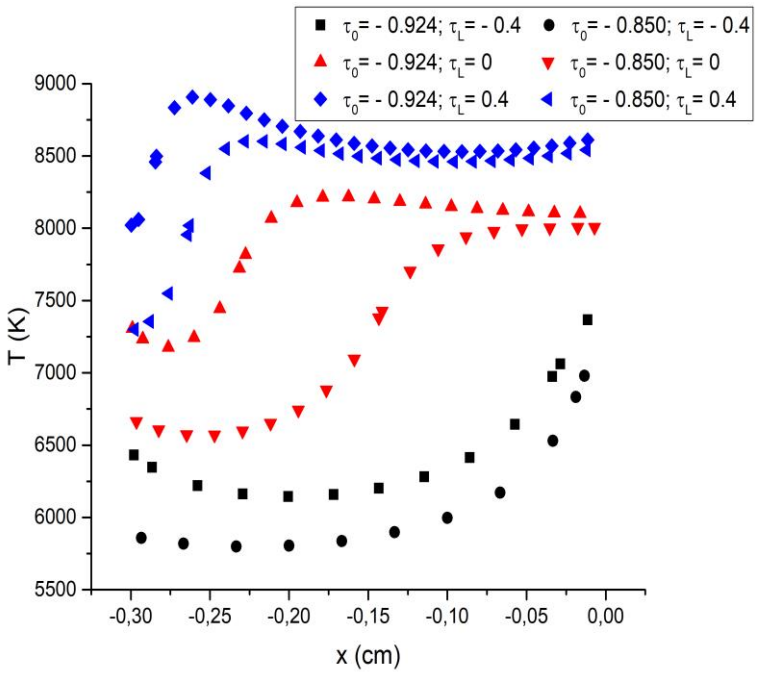



Fig. 4. The plasma temperature $T$ for the shapes of the cathode $\tau_0 = -0.924, -0.850$ and the shapes of the anode $\tau_L = -0.4, 0, +0.4$. The discharge parameters are as follows: $i = 10$ A; $N_{Th}^0 = 7 \cdot 10^{17}$ cm$^{-3}$, $N_{Xe} = 3 \cdot 10^{19}$ cm$^{-3}$.

A very important result of research is that the shape of the anode surface affects the plasma optical emission. A change in the plasma characteristics leads to a change in the composition and spatial distributions of plasma particles, in particular, xenon and thorium ions. The convex shape of the anode increases the UV radiation and IR xenon spectral lines emission (due to the higher plasma temperature), while the concave shape reduces these emissions and makes the radiation in the visible region preferred. This can be surely used to develop high current high pressure discharge light sources without any serious modification in the design of a light source.

1. Rokhlin G.N. Discharge light sources. Russia: Energoatomizdat (1991).
2. Benilov M., Plasma-physics aspects of high-intensity discharge lamps, Summer school on Plasma Physics PlasmaSurf, Portugal, Oeiras, (2016).
3. Timofeev N.A., Sukhomlinov V.S., Zissis G., Mukharaeva I.Yu., Dupuis P., IEEE Trans. Plasma Sci., 47 (2019) 3266-3271.
4. Korn A.G., Korn T.M.. A guide to mathematics for scientists and engineers. Moscow: Nauka (1973).
5. D. Stull, in American Institute of Physics Handbook, Third Edition. New York: D. E. Gray, Ed., McGraw Hill, (1972).

# COMPARISON OF DOUBLE PULSED REGIMES OF LASER PLASMA EXCITATION IN AIR AND INERT GASES

V. Kiris, K. Catsalap, M. Belkov

Institute of Physics, National Academy of Sciences of Belarus, Nezalezhnasci Ave. 68-2, 220072 Minsk, Belarus, yavasya@yandex.ru

LIBS (laser induced breakdown spectroscopy) is a rapid spectroscopic technique for elemental compositional analysis of different types of samples (solid, liquid, and gas). LIBS operates by focusing a short laser pulse onto or into a sample and when the breakdown threshold is reached, an optically-induced plasma (consisting of the target material and the surrounding gas) is formed [1].

One of the main disadvantages of LIBS compared to other analytical methods such as: atomic absorption spectrometry, inductively coupled plasma - optical emission spectrometry and mass spectrometry is its low sensitivity. Therefore, several methods have been proposed to improve the analytical capabilities of LIBS. The most common one is the double-pulse LIBS, which involves excitation of plasma with a pair of pulses separated in time [2,3]. The amplification of the signal in the double-pulse LIBS is explained by the change in the state and density of the environment after the first laser pulse, which provides an increase in the ablation of the material and a change in the conditions for the expansion of the plasma of the second laser pulse, in addition, the laser radiation of the second laser pulse interacts directly with the target vapor from the first laser pulse.

A change in the composition of the surrounding atmosphere also has a significant effect on the LIBS signal [3,4], on the one hand, a denser surrounding atmosphere should more effectively hold the laser plasma and prevent it from rapidly expanding and cooling down (especially if the spectrum is recorded over a long time interval exceeding the characteristic decay time of the plasma), on the other hand, a denser ambient atmosphere prevents the target material from being ejected during explosive evaporation, and a higher density of the medium will lead to a broadening of the spectral lines and an increase in the background radiation, in addition, molecular gases such as oxygen or nitrogen will take the energy of the plasma for the dissociation of molecules.

The carried out experiments on the installation are schematically depicted in (Fig. 1), it consists of a Nd: YAG laser operating in a double-pulse mode at a fundamental harmonic (1064 nm), an optical unit for focusing and collecting radiation, a compact spectrograph with an optical Czerny-Turner scheme and a turret with interchangeable gratings, a CCD was used as a recording system - matrix (Hamamatsu S10420). The focal length of the spectrograph is 200 mm.

The double-pulse mode is achieved by collinear convergence of beams from two active elements. At the output of the laser, the beam diameter was ~4 mm and the divergence was ~1.5 mrad; after passing through a triple telescope, the beam diameter increased to 12 mm, and the pulse duration at half height was ~10 ns. A convex lens with a focal length of 100 mm focused the radiation onto the sample surface. Plasma radiation is collected at the angle of ~ 25° to the laser beam axis by a convex lens with the focal length of 25 mm and the diameter of 25 mm, the radiation collected by the lens was focused on the end face of the quartz fiber (numerical aperture - 0.22, length 2 m). Air-cooled laser and compact optical system ensure low weight of the spectrometer. This allows one to make on-site analytical measurements. The delay between pulses can be adjusted from 0 to 80 μs, the maximum energy per pulse can be up to 50 mJ.

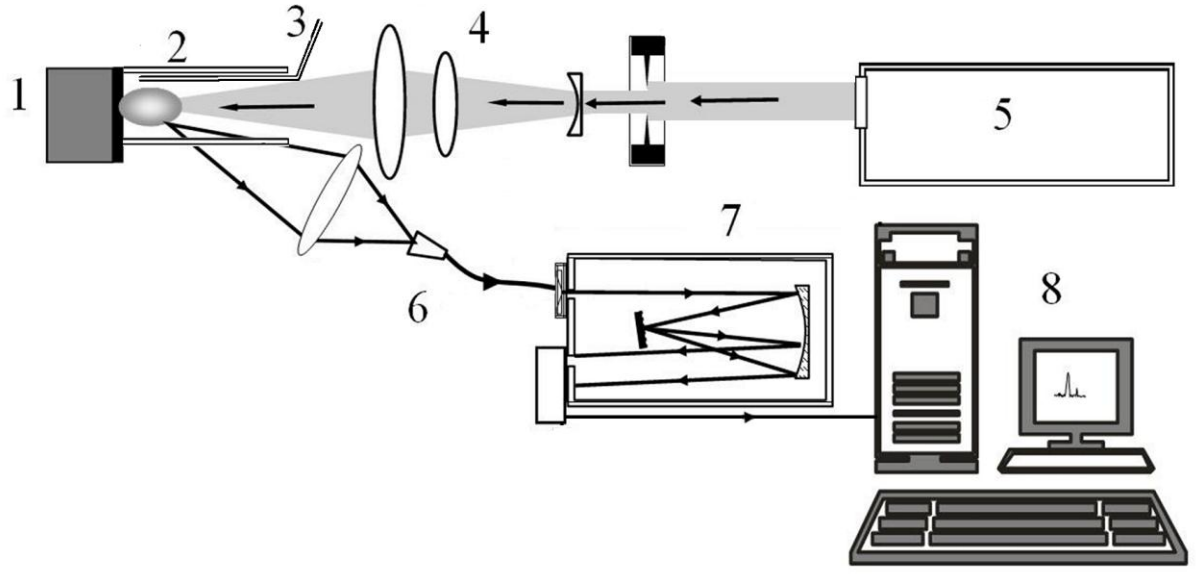



Fig. 1. Scheme of the LIBS spectrometer. 1) sample, 2)quartz tube, 3) gas purge line, 4) optics, 5) laser, 6) optical fiber, 7) spectrograph, 8) PC

To obtain representative data, the spectrum recording procedure included twenty double firing pulses, the spectra of which were not taken into account, and then eighty double-pulse spectra were recorded, which were averaged. The pulse energy was -47 mJ for the first one and 40 mJ for the second channel. The sample was positioned in such a way that the diameter of the radiation focusing spot on the sample was ~200 μm. The spectra of the UG88 steel sample recorded in the double-pulse excitation mode ($\Delta t$=5 mks) in various gases are shown in (Fig. 2). Fig. 3 shows the dependences of the intensity of the spectral lines of manganese (Mn II 293.931 nm) and copper (Cu I 324.754 nm) on the delay between laser pulses in various gaseous media. As it can be seen from (Fig. 2), the highest intensity of the spectrum is provided in the argon

atmosphere, and the lowest one in the helium atmosphere. At the same time, with single-pulse excitation [3,4], the maximum intensity of the spectrum (among these gases at atmospheric pressure) is achieved upon excitation in the helium atmosphere, the intensity in the argon medium is lower, and the minimum intensity is observed in the air.

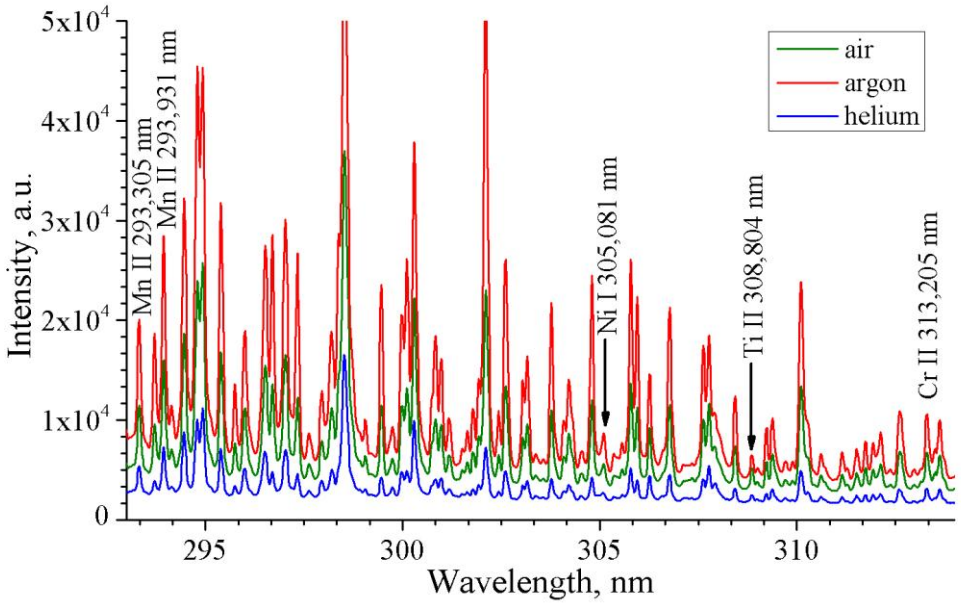



Fig. 2. Spectrum of the UG88 steel sample in double-pulse mode (Δt=5 mks), air-green, argon-red, helium-blue

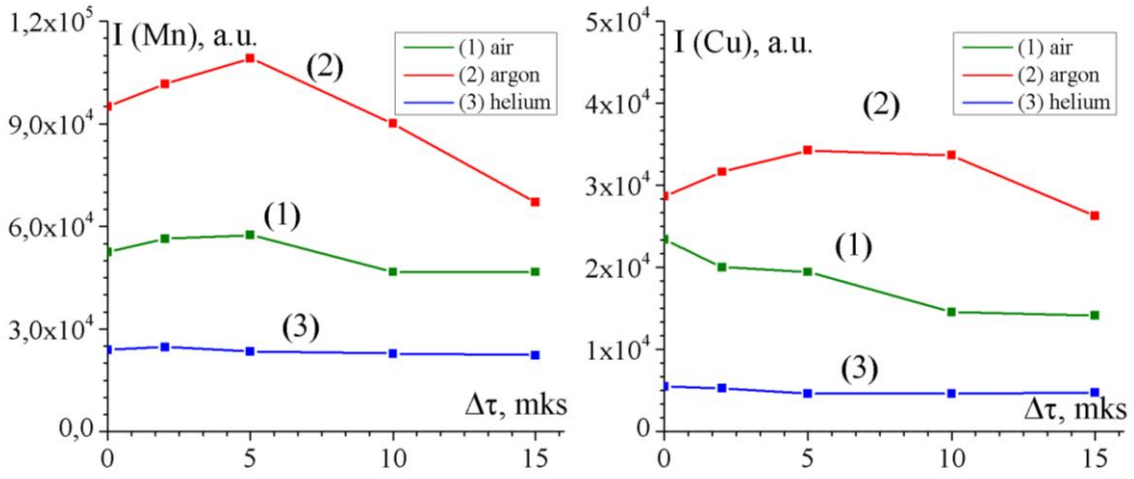



Fig. 3. Dependences of the intensity of the spectral lines of manganese (Mn II 293.931 nm) and copper (Cu I 324.754 nm) on the delay between laser pulses

However, even at zero delay, a different dependence of the signal intensity on the type of gaseous medium is observed in our experiments, probably due to the presence of interpulse delay jitter, so there is no exact convergence of pulses and we cannot obtain a truly single-pulse mode. In addition, it should be taken into account, that visually the dimensions of the plasma torch in the helium atmosphere are significantly higher, which may mean that the optimal detection zone is significantly shifted in relation to the air environment. The least pronounced effect of the time delay on the intensity of the spectral lines, in the considered range, is observed for helium, probably, the low density of helium does not provide sufficient efficiency of confining the plasma of the first pulse to ensure effective interpulse interaction. Among the gases used in our experiments argon has the highest density, the plasma formed in argon visually has the highest brightness, and the spectra obtained in argon have the highest intensity. In argon the most pronounced maximum is observed in the dependence of the intensity on the interpulse delay in the region of 5 μs, this maximum is also observed for the spectral lines of other elements Ni I 305.081 nm, Cr II 313.205 nm. In addition, when operating in argon with a delay between laser pulses of 5 μs, the minimum standard deviation of the intensity of the spectral lines between pulses is observed. When excited in the air, the maximum of the dependence of the intensity on the delay is less pronounced and shifted to the region of lower delays; moreover, for the resonance line of Cu I 324.754 copper, the maximum is observed for zero delay.

**Acknowledgements**. The work was partially supported by the State program for scientific research of the Republic of Belarus "Photonics and Electronics for Innovation" as part of tasks 1.5.

**References**

1. .**Laserna J., Vadillo J.M, and Purohit P.** Laser-Induced Breakdown Spectroscopy (LIBS): Fast, Effective, and Agile Leading Edge Analytical Technology, Appl. Spectrosc., 72 (2018) 35-50.
2. **Hahn DW, Omenetto N.** Laser-induced breakdown spectroscopy (LIBS), part II: review of instrumental and methodological approaches to material analysis and applications to different fields. Appl Spectrosc., 66(4) (2012) 347-419.
3. **Scaffidi J., Angel M., and Cremers D.** Emission Enhancement Mechanisms in Dual-Pulse LIBS, Anal. Chem. 78 (2006) 24–32.
4. **Jianlong Yu, Zongyu Hou, Yuanyuan Ma, Tianqi Li, Yangting Fu, Yun Wang, Zheng Li, Zhe Wang**, Improvement of laser induced breakdown spectroscopy signal using gas mixture, Spectrochimica Acta Part B: Atomic Spectroscopy, 174 (2020) 105992

# SIMULATION OF CHARGED PARTICLES MOTION IN THE CATHODE-FALL REGION OF AN ABNORMAL GLOW DISCHARGE IN CROSSED E×H FIELD

V. Shekelevski, D. Kotov

Belarusian State University of Informatics and Radioelectronics, 6 Petrusya Brovki str. Minsk, Belarus, kotov@bsuir.by

**Introduction.** Modern industry in the production of micro-, nano- and optoelectronic products most often uses magnetron sputtering method for thin film sputter deposition. Despite the prevalence of the method, it is currently relevant to develop methods for determining the uniformity of the formed coating based on a quantitative assessment of the processes occurring in crossed E×H fields during the glow discharge generation above the magnetron sputtering system target surface.

Plasma localization at the target surface by the magnetic trap that depends on the magnetic field value and its configuration. To determine the profile of the target erosion zone, it is necessary to know the profile of the ion current density distribution, which depends on the configuration of the magnetic and electric fields and the pressure in the chamber. The erosion zone profile can be calculated using the formula

$$(r_i, t) = t \cdot \vartheta_i(r_i) = t \cdot \frac{Y_i j_i(r_i) A_i}{e N_A \rho_i} \quad (1)$$

where $Y_i$ – the sputter yield; $j_i(r)$ – the ion current density over the target at the radius $r_i$, A/cm$^2$; $A_i$ – the atomic mass of the sputtered material, g/mol; $\rho_i$ – the density of the material, g/cm$^3$ [1].

The key step in calculating the profile of the target erosion zone is to find out the ion current density distribution profile, which can be estimated from the spatial distribution of electrons over the target surface using the Monte Carlo method. For this purpose, is necessary to solve the equation of an electron motion in the magnetic and electric fields according to the following formula

$$m \cdot \vec{a} = q(\vec{v} \times \vec{B}) + q \cdot \vec{E} \quad (2)$$

where $m$ – the particle mass, kg; $a$ – the acceleration, m/s$^2$; $q$ – the charge, C; $v$ – the velocity, m/s; $B$ – the magnetic field induction, T; $E$ – the magnitude of the electric field, V/m [2].

This equation is a second-order differential equation, which solution in

Cartesian coordinates it is necessary to divide into a system of three equations in order to find the projection of the velocity vector on each of the axes

$$\begin{cases} mv_x' = q(v_y B_z - v_z B_y + E_x) \\ mv_y' = q(v_z B_x - v_x B_z + E_y). \\ mv_z' = q(v_x B_y - v_y B_x + E_z) \end{cases} \quad (3)$$

To solve this equation numerically, it must be reduced to equations in first-order derivatives. Further, by calculating the set of electrons with different initial coordinates and velocities, it is possible to determine their general spatial distribution, which will define the spatial distribution of the anomalous glow discharge. In this case, it is assumed that the main factor in the plasma generation is the collision of electrons trapped in a magnetic trap with atoms of the working gas. Thus, the relativistic correction for the change in the mass of electrons can be neglected, since electrons with a speed over 106 m/s are not retained by the magnetic trap of the magnetic system. The movement of ions under the action of the Lorentz force can also be neglected due to their large mass, and only the case when they move rectilinearly to the cathode can be considered [3].

**Analytical determination of the spatial distribution of electrons in crossed fields E×H.** For the numerical solution of the system of equations 3, the Runge-Kutta method of the 4th order of accuracy was used. The built-in solver of this method in the SciPy library of the Python programming language was used. The solver takes as input each equation from the system and initial conditions and calculates for each moment of time an array of coordinates values and projections of the velocity vector. In our case, the calculations were carried out with a step of $10^{-11}$ s. The magnetic field was calculated applying the Python programming language using the free Magpylib library. The electrostatic field was calculated analytically, using the equations for the charged plane.

The trajectory of electrons in a magnetic trap of a planar magnetron with target 80 mm in diameter, using the Python 3.8 programming language by the SciPy, Matplotlib, Magpylib, Numpy libraries was calculated.

The calculations were performed for electrons uniformly distributed over the target surface and with random initial velocities ranging from 16 eV to 300 eV. The cathode potential is 600 V.

Next, to determine the distribution of electrons in the region above the target surface for each moment of time, the calculation region was divided into volumes of the same size, in which the electrons included in it were counted. Then the cross section passing through the axis of the magnetic system was taken, and the electrons entering the volumes crossing the section plane were summed along and across the target surface.

Examples of electrons distribution calculating in planes passing through the

z-axis and the x-axis are shown in Figure 1.

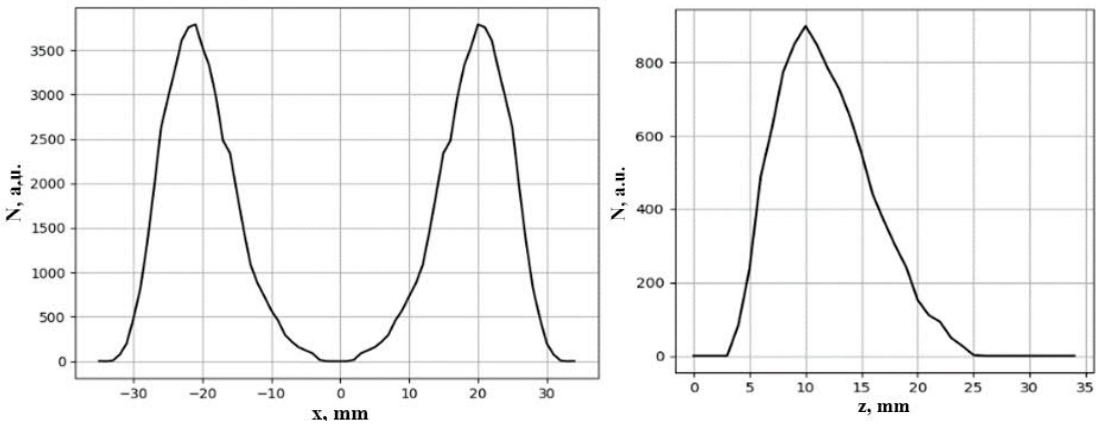



Fig. 1. The calculated electron density profile when summed along z and x, respectively

The result of the calculation gives pronounced maxima and minimum observed experimentally. After a certain number of calculated trajectories, the distribution pattern ceases to change, which indicates the inexpedience of further calculations.

It should be noted that the calculated profile describes only a qualitative rather than a quantitative distribution, which depends on the number of test particles, that in the calculations was from 12,000 to 100,000.

**Experimental verification.** To verify the proposed method for erosion zone profile determining, we compared the results of the erosion zone profile calculations and the experimental sputtered target measures.

Formula 1 was used to determine the target erosion zone profile, where the spatial distribution of the ion current density was determined analytically using the formula

$$j_i(r_i) = \frac{I_{dc}}{\pi(R_{max}^2 - R_{min}^2)} \frac{f(r_i)}{\int_0^\infty f(r_i)dr_i}, \quad (4)$$

where $R_{min}$ – the minimum target erosion zone, m; $R_{max}$ – the maximum radius of the target erosion zone, m; $f(r_i)$ – is the distribution function obtained by approximating the calculated electron density profile.

Next, the calculated curves were approximated by the Gaussian function using the built-in functionality of the SciPy library. An example of the fitted curve and its comparison with the experimental data is shown in Figure 2.

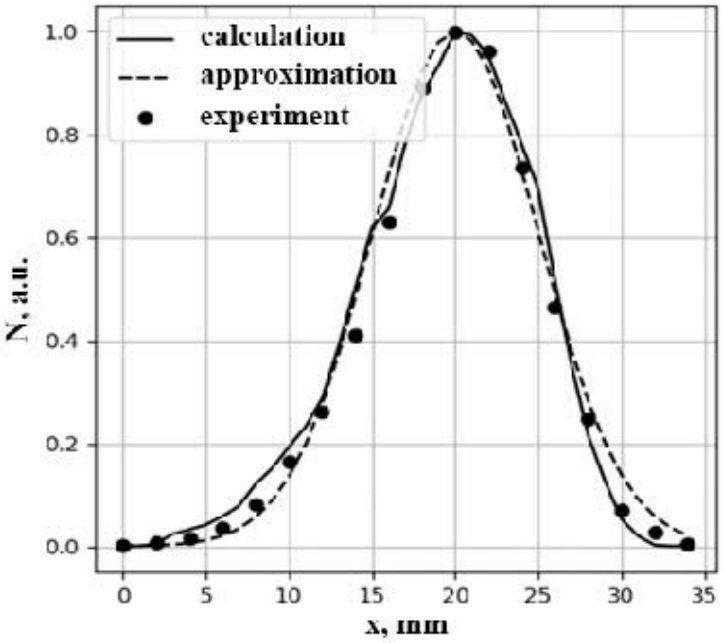



Fig. 3. Comparison of the experimental, calculated and approximated normalized curves of the target erosion zone profiles

As it shown in figure 2, the simulation displays a good agreement with the experimental data. The erosion zone error based on the target utilization factor is 6%.

**Conclusion.** Thus, a method for calculating the target erosion zone profile based on the spatial distribution of electrons over the target surface, calculated by the Monte-Carlo method, is presented. It can be said that the approximation using the Gaussian function makes it possible to mathematically describe the distribution of the discharge current in the magnetron sputtering systems (MSS) sputtering zone with sufficient accuracy and, based on this, subsequently obtain an erosion zone profile that corresponds to the experimental one with sufficient accuracy. The data obtained can be useful in designing MSS and predicting the results of the deposition uniformity thin-film coatings.

## References

1. **Golosov D.A., Zavadsky S.M., Melnikov S.N.** Vestnik Polotskogo gosudarstvennogo universiteta. Seriya C. Fundamental'nye nauki, 4 (2013) 76–82.
2. **Bogaerts A., Bultinck E., Kolev I., Schwaederl´e L., Aeken K.V., Buyle G. and Depla D.** J. Phys. D: Appl. Phys. 42 (2009).
3. **Yusupov M., Bultinck E., Depla D. and Bogaerts A.** New J. Phys. 13 (2011)

# CHARACTERISTICS OF A CYLINDRICAL PLASMA ANTENNA SYSTEM AND ITS ANALYSIS

A. Astafiev, A. Chirtsov, A. Lesiv, A. Altmark

Saint Petersburg Electrotechnical University "LETI", ul. Professora Popova 5, 197022, St. Petersburg,
E-mail: astafev-aleksandr@yandex.ru

A plasma antenna is a radio-frequency antenna that uses gas discharge as a conducting medium. The advantage of this type of antenna is that the parameters of the antenna can be quickly changed by switching on the appropriate gas discharge elements (or by changing the current). Numerous plasma antenna designs have been proposed and investigated, some of which have been reviewed in [1, 2]. Of particular interest is a symmetric round plasma antenna system that can shift radiation patterns from omnidirectional to unidirectional [3] without being turned. This type of system consists of a linear antenna surrounded by gas discharge tubes one or few times. By switching on selected lamps, the radiation pattern can be changed and rotated around the axis. An additional advantage of this symmetric cylindrical system is its relative simplicity, both for experiments and for theoretical analysis. Although this antenna system design has been repeatedly investigated, it has been studied for only few specifically selected modes (with one value of the operating frequency or discharge current). Nevertheless, increased interest has rendered the further study of such plasma antenna systems an urgent task.

This work is devoted to the measurement in a wide frequency range of the radiation pattern of a short linear antenna surrounded by 16 fluorescent lamps. As illustrated in Fig. 1, the experimental setup consisted of a spectrum analyzer with a tracking generator (1), a grounded short linear antenna (2), and 16 18 W fluorescent lamps (3), which were connected to the DC power supply (4) by connecting jumpers (5) and a switchboard (6). The antenna and lamps were placed on a metal plate (7) and mounted on a turntable. The antenna signal was measured by a receiving broadband horn antenna (8). The signal was recorded using a spectrum analyzer equipped with a tracking generator. The tracking generator output was connected to the 3 cm long linear transmitting antenna, and the spectrum analyzer input was connected to the receiving broadband horn antenna. The fluorescent lamps were combined into four groups (with four lamps in each group), each of which could be switched on and off independently of the others (Fig. 1 on the right). The radiation patterns under different numbers of switched-on lamps and different discharge current values (up to 200 mA) were investigated. Studies of the characteristics of the plasma antenna system were carried out in a fairly wide frequency range from 0.5 to 1.5 GHz.

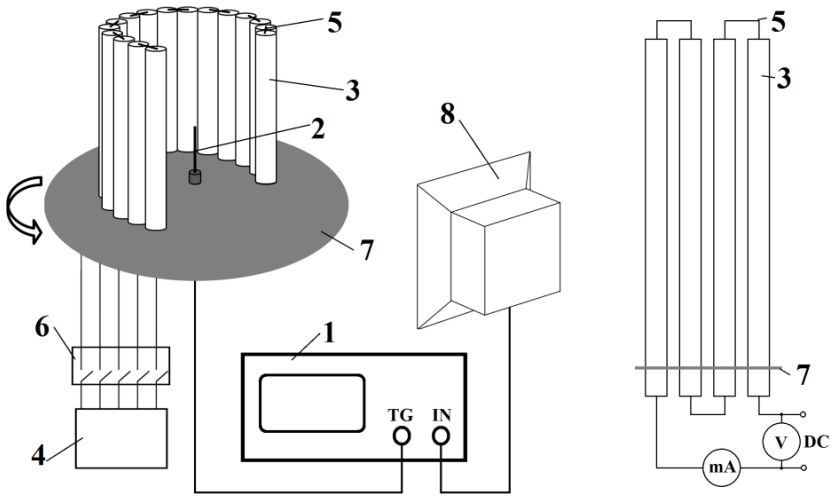



Fig. 1. A cylindrical plasma antenna system: 1 – generator; 2 – short linear antenna; 3 – fluorescent lamps; 4 – DC power supply; 5 – connecting jumpers; 6 – switchboard; 7 – metal plate; 8 – receiving broadband horn antenna. Connecting fluorescent lamps to a DC power supply (right).

The antenna system under study was numerically simulated in the Ansys HFSS, using a geometry that fully corresponded to the experimental one. The electron density and the electron collision frequency of the gas-discharge plasma were determined using the known results for the electron drift velocity in the Ar-Hg mixture [4]. Based on the simulation, the calculated radiation patterns were obtained, and were then compared with the measured ones. Moreover, for comparison with a metal analog in the analyzed model, a conductivity corresponding to the conductivity of copper was set. Another approach to the analysis of the investigated antenna system is its representation as a ring antenna array model. Each of the fluorescent lamps was replaced with an omnidirectional elementary antenna located on the axis of the lamp. Each of these elementary antennas re-radiated the field of a short linear antenna located in the center. The total field of the entire system in the far zone is the sum of the fields of the individual antennas determined by the corresponding array factor. The array factor of the N-element ring antenna array is expressed as follows [5]:

$$AF(\varphi) = 1 + \sum_{n=0}^{N-1} \left[ j_n e^{i\frac{\omega}{c}[D\cos(\varphi - \phi \cdot n)] + i\alpha_n} \right] \qquad (1),$$

where $J_n$ end $\alpha_n$ are, respectively, the excitation amplitude and excitation phase of the n-th ring antenna element; $D$ is the distance between the central antenna and other n-th antennas located around the ring; $\phi$ is the angle between two elementary antennas; $N$ is the number of switched-on fluorescent lamps (equal to the number of elementary antennas). For the studied plasma antenna system, the distance $D$ is 95 mm (the distance from the central antenna to the axis of

each fluorescent lamp), the angle between the two elementary antennas $\phi$ is 18 degrees. The relative power flux for the antenna system is determined by the product $AF \cdot AF^*$ which normalized to the $\frac{1}{2\pi}\int_0^{2\pi} AF \cdot AF^* d\varphi$. However, to calculate the relative power flux, it is necessary to determine the excitation amplitude $J_n$ and excitation phase $\alpha_n$ for each n-th elementary antenna. If the frequency is low or only 4 lamps ($N$=4) is on, then the values of the amplitudes and phases can be set the same for each of the equivalent elementary radiating antennas. Then the problem will reduced to minimizing the corresponding discrepancy functional with respect to these two parameters. In other words, such values of the amplitude $J$ and phase $\alpha$ are chosen so that they correspond as closely as possible to the experimental data. Since these two parameters are functions of frequency, it is necessary to calculate them for each frequency value.

The performed analysis shows that the in-phase ring antenna array representation in some cases can describe a real antenna system with good accuracy when only 4 lamps are turn on. Figs. 2 and 3 show the dependences on frequency for $J$ and $\alpha$, as well as comparisons of measured and calculated radiation patterns for the two current values (35 and 200 mA) and metal equivalent. According to Fig. 2, the excitation amplitude increases with increasing frequency, and the increase becomes larger with increasing electron density. However, an increase in the discharge current from 35 to 200 mA leads to an increase in the excitation amplitude by only about 2 times. The phase characteristics have a nearly linear dependence on the frequency which described by the approximate relation $\alpha \approx \pi + \frac{2\pi f}{c} D$. It can be noted that for the metal equivalent, the excitation amplitude is almost independent of frequency.

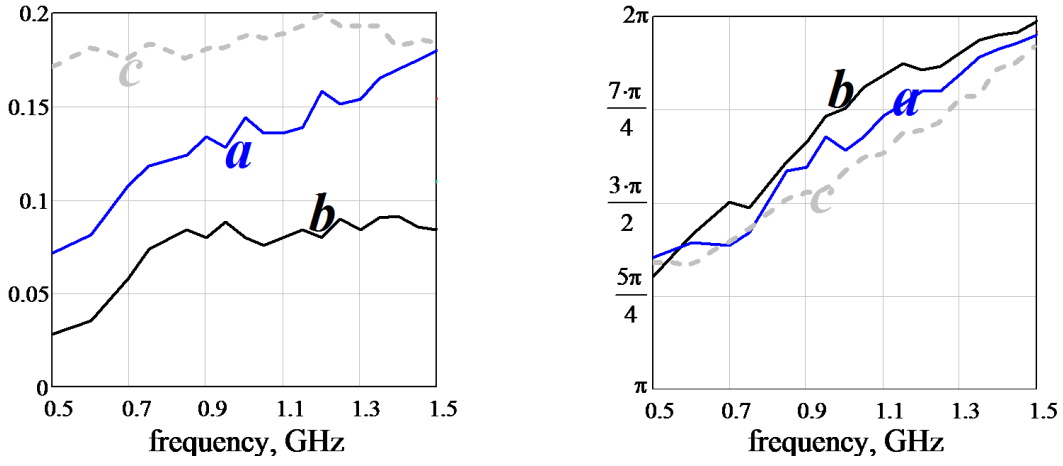



Fig. 2. Excitation amplitude (left graph) and excitation phase (right graph). ***a*** - 200 mA (blue curves); ***b*** - 35 mA (black curves); ***c*** - cupper conductivity (gray dashed curves).

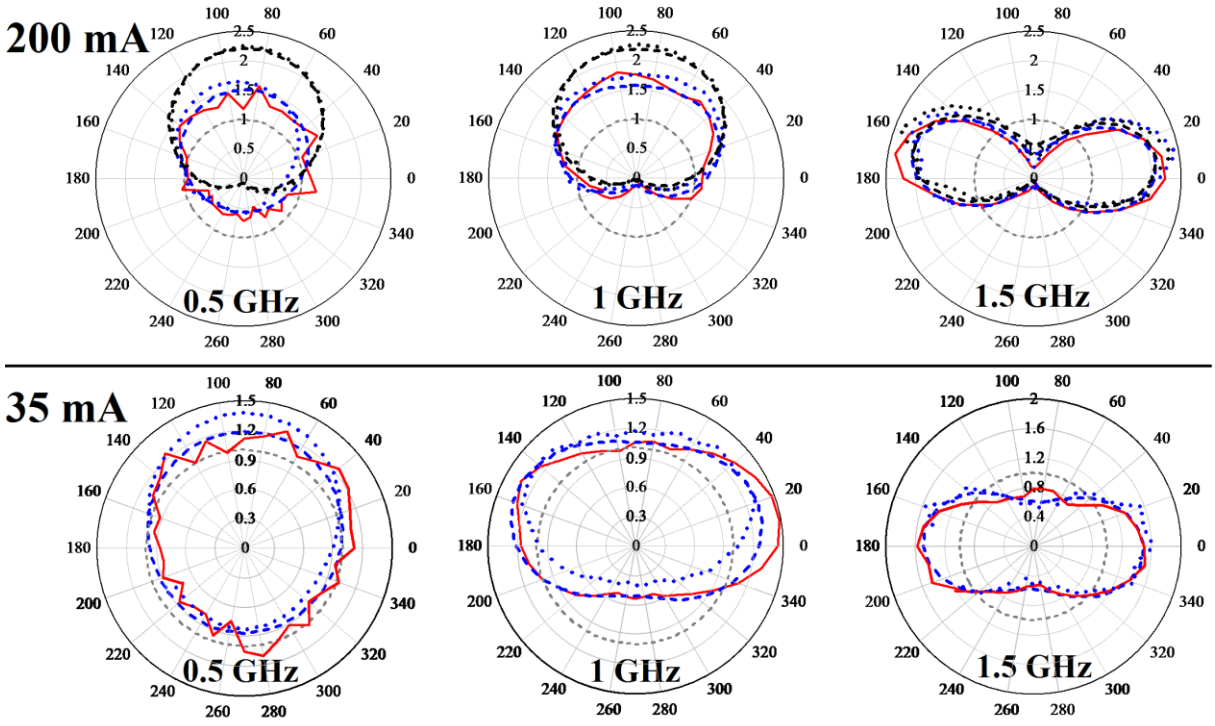



Fig. 3. Comparison of measured (red solid curves), ring antenna array model (blue dashed curves) and HFSS simulation (blue dotted curves) radiation patterns. Black dashed curves correspond to the ring antenna array model for the metal equivalent. Black dotted curves correspond to the HFSS simulation for the metal equivalent. The upper curves correspond to the 200 mA discharge current. The lower curves correspond to the 35 mA discharge current.

**Acknowledgements**. This work was supported by the Russian Science Foundation (project No. 22-22-20065) and St. Petersburg Science Foundation (project No. 17/2022).

## References

1. **T. Anderson.** "Plasma Antenna", Artech House, 2011.
2. **I. Alexeff, T. Anderson, S. Parameswaran, E. P. Pradeep, J. Hulloli and P. Hulloli,** "Experimental and theoretical results with plasma antennas" IEEE Transactions on Plasma Science, vol. 34, no. 2, pp. 166-172, 2006.
3. **H. Ja'afar, M. T. B. Ali, A. N. B. Dagang, H. M. Zali and N. A. Halili,** "A Reconfigurable Monopole Antenna With Fluorescent Tubes Using Plasma Windowing Concepts for 4.9-GHz Application", in IEEE Transactions on Plasma Science, vol. 43, no. 3, pp. 815-820, 2015.
4. **R. I. Golyatina, S. A. Maiorov,** "Characteristics of Electron Drift in an Ar–Hg Mixture", Plasma Physics Reports, vol. 44, no. 4, pp. 453-457, 2018.
5. **C. A. Balanis,** "Antenna Theory Analysis and Design", 2nd Edition, John Wiley & Sons, Inc., New York, 1997.

# RADIATION PATTERN OF A SYSTEM CONSISTING OF A SHORT LINEAR ANTENNA AND AN EXTENDED PLASMA JET

A. Astafiev, A. Chirtsov, A. Lesiv, A. Altmark

Saint Petersburg Electrotechnical University "LETI", ul. Professora Popova 5, 197022, St. Petersburg,
E-mail: astafev-aleksandr@yandex.ru

Over the past few decades, cold plasma at atmospheric pressure has been actively studied with the aim of using it for various applications, such as non-thermal sterilization of heat-sensitive surfaces, initiation of various chemical reactions and coating to the surface. To generate atmospheric plasma with about 300 K gas temperature, various types of discharges are used, which are most often not stationary. The problem of designing new low temperature plasma sources for specific applications is complex and is directly related to the need to measure dynamic processes in such discharges with high resolution. One of the most important characteristics of plasma is the electron density, which for atmospheric plasma with a low gas temperature can be less than $10^{19}$ m-3. However, the available methods for measuring the electron density of either have insufficient sensitivity or do not allow tracking dynamic processes in nonstationary discharges. One of the most useful methods for the diagnosis of atmospheric plasma jets are based on the interaction of microwave with plasma. The method in [1- 3] measures the dependence of the electron density on time for atmospheric pressure plasma and plasma jets, using a microwave scattering of signals with frequencies of about 10 GHz. A measured plasma volume with dimensions smaller than the wavelength was placed near two horn antennas, and the electron density of the discharge plasma was determined by measuring the level of the signal scattered from the plasma volume using a specific calibration procedure. The disadvantage of this method is the probing of plasma in free space, where various external factors, such as the supply wires of the discharge, can have a strong influence. Moreover, this method makes it possible to measure only the average electron density without being able to estimate the electron density distribution for inhomogeneous discharges and plasma jets. In this work, by means of numerical simulation and analysis of a simple analytical model, a method is developed that is based on registering changes in the radiation pattern of a grounded short linear antenna depending on the conductivity of a plasma jet located the near field zone of the short linear antenna and directed parallel to it. Such a close location of the investigated plasma region with respect to the antenna will significantly increase the sensitivity of measurements. In addition, the presence of a conductive base will make it possible to estimate the electron density distribution along extended plasma jets by their vertical moving.

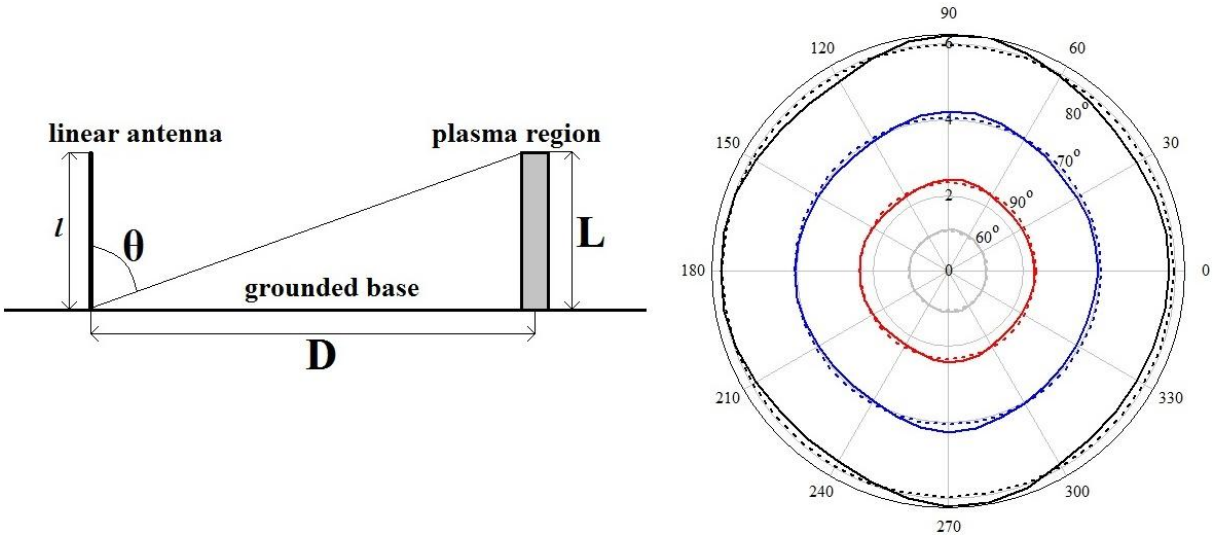



Fig. 1. Left – model of the Antenna system; right – polar plot of the antenna system gain at 2.5 GHz for 90, 80, 70 and 60 degrees of polar angle. Dashed curves – antenna gain without cylindrical plasma region; solid curves – antenna gain with cylindrical plasma region ($n_e$ =$10^{20}$ $m^{-3}$).

The antenna system under study was numerically simulated in the Ansys HFSS software, using a geometry that represented on Fig. 1 left. It consists of a round metal base (1) having a diameter of 700 mm, a central short linear antenna (2) having a length of $l$=30 mm and a diameter of 1 mm, and a cylindrical object simulating an atmospheric plasma jet (3), which is located at a distance of $D$=90 mm from the central antenna. Two values (15 and 30 mm) are chosen for the length $L$ of the cylindrical object. The region diameter was chosen equal to 4 mm and did not vary. The relative permittivity $\varepsilon_m$ and conductivity $\sigma$ of the investigated cylindrical plasma region are determined through the electron density $n_e$ and electron collision frequency $\nu_{eff}$ using known relations [4, 5]. The parameters of the plasma region were set on the basis of the available data for atmospheric plasma jets in a helium flow [2, 3]. Three values of the electron density are selected for analysis: $10^{19}$ $m^{-3}$, $5 \cdot 10^{19}$ $m^{-3}$ and $10^{20}$ $m^{-3}$. The electron collision frequency was set equal to 1.5 THz. For such values of the electron density and electron collision frequency, the conductivity and relative permittivity of the plasma are almost independent of the signal frequency in the considered frequency $f$ range from 0.5 to 3 GHz. This frequency range was chosen from the condition that a linear antenna could be considered as an elementary dipole. The analysis showed that the field maximum is formed in the region of 70-80 degrees of the polar angle $\theta$ and its position weakly depends on the frequency $f$ and does not depend at all on the parameters of the plasma region. The presence of a cylindrical region of plasma with the above values of the electron density leads to a dependence of the radiation field on the azimuthal

angle $\varphi$ by only a few percent and changes the radiation field of the linear antenna completely identical for different polar angles $\theta$ (Fig. 1 right).

The analytical model of the antenna system under consideration was built on the basis that the electromagnetic field of both the central antenna and the cylindrical region under study are described by known expressions for the field of an elementary Hertzian dipole [6]. It is known that, in a spherical coordinate system, the electric field of a dipole has radial $E_R$ and polar $E_\theta$ components. This electric field radiated by the dipole leads to the appearance of a current in the cylindrical plasma region which is described by the well-known drift theory [5]. Since the plasma region is located at a considerable distance from the central antenna and the polar angle $\theta$ differs little from 90 degrees, the radial component of the electric field can be discarded and only the polar component is taken into account (Fig. 1 left). In this case, the field that excites the current in the plasma region will be uniform. In order to fulfill this condition, the distance $D$ should be much greater than the length of the plasma region $l$. It should also be taken into account that the polar component $E_\theta$ of the electric field of a grounded short antenna is twice that for a short antenna in free space. Another important circumstance is that the current excited in the plasma region is very small compared to the linear antenna current, which is due to the very low plasma conductivity. In this case, the system under consideration can be represented as a ring antenna array [6] consisting of two elements, which array factor as a function of the azimuthal angle $\varphi$ is given by $AF(\varphi)=1+q\cdot e^{-ik\cdot D\cos(\varphi)}$. The dimensionless complex parameter $q$ is a quantitative characteristic of the effect of the plasma region on the radiation pattern of the linear antenna. This parameter is a function of the frequency and the total number of electrons $N_e$ in the plasma volume. For the conditions under consideration, the modulus of the parameter $q$ does not exceed 0.02.

Fig. 2 shows the dependences of the relative power flux on the azimuthal angle in Cartesian coordinates for the results of modeling using the Ansys HFSS (dashed lines) and for the results of the analytical model (solid lines). It can be seen that the effect of the plasma region on the radiation pattern (power flux) of a linear antenna is highly dependent on the frequency. With changing the frequency, not only the magnitudes of the maximum deviation change, but also their number and position. As expected, the dependences for a plasma region 15 mm long and with an electron density of $10^{20}$ $m^{-3}$ almost completely coincide with the dependences for a plasma region 30 mm long with an electron density of $5\cdot10^{19}$ $m^{-3}$. This circumstance confirms the fact that the field reradiated by the plasma region is determined by the total number of electrons. In general, a comparison of numerical simulations and a simple analytical model gives very good agreement. The overestimated values of the maxima of the analytical curves are explained by the fact that the model assumed the homogeneity of the

current excited by the linear antenna in the cylindrical region of the plasma, which is not entirely true. This error can be easily taken into account, since it does not depend on the frequency or the electron density.

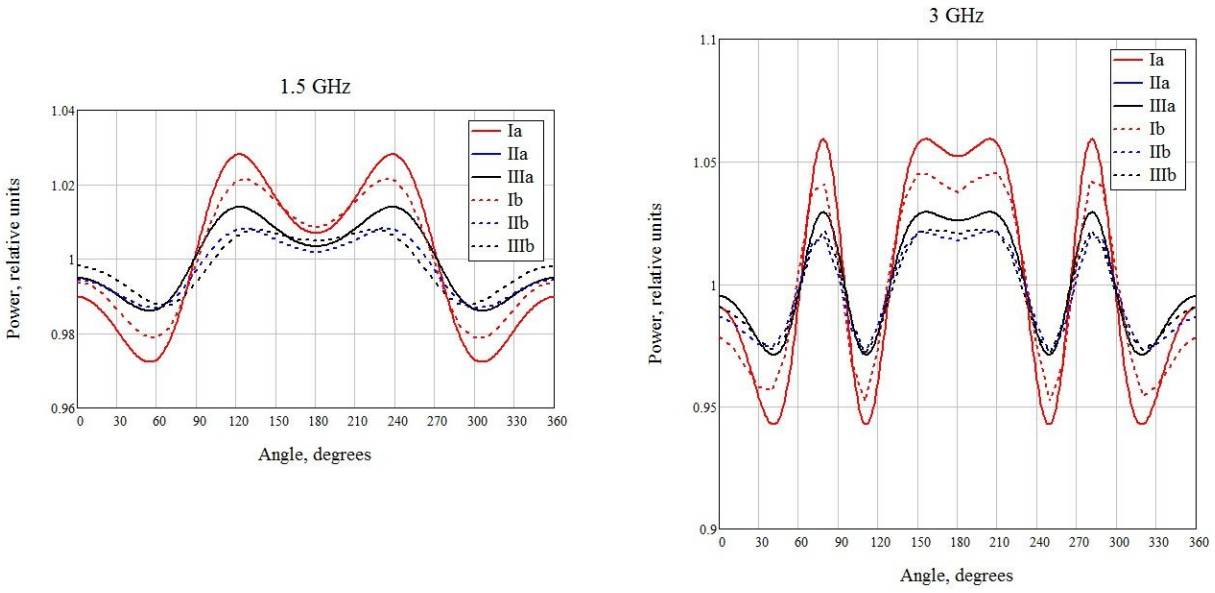



Fig. 2. Dependencies of the relative power flux on the azimuthal angle $\varphi$ for 1.5 GHz (left) and 3 GHz. Solid (a) curves – analytical model; dashed (b) curves – Ansys HFSS simulation. I (red curves) – 30 mm with $1 \cdot 10^{20}$ $m^{-3}$ electron density; II (blue curves) – 30 mm with $5 \cdot 10^{19}$ $m^{-3}$ electron density; III (black curves) – 15 mm with $1 \cdot 10^{20}$ $m^{-3}$ electron density.

**Acknowledgements**. This work was supported by the Russian Science Foundation (project No. 22-22-20065) and St. Petersburg Science Foundation (project No. 17/2022).

## References

1. **M. N. Shneider and R. B. Miles,** "Microwave diagnostics of small plasma objects," J. Appl. Phys. 98, 033301, 2005.
2. **X. Wang and A. Shashurin,** "Study of atmospheric pressure plasma jet parameters generated by DC voltage driven cold plasma source" J. Appl. Phys., vol. 122, no. 063301, 2017.
3. **A. Shashurin, M. Keidar,** "Experimental approaches for studying non-equilibrium atmospheric plasma jets", Phys. Plasmas, vol. 22, no. 12, 2015.
4. **V.L. Ginzburg,** "The propagation of electromagnetic waves in plasmas", Pergamon Press, Oxford, 1970
5. **Raizer, Y. P.,** "Gas Discharge Physics", Springer-Verlag, 1991.
6. **C. A. Balanis,** "Antenna Theory Analysis and Design", 2nd Edition, John Wiley & Sons, Inc., New York, 1997.

# OPTOGALVANIC OSCILLATIONS IN HOLLOW CATHODE LAMP

M. S.A. Eldakli, S. S. Ivković and B. M. Obradović

University of Belgrade, Faculty of Physics, Studentski trg 12, 11001 Belgrade, Serbia
E-mail: obrat@ff.bg.ac.rs

One of the simplest objects for the studying of low temperature plasma is a dc glow discharge, widely applied in spectrometry absorption techniques in the form of a hollow cathode discharge. Beside the use in optical emission spectroscopy, hollow cathode discharges are used in researching of the optogalvanic effect (OGE). OGE is the term given to the light-induced change in the impedance, which occurs because of absorption of resonant radiation by the atoms/molecules present in a gas discharge environment. Within a certain range of operational parameters of the discharge, instabilities and oscillations occur, which are sometimes mixed with the background and cannot be used for optogalvanic detection. These oscillations commonly occur at frequencies below a few hundred kilohertz and have been referred to as pseudosonic (ion) waves. These instabilities can be the inherent characteristics of the discharge (self-sustained oscillations) or can be produced by external perturbation (induced by voltage or by laser radiation). The oscillations usually occur in subnormal regimes, at low pressure and current, where the discharge usually exhibits negative differential resistance. In this article we studied self-sustained and laser induced current oscillations in a commercial hollow cathode lamp (HCL).

## Experiment

The schematic of the experimental setup is shown in Fig. 1.

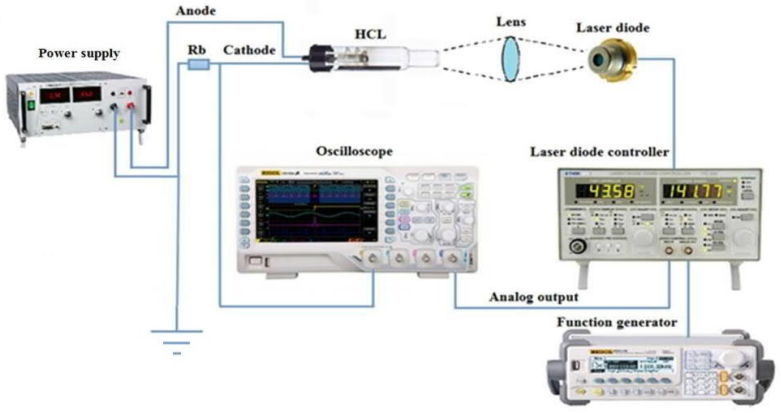



Figure 1. Experimental setup.

HCL with Sb cathode (D = 3.0 mm, L = 11 mm) is filled with neon at low pressure (< 3.5 mbar). To run the discharge, a voltage stabilized power supply is

used. A ballast resistor of 9.98 kΩ is placed in series with the discharge and power supply and it is used for monitoring the current oscillations and the OG signal. Laser diode controller is used for controlling the temperature and current of the laser diode and tuning the laser wavelength around the neon transition 3s – 3p at 659.89 nm. A function generator square pulse is used for modulation of the laser diode current. The laser beam is focused to the hollow cathode filling all its interior space. Four channels, wideband oscilloscope is used for measurement and recording the signals.

## Results and discussion

From the standpoint of voltage-current characteristic, the HCL is operated as an abnormal glow discharge. With the discharge current increase, four different ranges are observed: two with the stable current and two with the self-sustained oscillating current, see Fig. 2.

Current ranges describe the following states:

State I: 0.4 mA ≤ I ≤ 3.1 mA, self-sustained oscillations
State II: 3.2 mA ≤ I ≤ 3.9 mA, stable current region
State III: 4.0 mA ≤ I ≤ 7.5 mA, self-sustained oscillations
State IV: I ≥ 7.6 mA, stable current region.

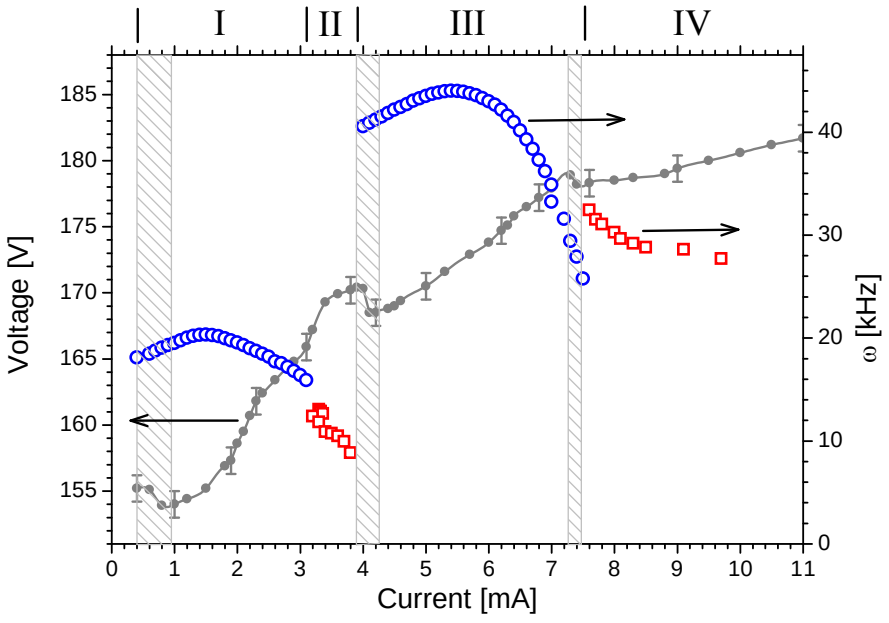



Figure 2. Steady state voltage-current characteristic of the Sb HCL (solid circles with error bars), and graph of current oscillations angular frequency vs. current (open circles and open squares). Self-sustained oscillations are marked by circles while laser induced oscillations are marked by squares. States I to IV and regions with negative differential resistance are also marked on the graphs.

In the State I the oscillations change their frequency with the current increasing. In the State II the discharge works without oscillations (DC or stable-current mode) until it reaches 4 mA. After that, the oscillations start again and prolong till I = 7.5 mA, but with different frequency than in the State I. Finally, for I ≥ 7.6 mA a new stable current state occurred. In Fig 2 also shows the current oscillations angular frequency ω vs. current. Fig. 2 shows that self-sustained oscillation angular frequencies have similar behavior in both current regions. They increase with the current increase and after reaching the maxima (at the middle of the regions) decrease to the values lower than the starting ones. The latter is especially pronounced in the second region where angular frequency rapidly decreases to the value more than 35% lower than the starting one. Examples of self-sustained current oscillations are presented in Fig.3.

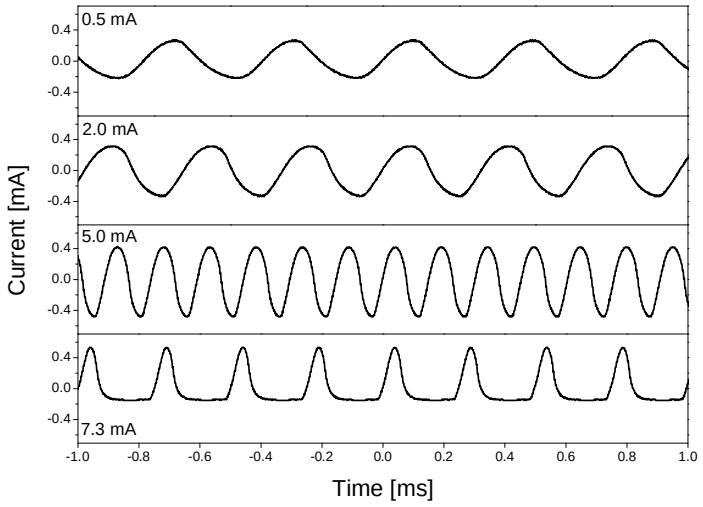



Figure 3. Example of steady-state oscillations for different discharge currents.

Analyzing the Fig.7 one can conclude that amplitudes of the self-sustained current oscillations cannot be approximated as small (e.g. they can be larger than 50% of the steady state current).

The experimental data of the damping constant α and the angular frequency ω for the laser induced current oscillations are acquired by fitting recorded OG signals by dumped sinus function (1). Two graphs in Fig. 4 present examples of OG signals with appropriate fits for two current regions noted as (a) and (b). In the both current regions α increases and ω decreases with the current growth, see Fig. 5. α and ω current dependences are fitted using functions (2) and (3). More details on α(*I*) and ω(*I*) are presented in ref. [1].

$$i(t) - i(0)e^{-\alpha t}\sin(\omega t + \phi_\perp) \qquad (1)$$

$$\alpha(I) = \frac{a_1 + a_2 I}{1 + a_3 I} \qquad (1)$$

$$\omega(I) - \sqrt{\frac{h_1 I}{1 + b_2 I}} - \alpha(I)^2 \qquad (2)$$

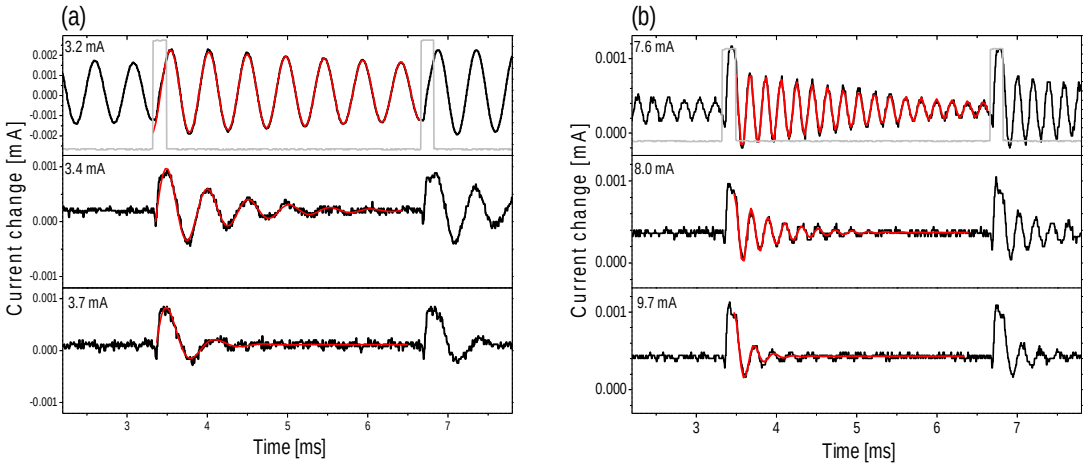



Figure 4. Examples of laser induced oscillations with appropriate fits for different discharge currents in two current regions. Rectangular signals are the laser diode's tuning currents.

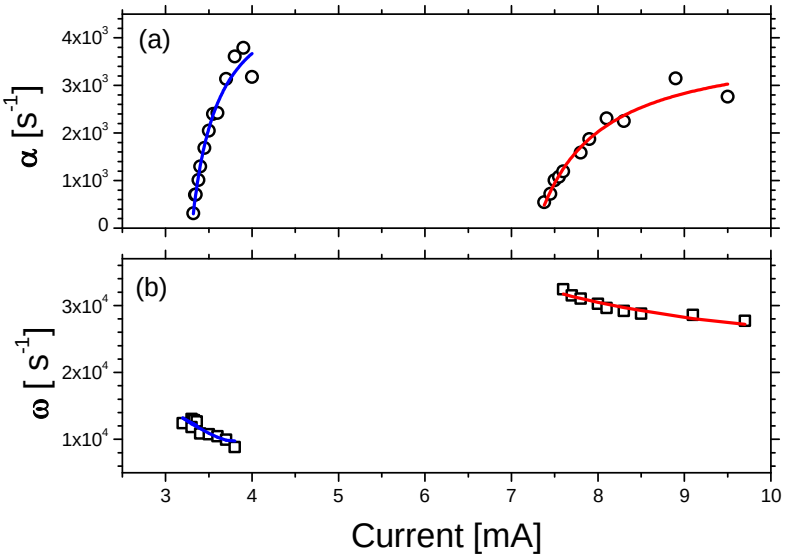



Figure 5. (a) The damping constant α and (b) the angular frequency ω, for the laser induced current oscillations. Appropriate fits for α and ω for two current regions (see Fig. 2) are presented with different colors.

## References

1. **Eldakli, M.S.A., Ivković, S.S., and Obradović, B.M.** European Journal of Physics (2017) 38 (2) 025210

# STUDIES OF ANALYTICAL CAPABILITIES OF LASER INDUCED BREAKDOWN SPECTROSCOPY FOR DETERMINATION OF SULFUR CONTENT IN OIL PRODUCTS

A. Nevar, M. Nedelko, N. Tarasenko

Institute of Physics of National Academy of Sciences of Belarus,
220072 Belarus, Minsk, Nezalezhnasti Ave. 68-2, e-mail: a.nevar@ifanbel.bas-net.by

**Introduction.** Crude oil is a natural combustible liquid with a specific odor, consisting mainly of a complex mixture of hydrocarbons of various molecular weights and some other chemical compounds of sulfur, oxygen, nitrogen, microelements. Oil sulfur compounds are complex mixtures consisting of mercaptans, sulfides, as well as disulfides and heterocyclic compounds. Sulfur is the most abundant of the heteroatoms in crude oil and oil products. Its content in oil ranges from hundredths of a percent (Baku, Turkmen, Sakhalin oils) to 5-6% (oils of the Ural-Volga region and Siberia).

The determination of sulfur in oil and its removal is of great importance, since sulfur compounds adversely affect the quality of petroleum products, cause a corrosion of equipment and poison expensive refinery catalysts and pollute the environment by producing toxic sulfuric anhydride when burned.

To date, many different methods have been developed for determining sulfur in oil, from chemical to X-ray diffraction [1].

All these methods can be divided into 3 groups:

1. Methods based on the oxidation of sulfur and the subsequent determination of oxides.

2. Methods based on the reduction of sulfur to $H_2S$.

3. Spectral methods: a) X-ray based and b) atomic emission.

In the present work, we analyzed capabilities of standard laser induced breakdown spectroscopy (LIBS) experimental equipment for determination of sulfur in crude oil and some oil products.

**Experimental.** The experimental setup is shown in Fig. 1. Laser plasma was produced by a radiation from a YAG:$Nd^{3+}$ laser (Lotis TII LS2137U, Belarus) operated on fundamental (1064 nm) and forth (266 nm) harmonics, with pulse energies 23-175 mJ/pulse and 40 mJ/pulse, respectively.

Since during ablation the plasma plume propagates perpendicularly to the target surface, the incident laser beam was directed not at a right angle to the target surface to avoid contamination of the optical elements. The cell with a sample was specially designed providing windows for introducing the laser beam and recording the plasma plume emission. In addition, there was a possibility for purging of the cell with gases. The cell filled with the oil sample under study contains a disc placed inside the cuvette, so that part of it was

immersed in oil. The disk was driven into rotation by an engine with a gearbox, catching the oil which covered the disc surface with a film.

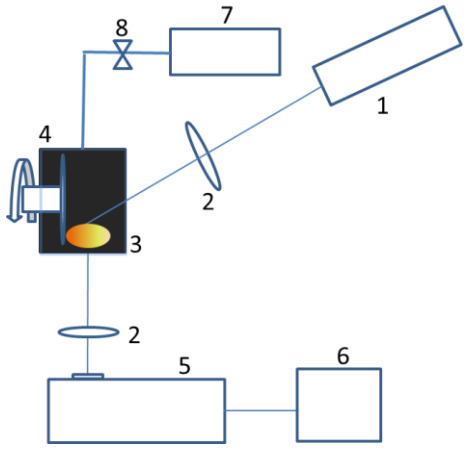



Fig. 1. Experimental setup: 1 – laser, 2 – lens, 3 – cuvette with oil, 4 – rotating target, 5 – spectrograph, 6 – computer, 7 – gas cylinder with helium , 8 – valve

A laser beam was focused onto the surface of the disk covered with oil film. The rotation of the disk provided mixing of the liquid sample and renewal of the film on the ablated surface. To prevent the formation of fog, the cell was purged with air or helium.

Plasma emission was collected by a quartz lens (focus 75 mm) and directed on the slit of the spectrometer (Solar TII, Belarus) with a grating containing 600 lines/mm.

Vacuum and machine oil, as well as 2 Ural crude oils taken from the Mozyr Oil Refinery (sample 1) and Novopolotsk Oil Refinery (sample 2) with sulfur concentration ~ 1.35% w/w were used as test samples.

**Results and discussions.**

The determination of sulfur in oil is a rather difficult task for LIBS: most of the sulfur energy levels are quite high (more than 7 eV), the most intense sulfur lines are in the UV region (180 – 190 nm), requiring a purge or vacuum spectrometer. In the visible region sulfur lines are overlapped by the emission bands of $C_2$, CH, CN molecules [2]. In the NIR region some authors detected the sulfur triplet at 921,291 nm, 922,811 nm, 923,749 nm [3].

Vacuum oil VM-1 and engine oil with sulfur of known concentration dissolved in them were studied as model samples. The aim of the study was to determine the minimum sulfur concentration that can be recorded by LIBS method. To obtain reliable results during the registration process, the sample was stirred to prevent sulfur from precipitating. The results of these experiments are presented in Fig. 2, where LIBS spectra of sulfur pressed tablet andvacuum and engine oils are presented. The spectrum of bulk sulfur is shown for

comparison. As can be seen from Fig. 2, both in vacuum and engine oils with 1%w/w sulfur concentration intensities of sulfur lines are observed at the background level.

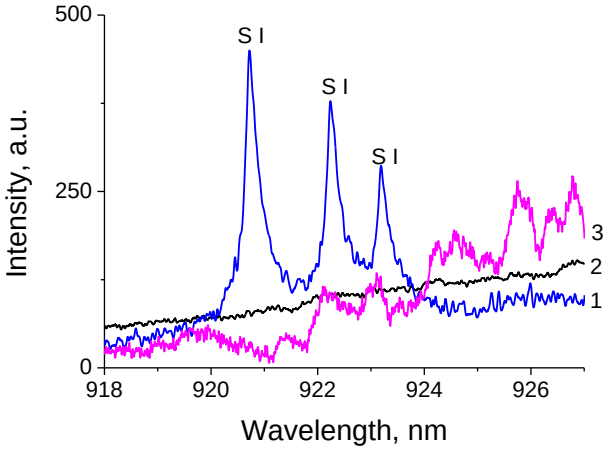



Fig. 2. LIBS spectra of sulfur (curve 1), vacuum (curve 2) and engine (curve 3) oils

Fig. 3 shows the emission spectra obtained during the ablation of oil (sample 2) by radiation of the fundamental and fourth harmonics of a YAG:$Nd^{3+}$ laser. The spectra obtained by purge with air are characterized by the presence of atomic carbon, nitrogen, oxygen, and weak sulfur lines in the region at 920 nm. Ablation in a helium atmosphere reduces the background level and eliminates the lines of oxygen and nitrogen containing in the air, but does not increase the intensity of the sulfur lines.

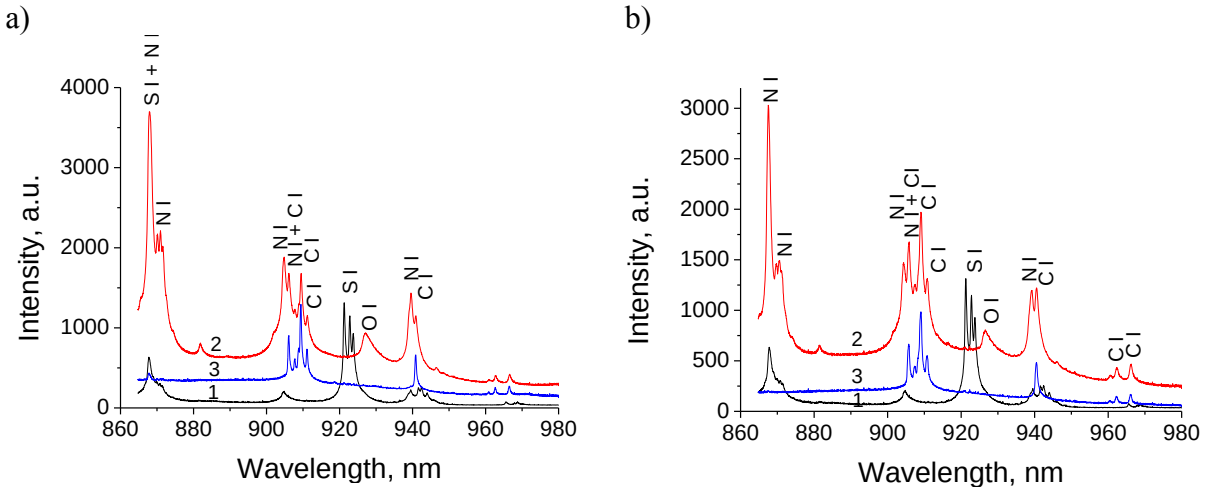



Fig. 3. LIBS spectra of bulk sulfur (curve 1), crude oil (sample 2) under air (curve 2) and helium (curve 3) atmosphere. Plasma created by irradiation of the fundamental (a) and forth (b) harmonics of YAG:$Nd^{3+}$ laser

In the spectra of the plasma from crude oil (sample 1) recorded at different energies at laser radiation of the fundamental harmonic of the YAG:$Nd^{3+}$ laser, low-intensity sulfur lines were detected (Fig. 4).

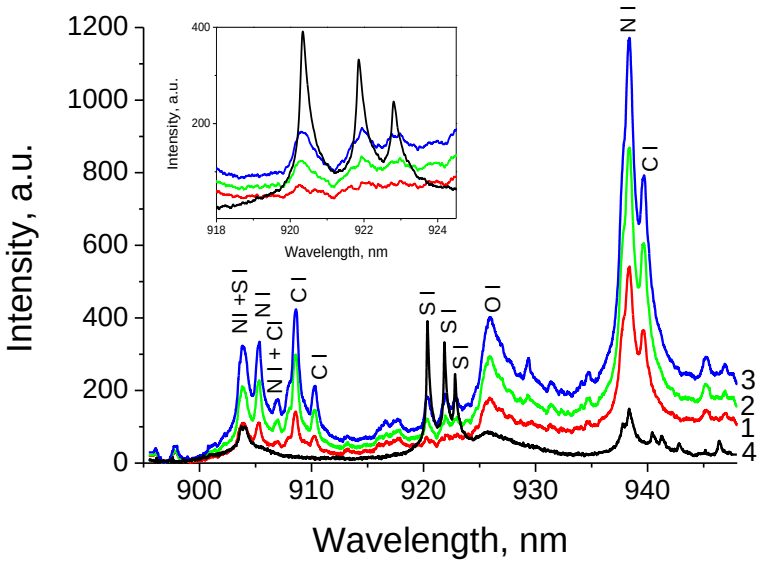



Fig. 4. LIBS spectra of bulk sulfur (curve 4) and crude oil (sample 1, curves 1-3) under air atmosphere at different intensity of laser irradiation (1 – 23 mJ/pulse, 2 – 34 mJ/pulse, 3,4 - 45 mJ/pulse)

**Conclusions.** The obtained results allow to conclude that the LIBS method with standard equipment can not provide a detection of sulfur content in crude oil and oil products at the level of 1% and below. The use of laser radiation of different wavelengths, as well as ablation in inert (helium) atmosphere, does not improve the analytical capabilities of the method.

**Acknowledgements**. The research was funded by NAS of Belarus under project Convergence 2.2.05.

## References

1. **Новиков Е.А.** «Мир нефтепродуктов. Вестник нефтяных компаний» № 1, 3, 4, 5 (2008).
2. **Bolshakov A.A., Pandey S.J., Mao X, Liu C.** Spectrochim. Acta Part B 179 (2021) 106094.
3. **Trichard F., Forquet V., Gilon N., Lienemann C-P., Baco-Antoniani F.** Spectrochim. Acta Part B 118 (2016) 72–80.

# 7. PLASMA APPLICATIONS AND ADVANCED PLASMA TECHNOLOGIES

# ENERGY DISSIPATION IN ARC DISCHARGE OCCURRING AFTER THE FUSE EXPLOSION

A.A. Kozlov, A.V. Shurupov, A.V. Kozlov, V.P. Polishchuk, M.A. Shurupov

Joint Institute for High Temperatures of the Russian Academy of Sciences,
Izhorskaya 13 Bd. 2, Moscow 125412, Russia; alexk5577@yandex.ru

Fuses are widely used in the electric power industry when it is necessary to quickly cut off the network current in the event of an accident. After a fuse breaks, an arc discharge usually occurs, and it may be necessary to maximize the amount of energy dissipated in this discharge. In particular, it is required for the efficient operation of current-limiting devices.

In this paper we consider the experiments with a model fuse, which was cut from an aluminum foil tape with thickness of 80 μm. The width and the length of the fuse were 44 and 260 mm respectively. The five rhombuses with increasing sizes were cut in the middle of the tape (Fig. 1), which facilitated the electric explosion of the fuse under the action of the passing current. The cross-sectional area of the fuse was changed in the limits of 1.6-3.5 $mm^2$. The fuse was immersed in quartz sand with a grain size of ~1 mm. The fuse was installed parallel or perpendicular to the sand surface at a distance of ~10 mm from it.



Fig. 1. The fuse before experiment

The electrical explosion of the fuse occurred under the action of a high-voltage pulse from the capacitive storage (CS) with capacity of 176 mF and maximum charging voltage of 6 kV. The inductance of 310 μH was connected to the circuit in series with the fuse. The total resistance of the circuit without fuse was 35 mΩ; the calculated resistance of the fuse was 2.4 mΩ.

The diagnostic system included measuring the current and voltage at the fuse, the emission registration from the minimum and maximum cross sections of the fuse using optical fibers. The fuse explosion was recorded on video with the speed of up to 7500 frames per second.

Fig. 2 shows the oscillograms of the current *I(t)* and voltage *V(t)* at the fuse. The charging voltage of CS was 1.5 kV; the fuse was set perpendicular to the

sand surface. The fuse position relative to the sand surface had little effect on the discharge current. In this experiment two current peaks were recorded - 12 kA at times of 3 ms and 9 kA at times of 14 ms. The second current maximum was realized at a falling voltage at the fuse. This means that at this stage of the process the resistance of the discharge gap has decreased.

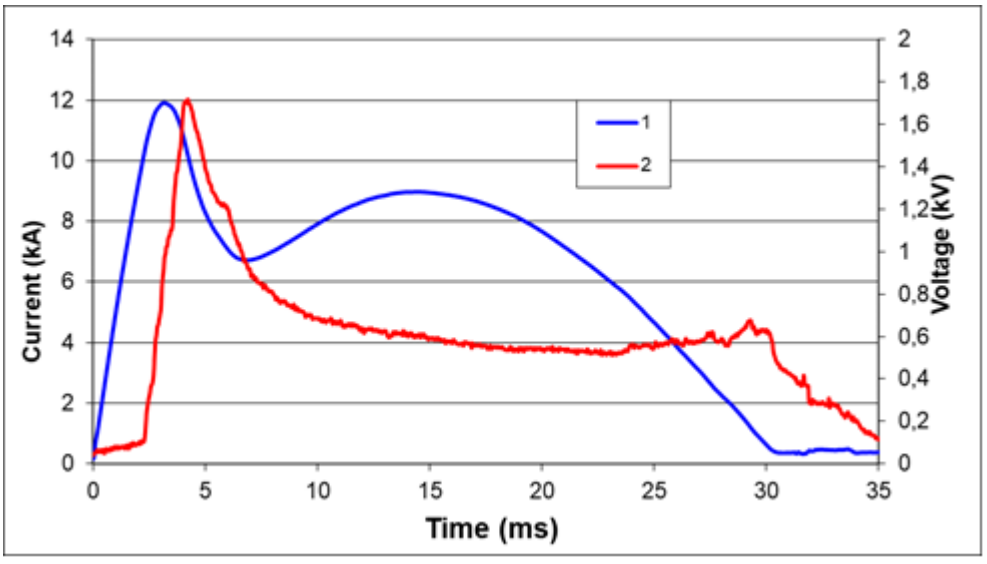



Fig.2. Waveforms of the current (1) and voltage (2)

Video filming confirmed that the fuse began to break down near the minimum section. This area began to glow ~1 ms after the voltage was applied, then, for ~1 ms, the glow gradually turned on from the zone of other constrictions on the fuse. The glow zone on the sand surface propagated at the speed of ~30 m/s. In ~2 ms after the voltage was applied, a plasma cloud appeared near the sand surface, this cloud expanded at the speed of ~60 m/s. If the fuse was installed parallel to the sand surface, then during the electric explosion, the hemispherical protrusions formed on the sand surface (Fig. 3). These protrusions grew at the rate of ~10 m/s, and their height reached ~70 mm; the plasma pressure, which may be estimated from these data, was ~0.3 MPa.



Fig. 3. The sand surface during discharge in the fuse, interval between frames – 1.3 ms

The modes of the fuse explosion with two current maximums (Fig. 2) have a considerable practical interest because in this case the significant electrical energy dissipates in the vicinity of the destroyed fuse. It is also important that the region of the fuse location ceases to conduct current, although the voltage on it can be quite large (~0.5 kV). The results from Fig. 2 were used to analyze the energy balance of the fuse distraction. The charge and the energy of the CS $W_C$ were calculated from the current. The energy released in the circuit $W_{r1}$ and in the fuse $W_{r2}$ were determined from the circuit resistance and the voltage drop on the fuse. The magnetic energy in the circuit $W_L$ was found from its inductance. The components of the energy balance $W_C$, $W_{r1}$, $W_{r2}$ and $W_L$ divided to the initial energy $W_0$ stored in CS ($W_0$=198 kJ) are presented in Fig. 4.

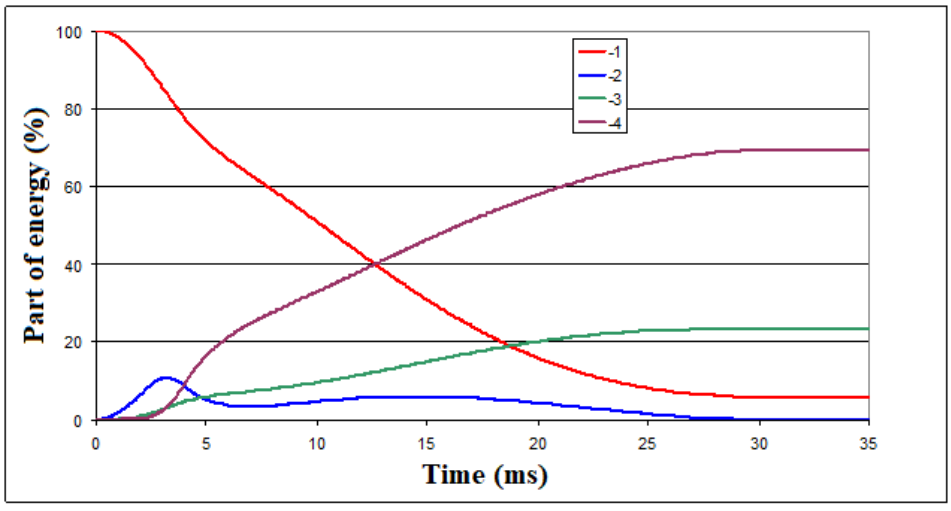



Fig.4. Energy balance: 1 - $W_C/W_0$; 2 - $W_L/W_0$; 3 - $W_{r1}/W_0$; 4 - $W_{r2}/W_0$

The destruction of the fuse and the appearance of the arc occurred before the evaporation of the most heated regions during the transition into the liquid phase. The further destruction of the fuse can be influenced by thermal stresses and mechanical stresses, which are created by magnetic forces. The local fuse temperature $T$ was calculated from the energy balance in its cross-section [2]:

$$h^2 d^2 \frac{d\rho_d c_p T}{dt} = I^2 \rho_0 (1+\alpha(T-T_0)) \qquad (1)$$

where $d$ and $h$ – the fuse width, $c_p$ and $\rho_d$ – heat capacity and density of the conductor, $\rho_0$ – its resistivity at the room temperature $T_0$ =20°C, $\alpha$ – temperature coefficient of resistance. The properties of aluminum were taken from [1].

It follows from equation (1) that for the current pulse shown in Fig. 2, melting in the minimum and maximum sections of the fuse occurred 2.2 and 3.5 ms, respectively, after the voltage pulse was applied to the fuse. The calculated times of the liquid phase formation in the different sections of the fuse agree with the appearance time of the glowing regions on the sand surface.

At the moment $t$=2.3 ms the sharp break is observed in the voltage oscillogram (Fig.2). At this moment the fuse resistance was 12 mΩ, it increased five times compared to the initial one. After this some peculiarities appeared on the sharply increasing voltage. The time of their appearance was consistent with the onset of melting in the other sections of the fuse. At this time the resistance of the fuse region began to increase abruptly and by the time t = 4 ms reached 170 mΩ, remained at this level for 2 ms. At this stage there was an intense fuse destruction with emergence of local microarcs. By the second maximum of the current ($t$=14 ms) the resistance of the discharge gap decreased to 65 mΩ; after it began to increase with decreasing current.

After the fuse destruction the current is distributed between two parallel conductors: the plasma and the molten metal. The typical value of the electrical conductivity of the arc plasma σ at the atmospheric pressure ~50 $(\Omega\times cm)^{-1}$ [3]. It is approximately three orders of magnitude less than the conductivity of liquid aluminum [1]. The currents passing through the plasma and melt could be comparable if the cross-sectional area of arc channel $S_a$ was large enough. The average electric field strength in the discharge gap $E$ at the first current maximum (Fig. 2) is ~60 V/cm. Therefore, the average current density is $J = \sigma E$ ~3 kA/cm$^2$, and the cross-sectional area $S_a$ must be ~4 cm$^2$. However, the cross-sectional area of the lumen, which was created in the sand by the fuse explosion, was an order of magnitude smaller. Consequently, a significant part of the current passed through the molten metal, which was squeezed out by high plasma pressure to the discharge periphery.

The fraction of the current flowing through the metal should decreased over the time, since aluminum loses its conductivity due to oxidation. Additionally, the discontinuities in the liquid metal with the expansion of the melt increased. High resistance of the discharge gap at the initial stage (~170 mΩ) was possibly due to the presence of many isolated small hot metal drops. Over time, these drops merged and cooled that led to the decrease of the gap resistance. The following increase of this resistance at the final stage of the discharge can be associated with the decreasing of plasma conductivity because of decreasing of its temperature due to falling current density. The above reasoning probably qualitatively explains the mode of the fuse explosion with two current maxima (Fig. 2).

## References

1. **Babichev A.P.** Handbook. Physical Values. Moscow: “Energoatomizdat”. (1991).
2. **Knoepfel H**. Pulsed High Magnetic Fields. London: North Holland (1972).
3. **Raizer Y.P.** Physics of gas discharge. Moscow: “Nauka” (1987).

# PLASMA INDUCED MODIFICATION OF ZnO-BASED PHOTOCATALYSTS DOPED WITH PLASMONIC NANOPARTICLES

N.A. Savastenko [(1)], A.A. Shcherbovich [(1,2)], A. V. Miadzvetski [(1)], V.A. Lyushkevich [(2)], I.I. Filatova [(2)], S.A. Maskevich [(1)]

[1] Belarusian State University, International Sakharov Environmental Institute BSU, 23 Dolgobrodskaya Str., 220070 Minsk, Belarus, nataliesavastenko@iseu.by
[2] B.I. Stepanov Institute of Physics, National Academy of Sciences of Belarus, 68 Nezavisimosti Ave., 220072 Minsk, Belarus, filatova@presidium.bas-net.by

Disposal of pharmaceutical waste is an important problem of ecology and safety of the population of countries [1]. Pharmaceutical waste contains bioactive chemicals that can have a negative impact on soil, water, air, and living organisms. Water is especially sensitive to bioactive chemical pollutants.

In this work, we investigated the use of plasma treatment to increase the photocatalytic activity of ZnO photocatalysts doped with plasmonic Ag nanoparticles for water purification from pharmaceutical waste. In [2–5], plasma treatment was successfully used to increase the efficiency of photocatalysts.

Materials and methods. Sodium citrate $C_6H_5O_7Na_3$ (5 Okeanov LLC, Belarus), silver nitrate $AgNO_3$ (UE Unidragmet, Belarus), sodium hydroxide NaOH, 7-aqueous zinc sulfate $ZnSO_4$ $7H_2O$, ascorbic acid $C_6H_6O_6$ (OOO Belreaktivpostavka, Belarus), sodium borohydride, distilled water. Caffeine was chosen as the model substance. Caffeine (a mixture of caffeine and sodium benzoate, $C_{15}H_{15}N_4NaO_4$ (PJSC SPC "BORSHHAGOVSKY CPP").

To prepare a photocatalyst based on zinc oxide (ZnO) doped with silver (Ag) by the doping method, the procedure described in [6] was used. Composite Ag-ZnO nanoparticles were obtained by adding 6 ml of 0.01 M ascorbic acid and 13 ml of $AgNO_3$ 0.01 M to a solution of NaOH and $ZnSO_4$, while stirring on a magnetic stirrer at a speed of 150 rpm, after which the solution was kept at 70 °C for 2 hours. The synthesized products were centrifuged, washed several times with distilled water, and dried for 24 h.

Plasma treatment of the Ag-ZnO catalyst was carried out in the plasma of a dielectric barrier discharge generated in air at normal pressure for 5, 10, 15, and 25 minutes.

A dielectric barrier discharge is created between a flat electrode made in the form of a grid and having a dielectric coating, and a flat metal grounded electrode. A power source operating at a frequency of 1 kHz was used to supply a pulsed voltage to the upper electrode. The effective energy ($E_{eff}$) absorbed by the catalyst during treatment can be estimated from the formula:

$$E_{eff} = E_{el} t_{tret} f, \quad (1)$$

where $t_{tret}$ is the catalyst treatment time in plasma, f is the frequency, $E_{el}$ is the energy injected into the gas-discharge plasma. For the discharge mode used, the $E_{el}$ value was 20 mJ per cycle.

Based on studies [7], it can be expected that a treatment time of 15 minutes is optimal for increasing the photocatalytic activity of the Ag-ZnO photocatalyst. Accordingly, for a treatment time of 15 minutes, the effective energy value was $E_{eff}$=18 000 J.

The existence of optimal conditions for the efficient absorbed energy by catalysts during plasma treatment, which provide an improvement in the characteristics of the catalyst, indicates that a small value may be insufficient to ensure the interaction of nanoparticles with the catalyst surface. On the other hand, too high a value of the effective energy can lead to violation of the interface between the nanoparticles and the solid surface of ZnO, which will lead to a loss of catalyst activity.

**Results and discussion.** The photocatalytic activity was studied in a model reaction of caffeine decomposition under the action of ultraviolet radiation (UVR source mercury-quartz lamp DRT-240 with a power of 240 W) in aqueous suspensions of the studied samples with constant stirring on a COLOR SCUID IKAMAG WHITE magnetic stirrer (IKA, Germany) at a speed 200 rpm During irradiation, the change in the concentration of caffeine in the solution was monitored using a SOLAR PB 2201 spectrophotometer (SOLAR, Belarus).

To prepare the suspension, a 40 mg sample of the catalyst was mixed with 20 ml of an aqueous solution of caffeine with a concentration of 300 mg/L. The chosen concentration of caffeine for the model reaction is in the range of concentrations of pharmacological wastes contained in wastewater [8, 9].

The relative concentration of the model substance $C_r$ was determined from the data of optical density measurements at the absorption maximum:

$$C_r = \frac{C(t)}{C_0} \cdot 100\% = \frac{A_t}{A_0} \cdot 100\%, \quad (2)$$

where $C_0$ is the initial concentration of the model substance, C(t) is the concentration of the model substance after irradiation with UV radiation at time t, $A_0$ and $A_t$ are the optical density of the solution of the model substance at the absorption maximum before the start of irradiation and at time t after the start of sample irradiation respectively.

The rate constant of the photodegradation reaction, determined from the slope of the graph of dependence of the concentration $C_r$ on time, was used as a quantitative characteristic of the photocatalytic activity of the samples.

Figure 1 shows graphs of changes in the optical density of caffeine during irradiation of a suspension of Ag-ZnO photocatalysts in solution of caffeine for 5, 10, 15, 20 and 25 minutes before (a) and after (b) plasma treatment.

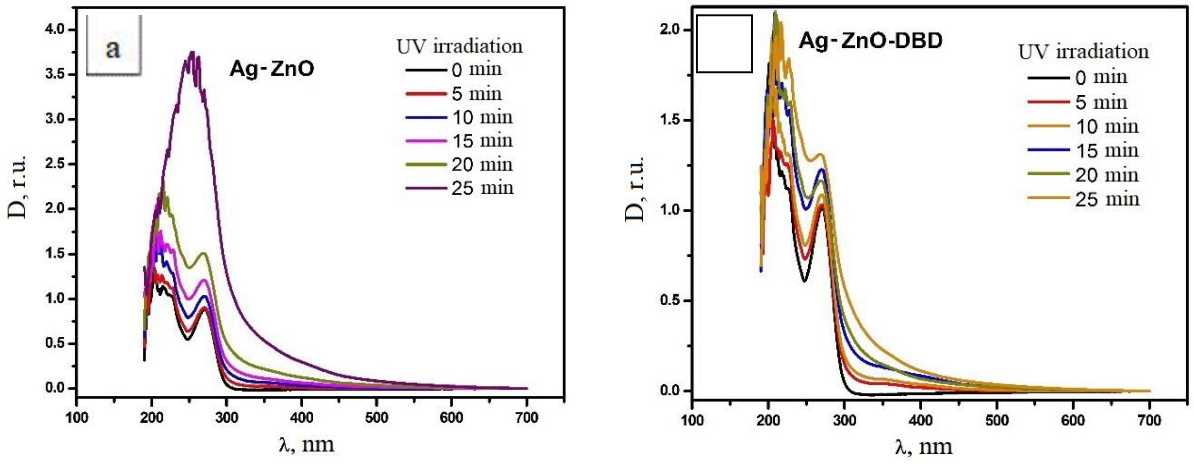



Fig.1 - Graphs of changes in the optical density of caffeine during irradiation of a suspension of Ag-ZnO photocatalysts in solution of caffeine for 5, 10, 15, 20 and 25 minutes before (a) and after (b) plasma treatment

The intensity of the absorption peak at a wavelength of $\lambda_{max}$ = 272 nm relative to the local minimum at a wavelength of $\lambda_{min}$ = 247 nm decreases with increasing irradiation time. However, the absorption of solutions in the range of 200-550 nm increases after UV irradiation of the studied suspension (caffeine-photocatalyst solution). The increasing absorption of the solution after the irradiation of the suspension can be explained by the formation of caffeine photodegradation reaction products with a wide absorption band in the range of 200–550 nm. The absorption maxima of the resulting reaction product are in the range of 217–255 nm. The position of the absorption maximum depends on the catalyst used and is 255 nm for Ag-ZnO and 217 nm for Ag-ZnO-DBD.

The rate constant of the photodegradation reaction was determined from the slope of the graph of dependence of the concentration Cr on time. The activity of the Ag-ZnO photocatalyst is $7.4 \cdot 10^{-4}$ $s^{-1}$, after DBD plasma treatment within 15 minutes the activity of the photocatalyst increased to $1.1 \cdot 10^{-3}$ $s^{-1}$.

**Conclusion**. In the summary of the studies carried out, data were obtained on the effect of plasma treatment on the photocatalytic characteristics of the synthesized Ag-ZnO nanostructures. The synthesized materials can be used as catalysts for the photodegradation of pharmaceutical waste in water.

**Acknowledgements.** This work was partially financially supported by the State Research Program “Convergence 2025. 2.2.02. NIR 8. Scientific basis of

plasma-activated interaction of nanoparticles with the surface of functional materials in order to develop new methods for aimed synthesis and modification of nanostructured catalytic materials" and "Convergence 2025. 2.2.02. NIR 1. Development of the basis of the combined effect of plasma, electromagnetic fields and dichromatic laser radiation on materials and biological objects for use in new technologies".

## References

1. Utilization of waste waste [**Electronic resource**] / Medical waste. - 2022. - Access mode: https://medservise24.ru/blog/medotkhody-i-obrashchenie-s-otkhodami/otkhody-na-farmatsevticheskikh-predpriyatiyakh-pravila-utilizatsii/ - Access date: 06/23/2022.

2. 2. **Liu C.-J., Li M., Wang J., Zhou X., Guo Q., Yan J. and Li Y. Chin**. J.Cat., 37 (2016) 340-348.

3. **Brueser V., Savastenko N., Schmuhl A., Junge H., Hermann I., Bogdanoff P. and Schroder K.** Plasma Process. Polym., 4 (2007) S94–S98.

4. **Savastenko N.A., Anklam K., Quade A., Bruser M., Schmuhi A. and Bruser V.** Energy Environ. Sci., 4 (2011) 3461–3472.

5. **Savastenko N.A., Filatova I.I., Lyushkevich V., Chubrik N., Shcherbovich A.A. and Maskevich, S.A**. High Temperature Material Processes, 24 (2020) 275-291.

6. **Tran Thi V.H., Cao T.-H., Pham T.-N., Pham T.-T. and Le M.-C.** Journal of Chemistry, (2019) 1–13.

7. **Scherbovich A., Lushkevich V., Savastenko N., Filatova I. and Maskevich S**. Sakharov readings 2020: environmental problems of the XXI century: materials of the 20th international scientific conference, (2020) 451-455.

8. **Mondal K., Sharma A.** Nanoscience & Nanotechnology for Minkind, (2014) 36–72.

9. **Rajeshwar K, Osugi M.E., Chanmanee W., Chenthamarakshan C.R., Zanoni Maria Valnice Boldrin, Kajitvichyanukul P. and Krishnan-Ayer, R.** Journal of Photochemistry and Photobiology C: Photochemistry Reviews, 9(4) (2009) 171–192.

# THE EFFECT OF DBD PLASMA ON THE MORPHOLOGY OF Ag NANOPARTICLES USED IN PHOTOCATALYSIS

N.A. Savastenko[(1)], A.A. Shcherbovich[(1)], V.A. Lyushkevich[(2)], I.I. Filatova[(2)], S.A. Maskevich[(1)]

[1]Belorussian State University, International Sakharov Environmental Institute BSU, 23 Dolgobrodskaya Str., 220070 Minsk, Belarus, nataliesavastenko@iseu.by
[2]B.I. Stepanov Institute of Physics, National Academy of Sciences of Belarus, 68 Nezavisimosti Ave., 220072 Minsk, Belarus, filatova@presidium.bas-net.by

Doping plasmonic silver nanoparticles (Ag NPs) into semiconductor catalysts can remarkably improve their photocatalytic activity [1-3]. In contrast to the study found in the literature [1-3], we observed a diminished photocatalytic activity after impregnation of ZnO with Ag NPs [4, 5]. However, it was shown in our previous work [4, 5] that plasma treatment of ZnO-based photocatalysts doped with Ag nanoparticles resulted in enhancement of their catalytic activity towards reactions of methyl orange and sodium caffeine benzoate photodegradation in aqueous solution exposed to ultraviolet (UV) light. Our previous studies have established that plasma treatment of Ag-NPs–doped ZnO-based photocatalysts improved their performance if the treatment time was less than 15 min and the value of the effective energy ($E_{eff}$) consumed by the catalysts during plasma treatment was less than 18,000 J. A further increase in the treatment time (i.e., by increasing the $E_{eff}$ value until it reached 30,000 J) inhibited the photocatalytic activity of hybrid Ag-NPs/ZnO catalysts [5]. It was also found that doping with Ag-NPs suppressed recombination (i.e., increased the value of characteristic recombination time $\tau$) of photoinduced electron–hole pairs in ZnO if the value of $E_{eff}$ was less than 18,000 J. A further increase in the value of $E_{eff}$ decreased the values for the recombination time and catalyst activity [5]. It was supposed that under optimal conditions in terms of $E_{eff}$ for the best catalyst performance, a low $E_{eff}$ value might be not enough to ensure the interaction between the NPs and the catalyst surface. On the other hand, an $E_{eff}$ value that is too high might disrupt the interaction between the NPs and the solid ZnO surface at the interface, leading to loss of catalyst activity [5].

In this study, the effect of dielectric barrier discharge (DBD) plasma on the morphology of Ag NPs was studied in detail by Atomic Force Microscopy (AFM) and UV-Vis Spectroscopy to elucidate the reason of the existence of optimal conditions in terms of the effective energy ($E_{eff}$) consumed by catalysts during plasma treatment in order to provide the best catalyst performance.

The samples were prepared as follows. At first colloidal silver nanoparticles were prepared by adding 1 ml of a 1% trisodium citrate ($C_6H_5O_7Na_3$) solution to an aqueous solution of 50 ml of a $10^{-3}$ M $AgNO_3$. Preliminarily aqueous solution

of $AgNO_3$ was heated to boiling. The mixture was boiled for 1 hour and then was cooled down. The detailed description of the method for preparation of colloidal Ag NPs can be found in [6, 7]. Then colloidal suspension was dissolved to Ag concentration of $10^{-5}$ M. Thereafter 250 µl of the Ag NPs colloidal suspension was deposited on to the quartz glass substrate. Then sample was dried at 80C. The preparation procedure was accomplished with plasma treatment by dielectric barrier discharge plasma. The DBD reactor was described in details in previous paper [5].

The value the effective energy ($E_{eff}$) consumed by catalysts during treatment time was calculated by the following relation:

$$E_{eff} = E_{el} t_{tret} f, \quad (1)$$

where $t_{tret}$ is the plasma treatment time and $f$ is the frequency of feeding voltage and $E_{el}$ is the energy consumed by DBD. The value of $E_{el}$ was estimated as the area of the characteristic Q-U Lissajous Figures [8]:

$$E_{el} = \oint U(t)dQ \equiv AREA\ of\ (Q-U)\ diagram. \quad (2)$$

A SOLAR PB 2200 single-beam spectrophotometer was used to perform the UV–vis absorption measurements. The morphology of untreated and plasma treated Ag NPs was investigated by non-contact mode atomic force microscopy in air at room temperature. The observations were performed using an Solver P47 Pro (NT-MDT»Ltd, Russia) system.

The UV–vis absorption spectra of untreated and plasma treated Ag NPs are presented in Fig.1. A photograph of the DBD plasma in use is also presented in Fig.1. Untreated Ag NPs exhibited a UV–Visible absorption maximum at 415 nm because of surface plasmon resonance [9]. Absorption at 730 nm assigned to the agglomerates of Ag NPs [10]. As it can be seen in Fig.1a, plasma treatment at $E_{eff}$= 51 and 153 J resulted in disappearance of absorption peak at 730 nm. These results imply that plasma treatment at medium energy cause the fragmentation of agglomerates. Plasma treatment at higher energy leads to a further decrease in the number of agglomerates and fragmentation of nanoparticles with the formation of small clusters of Ag atoms.

The fragmentation of Ag NPs agglomerates was confirmed by AFM (Fig. 2). From the AFM images, the height of the agglomerates and NPs were measured (Fig. 2b and d). The height of Ag NPs agglomerates was found to be ca 600 nm (Fig. 2b). The height of the structures was reduced after plasma treatment up to 50% (Fig. 2d).

In summary, our experiments confirm that there is a range of energy values $E_{eff}$ at which plasma treatment leads to the fragmentation of agglomerates of

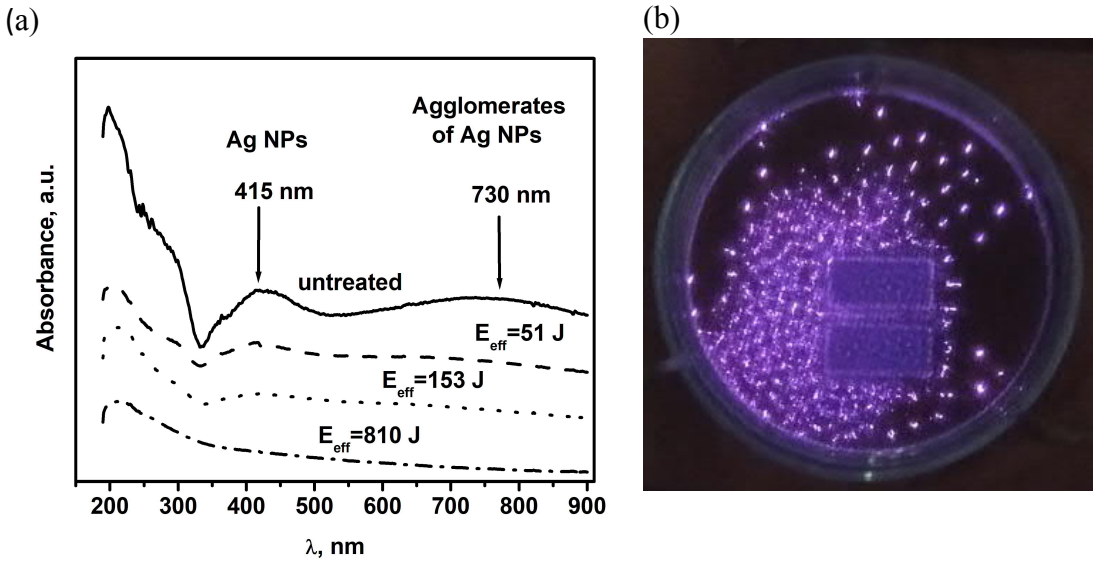



Fig. 1. UV–visible absorption spectra of untreated and DBD plasma treated Ag NPs (a) and a photograph of the DBD plasma during sample treatment (b).

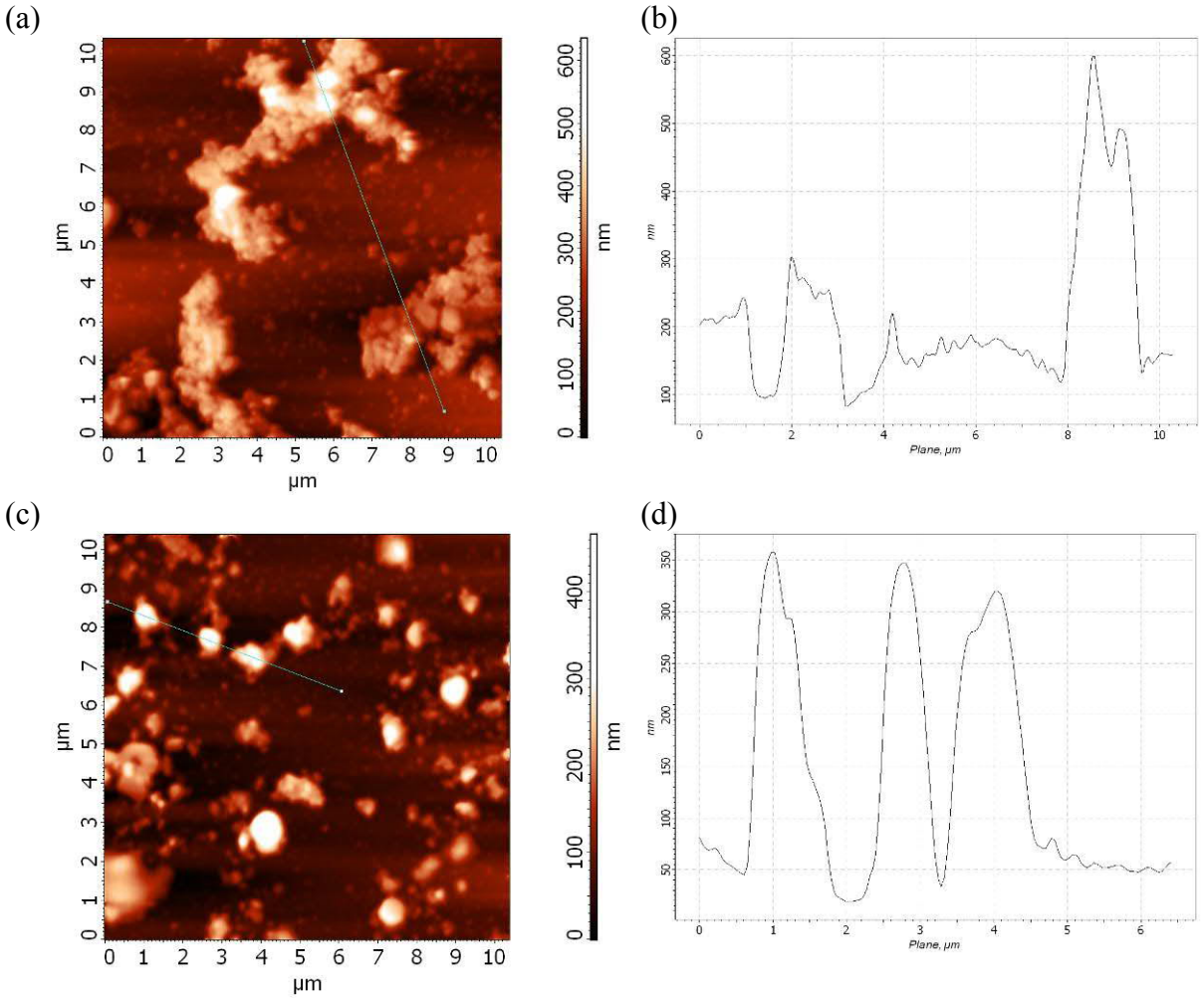



Fig. 2. AFM microphotograph images (a and c)of untreated (a) and DBD plasma treated Ag NPs at Eeff = 810 J (c); (b) line scan at position marked in picture (a); (d) line scan at position marked in picture (c)

NPs. In our experiments, this range was 50-150 J. The surface of samples treated with plasma at $E_{eff}$=50-150 J is covered rather with NPs than with agglomerates of NPs. Futhuer increase in $E_{eff}$ leads in destruction of NPs.

It was shown in our previous paper [5] that there were the optimal conditions in terms of the effective energy $E_{eff}$ consumed by catalysts during plasma treatment in order to provide the best catalyst performance. It may be assumed that the existence of optimal conditions is due to the fact that defragmentation of NPs agglomerates accrued during processing under optimal conditions. If the treatment of photocatalysts is carried out under optimal conditions their surface is covered with NPs. NPs enhance the activity of photocatalysts by any of known mechanisms [1-3]. On the other hand agglomerated NPs or small clusters can not promote the activity of catalysts. It should be stressed here, that the optimal value of $E_{eff}$ for catalysts treatment may differ from the value of $E_{eff}$ in model experiments due to the difference in amount of Ag deposited on the surface of catalysts and on the surface of substrate in model experiments.

**Acknowledgements.** This work was partially financially supported by the State Research Program “Convergence 2025. 2.2.02. NIR 8. Scientific basis of plasma-activated interaction of nanoparticles with the surface of functional materials in order to develop new methods for aimed synthesis and modification of nanostructured catalytic materials” and “Convergence 2025. 2.2.02. NIR 1. Development of the basis of the combined effect of plasma, electromagnetic fields and dichromatic laser radiation on materials and biological objects for use in new technologies”.

## References

1. **Nghia N.V., et al.** Open Journal of Synthesis Theory and Applications, 1 (2012) 18-22.
2. **Georgekutty R., et al.** J. Phys. Chem. C, 112 (2008) 13563–13570.
3. **Leong K.H., et al.** Beilstein J. Nanotechnol. 9 (2018) 628–648.
4. **Savastenko N.A, et al.** High Temperature Material Processes: An International Quarterly of High-Technology Plasma Processes, 24 (2020) 21–45.
5. **Savastenko N.A., et al.** High Temperature Material Processes: An International Quarterly of High-Technology Plasma Processes, 26 (2022) 25–42.
6. **Rivas L., et al.** Langmuir, 16 (2000) 9722–9728.
7. **Lee P.C and Meisel D**. J. Phys. Chem., 86 (1982) 3391–3395.
8. **Wagner H.-E., et al.** Vacuum, 71 (2003) 417–436.
9. **Sastry M., et al.** Colloids Surf. A: Physicochem. and Engi. Aspects, 127(1997) 221–228.
10. **Peng H., , et al.** Bioresources, 11 (2016) 385–399.

# ENHANCEMENT OF THE PHOTOCATALITYC EFFICIENCY OF NANOSTRUCTURED MATERIALS VIA PLASMA TREATMENT

N.A. Savastenko [(1)], A.A. Shcherbovich[(1)], V.A. Lyushkevich [(2)], I.I. Filatova[(2)], S.A. Maskevich[(1)]

[1]Belorussian State University, International Sakharov Environmental Institute BSU, 23 Dolgobrodskaya Str., 220070 Minsk, Belarus, nataliesavastenko@iseu.by
[2]B.I. Stepanov Institute of Physics, National Academy of Sciences of Belarus, 68 Nezavisimosti Ave., 220072 Minsk, Belarus, filatova@presidium.bas-net.by

Cold plasma represents an efficient technique for creating new materials with unique properties that are not obtainable by any other methods. A special place is occupied by catalytically active materials [1-4].

In this study, we report the results of systematic study on influence of plasma treatment on photocatalytic performance of ZnO-based photocatalysts, polymer-capped Ru sensitized $TiO_2$-based photocatalysts and ZnO-based photocatalysts impregnated with plasmonic nanoparticles (hybrid photocatalyst ZnO/Ag-NPs) as well as on the exciton-plasmon coupling in hybrid photocatalyst ZnO/Ag-NPs. The plasma-modified materials were employed for photocatalytic decomposition of methyl orange (MO) and sodium caffeine benzoate (caffeine) in aqueous solution exposed to ultraviolet (UV) light. Performance of the catalysts was assessed through the measurement of the reaction rate constant of photodegradation [5]. The performance of plasma-modified photocatalysts were compared with that of commercially available ZnO and $TiO_2$ – nanoparticles (NPs).

Diffuse Reflectance Infrared Fourier Transform Spectroscopy (DRIFTS), Infrared (IR) Spectroscopy, Time Resolved Photoluminescence (TR-PL), UV-Vis spectrophotometry (UV-Vis) and Atomic Force Microscopy (AFM) were used for catalysts characterization.

ZnO powders (ECOS-1, Russia, GR pure, 100 nm -- 1μm) were treated with dielectric barrier discharge (DBD plasma under different conditions to optimize their catalytic activity. The photocatalytic activity was approximately 8 times higher for the most active sample than that for untreated ZnO (Fig. 1a). The maximal value of rate constant was found to be 1.1 $10^{-2}$ $s^{-1}$. It was found that the performance of the catalysts depends on the effective energy ($E_{eff}$) consumed by catalysts during treatment time. The value of $E_{eff}$ was calculated by the following relation:

$$E_{eff} = E_{si} t_{tret} f, \quad (1)$$

where $t_{tret}$ is the plasma treatment time and $f$ is the frequency of feeding voltage and $E_{el}$ is the energy consumed by DBD. The value of $E_{el}$ was estimated as the area of the characteristic Q-U Lissajous Figures [6]:

$$E_{el} = \oint U(t)dQ \equiv AREA\ of\ (Q-U)\ diagram. \quad (2)$$

The optimal value of effective energy consumed by the most active catalyst was found to be 3180 J.

To elucidate the plasma treatment effects, DRIFTS was applied for catalysts characterization. It was found a weak correlation between DRIFT spectra peak area and activity of the catalysts for peaks in the regions of 2600-3800 $cm^{-1}$ (Fig. 1a) and 1200-1700 $cm^{-1}$ (not shown). The lowest value of peak area was reached for the most active catalyst. These peaks can be assigned to the hydroxyl groups [7]. These results imply that MO molecules and hydroxyl groups, may compete for adsorption sites on the surface. The catalysts with lower surface concentration of hydroxyl groups have the higher surface concentration of MO molecules. Usually, increase in concentration of MO molecules on the surface leads to the increase of the probability of heterogeneous reactions of MO.

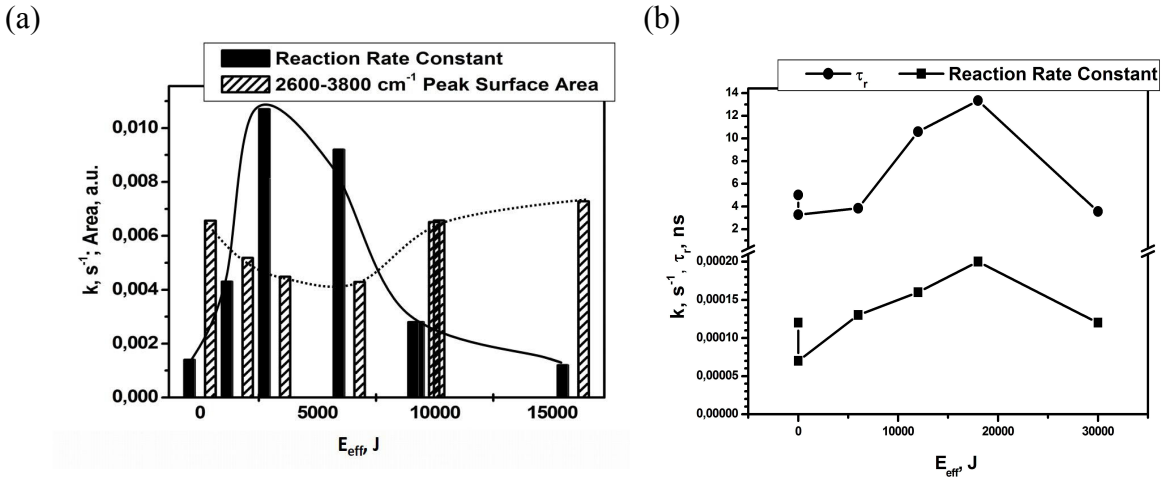



Fig. 1. Reaction rate constants and integrated areas under DRIFTS peak around 2800-3000 $cm^{-1}$ vs $E_{eff}$ for ZnO-based catalysts (a), reaction rate constants and photoluminescence decay lifetime vs $E_{eff}$ for ZnO/Ag-NPs catalysts (b)

Impregnation of ZnO with Ag-NPs followed by DBD plasma treatment at $E_{eff}$=18 000 J resulted in approximately 2-fold improvement of the photocatalytic activity for decomposition of caffeine (Fig. 1b). The maximal value of rate constant was $2.0 \cdot 10^{-4}$ $s^{-1}$.

No correlation was observed between the catalytic activity and surface concentration of various functionalities adsorbed on the surface of hybrid photocatalysts ZnO/Ag-NPs.

The TR-PL measurements imply that exciton–plasmon coupling occurred in the ZnO/Ag-NPs catalysts. For untreated ZnO/Ag-NPs, the Purcell factor ($F_p$) was calculated to be of 1.5.

As it can be seen in Fig. 1b, the photocatalytic activity of hybrid catalysts correlated with PL decay lifetime $\tau_r$ (i.e. with the recombination time of photogenerated electron-hole pairs). The most active photocatalyst had the longest recombination time and the lowest value of $F_p$ (13.34 ns, $F_p$= 0.38). Both the value of k and $\tau_r$ depended on the $E_{eff}$. Impregnation of catalyst with plasmonic Ag-NPs without plasma treatment resulted in decreasing of $\tau_r$. Plasma treatment of hybrid ZnO/Ag-NPs catalysts led to an increase of the $\tau_r$ if the value of $E_{eff}$ was less than 18 000 J. Further increasing of $E_{eff}$ resulted in decreased value of $\tau_r$ and catalysts activity.

The existence of optimal conditions in terms of effective energy consumed by the catalysts during plasma treatment ($E_{eff}$) providing the best catalyst performance might be explained by morphological changes in the structure of Ag-NPs. This fact was confirmed by the AFM and UV-Vis measurements before and after plasma treatment of Ag-NPs with different value of $E_{eff}$. According to the AFM and UV-Vis measurements, after impregnation of ZnO powders with Ag-Nps, the nanoparticles agglomerated and stuck together. The catalytic performance was reduced due to the formation of agglomerates. Plasma treatment of the Ag-NPS agglomerates on the surface resulted in formation of small Ag-NPs. The more the value of $E_{eff}$, the more agglomerates are broken down into smaller NPs. It may be assumed that there is a certain value of $E_{eff}$ that can be assigned as optimal value of effective energy ($E_{optim}$) consumed by catalysts during treatment time. When plasma treatment is carried out at this optimal energy $E_{optim}$, most of the agglomerates is converted into nanoparticles, but not into clusters Further increase in $E_{eff}$.results in formation of smaller clusters that do not participate in heterogeneous reactions.

It is shown [8, 9] that plasmonic NPs incorporated in semiconductor materials provide a few possibilities to influence on the photocatalytic activity. The plasmonic Ag NPs can act as an electrons trap. They suppress the recombination of photogenerated electron-hole pairs. It leads to enhancing the catalytic performance of semiconductor photocatalysts. Additionaly, an increase of the resonant electron density can occur due to the transfer of electrons from defect deep level of ZnO to Fermi level of NPs. These electrons transfer from the surface of nanoparticles to conduction band (CB) of ZnO. The increased number of electrons in CB promote the photocatalytic reactions.

The photocatalytic activity towards photodegradation of MO was approximately 4.4 times higher for the $TiO_2$-NPs covered with polymer thing films (100-200 nm) than that for untreated $TiO_2$-NPs. The activity of catalysts

did not depend on the thickness of polymer layer. There was no direct correlation between the recombination time of photogenerated electron-hole pair and photocatalytic activity. It might be implied that enhancement of photocatalytic activity towards methyl orange photodegradation by coating of $TiO_2$ with poly-allyl layers was due to the photogenerated electron transfer from polymer to $TiO_2$.

In summary, the present contribution demonstrates the potential of a plasma treatment and plasmonic NPs for the synthesis of nanostructured photocatalysts for photodegradation of organic pollutants in aqueous solution.

**Acknowledgements.** This work was partially financially supported by the State Research Program "Convergence 2025. 2.2.02. NIR 8. Scientific basis of plasma-activated interaction of nanoparticles with the surface of functional materials in order to develop new methods for aimed synthesis and modification of nanostructured catalytic materials" and "Convergence 2025. 2.2.02. NIR 1. Development of the basis of the combined effect of plasma, electromagnetic fields and dichromatic laser radiation on materials and biological objects for use in new technologies".

## References

1. **Wang Zh., Zhang Y., Neyts E.C., Cao X., Zhang, X. Jang B.W.-L., and Liu C**. ACS Catalysis, 8 (2018) 2093-2110.
2. **Witvrouwen T., Paulussen S. and Sel B**. Plasma Process Polym., 9 (2012) 750-760.
3. **Tyczkowski J.** in Plasma Science and Technology, T. Mino, Ed., Intech: Open access peer-reviewed (2016) 25–66.
4. **Liu C.-J., Li M., Wang J., Zhou X., Guo Q., Yan J. and Li Y. Chin.** J. Cat**.,** 37 (2016) 340-348.
5. **Savastenko N.A., Filatova I.I., Lyushkevich V., Chubrik N., Shcherbovich A.A. and Maskevich, S.A.** High Temperature Material Processes, 24 (2020) 275-291.
6. **Wagner H.-E., Brandenburg R., Kozlov K.V., Sonnenfel, A., Michel P. and Behnke J.F.** Vacuum, 71 (2003) 417–436.
7. **Davydov A.** in Molecular Spectroscopy of Oxide Catalyst Surfaces, N.T. Sheppard, Ed., Weinheim, Germany : Wiley-VCH Verlag GmbH (2003) 27–179.
8. **Leong K.H, Aziz A.A., Sim L.C., Saravanan P., Jang M. and Bahnemann D.** Beilstein J. Nanotechnol., 9 (2018) 628–648.
9. **Aby H., Kshirsagar A., and Khanna P.K.** J. Mater.. Sci. Nanotechnol., 4 (2016) 1–14.

# UNIFORMITY OF ION FLUX IN A LASER PLASMA SOURCE FOR DEPOSITION OF NANOFILMS

V.K. Goncharov[1], M.V.Puzyrev[1], N.I.Shulgan[2]

[1]A.N.Sevchenko Institute of Applied Physics Problems, Belarusian State University, 7 Kurchatova Street, Minsk 220045, Belarus
[2] Belarusian State University, 4 Niezalieznasci Avenue, Minsk 220030, Belarus

**Introduction** The laser-plasma method is perspective method for the formation of nanostructures. It has a number of advantages over others. This is, first of all, sterility, the ability to obtain plasma from substances in any aggregation state, including refractory materials, and the environmental friendliness of the process.

The usual laser-plasma method of deposition of nanofilms is that an erosion laser plume flows out into a half-space and a part of the destruction products the laser target falls on the substrate surface. It was proposed in [1] to place a grid between the laser target and the substrate for a smooth regulation of the energy of deposited particles. When a potential negative with respect to the target is applied to the grid, a flow of charged particles is formed after the grid, consisting mainly of ions. By applying a positive potential to the grid with respect to the substrate, we can smoothly change the kinetic energy of the ions. It allows changing the regime of the nanofilms deposition.

The experiments were carried out to study the deposition regimes of nanofilms of different materials of a laser target on the substrates surface which have been made from different materials [2].

However, these experiments were carried out with small substrates ($\sim 10$ cm$^2$ ). In practice, it is often necessary to deposit nanofilms on large surfaces. For this, it is necessary to find the regimes for the laser-plasma source, when it is possible to deposit uniform nanofilms on large surfaces.

This work is devoted to the study of the spatial distribution of the ion flux density on a circular substrate with the square of $\sim 200$ cm$^2$.

The general scheme of the experiment is described in /1/. The position of the target, grid, substrate and laser beam significantly depends on the volume and shape of the vacuum chamber. In the present experiments, the target - substrate distance was 12 cm, and the grid was located in the middle between them. It was 6 cm from the target surface.

**The experimental equipment** The target was irradiated by the LOTIS-TII pulsed YAG:$Nd^{3+}$ laser with a wavelength $\lambda = 1064$ nm and a pulse duration $\tau = 20$ ns (FWHM). The target was mounted at 45° with respect to the laser beam. The deposition was carried out in vacuum at the residual gases pressure

~ $10^{-3}$Pa. The target was rotated with a velocity of 2 rev/min to prevent formation of a deep crater on the target surface. The targets were made of aluminum.

**Discussion of results** The erosion laser plume in our laser plasma source is axisymmetric, the ion flux formed after the grid and moving towards the substrate is also axisymmetric. Therefore, to monitor the spatial distribution of the ion flux density on the substrate, it is sufficient to monitor the change in the ion current density along the radius of the substrate.

Two additional probes with a square of 1x0.5 cm each were placed in front of the substrate. One of them is stationary and located in the center of the substrate. Another had the ability to move along the radius of the substrate from the center to the edge. The general scheme of the experiment is shown in fig.1.

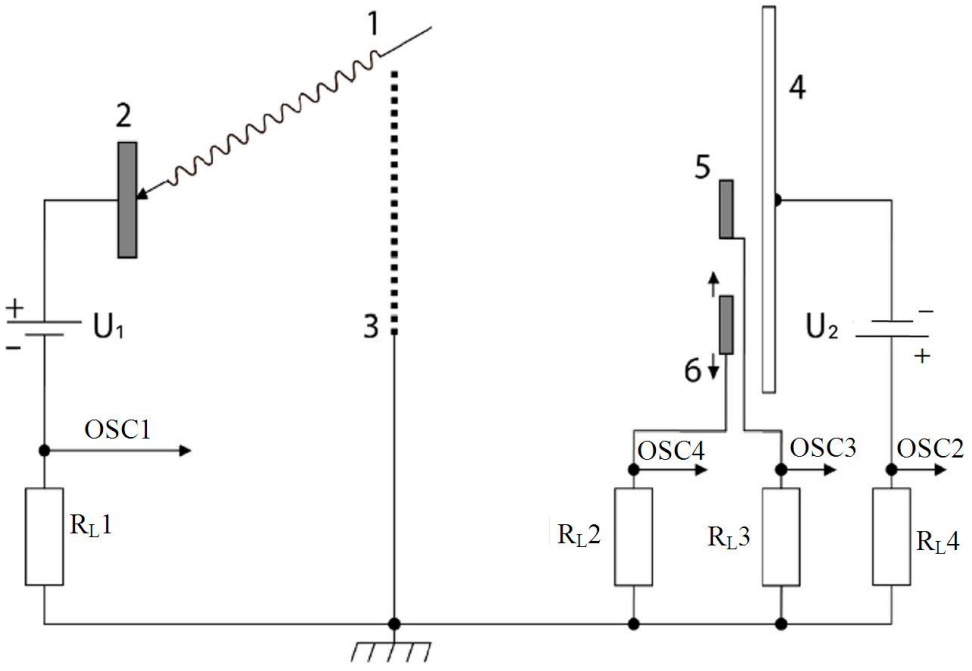



Fig. 1. General scheme of the experiment. 1 – laser radiation, 2 – aluminum target, 3 – grid, 4 – substrate, 5 – fixed probe, 6 – mobile probe. OSC1, OSC3— signals taken on the first, OSC2, OSC4 on the second beam, $U_1$ and $U_2$ – independent power sources

The energy level in each pulse can be unstable as a pulse-frequency laser with a long operating time was used in our experiments. Relative measurements of the movable probe current $I_2$ to the stationary probe current $I_1$ were carried out to eliminate the effect of laser instability on the experimental results. The $I_2/I_1$ measurements were taken in relation to squares and in relation to maximum amplitudes too. The results were very close.

The experiments were carried out with an aluminum target at a power density in a separate laser pulse of ~ $3 \cdot 10^8$ W/cm$^2$ at various electric field potentials on an oversized substrate.

The experimental results are shown in fig.2. Figure 2,a shows the curve of the relationship of currents movable and stationary probes along the radius of the substrate increased size without applying a potential to the grid-substrate interval.

It can be seen from the figure that some unevenness is observed along the curve. It can be determined by the unevenness of the laser beam spot and uneven form of erosion spot in the laser irradiation zone. Therefore, the ion flux is determined only by the kinetic energy of the ions due plasmodynamic pressure in the laser erosion plume in the target-grid interval after a grid in the absence of electrical potential in the grid-substrate interval. However, it is impractical to use such a regime in a laser-plasma source for deposition nanofilms.

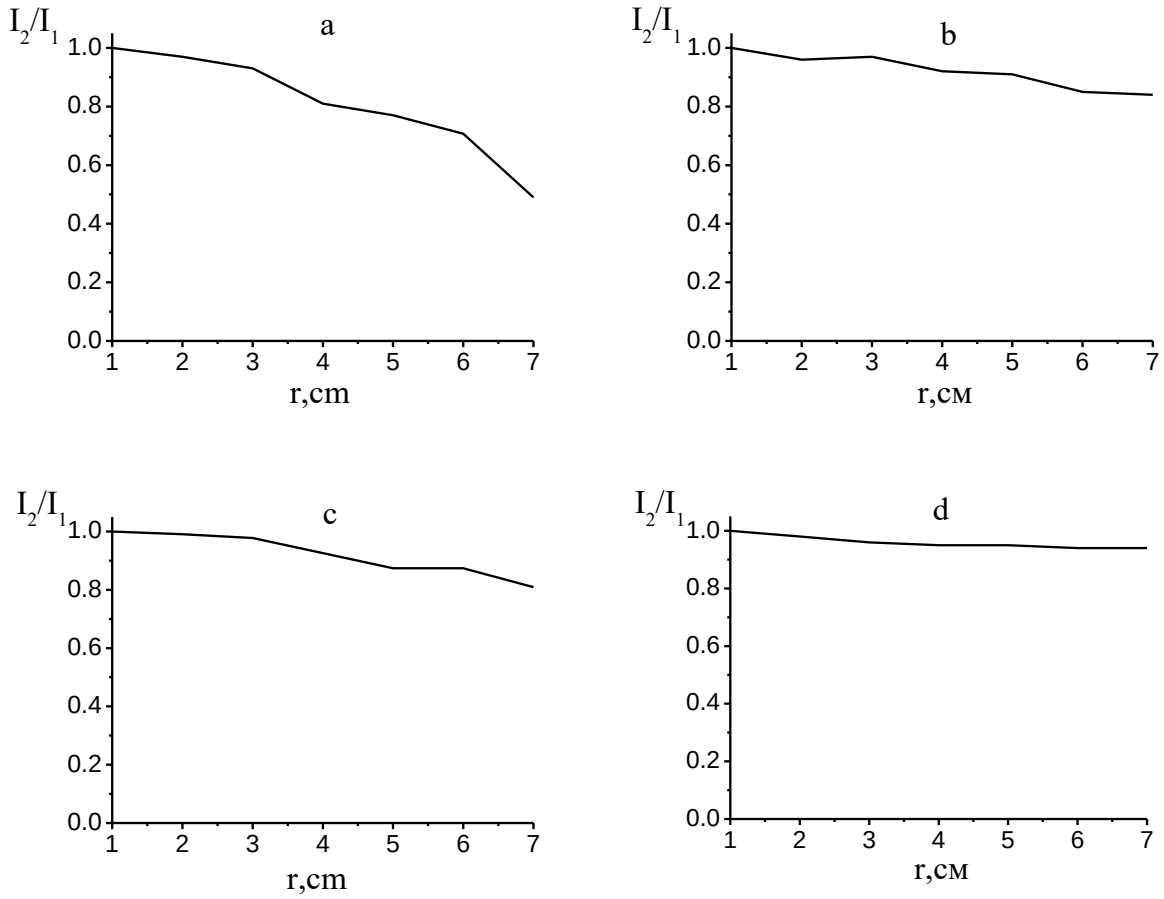



Fig. 2. The ratio of the current of a mobile probe to a stationary probe at acting laser radiation on an aluminum target at a power density of $3 \cdot 10^8$ W/cm$^2$ with a potential of the target – grid interval of 20V and at different potentials in the grid – substrate interval: a – $U_2 = 0$ V; b – $U_2 = 20$ V; c – $U_2 = 50$V; d – $U_2 = 100$V

When applied to the grid with respect to the substrate a positive potential 20 V, (see. fig. 2b) heterogeneity decrease due to an increase a kinetic energy in an electric field. It should be noted that, under such conditions, the material of the laser target is usually deposited on the substrate /2/.

When increasing the potential in the interval of grid - substrate up to 50 V, there is some increase of a nonuniformity of the density of the ion flux along the radius of the large dimensions substrate (fig. 2c). We can explain it the heterogeneity of the secondary ion emission from the substrate surface associated with inhomogeneity of substrate surface parameters of the large size.

The etching regime of the substrate surface is at secondary emission appears /2/. It favours to an increase an adhesion as the substrate surface is cleaned. The kinetic ion energy is increased at further increase of the electric field in the interval of the grid-substrate (see fig. 2d). This ions energy is enough for implantation a target material in a near-surface substrate zone. The figure shows, in this case, the minimum nonuniformity of the ion flux density on the substrate (~ 5%) is observed.

The pseudodiffusion layer is created on the substrate surface of the laser target material at this regime. The adhesion increases.

**Conclusion** Thus, the experiments have shown that the uniformity of the density of ion fluxes on a substrate of the large size (~ 200 $cm^2$ ) in a laser-plasma source of nanofilms deposition we can increase by supplying an accelerating potential to the substrate with respect to the grid. The difference between the density of ion flux in the center of the substrate and at a distance of 7 cm from it is ~ 5%. As a result, it is technologically possible to clean the substrate surface with ions of the laser target material (secondary emission), create a pseudodiffusion layer of the target material in the near-surface zone of the substrate, and deposit the laser target material on the substrate. All of these operations can be made consistently without depressurized a vacuum chamber.

It possible to obtain nanofilms with high adhesion on substrates of large size.

**References**

1. **Goncharov V.K, Puzyrev M.V and Stupakevich V.Yu.** Journal of Belarus State University 3 (2017) 79-87.

2. **Goncharov V.K, Puzyrev M.V and Stupakevich V.Yu.** Journal of Engineering Physics and Thermophysics. 91(4) (2018) 1056-1062.

# COMPOSITION AND STRUCTURE OF NANOPARTICLES SYNTHESIZED IN THE PLASMA OF AN ELECTRIC EXPLOSION OF METALS IN DISTILLED WATER

Znosko K.F., Tarkovsky V.V.

State University of Grodno, Ozheshko Street 22, 230023, Grodno, Belarus,
znosko@rambler.ru

Nanoparticles of metals and their alloys are widely used in science, electronics, energy, manufacturing of new materials, biology and medicine. They are used in microcircuits, sensors, chips, light emitters, superconductors, solar cells, batteries, drugs, etc. Metal nanoparticles are widely used in technologies to modify composite materials to give them specified properties. For these purposes, particles of a certain size range are needed. By changing the size, shape and structure of nanoparticles, it is possible to control the properties of the final products [1-2].

At present, nanomaterials are obtained by grinding macro samples into nanoparticles, or by synthesizing nanoparticles from individual atoms and molecules [3]. There are also combined methods. At the first stage, the macro-sample is crushed (transformed into plasma). At the second stage (at the stage of plasma recombination), the synthesis of nanostructures takes place.

Such methods of nanoparticle synthesis are pulsed laser ablation of solid materials in a liquid [4-5] and electrical explosion of conductors in a liquid [6-8]. A pulsed electric current is passed through a thin conductor in a liquid. The conductor material heats up, melts, evaporates, and ionizes. An electrical explosion of the conductor takes place. The formation of nanoparticles occurs during the recombination stage of the cooling highly nonequilibrium plasma. The liquid surrounding the discharge channel accumulates the formed particles and a nanosuspension is obtained.

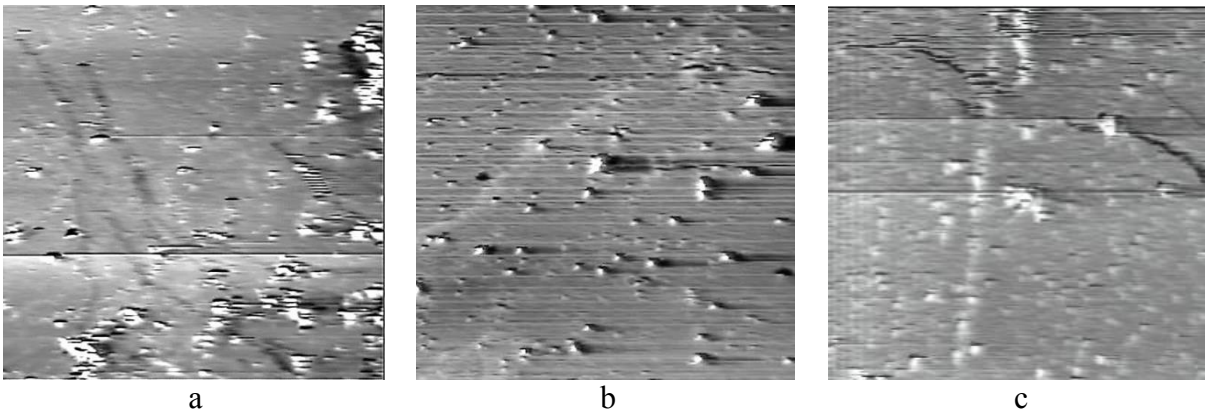
The aim of the present work is to experimentally investigate the composition, structure and size distributions of nanoparticles synthesized in electric explosion plasma of metals in distilled water, as a function of electric explosion parameters.

The investigations were performed on an experimental setup based on the excimer laser excitation systems [9-10] and lamps [11-12]. The dimensional distributions of the obtained nanostructures were investigated using an atomic force microscope NT-206 (AFM). For AFM studies, nanosuspensions in the form of droplets were applied to slides. The water was evaporated and the particles contained therein were deposited on the slides.

Electrical explosion of a 0.8 mm diameter aluminum wire in diethylated water resulted in a pale milky-colored nanosuspension with reduced translucency as compared to pure water. By the explosion of a 0.4 mm diameter

copper cap, a nanosuspension with a characteristic copper hue and reduced translucency was obtained. Electrical explosion of a nickel sample 0.6 mm in diameter in diethylated water resulted in a black-graphite-colored nanosuspension whose transmittance was significantly reduced, compared to pure water.

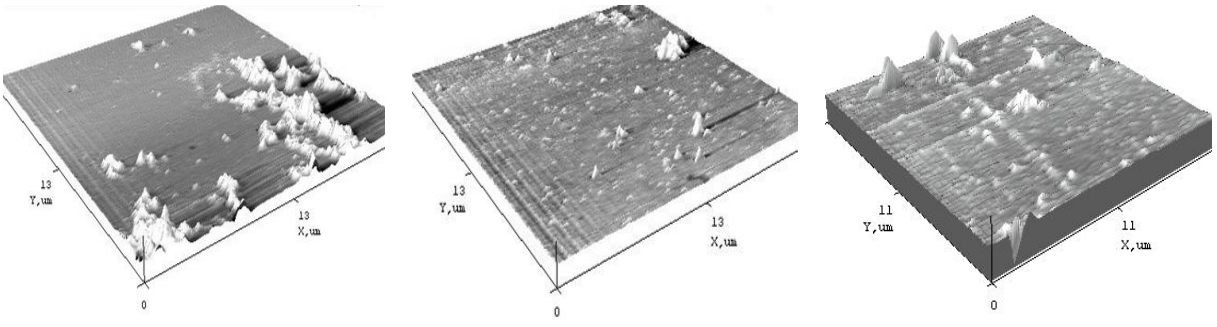
Figure 1 shows AFM images of aluminum, copper and nickel nanoparticles deposited from the obtained nanosuspensions. These images show that the electric blast produces particles of predominantly spherical or close to spherical shape. Analyzing the distribution of the particles on the slide, we can see that they are arranged chaotically. Clusters and conglomerates formed from nanostructures are not systematically arranged in the scanning field. The obtained nanoparticles have a clear boundary contour and a low profile height.



a b c

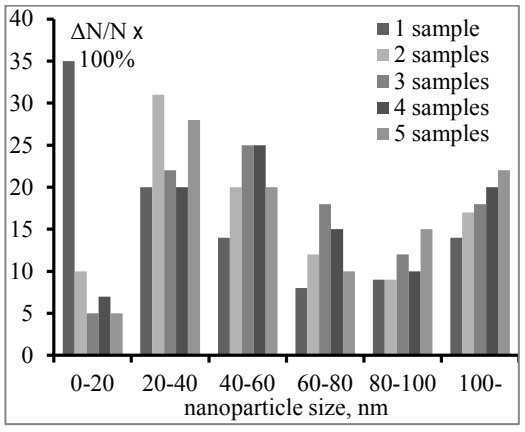
Fig. 1. AFM images of aluminum a, copper b and nickel c nanoparticles

Figure 2 shows 3D AFM images of aluminum A, copper B and nickel C nanoparticles deposited from the obtained nanosuspensions. Comparative analysis of 3D images and dimensional parameters of aluminum, copper and nickel samples electric explosion products in water revealed a number of differences in particle composition and surface morphology. Particles of copper are the most low-sized. A large number of aluminum particles up to 100 nm are

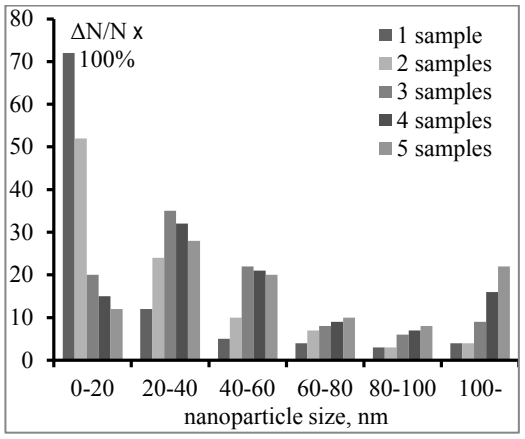



a b c

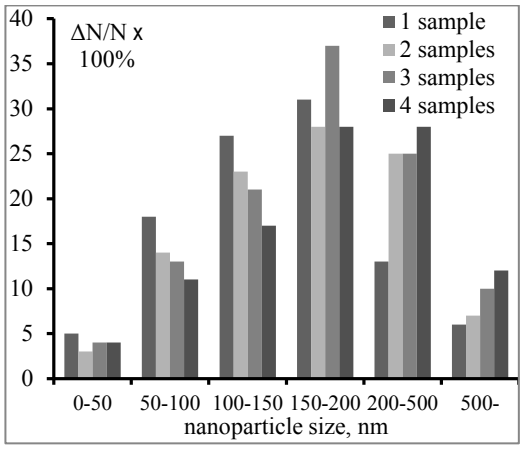
Fig. 2. 3D AFM images of aluminum a, copper b and nickel c nanoparticles




a




b




c

Fig. 3. Histograms of the size distribution of aluminum (a), copper (b), and nickel (c) nanoparticles as a function of the number of blasted samples

formed. Nickel nanoparticles have sufficiently clear boundary contour and low profile height. They resemble flattened spheres. They are larger than copper and aluminum nanoparticles. Among the many small scattered nanoparticles, the presence of large single particles measuring several hundred nanometers is observed. Clusters of nanoparticles and their conglomerates are also observed in the scanning field of the AFM microscope. Clusters and conglomerates formed from nanostructures are also arranged chaotically in the scanning field.

Figure 3 shows histograms of the size distribution of aluminum (a), copper (b), and nickel (c) nanoparticles as a function of the number of exploded samples in one volume of water. A characteristic feature of the morphology of the nanoparticles obtained is that the number of submicron-level particles and conglomerates increases as the number of conductor blasts in the same volume of water increases. Since the nickel nanoparticles are uniformly distributed over the volume of water in the reactor after the first sample explosion, they are affected by shock waves of subsequent explosions and ultraviolet ionization by the radiation of electroexplosive plasma of subsequent explosions. Shock waves and high pressure can lead both to additional crushing of synthesized nanostructures and to the formation of conglomerates of low-dimensional nanostructures. The direction of these processes and the factors influencing them require separate studies.

Intense ultraviolet ionization leads to the appearance of charge in nanoparticles formed after the first explosion, as well as free electrons. In general, the nanosuspension is electrically neutral, but at the nanoscale it will

have an uncompensated electric charge. In recombination processes, nearby nanoparticles with opposite charge will be attracted to each other and form conglomerates, which is observed in the experiments.

Thus, aluminum, copper, and nickel nanoparticles were obtained in electric explosion plasma. The composition, structure and morphology of the synthesized nanoparticles were determined by AFM microscopy. Particles up to 60 nm in size dominate for aluminum and copper. For nickel, particles 100-200 nm in size dominate. The profile of the size distribution of nanostructures depends on the number of blasted samples in one volume of water.

This work was performed within research task 2.2.03 of the Scientific Research Program "Convergence 2025", subprogram "Microworld, Plasma, and Universe".

## References

1. **Maier G.G.** Volumetric nanostructured materials: modern methods of creation and research. Tomsk: IFPM SO RAN (2013).
2. **Rempel A.A.** Russian Chemical Reviews, 76 (2007) 474-500.
3. **Boguslavski L.I.** Chemistry and Technology of Inorganic Materials, No. 5, (2012) 3-5.
4. **Makarov G.N.** Advances in Physical Sciences, 183 (2013) 673-718.
5. **Sergienko I.G., Znosko K.F. and Leshchyk S.D.** Vesnik of Yanka Kupala State University of Grodno. Series 6. Engineering Science, 7 No.2 (2017) 47–57.
6. **Nazarenko O.B.** Electrospray nanopowders: production, application, properties. Ed. by Ilyin A.P.. Tomsk: PTU (2005).
7. **Sergienko I.G., Znosko K.F. and Tarkovsky V.V.** Vesnik of Yanka Kupala State University of Grodno. Series 6. Engineering Science, 7 No.1 (2017) 56–65.
8. **Sergienko I.G., Znosko K.F. and Tarkovsky V.V.** Vesnik of Yanka Kupala State University of Grodno. Series 6. Engineering Science, 8 No.1 (2018) 50–61.
9. **Anufrik S. S., Volodenkov A.P. and Znosko K.F.** Journal of Applied Spectroscopy, 88 (1999) 702-707.
10. **Anufrik S.S., Volodenkov A.P. and Znosko K.F**. Journal of Optical Technology, 67 (2000) 961–967.
11. **Znosko K.F.** Vesnik of Yanka Kupala State University of Grodno. Series 2. Mat..Phys..Inform.,Computer Technol. and Contr., 8 No.3 (2018) 102-112.
12. **Znosko K.F.** Vesnik of Yanka Kupala State University of Grodno. Series 6. Engineering Science, 9, No.2, (2019) 81-91.

# PHOTOCATALYTIC AND STRUCTURAL PROPERTIES OF NANOSTRUCTURED TITANIUM DIOXIDE OBTAINED BY HYDROTHERMAL METHOD

A. V. Miadzvetski [(1)], N. A. Savastenko[(1)], S. A. Maskevich [(1)], I.I. Filatova [(2)], M. T. Gabdullin [(3)], T. S. Ramasanov [(3)], Kh. A. Abdullin [(3)], Zh. K. Kalkozova [(3)]

[1] Belarusian State University, International Sakharov Environmental Institute of BSU, 23 Dolgobrodskaya Str., 220070 Minsk, Belarus, aleksandr.miadzvetski@iseu.by
[2]B.I. Stepanov Institute of Physics, National Academy of Sciences of Belarus, 68 Nezavisimosti Ave., 220072 Minsk, Belarus, filatova@presidium.bas-net.by
[3]National Nanotechnology Laboratory of Open Type, Al-Farabi Kazakh National University, 71 al-Farabi Ave., Almaty, Kazakhstan

Wastewater treatment from organic impurities is the most critical task in restoring water resources polluted due to using organic dyes in technological processes. Water purification methods have been developed based on reverse osmosis, filtration, activated carbon absorption, etc. [1]. However, these methods are either insufficiently effective or have a high operational cost [2]. In this regard, the search for new and improved methods for removing organic impurities from aqueous media is relevant.

Heterogeneous photocatalysis using nanocatalysts based on zinc oxide and titanium dioxide is a promising method of purification of aqueous media from waste from the pharmaceutical industry [3].

One of the promising ways to increase the efficiency of photocatalysts is to change the morphology and increase the specific surface area, as well as use nanomaterials.

Currently, the hydrothermal method of materials synthesis is being intensively developed, which makes it possible to change the properties and morphology of the resulting material when varying the temperature of the technological process and the composition of the initial solutions [4].

This paper investigates the structural and photocatalytic properties of titanium dioxide-based catalysts synthesized by the hydrothermal method.

The synthesis of titanium dioxide samples was carried out in two ways.

In the first case, a solution of sulfuric acid was made in the proportion of 100 parts of water and four parts of concentrated sulfuric acid, which was added drop by drop to the water. The solution was placed in an ice bath during preparation to eliminate significant heat release during acid dissolution. After cooling to 0°C, two parts of titanium tetrachloride were added to the solution drop by drop. The solution was stirred for 1 hour; then, while stirring, it was heated to 60°C, followed by heating for 1-2 hours with continuous stirring on a magnetic stirrer.

At the same time, the gray solution became transparent. To increase the pH of the solution to 7, $NH_3$ * $H_2O$ was added drop by drop, after which the solution turned white. When the solution was cooled to room temperature, a gel was formed. The $TiO_2$ water gel was filtered and washed with distilled water, dried at room temperature and calcined at 400°C for two hours. The sample was named $TiO_2$-4.

Another way to synthesize a titanium oxide catalyst was as follows: $TiCl_4$ was added drop by drop to a cooled aqueous hydrochloric acid solution. The volume ratio of the components was HCl:$H_2O$:$TiCl_4$=1:2:1. The resulting solution was stirred on a magnetic stirrer for 6 hours at room temperature. Then the solution was poured into a Teflon beaker, which was placed in a hermetically sealed steel reactor container playing the role of an autoclave. The reactor was placed in an oven and annealed at 130°C and 160°C for 3 hours. After the synthesis was completed, the reactor was removed from the furnace and cooled to room temperature. The solution with the reaction products was poured from a Teflon beaker into a glass beaker; then the resulting sample was thoroughly washed with distilled water and dried. The sample was named $TiO_2$-2.

$TiO_2$-4 was processed in a dielectric barrier discharge plasma created in the air at standard pressure within 42 minutes. The sample was named $TiO_2$-4-DBD_42.

The photocatalytic activity was studied in a model decomposition reaction of methyl orange dye ($C_{14}H_{14}N_3NaO_3S$, MO) under the action of ultraviolet radiation in aqueous suspensions of synthesized samples. Suspensions of catalysts in aqueous solutions of model substances were exposed to UV radiation. A mercury-quartz lamp DRT-240 (240 W power) was used as a source of ultraviolet radiation. The illumination level in the affected area, estimated using the TKA-LUX luxmeter, in the visible and near UV range was 150 kLk. During irradiation, the change in the concentration of MO in the solution was monitored using a SOLAR PB2201 spectrophotometer (SOLAR, Belarus). The relative concentration of the model substance Cr was determined from optical density measurements at the absorption maximum:

$$C_r = \frac{C(t)}{C_0} \cdot 100\% = \frac{A_t}{A_0} \cdot 100\%, \quad (1)$$

where $C_0$ is the initial concentration of the model substance, C(t) is the concentration of model substances after irradiation of the UV radiation at time t, $A_0$ and $A_t$ the optical density of the solution of the model substance in the absorption maximum before irradiation and at time t after the start of irradiation of the samples, respectively.

The photodegradation reaction rate constant k was determined by the formula (2) from the slope of the graph of the dependence of the logarithm of concentration ln($C_r$) on time:

$$lnC_r = \ln\frac{C(t)}{C_0} = -kt \quad (2)$$

The photodegradation reaction rate constant was used as a quantitative characteristic of the photocatalytic activity of the samples.

Before the measurements, preliminary experiments were carried out to establish the possibility of reducing the model substance's concentration due to its molecules' adsorption on the surface of the catalyst in the absence of irradiation (determination of the sorption capacity of the catalyst, dark absorption).

Figure 1 shows the results of dark (in the absence of UV light irradiation) MO adsorption for titanium dioxide-based photocatalysts synthesized using the first ($TiO_2$-4 sample), the second ($TiO_2$-2 sample) methods and the first with plasma treatment ($TiO_2$-4-DBD_42 sample).

As can be seen from Figure 1, the sorption capacity of the $TiO_2$-4 catalyst is slightly higher than that of the $TiO_2$-2 and $TiO_2$-4-DBD_42 catalysts.

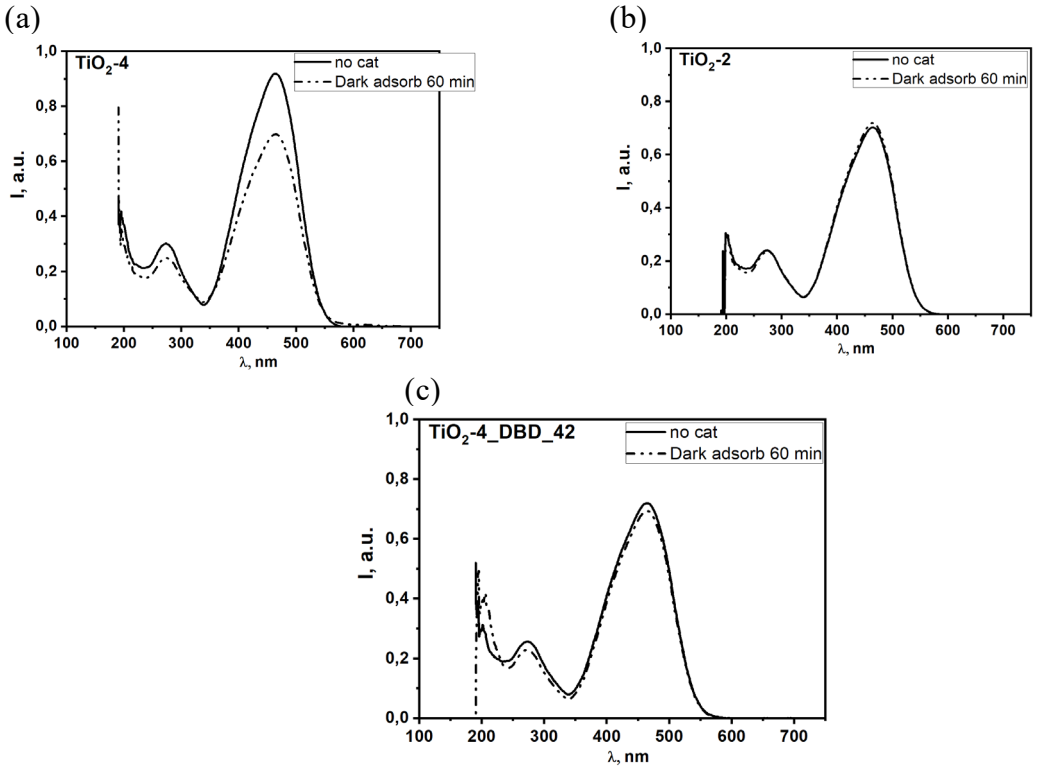



Fig. 1 – Changes in the absorption spectra of MO as a result of dark adsorption on the surface of $TiO_2$-4 (a), $TiO_2$-2 (b) and $TiO_2$-4-DBD_42 (c)

Figure 2 shows the kinetics of the MO photodegradation reaction in the presence of a $TiO_2$-4, $TiO_2$-2 and $TiO_2$-4-DBD_42 photocatalyst. The photodegradation reaction rate constants calculated by formula (2) are also given there

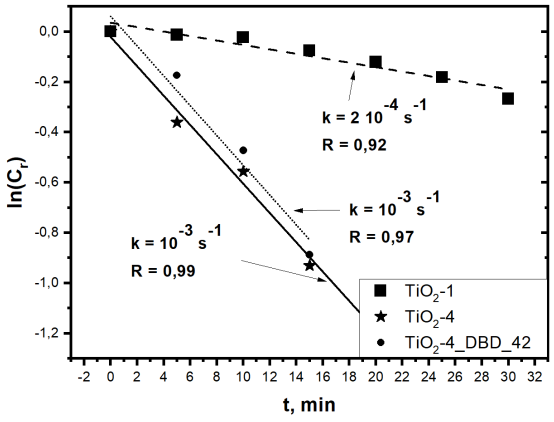



Fig. 2 – Kinetics of the MO photodegradation reaction in the presence of a $TiO_2$-4, $TiO_2$-2 and $TiO_2$-4-DBD_42 photocatalyst

The results of Raman studies show that the $TiO_2$ sample obtained by the second method consists of the rutile phase without an admixture of anatase, and the one obtained by the first method consists of the anatase phase.

Analysis of radiographs of $TiO_2$-4 and $TiO_2$-2 samples together with radiographs of standard rutile and anatase phase $TiO_2$ powders shows that the $TiO_2$-2 sample is a rutile lattice sample, and the $TiO_2$-4 sample is anatase. At the same time, the rutile ($TiO_2$-2) lines have a noticeable half-width, by which the sizes of nanocrystalline regions can be estimated. Estimates according to the Scherrer formula give sizes of 10.5 nm for reflex 110, 13 nm for reflex 101 and 8 nm for rutile reflex 211.

The $TiO_2$-4 sample has the greatest photocatalytic activity in the anatase phase, which confirms that the titanium dioxide phase is the determining factor for the MO photodegradation reaction. Plasma treatment did not affect the photocatalytic activity.

**Acknowledgements**. This work was partially financially supported by the State Research Program "Convergence 2025. 2.2.02. Scientific basis of plasma-activated interaction of nanoparticles with the surface of functional materials in order to develop new methods for aimed synthesis and modification of nanostructured catalytic materials." A.V. Miadzvetski acknowledge support by the Ministry of Education of Republic of Belarus (Grant No. 20220569).

## References

1. **Rajeshwar K.** J. Photochem. Photobiol, 9 (2008) 171–192.
2. **Atmani F.** Journal of Environmental Science and Technology, 2 (2009) 153–169.
3. **Sarkar S.** Ecotoxicology and Environmental Safety, 121 (2015) 263–270.
4. **Guo M.** // J. Solid State Chem, 178 (2005) 1864-1873.

# DEPOSITION OF TiSiCN NANOCOMPOSITE COATINGS IN HOLLOW CATHODE ARC DISCHARGE WITH ACTIVE ANODE

A. Menshakov[1,2], Yu. Bruhanova[1]
[1]Institute of Electrophysics of the Ural Branch of the Russian Academy of Sciences, 106 Amundsen St., Yekaterinburg, 620016, Russia, menshakovandrey@mail.ru
[2] Ural Federal University, 19 Mira St., Yekaterinburg, 620002, Russia

TiSiCN nanocomposite coatings began to be obtained relatively recently, about 20 years ago. Of particular interest are their physical properties. High temperature resistance and oxidation resistance [1] allow them to be used in extreme conditions in aggressive environments, for example, on parts of aircraft or rocket engines. Good anti-friction properties [2], high hardness and good toughness allow them to be used on cutting tools (cutters, drills, cutters, etc. high resistance to dust erosion makes it possible to use the coating to protect the blades of gas turbine engines [3]. They also have good biocompatibility [4] and are suitable for covering medical prostheses and implants. To date, such four-component coatings are synthesized using a number of physical and chemical methods. An alternative approach was proposed in [5], in which only a gas-discharge device with a hollow cathode and an active anode is used to create a multicomponent active medium. With the help of an arc discharge with a self-filling hollow cathode, a dense plasma is created in a large volume, as well as a stream of metal vapors is created and vapors of an organosilicon precursor decompose. With this method of deposition, filtration systems are not used, since the flow of the evaporated metal does not contain droplets that violate the structure of the coating. In comparison with existing methods, this approach provides higher deposition rates, high ion flux density, necessary for the formation of dense and high-quality coatings. In comparison with the chemical method, the advantage is the use of environmentally safe and harmful, affordable and inexpensive components. The main advantage of the method is the ability to independently and broadly control almost all synthesis conditions, and, consequently, the composition and properties of the resulting coatings, which makes it possible to obtain films with the required characteristics. The paper presents the results of a study of the conditions for obtaining TiSiCN coatings by this method.

The experiments were carried out on the facility schematically shown in Figure 1. The design of the gas discharge system is described in detail in [6]. The gas discharge system is equipped with a hollow cylindrical cathode made of TiN and a sectional anode. One section, made of stainless steel 12H18N10T, had water cooling, the second section of the anode was a crucible (graphite MPG-7) with a Ti-hitch (VT1-0).

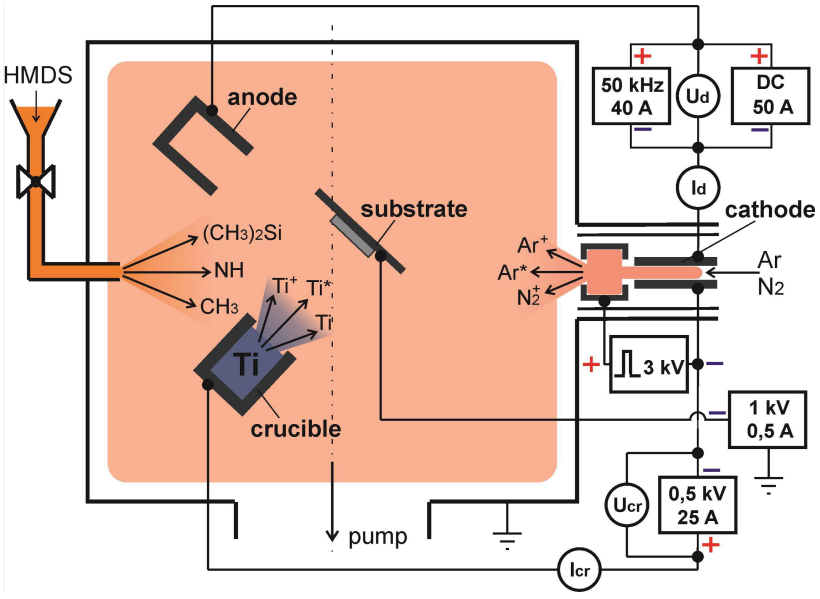



Fig. 1. Electrode diagram of the gas discharge system

Such a power supply scheme allowed to independently change the currents in the circuit of each anode section. The current in the cooled anode circuit varied in the range of 0-50 A, in the crucible circuit the current was regulated in the range of 0-15 A. The precursor vapor was released through an evaporator heated to a high temperature by a plasma stream and located at a distance of 10 cm from the samples. The flow was regulated in the range of 0-10 g/h using the Mini Cori-Flow digital liquid flow controller (Bronkhorst). Hexamethyldisilazane (HMDS) was used as a precursor. The samples were placed in the gap between the cathode and the anode at a distance of 8 cm from the crucible on an insulated holder, to which an offset voltage of up to -1 kV was applied.

Previous studies have shown [6] that this method makes it possible to create an active vapor-gas medium consisting of decomposition products of organosilicon molecules and titanium vapors, as well as independently control their content and degree of activation in the gas mixture. This makes it possible to create conditions for the formation of coatings from the active components of this mixture on the treated surface, as well as to change their properties.

Coatings were obtained at different values of the precursor flow. The bias voltage on the samples was -50 V relative to the anode. Before deposition, the surface of the samples was cleaned with argon ions with an energy of 1 kV, after which a Ti sublayer was applied. In the absence of precursor vapors in the gas mixture, a TiN coating with a predominant orientation (200) is formed on the treated surface (Figure 2), the microhardness, measured using Shimadzu DUH-211s microhardness meter, was 24-27 GPa, and the coating color was characteristically golden (Figure 3), the size of the crystallites is 6-7 nm. The

addition of hexamethyldisilazane led to a change in the shade of the coating to dark gray, as well as to a change in its X-ray phase state (Figure 2) and microhardness to 33-42 GPa (Figure 4). At discharge current 20 A a solid solution is formed based on TiCN (phases TiC0,3N0,7 (PDF No. 42-1488, cubic, period a=4.2644Å) and TiC0,7N0,3 (PDF No. 42-1489, cubic, period a= 4.2971Å) [7]. However, in the observed phases TiC0.3N0.7 (content 70%, OCR≈4.5 nm, period a=4.330Å) and TiC0.7N0.3 (content 22%, OCR≈7 nm., period a=4.388Å), the lattice periods are significantly increased in comparison with the literature data. Perhaps this indicates that there is a solid solution based on these phases, and the reason for the increase in the lattice may be silicon atoms embedded in it. In addition, an increase in the HMDS vapor flow in the range of 0-1.5 g/h leads to an increase in the deposition rate from 5 to 9 microns/h.

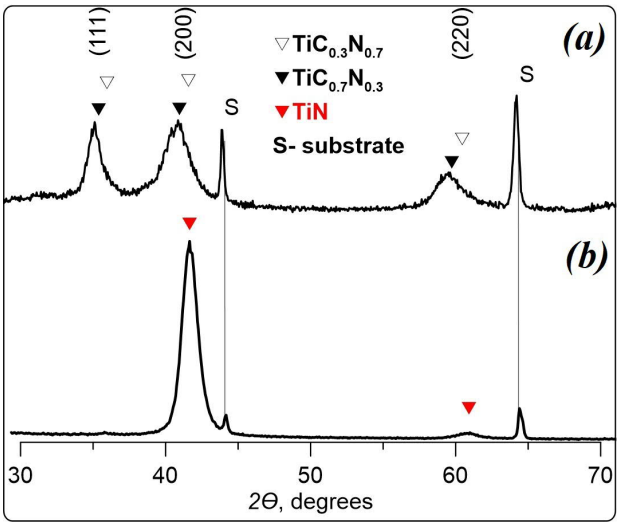



Fig. 2. XRD patterns of coatings in Ar+$N_2$ (b) and Ar+$N_2$+HMDS (0,5 g/h) (a) vapor-gas mixture.

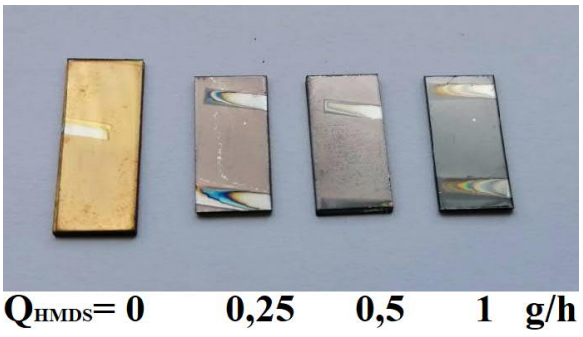



Fig. 3. Photos of samples obtained with different precursor flows.

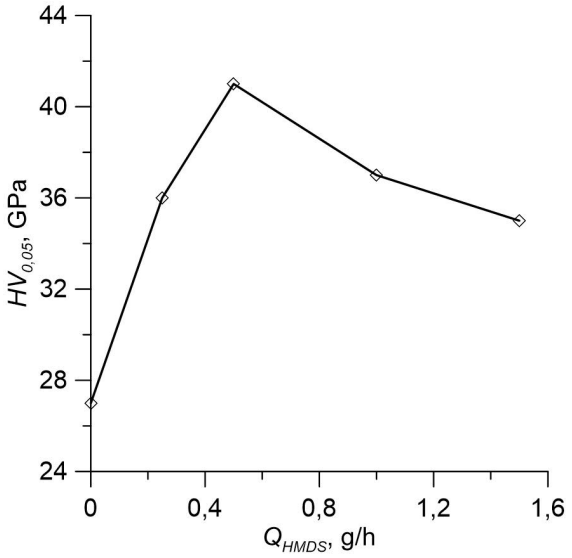



Fig. 4. Hardness of samples obtained with different precursor flows.

Probably, the decrease in hardness with an increase in the HMDS flow (Figure 4) is associated with an excess of the precursor and a decrease in the proportion of the nc phase in the coating composition.

Thus, by the method of anodic evaporation of titanium and decomposition of hexamethyldisilazane in an arc discharge with a hollow cathode, coatings based on TiSiCN with a nanocomposite structure up to 10 microns thick, with a hardness of up to 42 GPa and a speed of up to 9 microns/h were obtained.

**Acknowledgements**. This work was supported by the Russian Science Foundation (grant No. 20-79-10059).

## References

1. **Endler I., Höhn M., Schmidt J., Scholz S., Herrmann M., Knaut M.** Surf. Coating. Technol. 215 (2013) 133–140
2. **Xu H., Nie X., Wei R.** Surf. Coating. Technol. 201 (2006) 4236–4241.
3. **Wei R., Langa E., Rincon C., Arps J.H.** Surf. Coatings Technol. 201 (2006) 4453–4459.
4. **Hatem A., Lin J., Wei R., Torres R.D., Laurindo C., de Souza G.B., Soares P.** Surf. Coating. Technol. 347 (2018) 1–12.
5. **Menshakov A.I., Bruhanova Yu.A., Skorynina P.A.** J. Phys.: Conf. Ser. 1954 (2021) 012032.
6. **Menshakov A.I., Bruhanova Yu.A., Kukharenko A.I., Zhidkov I.S.** Membranes, 12(3) (2022) 321.
7. **El-Rahman A.M.A., Wei R.** Surf. Coatings Technol. 241 (2014) 74–79.

# DEPOSITION OF MICRO- AND NANOCRYSTALLINE DIAMOND COATINGS ON CARBIDE CUTTERS OF SMALL DIAMETER IN MW PLASMA

E. Ashkinazi[1], V. Sedov[1], M. Shevchenko [1], D. Vinogradov[2], E. Matasova [2], A. Khomich [3], R. Khmelnitsky [4], V. Ralchenko[1]

[1]A.M. Prokhorov General Physics Institute, Russian Academy of Sciences, 38 Vavilova St., Moscow, 119991, Russia e-mail: jane50@list.ru
[2]Bauman Moscow State Technical University 2nd Baumanskaya st. 5/1, 105005 Moscow, Russia e-mail: vdv2010@bk.ru
[3]V. A. Kotelnikov Institute of Radio Engineering and Electronics RAS, 1 Vvedenskogo sq., Fryazino, Moscow Region, 141190, Russia e-mail: antares-610@yandex.ru
[4]P. N. Lebedev Institute of Physics, Russian Academy of Sciences, 53 Leninsky prospect, 119991 Moscow; Russia e-mail: roma@lebedev.ru

## Abstract

Objects with a high aspect number (high height-to-width ratio), have a number of problems when used as substrates for the growth of diamond coatings in CVD reactors. One of them is the "edge" effect at the contact of plasma with the substrate, which leads to non-uniform heating and, as a result, non-uniform properties of the coating. To compensate for this effect, we used a "limiting" ring installed around a group of substrates, which made it possible to homogenize their temperature. We produced the diamond films on cutting tools in such geometry, and demonstrated a significant increase in their performance.

## Experiment

The diamond coatings a few microns thick were obtained on the surface of tungsten carbide with the addition of cobalt (6%) in ARDIS-100 microwave plasma CVD reactor using a hydrogen-methane-nitrogen gas mixture. Figure 1a shows the geometric configuration of the reactor chamber in cross-section with a substrate in the center.

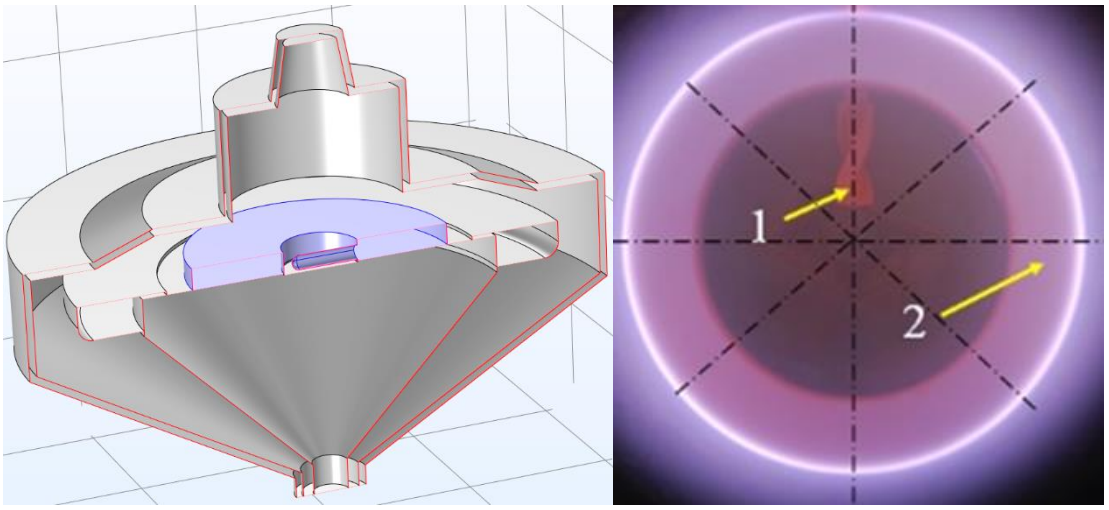



Fig. 1. (a) Geometry of reactor chamber; (b) Top-down photograph of the coating process of a cutter (1). The bright ring is enhanced plasma light emission on the edge of "limiting" ring (2).

As cobalt particles catalyze the diamond-graphite transition, it was chemically removed from the surface using Murakami's and Caro's etchants. To improve the coating adhesion and block the diffusion of cobalt from depth during deposition, single-layer tungsten buffer layers were used. A technology is proposed for uniform heating of an axial tool of small diameter by the plasma using a "limiting" ring [1,2] placed on the main conductive platform of the microwave reactor (Fig.1, b).

**Modeling**

To optimize the dimensions of the "limiting" ring, FEM computer simulations were used. Two different model types were used: axisymmetric 2D for calculation of heat and gas flow, and 3D model for electromagnetic field. The modeling showed that in the absence of direct contact between the plasma cloud and the sample located inside the ring, the edge effect is weakened. The gas flow model took into account the arrangement of gas inlets on top of reactor, vacuum pump at the bottom, and other details. The gas flow pattern revealed significant primary convection circulation of gas right above the growth region, as well as secondary vortex.

For heat distribution modeling, both convective and radiative heat transfer was considered, with temperature distribution accorded with optical spectroscopy diagnostics of the plasma [4]. The calculated heat distribution pattern is shown in Fig. 2. Due to convective cycle size and speed, as well as distance between substrate and plasma, significant part of non-radiative heat is removed from active area by gas flux while close proximity makes radiative

heating a significant factor. This results in more even heating of a substrate with complex shape and high aspect ratio.

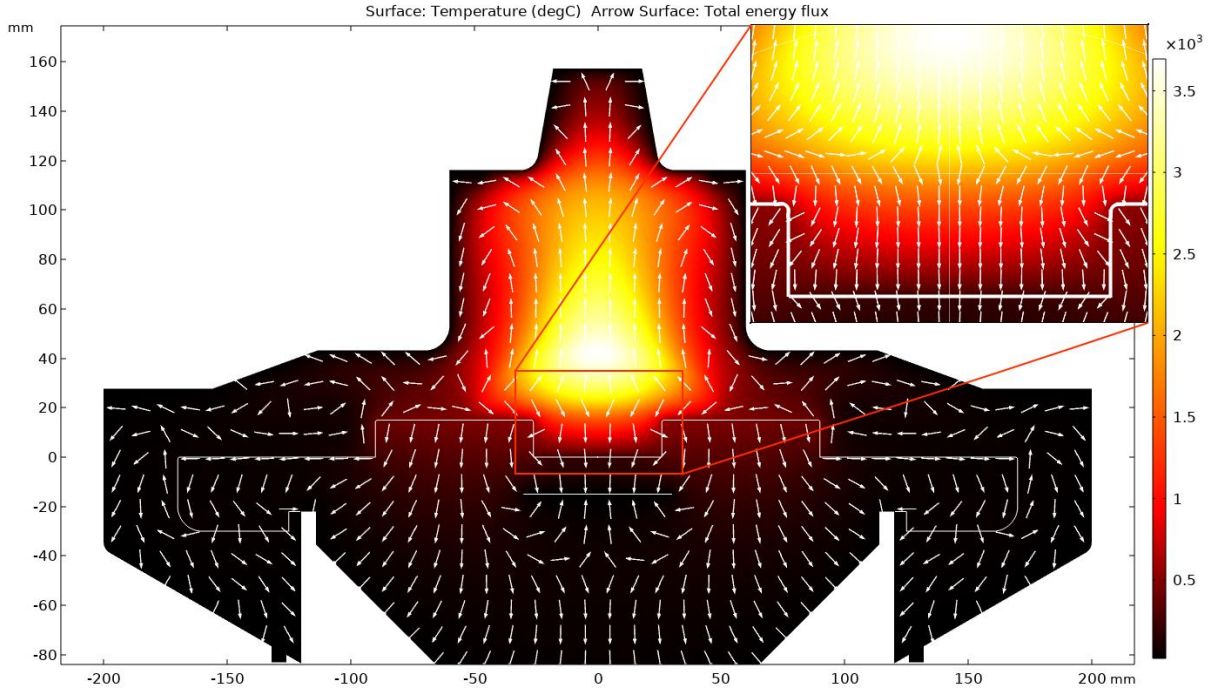



Fig. 2. Calculated pattern of temperature distribution and heat flux. Inset: zoomed temperature pattern in the central region of the cavity.

## Performance test

Comparative wear tests were carried out by milling a polymer composite material made of quartz fabric and a chromium aluminophosphate binder by 5mm diameter cutter. The tests were performed on the MULTICUT 3000 engraving machine and have shown that the back and front cutting edge of an uncoated cutter is subjected to intense build-up of the material of the processed composite, which changes its geometry. This problem was relaxed for the coated tools. The cutting test revealed a clear reduction of wear rate for the diamond-coated mill, up to 40% for edge of cutting tooth and 20% on average (Fig. 3).

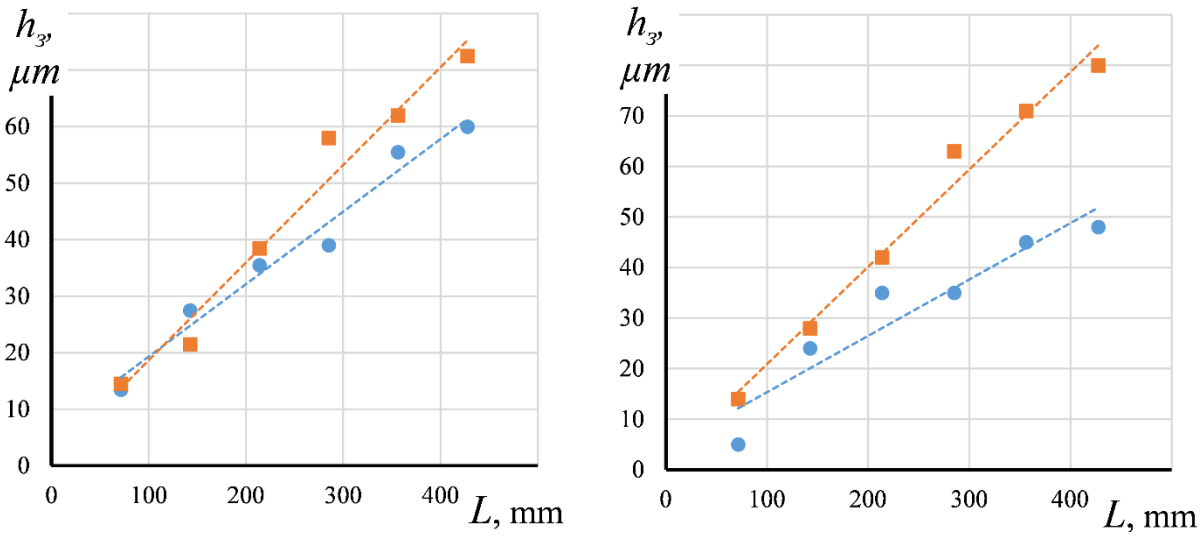



Fig. 3. Wear of coated (circles) and uncoated (squares) cutters: left panel – average wear; right panel – wear of a single cutter tooth

## References

1. **Plateholder design for deposition of uniform diamond coatings on WC-Co substrates by microwave plasma CVD for efficient turning application** / Ashkihazi E.E., Sedov V.S., Sovyk D.N., Khomich A.A., et al. // Diamond and Related Materials. 75 (2017) 169-175.
2. **Patent of the Russian Federation** No. 2644216 dated July 15, 2016 "UHF plasma reactor for obtaining a homogeneous nanocrystalline diamond film"
3. **Frictional Coefficients between Aluminum–Silicon Alloy and Cutting Inserts with MPCVD Diamond Coatings** / E. E. Ashkinazi, V. G. Ral'chenko, V. I. Konov [et al.] // Russian Engineering Research. – 2018. – Vol. 38. – No 6. – P. 457-461. – DOI 10.3103/S1068798X18060047. – EDN VBTZDG.
4. **Optical diagnostics of microwave plasma in process of micro/nanocrystalline diamond deposition on hard alloy tools** / V.Y. Yurov, E.E. Ashkinazi, E.V. Zavedeev, A.K. Martyanov, I.A. Antonova, V.G. Ralchenko // Materials Today: Proceedings, 2021, Volume 38, Part 4, Pages 1736-1739, DOI 10.1016/j.matpr.2020.08.241

**Acknowledgements**. This work was supported by the Russian Science Foundation for Fundamental Research (grant No. 22-19-00694).

# STUDY OF THE EFFECT OF PLASMA MODIFICATION OF A UHMWPE THREAD ON THE PHYSICAL AND MECHANICAL PROPERTIES OF POLYETHYLENE COMPOSITE

I.Sh. Abdullin[1], I.K. Nekrasov[2], A.V. Kormakov[3], A.S. Krainov[3], E.F. Kharchenko[3]

[1]Open Joint Stock Company “Plasma VST”, Russia, Kazan, plasma.vst@gmail.com
[2]Federal state autonomous educational institution of higher education "Kazan (Volga Region) Federal University, Russia, Kazan, igor05071997@mail.ru
[3]Open Joint Stock Company «Armocom», Moscow region, Khotkovo, mail@armocom.ru

The choice of UHMWPE materials as the object of study is explained by the unique combination of their properties. High strength, specific modulus, adsorption energy, combined with lightness, are the great interest in the manufacture of composite materials. Therefore, world interest in high-strength high-modulus polyethylene fibers and fabrics based on them is increasing [1].

The creation of polymer composite materials (PCM) based on UHMWPE fibers is an important direction, since such PCMs with a density of 1.0–1.4 g/cm$^3$ from nanocrystalline high-strength high-modulus UHMWPE fibers are promising for reducing the weight of products. The problem is the low adhesion properties of UHMWPE-fibrous material, which have been improved by plasma treatment in a high-frequency capacitive coupling discharge [2].

As samples, is used a roped untwisted plait of 10 UHMWPE threads, untwisted UHMWPE thread (330 cN/tex) and a fabric based on UHMWPE satin weave thread (80 g/m$^2$) made by compression-winding method. As matrices for the composite material, thermoplastic with an alcohol-acetone solvent, thermoplastic with distilled water as a solvent, and thermoplastic were used. Composite material samples were made under the same conditions with identical technological regimes by the method of infusion impregnation.

The studies were carried out with the following input parameters of the experimental setup (described in [3]): frequency - 13.56 MHz; operating pressure P - 13.3–100 Pa; plasma forming gas - air, from 1-2 kW, processing time - 5-10 minutes. The output parameters of the installation were: ion energy $E_i$ - 50-100 eV, current density on the fiber surface $j_i$ - 0.5-1 A/m$^2$, temperature - 323-343 K.

The effect of treatment on the strength of the original UHMWPE fiber was tested by determining the maximum breaking force of the tow before and after treatment. The test results are presented in table.1. From the data of Table 1, one can note a slight decrease in tensile strength and an increase in relative elongation within the coefficients of variation of the test results of the starting

Table 1. Determination of tensile strength.

| № | Material | Plasma treatment | Determination of tensile strength | |
|---|---|---|---|---|
| | | | Breaking elongation, N | Relative extension, % |
| 1 | Harness canted untwisted | No processed | 816 | 12.4 |
| 2 | | Processed | 793 | 13.5 |

Table 2. Dependence of the enhancement of stratification depending on the presence of treatment with a stream of low-energy ions.

| № | Sample characteristics | | | Results |
|---|---|---|---|---|
| | Availability of plasma treatment of UHMWPE | Matrix | Size, mm | Strengthening the delamination, N |
| 1 | No processed | React plastic, solvent - acetone | 25*150 | 5,3 |
| 2 | Processed | | 25*150 | 16,5 |

material. This is due to the fact that the introduced low-energy ions create point defects in the thread (penetration depth up to 50 angstroms, as determined using Auger spectrometry). These defects weaken the bonds between atoms in the UHMWPE chain, which leads to a weakening of the elongation at break. The low penetration depth of ions, which is typical for the method of treatment with low-energy ions in an RF discharge, practically does not weaken the interatomic bonds.

To test the effect of processing UHMWPE fibers on the physical and mechanical properties of woven polyethylene composites, samples were made to determine the magnitude of the interlayer adhesive bond and strength characteristics. Samples were made on the basis of SVPME satin weave fabric and epoxy binder, where acetone was used as a solvent. Table 2 shows the results of testing samples.

It can be seen from the results of table 2 that fiber treatment increased the delamination enhancement of PCM by more than three times. This is due to increased adhesion of UHMWPE tissue, which results in greater polymer-matrix bonding.

Analyzing the data in table 3, one can notice a twofold increase in bending strength and a more than fourfold increase in shear strength, which indicates a noticeable improvement in the structural characteristics of the polymer composite material.

Table 3. The dependence of the mechanical parameters of the samples depending on the presence of treatment with a stream of low-energy ions.

| Sample characteristics | | | | | | Test results | | | |
|---|---|---|---|---|---|---|---|---|---|
| Availability of UHMWPE fabric treatment | Matrix | Surface density of reinforcement, | Sample surface density, kg/m$^2$ | Thickness, mm | Binder content, % | Bending, σ, MPa | Bending, E, MPa | Cut, σ, MPa | Shear, σ, MPa |
| No | Reactoplastic, solvent - acetone | 4 | 6.41 | 6.25 | 37.6 | 76 | 10.8 | 142 | 2.5 |
| Yes | | 4 | 6.67 | 6.40 | 40.0 | 171 | 10.7 | 147 | 11.1 |

## Conclusion

Treatment of the fiber with a stream of low-energy ions reduced its initial strength by only 3%. This is a rather low value compared to other methods for improving the adhesive properties of UHMWPE fibers.

The use of processed fiber with thermosets significantly increased the physical and mechanical properties of PCM, as well as the adhesive strength at the fiber-matrix interface, which makes it possible to use it as a perspective structural material.

The presence of plasma treatment of UHMWPE fibers increased such tissue parameters as bending and shearing (table 3). The increase in the amount of binder is explained by the increase in adhesive properties, which led to a greater consumption of the binder. This leads to the need to reduce the time of impregnation of the tissue treated with UHMWPE plasma in order to prevent an excessive amount of binder in the PCM volume.

## References

1. **Kudinov V.V., Korneeva N.V., Krylov I.K.** Influence of components on the properties of polymer composite materials. Reference monograph. M. Nauka (2021).

2. **Sergeeva E.A., Korneeva N.V., Zenitova L.A., Abdullin I.Sh.** Modification of synthetic fibrous materials and products by non-equilibrium low-temperature plasma. Part. 2. Properties, structure, technologies. Kazan: Kazan State Technological University (KSTU) (2011).

3. **Abdullin I.Sh., Zeltukhin V.S., Kashapov N.F.,** High-frequency plasma-jet treatment of materials at reduced pressures. Theory and practice of application. Kazan: Kazan University Press (2000)

# EFFECT OF ION-PLASMA NITRIDING AND ELECTROLYTE-PLASMA POLISHING ON THE HARDNESS AND CORROSION RESISTANCE OF HIGH-CHROME STEELS

V.S. Kaplenko, S.I. Bahayeu, D.V. Zhuk, I.L. Pobol, I.P. Smyaglikov

Physical Technical Institute, National Academy of Science of Belarus,
220141, Minsk, 10 Kuprevicha str., pobol@phti.by

## Introduction

One of the most effective and high-tech industrial methods of surface hardening of workpieces of structural and tool steels is an ion-plasma nitriding (IPN). By means of IPN it is possible to obtain uniform hardened layers of high hardness [1]. The formation of a diffusion layer with a developed nitride zone (ε-phase) provides high corrosion resistance, and a diffusion layer without a nitride zone (γ'-phase) provides the ability to withstand alternating loads under wear conditions at high pressures. During IPN foreign inclusions, oxides and carbides of iron and other elements can be deposited on the surface of nitrided samples from the walls of the vacuum chamber, which leads to a decrease in the corrosion resistance of the treated surface. The method of electrolytic-plasma polishing (EPP) is effective processing of metals and their alloys providing the surface cleaning and surface roughness reducing [2]. The aim of the work is to determine the effect of EPP on the hardness and corrosion resistance of the IPN-hardened surface of samples of high-chromium AISI 304, AISI 316L and AISI 420 steels.

## Equipment, materials and research methods

The IPN of the samples was carried out using equipment developed at the Physical Technical Institute of the NAS of Belarus. A treatment was carried out at a temperature of 400 °C and exposure time of 16 h in a gas mixture of nitrogen, hydrogen, and argon. The EPP process was carried out in an aqueous solution of 5% ammonium sulfate at a constant voltage of 320 V, an electrolyte temperature of 85 °C during 60 and 120 s. The microdurometric properties of the materials were determined with the help of AFFRI-MVDM8 microhardness tester at a load on the indenter of 25 g with simultaneous identification of metallographic features of the microstructure. It should be emphasized that the results of measuring the microhardness of a thin near-surface layer are somewhat arbitrary, since the imprint diagonal is practically equal to the layer depth. The corrosion resistance of the samples was studied on Multi

Autolab/M204 potentiostat/galvanostat in a 10% NaCl solution in a three-electrode cell with an Ag/AgCl/KCl reference electrode by the electrochemical method of linear polarization. The surface roughness of the IPN samples was measured using Surtronic 25 profilograph.

**Research results and analysis**

As a result of IPN of AISI 304 sample, a uniform nitride layer is formed on the surfaces. The layer average depth is 9 μm and a microhardness at the surface is 470 $HV_{0,025}$, while a steel layer microhardness is 170 $HV_{0,025}$ (Fig. 1, *a*).

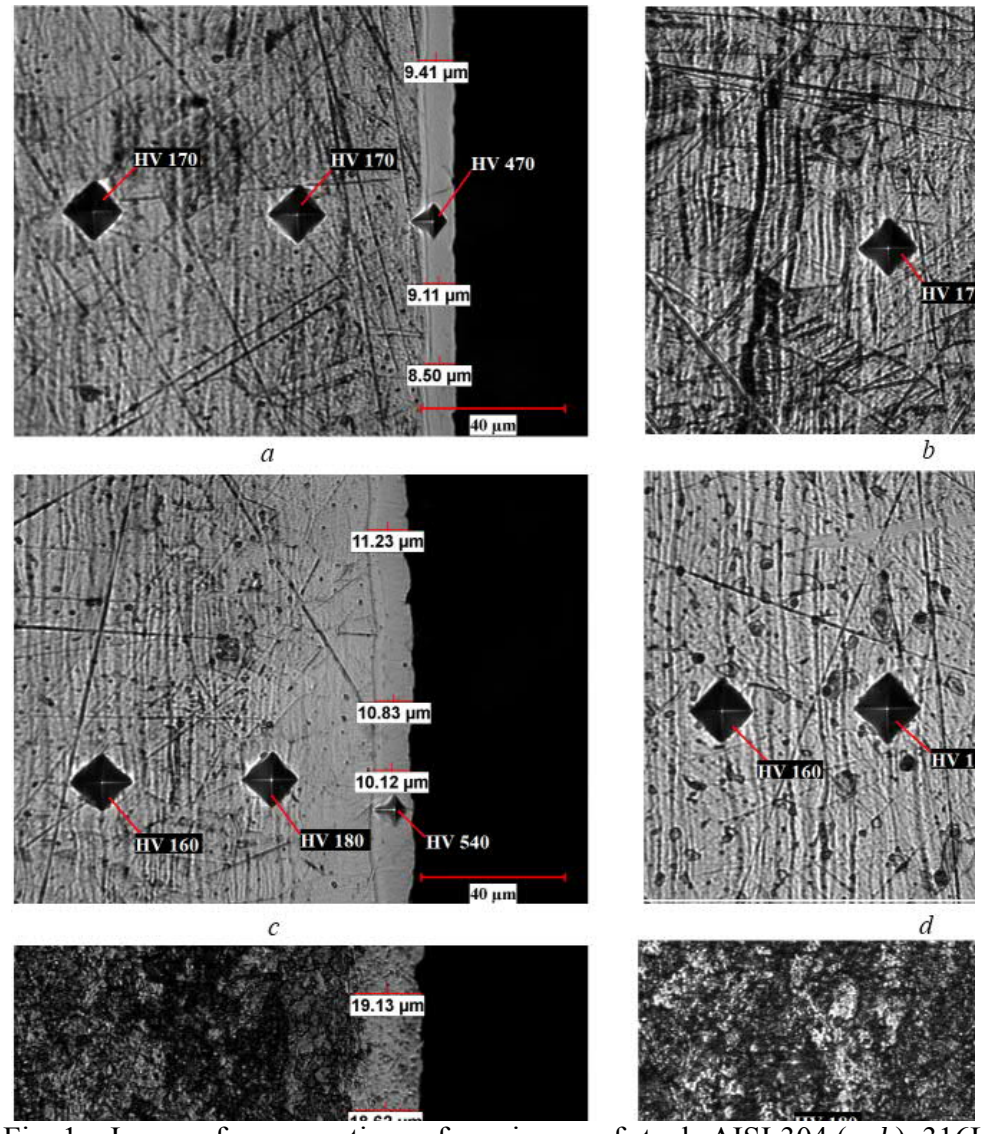



Fig. 1 – Image of cross-sections of specimens of steels AISI 304 (*a*, *b*), 316L (*c*, *d*), 420 (*e*, *f*) subjected to IPN (*a*, *c*, *e*) and subsequent EPP (*b*, *d*, *f*)

The average nitride layer depth on AISI 316L sample is 11 μm with microhardness of 540 $HV_{0,025}$ (the steel base microhardness is 160 $HV_{0,025}$)

(Fig. 1, c). For the AISI 420 sample, the depth of the nitride layer is 19 μm and microhardness is 840 $HV_{0,025}$ (Fig. 1, *e*). Non-equilibrium conditions during IPN make it possible to obtain a metastable corrosion-resistant S-phase (nitrogenous austenite). The composition of the S-phase corresponds to FeN and CrN.

The EPP process was used to remove contaminations from the surface of samples made of high chromium steels. The Table contains results of influence of processing IPN and the combined effect of IPN and EPP for 60 and 120 s on the properties of the steel sample surfaces.

Table. Surface properties of processed samples

| Steel | Sample surface conditions | Surface microhardness, $HV_{0,025}$ | | | | Layer depth, μm | | Corrosion potential, V | | Year corrosion, mm/year | | Surface roughness Ra, μm | |
|---|---|---|---|---|---|---|---|---|---|---|---|---|---|
| | | Treatment time of EPP, s | | | | | | | | | | | |
| | | 60 | 120 | 60 | 120 | 60 | 120 | 60 | 120 | 60 | 120 | 60 | 120 |
| AISI 304 | As-received | 170 | | | | – | | –0,164 | | 0,001 | | 0,26 | |
| | IPN | 1250 | | | | 8,5-9,4 | | –0,281 | | 0,050 | | 0,3 | |
| | IPN+EPP | 310 | 190 | 970 | 340 | 7,8 – 8,9 | 4,9 – 5,7 | –0,214 | –0,196 | 0,006 | 0,004 | 0,25 | 0,12 |
| AISI 316L | As-received | 160 | | | | – | | -0,071 | | 0,007 | | 0,22 | |
| | IPN | 1040 | | | | 10,1–11,2 | | –0,444 | | 0,104 | | 0,18 | |
| | IPN+EPP | 290 | 240 | 1000 | 350 | 8,8 – 9,3 | 5,1 – 6,5 | –0,194 | –0,153 | 0,010 | 0,008 | 0,13 | 0,12 |
| AISI 420 | As-received | 180 | | | | – | | –0,417 | | 0,066 | | 0,24 | |
| | IPN | 1060 | | | | 18,6–20,0 | | –0,521 | | 0,178 | | 0,3 | |
| | IPN+EPP | 1020 | 670 | 840 | 380 | 12,7 – 16,7 | 8,4 – 11,3 | –0,425 | –0,417 | 0,083 | 0,072 | 0,27 | 0,14 |

It can be seen from the data in the Table that EPP of nitrided samples leads to decrease of hardness of steel samples, but result value of surface microhardness still keeps more than that of initial state samples for all type of treated steel samples. The surface of AISI 304 steel after nitriding corresponds

to the 5th group of resistance, the class of medium resistance, and after EPP for 60 s it corresponds to the 3rd resistance group, the class of quite resistant. For AISI 316L steel, the values of annual corrosion after nitriding correspond to the 6th resistance group, the class of limited-resistant, and after EPP for 60 s it corresponds to the 3rd resistance group, the class of quite resistant. For AISI 420 steel, the value of annual corrosion after nitriding corresponds to the 6th resistance group, limited resistance class, and after EPP for 60 s it corresponds to the 5th resistance group, moderately resistant class.

## Conclusion

The effect of electrolytic-plasma treatment of the surface of samples made of high-chromium steels after ion-plasma nitriding on the properties of the hardened layer (depth, microhardness, corrosion resistance, surface roughness) has been studied. Combined surface treatment of specimens of high-chromium steels, including IPN followed by EPP, makes it possible to obtain hardened layers of the required depth, the surface microhardness is 2–6 times more than that of as-received steel microhardness. At the same time the preservation of the corrosion resistance of samples at the level of the untreated surface at the depth of the hardened layer not less than 5 microns occur. Additionally, as a result of processing, the surface is polished with the removal of the surface layer of foreign inclusion.

The recommended EPP processing time at a voltage of 320 V and electrolyte temperature of 85 °C for high-chromium steels after IPA is 60–120 s. These conditions provide the necessary operating performance.

The results obtained allow to recommend the combined processing for the manufacture of tools and industrial equipment used in the food industry and medicine.

## References

1. **Bosyakov M.N. et al.** Modern Methods and Technologies for Creating and Processing Materials: Collection of Scientific Papers, PTI NAS of Belarus, Minsk, 1 (2021) 60-80.

2. **Bahayeu, S.I., Parshuto A.A., Smyaglikov I.P.** J. High Temperature Material Processes, 19 (2015) 93–97.

# EFFECT OF PLASMA ELECTROLYTIC PRETREATMENT ON A ROUGHNESS AND COLORING UNIFORMITY OF THE OXIDE FILMS ON TITANIUM AND ITS ALLOYS

S.I. Bahayeu, I.P. Smyaglikov

Physical-Technical Institute of NAS of Belarus,
220141 Minsk, 10 Kuprevich str., ips.imaf@gmail.com

Electrolyte plasma is successfully used for polishing various metals and alloys (steel, copper, aluminum, titanium) [1]. As a result of processing, changes in the structure and elemental composition of the metal surface occur: a decrease in surface roughness and enrichment of the surface layer with oxygen [2]. For implants made of titanium alloy Grade 5, the aluminum and vanadium concentrations in the surface layer decrease from 7.3 to 3.5–4.4 at. % and from 2.1 to 0.1–0.3 at. % respectively [3], which ensures their biocompatibility by reducing the release of toxic metals into living tissues of the body. To increase the biocompatibility of titanium implants, oxide interference-colored coatings are additionally formed on their surface by an electrochemical method [4]. Color marking of implants with preservation of their biocompatibility reduces the risk of erroneous use of an inappropriate implant size and facilitates their operational use in medical practice [5].

The color uniformity of the titanium oxide layer is strongly affected by the state of the original titanium surface. For example, it was shown in [6] that metal grains with different crystallographic orientations emerge on the surface in polycrystalline titanium. Since different crystallographic planes have different atomic packing densities, this can affect the characteristics of the oxide layer formed on these planes. From the point of view of quality of titanium implants, the effect of electrolytic plasma pretreatment on the uniformity of their electrochemical coloring is of interest.

Titanium Grade 4 and Grade 5, which are used for the manufacture of medical implants, were chosen as the material for the study. The surface roughness parameter *Ra* of titanium samples of Grade 4 and Grade 5 after mechanical treatment (MT) was 0.28 and 0.38 μm, respectively. Three methods of the samples pre-treatment before electrochemical oxidation are considered, which make it possible to obtain a smooth polished surface:

1. Chemical polishing in a solution of 5.6 M HF and 10.4 M $HNO_3$ at a solution temperature of 60–70 °C for 0.3–1 minutes (CP1).

2. Chemical polishing in a solution of 6.3 M $H_3PO_4$, 3.5 M $HNO_3$ and 5.6 M HF at a solution temperature of 20–30 °C for 5–10 minutes (CP2).

3. Electrolyte-plasma polishing (EPP) in a solution of 0.3 M potassium fluoride, 0.3 M ammonium fluoride and 0.02 M surfactant at a solution temperature of 75–85 °C for 5–10 minutes [3].

Subsequent electrochemical oxidation (EO) of the samples was carried out in a potentiostatic mode in a two-electrode cell at a voltage of 20–100 V and a current density of 0.1 A/cm$^2$ in a 0.5 M phosphoric acid solution at a temperature of 20°C for 5–15 minutes. As a result the oxide layers with a wide range of colors are formed on the surface: shades of blue, yellow, red, and green.

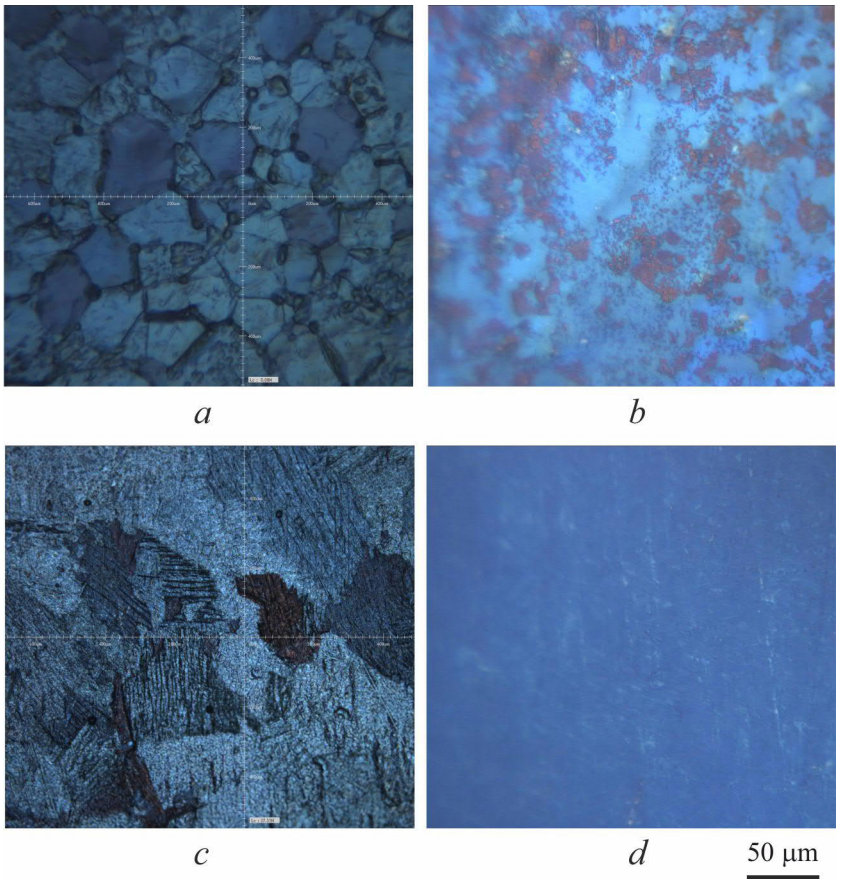



Fig 1. Surface images of titanium Grade 4 (*a*, *b*) and Grade 5 (*c*, *d*) samples oxidized at 30 V with different pretreatment methods (*a*, *c* – CP1; *b*, *d* –EPP)

The surface of titanium Grade 4 after chemical polishing is a grain structure with clear interfaces and grain sizes of 30–100 μm, which acquire different colors as a result of oxidation (Fig. 1, *a*). At a forming voltage of 30 V, areas of blue color of various shades are observed on the surface, and at a voltage of 90 V, blue, red, and yellow grains are found on the surface.

Chemical polishing of a titanium Grade 5 sample also reveals the structure of its surface. Grains of α-Ti and β-Ti after electrochemical oxidation have different colors (Fig. 1, *c*).

Preliminary electrolytic-plasma polishing of samples made of titanium Grade 4 and Grade 5 leads to their more uniform coloration as a result of electrochemical oxidation compared to the samples after chemical polishing (Fig. 1, *b*, *d*). The observed phenomenon can be explained by the fact that during EPP, in contrast to chemical polishing, the metal is uniformly removed both from the grains and along their boundaries; as a result, the metal structure does not appear [2]. In this case, it is possible that the initial oxide layer formed on the surface during electrolytic-plasma polishing suppresses the effect of grain orientation during subsequent anodizing. As a result, an oxide layer is formed with the same thickness over the entire surface of the sample, which is characterized by much smaller inhomogeneities.

It should be noted that the preliminary EPP of titanium leads to lower values of the surface roughness parameter of the oxidized samples compared to the use of preliminary chemical polishing (Table 1).

Table 1. The surface roughness parameter *Ra* of titanium samples, μm

| Titanium | Processing method | | | | |
|---|---|---|---|---|---|
| | MT | EPP | CP1 | CP2 | EO |
| Grade 4 | 0.28 ±0.06 | 0.08 ±0.03 | – | – | 0.09 ±0.04 |
| | | – | 0.16 ±0.06 | – | 0.17 ±0.05 |
| | | – | – | 0.19 ±0.06 | 0.19 ±0.07 |
| Grade 5 | 0.36 ±0.08 | 0.11 ±0.04 | – | – | 0.12 ±0,04 |
| | | – | 0.19 ±0.05 | – | 0.18 ±0,06 |
| | | – | – | 0.24 ±0.07 | 0.26 ±0.07 |

It follows from the data in the table that the use of preliminary EPP provides a 1.5–2.0 times lower surface roughness index *Ra* of oxidized samples than in the case of preliminary CP for all considered samples.

Thus the use of electrolytic plasma polishing as a preliminary treatment of titanium surface before electrochemical oxidation contributes to the formation of a uniformly colored oxide layer with the roughness parameter *Ra* in 1.5–2.0 times lower than that in the case of chemical pretreatment.

The discovered effect can be used in the manufacture of implants from titanium and its alloys used in cardiac surgery, dental implantology, maxillofacial surgery, traumatology and orthopedics, when their low roughness and bioinertness are required.

**Referenses**

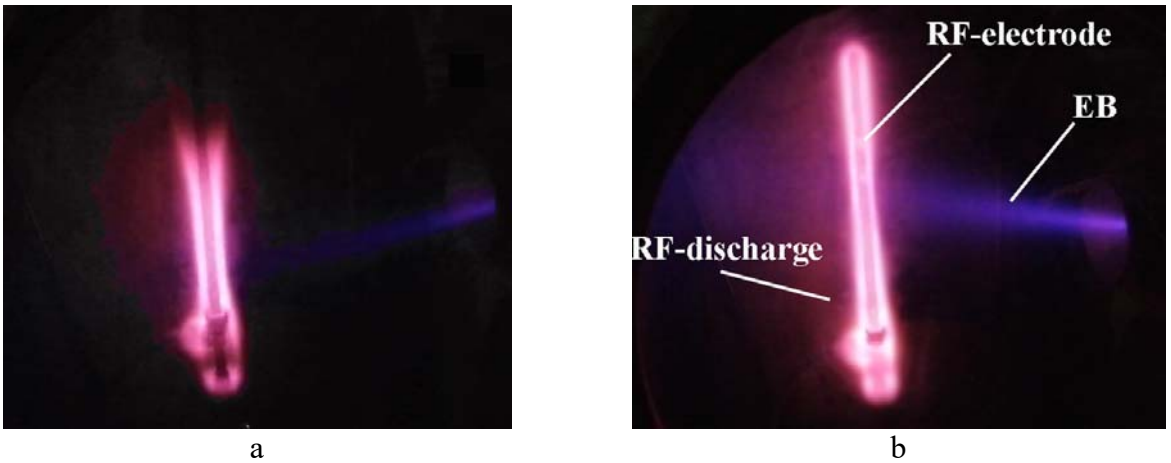
1. Kulikov I.S., Vazhenko S.V., Kamenev A.Y. Electrolytic plasma treatment of materials. (2010). Minsk: Belarusian Science, 232 p. (In Russian).
2. Bahayeu, S.I. Surface modification of titanium and aluminum alloys by electrolyte plasma treatment / S.I. Bahayeu, A.A. Parshuto, I.P. Smyaglikov // J. High Temperature Material Processes. – 2015. – Vol. 19, iss. 1. – P. 93–97.
3. Bahayeu, S.I. Electrolytic plasma polishing of titanium implants / S.I. Bahayeu, I.P. Smyaglikov // Plasma physics and plasma technology. IX International Conference (Minsk, September 17–21, 2018) / Editorial N.V. Tarasenko, A.A. Nevar, N.N. Tarasenka. – Minsk : Kovcheg LTD, 2018. – P. 421–424.
4. Karambakhsh, A. Corrosion Resistance and Color Properties of Anodized Ti-6Al-4V / A. Karambakhsh, A. Afshar, P. Malekinejad // Journal of Materials Engineering and Performance. – 2011. – Vol. 21. – P. 121-127.
5. Ross, A.P. Anodizing color coded anodized Ti6Al4V medical devices for increasing bone cell functions / A.P. Ross, T.J. Webster // Int. J. Nanomedicine. – 2013. – Vol. 8. – P. 109–117.
6. Diamanti, M.V. Thickness of Anodic Titanium Oxides as a Function of Crystallographic Orientation of the Substrate / M.V. Diamanti, M.P. Pedeferri, C.A. Schuh // Metall. Mater. Trans. A Phys. Metall. Mater. Sci. – 2008. – Vol. 39, iss. 9. – P. 2143–2147.

# BEAM-PLASMA REACTORS FOR FUNCTIONAL GRADIENT MATERIALS PRODUCTION

T. Vasilieva

Joint Institute for High Temperatures of the Russian Academy of Sciences (JIHT RAS), 125412, Izhorskaya str., 13 Bd.2, Moscow, Russia, tmvasilieva@gmail.com

Functionally graded materials (FGMs) are advanced engineering materials designed for a specific performance or function in which a spatial gradation in structure and/or composition lend itself to tailored properties [1]. Interest in FGMs has recently escalated while they are promising candidates for numerous high tech applications such as chemical industries, microelectronics, bioengineering and regenerative medicine.




a b

Fig. 1. The EB action on a RF-gas discharge near a cylindrical electrode. Gas pressure 2.0 Torr: (a) The EB is directed to the electrode bottom: the discharge glows on a half of the electrode length. (b) The EB is directed to the central part of the electrode: the discharge glows over the entire length of the electrode

Over the last few years several other techniques have been developed to prepare gradient surfaces including plasma chemical methods, e.g. treatment in corona and radio frequency glow discharges [2, 3]. To obtain gradients special masks and covers, which are moved over the polymeric surface, are applied [4]. Technically, however, the usage of such moving parts in the reaction chamber is difficult. Moreover, the formed gradient surfaces appeared to be derivatized beyond the length of the mask, possibly due to a small gap between the material and the cover [3].

The beam-plasma chemical reactors generating cold hybrid plasma (HP) for production of polymeric FGMs for tissue engineering and regenerative medicine are considered. The main hybrid reactor advantages are as follows:

1. The reaction volume is uniform and doesn’t contract with the increase

of the plasma generating gas pressure to values at which the RF-discharge is filamentary or does not glow at all;

2. The EB attracts RF-discharge and changes its shape and location at the surface of the polymeric substrate. Figure 1 illustrates the EB influence on the RF-discharge (13.56 MHz) plasma generated by cylindrical electrode 150 mm in length and 5 mm in diameter.
3. Electron beam scanning can instantly control the reaction volume geometry, while active plasma particles concentrations can be controlled by the beam power independently. This allows precisely localize the RF-discharge on the desirable zone of the polymeric surface forming abruptly structured or smooth gradient patterns of functionalities and also prevent the sample from radiation and thermal damages.

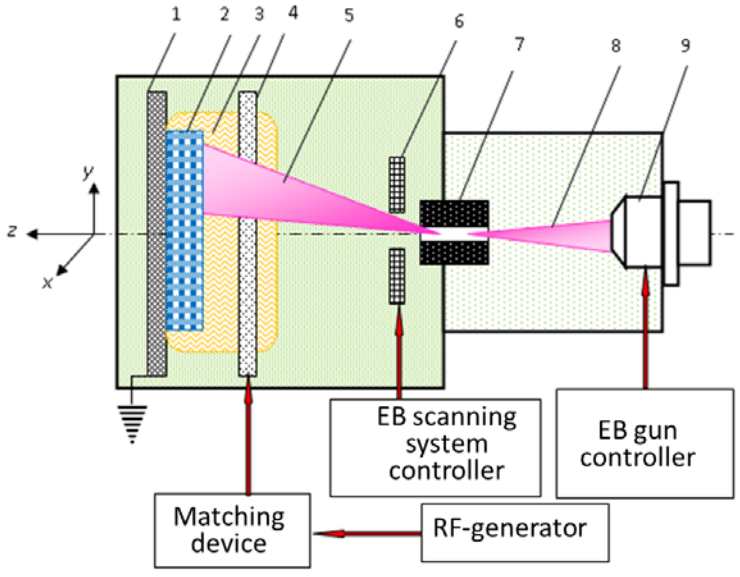



Fig. 2. The scheme of the hybrid type electron-beam chemical reactor: 1 – passive RF-electrode, 2 – treated polymeric object, 3 – RF-discharge, 4 – active RF-electrode, 5 – electron-beam plasma cloud, 6 – scanning EB system, 7 – injection window, 8 – electron beam (EB), 9 – electron-beam gun

Oxygen HP was generated in the special beam-plasma chemical reactor of hybrid type [5]. The scheme for polymers modification experiment as well as procedure of two-dimensional gradient structures formation on their surface are given in Figure 2. The HP was excited by joint action of a continuous or intermittent electron beam (EB) and a capacity coupled RF-gas discharge (13.56 MHz) on gaseous media at pressures (5-10 Torr). The scanning EB (accelerating voltage 30 kV and beam current 1-5 mA) was injected through the grid-shape active electrode into the gap of the planar double-electrode RF-discharge system; electromagnetic deflecting coils scanned the electron beam in the {x, y}

plane. The gas flow rate and the pressure of plasma generating gas were automatically controlled by mass flow and pressure controllers (MKS Instruments, USA). Samples were placed in the gap between the active RF-electrode and the flat grounded electrode for treatment.

As mentioned above, the EB characteristics can independently control the reaction volume geometry as well as active plasma particles concentrations. Several control techniques by intermittent EB were studied (Fig. 3), namely 1) rotation of the beam injection axis along concentric circles (or ellipses) and 2) linear displacement of the beam injection axis along a certain straight line with stops at certain points of each point of both the circuit path and linear trajectories. Thus, the following treatment parameters can vary:

- Amplitude of the EB linear scanning and diameters of circles (or lengths of the main axes of ellipses);
- Orientation and location of the scanning segment in the plane {x, y};
- Time duration of the EB stop at each point of the trajectory;
- Speed of the beam movement from point to point.



a b

Fig. 3. EB scanning patterns in intermittent mode in the {x, y} plane: (a) EB scanning along concentric ellipses; (b) EB linear scanning

The approach was tested on flat polymethylmethacrylate, polyethylenterphtalate, and polycarbonate samples. The hybrid plasma treatment resulted in oxygen-containing polar hydroxyl, carbonyl, and carboxyl groups formation in the polymers' surface layers. Surface free energy increase and wettability enchantment up to 1.5-2 times in comparison with original polymers were observed as well. Polymers biocompatibility improvement was found, which was attributed to changes in the chemical composition and hydrophilic sample surfaces properties due to HP processing.

**Acknowledgements**. This work was supported by the RSF grant 21-79-30062.

## References

1. **Naebe M., Shirvanimoghaddam K.** Applied Materials Today, 5 (2016) 223–245.
2. **Spijker H.T., Bos R., van Oeveren W., de Vries J., Henk J. Busscher H.J.** Colloids and Surfaces B: Biointerfaces, 15 (1999) 89–97.
3. **Pitt W.G.** Journal of Colloid and Interface Science, 133 (1989) 223–227.
4. **Mangindaan D., Kuo W-H., Wang Y-L., Wang M-J.** Plasma Processes Polymers, 7 (2010) 754–765.
5. **Vasiliev M., Vasilieva T., Aung Miat Hein.** Journal of Physics D: Applied Physics, 52 (2019) 335202.

# HYBRID-TYPE PLASMA CHEMICAL REACTORS: DEVELOPMENTS FOR NATURAL BIOPOLYMERS PROCESSING

T. Vasilieva[1], M. Vasiliev[2]

[1]Moscow Institute of Physics and Technology (MIPT), Institutskiy per., 9, Dolgoprudny, Moscow reg., 141700 Russia vasileva.tm@mipt.ru
[2]Joint Institute for High Temperatures of the Russian Academy of Sciences (JIHT RAS), Izhorskaya st., 13 Bd.2, Moscow, 125412 Russia

Natural polysaccharides chitin (linear heterocopolymer of β-1,4-linked 2-amino-2-deoxy-D-glucopyranose and 2-acet-amido-2-deoxy-D-glucopyranose units) and its deacetylated derivative chitosan are very promising for bioplastics production, pulp and paper industry, microbiology, food processing and agriculture [1-3]. For example, water soluble chitooligosaccharides (COS) have been used to augment foliar biomass, promote shoot and root growth, hasten flowering time and increase flower number, enhance fruit weight and productivity, spike number and grains per spike, improved seed germination in various plants [2, 3].

Plasma chemical processing of polysaccharides and COS production based on non-equilibrium low temperature plasmas could be an alternative to the conventional chemical hydrolysis and enzymatic degradation [4-6]. Our previous studies showed that non-equilibrium low-temperature electron-beam plasma effectively degrades high molecular weight chitosan due to combined action of high-energy electrons and chemically active particles [4-6].

Chitosan processing in non-equilibrium low-temperature hybrid plasma (HP) generated by joint action of a continuous electron beam and RF-gas discharge on gas (oxygen or water vapor) at pressures 0.1–10 Torr is considered in the present paper.

Several designs of the hybrid-type plasma chemical reactor of co-axial configuration were tested in experiments with crab shell high molecular weight chitosan destruction.

Figure 1 presents general scheme of the plasma chemical reactor specially designed for scientific and technological experiments. Cloud of the HP 12 is formed in reaction vessel 11 placed inside working chamber 10. Working chamber has connector 3 for evacuation and connector 4 to blow the main plasma-generating gas. In the present study oxygen was used as the plasma-generating gas. The reaction vessel can rotate by means of stepper electric motor 9 with variable rotation frequency Ω. Rotary feedthrough 6 with sealed holder for immovable RF-electrode 5 is combined with RF-feedthrough. Also the electrode holder has two connectors 8 and 7 for RF cable and for gas pipe respectively. Electrode 5 is made of porous metallic tube to blow additive gases

into the reaction vessel, if necessary. One end of the reaction vessel 11 is open and EB 2 is injected into the vessel through it. The electron beam (EB) is generated by electron gun 1 inside high vacuum chamber 14 and then is transported into working chamber 10 via special injection window (IW) 13 described in [7]. The IW is combined with the electromagnetic deflection system that can deflect the EB axis in two perpendicular directions and can also scan the EB to shape a desirable raster.

The other configuration of the hybrid reaction volume obtained using planar RF-electrodes is shown in Fig. 2. In that case the active RF-electrode was combined with piezoelectric plate which threw up the chitosan powder particles forming the mixing layer of the treated polysaccharide.

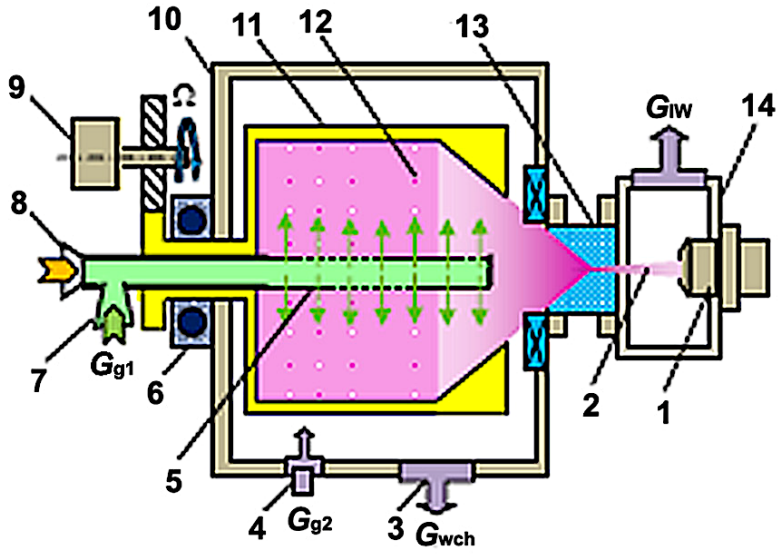



Fig. 1. General design of hybrid coaxial plasma-chemical reactor: 1 - electron gun, 2 - electron beam, 3 - vacuum pump connector, 4 - connector for plasma-generating gas feeder, 5 - active RF-electrode, 6 - rotary feedthrough combined with RF-feedthrough, 7- connector for additive gas feeder, 8 - RF-connector, 9 - stepper electric motor, 10 - working chamber, 11 - reactor vessel, 12 - plasma cloud, 13 - injection window combined with scanning system, 14 - high vacuum chamber

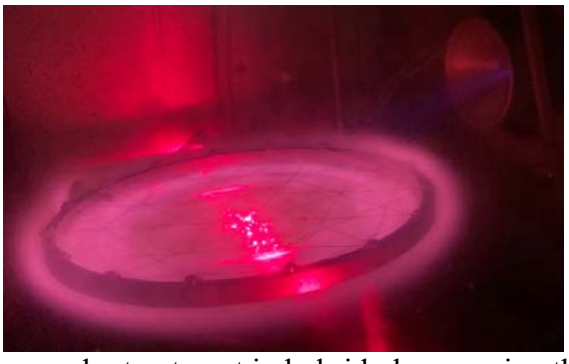


Fig. 2. The chitosan powder treatment in hybrid plasma using the system of planar RF-electrodes

Typical regimes for processing chitosan powders are given in Table 1 that also presents main parameters of the HP. The table shows that under typical conditions of the hybrid reactor operation particles of atomic oxygen, singlet oxygen and positive molecular ions of oxygen are responsible for plasma-chemical processes on the material surface because they are extremely chemically active forms of oxygen and their fluxes significantly exceed fluxes of other particles.

Table 1. Typical regimes of the plasma chemical reactor operation and treatment conditions

| Parameter | Value or characteristics | |
|---|---|---|
| Electron energy $E_{b0}$, keV | 25–30 | |
| Beam current $I_{b0}$, mA | 1–10 | |
| Scanning mode | Concentric circumferences of variable diameter | |
| Plasma generating gas | Pure oxygen, sulfur hexafluoride | |
| Gas pressure $P_m$, Torr | 0.1–10 | |
| RF-power, W | <50 | |
| RF-frequency, MHz | 13.56 | |
| Sample temperature $T_s = T_w$, °C | 40–70 | |
| Plasma density $n_{ep}$, $cm^{-3}$ | $10^8$–$10^{10}$ | |
| Maximal fluxes of neutral and heavy charged oxygen plasma particles falling on the sample surface, $1/(s \times cm^2)$ | Neutral<br>$O - 2 \cdot 10^{16}$;<br>$O_2(a) - 8 \cdot 10^{15}$;<br>$O_3 - 10^{11}$; | Charged<br>$O_2^+ - 4 \cdot 10^{15}$;<br>$O_2^- - 10^{13}$;<br>$O^+ - 5 \cdot 10^{13}$;<br>$O_4^+ - 2 \cdot 10^{11}$ |
| ($P_m = 5$ Torr, $E_{b0} = 30$ keV, $I_{b0} = 10$ mA, $z = 100$ mm) | | |
| Reactor vessel sizes: | | |
| Diameter, mm | 50–150 | |
| Length/diameter ratio | ≈ 1 | |

Water-soluble chitooligosaccharides with weight-average molecular mass $M_w$ = 800-2000 Da and polymerization degree varying from dimeres to heptamers were obtained; trimeres being the most predominant. Some increase in oxygen-containing carbonyl C=O and carboxyl –COOH groups and slight increase in deacetylation degree were observed after chitosan processing by the hybrid plasma of oxygen. The deacetylation degree of the HP-produced COS was determined by $^1$H NMR and its up to 98% increase with respect to original biopolymer was found. Water solutions of the produced chitosan oligomers enhanced germination in peas and decreased their microbial and fungal contamination [8].

The present experiments proved higher HP efficiency for COS production: the COS composition, properties and yield per unit mass of raw material were the same as after the chitosan processing in the electron-beam plasma [4, 5], however the COS formation was 20 percent faster.

**Acknowledgements**. This work was supported by the RFBR_№20-02-00501_a.

## References


1. **Bandara S., Du H., Carson L., Bradford D. and Kommalapati R.** Nanomaterials, 10 (2020) 1903.
2. **Faqir Y.H., Ma J.H. and Chai Y.L.** Plant, Soil and Environment, 67 (2021), 679-699.
3. **Shahrajabian M.H., Chaski C., Polyzos N., Tzortzakis N. and Petropoulos S.A.** Biomolecules, 11 (2021) 819.
4. **Vasilieva T., Sigarev A., Kosyakov D., Ul'yanovskii N., Anikeenko E., Chuhchin D., Ladesov A., Hein A.M. and Miasnikov V.** Carbohydrate Polymers, 163 (2017) 54-61.
5. **Vasilieva T., Chuhchin D., Lopatin S., Varlamov V., Sigarev A. and Vasiliev M.** Molecules, 22 (2017) 1908.
6. **Vasilieva T., Vasiliev M. and Aung Miat Hein.** Journal of Physics D: Applied Physics, 52 (2019) 335202.
7. **Vasiliev M. and Vasilieva T.** Encyclopedia of Plasma Technology (Ed.: J. Leon Shohet). Boka Ralton, FL, USA: Taylor & Francis Inc. (2016).
8. **Vasilieva T.M., Naumova I.K., Galkina O.V., Udoratina E.V., Kuvschinova L.A., Vasiliev M.N., Khin Maung Htay and Htet Ko Ko Zaw.** IEEE Transactions Plasma Science, 48 (2020) 1035-1041.

# TEMPERATURE EFFECTS UNDER PROCESSING OF NUCLEAR POWER PLANT CONSTRUCTIONS BY ION-PLASMA DEACTIVATION TECHNOLOGY

A. Petrovskaya[1], A. Kladkov[2], S. Surov[2], A. Tsyganov[1]

[1]InnoPlasmaTech LLC, 199034, Line 17th V.O., building 4-6, office K-202, St.Petersburg, Russia
[2]Science and Innovation, JSC ROSATOM, 115035, Kadashevskaya embankment, 32/2 bld., Moscow, Russia
Email: anita3425@yandex.ru

Today one of the global nuclear energy problem is technically and economically effective deactivation of decommissioned nuclear power constructions. In particular, it relates to a large volume of irradiate graphite which is accumulated around the world at about 260 thousand tons, in Russia - at 50-60 thousand tons. No less important problem is the deactivation of nuclear power plants metal structures, for example, radioactive contamination deposits on the primary circuit surfaces of NPPs. Known deactivation technologies are multi-stage, unsafe and lead to a secondary radioactive waste volume increase: plasma burning with graphite grinding into fine fractions [1-3], chemical treatment (e.g., [4]), etc. It is meaningful to note that the peculiarities of irradiated graphite deactivation are associated with the presence and spatial localization in graphite blocks of a number of active isotopes, such as $^{14}C$, $^{60}Co$, $^{134}Cs$, $^{137}Cs$ and others. Among these isotopes the main dose-generating (95% of activity) is $^{14}C$ (half-life of 5730 years), which is produced in significant quantities during graphite reactors operation. The spatial localization of $^{14}C$ has been studied in a number of modern experimental works [5–8], demonstrating that inside of the irradiated graphite masonry the $^{14}C$ isotope is concentrated mainly at no more than 5 mm from the surface. The inhomogeneous distribution of $^{14}C$ isotope is due mainly to neutron capture by $^{14}N$ which are presenting in a cooling nitrogen-helium mixture circulating in the graphite masonry of RBMK. Nitrogen molecules from cooling gas mixture are absorbed inside of graphite pores, are intercalated in between graphene-like layers of graphite grains and are converted to $^{14}C$ by neutron capture. Our experimental study of the reactor graphite (GR-280) samples porosity showed their developed specific surface and high ability for adsorption (and intercalation). Using BET and BJH porosimetry methods the specific surface area $S_{sp}$ = 2 m²/g, the pore volume ~ 0.004 $cm^3/g$ and the pore radius ~19 Angstrom were obtained.

To solve the above problem, we are developing new "dry" ion-plasma deactivation technology based on the high pressure “shortened” discharge in inert gas. According to the ion-plasma technology an area on the graphite surface or

metal structures is preliminary selected for the treatment, the congruent electrode plate is positioned parallel to the selected area with the fixed gap (0.1-2 mm), inert gas (e.g., argon) is supplied via perimeter into the gap at the pressure (76 – 760) Torr and is pumped out via central hole, the plasma discharge is ignited between the surface under treatment (the cathode) and the sputtered atoms collector (the anode). Electric ion-plasma technology parameters are: discharge voltage (100-1000) V, discharge current (0.01-1) A/cm$^2$. It is known that in the "short" discharge the main part of the voltage drop is concentrated in the cathode plasma layer (with the length of less than ~ 0.1 of the gap) and the most of the input plasma power (fast argon ions and atoms bombardment) falls at the surface under the treatment. At the same time the sputtered and desorbed atoms from the cathode are diffusing through argon buffer gas to the anode surface in mass-transfer mode. In our previous works [9-12] more details of the technology are described.

In this way, it is important to evaluate the temperature of the surface under the treatment in dependence on the input discharge power value. With increasing of the treated surface temperature, the thermal desorption/evaporation effect is added to the ion sputtering from the surface. So, we have calculated temperature distributions in the samples of reactor graphite GR-280 and reactor steel under ion-plasma deactivation process. Fig. 1 shows the longitudinal section of 3D temperature distribution in typical graphite masonry block under ion-plasma deactivation in argon at the pressure 76 Torr.

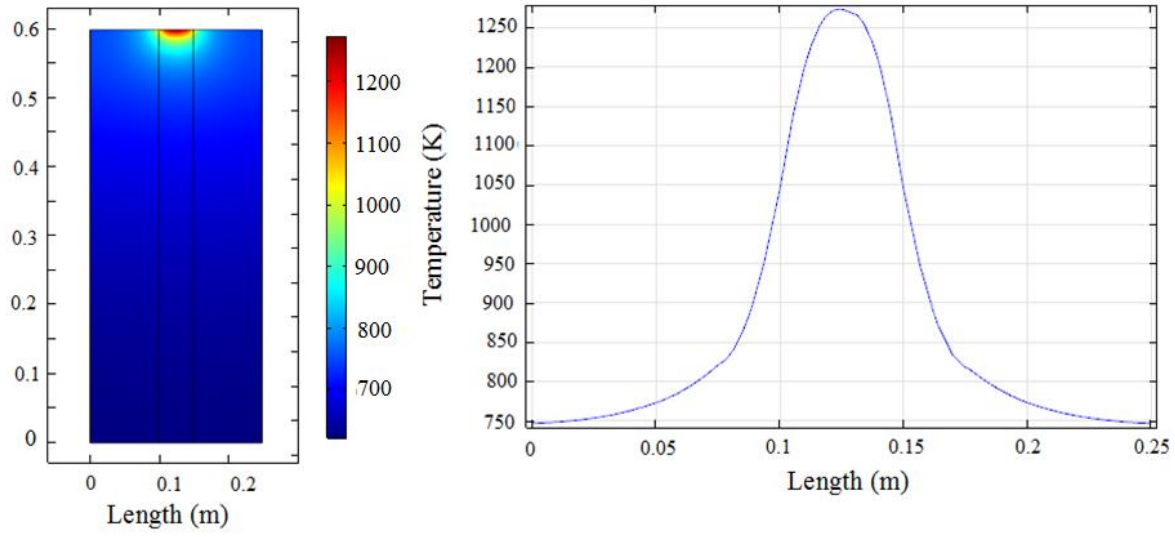



Fig. 1. The longitudinal section of 3D temperature distribution in graphite masonry block (left) and the temperature on the graphite surface under the treatment (right).

These results are obtained for the graphite masonry block (dimensions 25x25x60 cm, grade GR-280) of RBMK. The dimensions of the flat collector

electrode (tantalum) are 5x5 cm, the input discharge power value is $3 \cdot 10^6$ W/m$^2$ (current density 0.5 A/cm$^2$, voltage 600 V). At the input power level of $6 \cdot 10^6$ W/m$^2$ (current density is 1 A/cm$^2$, voltage is 600 V) the temperature of the surface under the treatment reaches 2250 K.

Fig. 2 shows the longitudinal section of 3D temperature distribution in reactor steel (08X18H12T) model sample under ion-plasma deactivation with the same collector electrode in argon at the pressure 76 Torr. As a model sample, we considered the ion-plasma treatment of the inner surface of the tube (0.25 m diameter, 0.063 m thin) fragment of 1 m length. For the model calculations this tube fragment was virtually slitted along and converted to the flat sample of 1.0x0.79x0.063 m size. During RBMK operation period, radioactive contamination in oxides form is deposited on the inner surface of such tube in steam-water communications pipelines and the main circulating pump of reactor.

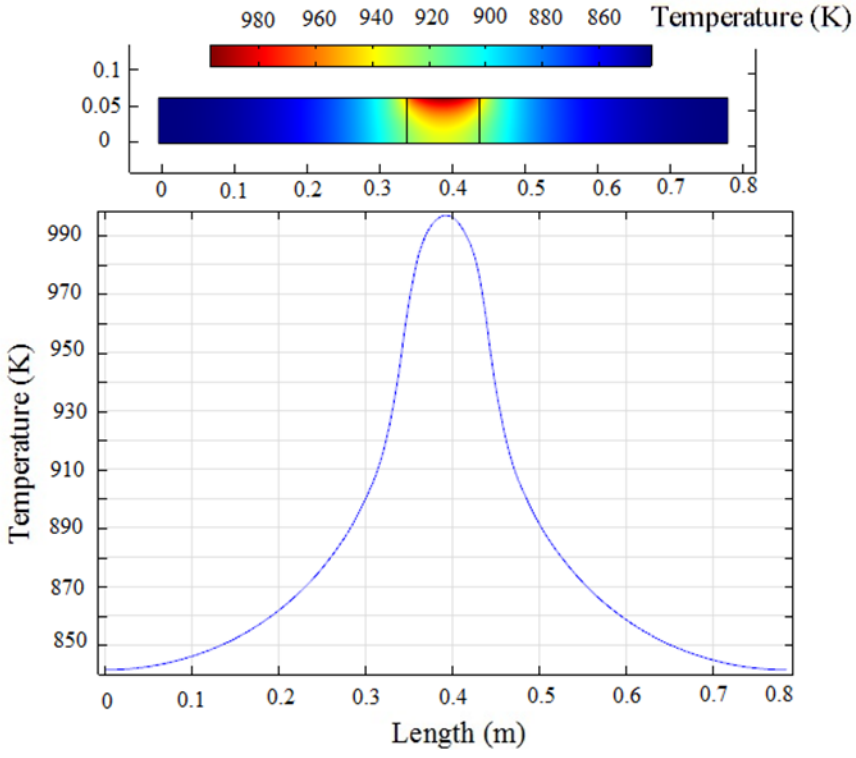



Fig. 2. The section of 3D temperature distribution in the fragment of the repeated forced circulation circuit (up) and the temperature on the treated surface (down).

These results were obtained for the ion-plasma treatment in argon under input power $-1 \cdot 10^5$ W/m$^2$ (current density - 0.0166 A/cm$^2$, discharge voltage - 600 V). Calculations of the temperature distributions in the graphite and the reactor steel elements under ion-plasma deactivation are necessary to estimate possible overheating of the treated surfaces and to select the ion-plasma

technology operating parameters. In addition, the thermal desorption/evaporation effect on graphite during its heating to the depth about 5 cm (see Fig. 1) lead to the de-intercalation of other radionuclides, as $^{60}Co$, $^{134}Cs$, $^{137}Cs$, etc., their removal and more profound deactivation of irradiated graphite block. The modified version of our technology can also be used to decontaminate metal constructions of the emergency reactors at the Fukushima nuclear power plant and to extract the corium (molten fuel assemblies). The temperature effects of ion-plasma technology are also important when the practical goal is to get nano/micro-sized layers of beta-active $^{14}C$ isotope concentrate during RBMK graphite deactivation.

## References


1. **Bespala E.V., Pavlyuk A.O., et al.** Patent RU № 2580818 (2016).
2. **Arustamov A.E., Vasendin D.R., et al.** Patent RU № 2320038 (2008).
3. **Theodosiou A., Jones A.N., et al.** Journal of Nuclear Materials, 507 (2018) 208-217.
4. **Klimov V.L., Karlina O.K., et al.** Patent RU № 2192057 (2002).
5. **LaBrier D., Dunzik-Gougar M.L.** Journal of Nuclear Materials, 448 (2014) 113-120.
6. **Dunzik-Gougar M.L., Smith T.E.** Journal of Nuclear Materials, 451 (2014) 328-335.
7. **Vulpius D., Baginski K., Kraus B., Thomauske B.,** Nuclear Engineering and Design, 265 (2013) 294-309.
8. **Luyken L.** Using intercalation to simulate irradiation damage of nuclear graphite: PhD thesis, University of Manchester (2012).
9. **Petrovskaya A.S., Tsyganov A.B., Stakhiv M.R.** European patent application EP 19888171.6, US patent application US 20210272715 (2021).
10. **Petrovskaya A.S., Tsyganov A.B., Stakhiv M.R.** Patent RU № 2711292 (2020).
11. **Petrovskaya A.S., Tsyganov A.B., Kladkov A.Yu., Surov S.V.** Journal of Surface Investigation: X-ray, Synchrotron and Neutron Techniques, 14 (2020) S175–S178.
12. **Petrovskaya A.S., Tsyganov A.B., Kladkov A.Yu., Surov S.V.** Problems of atomic science and technology, Series: Nuclear and Reactor Constants, 4 (2018) 185-197.

# SEM X-RAY MICROANALYSIS STUDIES OF THE NUCLEAR CONSTRUCTION MODEL SAMPLES PROCESSED BY ION-PLASMA DEACTIVATION TECHNOLOGY

A. Petrovskaya[1], A. Kladkov[2], S. Surov[2], A. Tsyganov[1]

[1]InnoPlasmaTech LLC, 199034, Line 17th V.O., building 4-6, office K-202, St.Petersburg, Russia
[2]Science and Innovation, JSC ROSATOM, 115035, Kadashevskaya embankment, 32/2 bld., Moscow, Russia
Email: anita3425@yandex.ru

Today, one of the very important problem for nuclear power engineering is the search of effective technology to deactivate irradiated reactor graphite arising after nuclear reactors decommissioning. In the world the irradiated graphite volume is estimated at 260 thousand tons, in Russia at 50-60 thousand tons. The world park of power and industrial uranium-graphite reactors (UGR) numbers more than 120 units (RBMK, EGP, AMB, MAGNOX, GCR, AGR, LWGR, etc.). For example, since 2004, the European Union has already allocated more than 1 Billion Euros to Lithuania for the Ignalina NPP decommissioning (2 units of RBMK-1500), but the dismantling of the reactors there has not even begun. Described in literature decontamination methods, such as plasma incineration of small-scale grinded irradiated graphite [1-3], chemical or thermal treatment of the irradiated graphite (for example, [4, 5]) lead to formation of the large volume of a secondary radioactive waste. In addition, these methods do not take into account the inhomogeneous distribution of the main dose-generating $^{14}C$ isotope (half-life 5700 years and 95% of all activity of irradiated graphite in most cases) in irradiated graphite.

In recent years the sufficient number of experimental studies have been aimed to explore $^{14}C$ isotope spatial localization in irradiated reactor graphite [6−9]. which have confirmed that $^{14}C$ isotope is concentrated mainly underneath the graphite blocks surface. These data were obtained [7] in complex experimental investigations of the graphite surface before and after neutron irradiation using SEM, XRD, XPS, ToF-SIMS, AES, EDX/EDS. It is also well known that one of the main channel of $^{14}C$ isotope formation is the neutron capture by $^{14}N$ atoms which are component of the cooling nitrogen-helium gas mixture ventilating the graphite masonry during the High Power Channel-type Reactor (RBMK) operation.

We are developing the ion-plasma technology for the irradiated reactor graphite and nuclear power plant metal structures deactivation, in particular, for the decontamination of the primary circuit internal surfaces. According to the ion-plasma technology, area on the graphite surface or metal structure is

preliminary selected for the treatment (deactivation), the congruent electrode plate is positioned parallel to the selected area with the fixed gap (0.1-2mm), inert gas (e.g., argon) is supplied from the perimeter inflow the gap at the pressure (76 – 760) Torr and is pumped out through the central hole, the plasma discharge is ignited between the treated surface (the cathode) and the collector of sputtered atoms (the anode). The ion-plasma technology parameters: voltage (100-1000) V, current discharge of (0.01-1) A/cm$^2$. During discharge the sputtered atoms from the cathode are diffusing to the anode surface in the mass-transfer mode. The technology is described in detail in our previous works [10-13].

To confirm the efficiency of the ion-plasma technology we have studied by SEM X-ray microanalysis the cathode surface (non-irradiated reactor graphite GR-280 as model sample) and the anode surface (Ni collector with thickness of about 1 mm) before and after treatment by the ion-plasma deactivation process. We have used the Merlin Zeiss scanning electron microscope with the Oxford X-Max 80 EDX detector. Figures 1 and 2 show the SEM image (at electron beam energy 20 keV) of nickel anode surface before and after sputtering (treatment) of reactor graphite GR-280 cathode sample. The fast electrons penetration and the integral generation of the X-ray signal depth is estimated 1 μm.

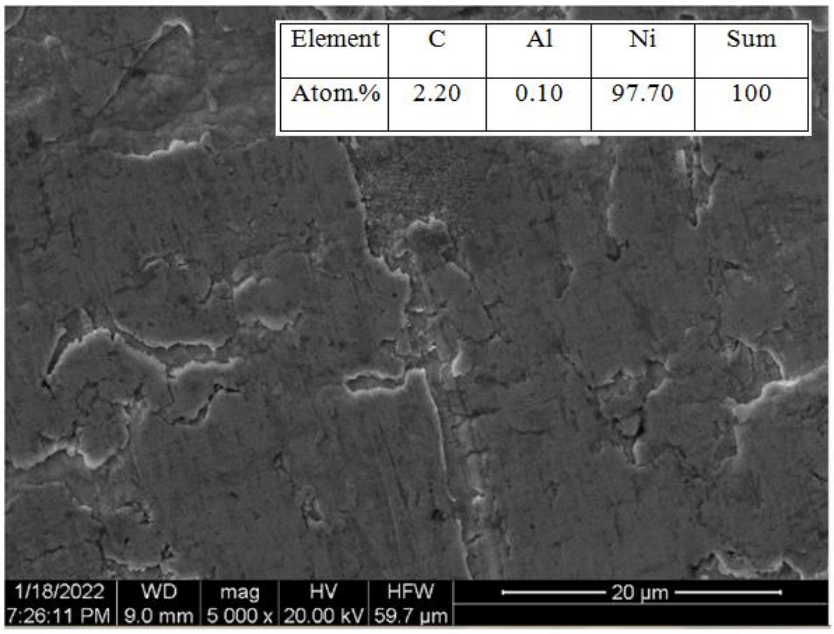



Fig. 1. The SEM image of nickel anode surface before graphite sputtering.

The carbon amount (~ 90 atom.%) covering and masking the nickel anode surface on Fig,2 confirms the sputtering of the graphite sample surface layer by the ion-plasma deactivation process and the sputtered carbon atoms deposition

in the diffusion mode on the anode surface (atop the nickel). Thus, the experimental evidence of the carbon coverage in a large percentage (90 at.%) of the nickel anode surface after graphite sputtering provides estimates of the ion-plasma deactivation technology efficiency in relation to the reactor graphite samples treatment. At the following ion-plasma decontamination technology parameters: discharge voltage - 600 V, current density - 1.5 A/cm$^2$, discharge exposure time - 10 sec, argon pressure - 0.8 atm., gap between the treated graphite surface and the anode - 0.5 mm, there have been found the thickness of the sputtered/deposited layer of carbon - 0.8 μm and the erosion depth rate constant $V_p = 8 \cdot 10^{-6}$ cm/s.

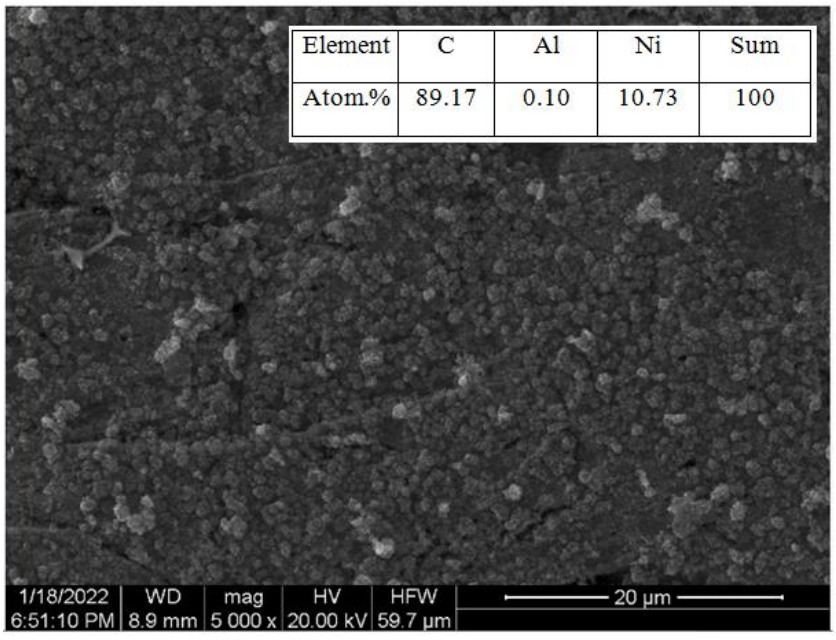



Fig. 2. The SEM image of nickel anode surface after graphite sputtering.

We also observed the SEM images of reactor graphite GR-280 surface (cathode) before and after plasma treatment. The surface of reactor graphite samples before plasma treatment seemed as the layered structure - oriented fragments of graphene-like layers at different angles to each other and to the surface plane. Some molten regions on the graphite surface after plasma treatment appeared due to the ion sputtering and thermal effects in the microplasma argon discharge. The ion-plasma deactivation technology seems to be very technically and economically effective for nuclear industry concerning decontamination of irradiated reactor graphite and any metal structures surfaces polluted by radionuclides. For example, it may be also used for the deactivation of the primary circuit inner surfaces during scheduled repairs of nuclear power plants. In general, any radionuclides contaminations may be removed from any conducting surface, as only said ion-plasma deactivation technology provides

argon ions with sufficient energy for sputtering, vaporization and mass-transfer of any surface pollution. Additionally, our technology will make it possible to obtain the useful product - enriched by $^{14}C$ isotope layers assembled on the anode (collector plate), for example, to create beta-voltaic batteries or radioactive beta-active sources for nuclear medicine (diagnostics and therapeutic purposes). The modified version of this technology can also be used to decontaminate the emergency reactors at the Fukushima NPP and to extract the corium (molten fuel assemblies).

## References


1. **Bespala E.V., Pavlyuk A.O., et al.** Patent RU № 2580818 (2016).
2. **Arustamov A.E., Vasendin D.R., et al.** Patent RU № 2320038 (2008).
3. **Theodosiou A., Jones A.N., Burton D., Powell M., Rogers M., Livesey V.B.** Journal of Nuclear Materials, 507 (2018) 208-217.
4. **Klimov V.L., Karlina O.K., et al.** Patent RU № 2192057, 2002.
5. **Romenkov A.A., Tuktarov M.A., Karlina O.A., Yurchenko A.Yu.** Patent RU № 2546981, 2015.
6. **LaBrier D., Dunzik-Gougar M.L.** Journal of Nuclear Materials, 448 (2014) 113-120.
7. **Dunzik-Gougar M.L., Smith T.E.** Journal of Nuclear Materials, 451 (2014) 328-335.
8. **Vulpius D., Baginski K., Kraus B., Thomauske B.,** Nuclear Engineering and Design, 265 (2013) 294-309.
9. **Luyken L.** Using intercalation to simulate irradiation damage of nuclear graphite: PhD thesis, University of Manchester (2012).
10. **Petrovskaya A.S., Tsyganov A.B., Stakhiv M.R.** European patent application EP 19888171.6, US patent application US 20210272715 (2021).
11. **Petrovskaya A.S., Tsyganov A.B., Stakhiv M.R.** Patent RU № 2711292 (2020).
12. **Petrovskaya A.S., Tsyganov A.B., Kladkov A.Yu., Surov S.V.** Journal of Surface Investigation: X-ray, Synchrotron and Neutron Techniques, 14 (2020) S175–S178.
13. **Petrovskaya A.S., Tsyganov A.B., Kladkov A.Yu., Surov S.V.** Problems of atomic science and technology, Series: Nuclear and Reactor Constants, 4 (2018) 185-197.

# STUDY OF PLASMA PARAMETERS IN COPPER/GRAPHENE NANOCOMPOSITE NUCLEATION ZONE IN EROSION PLASMA JETS

D.I. Kavyrshin[1,2], M.B. Shavelkina[1], V.F. Chinnov[1,2], A.S. Myazin[1,2]

[1]Joint Institute for High Temperatures of the Russian Academy of Sciences (JIHT RAS) 125412, Izhorskaya st. 13 Bd.2, Moscow, Russia. E-mail: dimakav@rambler.ru
[2]National Research University "MPEI" 111250, Krasnokazarmennaya st. 14, Moscow, Russia. E-mail: KavyrshinDI@mpei.ru

We studied the synthesis of composite Cu/graphene nanoparticles from the radiative characteristics of copper-containing plasma jets of helium/hydrocarbon mixture, flowing from the nozzle of the output copper electrode of a DC plasmatron. A mixture of propane and butane was used as a hydrocarbon. In order to find the conditions of nanoparticle formation during conversion of hydrocarbons in erosion jets, the concentration of copper was estimated by analyzing the optical emission spectra of Cu I lines observed in the spectrum. We have found that the maximum saturation of graphene by copper of 0.03 percentage by mass is reached at the copper concentration in plasma $[Cu]=N_{abs}\approx 3\cdot 10^{13}$ cm$^{-3}$, which is enough to form a chemical bond of copper with $sp^2$ carbon in a nanoparticle.

**Experiment setup and methods.** The most important characteristic of efficiency and reliability of electric arc plasma torch is the service life of electrodes In order to increase the lifetime of electrodes, they are made of smooth copper and in different forms: the cathode is the inner cylindrical electrode, and the anode is the outlet electrode in the form of nozzle. Plasma-forming gas is fed into the plasmatron through the gas twisting device, its rotation stabilizes the electric discharge arc column on the axis of the electrodes. Electrode erosion rate is usually reduced by rapid movement of the arc column section together with the gas flow, since greater flow rates of plasma-forming gas provide greater length of the electrode working zone facilitating less electrode erosion. Therefore, the flowing plasma jet from the plasma torch is more or less saturated with electrode erosion products.

We used a plasmatron with copper anode to synthesize graphene with carbon bonded to metal particles in its structure with the formation of 3D nanoparticles. The task was to create such conditions under which the copper impurity in the plasma jet would participate in the graphene nucleation rather than only be adsorbed on its surface. Additionally, the erosion of the electrode should not affect the stable operation of the plasma torch. We conducted experimental studies reducing the flow rate of plasma-forming gas down to a threshold at which the arc discharge binding region became the upper surface of the nozzle electrode channel, causing the maximum erosion. A series of

experiments showed that the threshold value for helium flow rate was 0.45 g/s. The experimental conditions are presented in Table 1.

Table 1: Technological conditions.

| Arc power (kW) | Current (A) | Gas pressure (Torr) | Helium flow rate (g/s) | Propane-butane flow rate (g/s) |
|---|---|---|---|---|
| 30 | 400 | 350-710 | 0.45 | 0.1 |

Optical emission spectra of the plasma were recorded using the optical fiber spectrometer AvaSpec2048 with the spectral resolution 0.2–0.5 nm and wavelength range 220–1000 nm under atmospheric pressure. A quartz condenser f=150 mm was used to form a sharp image of the plasma column at a scale of 1.0:1.0. The input end of the AvaSpec 2048 light guide was installed perpendicularly to the plane of this image and could be moved in this plane, selecting a circular image part with a diameter of 1 mm by means of collimator, enabling observation of the desired zone.

**Experiment results.** Fig. 1 shows the STEM image of nanoparticle morphology. It can be seen from Fig. 1a that particle morphology has the form of flakes with corrugated surface which is caused by the substrateless synthesis we used. This corrugated surface contains round black domains (Fig. 1b) related to metal particles. Metal scatters electrons when studied using electron microscopy and forms black spots on the image.

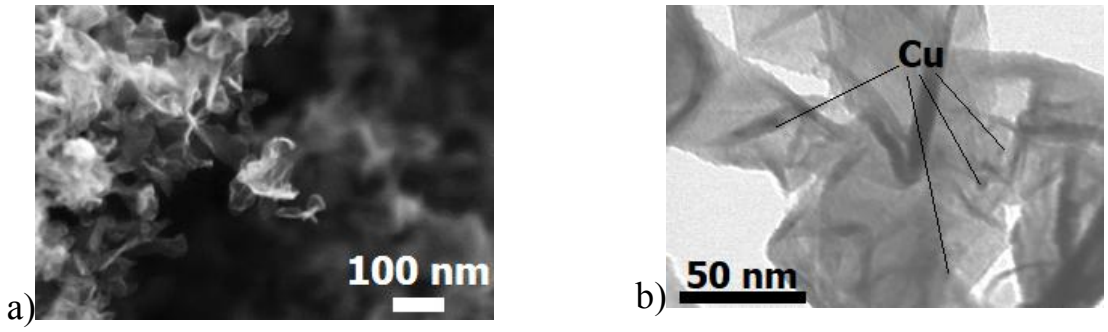



Fig. 1 — SEM (a) and TEM (b) image of a graphene/copper composite synthesized by mixture conversion $C_3H_8$-$C_4H_{10}$ /He at a pressure of 350 Torr.

Sample structure X-ray analysis showed that the graphene obtained in the experiments had up to 5 layers, because the samples are composed mostly of X-ray amorphous substance, which does not produce a clearly expressed halo in the spectrum. A number of weak spectral lines in the spectrum indicates the presence of small quantities of copper in the sample, which has a cubic face-centered structure with the lattice parameter a=0.3615 nm.

In order to study the conditions for the formation of composite nanoparticles, the emission spectra of the plasma jet were studied and its main

plasma parameters were determined. As seen from figure 2, the spectrum of helium hydrocarbon plasma, contains atomic lines of He and C, molecular $C_2$ bands, and atomic Cu I lines. The presence of Saha-Boltzmann equilibrium allowed to determine electron temperature from the relative intensities of C I 247.9 and C II 283.7 nm spectral lines [1], its value was found to be $T_e$=1.2 eV. Populations of helium atom excited states were not used to find $T_e$ because their nonequilibrium distrubution and absence of helium ion lines in the spectra [2,3]. Electron concentration $n_e \approx 1 \cdot 10^{16}$ cm$^{-3}$ was estimated from the widths of $H_\alpha$ and $H_\beta$ lines. The spectrum also contains molecular Swan band of the $C_2$ molecule, transition 0-0. In order to perform comparison with the model to determine the vibrational $T_V$ and rotational $T_R$ temperatures, the continuum was subtracted from the original spectrum and normalized to the maximum of $C_2$ band at 516.5 nm [4]. The best agreement between the experimental spectrum and the model was obtained for $T_V$=$T_R$=4500 K.

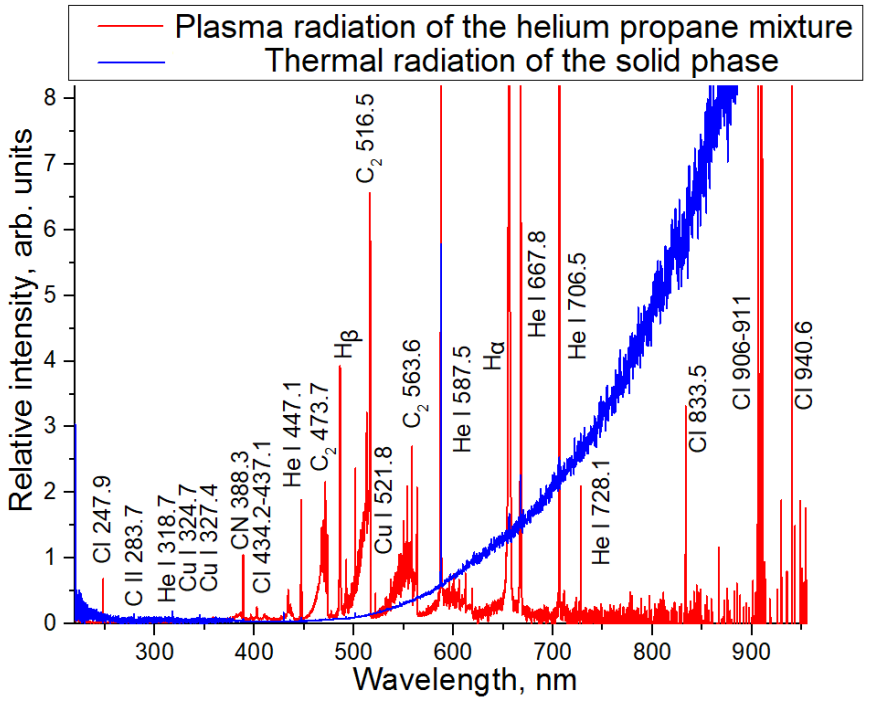



Fig. 1. Optical emission spectra when a hydrocarbon is added to helium and a dark coating is formed on the glass

The determination of the solid phase temperature formed in the reactor was carried out using its thermal radiation intensity $I_\lambda$ (see blue spectrum in Fig. 1) representing the radiation spectral density of the heated particles in the Wien coordinates. The resulting solid particle temperature was 1700 K.

To estimate the concentration of copper atoms in the plasma, we analyzed possible reabsorption of its resonant doublet spectral lines observed in the

spectrum. Spectral lines most sensitive to reabsorption are the ones with emitting levels containing an allowed radiation transition to the ground state of the atom, which is the state with maximum concentration.

Thus, we have established the following from the analysis of optical emission spectra of the plasma jet flowing from the anode nozzle:

Helium to copper concentration ratio ([He]/[Cu]~$10^4 \div 10^5$);

Hydrogen to copper concentration ratio ([H]/[Cu]~$10^3$);

Solid phase temperature (1700 K);

Copper atom concentration in plasma [Cu]=$N_{abs} \approx (0.5 \div 1.0) \cdot 10^{13}$ cm$^{-3}$.

**Conclusion.** We have successfully synthesized Cu/graphene composite nanoparticles in one step in the volume of DC plasma jets. A mixture of helium and propane-butane was used as the plasma-forming system. The obtained nanocomposite is a graphene layer with copper domains. It was found that copper forms chemical bonds with carbon, but does not affect the decomposition of pure graphene.

We used methods of optical emission spectroscopy to determine the concentration of copper in the helium plasma, which demonstrates the possibility to control the copper content in graphene.

We have obtained experimental data showing the possibility of utilizing plasma for the direct scalable synthesis of the nanocomposite, which can expand the fields of its potential applications.

**Acknowledgements**. The research was funded by RFBR and BRFBR project number 20-58-04013 in the part of plasma jet characterization, and by the Ministry of Science and Higher Education of the Russian Federation (state assignment No. 075-01056-22-00) in the part of samples characterization.

## References

1. **Belevtsev A.A., Chinnov V.F. & Isakaev E.K.** Plasma Sources Sci. Technol. 15 (2006) 450–457. http://dx.doi.org/10.1088/0963-0252/15/3/021
2. **Korshunov O.V., Chinnov V.F. & Kavyrshin, D.I.** Highly Ionized Arc He Plasma: Nonequilibrium, Nonideality, and Kinetics. *High Temp* 57 (2019) 147–155. https://doi.org/10.1134/S0018151X18060147
3. **Korshunov O.V., Chinnov V.F. & Kavyrshin D.I.** Highly Ionized Helium Arc Plasma. Determination of the Temperature in Nonequilibrium Conditions and the Effect of Plasma Microfields. *High Temp* 57 (2019) 308–315. https://doi.org/10.1134/S0018151X19020081
4. **Shavelkina M.B., Amirov R.K., Kavyrshin D.I.** *et al.* Spectroscopic Study of a Helium Plasma Jet with Hydrocarbon Additives. *High Temp* 58 (2020) 309–316. https://doi.org/10.1134/S0018151X20030165

# BEAM-PLASMA SYSTEMS FOR "GREEN" TECHNOLOGIES: MULTIFUNCTIONAL EXPERIMENTAL COMPLEX FOR R&D

M. Vasiliev[1], T. Vasilieva[2]

[1]Joint Institute for High Temperatures of the Russian Academy of Sciences (JIHT RAS), Izhorskaya st., 13 Bd.2, Moscow, 125412 Russia
[2]Moscow Institute of Physics and Technology (MIPT), Institutskiy per., 9, Dolgoprudny, Moscow reg., 141700 Russia vasileva.tm@mipt.ru

Plasma is undoubtedly considered to be an effective tool for solving various technological problems related to the green economy. Due to its high chemical activity at low temperatures the cold strongly non-equilibrium plasma definitely has advantages in comparison with widely used thermal plasma becoming a potential medium for the targeted treatment wide spectrum of substances, including bio-organic matters, in solid, liquid and gaseous states.

Plasmas can be used in renewable energy technologies for [1]:

- harmful gases decomposition such as nitrogen-, sulfur- and carbon-oxides, volatile organic compounds (VOC) and others;
- harmful solid and liquid particles removal;
- decomposition technology of harmful substances in liquid, such as gas–liquid interfacial plasma;
- flow control to enhance heat and mass transfer in chemical reactors, actuators and energy devices;
- plasma-assisted combustion, including aircraft propellants, and fuel reforming.

Plasma technologies is recognized as a game changer for green chemistry [2]. They allow optimizing the use of methane by converting it into raw materials for polymers and hydrogen, for example, without releasing $CO_2$. "Green" hydrogen can be produced in the process of splitting water and raw materials obtained from ammonia in biomass, biogas, bio-alcohols, and bio-oils processing [3]. Plasma treatment of ammonia is useful in hydrogen production since $NH_3$ is considered as one of the best $H_2$-carriers for developing hydrogen economy. However, this hydrogen usually turns out to be "grey" rather than "green" because of nitrogen oxides decomposition and conversion.

Non-thermal plasma applications for dry methane reforming and $CO_2$ reforming with $CH_4$ via plasma catalysis systems are known [4]. Non-equilibrium plasmas are also an effective tool to convert the greenhouse gases $CH_4$ and $CO_2$ to syngas ($H_2$/CO mixture) at low temperature. Synergy between catalyst and non-thermal plasma increases $CO_2$ utilization efficiency in plasma catalytic systems. The $CO_2$ utilization itself can reduce greenhouse gases exhaust. In this area, the focus is on converting $CO_2$ and reforming

hydrocarbons, with the goal of developing an efficient single-step ‘gas-to-liquid’ (GTL) process [5]. Reforming of methane into syngas in plasma chemical reactors is considered as an interim stage of synthetic liquid fuels production.

Plasma treatment is an effective way to utilize waste materials and move toward a circular economy [6]. With careful management of system processes, this is also a promising source of carbon neutral hydrogen for manufacturing and power industry. Dry plasma processes are considered as 'green' industrial processes in waste treatment with gasification of hazardous wastes and generation of valuable by-products. Direct synthesis of long-chain hydrocarbons by plasma-catalysis from syngas and $CH_4$-$CO_2$ mixtures is the example of this process [7].

Additive technologies (i.e. technologies in which CAD generated 3D models directly converted into three-dimensional object via layer-by-layer material input with further material particles joint into a whole) are compatible with plasma processing [8]. The architecture of these objects can be complex, and their chemical composition is usually multicomponent.

Plasma-based techniques show numerous advantages in fabricating nanomaterials from occupational health, safety and eco-aspects [9]. As to conventional materials, their production and modification by non-equilibrium plasmas have proved their potentials for environment friendly technologies [10].

Obviously, every particular technological problem requires preliminary scientific study and practically-oriented technique developments. The present paper aims to highlight experiments on novel and promising technologies based on a very special type of strongly non-equilibrium plasma, namely on Electron-Beam Plasma (EBP), generated by injecting an electron-beam (EB) into a dense medium [11] in the field of clean energy production, environment friendly industry and agriculture, resource saving and environmental remediation.

**Multifunctional experimental complex**

Multifunctional experimental complex for R&D in the field of eco-friendly EBP-technologies successfully operates in joint MIPT-JIHT RAS laboratory. Figure 1 presents basic configuration of the setup on which the majority of the above studies were carried out. It contains:

- EBP generator: electron gun (1) fed by high voltage power source and governed by specially designed controller, injection window (7) for the EB and deflecting system (8) combined with the injection window;
- Working chamber (10) equipped with reaction chamber (4), various feedthroughs to connect external and internal sensors, flanges to connect vacuum pipelines and gas/liquid feeders, vacuum optics;
- Vacuum system: pumps, gas feeders, valves and some other components;
- Accessory systems (coolers, filters, X-ray protection), and special units (gas nozzles, sprayers, samples holders and others);

- The EBP diagnostics facilities and experimental setup control system.

The EBP generator operates as follows. Electron gun (1) forms thin EB (3) in high-vacuum chamber (2) and directs the EB to the injection window inlet. Injection window (7) transports the EB into working chamber (10) and deflecting system (8) directs the EB along the reaction chamber axis (*z*).The controller of the electron gun sustains the EB generation with preset current value in both continuous and intermittent modes. Deflecting system can scan the EB over the reaction chamber volume, or change the EB position if required.

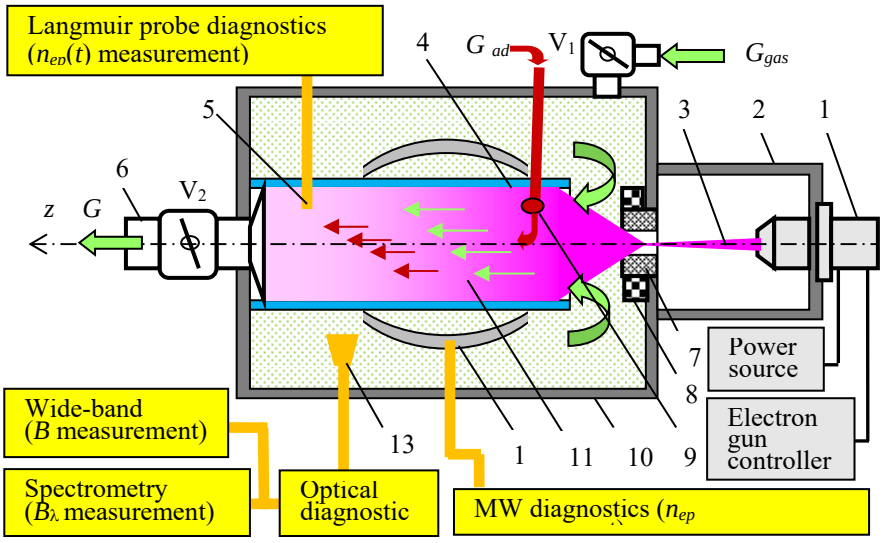



Fig.1. Scheme of the experimental setup in basic configuration:
1 – electron gun, 2 – high vacuum chamber, 3 – electron beam, 4 – reaction chamber, 5 – Langmuir probe, 6 – vacuum line, 7 –injection window, 8 – deflection system,9 – additives injector, 10 – working chamber, 11 – EBP, 12 – MW-resonator, 13 – optical fiber with collimating lens; $V_1$, $V_2$ – controlled vacuum valves

The working chamber is filled with plasma generating gas through the controllable valve $V_2$. The reaction chamber is connected to vacuum line (6) equipped with controllable valve $V_1$. As a result, the gas stream is formed in the reaction chamber; valves $V_2$ and $V_1$ controlling feeding ($G_{gas}$) and evacuated ($G_0$) gas flows maintain desirable stream velocity ($w$) and gas pressure ($P_m$). Various admixtures can be introduced ($G_{ad}$) into the main plasma generating gas stream by means of injector (9). It may be a nozzle for gaseous additives or a sprayer for liquid ones.

The following diagnostic facilities were used to get information about parameters of plasma volume and plasma-assisted processes:

- Barrel-shape MW-resonator (12) and Langmuir probe (5) were used for electron density ($n_{ep}$) measurements;
- Thermo-sensors of various types and optical pyrometers (they are not shown in Fig. 1) were installed inside and outside of the reaction chamber;

- CCD-cameras, wide-band photo-sensors and spectral devices were used for optical diagnostics of the processes in the reaction chamber and on the samples surface;
- Mass-spectrometer was connected to vacuum line (6) to monitor gas chemical composition at the reaction chamber outlet;

The main facility technical characteristics are:

- Electron energy – 25-40 keV;
- Beam power – 100-1000 W;
- Plasma generating media – gases and vapors, gas-vapor mixtures (air, $N_2$, $O_2$, $CO_2$, CO, $H_2O$, $CH_3OH$, $CH_4$, $NH_3$, $SF_6$…); aerosols (C, $C_2H_5OH$, kerosene…)
- Solid and liquid compounds introduced in the EBP – synthetic and natural polymers, biomass, lignin, cellulose, chitosan, crude oil, waste paper, gels…
- Reaction volume – still plasma clouds and flows in free space or in channels;
- Reaction volume pressure, $P_m$ – 0,01-100 Torr;
- Operation modes – continuous or intermittent.

## References


1. **Okubo M.** Energies, 12 (2019) 5-20.
2. **Grimbergen R.** https://www.voltachem.com/news/plasma-technology-recognized-as-a-game-changer-for-green-chemistry.
3. **Dimitrakellis P., Delikonstantis E., Stefanidis G.D., Vlachos D.G.** Green Chemistry, 24 **(**2022) 2680-2721.
4. **Abiev R.S., Sladkovskiy D.A., Semikin K.V., Murzin D.Yu. and Rebrov E.V.** Catalysts 10 (2020) 1358.
5. **Snoeckx R., Wang W., Zhang X., Cha M.S. and Bogaerts A.** Scientific Reports, 8 (2018) 15929.
6. **Diaz G., Leal-Quiros E., Smith R.A., Elliott J. and Unruh D.** Journal of Physics: Conference Series, 511 (2014) 012081.
7. **Li D.** Chemical and Process Engineering. Université Paris sciences et lettres. (2019).
8. **Sui Y., Zorman C.A. and Sankaran R.M.** Plasma Processes and Polymers, 17 (2020) 2000009.
9. **Han Z.J., Levchenko I., Kumar S., Yajadda M.M.A., Yick S., Seo D. H., Martin P.J., Peel S., Kuncic Z. and Ostrikov K.** Journal of Physics D: Applied Physics, 44 (2011) 174019.
10. **Vasilieva T., Vasiliev M. and Aung Miat Hein.** Journal of Physics D: Applied Physics, 52 (2019) 335202.
11. **Vasiliev M. and Vasilieva T.** Encyclopedia of Plasma Technology (Ed.: J. Leon Shohet). Boka Ralton, FL, USA: Taylor & Francis Inc. (2016).

# SPATIALLY RESOLVED LIBS AND XRF FOR ENVIRONMENTAL MONITORING IN AQUATIC ECOSYSTEMS

N. Sushkov[1], N. Kurian[2], S. Anuchin[2], S. Zaytsev[1], T. Labutin[1]

[1]Lomonosov Moscow State University, Leninskie Gory 1 building 3, 119234, Moscow, Russia
[2]Yanka Kupala State University of Grodno, Ozheshko 22, 230023, Grodno, Belarus

Elemental analysis of biosamples, aimed at both bioelements and pollutant elements, is important in ecological studies. There is abundant research dedicated to the determination of metals like Fe, Pb, Cd in fish [1, 2]. Large concentrations of metals have been noted in organs with active metabolism, such as liver, kidneys, and spleen [3]. Fish and plants are rich in biologically active substances, capable of binding macro- and microelements [4], plants usually containing more trace elements than animals [5, 6]. The elemental composition of fish and plants can be used to compose a biochemical profile of a water body and assess its ecological status [7]. Besides that, some organisms have shown unusual patterns of element accumulation (Li, As, U in marine zooplankton) [8].

The aim of the present research was to compare the performance of laser-induced breakdown and X-ray fluorescence spectroscopies (LIBS and XRF, respectively) in studying the elemental composition of tissues and organs of fish and plants of the Neman River (Belarus) in places with different extent of anthropogenic pollution. The elements of interest included Zn, Sr and Ca.

Aquatic plants (riverine horsetail, submerged hornwort) and fish (pike) were sampled according to guidelines [9]. Samples were taken in two replicates in two locations of the Neman River: in Grodno city and in Bogatyrevichi village 38 km upstream. Horsetail roots and stems were collected separately, and only the stem was taken from hornwort. Samples were cleaned, washed with water, dried at 40 °C to constant weight, ground and sieved. For fish, fins, scales, liver, muscles and bones were taken separately, dried at 100 °C, ground and sieved. The resulting powders were pelletised.

Preliminary LIBS experiments were carried out with a Nd:$YVO_4$ diode-pumped solid state (DPSS) laser (DTL-413, Laser-Compact, Russia, $\lambda$ = 527 nm, $\tau$ = 30 ns, 0.3 mJ, 200 Hz). With the help of a fast ICCD camera (Nanogate-2V, Nanoscan, Russia), spectra were obtained both with short and long acquisition gates (delay/gate 150/20 and 100/300 ns, respectively), so that both calibration-free (CF-LIBS) and calibration-based analyses were possible. Each spectrum was the average of signals from around 10000 laser pulses. Biological CRMs EK-1, LB-1, Tr-1, BOk-2 (Russia), IAEA-336, and IAEA-407 (Austria) were used for calibration.

High-quality calibration curves were obtained for Ca II and Sr II

($R$ > 0.999). The quantification limits were 0.05 % and 1.4 mg/kg, respectively. For CF-LIBS, plasma temperature was calculated using the line pair method (Mg I 517.268 nm and Mg I 383.830 nm), the electron density was estimated from the Stark broadening of the Mg I 383.83 nm line. The analytical results are shown in Table 1, including XRF data for comparison (the latter were obtained with CEP-01 Elvax ED-XRF spectrometer with tungsten anode (Elvatech, Ukraine), in the range of 0–35 keV). LIBS typically yields higher concentrations than XRF, probably because of matrix effects in both methods, especially in XRF, which suffers from the low efficiency of absorption of X-rays by the light organic matrices.

Table 1. Results of the analysis of biological samples by LIBS (DPSS laser) and XRF.

| Analytical lines | Hornwort | Horsetail | Pike |
|---|---|---|---|
| Ca II 396.847, % | 11.6±1.0 | 0.39±0.03 | 3.8±0.3 |
| Ca $K_\alpha$, % | 2.27±0.05 | 1.29±0.03 | 0.48±0.02 |
| Sr II 407.771, mg/kg | 387±49 | 19.4±0.8 | - |
| Sr $K_\alpha$, mg/kg | 28.3±1.2 | 4.1±0.3 | - |
| Sr II/Ca II (CF-LIBS) | $(1.9\pm0.3)\times10^{-4}$ | - | - |
| Sr $K_\alpha$ /Ca $K_\alpha$ | $(1.25\pm0.8)\times10^{-5}$ | $(3.2\pm0.3)\times10^{-4}$ | - |

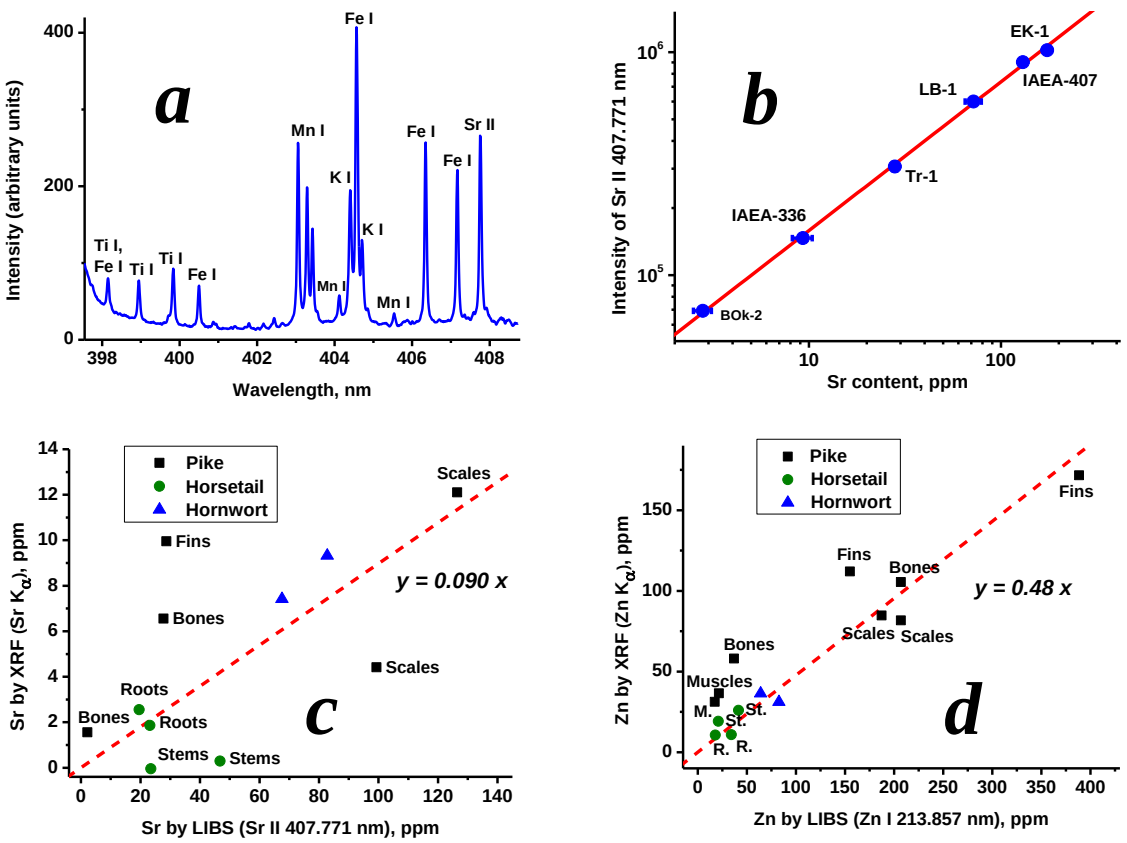



Fig. 1, *a*: emission spectrum of a natural sample (horsetail roots, delay/gate 0.8/1.7 μs); *b*: calibration curve for Sr II 407.771 nm (log-log scale); *c*: comparison of XRF and LIBS results for Sr; *d*: same for Zn.

The problems with the DPSS laser were the low efficiency of ablation of organic matter, low plasma temperature (5000 – 6500 K) and electron density ($N_e \leq 4.3\times10^{16}$ cm$^{-3}$), which limited the analytical capabilities. Thus, we continued the experiments with a more powerful laser (lamp-pumped Nd:YAG LOTIS TII LS-134UTF, Belarus, $\lambda = 266$ nm, $\tau = 8$ ns, 21 mJ, 5 Hz). Fig. 1 shows the results of these LIBS experiments in comparison with XRF data. There are again considerable discrepancies between the results of the two methods, XRF always yielding lower concentrations than LIBS. In principle, the discrepancies could be minimised using signal normalisation. However, the best way to check the accuracy will be the use of a reference method involving sample dissolution, like ICP-AES or ICP-MS, which will be done at the next stage of the work.

XRF results for different parts of aquatic organisms taken from the two locations in the Neman River are presented in Fig. 2. In most cases, urban samples present higher metal content than rural ones. The lowest level of metals is found in fish muscles, the highest — in fish scales and fins, as well as in horsetail roots.

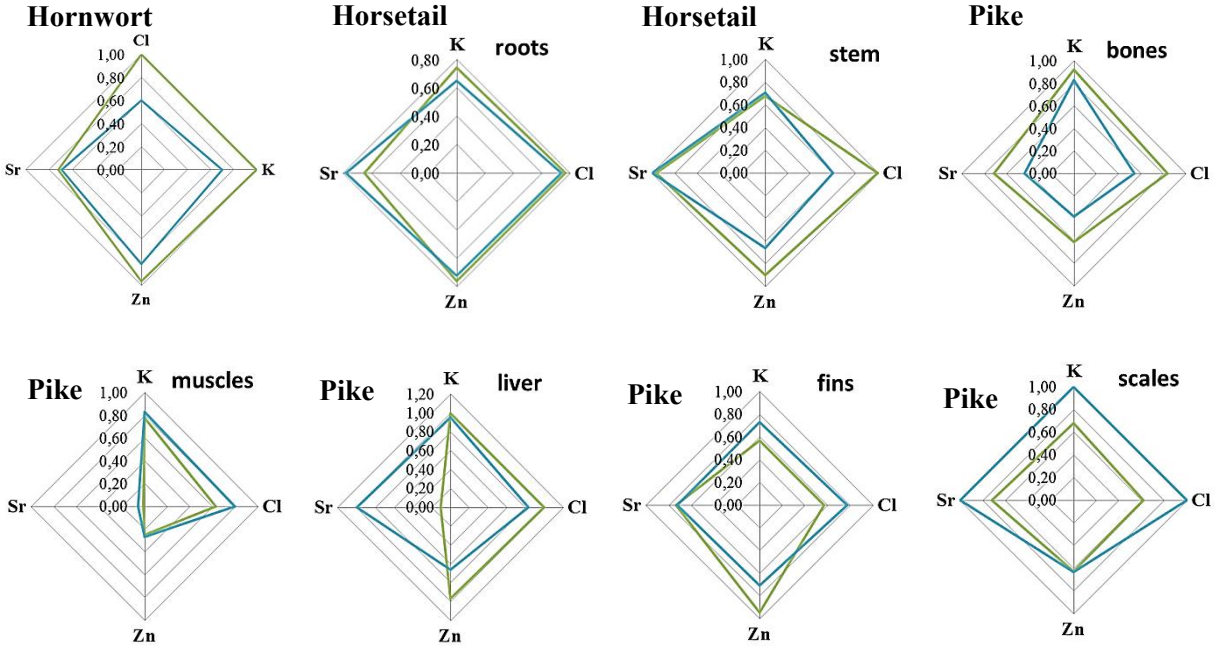



Fig. 2. Concentrations of Cl, K, Zn, Sr in biosamples as determined by XRF (divided by their respective maximum values). Green lines: Grodno city, blue lines: Bogatyrevichi village.

We also studied vertical emission profiles of laser-induced plasma. As the plasma is inhomogeneous, there may be areas with different self-absorption of analytical lines or variable extent of spectral interferences. This potentially may be used to improve analytical figures of merit (e.g., by eliminating curvature in

calibration graphs). Fig. 3 shows some examples for time-integrated signal acquisition mode (delay/gate 0.8/1.7 μs). It is clear that the profiles are substantially different (i.e., the time evolution characteristics are different), so that the construction of calibration curves based on the signals from a selected plasma section would be impossible. Thus, the vertical profiles should rather be used for calibration-free calculations where the intercomparison of different samples is not relevant.

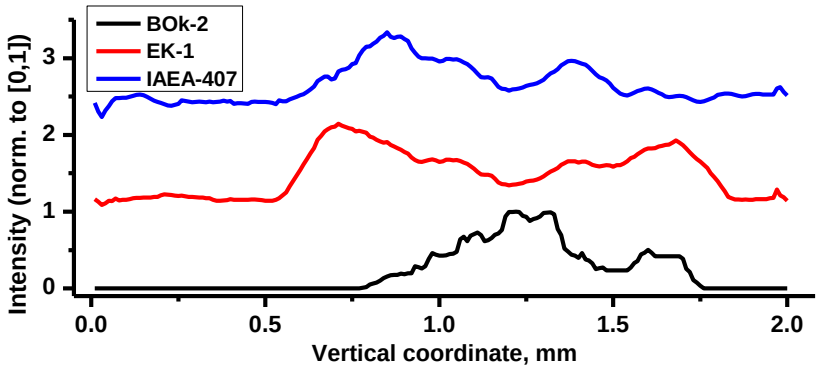



Fig. 3. Normalised vertical emission profiles of laser-induced plasmas of organic CRMs (time-integrated mode, delay/gate 0.8/1.7 μs).

**Acknowledgements.** The reported study was funded by RFBR (project number 20-53-04036) and BRFFR (project number Б21РМ-085).

## References

1. **Malkov A.V.** et al. Industrial Laboratory. Diagnostics of Materials, 12 (2017) 12–20 (in Russian).

2. **Celik U. et al.** Food chemistry, 87 (2004) 343–347.

3. **Rudic V., et. al.** In: Analele Ştiinţifice ale Universităţii de Stat din Moldova, Chişinău, 12 (2002) 168-172 (in Moldavian).

4. **Vlasyuk, P.A.**, in [Microelements in Environment], Kiev: Naukova Dumka (1980, in Russian).

5. **Zhiltsova, Yu.V.** et al. [Health and environment], 11 (2008) 87-90 (in Russian).

6. **Sushkov N.I., Kurian N.N., Labutin T.A.** Proceedings of the 11th Euro-Mediterranean Symposium on Laser-Induced Breakdown Spectroscopy (2021) 158.

7. **Savenok E.I. et al.** Sakharov Readings 2008: Environmental Problems of the 21st Century, (2008) 285-286.

8. **Lobus N.V.** Oceanology, 6 (2016) 890–900.

9. [Unified rules for the sampling of agricultural products, food products and environmental objects for the determination of trace amounts of pesticides, Aug. 21, 1979], №. 2051-79. Moscow: Kolos (1983, in Russian).

# CO-PRECIPITATION FROM SOLUTIONS OF IRON, NICKEL, COBALT NITRATES UNDER THE ACTION OF A GLOW DISCHARGE

K.V. Smirnova, P.A. Ivanova, D.A. Shutov, A.N. Ivanov, V.V. Rybkin

Ivanovo State University of Chemistry and Technology, Ivanovo, Russia
smirnovakv1@gmail.com

Over the past few decades, a new branch has emerged in the development of plasma research on the synthesis of nanomaterials, through the interaction of plasma with liquids [1]. Studies of the formation of nanoparticles in solution using various types of gas discharges are actively conducted all over the world. However, the amount of information on the formation of insoluble oxygen-containing compounds, in particular cobalt and nickel ferrites, when exposed to discharges on their aqueous solutions is extremely limited.

Furthermore, cobalt and nickel ferrites are among the most technically important transition metal oxides. Cobalt and nickel ferrites attract the attention of many researchers due to their properties, including chemical resistance, high mechanical strength, electrical, magnetic and catalytic properties. This allows them to be used as materials for various purposes. Materials based on cobalt and nickel ferrites are used as sensors [2, 3], drug delivery [4], catalysts [5], and recording devices [6]. The quality of the materials and the scope of their application are primarily related to the magnetic characteristics of the obtained powders, which, in turn, depend on the chosen method and synthesis conditions [7]. For this reason, in recent years there has been a lot of research on the synthesis of iron oxides using various methods of chemical precipitation, mechanical grinding and physico-chemical methods (hydrothermal, electrochemical, aerosol, chemical and metallurgical, etc.).

The determination of parameters that represent some influence on the synthesis process, as well as the optimal conditions for such parameters, are of decisive importance for obtaining powders with high magnetic properties [2, 8]. One of the promising, but little known technological processes is the use of a glow discharge, hydrothermal and microwave treatments [9].

The use of a glow discharge for the synthesis of ferrites has not been sufficiently studied [10, 11]. Depending on the parameters of the glow discharge, it is possible to change the rate of processes occurring between several inhomogeneous media and thereby changing the phase and morphological composition of the products obtained. In this paper, we present the plasma-solution synthesis of ultrafine particles of cobalt and nickel ferrites from solutions of their nitrates.

Plasma-solution cell, the scheme of the installation and the experimental technique was described in detail in the articles [12, 13]. We used aqueous

solutions of iron (III), cobalt (II), and nickel (II) nitrates as the liquid phase. The solution was prepared by mixing 5 mmol/l of $Fe(NO_3)_3$ and 50 mmol/l of $Co(NO_3)_2$. For other studies we used 1 mmol/l of $Fe(NO_3)_3$ and 50 mmol/l of $Ni(NO_3)_2$. The discharge current was 50 mA. After several seconds of plasma-solution interaction, the formation of an orange colloidal suspension was observed in the anode part of the cell. In the case of solutions where cobalt nitrate was added, after a few minutes, the colloid suspension changed its color from orange to dark brown. With solutions where nickel nitrate was added, no such color change was observed.

For qualitative and quantitative analysis of the phase composition of the powders, X-ray diffraction analysis was used (XRD, X-ray diffractometer DRON 3M, Burevestnik, Russia, CuKα radiation). The diffraction patterns were processed using QualX2 software [14] and the open crystallographic COD database [15].

The resulting sediments were analyzed by thermogravimetric (TGA) and differential scanning calorimetry (DSC). For this, an STA 449 F1 Jupiter thermal analysis instrument (Netzsch, Germany) was used. The temperature range was 20–900 ° C, the heating rate was 5 °C/min in an argon flow using a platinum crucible.

The average hydrodynamic diameter of the colloidal particles and their ʒ potential was determined by dynamic light scattering (DLS) using a Photocor Compact-Z size analyzer (Photocor, Russia).

Appearance of sediment particles and their elemental composition were deternined using scanning electron microscopy (SEM, Tesla Vega 3SBH, Czech Republic) with an EDX analysis system (Aztec EDS, Oxford Instruments Ltd., England).

After 10 minutes of plasma interaction with the solution in the anode cell, a stable colloidal suspension is formed (1-1.5 cm deep from the surface) and a huge amount of agglomerates uniformly distributed throughout the cell volume. The colloidal suspension uniformly distributed over the entire volume of the liquid anode was collected and centrifuged for 15 minutes at 15,000 rpm. The resulting precipitate was washed with distilled water (1 cycle in a centrifuge). After that, the powder was dried at a temperature of 50°C in air overnight. The study of the resulting product took place in several stages. In solution, immediately after plasma treatment (DLS), after drying and finally after high-temperature treatment of the obtained particles (XRD, TGA, DSC, SEM, EDX). The high-temperature treatment of the obtained powders was carried out at a temperature of 1000°C in an air atmosphere. The last step was necessary to obtain ferrites.

The results of X-ray diffraction analysis showed that the resulting powders are X-ray amorphous. At the same time, energy dispersive analysis showed that

they have a complex composition which can be represented as $Fe(OH)_3 \cdot Fe(OH)_2NO_3 \cdot MeOHNO_3$ (where is Me=Co, Ni). The data of TGA and DSC analysis confirm the data of EDX analysis. EDX and XRD analysis of powders after high-temperature treatment gives us cobalt and nickel ferrites with the general structural formula of spinel-type $Me^{2+}Fe_2^{3+}O_4$ (where is Me=Co, Ni). The micrographs of the obtained powders clearly show a well-developed surface with a grain size of approximately 300 nm (Fig. 1). This was confirmed by data obtained using Dynamic Light Scattering. The average size of the main fraction was 354 nm and the other one 6μm and the value of the zetta potential was 10.36 mV.

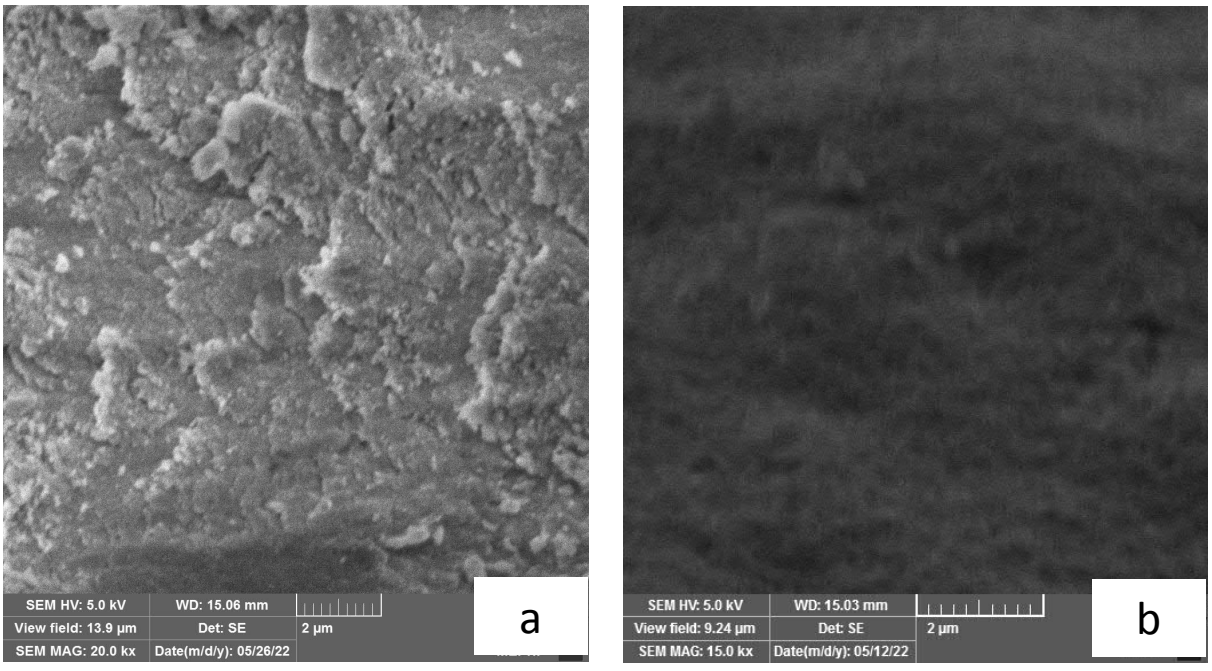



Fig. 1. SEM images of as-synthesized powder (a) - powders obtained from solutions of iron and nickel nitrates; (b) - powders obtained from solutions of iron and cobalt nitrates.

As a result of the work, shows the possibility of synthesizing cobalt and nickel ferrites from nitrate solutions under the action of a glow discharge at atmospheric pressure in air. The analysis of the obtained powders showed that we got chemically complex substances, which, after high-temperature treatment, became ferrites with the structural formula of spinel-type $Me^{2+}Fe_2^{3+}O_4$ (where is Me=Co, Ni). In the future, it is planned to study the magnetic properties of these substances and describe the mechanisms of formation in solution under the action of a glow discharge.

**Acknowledgements**. This work was supported by the grant of the Russian Federation President (MK-2607.2022.1.2).
The study was carried out using the resources of the Center for Shared Use of Scientific Equipment of the ISUCT (with the support of the Ministry of Science and Higher Education of Russia, No. 075-15-2021-671).

## References

1. **Valenzuela R.** Physics Research International, (2012) 1–10.
2. **Osman N.S., Thapliyal N., Alwan W.S., Karpoormath R., Moyo T.** Journal of Materials Science: Materials in Electronics, 26 (2015) 5097–5105.
3. **Akbarzadeh A., Samiei M., Davaran S.** Nanoscale Research Letters, 7 (2012) 144–151.
4. **Purkayastha M.D., Manhar A.K.** Nanoscience in Food and Agriculture, 2 (2016) 59–69.
5. **Zhou X., Chen Z., Yan D. and Lu H.** Journal of Materials Chemistry, 22 (2012) 13506.
6. **Hema E., Manikandan A., Karthika P., Antony S.A., Venkatrama B.R.** Journal of Superconductivity and Novel Magnetism, 28 (2015) 2539–2552.
7. **Motamedi E., Talebi Atouei M., Kassaee M.Z.** Materials Research Bulletin, 54 (2014) 34–40.
8. **Kang J., Lee H., Kim Y.N. et al.** Nanoscale Research Letters, 8 (2013) 376–383.
9. **Frolova L.A., Pivovarov A.A., Baskevich A.S., Kushnerev A.I.** Russian Journal of Applied Chemistry 87 (2014,1054–1059.
10. **Shabani M., Saebnoori E., Hassanzadeh-tabrizi S.A., and Bakhsheshi-Rad H.R.** Journal of Materials Science: Materials in Electronics, 32 (2021) 10424–10442.
11. **Frolova L.A., Derimova A.V.** Molecular Crystals and Liquid Crystals, 673 (2019) 109-119.
12. **Shutov D., Ivanov A., Rakovskaya A., Smirnova K., Manukyan A., Rybkin V.** Journal of Physics D: Applied Physics, 53 (2020) 445202.
13. **Smirnova K., Shutov D., Ivanov A., Rybkin V.** Journal of Physics: Conference Series, 2064 (2021) 012096.
14. **Altomare A., Corriero N., Cuocci C., Falcicchio A., Moliterni A., Rizzi R.** Journal of Applied Crystallography, 48 (2015) 598–603.
15. **Grazulis S., Daskevic A., Merkys A., Chateigner D., Lutterotti L., Quiros M., Serebryanaya N.R., Moeck P., Downs R.T., LeBail A.** Nucleic Acids Research, 40 (2012) D420–D427.

# MICROPLASMA PROCESSES DURING HIGH-VOLTAGE ELECTRIC PULSE CONSOLIDATION OF REFRACTORY METAL CARBIDES POWDERS

E. Grigoryev[1], O. Kuznechik[2], A. Chumakov[3], I. Nikonchuk[3], E. Strizhakov[4], S. Nescoromniy[4], S. Ageev[4]

[1]ISMAN, Academician Osipyan str., 8, Chernogolovka, Moscow Region, 142432, Russia, eugengrig@mail.ru
[2] SSI PMI, Platonova str., 41, Minsk, 220005, Belarus, pmi.nil26@gmail.com
[3] B.I.Stepanov Institute of Physics, Nezavisimosti Ave., 68-2, Minsk, 220072, Belarus, a.chumakov@dragon.bas-net.by
[4] DSTU, Gagarin square 1, Rostov-on-Don, 344000, Russia, strizhakov@inbox.ru

## Introduction

The method of high-voltage consolidation of powders is effective for the production of refractory composite materials that retain their strength properties at ultrahigh temperatures under aggressive external influences. The short duration of high-temperature exposure in the process of high-voltage consolidation makes it possible to preserve the structural-phase state of the initial powder material in the consolidated compact material. A feature of this method is the high density concentration of the released energy in the area of contacts between powder particles. Along with the characteristics of the powder, the determining factors are: the rate of input of the energy of the electromagnetic field into the powder material, the magnitude and nature of the mechanical pressure acting on the powder blank during high-voltage consolidation. The high energy density in the particle contact zones leads to a local change in the state of aggregation of the powder substance in these zones. The advantages of the high-voltage consolidation method can be fully realized with optimal process parameters, since intense electro-thermal action on the powder material can lead to instability of the consolidation process, the formation of an inhomogeneous structure of the material to be consolidated, and even to the destruction of the consolidated sample and technological equipment. The study of electro-thermal phenomena, both in the particle contact zones and on the scale of the entire consolidated sample, makes it possible to establish the optimal parameters of high-voltage consolidation.

## Theoretical analysis

As a result of theoretical analysis of electro-thermal processes in contacts between powder particles during high-voltage consolidation [1], the threshold

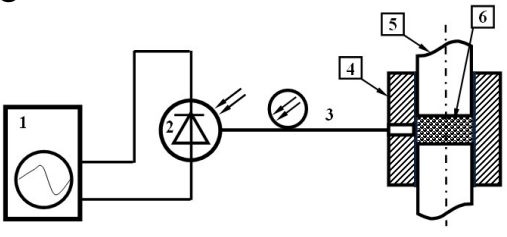
value of the current density $j_*$ in the interparticle contact was established, the excess of which causes an electrothermal explosion:

$$j_* = \sqrt{\frac{2\xi\sigma}{\rho h}} T_b^2 , \quad (1)$$

where: $\sigma$ is the Stefan-Boltzmann constant; $\xi \leq 1$; $T_b$ is the boiling point (loss of conductivity) of the powder material, $\rho$ is the resistivity of the material, $h$ is the thickness of the interparticle contact. The validity of criterion (1) was confirmed experimentally on grains of the nickel heat-resistant alloy (Ni-16Co-9Cr-5,5W-5Al-4Mo-2,5Nb-1,8Ti), and the results were published in [2].

## Experimental method

High-voltage consolidation uses the constant pressure and high voltage pulse electric current to provide the resistive heating of powder sample by Joule effect. High voltage pulse electric current are generated by experimental equipment described in [3]. Registration of the parameters of a high-voltage current pulse and the intensity of thermal radiation of the consolidated powder materials was carried out using a measuring complex developed by the authors. This complex consists of a Rogowski coil with an integrating circuit, which registers the parameters of a high-voltage current pulse, photodiode sensors that register the intensity of thermal radiation, which is transmitted through a special optical waveguide from the consolidated powder materials, systems for triggering and synchronizing the components of the measuring complex. The radiation during high-voltage electric pulse consolidation of powder materials was recorded by a calibrated photodetector with a maximum sensitivity in the spectral range of 800–900 nm based on a silicon photodiode (FD-21 KP) with a fiber optic light guide diameter 1.5 mm. To calibrate the photodetector, a light-measuring tungsten tape lamp (SI 10-300U No. 70) calibrated for the spectral density of the energy brightness of radiation in the region from 300 nm to 2500 nm was used. A schematic diagram of the measurement of powder thermal radiation is shown in Fig. 1.




1 - oscilloscope; 2 – photodiode; 3 - optical fiber (light guide);
4 – dielectric die; 5 - electrodes-punches; 6 - powder
Fig. 1. Scheme for measuring the thermal radiation of a powder during electropulse consolidation.

The compressive force of the punch electrodes provides a pressure on the powder of 20–25 MPa.

## Results and Discussion

Testing of the measuring complex for recording electro-thermal parameters of high-voltage consolidation was carried out in experiments with copper powder. Fig. 2 and 3 show synchronous oscillograms of current pulses recorded using a Rogowski coil (in Fig. 2 the maximum value corresponds to current amplitude of 41 kA, and in Fig. 3 - 94 kA) and oscillograms of signals from a photodetector that registers the radiation of a powder material during consolidation process.

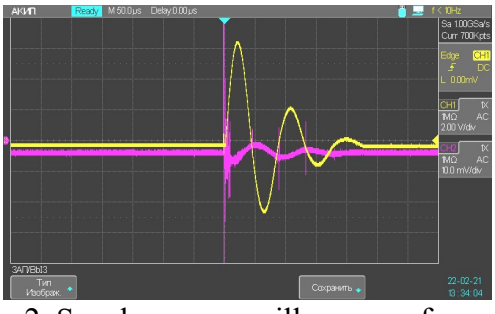


Fig. 2. Synchronous oscillograms of current pulses (CH1) and the radiation of a powder material (CH2) during consolidation process (capacitive energy storage voltage $U_{max}$ = 1,5 kV)



Fig. 3. Synchronous oscillograms of current pulses (CH1) and the radiation of a powder material (CH2) during consolidation process (capacitive energy storage voltage $U_{max}$ = 3 kV)

The radiation brightness of the studied sample Bexp was determined by comparison with the brightness of the reference sample Bet, taking into account the corresponding solid angles Ωet and Ωexp, the cross sections of the optical fiber (receiver) during calibration and in the experiment, as well as the amplitudes of the photodetector signals during calibration Uet and during experiments Uexp according to the following formula (2):

$$Bexp = Bet \times (\Omega et/\Omega exp) \times (Set/Sexp) \times (Uexp/Uet) \quad (2)$$

The experimental value of the radiation brightness of the studied sample Bexp obtained in this way was compared with the brightness of the black body radiation at the effective wavelength of the calibrated photodetector (900 nm) using the Wien formula, which is true for the conditions of our experiments. Thus, from the ratio for the brightness of black body radiation (Wien's formula):

$$B_{exp} = (2\pi hc^2/\lambda^5) \times \exp(hc/\lambda kT) \quad (3)$$

where h is Planck's constant, c is the speed of light, λ is the radiation wavelength, k is Boltzmann's constant, and T is the desired brightness temperature of the source under study.

Based on the above approach, when processing the data of test experiments on electropulse consolidation of copper powder when charging the energy storage device to 3 kV, we obtain the amplitude value of the brightness temperature of the sintered sample of 1465 K, which slightly exceeds the value of the copper melting temperature of 1356 K under stationary conditions. When the voltage on the energy storage device decreases to 1.5 kV, the amplitude value of the brightness temperature of the consolidated copper sample, determined by this method, drops to 1366 K, which is only 10 degrees higher than the melting point of copper under stationary conditions.

Testing of the measuring complex capable of recording the electrothermal parameters of the impact on materials by a high-voltage current pulse was also carried out in experiments on high-voltage welding of dissimilar materials and in electric discharges in water.

## Conclusion

It is worth mentioning that the fabrication of high-density refractory samples by the HVC method requires accurate identification of the optimal values of the pulsed current amplitude applied to the specimen since the optimal values of this parameter are close to the critical ones, which define the boundary between stable and unstable modes of HVC.

**Acknowledgements**. This work was supported by the Russian Science Foundation № 22-29-01119

## References

1. **Grigoryev E., Abedi M., Goltsev V., Osintsev A., Plotnikov A., Moskovskikh D.** Specific Features of High-Voltage Consolidation of Powders: Theoretical and Experimental Study. Metall Mater Trans B (2022). https://doi.org/10.1007/s11663-022-02465-x
2. **Grigoryev E.G., Olevsky E.A.** Thermal processes during high-voltage electric discharge consolidation of powder materials. Scripta Materialia, v. 66, Iss. 9 (2012) p. 662-665.
3. **Strizhakov E.L., Neskoromny S.V., Minko D.V.** Discharge-pulse processing of materials. Rostov-on-Don: DSTU, 2016, 152 p. (in Russian).

# BEHAVIOR OF $SF_6$ IN THE PLASMA MEDIUM OF AN ELECTRON BEAM

S. Sosnovskiy

Tomsk State University, Tomsk, Altaiskaya st., 126, apt. 261, ssa777@mail.ru

## Introduction

Sulfur hexafluoride ($SF_6$) is commonly used as an etching/etching-aid gas in fabricating the submicrometer features of modern integrated circuits because it has a higher fluorine content than $CF_4$ but does not undergo polymerization. However, the destruction of $SF_6$ has attracted much interest because of the important environmental issues and the toxicity of sulfur compounds. In this work, plasmas in medium of an electron beam were used to decompose $SF_6$ [1,2].

## 1. Experimental setup

Fig. 1a-c shows of the experimental bench which was used for the performance of experiments [3].

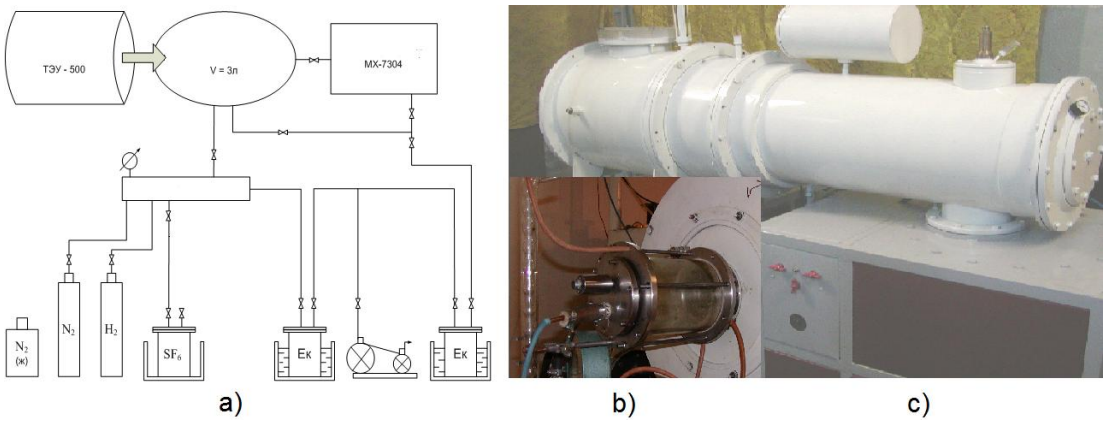



Fig.1. Experimental bench which was used for the performance of experiments: a) schematic diagram of the installation, b) photo of a plasma-chemical reactor with a volume of 6 liters, c) general view of the accelerator

The non-equilibrium plasma is formed due to the action of pulsed electron beam with the duration of not more than $10^{-9}$ s to the mixture of halogenides and gas-carrier. Nitrogen, hydrogen and oxygen are used as the gas-carrier. The processing of halogenides is performed by adding of diluent gas to the mixture of halogenide and gas-carrier up to the total pressure providing full absorption of

nanosecond pulsed electron beam energy. The modeling of chemical processes in the low-temperature plasma for equilibrium stage of the process was executed with the use of automotive system of thermal dynamic calculations “TERRA” Fig. 2a [4].

## 2. Results and discussion

Accomplished studies have shown that sulfur difluoride-oxid ($SOF_2$) is a major gas phase sulfur compound, synthesized in the conversion of sulfur hexafluoride (as a mixture with hydrogen and oxygen) in the plasma of a pulsed electron beam.

The studies of the sulfur reduction from $SF_6$ under the action of pulsed electron beam to the gas-phase mixture $SF_6 + H_2 + O_2 + Ar$ have been done. Argon (m/z = 40) was introduced to normalize the recorded mass spectrum. Major peaks characteristic of the gas mixture in the reactor after exposure to the electron beam correspond to the m/z = 2, 67, 86 and 127. The peaks at m/z = 18 and 28 correspond to the background of the mass spectrometer, the amplitude is not changed. Fig. 2b presents the mass spectra of positive ions.

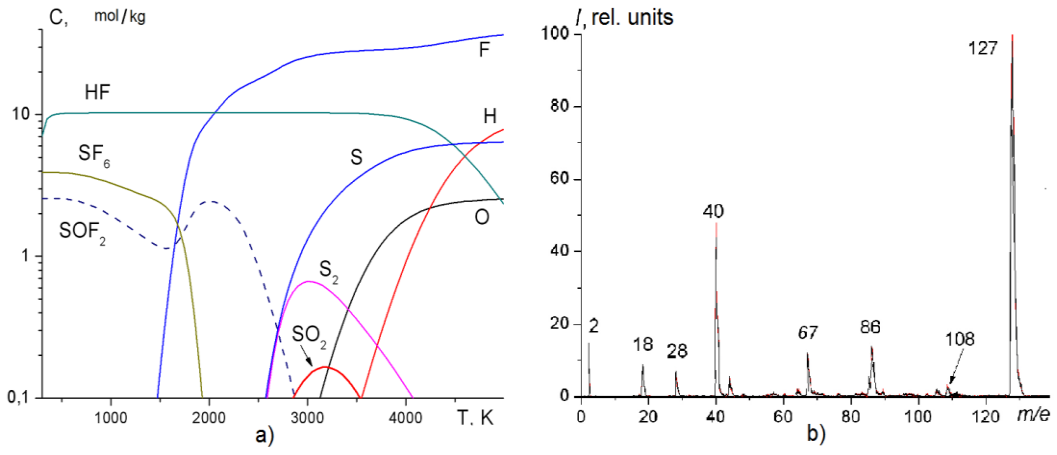



Fig.2. Thermodynamic modeling conversion of sulfur hexafluoride and mass spectra ions: a) thermodynamic modeling conversion of sulfur hexafluoride in a mixture of oxygen and hydrogen, the feed mixture (volume fraction) $SF_6 + H_2 + O_2$, b) mass spectra of positive ions of hexafluorides sulfur and difluoride sulfur oxide

When sulfur hexafluoride decomposes the electron beam energy consumptions for the dissociation of one molecule of $SF_6$ did not exceed 2.1 eV. The performed studies of sulfur hexafluoride decomposition in the mixture with hydrogen and under the action of pulsed electron beam showed that in our

experimental conditions $SF_6$ radiolysis goes according to the chain mechanism. When calculating the energy input of electron beam for sulfur hexafluoride decomposition we did not consider the energy losses for argon molecule excitation and for reagent gas heating. That is why the real values of electron beam energy input for $SF_6$ dissociation is lower than 2 eV and correspondently lower than the standard enthalpy of $SF_6$ formation which equals 12.4 eV/molecule.

Fig. 3b presents dependence of the peak area on the number of electron beam pulses and photograph of a film formed on the surface of a glass slide placed in a reactor.

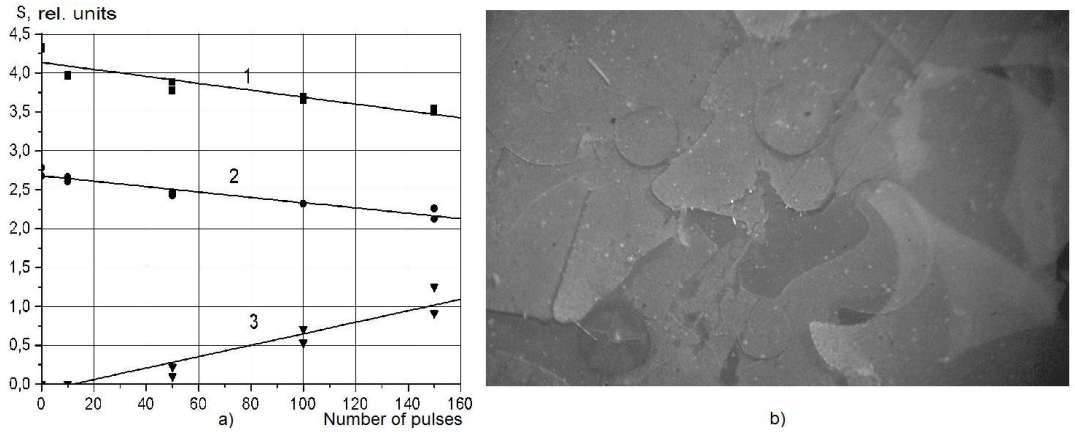



Fig.3. Dependence of the peak area on the number of electron beam pulses: a) 1- fragment ion of sulfur hexafluoride $SF_5$+, 2- $H_2$+, 3- sulfur dimer 2S+, b) photograph of a film formed on the surface of a glass slide placed in a reactor

In this study, the effect of plasma on isotope separation has been demonstrated [5]. Plasma was initiated due to the effect of pulsed electron beam with the duration of not more than $10^{-9}$ s on the mixture of hexafluorides sulfur and gas-carrier. As a gas-carrier, nitrogen, hydrogen and oxygen have been applied. The processing of halogenides sulfur is performed by adding of diluent gas and gas-carrier to the mixture of halogenides until the total pressure providing full absorption of nanosecond pulsed electron beam energy is reached. The studies showed that in the conversion of sulfur hexafluoride plasma pulse the electron beam is realized isotope effect. The content of $S^{34}$ in the products exceeds the original 1.8 times, significantly higher than the measurement error.

The thermal dynamic modeling showed that in case of plasma of $SF_6$ and $H_2$ all the elements such as S, HF, $H_2F_2$ and $SF_4$ are stable products of decomposition of sulfur hexafluoride in the mixture with hydrogen. The

calculations showed the possibility of condensed phase formation of sulfur monomer S, sulfur dimmer S2 and of other clusters.

In our case, at the expense of dissociation of sulfur hexafluoride by electronic shock: $SF_6 + e \rightarrow S + 6F$ and dissociative adhesion of low-energy electrons: $SF_6 + e \rightarrow SF_6^- \rightarrow S + 6F$. The atomic fluorine is formed, which initiates reactions in a mixture with molecular hydrogen. The major reactions are: $H_2 + F = HF + H + 1.47$ eV. The energy which is released in the exothermic reaction can be spent for initial decomposition of sulfur hexafluoride.

## Conclusion

The results of experimental study of plasmachemical processes which are flowing past at injection of a high-current pulsed electron beam in a mixture of the gases $SF_6$ , $H_2$ , $N_2$ , $O_2$ and Ar are introduced. Effective excitation of vibrational levels of the molecules occurs in the plasma of pulsed electron beam. The studies showed that in the conversion of sulfur hexafluoride plasma pulse the electron beam is realized effect. The parameters of electron beam are the following: electron energy is 400-500 keV, pulse duration at the half-height is 60 ns, frequency rate is up to 5 pulses per second, energy per pulsed is up to 200 J. The electron beam is injected to the closed reactor through the anode foil. The isotope effect under the action of a pulsed electron beam on a gas mixture is considered.

## References

1. **Dobslaw C., Glocker B.** Plasma technology and its relevance in waste air and waste gas treatment. Sustainability 12 (2020) 8981.
2. **Mesyats G.A.** Pulsed Energy and Electronics. – M.: Nauka, 2004. (in Russian)
3. **Ezhov V.V., Vlasov V.A., Pushkarev A.I., Remnev G.E., Sosnovskiy S.A.** Sulfur reduction from $SF_6$ by pulsed electronic beam // 8th Korea-Russia International Symposium on Science and Technology, Tomsk, 2004, v. 2, p. 212-215.
4. **Trusov B.G.** TERRA software package for calculation of plasma-chemical processes // Mater. 3 Intern. symp. in Theoretical and Applied Plasma Chemistry. - Ples, 2002. - S. 217-218.
5. **Pushkarev A.I., Sazonov R.V., Sosnovsky S.A.** Study of the isotopic composition of the products of the plasma-chemical conversion of sulfur hexafluoride // Proceedings of the Tomsk Polytechnic University, 2007 - v. 311. - No. 3, pp. 69-72.

# INVESTIGATION OF THE INTERACTION OF ULTRATHIN $MOS_2$ FILMS WITH $H_2$, $O_2$, AND $N_2$ PLASMA

D.E. Melezhenko[1], D.V. Lopaev[2], A.I. Zotovich[2], E.N. Voronina[1,2]

[1] Lomonosov Moscow State University, Faculty of Physics, Russia, 119991, Moscow, GSP-1, 1-2 Leninskiye Gory, dmelezhenko2301@gmail.com
[2] Skobeltsyn Insitute of Nuclear Physics, Lomonosov Moscow State University, Russia, 119991, Moscow, GSP-1, 1-2 Leninskiye Gory

**Introduction.** Two-dimensional (2D) $MoS_2$ films consisting of a few monolayers are currently considered as the most promising semiconductors for next-generation nanoelectronic devised owing their unique and fascinating properties, including high charge carrier mobility and tunable electronic properties, critically important for nanoelectronic industry [1,2]. Low-temperature plasma is widely applied at most stages of the modern technological processes, such as etching, surface functionalization, surface cleaning etc. However, active plasma species, in particular low-energy ions and radicals, may induce various damages of these ultrathin materials, which can lead to undesirable changes not only in their structure, but also in their properties (electrical conductivity, refractive index, etc.). To create a reliable technology for plasma processing of 2D materials, a detailed analysis of effects induced by ions, radicals and UV (direct plasma) or radicals only (remote or downstream plasma) is required.

The goal of this work is to study the effect of direct and remote $H_2$, $N_2$ and $O_2$ plasma treatment on ultrathin $MoS_2$ films.

**Experimental details.** Ultrathin disulfide films grown by the PECVD method on a substrate Si + $SiO_2$ + $Al_2O_3$ were used in this experiment. The 13.56 MHz ICP plasma source in a water-cooled quartz tube (16 mm of the inner diameter and ~84 cm of length) was used as a remote source of H, N and O atoms. The discharge conditions were the following: 200 W rf power, 100 mTorr pressure, 20 sccm flow, $H_2$, $N_2$, and $O_2$ gases. The atoms produced due to electron impact dissociation in the ICP discharge zone are transported by flow to the downstream reactor tube (9 cm in diameter and 60 cm length) where the samples were located. Since the tube walls are cold due to water cooling, the atom surface loss probability is low enough which provided high atom concentrations at the tube exit. A stainless steel mesh with a cell ~ 70 μm was used to exclude the plasma penetration of into the reactor tube.

In the case of the direct plasma treatment, an additional low-power surface wave discharge, SWD (10W at 81 MHz) was ignited in the reactor tube. The ion energy spectrum measured by RFEA was peaked at energy corresponding to

plasma potential (~20-22 eV for $N_2^+$ and $O_2^+$ and ~35 eV for $H_3^+$ - the main ion in $H_2$ plasma). The SWD plasma also allowed using the method of differential actinometry [3] to estimate the concentration of atoms and correspondingly atom flux to the surface of the samples.

The Raman spectra with the resolution of ~2 Å were measured by home-made raman spectrometer using Horiba Triax 550 spectrometer and solid-state laser ATC-53-1000 (532 nm). The samples thickness and optical properties of the treated samples were analyzed by spectroscopic ellipsometer SENTECH 800. Elemental composition of the samples was analyzed with XRF (Oxford Instrument X-act, via 5 keV electron irradiation) and XPS (Kratos Axis Ultra DLD).

**Result and discussion.** Measured Raman spectrum of the pristine samples (Fig. 1a) has two prominent narrow peaks corresponding to two normal modes $E^1_{2g}$ and $A_{1g}$, thereby confirming the high quality of samples under the study. The obtained difference between the peak frequencies is typical for $MoS_2$ films of more than 6 layers [4]. After the plasma treatment the Raman spectrum remains almost the same, but with increasing the exposure dose we observe a gradual weakening of peak intensities, which proceeds much faster for direct plasma (a dash line in Fig. 1a and filled symbols in Fig. 1b) than for treatment only by atoms (empty symbols in Fig. 1b).

It is also seen that for O and N atoms this process stops at relatively high doses of ~$10^{20}$, while for H atoms it does not saturates even at the highest applied doses, $10^{22}$.

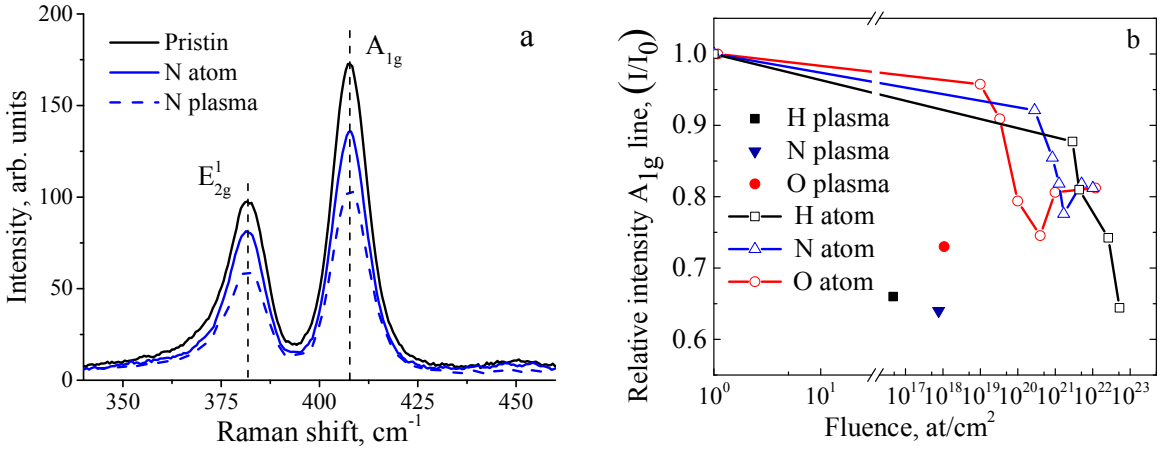



Fig. 1. Raman spectra of pristine and treated films (a); $A_{1g}$ peak intensity vs. doses of ions (filled symbols) and atoms (empty symbols) (b).

The observed changes in Raman spectra are explained by modification of the uppermost surface layers of the treated $MoS_2$ films. Analysis of the XRF and

XPS spectra shows some changes in the elemental composition, including a partial removal of sulfur by active plasma species. Such a removal is accompanied by sequential incorporation of oxygen and nitrogen into S vacancies; the appearance of Mo–O/Mo–N bonding at the surface of treated samples is confirmed by high-resolution XPS spectra.

Optical properties of pristine and treated $MoS_2$ films are studied by the ellipsometry method. Since plasma-induced changes of these properties depend on the exposure regime and plasma composition, we apply several different optic models for films under study. These models consist of three main parts: dielectric substrate + semiconducting $MoS_2$ + semiconducting/dielectric layer for modified $MoS_2$. Semiconducting layers are described with Tauc-Lorentz model [5], while for dielectric layers Caushy model with non-zero extinction coefficient is used. The thickness and optical properties of the substrate (Si + $SiO_2$ + $Al_2O_3$ + $Al_2O_3/MoS_2$ interface) are determined for pristine films and remain fixed in further analysis of the treated samples. The initial thickness of pristine $MoS_2$ film is estimated as ~ 4.5 nm.

The analysis of the ellipsometric data indicates that after the direct plasma treatment, the properties of the upper surface layers change slightly and the thickness of the semiconducting 'pure' $MoS_2$ films decreases (Fig. 2a). The best fitting for all treated samples is achieved using the model with an upper modified semiconducting layer (its thickness is approximately equal to that of one $MoS_2$ monolayer). For $O_2$ and $N_2$ plasma there is a noticeable reduction of the overall film thickness indicating a partial removal of the material.

Under the remote plasma exposure (treatment with atoms), the picture is different: the film thickness remains almost the same (Fig. 2b), but notable changes of optical properties of $MoS_2$ films are observed. For samples treated with N atoms, the best fitting is obtained with the same model as used for plasma treatment samples indicating that a thin uppermost surface layer remains to be semiconducting but with a slightly narrower bandgap. Under the O and H atom treatment the upper part of $MoS_2$ films behaves as dielectric one; the presence of such a modified layer can be explained by formation of surface $MoO_x$ clusters due to oxygen incorporation into S vacancies (both during remote plasma exposure and under ambient conditions) [6,7]. It is important that the described results of the ellipsometric analysis are well correlated with the dynamics of peak intensities in Raman spectra (Fig. 1b) and in XRF spectra. In addition, it should be noted that at high doses of H atoms the ellipsometric analysis indicates the appearance of a loose dielectric layer with a thickness of 1.0–1.5 nm and refraction index close to $n_{SiO2}$, which is related to deposition of $SiO_x$ (volatile $SiH_xO_y$ species can formed due to ion-assisted etching of the discharge tube walls in $H_2$ ICP plasma). The presence of $SiO_x$ species on treated samples is also confirmed by XPS.

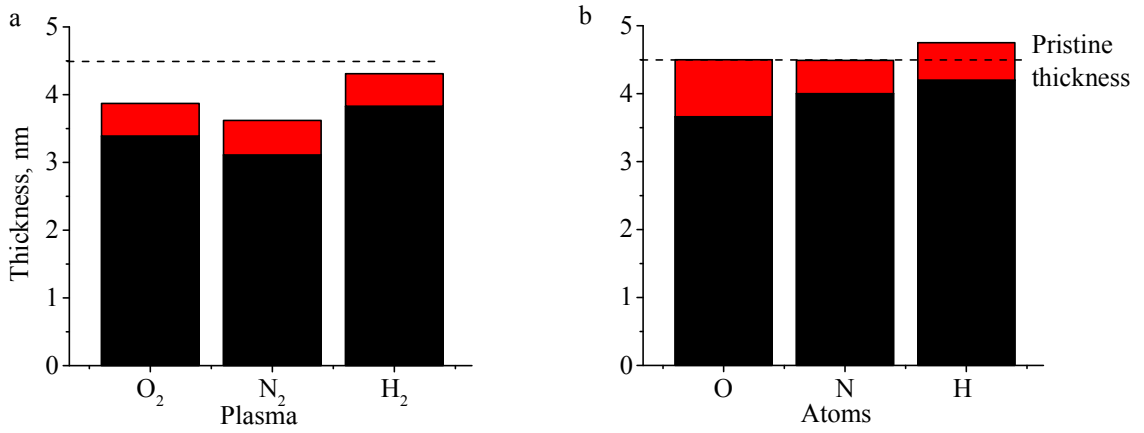



Fig. 2. Thickness of $MoS_2$ films (without substrate) after direct (a) and remote (b) plasma treatment on the base of ellipsometry data. The values of the layer thickness for samples treated with different atom species are given for an equal fluence $10^{22}$ at/cm$^2$. The 'pure' $MoS_2$ film and modified (dielectric or semiconducting) layer are shown with black and red, correspondingly. Horizontal dash lines indicate the thickness of pristine $MoS_2$ films.

**Conclusions**.

1) As a result of treatment with low-pressure plasma, even at low ion energies (≤20 eV for $O_2$ and $N_2$ plasmas and ~35 eV for $H_2$ one), the surface layer of the $MoS_2$ films is gradually destroyed, accompanying by partial removal of the material.

2) The impact of atoms is more selective. It leads to the functionalization of the film surface by incorporating attacking atoms into its upper layers and some changes of its physical properties but does not cause significant removal of the material.

3) O atoms have a most-pronounced destructive effect on the material as compared to N and H atoms due to higher reactivity of O atoms.

**Acknowledgements**. This work is supported by the Russian Science Foundation (Grant No 22-22-00178)

**References**

1. **Z. M. Wang** Materials, Physics, and Devices, 21 (2014)
2. **L.A. Chernozatonskii, A.A. Artyukh** Physics-Uspekhi, 61 (2018)
3. **D.V. Lopaev, et al.** Journal of Physiscs D: Applied Physics, 50 (2017) 075202
4. **C. Lee, et al.** ASCNano, 4 (2010)
5. **G.A. Ermolaev, et al.** npj 2D Materials and Applications, 21 (2020)
6. **K.C. Santosh, et al.** Journal of Applied Physics, 117 (2015)
7. **M. R. Islam, et al.** Nanoscale, 17 (2014)

# A REAGENT-FREE METHOD FOR MODIFYING CHITOSAN

A. Khlyustova[1], N. Sirotkin[1], I. Naumova[2], V. Titov[1]

[1]G. A. Krestov Institute of Solution Chemistry of RAS, Academicheskaja str., 1, Ivanovo, 153045, Russia, kav@isc-ras.ru
[2]Ivanovo State University, Yermak str., 39, Ivanovo, 153025, Russia

Low molecular weight chitosan, chitosan oligosaccharides, and modified chitosan are of interest for agriculture and biomedicine [1, 2]. These compounds are usually obtained using physical, chemical, and biological methods. Before exposure to chitosan for obtaining the low-molecular and water-soluble fractions, it is dissolved in an acidic medium. The procedure for isolating the water-soluble fraction requires the using a sufficient amount of chemical reagents. To reduce the use of chemicals, the possibility of obtaining a water-soluble fraction of chitosan without its preliminary conversion into a soluble form should be considered. In work [3], the authors studied the effect of underwater plasma on the dispersion of chitosan in aqueous salt solutions. It was found that in sulfate and sodium chloride solutions, the most compact structure of chitosan (the low molecular weight) is formed. The aim of this work was to study the possibility of obtaining a water-soluble fraction of chitosan by exposing two types of plasma (glow and underwater discharges) to aqueous solutions of chitosan dispersion.

4 g chitosan powder was dispersed in 400 mL distilled water in plasma cell with stirring by magnetic stirrer during the experiments. Two types of electrical discharge plasma were used [4]. The AC underwater discharge was excited between two graphite electrodes immersed in aqueous dispersion one of them was placed in quartz tube. The DC glow discharge burning above surface of water dispersion of chitosan. The discharge current was 50 mA in all experiments. The time of treatment was 20 minutes. The precipitate was separated and dried to constant weight. The difference in mass means that part of the chitosan has passed into the water-soluble fraction.

The structure of chitosan before and after plasma treatment was registered by FTIR spectroscopy (Brucker Optics) in the range of 4000-450 $cm^{-1}$ and X-ray diffraction (D8 PHASER) in the range of $2\theta$=5-60. FTIR spectroscopy data were used to determine the change in the degree of chitosan deacetylation during exposure to two types of plasma [5]. During the plasma treatment, the accumulation of $H_2O_2$, $NO_2^-$, and $NO_3^-$ was detected. Hydrogen peroxide was registered by the colorimetric method using $TiOSO_4$. The nitrite and nitrate ions were detected by the ion-selective electrodes.

FTIR spectra of untreated and plasma treated chitosan are presented in Fig. 1a. Obtained data show the presence of all the main peaks related to the

structure of chitosan. Peaks at 2929, 2866, 1420, 1325 and 1259 $cm^{-1}$ can be associated with various vibrations of $CH_2$ groups. A broad band in the region of 3600-3200 $cm^{-1}$, which centered at 3420 $cm^{-1}$ is assigned to the stretching vibrations of OH and amines groups. Peaks at 1080 and 1160 $cm^{-1}$ are attributed to the pyranose rings with the glucosidid linkage. The appearance of a shoulder at 1730 $cm^{-1}$ was noted in the spectra after the action of both types of plasma. This can be related to carbonyls band in the aldehide, ketone and carboxylic groups.

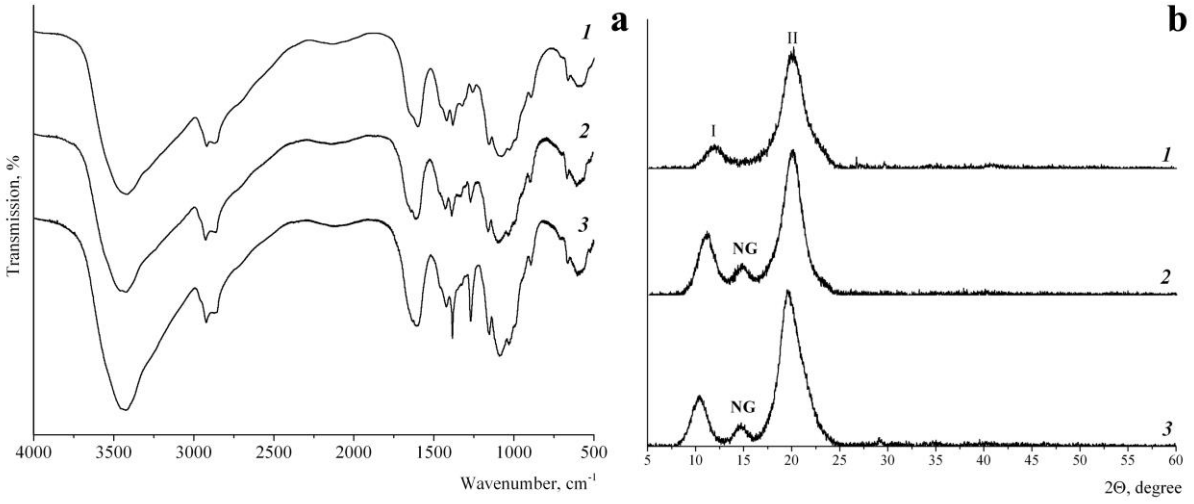



Fig. 1. FTIR spectra (a) and XRD patterns (b) of untreated (1) and after treatment by glow discharge (2) and underwater discharge (3) (I is crystalline Form I, II is crystalline Form II, and NG is N-acetyl-glucosamine)

The decrease in the intensities of the carbonyl bands indicates the deacetylation of the remaining N-acetyl groups arising from the action of the plasma. Table 1 shows the change in the degree of deacetylation during plasma treatment. The data show that the underwater discharge action causes a more loss of side groups from the chitosan chain.

Table 1 Degree of deacetylation of the chitosan at different time of treatment

| Time of treatment, min | Glow discharge | Underwater discharge |
|---|---|---|
| 0 | 73.08 | |
| 4 | 70.38 | 72.27 |
| 8 | 69.23 | 71.17 |
| 12 | 68.97 | 68.99 |
| 16 | 66.53 | 65.93 |
| 20 | 64.9 | 62.4 |

Figure 1b shows the XRD patterns of native chitosan and after plasma

treatment. The native chitosan powder contains two peaks related to the Form I and Form II of crystal structure of chitosan [6]. The X-ray patterns show that the action of both types of plasma leads to a modification of chitosan. It appeared in the presence of an additional reflex at 2θ=14.85º related to N-acetylglucosamine [7].

It is known that the ignition of electrical discharges above the surface or inside the volume of a liquid leads to the formation of chemically active particles. In the case of a glow discharge, the main stable species are nitrite, nitrate ions, and hydrogen peroxide (Table 2). In the experiments with underwater plasma, where there is no contact between the plasma and air, only the accumulation of $H_2O_2$ was recorded. A small change in the concentration of hydrogen peroxide during glow discharge combustion can be explained by its participation in the oxidation of the nitrite ion. These reactive species take part in the processes of depolymerization and modification of chitosan [4].

Table 2 The concentration of reactive nitrogen and oxygen species during the plasma treatment

| Time, min | $C(NO_3^-)$, mM | $C(NO_2^-)$, mM | $H_2O_2$, mM | |
|---|---|---|---|---|
| | | | Glow | Underwater |
| 4 | 1.12 | 12.52 | 0.77 | 0.65 |
| 8 | 5.73 | 5.34 | 0.78 | 0.69 |
| 12 | 6.77 | 6.38 | 0.78 | 0.73 |
| 16 | 7.87 | 6.83 | 0.79 | 0.75 |
| 20 | 8.77 | 6.85 | 0.8 | 0.85 |

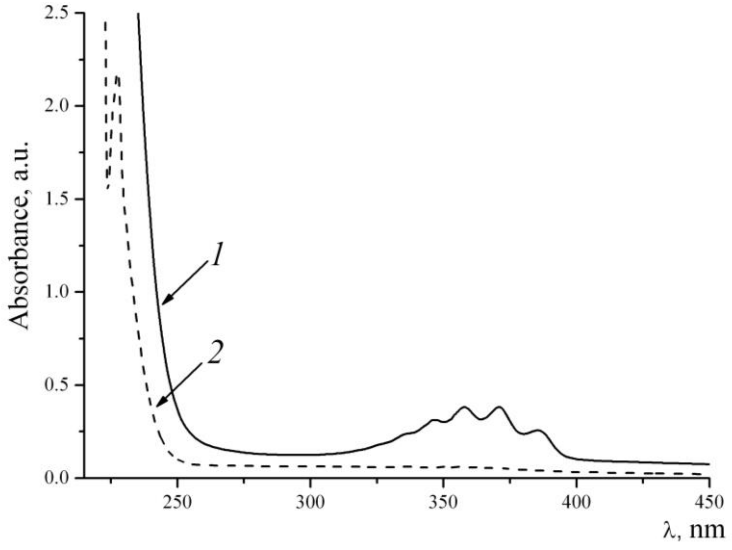



Fig. 2. UV spectra of water-soluble fraction of chitosan after action of glow (1) and underwater (2) discharges

Fig. 2 shows the UV absorption spectra of the native solution (water-soluble fraction of chitosan). After exposure to a glow discharge, the spectrum contains peaks at 345, 358, 370, and 387 nm, which correspond to n-π* transitions of carboxylic groups. After exposure to an underwater discharge, the spectrum exhibits a peak at 227 nm relating to the n-σ* transition of the hydroxyl and amide groups. This means the formation of a water-soluble fraction of chitosan. The difference in the masses of the initial chitosan and after plasma treatment is 0.12 and 0.15 g in the case of glow and underwater discharges, respectively. It gives us 0.03 and 0.05% solutions of water-soluble chitosan.

Thus, it was established that the treatment of an aqueous dispersion of chitosan by glow and underwater discharges leads to its modification and the formation of a water-soluble fraction of chitosan. In the process of modification and depolymerization, chemically active particles formed during the action of plasma take part. The proposed method is reagent-free. The resulting modified chitosan and 0.03-0.05% chitosan solution can be used in agriculture at the seed germination stage, watering sprouts, and soil fertilization.

**Acknowledgements**. This research was supported by Russian Foundation for Basic Research (project №20-02-00501).

## References

1. **Orzali L., Corsi B., Forni C., and Riccioni L**. Chitosan in agriculture: a new challenge for managing plant disease. InTech, Rijeka, (2017).
2. **Azmana M., Mahmood S., Hilles A. R., Rahman A., Arifin M. A. B., and Ahmed S.** International Journal of Biological Macromolecules, 185 (2021) 832-848.
3. **Chokradjaroen C., Theeramunkong S., Yui H., Saito N., and Rujiravanit R.** Carbohydrate Polymers, 201 (2018) 20-30.
4. **Khlyustova A., Sirotkin N., Naumova I., Tarasov A., and Titov V.** Plasma Chemistry and Plasma Processing, 42 (2022) 587-603.
5. **Domszy J.G. and Roberts G.A.** Macromolecular Chemistry Physics 186 (1985) 1671-1677.
6. **Ogawa K. and Yui T.** Bioscience, Biotechnology and Biochemistry, 58 (1994) 968-969.
7. **Herdyastuti N., Cahyaningrum S.E.** Rayasan Journal of Chemistry, 10 (2017) 226-233.

# PLASMA-LIQUID TREATMENT OF THE SURFACE OF METAL PRODUCTS

Al. Gaisin[1], D.N. Mirkhanov[1], S.Yu. Petryakov[1]

[1]Kazan National Research Technical University named after A. N. Tupolev – KAI, 420111, Russia, Kazan, K.Marx St., 10, almaz87@mail.ru

Low-temperature plasma discharges with liquid (non-metallic) electrodes is a rapidly developing interdisciplinary field of research, including the science of plasma, heat and mass transfer, fluid dynamics, photolysis, and multiphase chemistry [1]. Discharges in plasma-liquid systems are generated by direct or alternating current in the interelectrode space, where liquid is used as one of the electrodes. As a liquid electrode, solutions of salts of various concentrations in distilled, technical or purified water are usually used. The discharge is ignited in gas-discharge chambers with various types and configurations of electrodes. The most common discharge ignition schemes are carried out when a metal electrode is immersed in an electrolyte, or when a metal electrode is located at a certain distance from the electrolyte surface [2–3]. Interest in plasma-liquid systems is due to the fact that in this area of research three subsystems are intertwined in a complex way, describing, respectively, the physics of processes in the plasma (gas discharge), liquid (non-flowing and flowing electrolyte) and gas (surrounding air) phase states. In these systems, there are more than 50 charged, neutral atomic and molecular particles that react with each other and affect the energy balance in the discharge [4]. This is the reason for the complexity of carrying out numerical work, since the mathematical modeling of plasma-liquid systems can include more than 30 equations, depending on the number of particles taken into account. The results obtained in this case do not correlate well with the experimental data. All this makes it difficult to create a unified classification of plasma-liquid systems similar to the one that exists for discharges with solid electrodes (spark, arc, glow, corona, etc.). At the same time, one of the possible directions for systematizing discharges with liquid electrodes is their classification according to elementary processes, therefore, conducting search work and developing mathematical models based on them that are qualitatively and quantitatively consistent with experimental data is an urgent task. At the same time, plasma-liquid systems are of great interest for solving various applied problems in the field of mechanical engineering, metalworking, medicine, and the space industry. Specialists from various scientific schools are investigating the use of discharges with liquid electrodes for processing products with complex geometry of the outer and inner surfaces, made using both traditional production methods (stamping, casting, etc.), and using additive methods of laser sintering of metal powders. A number of foreign and domestic publications present the results on the use of

plasma-liquid systems for the production of fine metal powders and the production of nanoparticles, the application of functional coatings on products, the analysis of particle content in liquids, plasma-chemical reactors, sterilization and purification of solids, water and air. A wide variety of applications of these systems is associated with a large number of configurations of gas discharge chambers, modes and parameters of ignition and discharge combustion, as well as common plasma-chemical processes associated with the transfer of matter and charge at the phase boundary. The purpose of this work is to study the effect of low-temperature plasma of electric discharges with liquid (non-metallic) electrodes on the surface of a metal plate made of steel. Experimental studies of the discharge were carried out at voltage parameters U = 100 -1000 V, anode current density j_a = 0.2 - 0.6 A/cm$^2$, pressure p = 10^5 Pa, electrolyte temperature T = 10 - 25 °C, diameter anode d_a = 5 mm, electrical conductivity of the electrolyte σ = 0.1 - 0.12 Om$^{-1}$ cm$^{-1}$. The discharge was ignited by immersing a metal anode (workpiece) into an electrolytic cell with an electrolyte. Also, a metal plate made of copper was previously immersed in the electrolytic bath to supply a negative potential to the electrolyte. To obtain micrographs and measure the elemental composition of the samples, a Carl Zeiss Auriga Crossbeam scanning electron microscope with a built-in Inca X-Max energy-dispersive spectrometer was used. During the electron microscopic analysis, the SE2 mode (secondary electrons) was used for better visualization of the surface morphology, as well as for microprobe quantitative and qualitative analysis (15 kV, 250 pA). The X-ray microprobe analysis of the samples was performed using an INCA X-Max energy-dispersive spectrometer (resolution 127 eV). To obtain the most reliable results, spectra were collected from several areas for each sample and for each group of objects, and then the values were averaged accordingly. During the work, a magnification of 100 – 5000 times was used.

Figure 1 shows a photograph of the microrelief of the sample surface before electrolytic plasma treatment. The initial surface is a regularly rough structure covered with microheterogeneities of various diameters. The surface is also covered with microcavities and microprotrusions of various heights. Also on the surface there are various types of corrosion, burrs, as well as elements of organic and inorganic contaminants.

After electrolytic-plasma treatment (Fig. 2), the surface is smoothed, acquires a shine, turning into polishing. Micro-irregularities, impurities and elements of metal corrosion that were in the original sample disappear from the surface.

Thus, it can be concluded that plasma-liquid systems in this configuration of electrodes can be successfully used to modify and treat the surface of metal products made of steel.

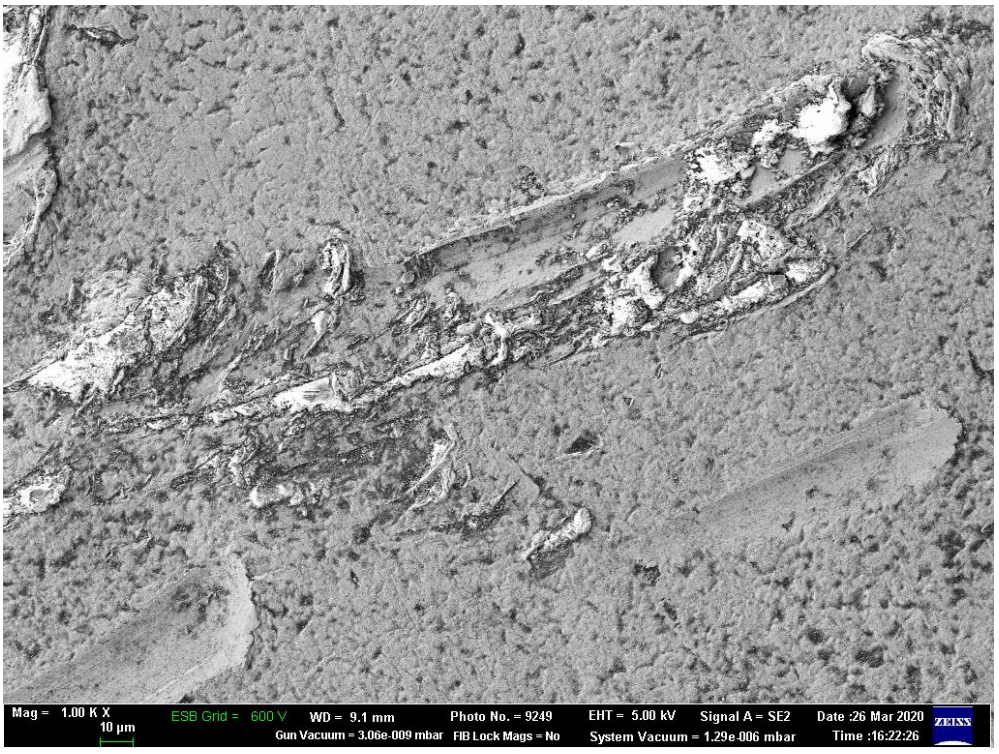



Fig.1. The surface of a metal product before electrolytic-plasma treatment.

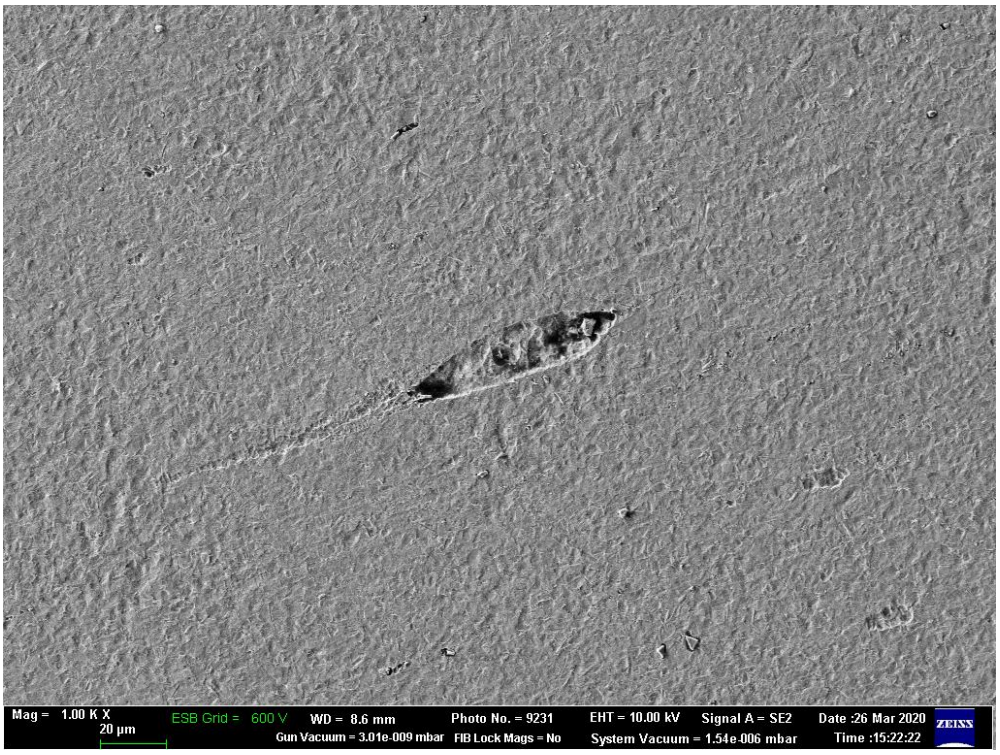



Fig.2. The surface of a metal product after electrolytic-plasma treatment.

**Acknowledgements.** The study was financially supported by the Russian Science Foundation (project no. 21-79-30062).

## References

1. **Bruggeman P.J., Bogaerts A., Pouvesle J.M., et al.** Journal of Applied Physics, 130 (20), 200401 (2021).
2. **Gaysin A.F., Gilmutdinov A.K.** Inorganic Materials: Applied Research, 12 (3), 633 (2021).
3. **Gaysin A.F., Gil'mutdinov A.K., Mirkhanov D.N.** Metal Science and Heat Treatment, 60 (1 – 2), 128 (2018).
4. **Sakiyama Y., Graves D.B., Chang Hung-Wen, et al.** Journal of Physics D: Applied Physics, 45, 425201 (2012).

# PLASMA-LIQUID PRODUCTION OF METAL POWDER FOR 3D PRINTING APPLICATIONS

Al. Gaisin[1], R. Kayumov[1], A. Kuputdinova[1]

[1]Kazan National Research Technical University named after A. N. Tupolev – KAI, 420111, Russia, Kazan, K.Marx St., 10, almaz87@mail.ru

Gas-discharge plasma with liquid (non-metallic) electrodes is a rapidly developing interdisciplinary field of research, including the science of plasma, fluid dynamics, heat and mass transfer, multiphase chemistry, and photolysis [1]. Unlike gas discharges with traditional electrodes (glow, arc, spark, etc.), this type of discharge is generated by direct or alternating current in the interelectrode gap, where one or both electrodes are a flowing or non-flowing liquid. As a liquid electrode, as a rule, solutions of salts of various concentrations in technical, distilled or tap water are used.

Plasma-liquid systems use in various industries, including metal surface treatment [2 - 3], removal of dielectric coatings, water and air purification [4], and others. Additive 3D printing technologies are increasingly replacing traditional methods of manufacturing products, as in most cases they surpass them in terms of physical and mechanical characteristics.

Additive technologies make it possible to produce high quality products with virtually unlimited complexity of surface geometry. For the manufacture of such products, specially prepared fine metal powders of various grades are used. A significant disadvantage is their high cost, for example, the price of powder based on nickel «Superalloy IN738» can reach $ 200 per kilogram, and based on stainless steel «PH1» exceeds $ 15 per kilogram. Along with this, the amount of defects and illiquid assets during the operation and manufacture of such products can reach high values. Together, this leads to increased costs for enterprises and may devalue the competitive advantages of the final product. Thus, the search for new methods for obtaining finely dispersed metal powders is an urgent task. Today, there are several methods for the production of powders, including: mechanical grinding in ball or hammer mills, mechanical grinding in vortex mills, spraying of liquid metals, reduction, electrolysis, decomposition of carbonyl compounds. The most common technologies for the production of metal powders are gas atomization and plasma atomization. Plasma atomization characterizes by the fact that the metal raw material in the form of a wire fed into the top of the atomizer, then it melts with a torch, and the molten metal solidifies in the fall and forms spherical particles.

As part of this work, it is planned to investigate plasma-liquid systems in the processes of recycling finished metal products of additive manufacturing back into powder for its reuse in 3D printing.

The initialization of the direct current electric discharge by the contact method between the metal anode and the electrolytic cathode showed that when the voltage is set in the range from 0.1 to 0.4 kV, evaporation begins in the region of interaction of the electrodes, which then turns into boiling of the electrolyte with intense vaporization, which proceeds as the free surface of the liquid, and around the metal anode. As a result, a region of phase separation is formed in the region of the metal anode, that is, vapor-gas bubbles are formed on its surface. The current flowing in the circuit induces the processes of chemical separation of dissolved substances from the electrolyte and Joule heat release from the surface of the metal anode. In an electrolytic cell with an electrolyte, a process characteristic of electrolysis takes place. By changing the parameters of temperature and electrolyte concentration, it is possible to change near-electrode processes in the desired direction. Breakdown at the interface between the media does not occur, since the power invested in the electric discharge is insufficient for ionization of the vapor-air medium and the occurrence of an electron avalanche.

With an increase in voltage to 500 V, the electric field strength reaches values sufficient for the occurrence of an electron avalanche and breakdown of the gas-vapor interelectrode gap. The source of free electrons is their emission from the surface of the metal electrode. After breakdown, the formation of free electrons in an electric discharge can be affected by direct electron impact ionization, stepwise, photo- and dissociative ionization in the volume, as well as plasma-chemical reactions between dissociation products at the electrolyte boundary and in the volume. Electric discharge burns in multi-channel mode.

Using an energy-dispersive spectrometer, elemental analysis was carried out, spectra, images with sections of a set of spectra, and summary tables of the weight and atomic % composition before and after sputtering of the samples were plotted (Fig. 1).

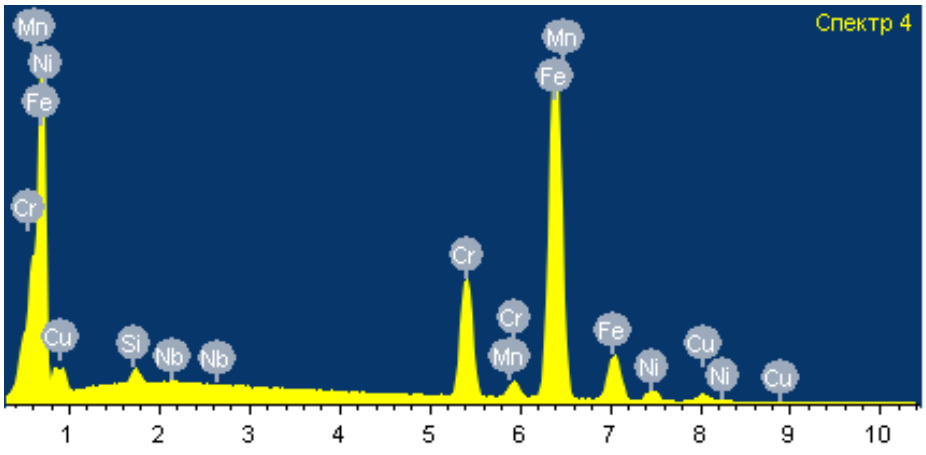



Fig. 1. Elemental analysis of metal powder

Based on the measurements, it follows that, in the studied spectrum of the sample before sputtering, there are atoms of various names, including: silicon Si, chromium Cr, manganese Mn, iron Fe, nickel Ni, copper Cu and niobium Nb, which generally corresponds to the chemical composition of the powder PH1 . After spraying the sample onto the metal powder, its chemical composition changes, the elements of oxygen O, magnesium Mg, chlorine Cl and calcium Ca appear, at the same time niobium Nb and manganese Mn disappear. Of particular note is the significant content of oxygen O in the resulting metal powder (about 33%), due to the contact of the molten metal anode under the influence of plasma with the surrounding air, which results in the dissolution of oxygen in the metal. As you know, oxygen O negatively affects the physical and mechanical properties of steel, including an increase in the corrosion rate and a sharp decrease in ductility. The appearance of other elements in small amounts may be due to their initial content in the electrolyte, which was based on purified tap water.

The method of scanning electron microscopy (SEM) was used to study the morphology of the resulting finely dispersed metal powder as a result of exposure to an electric discharge plasma with electrolytic electrodes at atmospheric pressure (Fig. 2). The shape of a significant volume of particles corresponds to the original powder, from which the initial product was “grown” by the laser. Also on the image there are particles corresponding to iron oxide.

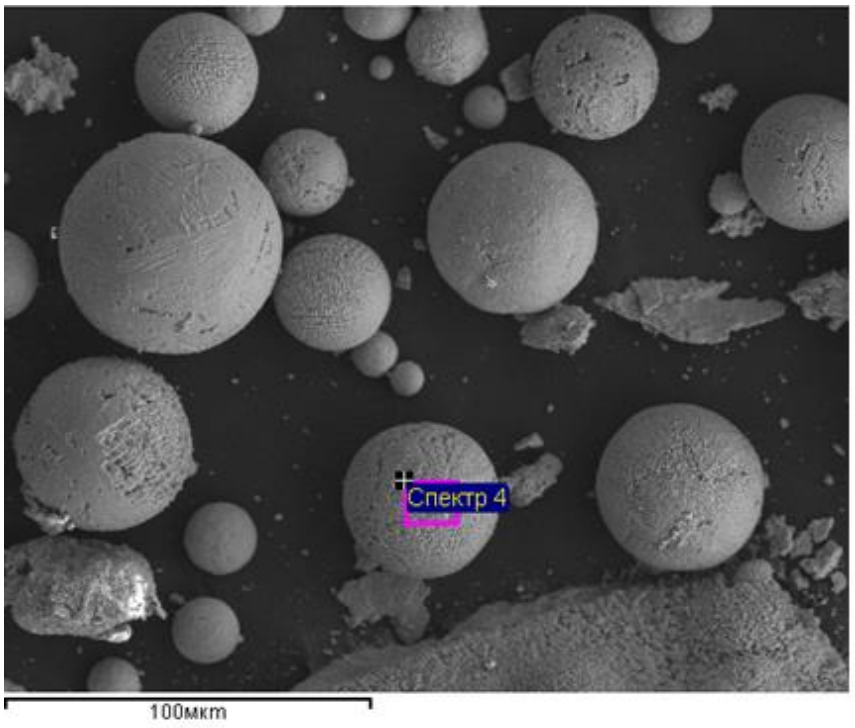



Fig. 2. SEM image of fine metal powder

**Acknowledgements.** The study was supported by the Russian Science Foundation grant No. 22-29-00021, https://rscf.ru/project/22-29-00021/

## References

1. **Bruggeman P.J., Bogaerts A., Pouvesle J.M., et al.** Journal of Applied Physics, 130 (20), 200401 (2021).
2. **Gaysin A.F., Gilmutdinov A.K.** Inorganic Materials: Applied Research, 12 (3), 633 (2021).
3. **Gaysin A.F., Gil'mutdinov A.K., Mirkhanov D.N.** Metal Science and Heat Treatment, 60 (1 – 2), 128 (2018).
4. **Son E.E., Suvorov I.F., Kakaurov S.V., et al.** High Temperature, 52 (6), 942 (2014).

# RESEARCH OF AIR IONS DISTRIBUTION GENERATED BY DIELECTRIC BARRIER DISCHARGE PLASMA

Y.V. Zaparozhchanka, A.V. Aksyuchits, D.A. Kotov, A.N. Osipov

BSUIR, Belarus Minsk, str. Petrusya Brovki,6,
yliyazaporozchenko@gmail.com

## Abstract

In our research, the source of negative and positive air ions is generated in the coaxial system with a dielectric barrier discharge (DBD). The spatial distribution of the negative and positive air ions concentration in different positions relative to the generation system was established. This investigation allow us to conclude that DBD can used to generate negative air ions for therapeutic application in medicine.

## Introduction

The purity and physico-chemical composition of the air we breathe largely determine the duration of human life. With the development of any disease, a metabolic disorder occurs in the cells of the body, as a result, their negative charge decreases. To restore the amount of negative air ions in the air to normal different generation systems are used . In our research, the source of negative and positive air ions is plasma that is generated in the coaxial DBD system at atmospheric pressure. The spatial distribution of the concentration of negative and positive air ions in different positions relative to the generation system was investigated.

## Materials, methods, and experimental set-up

Air ions are atmospheric air particles that carry a positive or negative charge and are obtained using ionizers or in other ways. The source of their formation is cosmic or ultraviolet rays, atmospheric discharges, soil radioactivity, etc. Among the air ions, the following ions have the highest chemical activity: $O_3^+$, $O_2^-$, $CO^+$, $NO_2$. In medical practice, mainly negatively charged air ions are used. The light negative ions have a depressing effect on the redox processes in the body of humans, animals and plants, on maintaining the process of homeostasis, and on the state of the immune system. In our research, the source of negative and positive air ions is plasma that is generated in a coaxial system with a dielectric barrier discharge.

Plasma at atmospheric pressure in a coaxial system is a dielectric barrier discharge in the form of a streamer or diffuse area and is characterized as a non-stationary and non-thermal discharge that arise when high voltages are

applied to small discharge gaps, in which the dielectric coating of one or both electrodes prevents the discharge from entering the arc mode.

The plasma produces reactive species by ionizing a flow of argon gas that subsequently reacts with ambient air oxygen and nitrogen to form gas-phase reactive oxygen and nitrogen species (ROS/RNS) (fig.1). [1]

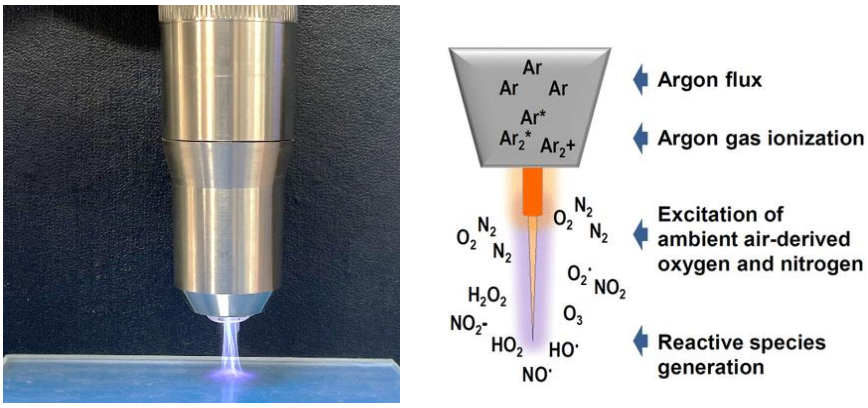



Fig. 1. The atmospheric pressure argon plasma jet and principle of reactive species generation. [1]

An experimental stand was used for our research. It includes gas system, discharge unit and power supply. The layout of the experimental complex is show in figure 2. The setup consists of a balloon with a working gas argon (1), a mass flow controller MFC-12 (2), a treated substrate (3), a tripod (4), a power unit (5) and a discharge system (6). Argon was used as the plasma gas.

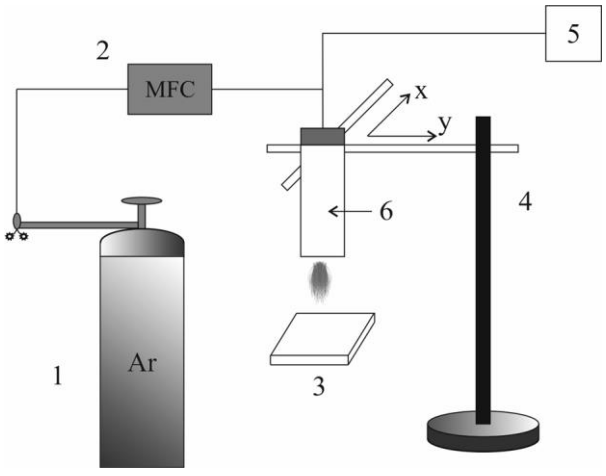



Fig. 2. The block diagram of the experimental setup

## Results and discussion

In our research, the rate of ionization of the air environment was determined using an AIM-1 device, which allows simultaneously measuring the concentration of positive and negative light ions. The range of concentrations of light air ions measured by the device is 100 ... 1,9-$10^3$ ion/$cm^3$ [2].

With artificial air ionization, the lifetime of an air ion is several seconds. Since the source of air ions is local, the distribution of air ions in space is especially non-uniform and the study of the concentration of air ions depends significantly on the choice of a point in space for which measurements are taken. In this study, the positions in front of the experimental complex were checked according to the following scheme (Figure 3).

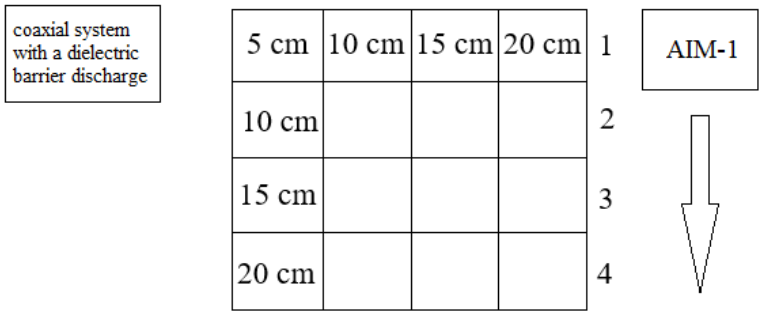



Fig. 3. Scheme of mutual arrangement of devices

In the course of the study, the distribution values of the concentration of negative and positive air ions were obtained in different positions relative to the generation system (Fig. 4-5).

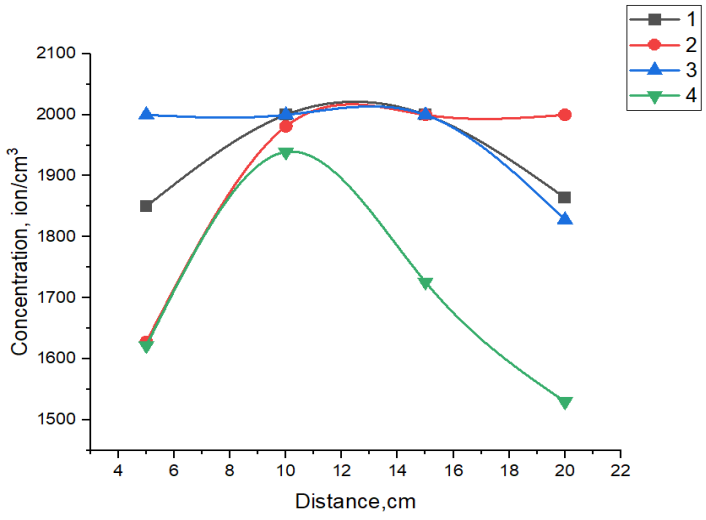



Fig. 4. Distribution of the concentration of negative air ions in front of the discharge system

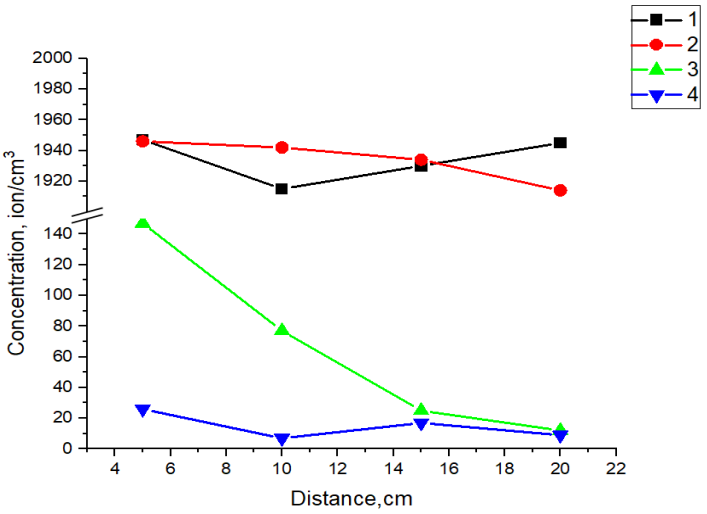



Fig. 5. Distribution of the concentration of positive air ions in front of the discharge system

The results of the study show, that with an increase in the distance of the AIM-1 device from the experimental complex, the concentration of positive air ions is reduced , and the concentration of negative air ions at almost all positions remains quite high.

By analyzing the distribution of the concentration of negative and positive air ions, it is possible to identify positions in the range of distances from 10 to 15 cm as the most favorable from the position of the maximum value of the concentration of negative air ions and the minimum positive air ions. It can be supposed that the plasma generated in a coaxial system with a dielectric barrier discharge can be used as a source of negative air ions for therapeutic applications in medicine.

**Acknowledgements**. This work was supported by the National Academy of Sciences of Belarus «Convergence – 2025».

## References

1. **Bekeschus, S., Lippert, M., Diepold, K.** et al. Physical plasma-triggered ROS induces tumor cell death upon cleavage of HSP90 chaperone. Sci Rep 9, 4112 (2019)
2. **H.F. Tammet.** Air ion counter. Methodological guide / Compiler - Haapsalu. 1985. - 44 s

# INCREASE THE GLASS SURFACE HYDROPHILICITY BY TREATMENT IN PLASMA AT ATMOSPHERIC PRESSURE

D.A. Kotov[1], A.V. Aksyuchits, Y.V. Zaparozhchanka, K.K. Zheliaznova

[1]Belarusian State University of Informatics and Radioelectronics, P. Brovki 6, 220013 Minsk, Belarus, kotov@bsuir.by

The surface properties of glass are studied after the treatment of a low-temperature plasma of dielectric barrier discharge (DBD). To estimate the magnitude of the glass surface hydrophilicity, a sessile drop method was selected to measure the wetting angle. It is established that such treatment leads to the surface cleaning and activation. The dependences of the wetting angle on the processing time, gas consumption and operation distance are obtained.

## Introduction

Nowadays modification of surface and its activation represents huge practical interest. One of the methods for materials surface properties improving is plasma treatment. This method of processing could be realized using vacuum or atmospheric pressure. Processing at atmospheric pressure offers a number of advantages: simple equipment, since no vacuum chamber with sample airlock, pumps and vacuum fitting are required, plasma processing can be combined with other technological processes, such as gluing, the material surface processing at atmospheric pressure is exposed much less or at all to bombardment high-energy electrons, X-ray irradiation, extreme ultraviolet, etc.

## Materials, methods, and experimental set-up

An experimental system for generation dielectric barrier discharge plasma at atmospheric pressure was used in research, it consisting of discharge unit, gas supply unit and power supply. Generation of plasma begins by pumping working gas (argon) throughout discharge gap of the coalxial type system. This discharge unit allows to form plasma torch up to 3 cm long with a treatment area up to 1cm in diameter.To evaluate the wettability value of a surface glass a sessile drop method was used, which allows measuring the edge of wetting angle. Measuring were taken in a way: a drop of 0.2 ml was applied to the treated part of a glass surface, then it was photographed and in COMPAS-3D program the edge of the wetting angle was determined. [1] The experimental setup is shown in fig.1.

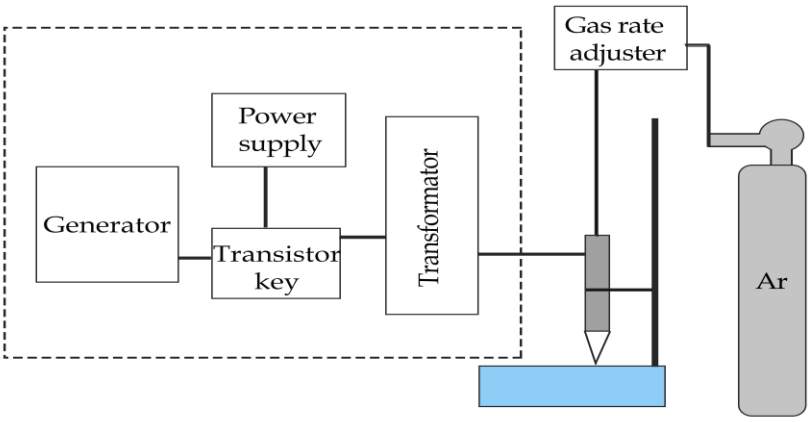



Fig.1. Schematic representation of the experimental setup

## Results and discussion

Surface activation occurs at the expense of formation of chemical active layer from broken bonds in processing. To quantify the impact of low-temperature plasma on surface properties of a glass dependences of wetting angle from processing time were studied (with fixed distance from sample to discharge system and gas consumption), from distance (with fixed time and gas consumption), and from gas consumption (with fixed time and distance). [2]

To measure the edge angle dependence on time, the time parameter varied from 10 to 300 seconds. Distance between the end of discharge unit and sample was 10 mm, gas consumption was 125 l/h, power consumption of discharge was 10 W. Based on measurements through the COMPAS-3D program (fig. 2) were obtained experimental data, presented in Figure 3.

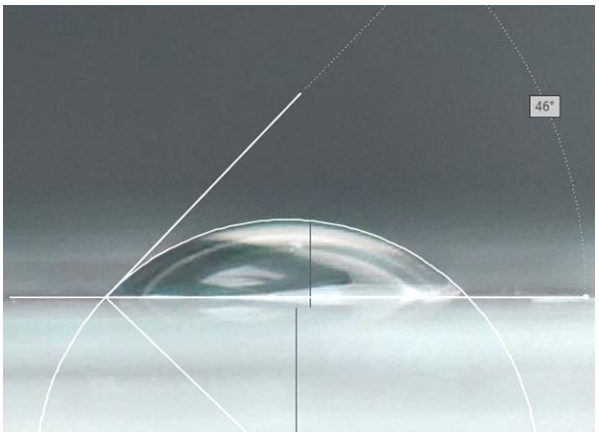



Fig. 2. Image of sesille drop on glass surface with measured wetting angle in COMPAS-3D program

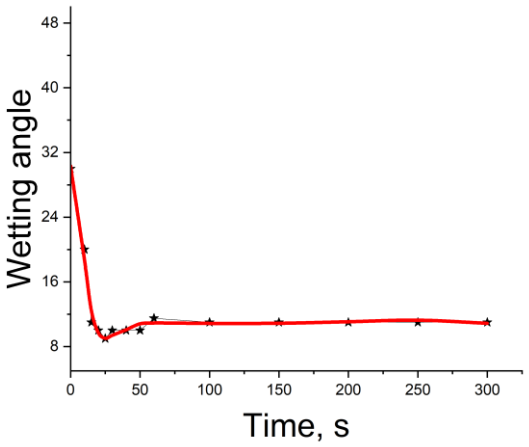



Fig. 3. Dependence of wetting angle on processing time

As it shown in fig.3 effective processing time is 25 seconds, which indicates active surface cleaning of a glass and improved wettability. With processing time over effective value is no significant improving in wettability.

At figure 4 is shown dependence of wetting angle on distance from sample to the end of the discharge system with following constants: time – 40 s, power consumption of discharge – 10 W, gas consumption – 125 l/h.

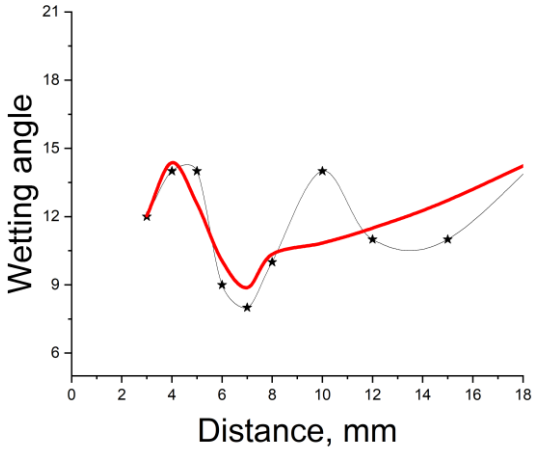



Fig. 4. Dependence of wetting angle on the end discharge unit – sample distance

As it shown in fig. 4, the edge-wetting angle reaches a minimum value at a distance of 7 mm. Thus, we can conclude that the efficiency of glass treatment is determined by the distance between the sample and the end of the discharge system.

The dependence of the wetting angle on gas consumption was investigated at the following constants: time – 40 seconds, distance sample – the

end of the discharge unit – 10 mm, discharge power – 10 W. The graph is shown in Figure 5.

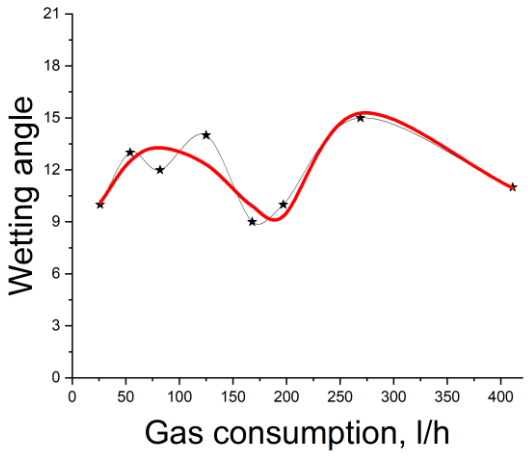



Fig. 5. Dependence of wetting angle on gas consumption

In this dependance minimum reachs in 194 l/h value, which is an optimal regime from point of view of active particle concentration for glass processing in «cold» plasma.

As a result of researches of changing the edge of angle of wetting of glass surface depending on parameters of technological process of its processing in plasma of a dielectric barrier discharge, effective modes have been established. The edge wetting angle decreased by 5.5 times (from 44° to 8°), indicating an increase in the work of adhesion forces. It was found that the best time parameters for glass treatment – 30-40 seconds, sample-the end of the discharge unit distance – 7 mm, and the gas consumption – 194 l/h.

As a result of the experimental studies it was found that the used method of cleaning and activation in the plasma torch of dielectric barrier discharge is effective both from the position of increasing hydrophobicity and from the point of view of energy and resource saving.

**Acknowledgements**. This work was supported by the National Academy of Sciences of Belarus «Convergence – 2025».

## References

1. Metod lezhashchej kapli [Electronic resource]. URL:https://tirit.org/articles/surface_theory_sessile.php. – in Russian.
2. **Y.V. Zaparozhchanka D.A. Kotov, T.A. Kuznetsova** Increace in the silicon surface adhesion by treatment in atmospheric plasma / PPPT-2018 Minsk – 49 p.

# INVESTIGATION OF ZIGZAG WIRES LAYOUT IN EXPLODING WIRE ARRAY

S. Anishchenko[1], A. Gurinovich[1], E. Gurnevich[1], D. Leonenko[2], A. Rouba[1]

[1]Research Institute for Nuclear Problems, Minsk 220030, Belarus, rouba@inp.bsu.by
[2]Electrophysical laboratory, Minsk 220088, Belarus

## 1. Introduction

Exploding wires serving as opening switch are widely used for generation of high-voltage pulse and for switching energy stored in inductive storage to a load. Two factors should be taken into account when designing an exploding wire array (EWA). First, the specific high-voltage pulse amplitude and duration are necessary for specific load. Second, dynamics of wires explosion depends on coating of wire and impurities in metal. So parameters of EWA such as wires material and environment, length, diameter and number of wires should be taken into account and experimentally tested. Geometry of EWA could also significantly influence on the output parameters of the opening switch [1, 2].

Compacting EWA could be useful for parameters of pulse forming network and minimization of inductance of the load connection to EWA. Compact EWA design implies use of non-strait wires, for example, zigzag layout [3]. High-voltage breakdown should be thoroughly considered for a compact EWA design: insulating gas should be considered as an option.

## 2. Experimental setup

Figure 1 shows a circuit diagram of the experimental setup for EWA test. Primary energy is stored in capacitor bank C. Inductance L1 is used as inductive storage. Controlled spark gap SG1 serves as closing switch. Uncontrollable spark gap SG2 picks voltage pulse over the load (high-power microwave source with impedance ~ 37 Ω).

Test of EWA with straight wires layout was used for reference. The supporting frame enables operate with straight wires of 750 mm length in air without extra pressure at full EWA length 750 mm. Frame for zigzag layout has length 300 mm for wires of 750 mm length. Seven supports are used for zigzag layout. The frame for zigzag layout is placed in a sealed casing suitable for filling with pressurized gas. Copper wire with diameter 100 μm is used. The number of wires in EWA used for reference tests is 28, but in some experiments the number of wires was varied according to specific purpose of test. Photo of EWA with zigzag layout is shown in Fig. 2.

Comparison of EWA operation for different wire layouts was done by comparison the amplitude and duration of the produced current pulse at the load.

Current was measured by Rogowski coil. Circuit diagram of experimental setup is shown in Figure 1 with values for the components.

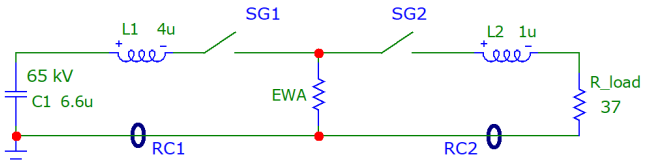



**Fig.1.** Circuit diagram of experimental setup. (C is the capacitor bank, L1 and L2 are the inductances, SG1 and SG2 are the switches (spark gaps), RC1 and RC2 are the Rogowski coils.)



**Fig.2.** Exploding wire array with zigzag layout (No. of wires is 28).

## 3. Results

SF6 was used to prevent electrical breakdown in EWA with zigzag layout. Measured current pulse in the load for different values of SF6 pressure is shown in Fig.3. It is seen that for regular operation of considered EWA, the pressure of SF6 should be higher than 2 atm. The surface breakdown in EWA revealed itself at 2 atm pressure as decrease of amplitude of current transfered to the load.

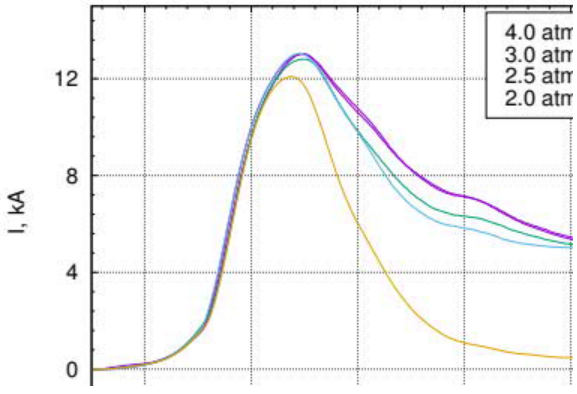



**Fig.3.** Current in the load for different values of SF6 pressure in EWA with zigzag layout (No. of wires is 28).

Tests of EWA with 28 wires in straight and zigzag layouts were carried out in same conditions using the circuit shown in Fig.1; gas type and pressure were varied. The distance between wires was about 11 mm in straight layout. The minimal distance between wires for zigzag layout was 5 mm. The amplitude of load current and pulse duration for different EWA are shown in the Table 1.

**Table 1.** Comparison of EWAs with different wires layout (No. of wires is 28)

| **Wires layout** | **Medium** | **Pressure, atm** | **Current (±5%), kA** | **FWHM of current pulse (±10%), ns** |
|---|---|---|---|---|
| Straight | Air | 1 | 14.5 | 150 |
| Zigzag | SF6 | 4 | 13 | 260 |

We can see from the Table 1 that the amplitude of load current drops by 10% for zigzag layout. It is not critical for load operation. The possible reason of such drop is smaller distance between wires in zigzag layout as compared to straight wires. Pulse duration for zigzag layout increases up to 70 % due to pressurized SF6.

To study influence of distance between wires on EWA operation, the minimal distance between wires was increased to 10 mm for zigzag layout. 20 wires were installed in straight and zigzag layouts. The distance 11 mm between the straight wires remained the same as in previous test. Parameters and current amplitudes are shown for both layouts in Table 2.

**Table 2.** Comparison of EWAs with different wire layouts (No. of wires is 20)

| **Wires layout** | **Medium** | **Pressure, atm** | **Current (±5%), kA** | **FWHM of current pulse (±10%), ns** |
|---|---|---|---|---|
| Straight | Air | 1 | 13 | 190 |
| Zigzag | SF6 | 4 | 12.8 | 200 |

From Table 2 it follows that the amplitude and duration of current pulse in the load are almost the same for two wire layouts. So, the distance between wires is recommended to exceed 5 mm (value approaching 10 mm is better).

We observed the variation of current amplitudes while working with EWA with zigzag layout. A possible reason of this is wire damage due to extra tension applied to wires during installation. Additional experiments were carried out to

check the influence of extra tension on EWA with zigzag layout. Experiments were done with use of the set-up shown in Fig.1 with changed parameters: voltage at capacitors bank C1 was 57 kV, load impedance was ~33 Ohm, the number of wires was 22. Results of this test are shown in Table 3.

**Table 3.** Comparison of EWAs with different tension applied to wires during installation (No. of wires is 22)

| | **Current pulse amplitude at the load (±5%), kA** | **FWHM of current pulse at the load (±10%), ns** |
|---|---|---|
| No or weak tension | 10 | 230 |
| Extra tension | 8.5 | 320 |

According to results in Table 3, extra tension applied to wires during installation could cause reducing of current amplitude by 15%.

## 4. Conclusion

Compact EWA design implies use of non-strait wires, for example, zigzag layout. High-voltage breakdown should be thoroughly considered for a compact EWA design: insulating gas should be considered as an option. According to multiple studies SF6 looks to be the best choice for EWA.

Minimal SF6 pressure is shown to be higher than 2 atm to prevent EWA breakdown in the proposed EWA design enabling to reduce the EWA length twice as many by zigzag layout in pressurized SF6. Use of pressurized SF6 also increase the pulse duration in the load by 70% as compared to the pulse produced with straight wires exploded in air. Wires damage is shown to be of high importance during installation. Any extra tension, applied to wires, can reduce the amplitude of high-voltage pulse by 15%.

## 5. References

[1] **G.A. Mesyats**, "Pulsed power," Springer, Boston, MA, 2005; ISBN: 978-0-**306-48654-8.**

[2] **A.E. Borisevich, S.L. Cherkas**, Technical Physics. **57**, No. 10, P. 1380–86, 2012; doi:10.1134/S1063784212100027.

[3] **D. McCauley, D. Belt, J. Mankowski, J. Dickens, A. Neuber, and M. Kristiansen,** "Electro-explosive fuse optimization for helical flux compression generator using a non-explosive test bed," Proc. of 16th IEEE Int. Pulsed Power Conf. 2007; doi: 10.1109/PPPS.2007.4652362.

# RESEARCH OF MAGNETIC FIELD AND GAS DISTRIBUTION INFLUENCE ON PLASMA GENERATION AND THIN DIAMOND-LIKE FILM UNIFORMITY

N. Leonovich[1], D. Kotov[1], P. Tovt[1], A. Zanko[2]

[1] Belarusian State University of Informatics and Radioelectronics, 6 Petrusya Brovki str. Minsk, Republic of Belarus, nickxz51@gmail.com

[2] JSC «INTEGRAL» - Holding Management Company, 121A, Kazintsa I.P. Str., Minsk, 220108, Republic of Belarus, zanko.andrei@inbox.ru

**Abstract.** This research is devoted to the study of the magnetic field influence and gas distribution on the inductively coupled plasma generation and the uniformity of diamond-like carbon thin film deposition. It has been determined that the presence of magnetic field up to 1 mT allows to reduce the operating pressure of plasma combustion up to $5\times10^{-2}$ Pa, which makes it possible to more flexibly control the structure of the resulting coatings. As a result of our research is the choice of the gas distributor effective configuration and value of electromagnets current for HDP-CVD cylindrical reactor with flat ICP plasma source.

**Introduction.** Application of thin-film optical protecting coatings is a problem, which includes scientific and technical aspects, related to physics and chemistry. Realization of this requirements depends directly on achievements in design of equipment and improvement of technological generation processes of thin-films. Nowadays plasma-chemical deposition from high-density plasma technique is one of the perspective tendencies in forming diamond-like carbon coating methods. The advantage of this method in comparing with traditional chemical methods is ecological safety, high cleanliness of technological processes, product quality, flexible parameter management of high-density plasma and as a result, the control of not only composition, but the structure of depositing layer.

**Experimental setup.** For generation diamond-like carbon coating technology realization by HDP-CVD method, there was developed cylindrical reactor 280 mm in diameter with pumping from the bottom, which is shown in fig.1. At the top of reactor coaxially located flat source of inductively coupled plasma 220 mm in diameter as a four-entry spiral, operating at a frequency of 13.56 MHz, ring-type gas distribution system outputs are directed to the plasma generation area, Helmholtz coil and cooled substrate holder are located in working chamber bottom.

General criteria in uniformity deposition of diamond-like carbon coating by CVD method with usage of the flat inductively coupled plasma source are

generating of high-density plasma in space between the plane antenna system and working surface of substrate holder, and distribution of gas stream in plasma forming area. There was established, that generating of plasma with uniform distribution of the charged particles with working pressure below $10^{-1}$ Pa depend on configuration and value of magnetic induction in a gap between plasma forming area and substrate holder.

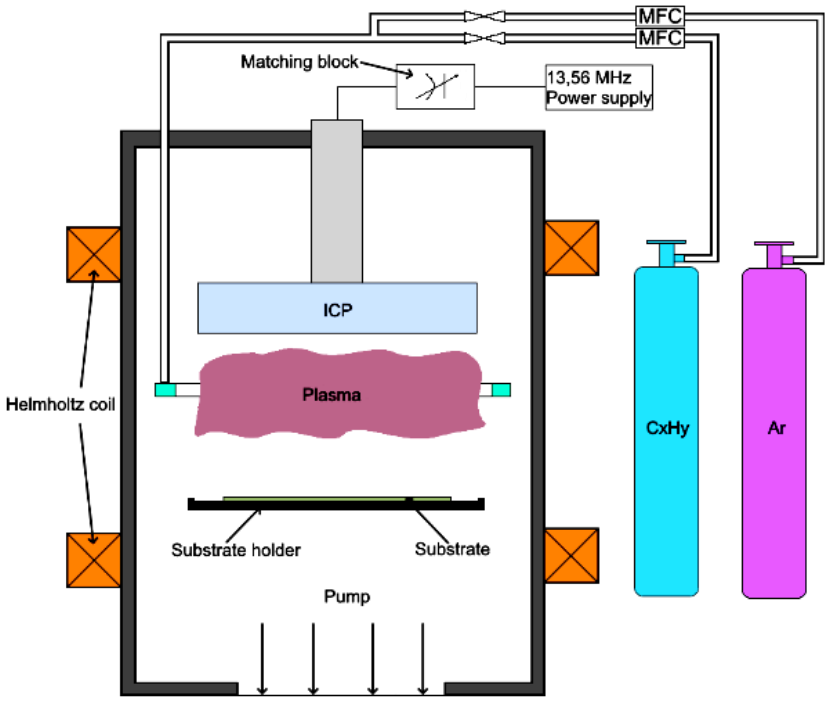



Figure 1 – Schematic image of deposition reactor DLC

Axial magnetic field in reactor was formed by two solenoids included in a coordinated manner as a Helmholtz coil. The source of inductively coupled plasma in reactor without outer magnetic field provides sustainable plasma generation at pressure above $5\times10^{-1}$ Pa, such as reflected power exceed 1%. Reduction of working pressure perhaps in the presence of axial magnetic field, which increases electron "lifetime" of plasma and, therefore, ionization probability.

For carrying out research influences of magnetic field on range of working pressure pursue initialization charge at 1 Pa pressure. Then, working pressure was reduced with decrease working gas consumption unless reflected RF power did not begin to grow so that matching system no longer allowed to compensate for it. There were established, that axial magnetic field at 1 mT inductivity optimally provides plasma generation of inductive charge with working parameters: working pressure in reactor – $6\times10^{-2}$ Pa, working gas consumption (argon) – 10 sccm, discharge power 1000 W, reflected power exceed 1%. With further pressure decrease in working chamber observed

increase of reflected power above 1%, and as a result, inductive discharge generation stopped at the pressure in working chamber below $4.7\times10^{-2}$ Pa.

From technological side for uniformity deposition of layers by HDP-CVD method, gas distribution could be laminar at substrate holder surface and uniform distributed at the gap between substrate holder and plasma source. From the other side, distribution film-forming precursor (acetylene) has a decisive influence on the condensation conditions and distribution of charged particles, radicals, neutral atoms and molecules in plasma-forming area, which determines geometric plasma borders [1]. Considering the above and reactor geometric parameters, it is critical to deliver working precursor to the center of plasma-forming area outside plasma source shield. Then, a two-stage gas distribution system with uniform gas supply around the perimeter of the reactor with the direction of the gas stream into the central eddy currents formation area of the ICP plasma source inductor was developed. That position of gas distribution ensures laminar precursor flow over the surface of the substrate holder and its uniform distribution in a gap between substrate holder and the walls of working chamber, which provides DLC coating with defined structure and uniformity in thickness.

To estimate the non-uniformity deposition of DLC was experimental researches on deposition of coatings with different working precursor consumption were performed. The criteria for uniform deposition was the non-uniformity below ±10%. In Fig. 2 is shown diameter of uniform DLC film deposition dependence on working precursor consumption is shown.

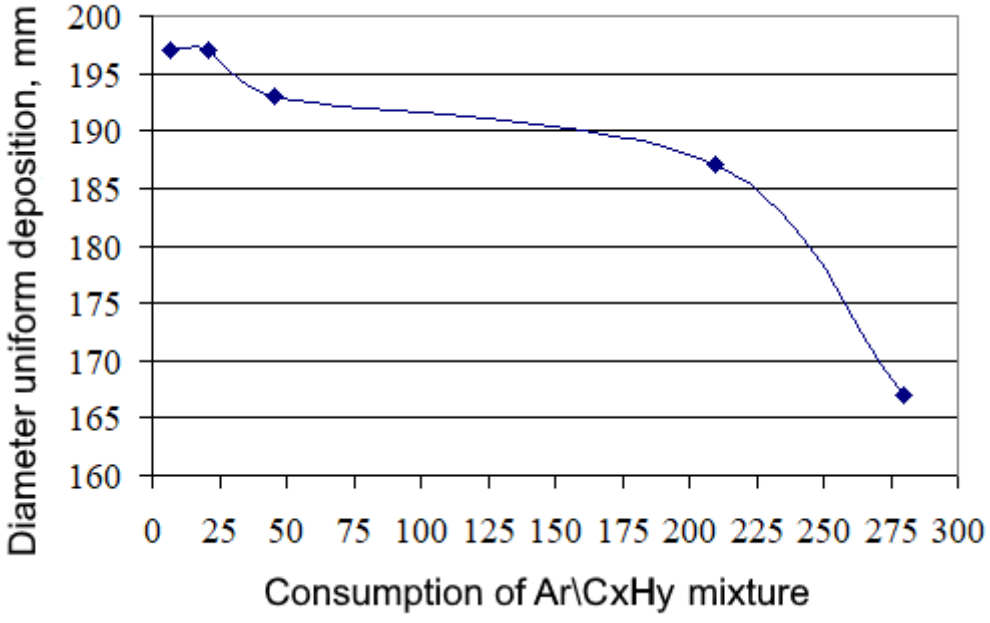



Figure 2 – Dependence of DLC coating uniform deposition diameter on working precursor consumption

**Conclusions.** The presence of an external axial magnetic field with a value of 1 mT allows to increase the lifetime of the electrons and reduce the operating pressure of the inductively coupled plasma source. This permits the process to be carried out without additional heating and, at the same time, to increase sp3-hybridization composition into created coatings. Deposited DLC films with high thickness uniformity on a substrate diameter up to 190 mm is possible at a total working precursor consumption not exceeding 150 sccm. Using Raman spectroscopy and friction coefficient determination by atomic force microscope deposited DLC films were studied. Based on the results of the I(D)/I(G) intensity peak ratio we can state, that the quantitative concentration of sp3-hybridization reaches up to 50%. The measured coefficient of friction is in the range of 0.03 - 0.08. This indicates that we have DLC coatings with the ta-C:H structure, which is mentioned by author [2, 3].

## References

1. Chen F. Introduction to Plasma Physics, (1987) 13-27.
2. Robertson J., O'Reilly E.P. Electronic and atomic structure of amorphous carbon // Phys. Rev. B. 1987. V.35. No.6. P. 2946-2957.
3. Tay B.K., Shi X., Liu E.J., Tan H.S., Cheah L.K. Effects of substrate temperature on the properties of tetrahe*D*ral amorphous carbon films // Thin Soli*D* Films. 1999. V.346. No.1-2. P. 155-161.

# THERMOSENSITIVE PROPERTIES OF VANADIUM OXIDE FILMS DEPOSITED BY PULSED DC REACTIVE MAGNETRON SPUTTERING

A. Zanka[1], D. Kotov[2], N. Leonovich[2], V. Kolos[1], N. Kovalchuk[1]

[1]JSC «INTEGRAL» - Holding Management Company, 121A, Kazintsa I.P. Str., Minsk, 220108, Republic of Belarus, zanko.andrei@inbox.ru

[2]Belarusian State University of Informatics and Radioelectronics, 6 Petrusya Brovki str. Minsk, Republic of Belarus, kotov@bsuir.by

**Abstract**

It was studied the structure and electrical properties of vanadium oxide films deposited by pulsed DC reactive magnetron sputtering. We have studied the change in the temperature coefficient of resistance (TCR) and resistivity of vanadium oxide films depending on their production conditions. The structure of the sputter deposited films was studied by the Raman spectroscopy. As a result of the research, thermoresistive layers with TCR = 2.1 %/℃ were obtained with a resistivity of 2.8 Ohm·cm.

**Introduction**

Vanadium oxide thin films ($VO_x$) are used in microbolometers as a thermosensitive resistor due to their high temperature coefficient of resistance (TCR) with a resistivity of $\rho \approx$ from 0.1 to 10 Ohm·cm and low noise equivalent differential temperature (NEDT). Vanadium oxide has many phase states that have different electrophysical parameters, which requires fine-tuning of the sputtering process to obtain films with specified electrophysical parameters. Microbolometers typically use $VO_x$ layers based on a mixture of several phases, in which there is no hysteresis dependence of resistivity on temperature in the range from -50 to 100 °C.

**Experimental details**

In our research paper, we obtained $VO_x$ films by pulsed reactive magnetron sputtering using the UHVPVD equipment (SysKey Technology Co., Taiwan) from a vanadium target (4 inches, 99.5% purity). For sputtering $VO_x$ at a power of 300 W in a mixture of argon and oxygen, a switching power supply with a fixed frequency of negative pulses of 100 kHz and a duration of positive pulses of 1 microsecond (+75 V) (Pinnacle™ Plus + 1.5 kW Advanced Energy Inc) was used. Silicon wafers with silicon nitride were used as a dielectric substrate. The substrates were heated to 50 °C. Before thin film deposition, the chamber was pumped to a pre-pressure of $5x10^{-6}$ Pa. The process pressure in the chamber was set to 0.6 Pa by mixing the process gases. To clean the surface of the target, its preliminary sputtering is carried out on the shutter for 3 minutes in an atmosphere of pure argon. Then a mixture of argon and oxygen was supplied through an

annular gas distributor to the plasma formation area above the target surface with a total flow rate of 12 sccm. To determine the ρ(T) and TCR $VO_x$ film, a four-probe measurement method was used on the SF P2000 equipment (Flex T&M, Taiwan) in the temperature range from 25 to 85 °C. The phase composition of $VO_x$ was studied by Raman spectroscopy using a Confotec® NR500 microscope (SOL Instruments, Republic of Belarus).

**Results and discussion**

Subsequently, the resistivity, TCR and phase composition of $VO_x$ were compared with the cathode current of the vanadium target during sputtering.

For reactive magnetron sputtering, as a rule, the presence of a hysteresis dependence of the current and/or voltage of the cathode on $O_2$ is typical. Figure 1 shows the hysteresis dependence of the cathode current on the percentage of oxygen $K(O_2)$ in a mixture of $Ar/O_2$ gases at a fixed power. The arrows show the increase and decrease of oxygen in the chamber.

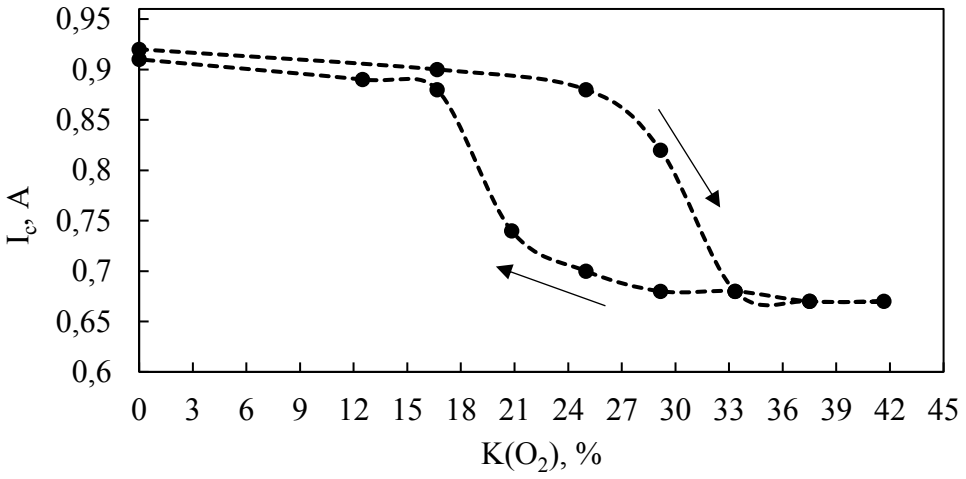



Figure 1. Dependence of the cathode current on the percentage of oxygen in the $Ar/O_2$ gas mixture

When $K(O_2)$ is up to 25 %, the cathode current decreases slightly from 0.91 to 0.88 A. When $K(O_2)$ is more than 25 %, the current drops sharply to 0.68 A and practically does not decrease in the future. With an increase in $K(O_2)$ in the chamber, the vanadium target passes from the metallic state (low degree of oxidation) through the transition zone to the oxidized state (high degree of oxidation). When $K(O_2)$ decreases, the cathode current slowly increases with the formation of a hysteresis dependence of the cathode current on $K(O_2)$, and is practically compared with the initial values when $K(O_2)$ is 18 %. This state can be explained by the different rates of simultaneous sputtering and oxidation of the target, the change in the behavior of the electron output from the metallic to the

oxidized target, which in turn leads to a change in the cathode impedance, current and its voltage.

Such cathode behavior directly affects the resistivity and TCR $VO_x$ film (Fig.2). The most suitable films for microbolometers according to electrophysical parameters are obtained when the values of $K(O_2)$ are in the hysteresis range from 23 to 28 %. In this mode of $VO_x$ film deposition, TCR is from 2 to 2.1 at resistivity is from 2.3 to 2.8 Ohm cm. When the surface of the vanadium target is close to the extreme states (to metallic $K(O_2) < 23$ % or coated with oxide on a significant part $K(O_2) > 28$ %, the films have a low TCR (<2%/°C) at low (< 0.1 Ohm cm) or high (>10 Ohm cm) resistivity. The decrease in TCR to 1.5 %/°C when $K(O_2) = 33$ % is apparently due to the formation of transition phases close to the metallic type of conductivity, which have a low activation energy and, accordingly, TCR. All the films obtained had a hysteresis dependence of resistivity on temperature.

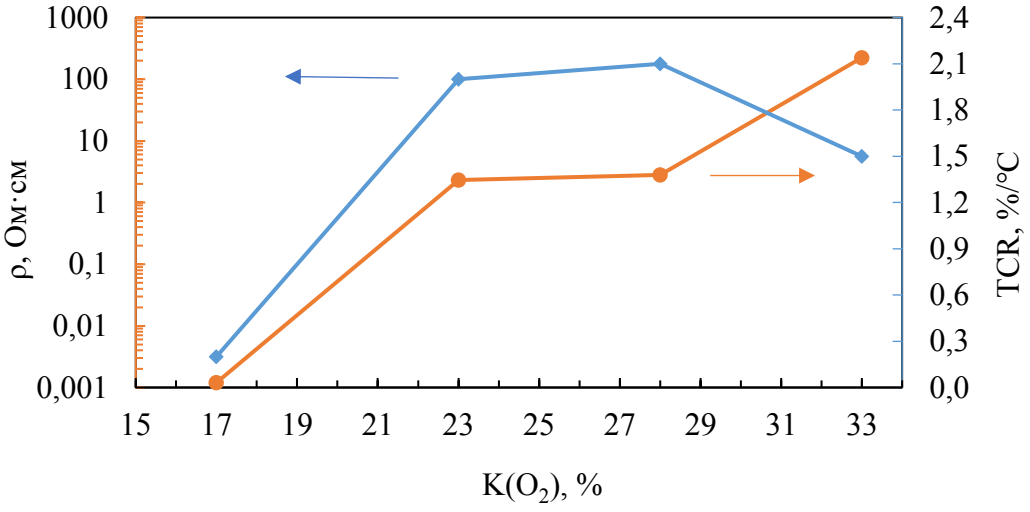



Figure 2. Dependence of resistivity and TCR on $K(O_2)$

Figure 3 shows the Raman spectra of samples with $VO_x$ films deposited when $K(O_2)$ is 23, 28 and 33 %, respectively. It can be seen from the obtained spectra that the films have a mixed phase composition, with typical Raman shifts for $VO_2$,$V_2O_5$ and shifts that are difficult to interpret, which can be attributed both to these phases and to transition oxides ($V_3O_7$, $V_4O_9$, $V_6O_{13}$, etc.); on the spectra such shifts are indicated as $VO_x$ (137, 301, 750-820 $cm^{-1}$). With an increase in $K(O_2)$, the intensity of typical shifts for the phase $V_2O_5$ increases (159, 266, 702, 942-1006 $cm^{-1}$), which indicates an increase in the phase $V_2O_5$ in the film, which has a greater resistivity, which is consistent with the data in Fig.2. The $VO_2$ phase can be found in several polymorphic modifications of $VO_2$ (M1), $VO_2$ (M2), $VO_2$ (R), $VO_2$ (A), $VO_2$ (B), etc. Such modifications differ in a different spatial

group and we found Raman shifts typical for $VO_2$ (M1) 618 $cm^{-1}$, $VO_2$ (M2) 229, 435 $cm^{-1}$ and $VO_2$ (B) 670, 880 $cm^{-1}$[1]. Only the phase with VO2 (M1) [2] has a hysteresis character ρ (T) in the temperature range under consideration, where the phase transition occurs at the level of 67 °C. Although we found the presence of the $VO_2$ phase (M1) in the films, but presumably, due to its low concentration, hysteresis is not observed.

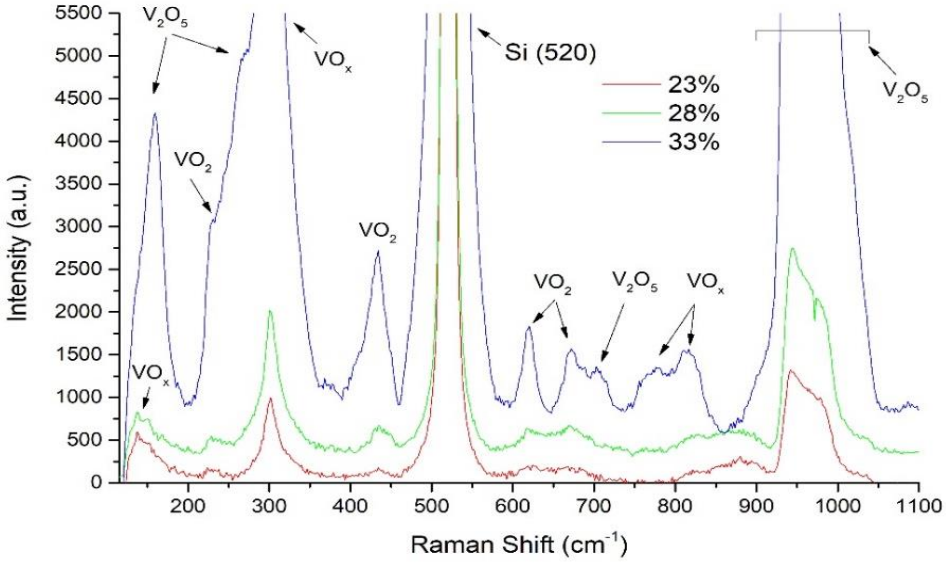



Figure 3. Raman spectrum of $VO_x/Si_3N_4/Si$

**Conclusions**

As a result of the studies carried out, thermoresistive layers based on a mixture of several phases of $VO_x$ with TCR 2.1%/°C with a resistivity of 2.8 Ohm·cm by a method of reactive pulsed magnetron sputtering were obtained, which allows them to be used in the production of microbolometer.

**References**

1. **Shvets P.**, Dikaya O., Maksimova K., Goikhman A. A review of Raman spectroscopy of vanadium oxides. Journal of Raman spectroscopy. 2019; DOI: 10.1002/jrs.5616.

2. **Shinbuhm Lee,** Ilia N. Ivanov, Jong K. Keum & Ho Nyung Lee, Epitaxial stabilization and phase instability of $VO_2$ polymorphs. 2016; DOI: 10.1038/srep19621.

# PLASMA TREATMENT AND SYNTHESIS OF POWDERS FOR ADDITIVE MANUFACTURING

A.Kh. Gilmutdinov[1], K.Yu. Nagulin[2], I.V. Tsivilskiy[3]

[1] Kazan National Research Technical University named after A.N. Tupolev, Dept. of Laser and Additive Technologies, albert.gilmutdinov@kai.ru
[2] Kazan National Research Technical University named after A.N. Tupolev, Dept. of Laser and Additive Technologies, knagulin@mail.ru
[3] Kazan National Research Technical University named after A.N. Tupolev, Dept. of Laser and Additive Technologies, icivv@mail.ru

Today, the main way to control the physicochemical and mechanical properties of 3-D printed material is to select the appropriate chemical composition of the powder used. This project proposes a fundamentally different, non-chemical, method for modifying the basic characteristics of the initial powder. It consists in the synthesis of new structure-gradient powders of two types in thermal plasma:

a) micro-reinforced composite powders, in which, due to plasma-chemical reactions, the base particle (alloy, ceramics) is impregnated with another metal in the interdendritic space,

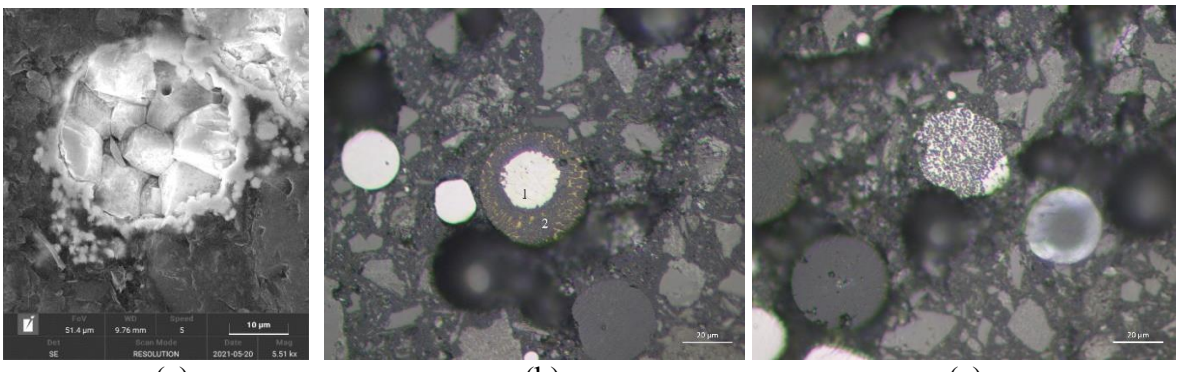
b) powders with a core-shell spatial structure.

As specific materials, the technology of metallization of ceramic microparticles will be comprehensively studied and developed when they are impregnated in plasma or covered with a metal shell. In this case, such a structural-gradient cermet powder has both the properties of a core (ceramics, provides strength) and a shell (metal, provides plasticity). Accordingly, the material printed from such a structurally graded composite powder will have characteristics that are difficult to match: it will be both strong and ductile. By selecting pairs "core-shell", "base-micro-reinforcement", as well as changing their geometric dimensions (diameter of the core, thickness of the shell), it is possible to vary widely the physicomechanical properties of the material printed from such powder compositions. In fact, we get materials in which the composite structure appears at the micro level, at the level of a single particle.

A laboratory system based on a radio-frequency (5.2 MHz) quartz plasmatron with a power of up to 40 kW was used for the plasma treatment of powder materials [1]. The argon (99,993% pure) was used as a plasma-forming, protective and transport gas.

Preliminary experiments on the synthesis of composite metal-ceramic particles in ICP have been carried out. Plasma treatment of a mixture of spheroidized particles of corundum powder and PTOM-1 titanium powder was carried out. According to calculations, in the process of passing the particles of

the initial materials through the plasma torch, their melting and mutual collisions occur due to the vortex structure of the flow. Particles of titanium, due to their small size, melt completely and partially evaporate. For corundum, which has a higher melting point (2050 ° C versus 1668 ° C for titanium), only particle melting prevails. When the molten particles collide with each other, titanium penetrates into the thickness of the corundum particle with the formation of a composite material. Even if the corundum particle did not have time to melt, the molten titanium fills the space between the microcrystals of the polycrystalline structure of the corundum particle. Fig. 1 shows an image of a thin section of a corundum particle in polycrystalline form. The SEM image clearly shows individual grains of corundum polycrystal that make up the particle under study. The cooling rate of such a particle was most likely slow, which made it possible to realize the growth of large crystals.




(a) (b) (c)

Fig.1. a - SEM image of a thin section of a corundum particle after plasma spheroidization; b, c - SEM image of a thin section of a corundum-titanium composite particle: 1 - titanium; 2- corundum.

Depending on the internal structure of corundum particles, two main types of corundum-titanium composite particles can be obtained. For corundum particles in amorphous form, a drop of molten titanium penetrating inside retains its structure and a clear boundary. In this case, we get a composite particle of the core-shell type, as shown in Fig. 1 b. Depending on the synthesis conditions, the composite particles have different sizes and locations of the titanium core. Also, on thin sections shown in Fig. 1b, a slight dispersion of titanium is observed in the subsurface layer of particles in the form of thin veins. In the case of a clearly expressed polycrystalline structure of a corundum particle, titanium penetrates into its thickness along the boundaries between grains, and a dispersed distribution of titanium over the entire volume of the corundum particle is obtained. Examples of such composite particles are shown in Fig. 1 c.

A mathematical model of the process of plasma treatment and synthesis of materials was developed at two scale levels. Macroscale modeling is performed

in Matlab. A self-written finite-difference solver of differential equations describing the evolution of discrete particles in the condensation chamber of the plasma reactor has been implemented. The algorithm includes solving the equations of particle transport, their phase transitions, as well as vapor dynamics. The influence of additional effects of Brownian force and thermophoresis is taken into account.

The mesoscale model is implemented in Python, and the particle with the bulk gas is considered as a continuous binary mixture moving in accordance with the system of Navier–Stokes equations. The source term includes additional accelerations caused by forces of gravity, thermophoresis, convective flows and surface tension. The spheroidization, phase transitions, coagulation of several particles phenomena, as well as the formation of composite core–shell particles with coating films are considered.

The combined use of models on macro- and mesoscale with a mutual transition between scales according to the boundary conditions will make it possible to obtain a coupled multiscale model of plasma synthesis in ICP of multicomponent particles, to evaluate the characteristics of the final powder material based on the input parameters of the reactor and the properties of the feedstock.

A series of computational experiments were carried out to determine the trajectories of motion powder particles motion in the condensation chamber with known distribution fields of temperature, pressure, gas flow velocity. Particles of powder of nickel with and aluminum oxide are considered. The ICP parameters under consideration are taken from [2].

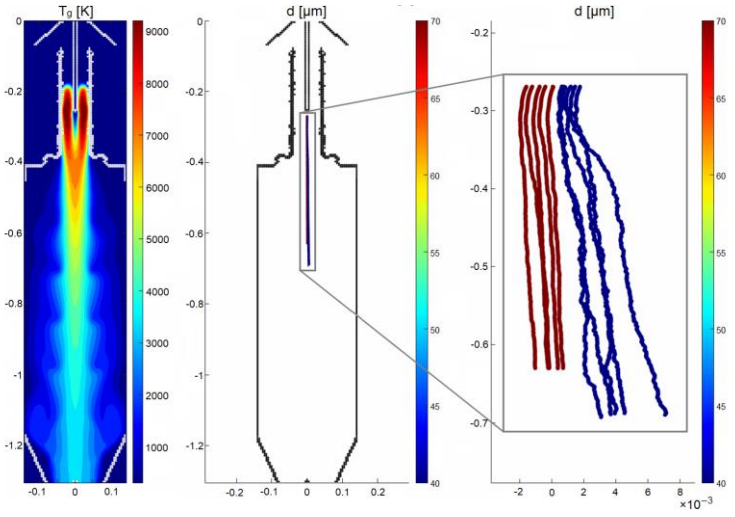



Fig. 2. Plasma temperature field $T_g$ and particles trajectories at different scales. The color of the graphs corresponds to the particle diameter

In fig. 2 shows the results of modeling the motion of the particles taking

into account the equation of motion, Brownian motion, and thermophoresis. The deviation of the particles from the initial trajectory of the carrying gas flow is noticeable. This is due to the motion of particles in a sharp temperature gradient, while small particles deviate more heavily due to less inertia.

At the mesoscale, the separate nickel particles of irregular shape are considered (fig. 3). Under the action of the surface tension force, the particles become more rounded. The mode of a flow around a particle in a downward hot gas flow is simulated. The driving force is caused by a pressure gradient that is directly proportional to temperature. The particles coagulate and then begin to spheroidize as a single particle. According to the same principle, heterogeneous condensation occurs, when the microdroplets formed from the vapor move to the colder surface of the core particle, thereby forming a uniform film coating.

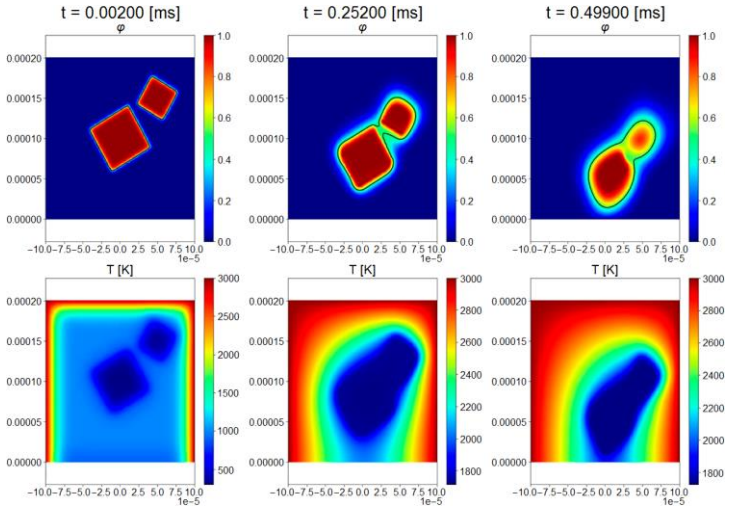



Fig. 3. The phase and temperature fields during coagulation of two particles

**Acknowledgements**. This work was supported by the Ministry of Education and Science of the Russian Federation State Order No. 075-03-2020-051 (fzsu-2020-0020).

## References

1. **Nagulin K., Nazarov R., Efimochkin I., Gilmutdinov A.** Optimization of radio-frequency plasma parameters for spheroidization of zirconium oxide powders, Surface & Coatings Technology (2019), https://doi.org/10.1016/j.surfcoat.2019.125196
2. **Tsivilskiy I. V.** et al. An experimentally verified three-dimensional non-stationary fluid model of unloaded atmospheric pressure inductively coupled plasmas, Journal of Physics D: Applied Physics, 53 (45) (2020). http://dx.doi.org/10.1088/1361-6463/aba45f

# PLASMOCHEMICAL RECOVERY OF POWDER MATERIALS FOR ADDITIVE MANUFACTURING

A.Kh. Gilmutdinov[1], K.Yu. Nagulin[2], A.A. Terentiev[3]

[1] Kazan National Research Technical University named after A.N. Tupolev, Dept. of Laser and Additive Technologies, albert.gilmutdinov@kai.ru
[2] Kazan National Research Technical University named after A.N. Tupolev, Dept. of Laser and Additive Technologies, knagulin@mail.ru
[3] Kazan National Research Technical University named after A.N. Tupolev, Dept. of Laser and Additive Technologies, aaterentev@kai.ru

The most important priority in the technological development of all advanced countries is metal-powder additive technologies, which form the basis of an actively emerging new technological order. The applications of these technologies demonstrate exponential growth in almost all sectors of the modern economy: engine-aircraft-ship-car and rocket building, energy, medicine (implants), etc. One of the key problems hindering the development of additive manufacturing in Russia is the lack of high-quality powder materials and their compositions for layer-by-layer synthesis of products.

During the process of 3D printing in SLM, DLMS, DMD machines the powder gradually degrades - the chemical composition and morphological characteristic are changing. The powder must dispose a maximum of 10 cycles of use. It was shown [1] that every printing cycle increases the oxygen content in the powder particles. Such spent powder can be recovered by treatment in inductively coupled plasma [2]. When the powder particles pass through the argon plasma, the thermomechanical detachment of the satellites, the particle spheroidization, their degassing, and the restoration of oxide films on the surface occur. Obviously, it makes economic sense to recover only expensive powders, the cost of which exceeds the cost of the recovery process. These include most powders of alloys based on iron, chromium and nickel used in aircraft and engine building. Figure 1 shows SEM images of defective particles of powders of Hastelloy X alloys (a), heat-resistant alloys EP648 (b), V3K (c), ZhS32 (d) that are widely being used in 3D printing systems. It can be seen (Fig.1) that the waste powders are characterized by an increased number of satellites and a non-spherical particle shape, which can lead to 3D printing defects.

The objective of this study is developing a technology for the recovery of spent powders in inductively coupled plasma.

A laboratory system based on a radio-frequency (5.2 MHz) quartz plasmatron with a power of up to 40 kW was used for the plasma treatment of powder materials [3]. The argon (99,993% pure) was used as a plasma-forming, protective and transport gas.

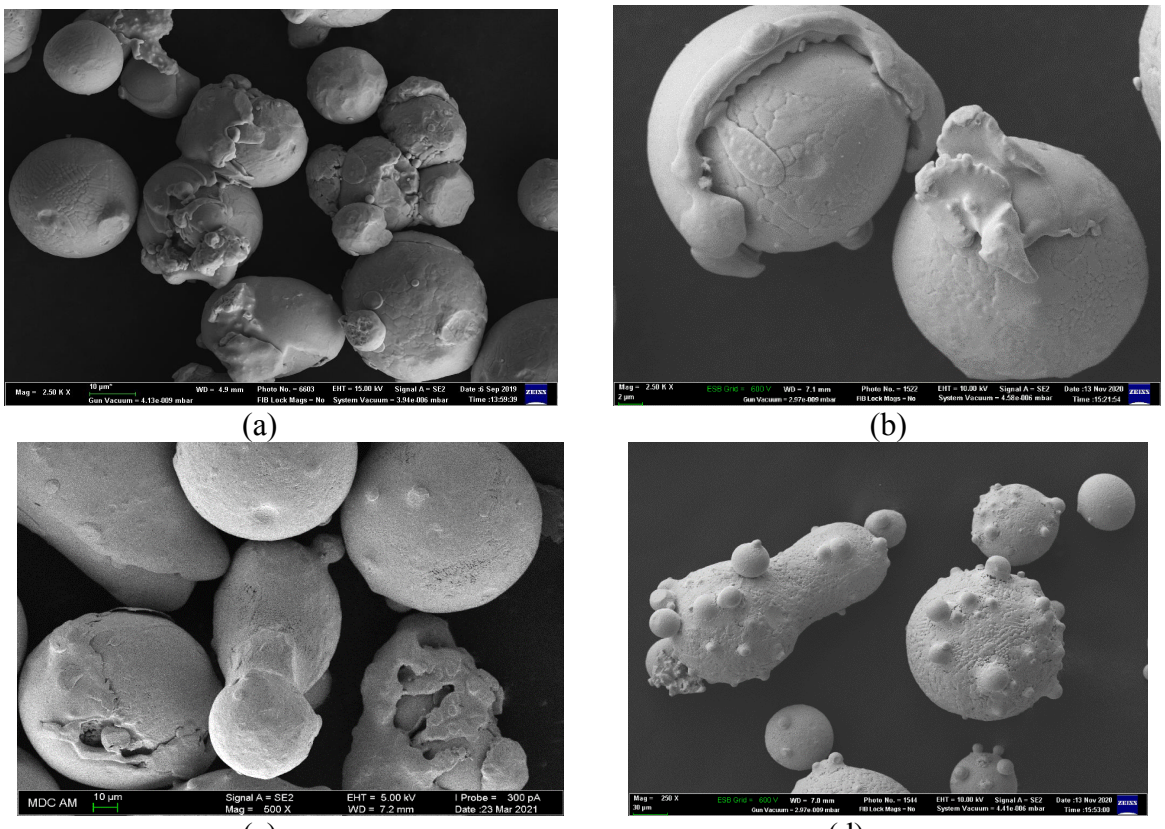
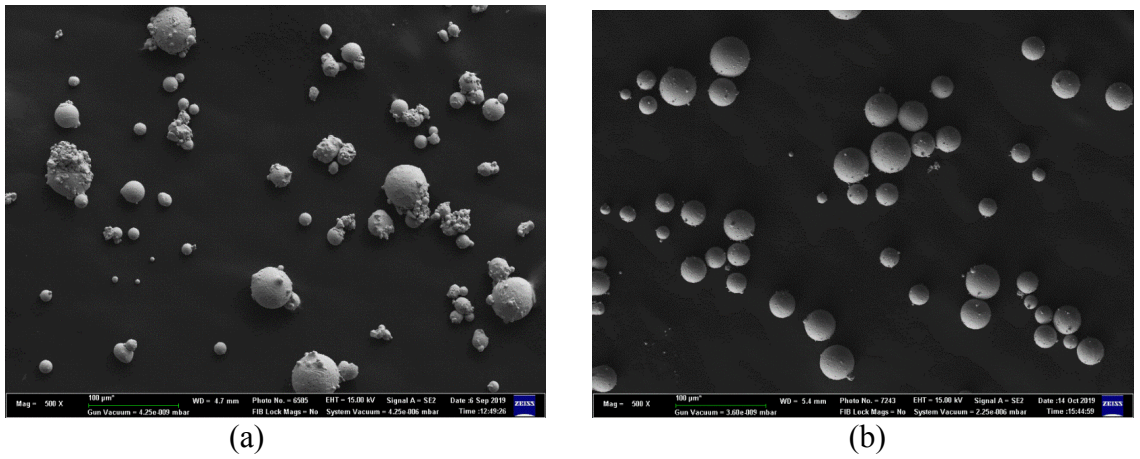



Fig. 1. SEM images of defective particles of powders of Hastelloy X alloys (a), heat-resistant alloys EP648 (b), V3K (c), ZhS32 (d)

The results of reduction in inductively coupled plasma of spent powder materials are presented in Fig.2. It can be seen that the particles of the reduced powder have acquired a spherical shape and are free from satellites. The analysis of the gross chemical composition by RFA showed compliance with the standard of the chemical composition of the recovered powder for all examples.



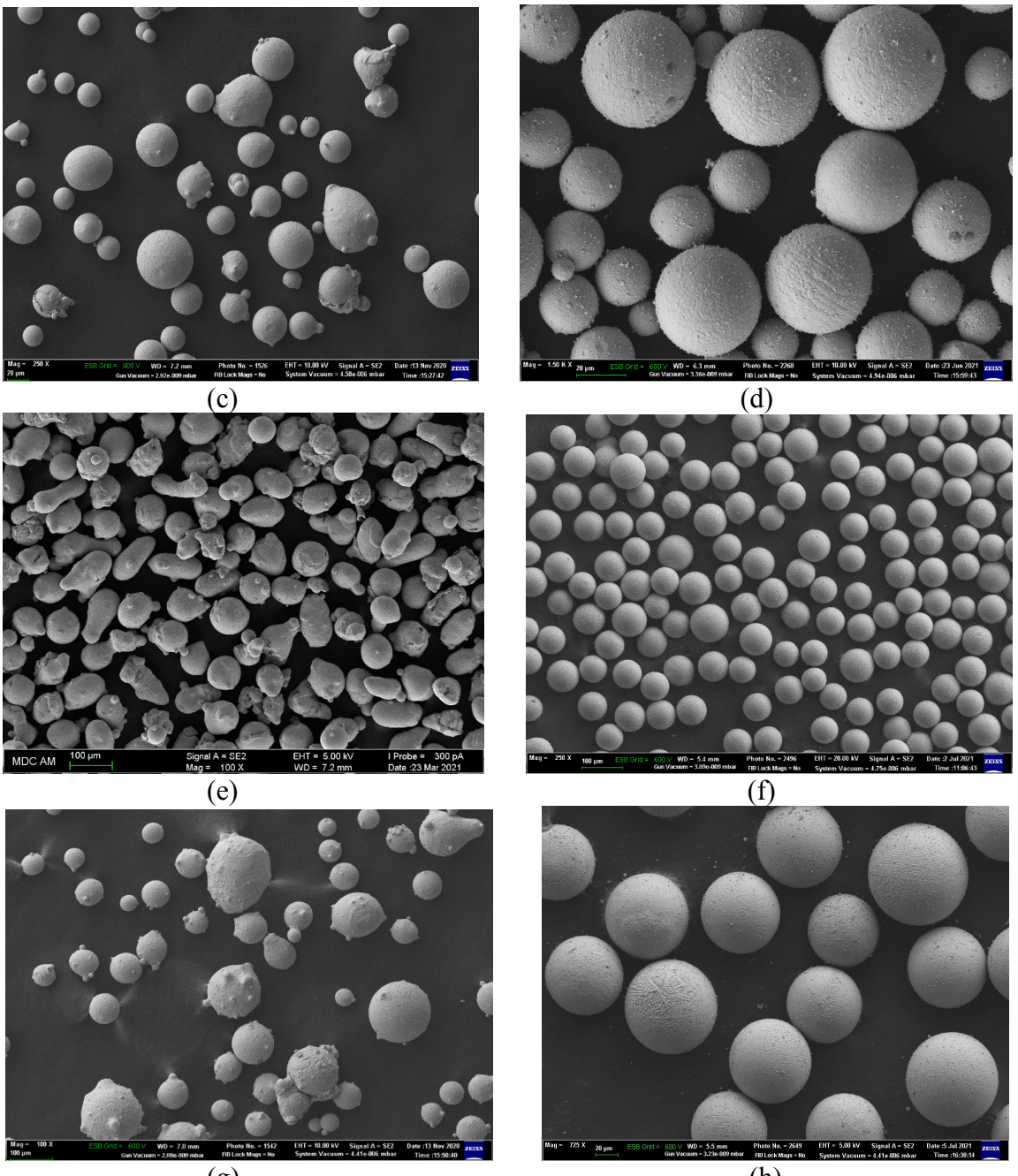



Fig. 2. SEM images of particles processed in 3D printing systems (left column) and recovered in inductively coupled plasma (right column) powders of Hastelloy X alloys (a, b), heat-resistant alloys EP648 (c, d), V3K (e, f), ZhS32 (g, h)

To exclude the burnout of alloying additives during the plasma treatment of the powder, the optimal operating mode of the plasma installation for each alloy was preliminarily selected with the obligatory real-time control of the plasma radiation spectra at the moment the powder was fed into the plasma torch. The operating mode was chosen in which the radiation on the spectral lines of the elements that make up the alloy was minimal. Also, such optimization makes it

possible to exclude the ingress of powder particles into the vortex zone of the plasmatron [4] and provides uniform processing conditions for all particles.

Tensile test specimens were printed from new, used, and reclaimed Hastelloy X powder by DMD on an INSSTEK Mini 3D machine using a Multi Actuator Test System Model Bi-04-CP-310 electronic tensile testing machine. The results of static tests of three groups of samples (new 1, used 2 and recovered powder 3) of Hastelloy X alloy are shown in the Table 1.

Table 1. Results of static tests of Hastelloy X specimens

| Sample | Maximum stress, MPa | Modulus of elasticity, GPa | Maximum deformation, % |
|---|---|---|---|
| 1 | 732 | 160 | 20 |
| 2 | 774 | 168 | 12 |
| 3 | 795 | 169 | 20 |

According to the results of static tests, it can be seen that for the used powder, an almost twofold reduction in the maximum deformation is observed - the samples become brittle. After plasma treatment of the powder, the strength of the samples returns to its original value.

Thus, the processing of powders used in 3D printing systems will make it possible to use them for printing working products without changing the physical and chemical properties of the material and the mechanical characteristics of the products.

**Acknowledgements**. This work was supported by the Ministry of Education and Science of the Russian Federation State Order No. 075-03-2020-051 (fzsu-2020-0020).

## References

1. **Samant R., Lewis B.** Metal Powder Recycling and Reconditioning in Additive Manufacturing. EWI: Columbus, OH, USA. – 2017.
2. **Bulos M.I.** Thermal Plasma Processing, IEEE Transactions on Plasma Science, 1991, V. 19, N. 6, pp. 1078-1089
3. **Nagulin K., Nazarov R., Efimochkin I., Gilmutdinov A.** Optimization of radio-frequency plasma parameters for spheroidization of zirconium oxide powders, Surface & Coatings Technology (2019), https://doi.org/10.1016/j.surfcoat.2019.125196
4. **Voronov, M., Tsivilskiy, I., Nazarov, R., Nagulin, K., Gilmutdinov, A.** Force-based analysis of vortices in atmospheric pressure ICPs, Plasma Sources Sci. Technol., 2018, DOI: 10.1088/1361-6595/aaef1c

# ELECTROLYTE-PLASMA POST-TREATMENT OF THE SURFACE OF ADDITIVE MANUFACTURING PRODUCTS

A.Kh.Gilmutdinov[1], K.Yu.Nagulin[2], A.A.Terentiev[3]

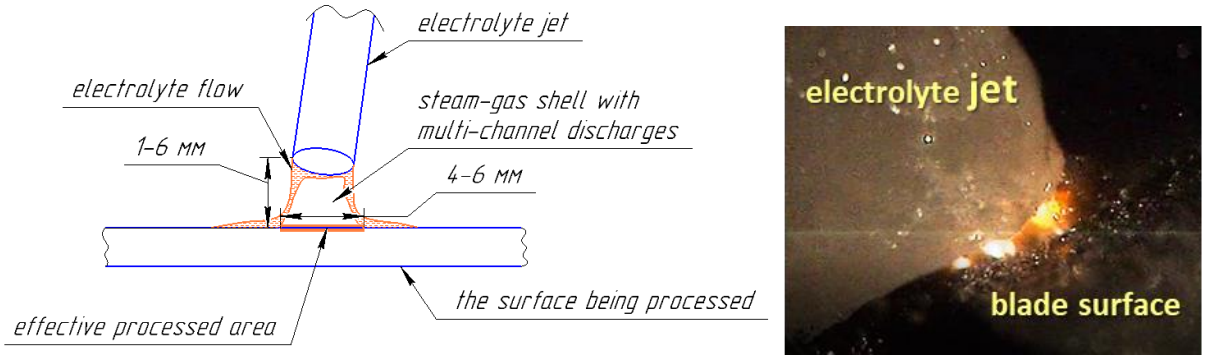
[1] Kazan National Research Technical University named after A.N. Tupolev, Dept. of Laser and Additive Technologies, albert.gilmutdinov@kai.ru
[2] Kazan National Research Technical University named after A.N. Tupolev, Dept. of Laser and Additive Technologies, knagulin@mail.ru
[3] Kazan National Research Technical University named after A.N. Tupolev, Dept. of Laser and Additive Technologies, aaterentev@kai.ru

All the additive manufacturing technologies based on metal powders produce items with increased roughness. The trigger for increased roughness is the principle of producing the item, which is being printed by layers of metal powder that are sintered together with sizes from 20 to 100 microns. In addition to the size of the powder particles, the surface roughness is also being affected by the geometry of the product, the strategy of its construction and the spatial orientation of the product in the working area of the 3D machine. As a result, the surface roughness of the same product can vary within fairly wide limits (Ra from 10 to 100 μm). In aircraft and gas turbine engine building, as well as in the field of medical instruments and implants, high surface roughness is unacceptable. Therefore, post-processing is necessary, the main purpose is to reduce the surface roughness of the product to acceptable values. There is a great variety of mechanical post post-processing methods (sandblasting, hydroabrasive processing, cryoblasting), chemical and electrochemical methods for polishing the surface of metal products. As for the electrochemical methods, the most popular are electrolytic plasma treatment [1] and polishing with a “dry” electrolyte [2-3]. The main problem for polishing additive manufacturing items is ones` complex surface geometry which complicates the polishing process. Therefore, there are certain limitations for electrolytic plasma treatment technology. Firstly, the shielding of half-open cavities and channels, as a result the potential in the shielded region is constant and an electric discharge does not occur inside. Secondly, inhomogeneities in the geometry of the part itself increase the electric field strength and intensify the process of substance removal. As a result, for instance, the edges of the blade are processed faster than its back or trough, which leads to a change of the geometry of the item.

In this regard, the purpose of the study was to develop the technology of jet dimensional electrolytic plasma treatment in order to treat the surface of complex-shaped products of additive manufacturing.

Unlike the traditional EPP method, which includes the polishing over the entire surface (The item is being immersed in an electrolyte bath [1]), the jet

EPP [4] polishing is carried out locally at the point where the electrolyte jet interacts with the metal surface, as shown in Fig. 1a. When an electrolyte jet hits the treated surface, the electrolyte rapidly heats up and boils up due to the electric current flowing through it. A vapor-gas shell is formed on the surface of the metal, and multichannel electric discharge occurs inside the shell (Fig. 1b). Figure 2 shows an oscillogram of the current of a typical jet discharge. The average value of the pulsed component of the discharge current is about 5-8 A, the constant component is 3A, the pulse frequency is tens and hundreds of kHz. Due to the high frequency of the pulses, the impact of the discharge on the surface in the processing zone occurs. A high-speed video recording shows that the discharges continuously move over the surface of the product, each time interact with a new point on the surface.




(a) (b)

Fig. 1. Scheme of the jet EPP process (a); Micrograph of the discharge (b)

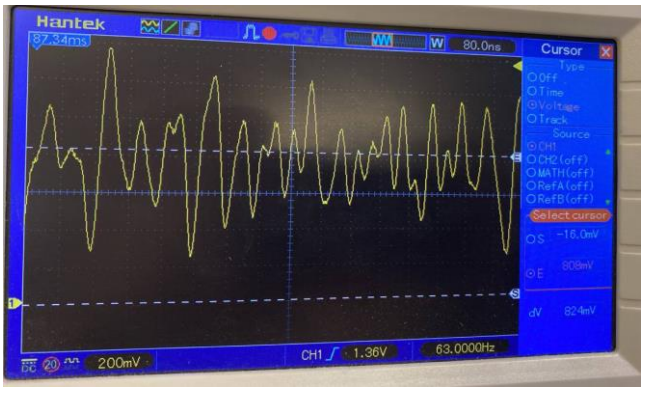
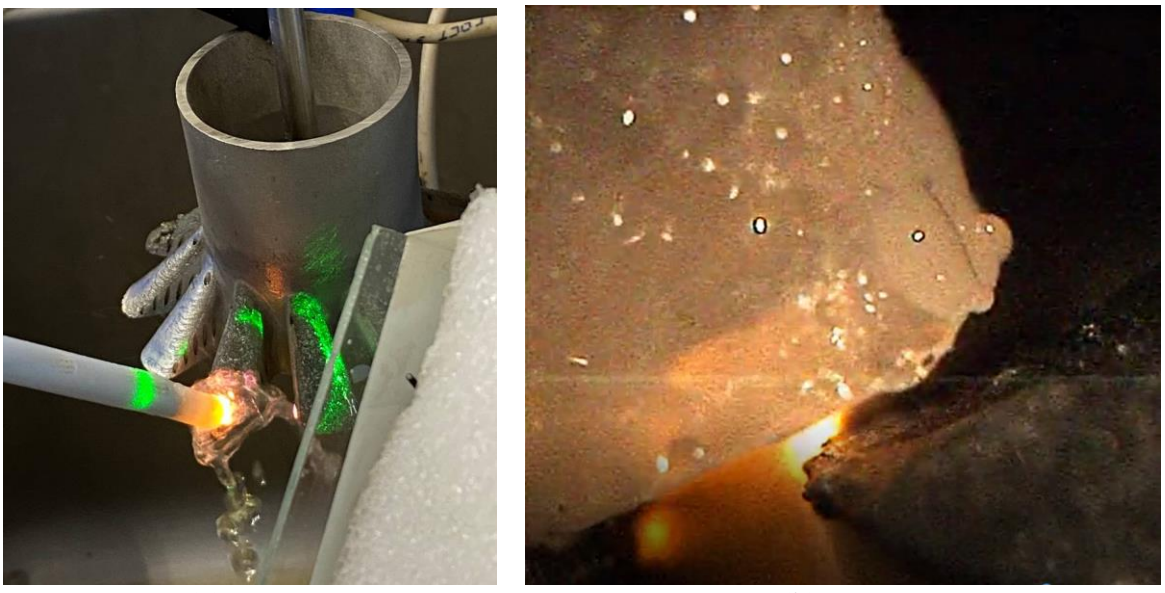



Fig. 2. Current waveform of a typical EPP jet discharge, measuring resistance 0.12 Ohm

The high intensity of EPP jet processing and the ease of its automation make it possible to use it for polishing large-sized parts, since in the classic submersible version of EPP, significant starting currents are required to form a vapor-gas shell (up to thousands of amperes). Another important advantage is the possibility of processing channels and cavities, since the shielding effect

does not work here. And, finally, the possibility of dimensional processing by implementing a local impact on the surface of the sample.

Let us consider examples of the use of jet EPP for polishing parts of gas turbine engines manufactured by additive methods. A Figure 3 shows a photograph of the combustion stabilizer processing process in the support area (a), as well as a frame from high-speed shooting of this process (b). Initial surface roughness Ra> 100 μm, after processing 2 μm. The jet EPP copes well with such large inhomogeneities even without prior sandblasting. Figure 3b shows the process of escaping of the large particle from the surface by discharge then the particle is being carried away by the electrolyte flow.



(a) (b)

Fig. 3. Jet EPP of the flame stabilizer surface in the support area (a) and a frame from high-speed video filming of this process (b)

Another characteristic example is swirlers made by additive methods. This part has many internal channels and cavities in which sintered powder can remain after 3D printing. Figure 4a shows a photograph of the surface of the inner annular chamber of the swirler, the roughness of which corresponds to Class 1a (Ra= 82.3 μm). After inkjet EPP (Fig. 4. b) the roughness of the same surface corresponds to Class 6v (Ra= 1.64 μm). Small channels in the space between the swirling blades are also processed well. These areas before (c) and after (c) processing are also shown in Fig.4. It should be noted that a whole swirler was processed and only then, to study its surface, it was cut on an electroerosive CNC machine.

Thus, the jet EPP method is well suited for post-processing the surface of additive manufacturing products, implementing automated dimensional processing of both external surfaces and cavities and channels. The achieved

level of roughness of the treated surface fully satisfies the requirements of aircraft engine building, and the locality of the impact ensures the preservation of the original geometry of the product.

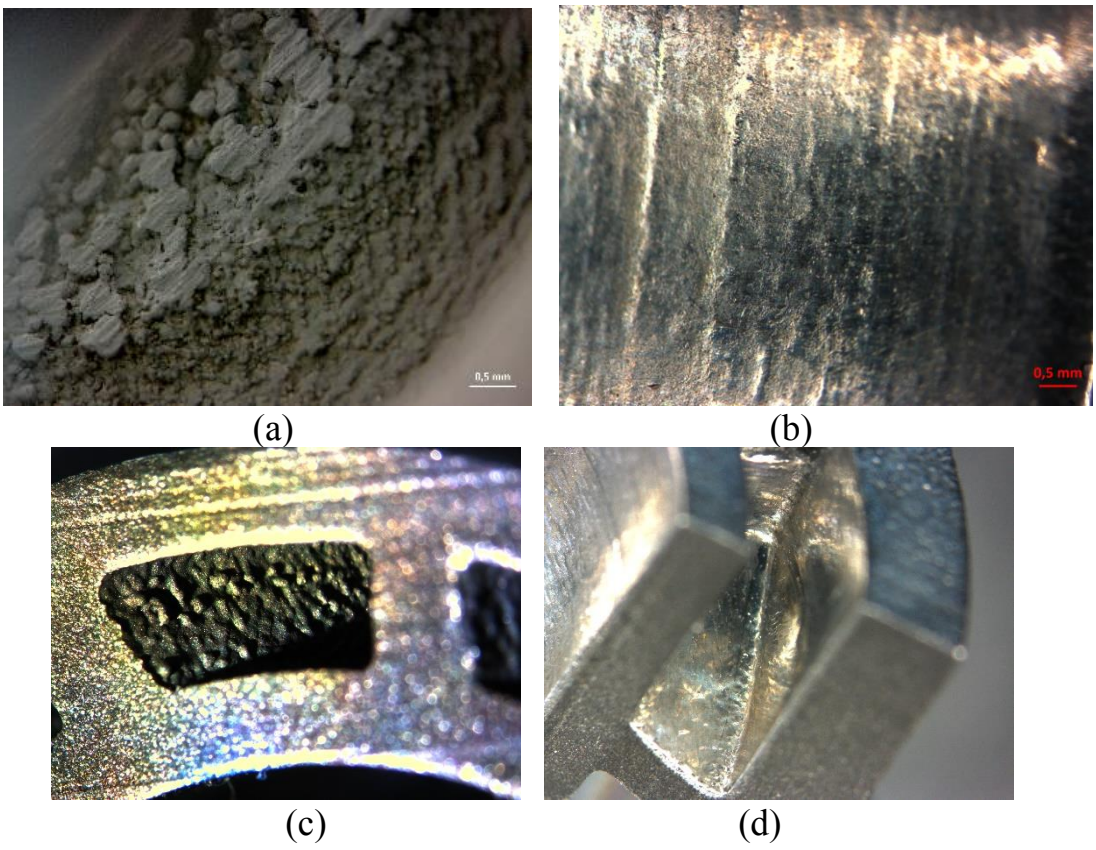



Fig. 4. Jet EPP of the fuel swirler surface before (a, c) and after processing (b, d)

**Acknowledgements**. This work was supported by the Ministry of Education and Science of the Russian Federation State Order No. 075-03-2020-051 (fzsu-2020-0020).

## References

1. **Kulikov I. S., Vashenko S. V., Kamenev A. Ya.** Electrolyte-plasma processing of materials. Minsk : Belarus. navuka, (2010).
2. Patent WO2017186992 A1 - Method for smoothing and polishing metals via ion transport by means of free solid bodies, and solid bodies for carrying out said method. Publ. 2017.11.02
3. Patent RU 2 730 306 C1 - Method for dry electropolishing of a patr. Publ. 2020.08.21
4. Kranhold Ch., Kröning O., Schulze H.-P., Herzig M. and Zeidler H. Investigation of stable boundary conditions for the Jet-electrolytic Plasma Polishing (Jet-ePP). Procedia CIRP 00 (2019) 000–000

# THE ROLE OF MONOLAYERS THICKNESSES RATIO FOR OXIDATION RESISTANCE OF AlN/$SiN_x$ MAGNETRON SPUTTERED COATINGS

I.A. Saladukhin[1], G. Abadias[2], V.V. Uglov[1], S.V. Zlotski[1]

[1] Faculty of Physics, Belarusian State University, 4 Nezavisimosti ave., 220030 Minsk, BELARUS, solodukhin@bsu.by
[2] Institut P', Université de Poitiers-CNRS-ENSMA, SP2MI, Téléport 2, F86962 Chasseneuil-Futuroscope, FRANCE, gregory.abadias@univ-poitiers.fr

## Introduction

Physically-vapor deposited transition metal nitride coatings based on MeN mononitrides of transition metal (Me=Ti, Zr, Cr, Al and others) are widely used in the industry as solid protective coatings. However, mononitride films often lose their protective role under harsh external conditions like friction, high temperatures, influence of corrosive media or irradiation. At the present, the multilayer film structures show considerable promise for improvement of the coatings operating abilities. In particular, multilayer coatings, where the layers of transition-metal nitrides alternate with layers of $SiN_x$, are characterized by the mutual insolubility of these two phases and display good thermal and oxidation stability and properties [1–3]. The presence of a large number of interfaces between layers and fine-grained structure are the reasons of it.

As it was shown in our previous studies, the resistance to high temperature oxidation of ZrN/$SiN_x$ and CrN/$SiN_x$ coatings depends on the thicknesses ratio of elementary layers [4]. In this work, the stability of AlN/$SiN_x$ coatings with different ratio of monolayers thicknesses upon annealing in air is investigated.

## Experimental details

AlN/$SiN_x$ multilayer coatings as well as reference AlN and $SiN_x$ monolithic reference films were deposited by reactive magnetron sputtering method in a high vacuum chamber (base pressure < $10^{-5}$ Pa) equipped with three confocal targets configuration and a cryogenic pump. Coatings were deposited on Si substrates at 300 °C. A constant bias voltage of −60 V was applied to the substrate during deposition. Al (99.9995% purity) and $Si_3N_4$ (99.99% purity) targets were used under Ar+$N_2$ plasma discharges at constant power mode. The Al target was operated in magnetically unbalanced configuration using a DC power supply, while a RF power supply was employed for the $Si_3N_4$ target in balanced mode. The Ar/$N_2$ flow ratio was optimized to obtain stoichiometric nitrogen content in the coatings based on earlier results. AlN/$SiN_x$ multilayers

with AlN and $SiN_x$ layer thickness varying from 2 to 10 nm were synthesized. The total film thickness was ~300 nm. Isothermal air annealing was performed at different sequential temperatures from 400 to 950 °C. The total duration of annealing procedure was 8-9 hours. The elemental composition of the coatings in their as-deposited and air-annealed states was determined using elemental probe microanalysis method by wavelength dispersive spectrometer attached to a JEOL 7001 TTLS scanning electron microscope. X-ray Diffraction (XRD) analysis for identification of phase composition and structure state of the coatings was performed using a Bruker D8 AXS X-ray diffractometer.

## Results and discussion

As described in the previous section, the AlN/$SiN_x$ coatings were formed with different AlN to $SiN_x$ layer thickness ratios, namely, 5 nm/2 nm, 10 nm/5 nm, 5 nm/5 nm, 10 nm/10 nm, 5 nm/10 nm, 2 nm/5 nm. The elemental composition of the elementary layers in multilayer systems corresponds to the composition of AlN and $SiN_x$ monolithic reference films: 43.6 at.% Al and 56.4 at.% N for AlN film, 43.3 at.% Si and 56.7 at.% N for $SiN_x$ film.

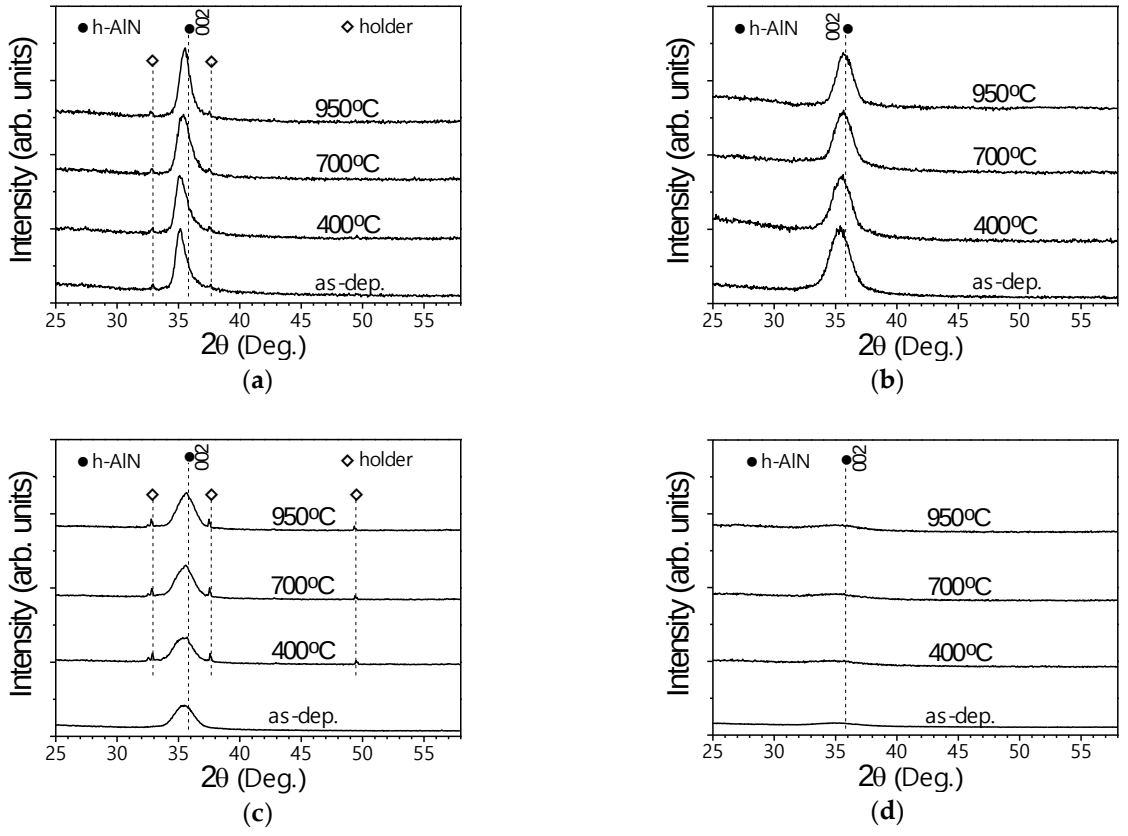



Fig. 1. Evolution of XRD patterns under air annealing for AlN reference coating (a); and AlN/$SiN_x$ multilayer coatings with different thicknesses ratio of AlN and $SiN_x$ elementary layers: (b) 5 nm/2 nm; (c) 5 nm/5 nm; and (d) 2 nm/5 nm.

The results of XRD analysis of AlN monolithic reference film in comparison with $AlN/SiN_x$ multilayer coatings during annealing in air in the temperature range of 400–950°C are given in Fig. 1. It is known that $SiN_x$ films are X-ray amorphous. That is why, in our case, the preferred orientation along the [002] direction for h-AlN layers is only observed. Broadening of AlN peak with decreasing AlN thickness takes place that can be connected with the decrease in grain size of AlN phase, and the coating appears to be nearly X-ray amorphous when the thickness of AlN layer is equal to 2 nm (Fig. 1d).

The main result consists in that no any change of phase composition for all synthesized coatings during annealing in air is detected by XRD method. The peak of the AlN phase retains its intensity up to a temperature of 950°C and oxide phases are not registered for AlN monolithic reference film as well as for $AlN/SiN_x$ multilayers. There is a decrease in lattice parameter with an increase of annealing temperature that can be caused by a relaxation of the compressive stresses. The structure of the $AlN/SiN_x$ multilayer coating with an elementary layer thickness ratio of 2 nm/5 nm remains X-ray amorphous at all temperatures of annealing (Fig. 1d).

The data of elemental analysis of the AlN, $Si_3N_4$ monolithic reference films and $AlN/SiN_x$ multilayer coatings after annealing in air are given in Table 1.

Table. 1. Results of the oxygen content analysis for AlN, $Si_3N_4$ monolithic reference films as well as for $CrN/SiN_x$ multilayer coatings after air annealing in the temperature range of 400–950 °C.

| Type of coating | Oxygen content, at. % |
|---|---|
| AlN | 33.9 |
| $Si_3N_4$ | 28.0 |
| $AlN/SiN_x$ (5 nm/2 nm) | 18.2 |
| $AlN/SiN_x$ (10 nm/5 nm) | 6.8 |
| $AlN/SiN_x$ (5 nm/5 nm) | 13.4 |
| $AlN/SiN_x$ (10 nm/10 nm) | 6.0 |
| $AlN/SiN_x$ (5 nm/10 nm) | 8.0 |
| $AlN/SiN_x$ (2 nm/5 nm) | 15.6 |

Quite lower oxygen content in the $AlN/SiN_x$ multilayer coatings exposed to annealing in air should be noted (Table 1). The minimal oxygen content in the $AlN/SiN_x$ multilayer coatings after annealing is 6-8 at % in the case of elementary layer thickness ratios of 10 nm/5 nm, 10 nm/10 nm and 5 nm/10 nm, it means, in the case of bilayer period of 15 nm or higher. Such a result differs from earlier obtained results for the $ZrN/SiN_x$ system where highest oxidation stability was observed for the case of ZrN to $SiN_x$ thicknesses ratio of 2 nm/5 nm [4]. The oxidation rate of $AlN/SiN_x$ multilayer coatings does not change significantly upon varying the MeN elementary layer thickness to that of $SiN_x$

that similar to the case of $CrN/SiN_x$ coatings [4]. However, the main result consists in that the $AlN/SiN_x$ multilayers are more resistant to high-temperature oxidation for all used MeN to $SiN_x$ thickness-ratio values as compared with $CrN/SiN_x$ and, especially, with $ZrN/SiN_x$ multilayers.

Figure 2 shows the surface topography of the $AlN/SiN_x$ (10 nm/10 nm) multilayer coating which is characterized by the best oxidation resistance. There are no any delamination of the coating and no presence of clearly defined surface centers of high-temperature corrosion.

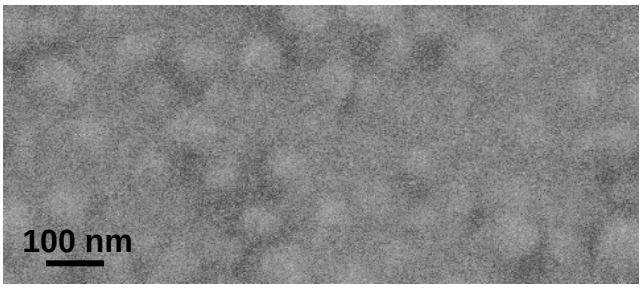



Fig. 2. Top-view SEM micrograph of $AlN/SiN_x$ multilayer coating with the ratio of thicknesses of AlN and $SiN_x$ elementary layers equal to 10 nm/10 nm after air annealing at 950 °C.

## Conclusions

$AlN/SiN_x$ multilayer coatings demonstrate higher resistance to high-temperature oxidation as compared to the AlN, $Si_3N_4$ monolithic reference films as well as $ZrN/SiN_x$ and $CrN/SiN_x$ multilayer coatings studied earlier. Observed relaxation of the compressive stresses during annealing can be one of the reasons of this fact. $AlN/SiN_x$ multilayers with the elementary layer thickness ratio of 10 nm/5 nm, 10 nm/10 nm and 5 nm/10 nm are the most stable to oxidation at the high temperatures (only 6-8 at.% of oxygen in their composition after air annealing procedure). Further decrease in thickness of any elementary layer down to 5 or 2 nm leads to deterioration of their oxidation resistance.

## References

1. **Bai X., Zheng W., An T., Jiang Q.** J. Phys. Condens. Matter, 17 (2005) 6405–6413.
2. **Hultman L., Bareño J., Flink A., Söderberg H., Larsson K., Petrova V., Odén M., Greene J.E., Petrov I.** Phys. Rev. B, 75 (2007) 155437.
3. **Abadias G., Uglov V.V., Saladukhin I.A., Zlotski S.V., Tolmachova G., Dub S.N., Vuuren A.J.** Surf. Coat. Technol., 308 (2016) 158–167.
4. **Saladukhin I.A., Abadias G., Uglov V.V., Zlotski S.V., Malashevich A.A.** Poverkhnost', 4 (2020) 40–48 (in Russian).

# PROSPECTS FOR THE USE OF LASERS FOR THE FORMATION OF CONFIGURABLE PLASMA ANTENNAS

N.G. Gusein-Zade[1], S.Y. Kazantsev[2], S.V. Podlesnikh[1,2], A.A. Smolsky[2], P.A. Titovets[2]

[1]Prokhorov General Physics Institute of the Russian Academy of Sciences, 38 Vavilov St., 119991, Moscow, Russia
[2] Moscow Technical University of Communications and Informatics, 8A Aviamotornaya St., 111024, Moscow, Russia and p.a.titovets@mtuci.ru

The main problem of modern antenna systems, which the efforts of many researchers aimed at solving, is the task of quickly switching antenna characteristics to changing tasks [1]. Therefore, in the past, plasma channels formed by a laser in atmospheric air were already discovered as appropriate plasma antennas for controlling the flow of electromagnetic radiation [2, 3]. Methods for creating plasma antennas without the use of lasers are considered in detail in [4-6]. The purpose of this article is to briefly review the various approaches in which lasers have been found to create tunable plasma antennas, as well as to describe new observations and research results on semiconductor configurable antennas.



Fig. 1. Photo of the laser spark obtained by focusing the radiation of a pulsed $CO_2$ laser using a spherical mirror.

By focusing laser radiation in the atmosphere, one can obtain long laser sparks [7], which were proposed to be used for energy transfer, lightning interception [8, 9], and as plasma antennas [2, 3]. Photograph of a typical laser spark obtained by focusing in the atmosphere using a spherical mirror of pulsed CO2 laser radiation (figure 1). This laser spark is a separate plasma formation, which largely determines the low efficiency of such a spark, both for lightning interception and for use as a plasma antenna. Much more efficient, for all the applications listed above, is a solid laser spark obtained by focusing laser radiation with conical optics [10, 11]. A photograph of a continuous laser spark and a schematic representation of a setup for studying the characteristics of plasma antennas is shown in figure 2. However, the energy costs for creating a continuous laser spark even with the use of an efficient pulsed $CO_2$ laser are 200 J/m, and for other available lasers they will be even higher [10]. This circumstance, as well as the fact that the duration of the high conductivity of the

plasma channel, when the electron density in the plasma is $10^{16}$–$10^{18}$ $cm^{-3}$, does not exceed a few microseconds [11], has become the main reason that the laser spark is not used in practical applications for the formation of antennas [12]. In addition, the creation of high-power lasers for obtaining long laser sparks and their maintenance requires significant material costs.

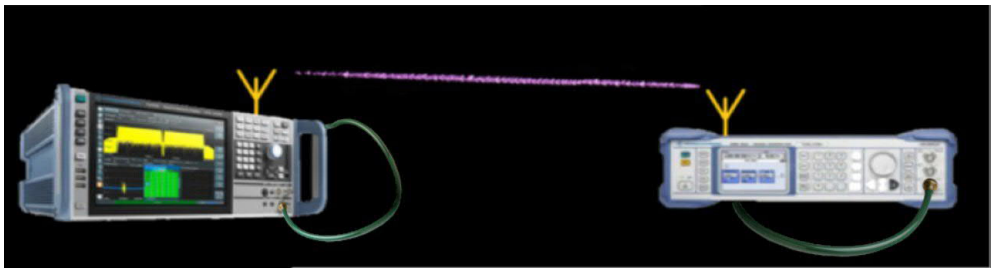
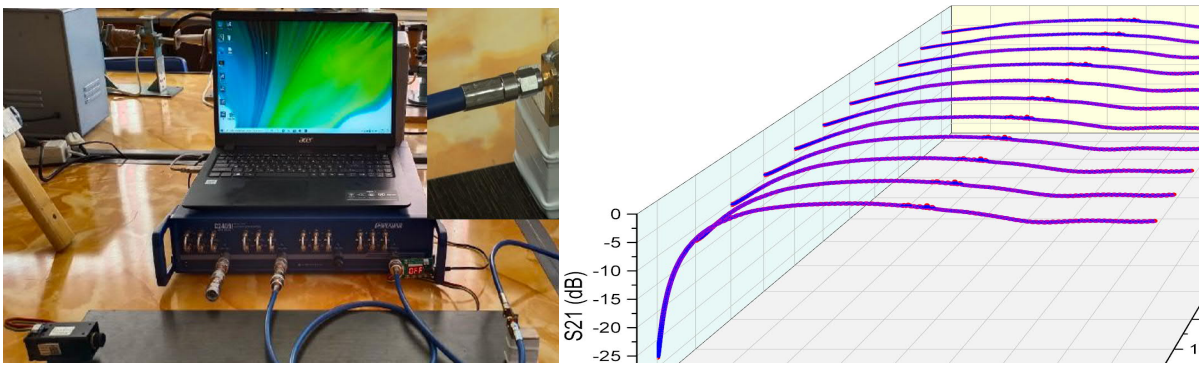


Fig. 2. Scheme of experiments to study the characteristics of a plasma antenna based on a continuous laser spark.

At the beginning of this century, the possibility of obtaining long conducting channels using pulsed UV lasers was demonstrated [13–15]. Plasma channels obtained in this way were used to direct electrical discharges in the atmosphere and could be used to form plasma antennas [14]. The lifetime of a high-conductivity channel created by a pulsed UV laser is even shorter than in a laser spark [12]. The electrical conductivity of filaments that arise in the atmosphere during the propagation of femtosecond laser pulses, which were also used to create plasma antennas [16–17], is also low. Taking into account the fact that repetitively pulsed UV lasers and lasers emitting powerful femtosecond pulses are very complex and expensive devices, it should be recognized that the creation of plasma antennas with their help is only for scientific interest and the wide practical application of such plasma antennas seems doubtful.

To create adaptive plasma antenna systems, a more promising approach was first demonstrated in [18], where a plasma antenna was formed by irradiating a semiconductor with a diode laser. In [12], in addition to a diode laser, a fiber laser was also used to create a semiconductor plasma antenna, which made it possible to increase the maximum irradiation intensity of an antenna made of single-crystal Ge at a low average laser power. In [12], the possibility of creating laser-controlled plasma reflective antennas based on Ge was also analyzed. A plasma receiving antenna based on single-crystal GaAs was studied in [19]. Comparison of the results of numerical simulation with experimental estimates of the concentration of photoplasma formed in semiconductor crystals due to the internal photoelectric effect revealed the need to take into account charge diffusion and recombination losses in the surface layer of a semiconductor [19]. The difficulties of forming a stable electric contact with semiconductor wafers under laboratory conditions have led to the

need to use semiconductor elements with more stable characteristics in experiments. In a series of works [20, 21], serial photoresistors were used to create plasma antennas, after which the concept of creating a configurable plasma antenna based on serially produced discrete semiconductor elements was proposed in [1]. Installation scheme and dependence of the coefficient S21 of an individual element of such a configurable antenna is shown in figure 3, when this element was a photodiode. These studies were carried out according to the methodology described in detail in [1]. With an increase in the intensity of irradiation of the photodiode by a semiconductor laser, the losses introduced by the diode decrease, and confirms the possibility of operational control of the characteristics of the configurable antenna.




(a) (b)

Fig.3. (a) - experimental setup; (b) - dependences of the transmission coefficient (S21) for a photodiode on the laser radiation power in the frequency range from 1 to 9000 MHz.

In this work, methods of using laser radiation to form plasma antennas were analyzed. It is shown that for practical applications the concept of a configurable plasma antenna proposed in [1] is more appropriate.

## References

1. **Kazantsev S.Y., Brusentsev A.S., Titovets P.A., et al.** *2022 Systems of Signals Generating and Processing in the Field of on Board Communications*, (2022) 1-6. doi: 10.1109/IEEECONF53456.2022.9744361.
2. **Dwyer T.J. et al**. IEEE Trans, on Antennas and Propagation, AP-32 (1984) 141.
3. **Askaryan G.A., and Raevsky I.M.** *Letters in ZhTF (in Russian)* 8 (1982) 1131-1137.
4. **Bogachev N.N., Gusein-Zade N.G., Nefedov V.I.** Plasma Physics Reports, 45 (2019) 372-375.
5. **Gusein-Zade N.G., Minaev I.M., Rukhadze A.A., Rukhadze K.Z.,**

Journal of Communications Technology and Electronics, 56 (2011) 1207-1211.
6. **Kumar R. and Kumar P.** AIP Advances, 8 (2018) 045306.
7. Raĭzer Y.P. Soviet Physics Uspekhi. 23 (1980) 789.
8. **Kononov I.G., Firsov K.N., Vasilyak L.M. et al.** High Temperature, 41 (2003) 166-175.
9. **Apollonov V.V. et al.** Quantum Electronics, 32 (2002) 523-527.
10. **Apollonov V.V. et al.** Quantum Electronics. 32 (2002) 115-120.
11. **Apollonov V.V. et al**. XIV International Symposium on Gas Flow, Chemical Lasers, and High-Power Lasers. – Proc. SPIE, 5120 (2003) 631-639.
12. **Bogachev N.N. et al.** XIV International Conference on Pulsed Lasers and Laser Applications. – Proc. SPIE, 11322 (2019) 357-365.
13. **Zvorykin V.D. et al.** Quantum Electronics. 43 (2013) 339–346
14. **Zvorykin V.D. et al.** Applied Optics. 53 (2014) 131-140.
15. **Bogatskaya A.V., Gnezdovskaia N.E., Popov A.M**. Physical Review E. 102. (2020) 043202.
16. **Ionin A.A., Seleznev L.V., Sunchugasheva E.S.** Proc. SPIE, 8898 (2013) 254-261. doi: 10.1117/12.2028118.
17. **Brelet Y. et al.** Applied Physics Letters, 101 (2012) 264106.
18. **Bogachev N.N. et al.** Technical Physics Letters. 45 (2019) 1223-1225.
19. **Brusentsev A.S. et al.** Journal of Physics: Conference Series. IOP Publishing, 2103 (2021) 012187.
20. **Kazantsev S.Y. et al.** 2021 Systems of Signals Generating and Processing in the Field of on Board Communications. – IEEE, (2021) 1-7.
21. **Kazantsev S.Y. et al.** Systems of Signal Synchronization, Generating and Processing in Telecommunications. SYNCHROINFO. – IEEE, (2021) 1-4.

# MAGNETRON DEPOSITION OF W-COATINGS WITH IN D-HE MIXTURE

M.M. Kharkov[1], D.V. Kolodko[1,2], G.S. Lomonosov[1], M.S. Kukushkina[1], A.V. Kaziev[1]

[1]National Research Nuclear University MEPhI (Moscow Engineering Physics Institute), 31 Kashirskoe sh., Moscow, 115409, Russia
[2]Kotelnikov Institute of Radio Engineering and Electronics, RAS, Fryazino Branch, 1 Vvedeskogo pl., Fryazino, 141190, Russia

Works on magnetron deposition of structured coatings in light gases have been carried out since 2014 [1, 2]. To form a structured layer (~ 1 μm) it takes quite a long time, usually 5–10 hours, with an ion flux of He ~ $10^{20}$ $m^{-2}s^{-1}$.

The studies were carried out in the hot-target magnetron deposition setup of the PINCH laboratory (MEPhI) (Fig. 1). Ultimate pressure in the vacuum chamber was $p_{base} = 4\times10^{-6}$ Torr. After reaching the ultimate vacuum, to reduce the load on the turbopump, the pumping was slowed by gradually closing the gate valve, and the actual residual pressure after that was $p'_{base} = 3\times10^{-5}$ Torr. Then the working gas mixture was introduced up to the operating pressure of $3.5\times10^{-2}$ Torr and the magnetron discharge was ignited. The discharge power supply operated in the HiPIMS mode with power stabilization. The electrical parameters were measured for the pulse frequency $f = 0.5$ kHz , pulse time $\tau = 500$ μs and $f = 2$ kHz, $\tau = 80$ μs at different discharge power $P_d$ in $H_2$/He mixtures at ratios of 90/10; 75/25; 50/50; 25/75.

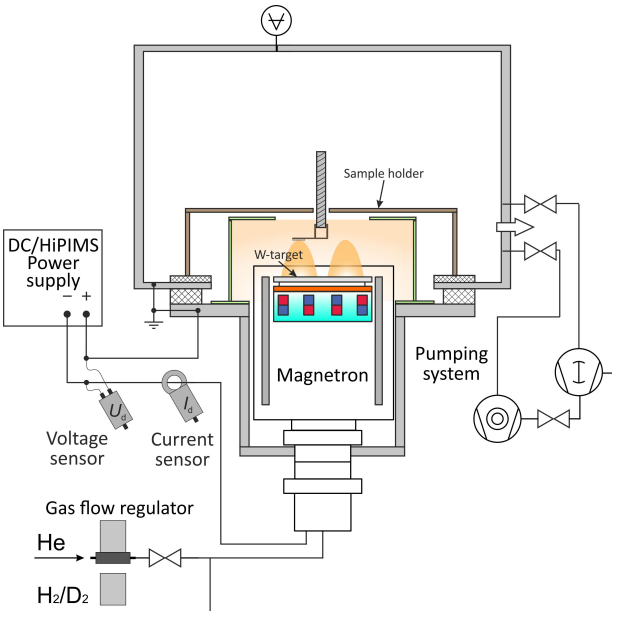



Fig. 1. Hot-target magnetron setup scheme used for deposition and measurements

In the regimes with fixed repetition frequency at power $P_d$ = 1500 W in $D_2$/He and $H_2$/He mixtures with ratio 90/10, tungsten was deposited from a thermally insulated pure W target for $t_{dep}$ = 30 min. For the first 2 minutes, the target was heated in the DC mode to the equilibrium temperature, and the remaining time was in the HiPIMS mode.

With an increase in helium content in the working mixture, the rate of current growth decreases, a distinguished peak appears, and the maximum current increases. At a power of less than 1000 W, the current pulse can be considered as quasi-stationary starting from 20–40 μs depending on the amount of helium in the mixture. However, with an increase in the discharge power, the magnitude of high-frequency oscillations in the current increases. When the discharge is operated in pure gases, the magnitude of these oscillations is less than for mixtures with helium. The minimum magnitude is observed in pure helium and does not exceed 0.8 A, while the maximum value ~ 3 A is observed for $H_2$/He = 25/75 and 50/50 mixtures.

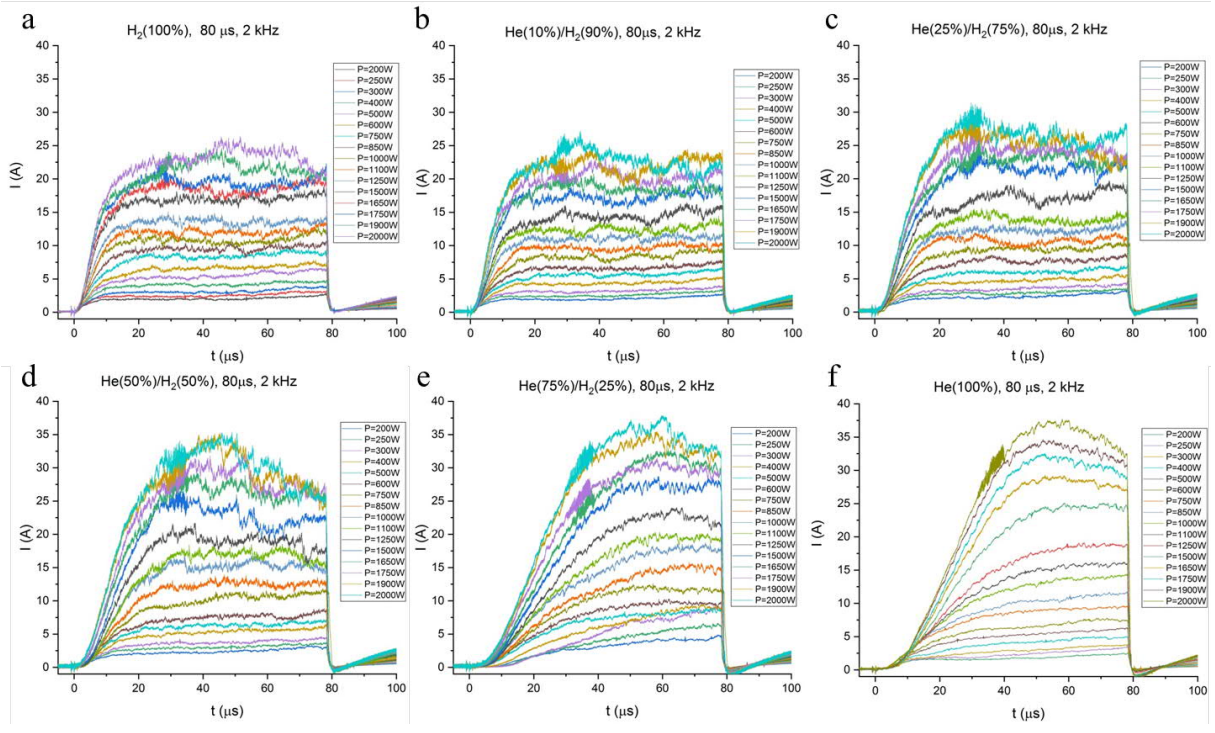



Fig. 2. Waveforms of the current of a pulsed magnetron discharge for different discharge power values and for various $H_2$/He mixtures: a) pure $H_2$; b) 90/10; c) 75/25; d) 50/50; e) 25/75; f) pure He.

The layers were deposited on tungsten samples with dimensions 10×10×0.05 mm. The structures were analyzed with a Tescan Vega 3 scanning electron microscope. Surface images obtained from both the backscattered electron (BSE) and secondary electron (SE) detectors are shown in Fig. 3.

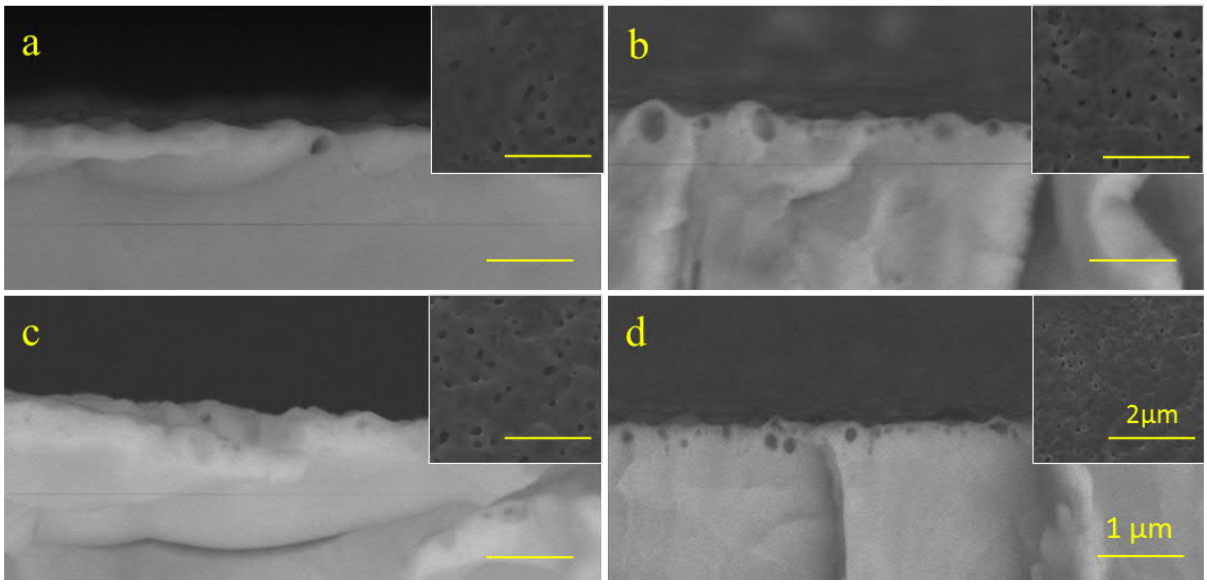



Fig. 3. Image of a fracture region of a tungsten sample after deposition in HiPIMS in $H_2$/He and $D_2$/He gas mixtures with different pulse times $\tau$ and frequency values $f$:
a) $H_2$ (90%)/He(10%), 80 µs, 2 kHz; b) $H_2$ (90%)/He(10%), 500 µs, 0.5 kHz;
c) $D_2$ (90%)/He(10%), 80 µs, 2 kHz ; d) $D_2$ (90%)/He(10%), 500 µs, 0.5 kHz

In the case of deposition in regimes with 500 µs pulse for hydrogen and deuterium mixtures, the coating structure is more porous than with a short pulse. However, the pore sizes turn out to be much smaller in case of $D_2$/He mixture than in $H_2$/He. The thickness of the coatings in the case of short pulses, but with higher frequency, turns out to be greater than in the case of longer pulse and lower frequency: 0.60±0.10 µm and 0.40±0.15 µm , respectively. The deposition rates were 0.33±0.06 and 0.22±0.8 nm/s, which is comparable with the deposition rates reported in [3] for the ratio $D_2$/He = 25/75 [3].

**Acknowledgements**. This work was financially supported by the Russian Science Foundation (project No. 20-12-00203).

**References**

1. **Petty T.J. et al.,** Journal of Nuclear Materials, 480 (2016) 374–385
2. **Petty T.J. and Bradley J.W.**, Journal of Nuclear Materials, 453(1–3) (2014) 320–322
3. **Krat S.A. et al.,** Bulletin of the Russian Academy of Sciences: Physics, 2022, 86(5) 521–525

# PLASMA CHEMICAL PRODUCTION OF WATER-SOLUBLE CHITOSAN AND TESTING OF ITS BIOLOGICAL ACTIVITY

V. Titov[1], I. Naumova[2], A. Khlyustova[1], N. Sirotkin[1]

[1]G.A. Krestov Institute of Solution Chemistry of the Russian Academy of Sciences, Akademicheskaya street 1, Ivanovo, Russia, 153045, titov25@gmail.com
[2]Ivanovo State University, Ermaka str. 39, Ivanovo, Russia, 153025, irinauma@mail.ru

**Introduction.** One of the promising fields of applied plasma chemistry is application of low-temperature plasma in agriculture and in the production and storage of food products [1–3]. A number of studies reported that the use of plasma improves the germination of seeds of grain, vegetable and flower crops. Three main approaches can be noted: (i) direct pre-sowing treatment of seeds in plasma at reduced or atmospheric pressure, (ii) plasma treatment of water used for soaking seeds during germination and for watering seedlings, and (iii) plasma chemical obtaining of phyto-stimulants from natural raw materials. In particular, it has been shown that treatment of chitosan powders in low-pressure plasma or plasma treatment of its solutions leads to depolimerization with production of low-molecular water-soluble chitosan with phyto-stimulating properties [4, 5]. In this work, a comparative study of plasma-activated water (PAW) and water-soluble chitosan (WSC) as stimulators of germination and growth of pea (*Pisum Sativum Convar. Sativum*) was carried out.

**Experimental part.** Two types of discharges were used for treatment of water and chitosan solutions: a direct current (DC) discharge in air, in which the solution itself was the discharge cathode, and a pulsed discharge in vapor-gas bubbles near the surface of an electrode immersed in a solution ("underwater" discharge). The experimental sets were described in detail in [5]. DC discharge was excited in atmospheric air between a graphite anode and the surface of water or chitosan solution (Fig. 1a). The interelectrode distance was 4 mm, the discharge current – 50 mA and voltage – 970 V. The underwater discharge was excited by applying an alternating voltage ($U \leq 2$ kV, $f = 50$ Hz) to graphite electrodes placed in glass tubes and immersed in a liquid. The discharge appeared quasi-periodically in gas-vapor bubbles formed due to electrochemical processes and overheating of the liquid near the end surface of the electrode (Fig. 1b). Digital oscilloscope and a multichannel analog-to-digital converter were used to determine the amplitude and average values of discharge current and voltage. These data were used for calculating the power dissipated in the discharge cell. Plasma emission spectra were recorded with an AvaSpec ULS3648 spectrometer. Tap water ($V$=400 ml) was treated at amplitude values of the voltage of about 800 V and a current of 200 mA for 5–30 minutes. The

pH value and concentrations of nitrite and nitrate ions were measured with an I-160MI ion-meter using ion-selective electrodes.

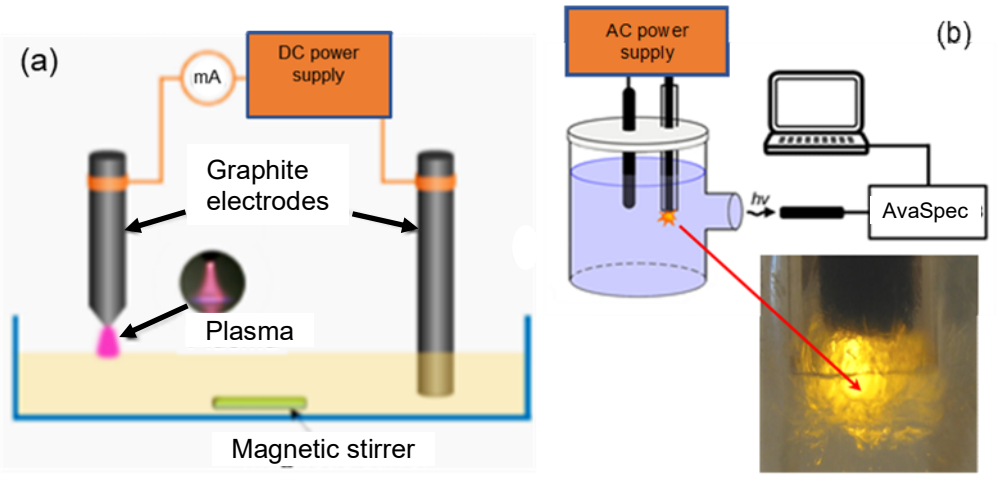



Fig. 1. Experimental setup: (a) – DC discharge with liquid cathode, (b) – underwater discharge

**Results and discussions.** The concentration of hydrogen peroxide after plasma treatment was determined spectrophotometrically using $TiOSO_4$ as a chemical probe. After 20 min of DC discharge treatment, PAW contained 3.2 mmol/L of $NO_2^-$, 5.6 mmol/L $NO_3^-$, and 1.3 mmol/L $H_2O_2$. Water-soluble chitosan (WSC) was obtained by plasma treatment of 1% (wt/v) chitosan solution in acetic acid. Water-soluble fractions were isolated from the solutions according to the procedure described in [6]. The yield of WSC depends not only on treatment time and discharge power but on the concentration of acetic acid. The maximum yield (24% wt/wt) was obtained when using DC discharge with chitosan solution in 2% acetic acid. The WSC was characterized by X-ray diffraction and IR spectroscopy. The degradation rate constants $k = (1.31\pm0.2)\times10^{-5}$ $s^{-1}$ and $k = (8.75\pm0.9)\times10^{-5}$ $s^{-1}$ for underwater and air DC discharges, respectively, were estimated from the change in the average viscosity molecular weight of chitosan.

For seed germination and soil irrigation, PAW and 0.2% (wt/v) solution of WSC in distilled water were used. Seed germination was studied according to the methods described in [7]. Seeds were germinated in Petri dishes on filter paper moistened with PAW or WSC solution. The seeds were kept at room temperature (20±2°C) for 12 days, wetting the paper with PAW or WSC every day. Untreated tap water was used in the control experiments. Fig. 2 shows the photos of pea seeds during germination, the data on germination and swelling of seeds *in vitro* are given in Table 1. The use of WSC increased germination by 3%. More significant increase was obtained for soil germination (Table 2): WSC gave increase in 5%. The use of PAW leads to similar results (Table 1 and 2).




Fig. 2. Pea seeds on the third day of germination: (1) – control, (2) – PAW, (3) – WSC.

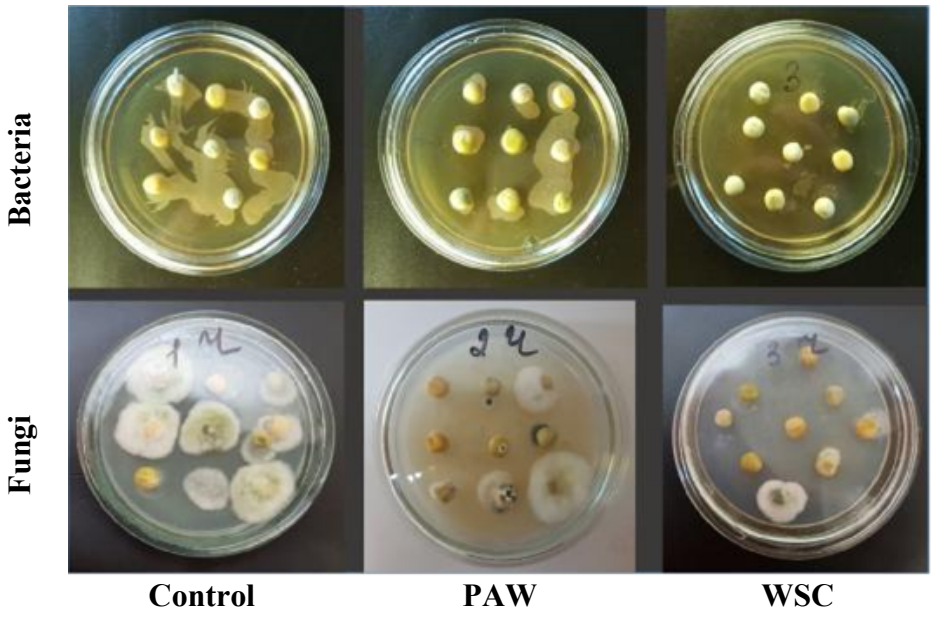



Fig. 3. Inhibition of pathogenic microflora on the surface of pea seeds using PAW and WSC

Table 1. Characteristics of the germination of pea seeds *in vitro*

| Phyto-stimulant | Germination (%) | Swelling (%) |
|---|---|---|
| Control (tap water) | 85 | 238 |
| PAW | 86 | 257 |
| WSC | 88 | 250 |
| Epin-extra | 87 | 242 |

Table 2. Germination and length of pea sprouts in soil

| Phyto-stimulant | Germination energy (%) | Soil germination (%) | Seedlings length (mm) | |
|---|---|---|---|---|
| | | | 8 day | 12 day |
| Control (tap water) | 65 | 80 | 51 | 133 |
| PAW | 94 | 96 | 83 | 173 |
| WSC | 70 | 85 | 49 | 101 |

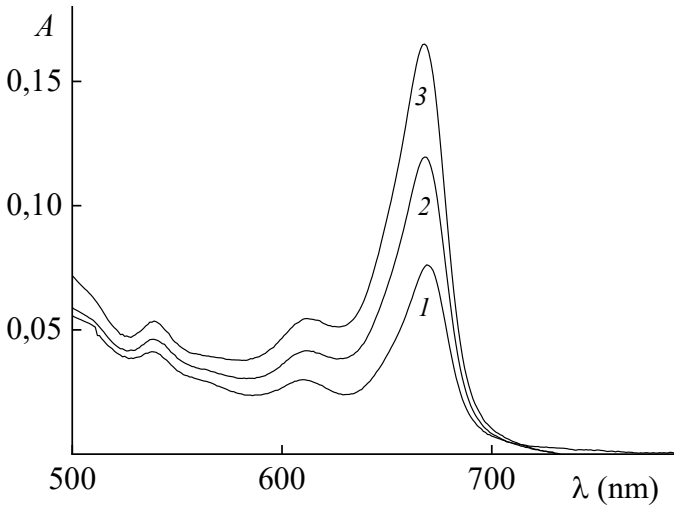



Fig. 4. Electronic absorption spectra of chlorophyll extracts from leaves of pea grown with PAW (2) and WSC (3). 1 - control

In terms of phyto-stimulating properties, WSC is not inferior to the commercial phyto-stimulant “Epin-extra” (Table 2). Photos in Fig. 3 show the good ability of PAW and WSC to inhibit the growth of bacteria and fungi on the surface of seeds. It should be noted that the use of both PAW and WSC stimulates the production of chlorophyll in the leaves of seedlings as can be seen in Fig. 4. At the same time, the data in Table 2 show that the use of PAW in the early stages of plant development is more preferable than WSC.

**Acknowledgements.** This work was supported by the Russian Foundation for Basic Research (project no. 20-02-00501 A).

## References

1. **Ranieri P., Sponsel N., Kizer J., Rojas-Pierce M., Hermandez R., Gatiboni L., Grunden A., Stapelmann K.** Plasma Process. Polymers, 18 (2020) e2000162.
2. **Rifna E. J., Ramanan K. R., Mahendran R.** Trends in Food Science & Technology, 86 (2019) 95.
3. **Attri P., Ishikawa K., Okumura T., Koga K., Shiratani M.** Processes, 8 (2020) 1002.
4. **Vasilieva T.M., Naumova I.K., Galkina O.V., et al.** IEEE Transactions on Plasma Science, 48 (2020) 1035.
5. **Khlyustova A., Sirotkin, N., Naumova I., Tarasov A., Titov V.** Plasma Chem. Plasma Process., 42 (2022) 587.
6. **Tantiplapol T., Singsawat Y., Naringsil N., Damrongsakkul S., Saito N., Prasertsung I.** Innov. Food Sci. Emerg. Technol., 32 (2015) 116.
7. **Vasko V.T**. Fundamentals of field crops seed science. S-Pb.: Publishing house "Lan" (2012) [in Russian].

# APPLICATION OF COLD PLASMA AND HIGH FREQUENCY ELECTROMAGNETIC FIELDS FOR TREATMENT OF LONG-STEMMED FLAX SEEDS

V. A. Lyushkevich[1], I. I. Filatova[1], S. V. Goncharik[1], N. V. Pushkina[2], N.M. Leschinskaya[2]

[1] B. I. Stepanov Institute of Physics, National Academy of Sciences of Belarus, 68-2 Nezavisimosti Ave., 220072 Minsk, Belarus, v.lyushkevich@ifanbel.bas-net.by

[2] Institute of Nuclear Problems of the Belarusian State University, 11 Bobruiskaya str., 220006, Minsk, Belarus, nadyapushkina@gmail.com

## Introduction

Recently, much attention in the world has been paid to the development of efficient and environmentally friendly (non-chemical) technologies for the production of agricultural plants. For pre-sowing seed treatment, physical methods are being actively developed using cold plasma and electromagnetic fields (EMF), which have a high biological activity in relation to the processed plant objects and make it possible to activate the biological catalysts of the germinating seed [1, 2]. In addition, physical methods can be used to induce mutations used in plant breeding. The induced mutation can provide the desired genetic changes, such as early maturation, resistance to various diseases, etc. [3].

We have demonstrated in our previous papers that the yield and growth parameters of number of annual and perennial plants (red clover [4], maize, winter wheat, narrow-leaved lupine [5], etc.) may be substantially improved as a result of cold plasma and electromagnetic fields treatment of seeds. In this paper, we studied the effect of pre-sowing seed treatment with cold plasma and high frequency electromagnetic fields of different intensity and frequency range on germination and morphometric parameters of long-stemmed flax, one of the most important crops in Belarus.

## Experimental part

Seeds were exposed to low-energy (without heating) and thermal (with heating) EMF in the gigahertz frequency range as well as to EMF in radio frequency range (5.28 MHz) and plasma produced in gas discharges at low and atmospheric pressure. The operating modes of seed treatment by a microwave EMF were as follows: Mode P1 (53.57-78.33 GHz, treatment duration – 20 min), Mode P2 (53.57–78.33 GHz, 12 min), Mode P3 (64.0–66.0 GHz, 12 min), Mode (64.0–66.0 GHz, 8 min), Mode P5 (2.45 GHz, power was 90%, 1 min), Mode P6 (2.45 GHz, power was 50%, 3 min).

The treatment duration for RF (5.28 MHz) EMF was 15 and 25 min (these treatments are further abbreviated as Mode P7 and Mode P8, respectively).

Seed treatment with low pressure RF (5.28 MHz) plasma was carried out in air at a pressure of 200 Pa. The power density was not more than 0.025 W/cm$^3$. The duration of plasma exposure was 10 min (abbreviated as Mode P10).

Dielectric barrier discharge (DBD) plasma reactor with a disk-plate electrode configuration was used for plasma treatment at atmospheric pressure. The upper mesh electrode with 98 mm diameter was covered by 2.0 mm quartz glass layer and connected to an alternating power source. The lower electrode made of cooper was grounded. The peak to peak of applied voltage value was 25 kV. The repetition rate of the packets of voltage pulses was 1 kHz. The distance between upper electrode and bottom one was 3 mm. The treatment duration was 7 min (abbreviated as Mode P9).

The seed germination tests were laid in triplicate for control and all treatment regimes. Seeds germinated in the substrate for 35 days at a temperature of 20-21 C, measurements were made every 7 days. Seed germination was assessed on the 7th day of growth. Sprouted seeds with an embryonic root about 2 mm were calculated as germinated. The results obtained during the experiments were processed using the statistical package M.Exel, Stadia 7.0. The histogram was built in Microsoft Excel 2010, which displays the average deviation in bars.

**Results and discussion**

The results of experiments demonstrate that pre-sowing treatment of flax seeds with a low-energy microwave electromagnetic field in certain modes increases the germination of the studied crop, and seed treatment with thermal microwave electromagnetic radiation and DBD plasma inhibits this parameter (Fig.1). The maximum increase in seed germination by 7.8% was observed as a result of their irradiation with microwave electromagnetic field in the P1 mode. The treatment of seeds with a microwave field in the P5 and P6 modes inhibited significantly the germination of the studied culture by 17.5 and 23.5% respectively. The treatment of seeds with plasma in the P9 mode inhibited the germination of seeds by 8.2 %. Modes P3, P8 and P10 did not have a significant effect on seed germination.

Seeds exposure to microwave EMF (P1, P2, P3 modes) and RF EMF (P7 mode) contributed to an increase in morphometric parameters (Fig.2). The seedling length increased from 12.3% (P7 mode) to 15.9% (P3) relative to the control. It was established that exposure to plasma and electromagnetic fields of the microwave and RF range affects the germination and growth processes of long-stemmed flax seeds. The most optimal modes of seeds treatment contributing to the improvement of their sowing conditions are exposure to microwave electromagnetic radiation at 53.57–78.33 GHz and 64.0–66.0 GHz

for 8 to 20 min (P1, P2, P3 modes), as well as exposure to radio waves (5.28 MHz) for 15 min (P7 mode).

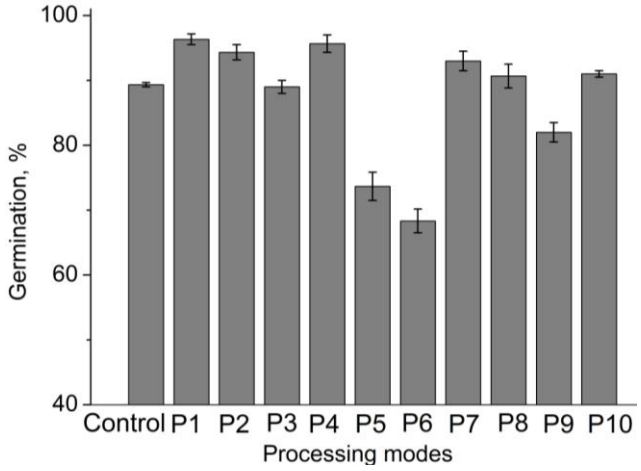



Fig. 1. – Germination of long-stemmed flax after treatment of seeds by cold plasma and electromagnetic fields

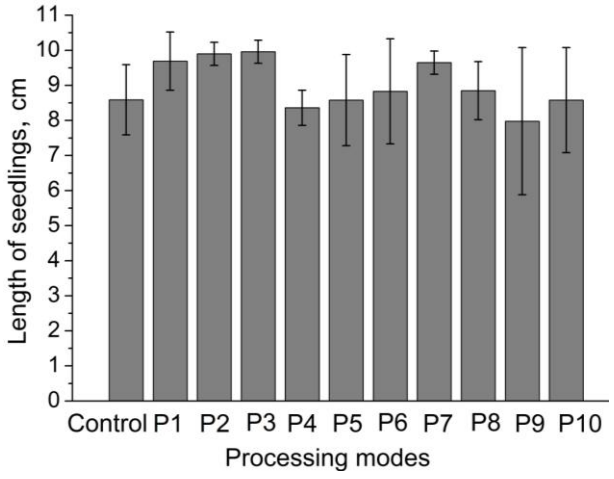



Fig. 2. – Morphometric characteristics of long-stemmed flax after treatment of seeds by cold plasma and electromagnetic fields

The use of physical factors in pre-sowing treatment of seeds is aimed at increasing the activity of the corcule by accumulating energy in the form of free radicals in a multi-level membrane structure of the shell with increased permeability [6]. Electromagnetic fields cause complex molecular processes, such as breakdown of sugars, increase the content of proteins and amino acids, increase the antioxidant activity of seeds [7]. Recent studies have reported new findings that reveal the complexity of the molecular mechanisms involved in plant response to stress caused by short-term seed treatment with cold plasma [8]. The main biologically active component of air plasma is a complex mixture

of reactive oxygen and nitrogen species (ROS and RNS), such as NO, hydrogen peroxide ($H_2O_2$), OH that are involved in the regulation of seed dormancy, germination [9], and plant physiology [10].

In the future more detailed studies are required to identify treatment modes that inhibit the germination and development of seedlings more strongly. Probably we should increase the doze of influence and use harder modes in order to detect possible mutational changes in plants. Such changes can be used as the basis for breeding new domestic varieties and lines of fiber flax.

**Conclusions**

Seeds of long-stemmed flax were treated with high frequency electromagnetic fields of different frequency ranges (from MHz to GHz) and with non-thermal plasma generated by two different plasma sources to identify the positive or negative effects on seed germination and early growth parameters. It has been identified several treatment modes contributed to the improvement of growth parameters, as well as modes inhibited seed germination. The treatment with low-intensity EMF increased the germination by 7.8%, and the length of the seedlings by 12.3% relative to the control. Seeds exposure to dielectric barrier discharge plasma for 7 min and to high-intensive EMF (with thermal heating) caused negative effects on the germination parameters that perhaps, will stimulate mutational changes in plants during the next stages of vegetation which is important in selection of long-stemmed flax plants. It is necessary to increase the exposure dose to stimulate mutational processes in plants.

**Acknowledgements**. This work was supported by the Belarusian Republican Foundation for Fundamental Research (grant No F21MC-016).

**References**

1. **Waskow, A.** Front. Phys., 9 (2021) 617345.
2. **Song J-S. et al.** Front. Plant Sci., 11 (2020) 988.
3. **Bhoi A. et al**. Plant Stress, 3 (2022) 100053.
4. **Mildaziene V. et al**. J. Physics D: Appl. Phys., 53(26) (2020) 264001.
5. **Filatova I. et al**. J. Physics D: Appl. Phys., 53(24) (2020) 244001.
6. **Spiridonov A. et al**. WSEAS transactions on environment and development, 15 (2019), 334-339.
7. **Wang J. et al**. Food Science and Technology Research, 25 (4) 2019 489-497.
8. **Mildaziene V. et al.** Plants 11 (2022) 856.
9. **Jeevan Kumar et al.** Ann. Bot. 116 (2015) 663–668.
10. **Del Rio, L.A. J.** Biol. Chem. 66 (2015) 2827–2837.

# PLASMOCHEMICAL MODIFICATION OF NONWOVEN POLYPROPYLENE MATERIALS TO INCREASE ANTIBACTERIAL AND FILTRATION PROPERTIES

K. Avdeeva[1], A. Mikhalko[2], N. Dudchik[3], V. Agabekov[1], A. Rogachev[1]

[1]State Scientific Institution "Institute of Chemistry of New Materials of the NAS of Belarus", Minsk, Belarus.
[2]International Chinese-Belarusian Scientific Laboratory for Vacuum-Plasma Technologies, Gomel State University named after Francisk Skorina, Gomel, Belarus.
[3]Republican Unitary Enterprise "Scientific and Practical Center for Hygiene", Minsk, Belarus.

Composite systems with surface modification based on polymers with unique physicochemical, mechanical, electrophysical and biological properties are relevant objects of research. Of particular interest are plasmochemical methods of modification of polymer nonwovens, which allow the formation of layers of different nature (organic and inorganic), giving new functional properties to the starting material. The growth rate and thickness of the coating on the substrate surface depend on the nature of the dispersed target, the features of the mass transfer process in vacuum and structure formation in the thin layer being formed [1, 2].

**Instruments and methods.** As a target for electron beam dispersion, we used polytetrafluoroethylene (PTFE, GOST 10007-80), metal zinc powder (CAS 7440-66-6), octenidine dihydrochloride (TU BY 100289145.023-2016) OCD, synthesized at IChNM [2]. The target was dispersed by an electron beam with an energy of 800-1600 eV and a current density of 0.01-0.03 A/cm$^2$. Coating was carried out at an initial pressure of residual gases in a vacuum chamber of ≈ $4 \cdot 10^{-3}$ Pa. The average distance from the electron gun to the target was 150 mm, and from the target to the sample - 200 mm. The thickness of the deposited thin-film coatings in vacuum was controlled by a quartz thickness gauge. Non-woven materials based on polypropylene of the Aquaspan brand with a surface density of 80 g/cm$^2$ (produced by SvetlogorskKhimvolokno, RB) were used as a substrate.

The morphology of the coatings was studied using a JEM-6000 electron microscope (Jeol, Japan). The air filtration efficiency was determined using a specially designed laboratory bench. The surface properties of the original and modified samples were assessed by the contact angle of 5 μL water. The determination of the antibacterial activity of the coatings was carried out at the RUE "Scientific and Practical Center for Hygiene" in direct contact with standardized test cultures E. coli ATCC 11229, St. aureus ATCC 6538, Kl. pneumoniae ATCC 13883 [3].

**Results and discussion.** The analysis of the images of the initial samples of AquaSpun polymer nonwovens by scanning electron microscopy showed that this material consists of disordered fibers with a diameter of 19.0 ± 2.0 microns, which have a homogeneous, smooth surface (Fig. 1a). The presence of a thin layer of functional PTFE coating on the fibers of materials with a thickness of 650 nm, zinc oxide 150 nm is shown. The thin-film coating (20 nm) of OCD includes, in some cases, individual crystals (Fig. 1d).

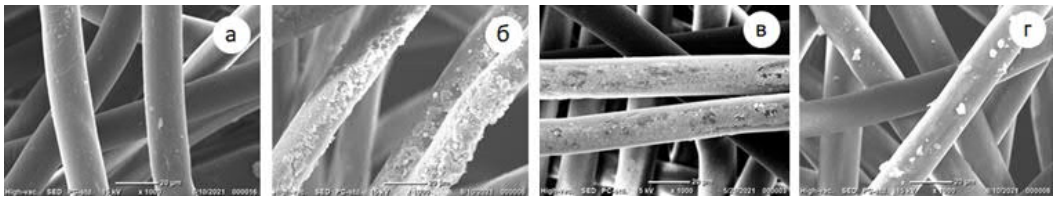



Fig. 1. SEM images of the original AquaSpun nonwoven (a) and modified: PTFE (b), zinc oxide (c), OCD (d).

AquaSpun has hydrophobic properties, with a wetting angle of 121.4±2.3°. Modification of the OCD surface lowers the wetting angle of the material from 121.4° to less than 5°, zinc oxide increases the wetting angle to 137.8± 2.3°. Application of PTFE to AquaSpun leads to a significant increase in wetting angle to 152.7±2.7°, EAF from 78.3% to 83.4%. Apparently, this is due to the formation of a mechanically stable layer on polypropylene fibers. Modification of AquaSpun with OCD and zinc oxide reduces EAF from 78.3% to 52.4% and 76.7% due to changes in the morphology and chemical composition of the fiber surface, and hydrophilic/hydrophobic properties of substances.

AquaSpun showed no antibacterial activity, which is confirmed by the absence of inhibition of bacterial growth in the contact area and suppression of bacterial growth. Samples with zinc oxide are characterized by a minimal manifestation of the effect, which is interpreted as the limit of effectiveness for *E. coli* and *Kl. pneumoniae* and an insufficient effect for *St. aureus.*

The most pronounced antibacterial properties were as a result of treatment of OCD against 3 test strains. The modification led to the formation of an inhibition zone up to 1 mm (0.25-0.5 mm) with respect to *E. coli* and Kl. *pneumoniae* up to 1 mm, the absence of growth of St. aureus in the absence of growth of all tested cultures under the samples.

Modification of PTFE materials increases the hydrophobic properties and EAF. Surface treatment with OCD suppresses the growth of bacteria *St. aureus*, *E. coli*, *Kl. pneumoniae* (100%).

The proposed method of plasma chemical modification makes it possible to form functional thin layers of various nature (organic or inorganic) and is

promising for giving non-woven polypropylene materials for medical purposes antibacterial and filtration characteristics.

**Acknowledgements**. This work was supported by the Belarusian Republican Foundation for Fundamental Research Х21УЗБГ-030.

## References

1. Applied Surface Science Molecular structure and optical properties of PTFE-based nanocomposite polymer – metal coatings / A.V. Rahachou, A. A. Rogachev, M. A. Yarmolenko, J. Xiao-hong, and L. Zhu // Appl. Surf. Sci., vol. 258, no. 6, pp. 1976–1980, 2012, doi: 10.1016/j.apsusc.2011.05.084.
2. Growth of polymer coatings from the active gas phase / A.V. Rogachev, V.P. Kazachenko, M.V. Bui, A.I. Egorov // Materials, technology, instrument. – 1998. – Vol. 3, No. 1. – pp. 60-64.
3. ISO 20645:2004 Textile fabrics - Determination of antibacterial activity-agar diffusion plate test).

# PREPARATION AND PARAMETERS ADJUSTING OF NANOPARTICLE SUSPENSIONS FOR A WORKING MEDIUM OF A LASER MICROENGINE

V.V. Kiris, A.N. Chumakov, M.I. Nedelko, N.N. Tarasenka, A.A. Nevar, N.V.Tarasenko

B.I. Stepanov Institute of Physics of National Academy of Sciences of Belarus , 68 Nezalezhnasti Ave., 220072 Minsk, Belarus

## Abstract

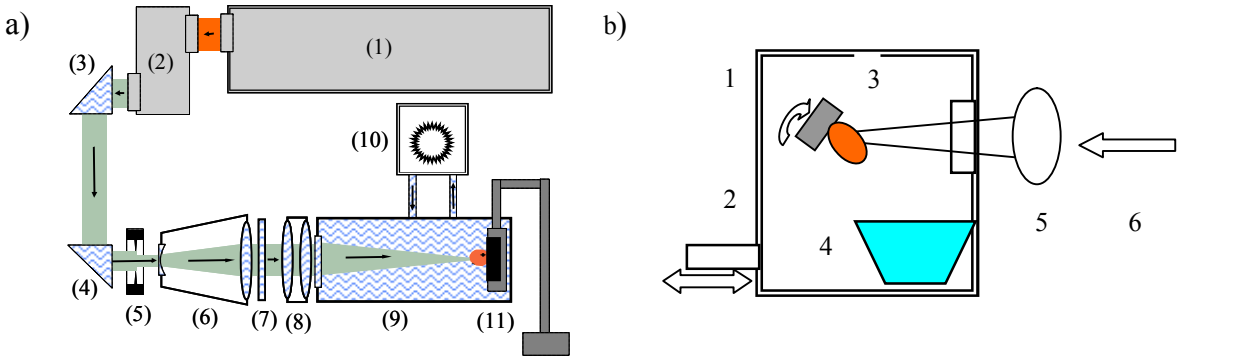
The dependence of the characteristics of nanoparticle suspensions on the synthesis conditions and adjusting them for using as a working fluid of a laser micromotor are presented. The experiments were curried out by varying the laser radiation wavelength, the time of particle production, and the spatial positioning of the target in the cuvette with liquid. The range of the optimal parameters for the synthesis of carbon-containing nanoparticles suitable for using in laser micromotors has been determined including laser ablation in a gaseous medium followed by deposition of the ablated products into vacuum oil or ionic liquid.

## Introduction

The problem of precision control of small spacecraft - micro-satellites can be solved by using a laser ablation plasma jet to generate thrust pulses, which is formed when a series pulses of solid-state microlaser acts on the assembly of the target with the working body [1]. The short duration of the laser pulse in combination with the high energy density on the target surface makes it possible to generate a plasma jet with a high plasma outflow rate. The problem associated with the non-reproducibility of the ablation conditions when using a solid target due to the removal of the working substance during ablation can be eliminated by replacing the solid target with a liquid-phase one with the supply of the working fluid through the capillary under the action of surface tension. In this paper, we discuss the results of studies aimed at obtaining suspensions of nanoparticles. For this purpose, a special technology for the preparation of a working fluid of a laser micromotor has been developed, based on the laser-plasma method for the synthesis of nanoparticles in liquid media [2]. Two approaches have been tested for the implementation of the laser-ablation method: the formation of colloidal nanoparticles directly by laser ablation inside a liquid medium and laser sputtering of the material in a gaseous medium, followed by deposition of the ablation flow into a liquid.

## 1. Experimental

The block diagram of the experimental setup for the synthesis of suspensions of nanoparticles is shown in fig. 1. It consists of a power supply and control unit for a solid-state laser LS-2137U, a laser emitter with the second and third harmonics, a laser cooling unit, a unit for converting radiation into the fourth and fifth harmonics, a focusing objective, cuvettes with liquid (oils, ionic liquids, etc.), submersible target, and also includes an additional unit for laser sputtering of the material in a gaseous medium. The unit consists of a vacuum chamber, a cuvette with working fluid, and the ablated target above it.




(1) - laser, (2) - harmonic converter, (3,4) - prisms, (5) - diaphragm, (6) - telescope, (7) - light filter, (8) - lens, (9) - cuvette with liquid, (10) - pump, (11) - sample

(1) - vacuum gauge, (2) - pumping out and inlet of gas, (3) - target, (4) - cuvette with working fluid, (4 ) - focusing lens, (6) – laser beam

Fig. 1. Structural diagram of the layout of the technological module for the synthesis of suspensions of nanoparticles by laser sputtering of material in liquid (a) and gas (b)

Setting the target above the liquid surface made it possible to circumvent the limitations associated with the effect of target screening as particles were produced. In this case, the target and the cuvette with liquid were placed in a vacuum chamber to eliminate the effect of the atmosphere on the process of nanoparticle formation. The vacuum chamber was connected to the pumping system and filled with an inert gas (neon, helium).

The laser module includes a solid-state laser, a beam positioning and focusing system, and also a cuvette with a target holder. The maximum energy of the laser pulse during ablation did not exceed 300 mJ. Vacuum oil VM-1, ethanol, and ionic liquid were used as working liquid media in the experiments. The size and shape of the synthesized NPs were controlled using transmission electron microscopy (LEO 906E electron microscope), the maximum accelerating voltage was 120 kV. To measure the absorption coefficient of the obtained samples at the wavelength of laser radiation, a Carry 500 Scan spectrophotometer was used. The optical density of the obtained colloidal nanoparticles was measured using a cuvette of 1 mm thick.

## 2. Results and Discussion

As shown by the results of measuring the optical density of the solution depending on the operating time (the number of laser pulses), the concentration of the produced substance demonstrates a tendency to saturation, probably associated with an increase in absorption and scattering of the probing laser radiation with an increase in the optical density of the solution, which leads to a decrease in the radiation energy reaching the surface of the target and to reduce the ablation efficiency. At the same time, in the scheme of the experiment on laser ablation in a gaseous medium and deposition of the ablation flow into the working liquid, the dependence of the optical density of suspensions on the operating time was linear, which indicated that the conditions for the technological process of NPs generation were preserved with time. In this case, to exclude the agglomeration of NPs, it is necessary to mix the liquid. In addition, it was found that the rate of particle production when the target is exposed to laser radiation with a wavelength of 266 nm is about 5 times higher compared to the action of radiation with a wavelength of 1064 nm under comparable conditions. When the target was exposed for half an hour to the radiation of the fourth harmonic of a Nd:YAG laser with a pulse energy of 15 mJ and a pulse repetition rate of 10 Hz, carbon-containing colloidal NPs were obtained in VM-1s vacuum oil and ionic liquid. Colloidal particles were also formed when a graphite target was exposed to the fundamental harmonic of a Nd:YAG laser with an energy of less than 100 mJ under comparable experimental conditions. The absorption spectra of a suspension of carbon nanoparticles in an ionic liquid are shown in Figure 2a. For Nd:YAG laser radiation at the fundamental harmonic of 1064 nm, the achieved optical density corresponds to an absorption coefficient of 7 $cm^{-1}$.

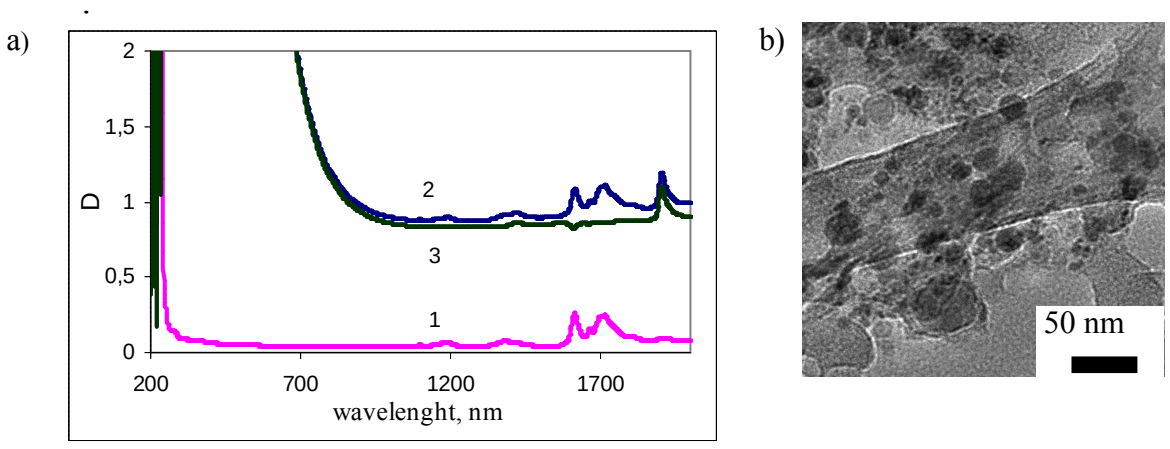



Fig. 2. a) Optical density of ionic liquid (1), of carbon nanoparticles suspension in ionic liquid (2), and also difference between 2 and 1 (3); b) typical TEM image of carbon nanoparticles formed by laser ablation

Single-stage laser synthesis of nanoparticles suspensions by laser radiation at wavelengths of 266 nm and 213 nm in the energy range of 15–30 mJ led to the formation of nanoparticles with average particle sizes in the range of 5–60 nm (Fig. 2b). Based on the developed technology for the synthesis of nanoparticles suspensions, a technological process was implemented and suspensions of carbon nanoparticles in vacuum oil VM-1C were obtained (Figure 3).

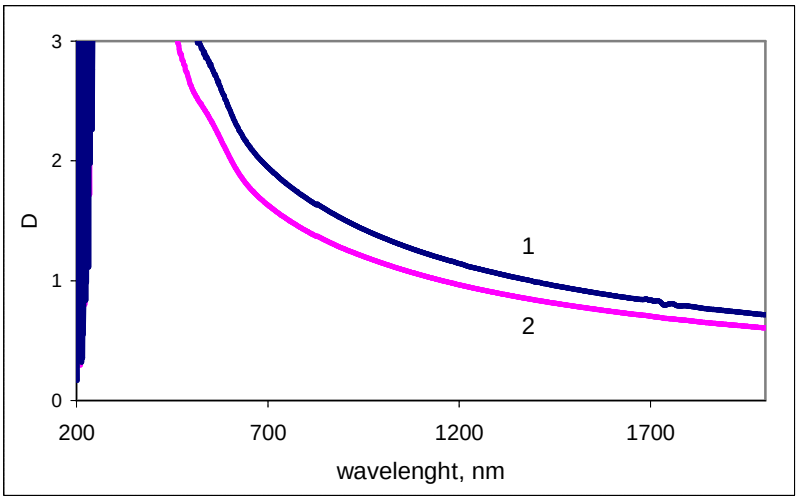



Figure 3 - Optical density of a suspension of carbon nanoparticles in VM-1C vacuum oil immediately after synthesis (1) and 4 months after synthesis (2);

Figure 3 shows how the optical density changes with the storage time of the accumulated suspensions of nanoparticles. For the radiation of Nd:YAG - laser at the fundamental harmonic of 1064 nm, the achieved optical density corresponds to an absorption coefficient of 12.8 cm-1. Repeated measurements of optical density after 4 months confirmed the long-term stability of the obtained suspensions of nanoparticles.

**Conclusion**

The technology has been developed for preparing a liquid working fluid of a laser micro-engine, which is based on a laser-ablation method for the synthesis of nanoparticles in liquid media. Two approaches have been tested for the implementation of the laser-ablation method, including the formation of colloidal NPs directly by laser ablation inside a liquid medium, as well as laser sputtering of the material in a gaseous medium, followed by deposition of the ablation flow into a liquid.

**References**

1. F.N. Ljubchenko, A.V. Fedenev, A.N Chumakov, N.A Bosak et al. // Proc. SPIE Vol. 7005, 700520-1 (13 October 2009); doi: 10.1117/12.786659.

2. N.V. Tarasenko, A.V. Butsen. Laser synthesis and modification of composite nanoparticles in liquids// Quantum electronics, 2010, vol. 40, No. 11, p. 986–1003.

# PROPERTIES OF BIOGENIC METAL NANOPARTICLES PREPARED BY PLASMA ASSISTED ELECTROCHEMISTRY

N. Tarasenka, A. Nevar, V. Kornev, M. Nedelko, N. Tarasenko

B.I. Stepanov Institute of Physics National Academy of Sciences of Belarus, 68 Nezalezhnasti Ave., Minsk, Belarus, n.tarasenko@ifanbel.bas-net.by

Recently, the studies of nanomaterials effect on the processes of plant growth and development were a subject of intensive research. Specifically, the impact of nanoparticles (NPs) uptake on seed germination and seedling development, which are considered as most sensitive stages of the plant life cycle, have attracted a great interest. The use of colloidal solutions of biogenic metals at this stage can lead to both positive and negative effects, inducing the morphological and physiological changes in plants depending on the type, size and concentration of NPs, duration of exposure or growing conditions [1]. In result, under proper selection of parameters, biogenic metal NPs can be promising for agricultural applications, allowing to use them as phytopathogens as well as for stimulation of seed germination and plant growth, i.e. as nanofertilizers [2,3].

In this paper, studies were carried out on the biogenic metals NPs preparation in colloids and analysis of their properties. For the synthesis, a reactor was developed based on an electrical discharge in contact with a liquid modified in a way to enable simultaneous formation of NPs of several metals. Liquid-assisted non-equilibrium atmospheric pressure plasmas have recently proved to be effective both for NPs fabrication as well as for their surface modification with various chemically active species formed during the discharge. This type of discharge can be considered as a “green synthesis” technique that enables NPs production without a need in additional reducing agents and without production of toxic by-products thus assuring their biocompatibility that is important for further agricultural applications. At the same time, the NPs stabilization remains an issue so apart from the synthesis of NPs, the studies were also aimed at increasing the stability of the colloidal solutions, using NPs preparation in solutions of various compositions. In general, the composition of a solvent is the decisive factor influencing the NPs production process. Therefore, aqueous solutions of two different stablilizers (glucose or carboxymethylcellulose (CMC) with a concentration of 1.8 g/l) as well as distilled water (with the addition of nitric acid) were used as solvents in order to find the optimal synthesis regimes towards the NPs of the required components ratio, size and stability.

For the synthesis of a colloidal solution containing NPs of several metals, a modification of the reactor was performed in a way that copper, zinc, iron and

molybdenum plates were used as an anode, connected in parallel to an electrical circuit and immersed in a liquid. As a cathode, an iron capillary was used, with argon flowing through it with a flow rate of 20 ml/min. To initiate a discharge between the electrodes, a voltage of 2.6-3.0 kV (depending on the composition of the solution) was applied while the discharge current was maintained at 5 mA for all the samples. The synthesis time was 30 min.

After several minutes of the synthesis, the colloidal solutions acquired a yellowish color, indicating the formation of NPs. These observations were further confirmed by the study of the absorption spectra of colloidal solutions and by the results of TEM studies (Fig. 1).

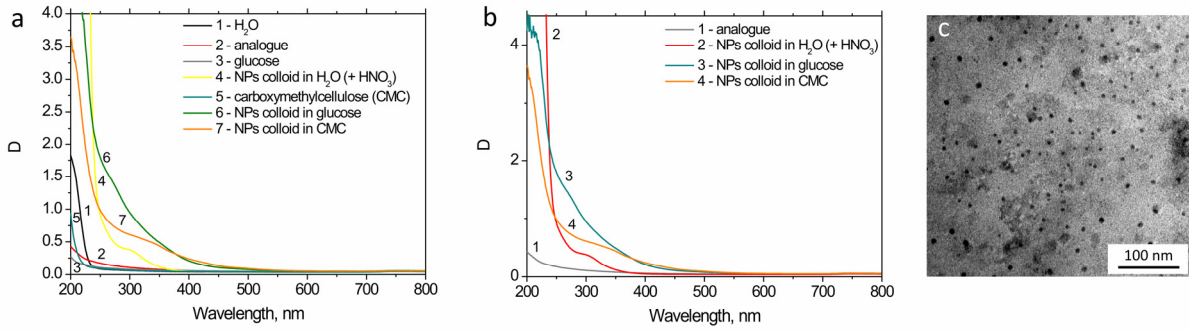



Fig. 1. – Properties of nanoparticles prepared by atmospheric pressure plasma in contact with different solutions with an anode composed of parallelly connected Cu, Fe, Mo and Zn plates: a - absorption spectra of the prepared samples and initial solvents. The absorption spectrum of a commercial analogue is presented for comparison; b - comparison of the absorption spectra of the colloids of NPs in water, and aqueous solutions of glucose and CMC with the commercial solution; c – typical TEM image of NPs prepared in CMC aqueous solution.

In the sample without the stabilizers, plasma-activated synthesis leads to the observation of the absorption bands in the 200–550 nm region, whose position and shape can be attributed to the characteristic absorption bands of metal oxides [4]. It should be noted that the commercial sample is featureless. The use of stabilizers (glucose and CMC) in the synthesis process results in different absorption spectra of the samples (Fig. 1b). According to the literature data, intense absorption bands below 400 nm can be associated with the formation of metallic NPs, in particular, Mo [5], Fe [6], and Zn [7]. As for copper NPs, their absorption is usually charactarized by the surface plasmon band at around 570 nm [8]. However, if a particle size of less than 4 nm, the characteristic plasmon peak broadens and is replaced by an indistinct optical absorption band, which monotonically increases towards higher photon energies [9]. In colloids obtained in aqueous solutions of glucose and CMC, there is a slight increase in absorption in the 400–500 nm region, which can be attributed to small Cu NPs.

The formation of NPs was further proved by microscopic characterization. The typical TEM image of the sample prepared in CMC solution is presented in

Fig. 1c. As seen, well-separated NPs with sizes below 10 nm are formed having rather narrow size distribution. Note that NPs of different structure and shape were found in the TEM images that can be indicative of their different composition.

To study the NPs composition, optical emission spectroscopy with inductively coupled plasma was used. The spectra were calibrated against standard aqueous solutions. For this, 2 ml of a colloidal solution was mixed with 0.25 ml of concentrated nitric acid, followed by the mixture dilution to 10 ml. The metal content was determined using an ICP spectrometer analyzing the lines Cu 324.7 nm, Fe 259.9 nm, Mo 202.0 nm, Zn 213.8 nm. The results of the components concentrations determination in the samples prepared in glucose and CMC solutions are shown in Table 1. For comparison, the known contents of the corresponding metals in the commercial sample (100 fold diluted) are also presented.

| Sample | Concentration, mg/l | | | |
|---|---|---|---|---|
| | Cu | Fe | Mo | Zn |
| 1* | 2.467 | 3.117 | 1.890 | 5.351 |
| 2 | 0.7249 | 1.623 | 0.4998 | 7.533 |
| 3 | 4.500 | 6,000 | 4.500 | 2.500 |

*

1 - colloidal solution of Cu, Fe, Mo, Zn NPs in aqueous glucose solution (1.8 g/l)

2 - colloidal solution of Cu, Fe, Mo, Zn NPs in an aqueous solution of CMC (1.8 g/l)

3 – commercial analogue

Table 1. - The results of the element concentrations determination in the prepared colloidal solutions (samples 1 and 2), compared with the commercial analogue (sample 3)

As it follows from the data in Table 1, plasma-activated synthesis enables the formation of NPs that contain the elements from all the electrodes immersed in a solution. According to the mechanism of NPs synthesis in a plasma with liquid electrode, at the initial stage, the anode material dissolves, which is associated with the transition of metal ions into the solution. Subsequently, metal ions are reduced as a result of the reactions with electrons and radicals formed due to the plasma cathode jet interaction with a liquid surface. However, it can be seen that the ratio of the components is different, which is associated with different electrochemical potential of metals. It is also noteworthy that the

dissolution rate of zinc increases markedly when CMC is used as a stabilizer. Namely, the Cu:Fe:Mo:Zn atomic ratio in a glucose solution is 1.97 : 2.83 : 1 : 4.15, while in a CMC solution this ratio is 1.19 : 5.58 : 1 : 22.11. A possible reason for the significant increase in the content of active metals (Zn and Fe) may be the anionic type of conductivity of CMC macromolecules. As known, CMC is a linear polymeric derivative of cellulose, consisting of β-linked glucopyranose residues with hydroxyl groups partially substituted with carboxymethyl ($–CH_2COO–$) groups, that are responsible for anionic conductivity of the polymer and can therefore establish a strong bond with oppositely charged ions, forming a polyelectrolyte complex [10]. Thus, the obtained results show that a type of stabilizer used affects the mechanisms of formation and growth of NPs; therefore, the choice of the composition and concentration of the stabilizer is important for optimization of the NPs synthesis process.

**Acknowledgements**. The work was partially supported by the National Academy of Sciences of Belarus under project Convergence 2.2.05 and by the State Committee on Science and Technology of the Republic of Belarus (grant No. F21UKRG-009).

## References

1. **Bayat M.; Zargar M.; Murtazova K.M.-S.; Nakhaev M.R.; Shkurkin S.I.** Agronomy, 12 (2022) 811.
2. **Singh A.; Singh N.B.; Afzal S.; Singh T.; Hussain I.** J. Mater. Sci. 53 (2018) 185–201.
3. **Guilger Casagrande** M.,**Bilesky-José** N., **Sousa** B., **Oliveira** H., **Fraceto** L., **Lima** R. BMC Plant Biology, 22 (2022) *255.*
4. **Bouafia A., Laouini S. E., Khelef A., Tedjani M. L., & Guemari F.** J. of Cluster Science 32 (2020) 1033–1041.
5. **Zamora-Romero N.O.E., Camacho-Lopez M.A., Vilchis-Nestor A.R., Castrejon-Sanchez V.H., Aguilar G., Camacho-Lopez S., Camacho-Lopez M.** Materials Chemistry and Physics, 240 (2019) 122163
6. **Khan Z, Al-Thabaiti S.A., Hussain S.** RSC Adv 6 (2016) 7267–7278.
7. **Singh S., Gopal R.** Bulletin of Materials Science. 30 (2007) 91-293.
8. **Xiong J., Wang Y., Xue Q., Wu X.** Green Chemistry, 13 (2011) 900-904.
9. **Lisiecki I., Billoudet F., Pileni M.P.**, J. Phys. Chem., 100 (1996) 4160–4166.
10. **Dueramae I., Okhawilai M., Kasemsiri P. *et al.*** Sci Rep 10 (2020) 12587.

# PLASMA REACTOR FOR INVESTIGATION OF BIOMASS HIGH TEMPERATURE GASIFICAION

A. Liavonchyk[1], I. Khvedchyn[1], V. Sauchyn[1]

[1]A.V.Luikov Heat and Mass Transfer Institute of the National Academy of Sciences of Belarus, The Republic of Belarus, Minsk, P.Brovka str. 15, sauchyn@itmo.by

Pilot plasma reactor with capacity up to 100 kg/h was designed for investigation of high temperature gasification of different types of biomass such as agriculture waste, municipal or industrial waste. The proposed reactor is intended for conversion of organic part of waste into syn-gas and melting and vitrification of inorganic one to produce homogeneous compound that suits for safety long-term storage or utilizing in building industry.

Arc plasma torches with power 80-150 kW and plasma jet temperature 3000-5000°C are used as main source of energy in the reactor. Mass average temperature in the reaction zone inside the reactor is 1100-1300°C. In ash melting zone temperature can reach 1500°C. Melted ash is discharged from the reactor with special high temperature valve intermittently.

The reactor was also designed for processing organic materials with high (up to 50%) ash content. The 3D model is shown in Fig 1. The distinctive features of this reactor are its high energy density of 1.5-2 MW/m$^3$ and low inertia. This reactor goes into operation in less than 1 hour.

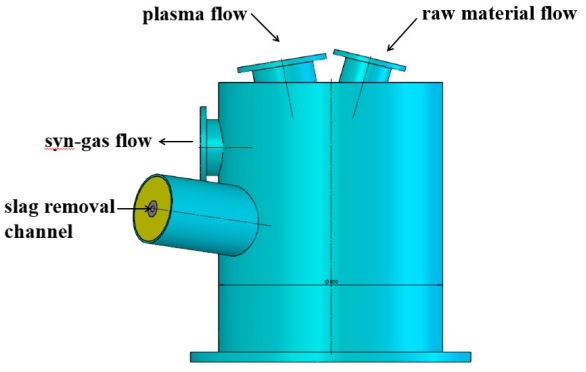



Fig. 1. The 3D model of a reactor for processing high-ash organic materials

During experiments different parameters can be varied such as type of biomass, granulometric and morphological composition, caloricity, part of volatile substances in biomass, moisture content, ash content as well as composition of gas that is used as gasifying agent (air, oxygen, water steam and their mixture in different composition).

Experimental researches were conducted on dehydrated sludge wastewater processing in the reactor. Chemical composition of fed material is presented in the Table 1. Total waste stream is 100 kg/h. The composition of the syn-gas obtained from high temperature processing of dehydrated sludge wastewater is shown in the Table 2.

Table 1. Chemical composition dehydrated sludge wastewater

| Waste composition | mass % |
|---|---|
| **Moisture** | 8,882 |
| **Ash content** | 39,682 |
| **C** | 26,545 |
| **H** | 3,775 |
| **O** | 15,518 |
| **S** | 1,332 |
| **N** | 4,266 |
| **Heating value LHV, MJ/kg** | 10,835 |

Table 2. The composition of the synthesis gas.

| **Chemical component** | **CO** | **$H_2$** | **$CO_2$** | **$C_mH_n$** | **$O_2$** | **$N_2$** | **$H_2O$** | **other** |
|---|---|---|---|---|---|---|---|---|
| **Concentration vol.,%** | 24,45 | 22,70 | 15,42 | 0,08 | 0,02 | 28,65 | 7,12 | 1,56 |

A numerical simulation of the processes occurring in the reactor during the partial oxidation of a given mixture by a stream of air plasma has been performed.

The Coupled method was used in the calculation [1, 2]. It made it possible to reduce the continuity discrepancy from 3% to less than 1.5%. The coefficient of mixing the material with the oxidizing agent was chosen to be 0.7.

Air was supplied to the entrance of the plasma torch with a flow rate of 15 g/s at a temperature of 3800 K, which corresponds to 105 kW of useful power.

The wall of the reactor was introduced into the task with a thickness of 50 mm.

Wall material properties:

thermal conductivity — 1 W/m·K,

heat capacity — 1000 J/kg·K

density — 2000 kg/$m^3$

This corresponds to the average properties of bricks or ceramics.

The temperature of the outer wall was set equal to 350 K. Losses in the side wall was approximately 6.3 kW. The loss in the cover was about 0.5 kW (flux density is 5 kW/m$^2$)

The distributions of temperatures, flow rates and the mole fractions of $H_2$, $CO_2$, CO and water over the cross section of the reactor are given. The heat flux density through the bottom of the reactor is set to 100 kW/m$^2$.

The distribution of heat flow across the bottom of the reactor was set to be uniform.

The distribution of temperature, flow velocity, and mass fractions of gas components by volume of the reactor is presented in Fig. 2.

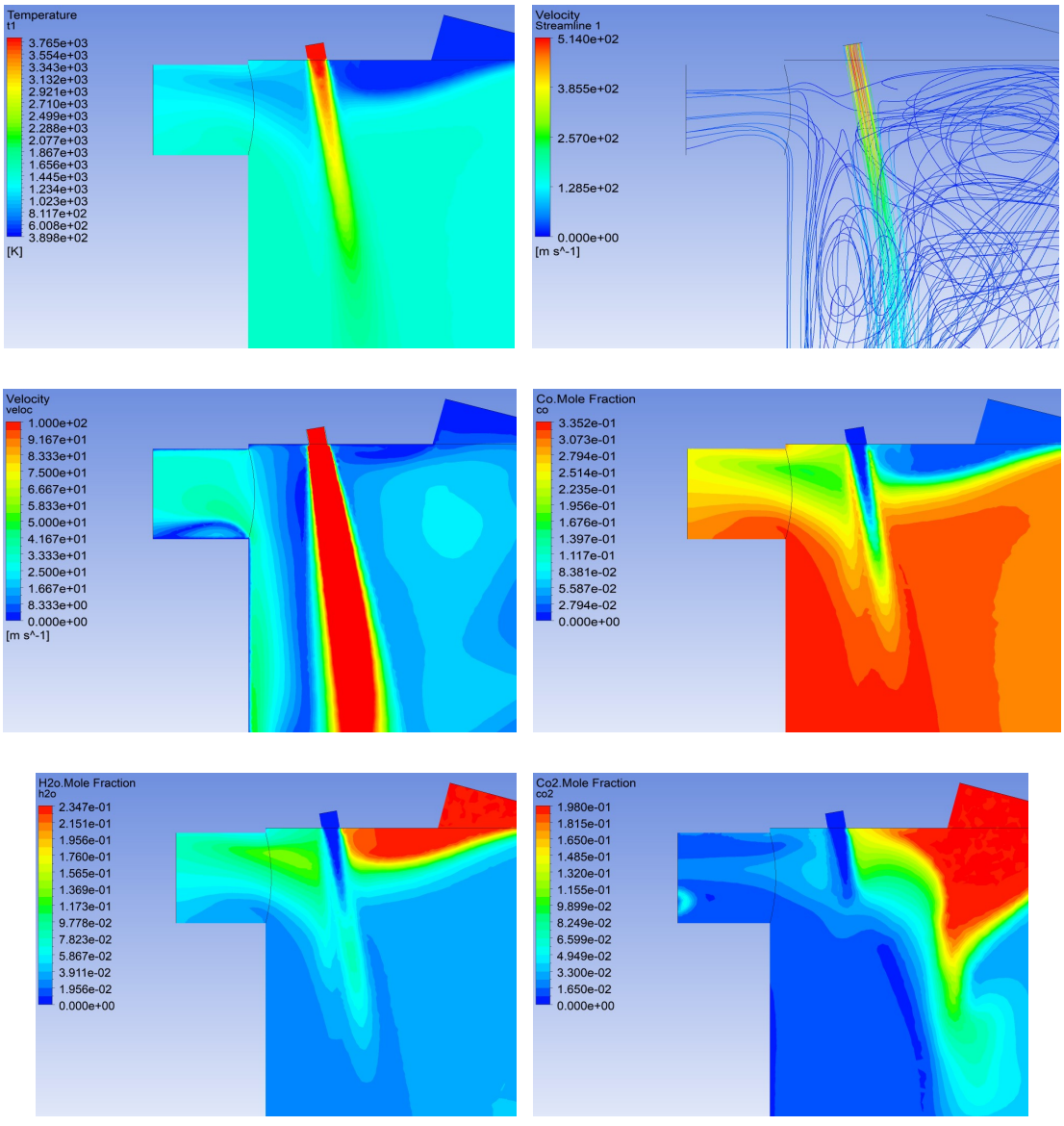



Fig. 2. Results of simulation

**Conclusion**. Results of simulation and experimental research show great opportunity of plasma technology application for waste management. Dehydrated sludge wastewater was processed in the plasma reactor with production of syn-gas and vitrified slag. The syn-gas can be used as a fuel for heat or electricity production. Vitrified slag is environmentally friendly material and can be stored without any special treatment.

**Acknowledgements.** The project was supported by A.V.Luikov Heat and Mass Transfer Institute of NAS of Belarus.

## References

1. **Liavonchyk A., Morozov D., Sauchyn V., Dalholenka H.** Numerical modeling of processes in plasma reactor for hydrocarbons conversion. High Temperature Material Processes Volume 21, 2017 Issue 4 359-375.
2. **Liavonchyk A., Sauchyn V., Khvedchyn I., Dalholenka H., Olenovich A., Kurbanov N.** Hydrocarbons conversion in to syn-gas in plasma reactor. The X III Symposium of Belarus and Serbia on Physics and Diagnostics of Laboratory and Astrophysical Plasmas (PDP-X III'2021) 169-171.

# ATMOSPHERIC PRESSURE PLASMA-ASSISTED FABRICATION OF IRON OXIDE NANOSTRUCTURES

A.A. Nevar[1], M.I. Nedelko[1], A.O. Radomtsev[1], E.V. Beletskii[2], N.V. Tarasenko[1]

[1]Institute of Physics of National Academy of Sciences of Belarus, 220072 Belarus, Minsk, Nezalezhnasti Ave. 68-2, e-mail: a.nevar@ifanbel.bas-net.by
[2]Institute of Chemistry, St. Petersburg State University, St. Petersburg, Universitetskaya Emb.7/9, 199034, Russian Federation

In the last decade, the special interest of researchers has been focused on the synthesis and study of the properties of iron oxide and oxyhydroxide nanoparticles in view of the prospects for their practical applications [1-3]. One of the methods for such structures obtaining is the low-temperature plasma electrolysis based on a glow discharge at atmospheric pressure between a metal and liquid electrodes.

Although the exact mechanisms of the nucleation and growth of nanoparticles in the plasma of a glow discharge with a liquid electrode remain not fully understood, it is obvious that this occurs due to the reduction of the ions in liquid to atoms, their combination into clusters, and the subsequent growth.

The process of nanoparticle synthesis can divide into two stages: nucleation and growth. During plasma initialization, a large number of free electrons and high-energy particles are formed at the interface between the plasma and the solution, which cause the activation of metal ions and lead to a rapid nucleation process in this region. Nascent atoms in collisions grow into larger nanoparticles, which leave the "reaction zone" and fall into a solution with a lower concentration of ions. Once far from the zone of nucleation and diffusion, without a sufficient amount of activated raw material, the nanoparticles stop their growth and settle to the bottom.

Recently [1,3] it was shown that in the pulsed discharge with a liquid electrode, the synthesis of iron oxyhydroxide nanoparticles mainly occurs due to the redox properties of active particles formed in the plasma discharge. The synthesis mechanism described by these authors showed that the hydroxyl radical formed during the discharge plays a decisive role in this process.

In the present work, experimental studies of the process of formation of iron oxide nanostructures by low-temperature plasma electrolysis, including spectroscopic studies of plasma in contact with a solution and characterization of the structure and composition of formed nanoparticles, were carried out. The method of low-temperature plasma electrolysis is based on a glow discharge at atmospheric pressure between metal and liquid electrodes. The metal electrode was a stainless steel capillary through which argon was supplied (flow rate ~ 20 ml/min). The outer diameter of the electrode was 800 μm, and the inner diameter was 500 μm. The gas flow was regulated using a leak valve. The electrode was located at a distance of 2–6 mm from the liquid surface. An iron sulfate solution with a graphite electrode immersed in it served as a "liquid electrode". The discharge was powered from a stabilized direct current source with a maximum

voltage of 3.6 V. The discharge current varied during the experiments from 3.2 to 5.6 mA. As the power supply voltage increased, the discharge gap between the surface of the solution and the electrode end brokes down, and a glow discharge of atmospheric pressure was ignited. The stable state of the plasma was ensured by selecting the parameters of the discharge circuit and the rate of the argon flow.

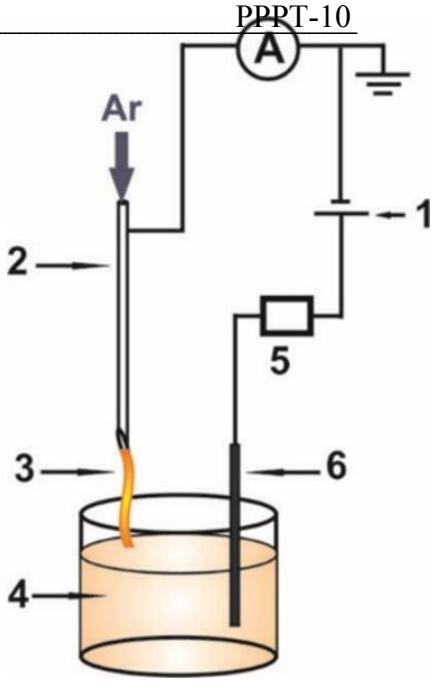



Fig. 1. Experimental setup: 1 - power supply, 2 - needle, 3 - plasma, 4 - ferrous sulfate solution, 5 - resistor, 6 - graphite electrode

Both the modes : mode 1 (needle - "anode", liquid - "cathode") and mode 2 (needle - "cathode", liquid - "anode") were investigated in the work.

The results of spectroscopic studies of a plasma jet generated in an argon flow between metal and liquid electrodes are shown in Fig. 2-4. The main emission of the glow discharge is concentrated in the spectral range of 300–400 nm and is represented by the bands of hydroxyl OH(X-A) and the second positive system of the nitrogen molecule $N_2$ (337.1 nm (0 - 0) with the most intense emission band and the less intense bands 357.7 (0 - 1), 375.5 (1 - 3), 380.5 nm (0 - 2)). In the visible region of the spectrum, the spectral line of the hydrogen atom Hα (656.28 nm), Hβ (486.133 nm) and argon lines were observed. We note that it was not possible to detect the emission of iron atoms, most likely due to the insufficiently high plasma temperature and high excitation energies of the upper levels of iron atoms.

The temperature estimation methods used in our work are based on the search for the best fit between the experimental and simulated emission spectra of OH radicals or the second positive $N_2$ system. Fig. 2-3 show an approximation of the $N_2$ and OH (in insets) spectra by a theoretically calculated ones for estimating the vibrational and rotational temperatures of the plasma. The difference between the vibrational (~2800 K (mode 1) and ~3000 K (mode 2)) and rotational (~900 K (mode 1) and ~850 K (mode 2)) temperatures indicates a non-equilibrium state of the microplasma of this type of discharge. The gas temperature (rotational temperature Trot) calculated from molecular spectra is in good agreement with the data of [4], where the discharge conditions are similar (discharge at atmospheric pressure in argon at a current of several mA).

A widely used method for estimating the temperature of plasma electrons is the method of relative intensities of spectral lines [5]. However, suitable emission lines for determining the electron temperature of the plasma from the ratio of atomic lines with different excitation energies or atomic and ion lines in the discharge emission spectrum have not been found.

Therefore, when estimating the electron concentration from the broadening of spectral lines, it was assumed that the electron temperature in our experiment is about 10,000 K, similar to the electron temperature estimated in [4].

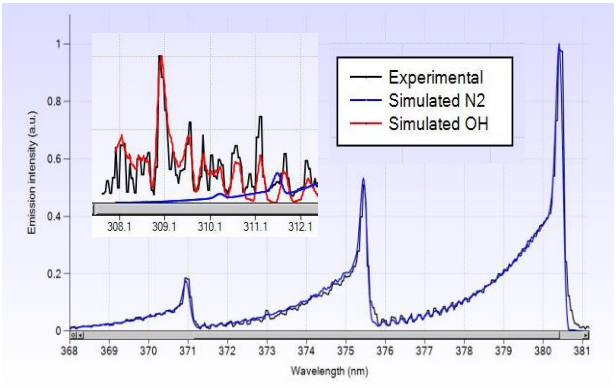



Fig. 2. $N_2$ and OH (in inset) spectra approximated by the theoretically calculated spectrum (mode 1, Tvib = 2800K, Trot = 900K)

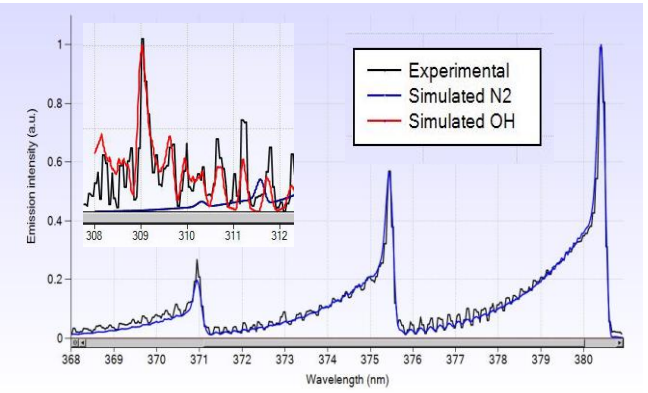



Fig. 3. $N_2$ and OH (in inset) spectra approximated by the theoretically calculated spectrum (mode 2, Tvib = 3000K, Trot = 850K)

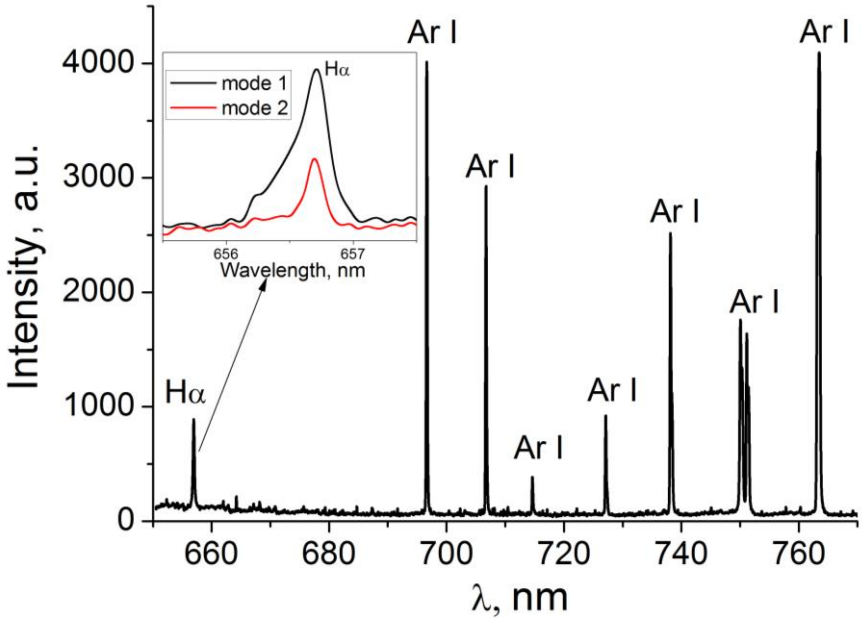



Fig. 4. The emission spectrum of the discharge plasma in the region of 650 – 770 nm. Inset – enlarged region with Ha

The electron concentration was determined from the measured Stark width of the hydrogen atomic line Ha 656.28 nm (Fig. 4) [6]. The electron density was $8.02 \cdot 10^{15}$см$^{-3}$ (mode 1) and $5.9 \cdot 10^{14}$см$^{-3}$ (mode 2).

To investigate the effect of polarity of discharge on the morphology and composition of nanoparticles formed, the SEM images and EDX mapping were performed using SUPRA 55WDS (Carl Zeiss, Germany) microscope. SEM images (Fig. 5) reveal that the samples consist of hierarchical urchin-like spheres (up to 1μm) assembled from nanorods. When the needle acts as an anode (Fig.5a),

particles are composed of subunits with small (less 100 nm) needles. In this case the length of the needles reaches up to 0.5 μm.

EDX spectra (not presented) confirmed that the obtained samples mostly consist of iron and oxygen with the presence of trace amount of sulfur.

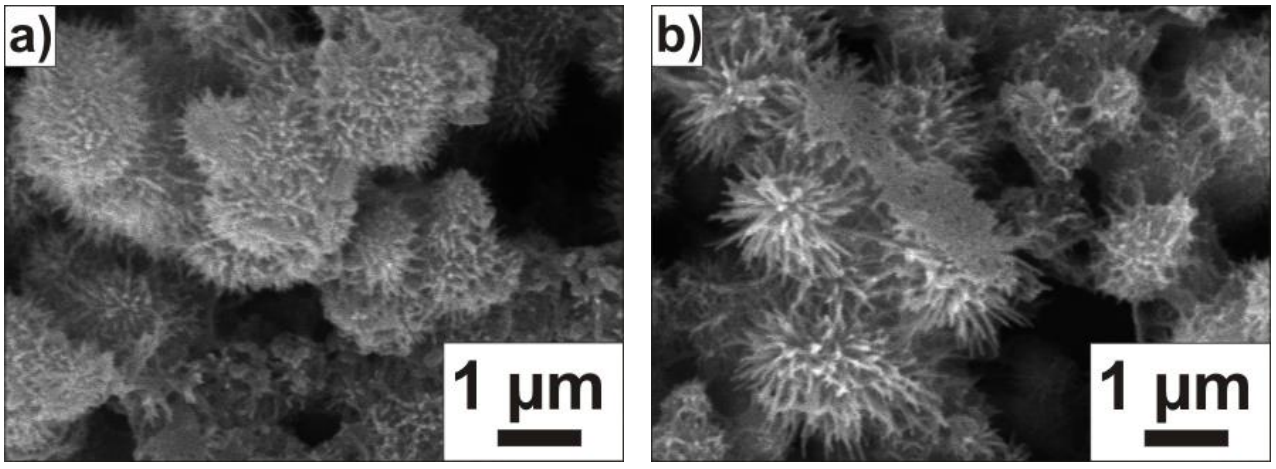



Fig. 5. SEM images of urchin-like spheres synthesized at atmospheric pressure discharge in contact with solution in mode1 (a) and mode 2 (b)

In summary, the iron oxyhydroxide nanoparticles were fabricated via glow discharge at atmospheric pressure between metal and liquid electrodes. It has been established that the polarity of the electrodes affects to the characteristics of the plasma and the morphology of the synthesized particles. Further research will focus on studying the electrochemical characteristics of hierarchical urchin-like FeOOH spheres in anodes for lithium-ion batteries.

**Acknowledgements**. This work was supported by the National Academy of Sciences of Belarus (project Convergence 2.2.05), by BRFFR (grant number F21RM-104) and by RFBR (grant number 20-53-04010).

**References**

1. **Bratescu M. A., Saito N., Takai O.** Current Applied Physics, 11 ( 5 ) (2011) S30-S34.
2. **Bao Wang, Haobin Wu, Le Yu, Rong Xu, Teik-Thye Lim, and Xiong Wen (David) Lou** Adv. Mater., 24 (2012) 1111–1116.
3. **Tiya-Djowe, A. Laminsi S., Noupeyi G.L., Gaigneaux E.M.** Applied Catalysis B: Environmental, 176 (2015) 99–106.
4. **Arkhipenko V.I., Kirillov A.A., Safronau Y.A., Simonchik L.V., Zgirouski S.M.** Eur. Phys. J. D, 66 (2012) 252.
5. **Грим, Г.** Спектроскопия плазмы / Г. Грим. – М.: Атомиздат, 1969
6. **Gigososy M.A., Cardenoso V.** J. Phys. B: At. Mol. Opt. Phys., 29 (1996) 4795–4838.

# THE MECHANISM OF SINGLE-FREQUENCY HIGH POWER MICROWAVE GENERATION BY RELATIVISTIC VIRTUAL CATHODE OSCILLATORS

P. Molchanov[1], A. Rouba[1]

[1] Institute for Nuclear Problems of Belarusian State University, Bobruiskaya str., 11, 220006, Minsk, Belarus, molchanov-p-v@mail.ru

## 1. Introduction

Virtual cathode oscillators (vircators) are one of the promising microwave sources of gigawatt power level pulses, generating an efficiency level of 8-12% under conditions of single-frequency generation [1,2,3]. For the first time assumptions about the parametric resonance gaining and the implementation of single-frequency generation were put forward in the work of A.N. Didenko for a reflex triode oscillator with a virtual cathode (VC) [4]. In this paper, we study the conditions for establishing a single-frequency generation regime of high power microwaves based on the results of numerical simulation of an axial vircator with a three-cavity resonator and a reflex triode vircator with an electron beam energy of 400÷500 keV.

## 2. Numerical simulation

The electrodynamics structures of the investigated vircators are shown in Fig. 1., where 1 is the emitting cathode, 2 is the transparent anode mesh of the diode unit, 3 and 4 are the internal elements of the vircator's resonators, serving to form the internal feedback. The presented vircators were developed and experimentally studied by researcher team from the INP BSU for electron beam energies of 400÷500 keV [5, 6].

Simulation and optimization were carried out using 2.5D particle-in-cell code XOOPIC [7]. An electron beam with given values of current, energy, and velocity spread was injected into the computational domain from the left side.

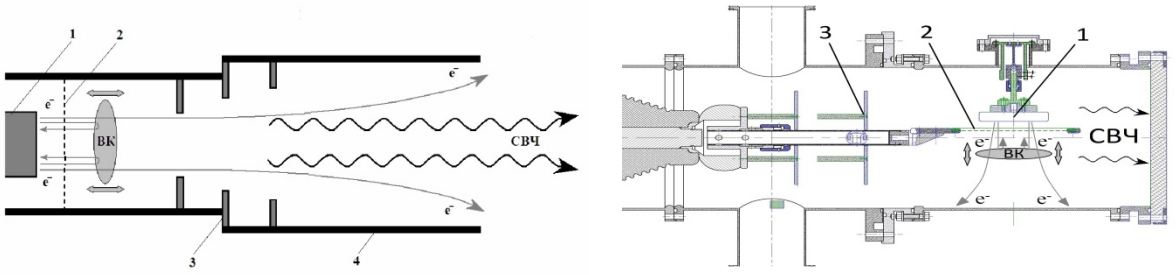



Fig.1. Schematic layouts of the three-cavity axial vircator (left) and reflex triode vircator (right).

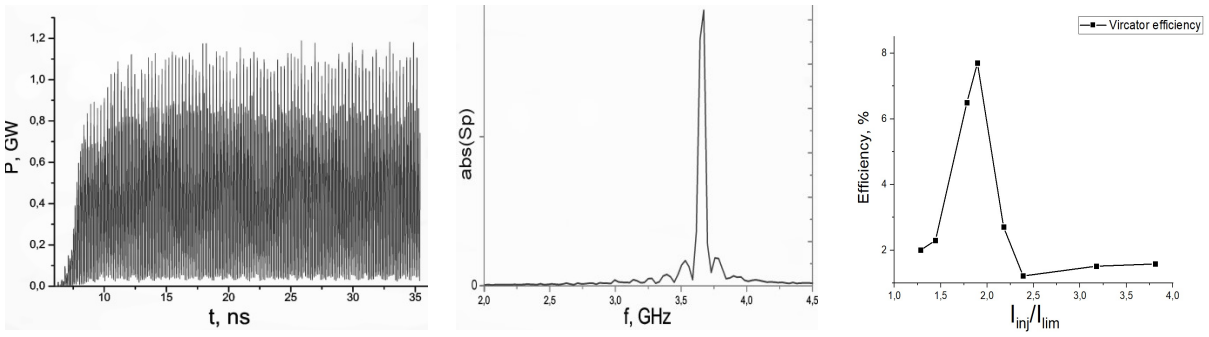



Fig.2. Radiation power (left), microwave spectrum (center) and generation efficiency (right) of the three-cavity axial vircator layout simulated for the injected beam of energy 450 keV.

The microwave power was determined by integrating the flow of the Poynting vector (see Fig. 2 (left)). The Fourier transforms of the *r*- and *z*-components of the electric field at several points near the right boundary were used to calculate the radiation spectrum (see Fig. 2(center)). Measuring current monitors detecting the magnitudes of electrons flow oscillations in the fluxes of reflecting, transmitting electrons and the oscillations of the virtual cathode (VC) were used in numerical simulations (see Fig. 3 (left, center)).

The principle underlying vircator operation consists in the formation of an oscillating virtual cathode (VC) in the electron flow whose current exceeds the threshold vacuum (critical) current $I_{lim}$ of the oscillating VC. The maximum efficiency of generation of the axial vircator is achieved when the operating current are about twice the critical current determined in the section with beam-microwave conversion see Fig. 2 (right). Formation of a nonstationary vircator is deterring to a complete transmission of the electron beam current through the drift tube and leads to formation of the flows of electrons reflected and transmitted by the VC. The current through a VC oscillates near the value determined by the critical current $\langle I_{VC} \rangle = I_{lim}$ [8].

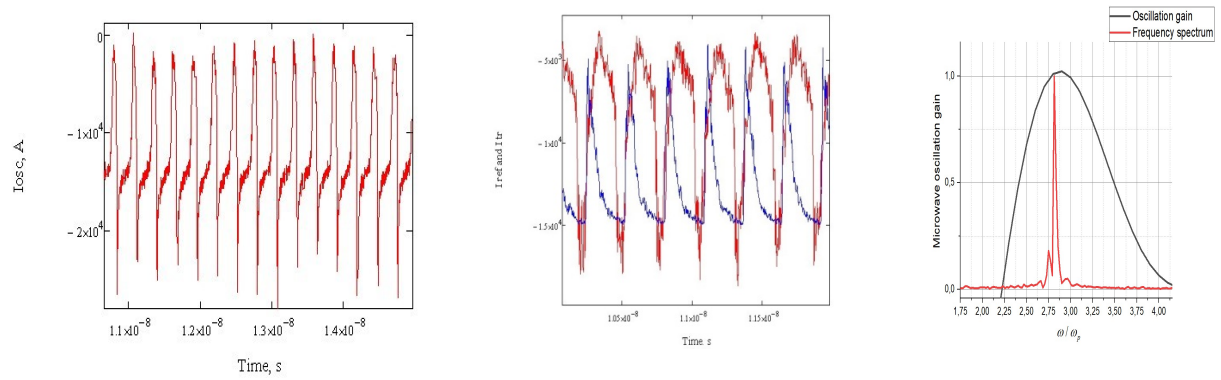



Fig.3. Oscillations of the electron flows of the VC (left), reflecting and transmitting electron streams (center) and the analytic curve for the predicted oscillation gain and spectrum (right).

According to a one-dimensional analytical theory [9] microwave gain of the vircator oscillations grows and amplification can be expressed as:

$$F(\omega) \sim -\frac{\omega_p}{\omega}\sin^2\frac{\omega}{\sqrt{2}\omega_p}\sin\frac{\sqrt{2}\omega}{\omega_p}\quad,\quad \omega_p = \left(\frac{n_0 e^2}{\varepsilon_0 m \gamma_0}\right)^{1/2} \qquad (1)$$

Where $\gamma_0$ and $n_0$ are the relativistic factor and the electron density and $\omega_p$ is called the plasma frequency. It can be found from Fig. 3(right) that the vircator microwave generation gain is predicting a maximum value at the parameter of the beam plasma frequency with the radiation frequency $\omega \approx 2.8 \div 2.9\omega_p$.

At present the general concept is accepted, that the two generation mechanisms are simultaneously implemented in high power microwaves vircators: those caused by oscillations of the reflected electron flow in the cathode-virtual cathode space $\omega_{ref}$ and due to oscillations of the virtual cathode bunch as it all $\omega_{VC}$. The most optimal and highly effective regime will be single-frequency generation under $\omega=\omega_{VC}=\omega_{ref}$ these frequencies coincide. The results of numerical studies to determine the frequencies of electron fluxes oscillations presented in this work on the graphs of Figure 4 (left, center) for the axial vircator and the reflex triode vircator confirm this conclusion. The relationship between the frequency of inducing and the frequency of beam plasma oscillations can be established as follows [10], as that fast space charge waves propagating in the injected beam can have characteristic frequencies $\omega_q = 2\omega_p$. Taking into account that in the considering vircator layouts the current of the injected beam is close to the value $2I_{lim}$, i.e. $\omega_q = 2\sqrt{2}\,\omega_{p(VC)}$, we defined the resonance conditions as: $\omega_{VC} \approx \omega_{ref} \approx \omega_{res} \approx 2.8 \div 2.9\ \omega_{p(VC)}$. Where $\omega_{p(VC)}$ - beam plasma frequency determined by the critical current $I_{lim}$, $\omega_{res}$ – intrinsic resonator frequency.

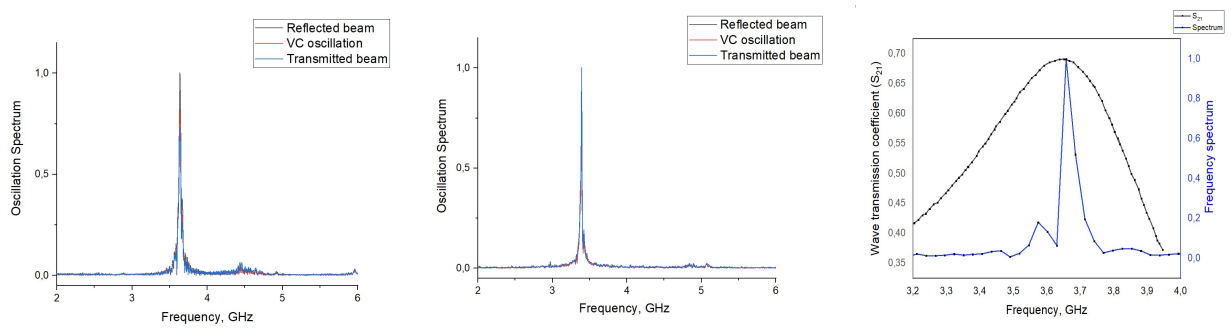



Fig.4. Oscillation spectrums of the electron flows for the axial vircator at frequency 3.65 GHz (left), for case of the reflex triode vircator at frequency 3.37 GHz (center) and the curve of $S_{21}$ parameter of the calculated passband for axial vircator resonator and the spectrum (right).

In the case that VC originated in the resonator whose the natural frequency is closed to the virtual cathode oscillator frequency is attained the resonant feedback (see Fig. 4 (right)).

## 3. Conclusion

The single-frequency operation regimes of the relativistic vircators have been numerically simulated and investigated. The computed results are in good agreement with the experimental data on observation of a single-mode generation in the axial and the coaxial vircators with a three-cavity resonator [3, 5], reflex triode vircator [6]. It has been found out that the resonant generation regime in the vircator is determined by the arising self-consistent state between the electron beam and the VC oscillations in the presence of two modulated electron flows. Under resonance conditions the vircator is a parametric generator operating in the mode of auto-generation. At the same time, the VC acts as a valve (gate), transmitting or reflecting the beam's electrons, depending on the oscillation phase. The periodicity of this process in the considered generators is determined by the generation frequency in the dependence from beam plasma frequency $\omega \approx 2.8 \div 2.9 \omega_{p(VC)}$.

## References


1. **Didenko A.N.** et al. Proc. 3rd Int. Topical Conf. High-Power Electron Ion Beam Res. Technol., 2 (1979) 683 - 691.
2. **Jiang W.** et al. IEEE Trans. Plasma Sci., 1 (2004) 54-59.
3. **Qiangjiguang Yu Lizishu** et al. High Power Laser and Particle Beams, 19 (2007) 91-94.
4. **Didenko A.N.** Doklady Akademii nauk SSSR, 321 (1991) 727-729.
5. **Baryshevsky V.G.** et al. IEEE Trans. Plasma Sci., 10 (2015) 3507-3511.
6. **Baryshevsky V.G.** et al. IEEE Trans. Plasma Sci., 45 (2017) 631-635.
7. **Verboncoeur J.P., Langdon A.B., Gladd N.T.**, Computer Physics Communications 87 (1995) 199-211.
8. **Dubinov A.E. and Efimova I.A.** Technical Physics, 48 (2003) 126-129.
9. **Jiang W.** et al. Phys. Plasmas, 8 (2001) 3781–3787.
10. **Louisell William H.** Coupled Mode and Parametric Electronics, Hassell Street Press (2021).

# INVESTIGATION OF THE EFFECTIVENESS OF THE INTERACTION OF PLASMA BEAMS WITH A MAGNETIZED TARGET

N.V. Batrak, M.V. Kutyrev, N.G. Kopaleishvili

Bauman Moscow State Technical University (BMSTU), 2-nd Baumanskaya, 5, 1, Moscow, 105005, Russia, nik.nikita02@mail.ru

An interaction of plasma beams with a target located in a seed magnetic field is considered by authors. Two types of designs of pulse choke-transformers used in experiments are presented.

For a coaxial magnetoplasma accelerator [1-14], various injectors have been designed and built. Note that the experiments used different types of designs of pulsed choke - transformers Tr1.

The construction of the first type did not have a ferromagnetic core, and a dielectric ring (kaprolon) was used as a frame. The design of the second type had an annular (pseudo-toroid) ferromagnetic core (ferrite). This type of design made it possible to significantly reduce the number of turns of the secondary winding (reduce ohmic resistance) compared to the first type, due to the concentration of the magnetic flux and ensured reliable operation at the first stage of the injector working process (step-up pulse transformer mode). The cross section of the ferromagnet was selected in such a way that during the discharge of the power capacitor C1 in the second stage of the working process (throttle mode), the core material was guaranteed to saturate. This led to "pauses" of the discharge current, but significantly increased the amplitude and reduced the temporal parameters of the current characteristic (increased the instantaneous power of energy release) compared to the "classical" sinusoidal current characteristic, which was realized when using a choke - transformer of the first type.

It is necessary to dwell on the design of the choke - transformers, as one of the main elements of the energy-generating part of the injector power circuit.

Two “air” toroidal pulse step-up transformers were assembled on a caprolon ring, differing in the design of the secondary windings. In the first case, the winding of the secondary winding was carried out with a single-core standard winding copper wire with a diameter of 1.5 mm. in lacquered insulation. The total number of turns of the secondary winding was 302 turns, the inductance of the secondary winding was about 270×10-6 H.

The excitation winding of the transformer was wound with a stranded network wire soldered "in parallel" in PVC insulation, "dressed" in an additional insulating cambric. The wire diameter was 1.8 mm, the winding consisted of 6 turns.

In the second case, the winding of the secondary winding was carried out with a double MGTF wire with a cross-sectional area of \u200b\u200beach wire 0.35 mm2 and amounted to 217 turns, while its inductance was 166 × 10-6 H. The ohmic resistance of the secondary in both cases was 0.4 ohm.

Structural parameters of the caprolon ring (pseudotoroid) for winding are shown in Fig. one.

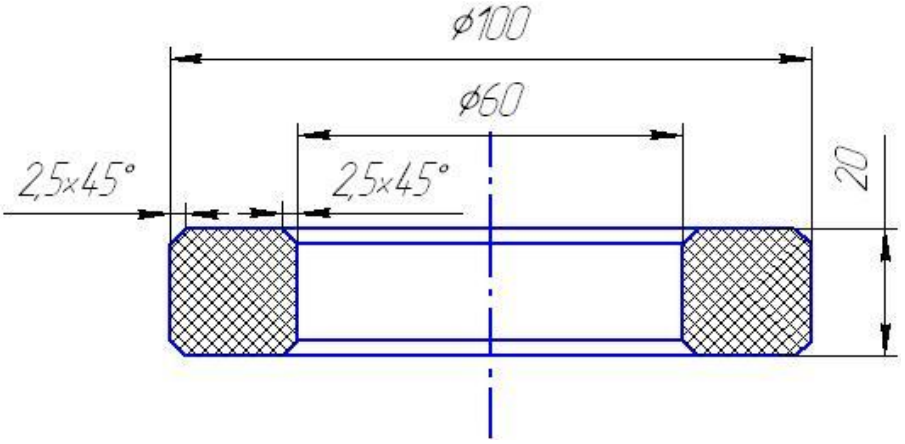



Fig. 1. Design of a caprolon ring (pseudo-toroid) for winding

During the operation of the “air” transformer, the discharge current through an injector of any type was a sonusoidal shape. The parameters of the discharge current from the design of the injectors practically did not change and depended only on the capacitance of the capacitor and the parameters of the secondary winding of the choke-transformer.

In the experiments, pseudo-toroidal transformers of the second type on ferromagnetic cores were also used. Three transformers were assembled parameters of ferromagnetic cores.

Fig. 2 shows diagram of a choke-transformer and an injector for creating a high-speed plasma jet.

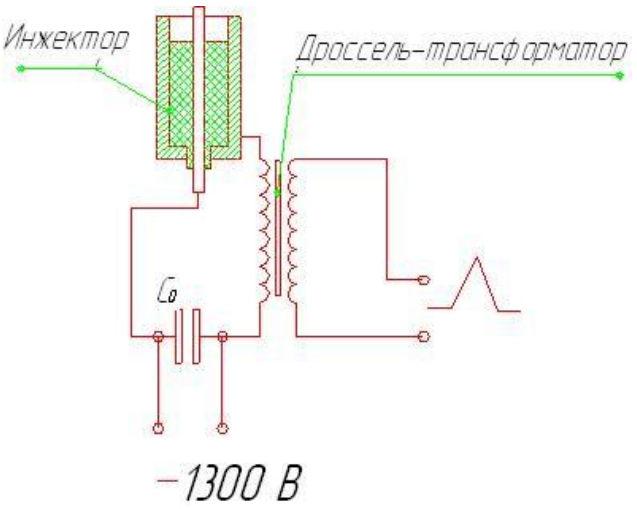



Fig. 2. Throttle - transformer and injector for plasma jet generation

The oscillogram of the discharge on the injector 2-2 (chamber 1mm) 4uF, TR-1A is shown in Fig. 3. As can be seen from the comparison with the oscillogram in the case of the pressed state, they are almost completely identical, with the exception of a slight increase in the time between the 3rd and 4th half-cycles.

V, мВ

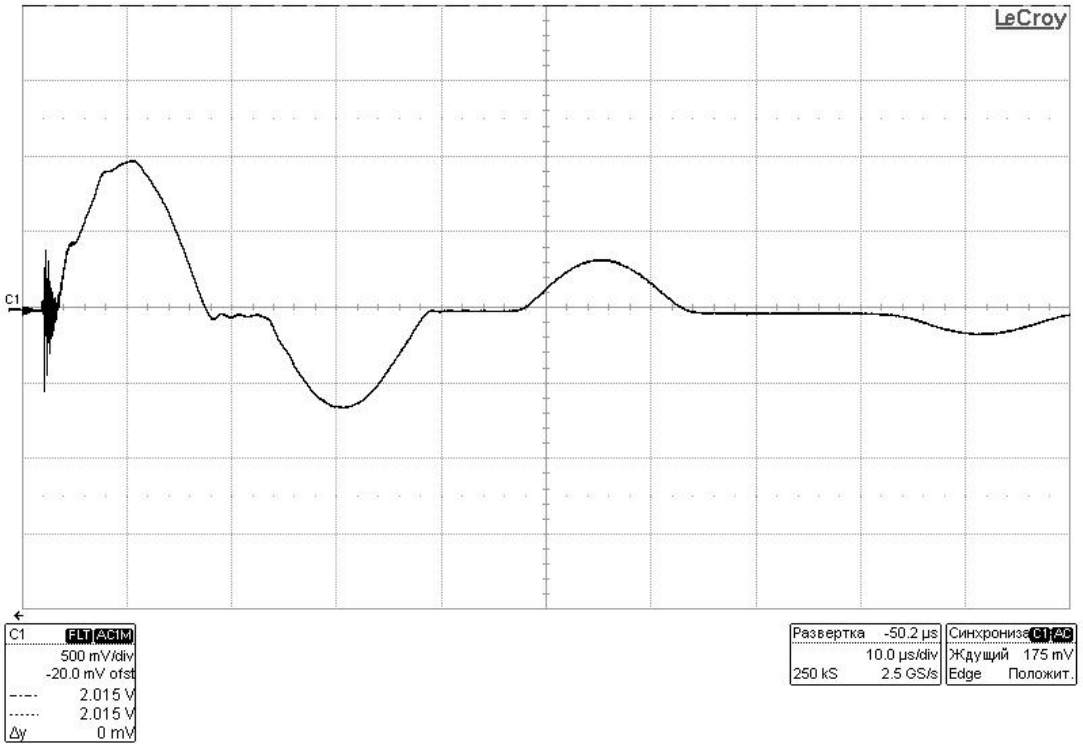



Fig. 3. Principal oscillogram of the discharge on the injector TR-1A, 4 µF

## References


1. **Astashynski V.M., Dzahnidze H.M., Kostyukevich E.A., Kuzmitski A.M., Shoronov P.N., Shymanski V.I. and Uglov V.V.** High Temp. Material Processes, 24 (2020) 99–107.
2. **Garkusha I.E., Chebotarev V.V., Herashchenko S.S., Makhlaj V.A. Kulik N.V., Ladygina M.S., Marchenko A.K., Petrov Y.V., Staltsov V.V., Shevchuk P.V., Solyakov D.G. and Yelisyeyev D.V.** Nuclear Fusion, 57 (2017) 116011.
3. **Kuzenov V.V., Ryzhkov S.V., Gavrilova A.Yu. and Skorokhod E.P.** High Temperature Material Processes, 18 (2014) 119–130.
4. **Nosov K.V., Pavlov A.V., Protasov Y.Y., Telekh V.D. and Tshepanuk T.S.** J. of Phys.: Conf. Ser., 1115 (2018) 032011.
5. **Sivkov A., Naiden E., Ivashutenko A. and Shanenkov I.** Journal of Magnetism and Magnetic Materials, 405 (2016) 158–168.
6. **Kuzenov V.V., Ryzhkov S.V. and Frolko P.A.** JPCS, 830 (2017) 012049.
7. **Bakhtin V.A., Zakharov D.A., Kozlov A.N. and Konovalov V.S.** CEUR Workshop Proc., 2543 (2020) 59-70.
8. **Kuzenov V.V., Ryzhkov S.V. and Varaksin, A.Yu.** Applied Sciences, 12 (2022) 3610.
9. **Shanenkov I.I., Pak A.Ya., Sivkov A.A. and Shanenkova Yu.L.**, MATEC Web of Conferences, 19 (2014) 01030.
10. **Ryzhkov S.V., Chirkov A.Yu.** Alternative Fusion Fuels and Systems (CRC Press, Taylor & Francis Group, 2019) 200 p.
11. **Kuzenov V.V. and Ryzhkov S.V.** Physics of Plasmas 26 (2019) 092704.
12. **Kuzenov V.V. and Ryzhkov S.V.** Applied Physics, № 3 (2014) 26-30.
13. **Kuzenov V.V. and Ryzhkov S.V.** Symmetry, 13 (2021) 927.
14. **Kuzenov V.V. and Ryzhkov S.V.** Computational Thermal Sciences, 13 (2021) 45-56.

# BACTERICIDAL COMPONENTS OF AIR PLASMA JETS DIAGNOSTICS USING ABSORPTION IR AND UV SPECTROSCOPY

A.V. Kazak[1], A.A. Kirillov[1], L.V. Simonchik[1],
M. M. Kuraica[2], B. M. Obradovich[2], G. B. Sretenovich[2]

[1]B.I. Stepanov Institute of Physics, NAS of Belarus, Ave. Nezavisimosti 68, 220072, Minsk, Belarus, E-mail: a.kirillov@dragon.bas-net.by
[2]University of Belgrade, Faculty of Physics, Studentskitrg 12, 11001, Belgrade, Serbia,E-mail: obrat@ff.bg.ac.rs

## 1. Introduction

Plasma medicine is one of the most innovative and developing fields, integrating plasma physics, biology and clinical medicine. [1]. One of the most important unresolved problems is related to the controlled delivery of plasma agents to the affected targets for the correct determination of the "plasma dose". This work discusses the application of UV and IR absorption spectroscopy to determine the mole fraction of chemically active molecular components in air plasma jets of a direct current glow discharge and a dielectric barrier discharge (DBD) at atmospheric pressure, the effect of which on bacteria in the case of air jets is the main mechanism of inactivation of microorganisms [2, 3].

## 2. Experimental

Plasma jets of a direct current glow discharge are generated in a two-electrode gas discharge chamber with an interelectrode gap of about 1 mm at an air flow rate of 5 l/min from a DC source of 30 mA. Air is supplied to the gas-discharge chamber, passes through the discharge region, and forms a plasma jet through a hole 1.5 mm in diameter at the outlet of the anode [2].

The discharge chamber of the DBD, which generates a plasma jet, consists of two electrodes [4]. The high-voltage tubular electrode was placed into a quartz tube of inner diameter 2 mm and outer diameter 4 mm that acted as a barrier dielectric. The second electrode was grounded and located near the end of the tube. Air at flow rate 5 L/min was blown through the quartz tube. The discharge was generated using a laboratory pulsed high-voltage power supply with a step-up transformer that gave an output voltage up to 4.5 kV. The plasma generated in the DBD was carried into the surrounding medium by a flow of plasma-forming gas, which led to the formation of a plasma jet.

In the case of IR spectroscopy, a Cary 600 Series FTIR Spectrometer with a Pike 163-4100230 gas cell was used. The optical path of the gas cell is $L_{IR}$ = 10 m. The spectra were recorded with a Gaussian instrumental function with a

resolution of 1 $cm^{-1}$. For UV absorption spectroscopy, we used an NS-617831 deuterium lamp, a cuvette with a length of $L_{UV}$ = 50 cm, and an Ocean Optics Inc. QE65000 spectrometer. The absorption spectrum was recorded with a resolution of 0.4 nm. The gas was taken into the cells using a tube 4 mm in diameter, which was placed on the jet axis.

Subtracting from the experimental IR absorption spectra of plasma jets the vibrational-rotational bands of $H_2O$ and $CO_2$ molecules present in air, we obtain the spectra of the bactericidal components NO, $NO_2$, and $HNO_2$ in the glow discharge jet and $O_3$ in the DBR jet (Fig. 1a).

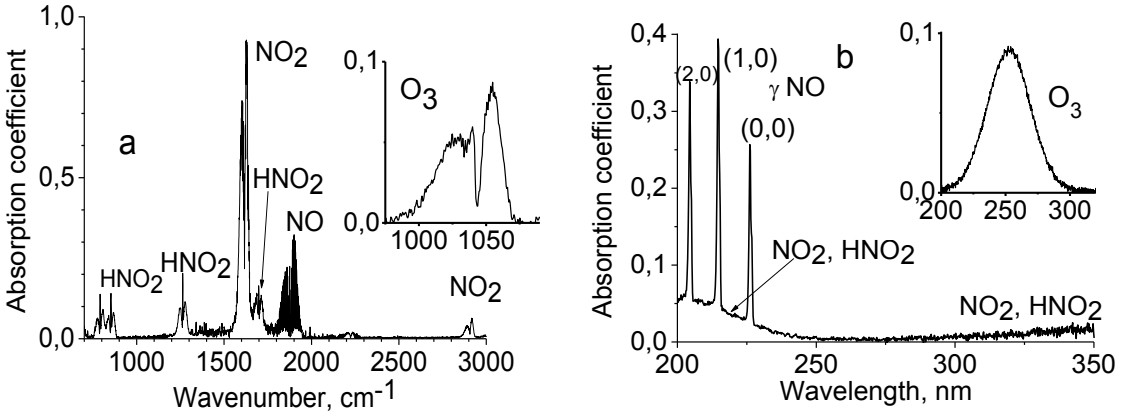



Fig.1. IR (a) and UV (b) absorption spectra of bactericidal components of air plasma jets

Fig. 1b shows the UV absorption spectra, the main contribution to which is made by the bactericidal components NO, $NO_2$, $HNO_2$ and $O_3$. In the case of a glow discharge jet, the continuous spectrum of $NO_2$ and $HNO_2$ is superimposed on the vibrational-rotational bands γ of the NO system. In a DBD jet in the spectral range 200 – 300 nm, absorption is almost completely determined by $O_3$ molecules.

## 3. Result and discussion

In the case of IR spectroscopy, the molar fractions of the bactericidal components NO, $NO_2$ and $O_3$ were determined by comparing the experimental transmission spectra and the transmission spectra calculated using the Hitran [5] spectral database, which contains data allowing the calculation of the absorption coefficient in vibrational-rotational bands $k(\nu)$ depending on the mole fraction of molecules $\alpha_i$. Applying the Beer - Lambert law, and performing convolution with the instrumental function $G(\nu - \nu')$, we obtain the spectral transmittance intended for comparison with experiment:

$$T_G(\nu) = \int \exp[-k(\nu')L_{IR}]\, G(\nu - \nu')d\nu' . \qquad (1)$$

At atmospheric pressure, the lines of the $HNO_2$ molecule overlap to form a continuous spectrum. The molar fraction of $HNO_2$ having a continuous absorption spectrum was determined in a standard way using the Beer - Lambert law and the spectral absorption cross sections of nitrous acid molecules $\sigma_{HNO2}(\nu)$ [5]. The problem is reduced to the selection of $\alpha(HNO_2)$ in the calculated absorption spectrum $k(\nu) = \alpha(HNO_2)\sigma_{NO2}(\nu)nL_{IR}$, which provide the best agreement with experiment. Here $n$ is the concentration of gas molecules in the cell. Examples of determining the mole fractions of molecules with a band spectrum ($NO_2$) and a continuous spectrum ($HNO_2$) are shown in Fig. 2.

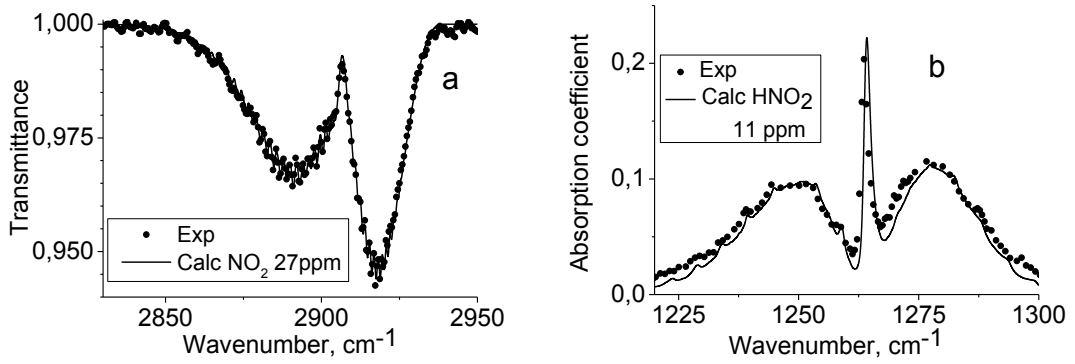



Fig.2. Experimental and calculated IR spectra of the $NO_2$ (a) and $HNO_2$ (b) bands

When using UV spectroscopy, the molar fraction of $NO_2$, $HNO_2$ and $O_3$ having a continuous absorption spectrum was determined in a standard way using the Beer - Lambert law and the spectral absorption cross sections of nitrogen dioxide molecules $\sigma_{NO2}(\lambda)$ [6], nitrous acid $\sigma_{HNO2}(\lambda)$ [7] and ozone $\sigma_{O3}(\lambda)$ [8] available in the literature.

In the case of the vibrational-rotational bands (0,0), (1,0) and (2,0) $\gamma$ - NO system, the application of the Beer - Lambert law with the published values of the cross sections is unacceptable, since they significantly depend on pressure, temperature, hardware resolution and their use in other conditions can lead to an error several times. For example, application of the absorption coefficient from [9] results in a mole fraction of NO 6 times higher than that determined using IR spectroscopy. The technique used by us consists in calculating the spectral transmittance $T(\lambda)$ of the gas in a cuvette with a given concentration of NO using the absorption coefficients of the true spectrum calculated in the Specair program [10], convolution of $T(\lambda)$ with the

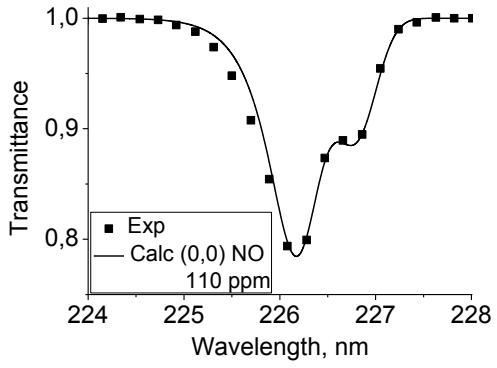



Fig. 3. UV transmission spectra in the (0,0) NO band

instrumental function and comparing the calculated spectrum with the experimental one. In fact, this coincides with the procedure for determining the concentrations of NO, $NO_2$ and $O_3$ by the IR method (see formula (1)). In the spectrum [10], it was necessary to make changes to achieve compliance with the literature data of the oscillator strengths of the bands [11] and collisional broadening of the lines [12]. Determination of the molar fraction of NO was carried out using the most represented in the literature band (0,0) (Fig. 3).

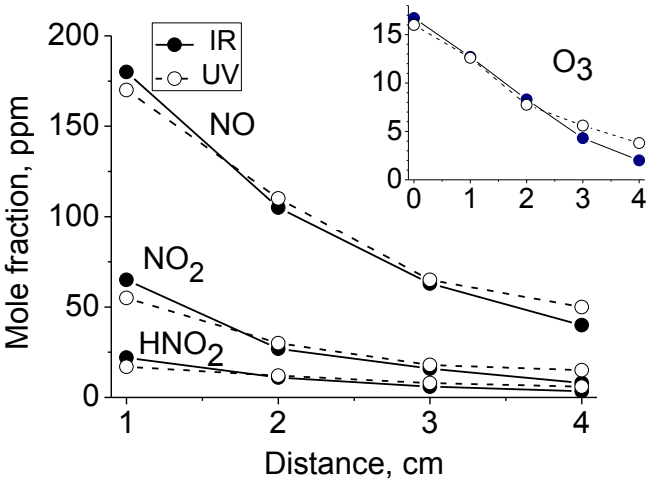



Fig. 4. Axial distribution of molar fractions of bactericidal components

There is a good agreement between the mole fractions of the bactericidal components determined by UV and IR absorption spectroscopy at short distances from the discharge chamber (Fig. 4). With an increase in the distance, IR spectroscopy leads to underestimated results due to the difficulty of achieving a large volume of concentrations in the jet in a multi-pass cuvette, due to the low velocity of the gas flow.

## References

**1. Laroussi M., et.al**. IEEE Transact. Rad. Plasma Med.Sci., 6 (2022) 127-157.
2. **KirillovA.A., et.al.** Appl. Phys., 5 **(**2013) 52-55.
3. **Kazak A., et.al**. J. Appl. Spectrosc., 88 **(**2021) 293-298.
4. **Sretenovic G. B., et.al.**, Plasma Sour. Sci. Technol., 27 (2018) 07LT01.
5. http://www.cfa.harvard.edu/HITRAN/
6. **Vandaele A. C., et.al.** J. Quant. Spectrosc. Radiat. Transfer, 59 (1998) 171-184.
7. **Kenner R. D., et.al.** J. Phys. Chem., 90 **(**1986) 2635-2639.
8. J. Viallon, **et.al.** Atmos. Meas. Tech., 8, (2015)1245–1257.
9. **Watanabe K., et.al.** Geophys. Res. Papers, No. 21 **(**1953**).**
10. http://www.specair-radiation.net/
11. **Farmer A.J.D., et.al.** J. Quant. Spectrosc. Radiat. Transfer, 12 (1972) 627-633.
12. **Chang A.Y., et.al.** J. Quant. Spectrosc. Radiat. Transfer, 47 **(**1992) 375-390.

# CONVERSION OF $CO_2$-$CH_4$ MIXTURE IN DIRECT CURRENT NON-SELF-SUSTAINED GLOW DISCHARGE AT ATMOSPHERIC PRESSURE

A.V. Kazak, A.A. Kirillov, L.V. Simonchik, M.U. Tomkavich

B.I. Stepanov Institute of Physics of NAS of Belarus, Ave. Nezavisimosti 68-2, 220072 Minsk, Belarus, Email: mikalaitomkavitch@yandex.by

## 1. Introduction

Biogas is a promising renewable energy source and an important component for the future energy supply. It mainly consists of methane (50–75%) and carbon dioxide (50–25%) with admixtures of other gases such as hydrogen sulfide, ammonia, hydrogen, nitrogen, oxygen, and water vapor [1]. The most common use of biogas is direct combustion to produce heat and electricity. However, the thermal value of biogas is reduced due to the high concentration of carbon dioxide in it. It is more efficient to convert biogas into synthesis gas (CO + $H_2$).

Catalytic and plasma technologies are considered to be promising for such conversion purpose. The main advantages of plasma-based conversion technologies include acceptable operating modes (atmospheric pressure, fast start-up, compact size, etc.). Various types of atmospheric pressure discharges namely corona, spark, barrier, arc and glow discharge are proposed as plasma sources for these purposes, but they account for differing degrees of productivity. Conversion devices based on "cold" plasma have very low productivity. Productivity increases when using the plasma sources with high currents such as arc [2] or glow discharge [3]. No matter type of discharges, the plasma-chemical reactors for biogas conversion are still far from a sufficient degree of energy efficiency and degree of conversion.

In the works [4, 5], high efficiency of the ethanol conversion into synthesis gas was demonstrated in a DC non-self-sustained atmospheric pressure glow discharge in a three-electrode configuration. The plasma chemical reactor based on such a discharge was adapted in this work for conversion of mixture of $CH_4$ and $CO_2$ into synthesis gas. The experimental results of the resulting conversion process investigations are presented.

## 2. Experimental setup

The design of the plasma-chemical reactor is based on a three-electrode system developed in [6] for generating stable large volume gas discharges. The photo and the setup of the plasma-chemical reactor is shown in Fig. 1, *a* and *b*, correspondingly. The reactor consists of a three-section discharge chamber (Fig.1, *b*). The segments of cylindrical quartz pipes form sections of the

chamber. In section A there is a cathode (steel rod with a diameter of 8 mm). A 1 mm thick brass insert in a duralumin disk 1 acts as anode. The interelectrode gap is 1-2 mm. A flow of $CO_2$ is provided through section A; $CO_2$ exits into

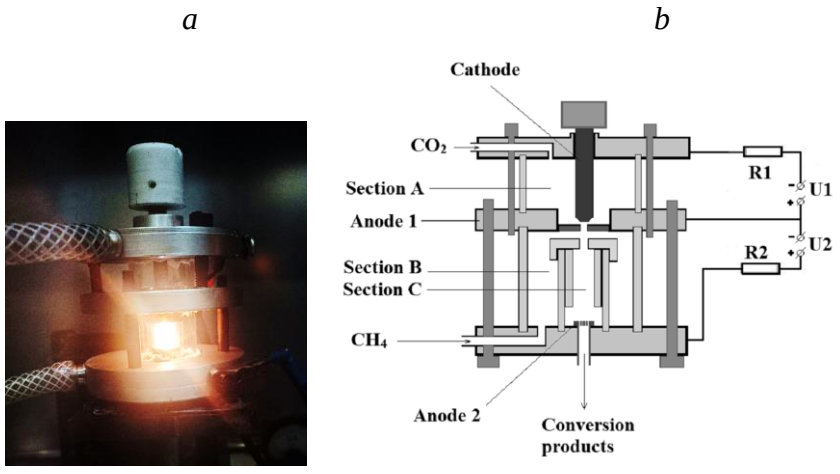



**Fig. 1.** Photo (*a*) and schematic (*b*) of the plasma–chemical reactor

section C through a hole in the center of the brass insert. At the same time, methane enters section C from section B. The flow rates of $CO_2$ and $CH_4$ are set so that the mixture in section C is realized at about 1:1 ratio.

In section A, a self-sustained normal glow discharge is ignited in $CO_2$. The discharge current (~200 mA) is controlled by the power supply U1 (1500 V, R1~ 5 kΩ). This discharge serves as a plasma cathode for a non-self-sustained discharge in $CO_2$-$CH_4$ mixture in section C. This discharge is ignited from another DC power supply U2 (3000 V, R2 ~ 10 kΩ), voltage of which is applied between anode 1 and anode 2. The interelectrode gap in section C is fixed at ~18 mm. The discharge current of the non-self-sustained discharge is 150-200 mA.

## 3. Experimental results

The fact that the reaction mixture gets additional energy after conversion

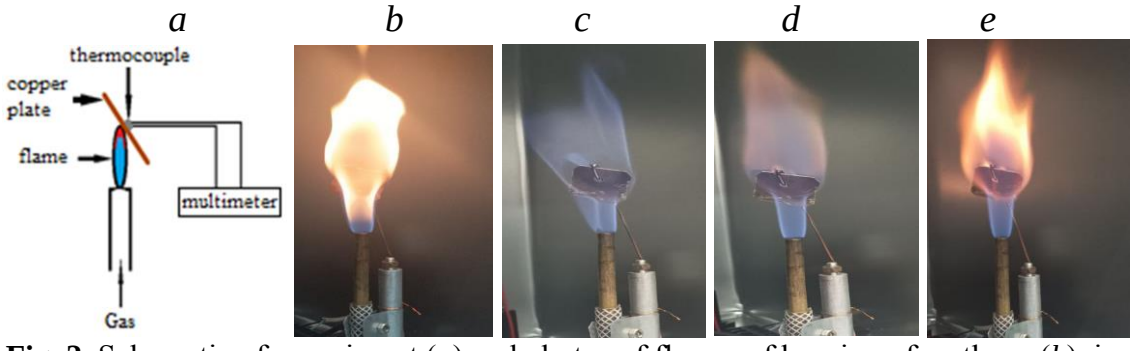



**Fig. 2.** Schematic of experiment (*a*) and photos of flames of burning of methane (*b*), input mixture (*c*) and conversion products (*d*, *e*).

was demonstrated in experiment, schematically shown in Fig. 2, *a*. A copper plate was placed at a distance of ~2 cm from the nozzle, and the temperature of its reverse side was measured with a thermocouple. When methane burned in air (Fig. 2, *b*), the temperature reached about 400 °C. Dilution of methane with the same volume of carbon dioxide (Fig. 2, *c*) leads to a decrease in the temperature of the plate to 250 °C. Turning on the discharge in chamber A (Fig. 2, *d*) increases the temperature to 330°C. The addition of a discharge in chamber C (Fig. 2, *e*) brings the temperature of the plate to 530°C.

The composition of the conversion products of the mixture of CH4 and CO2 was determined by an infrared absorption spectroscopy method, similar to [7]. For this, NEXUS (Thermo Nicolet) infrared spectrometer was used. The conversion products was passed through a diagnostic cuvette with germanium windows, preheated to 100 ºC to prevent water vapor condensation.

The mole fractions of the IR-active components of biogas and its conversion products were determined by comparing the experimental absorption spectra and those calculated using the Hitran spectral database [8]. The molar fraction of hydrogen was calculated taking into account the mole fractions of the IR active components in the biogas conversion products, determined experimentally and additionally controlled by the balance of hydrogen atoms at the inlet and outlet of the plasma chemical reactor.

Without discharges, the IR spectrum of the initial $CO_2$-$CH_4$ gas mixture contains three vibrational-rotational bands for $CO_2$ and two vibrational–rotational bands for $CH_4$ (Fig. 3, *a*). When the discharges were switched on in both sections, bands of $CO_2$, $CH_4$, CO, $H_2O$, and $C_2H_2$ molecules were identified in the gas absorption spectrum at the reactor outlet (Fig. 3, *b*).

The mole fractions of $CO_2$ and $CH_4$ were determined from the bands 3500-

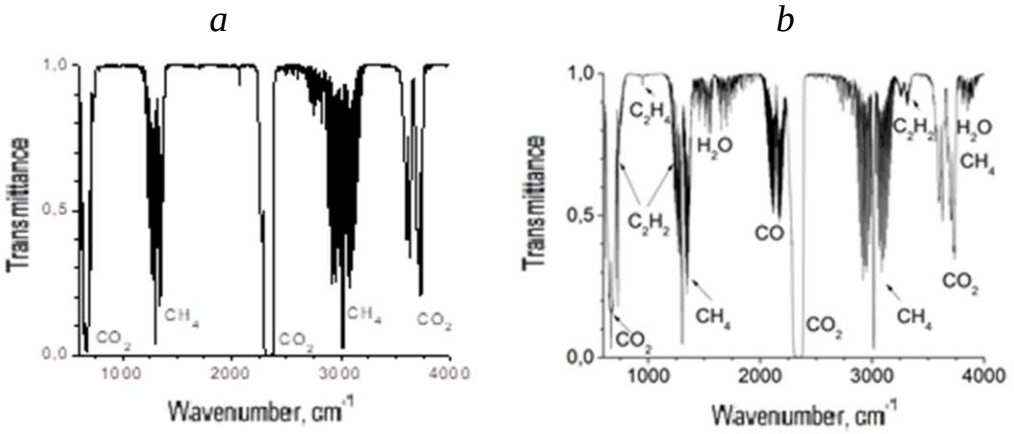



**Fig. 3.** IR absorption spectra of initial mixture (*a*) and conversion products (*b*).

3800 $cm^{-1}$ and 2800-3200 $cm^{-1}$, CO, $H_2O$ and $C_2H_2$ by bands 2000-2200 $cm^{-1}$, 1300-2000 $cm^{-1}$ and 3200-3400 $cm^{-1}$, respectively. We can assume that the remaining fraction will belong to $H_2$. The mole fraction of $H_2$ obtained in this

way was also controlled with consideration of the conservation of the hydrogen atoms number at the inlet and outlet of the reactor [7].

Table 1 shows conversion data for a mixture of 45% $CH_4$ and 55% $CO_2$ at two total flow rates of 0.7 l/min and 1.4 l/min. The operating modes of self-sustained and non-self-sustained discharges were about 200 mA. The total electrical power of both discharges was about 0.5 kW.

**Table 1.** Mole composition (percentage) of biogas conversion products.

| | flow 1.4 l/min | flow 0.7 l/min |
|---|---|---|
| $CO_2$ | 18 | 6 |
| $CH_4$ | 22 | 7 |
| $C_2H_2$ | 1.8 | 1.4 |
| $H_2O$ | 2.53 | 1.45 |
| CO | 35 | 45 |
| $H_2$ | 20.5 | 39 |
| $C_2H_4$ | 0.17 | 0.15 |

Analyzing the data in Table 1, we can conclude that with a decrease in biogas flow from 1.4 l/min to 0.7 l/min, the amount of CO and $H_2$ increases, while $CH_4$ and $CO_2$ decreases. As a result, the degrees of conversion of $CO_2$ and $CH_4$ increase from 58% to 83% and from 40% to 78% respectively. Apparently, the reasons for this increase in the productivity/conversion rate are higher gas temperature and longer residence time of the reaction mixture in the reactor core at lower flow rate.

## References


1. **H.J. Alves, C.B. Junior, R.R. Niklevicz et al.,** Int. J. Hydrogen Energy 38, 5215 (2013).
2. **A. Huang, G.G. Xia, J.Y. Wang et al.,** J. Catal. 189, 349 (2000).
3. **D. Li, X. Li, M. Bai et al.,** Int. J. Hydrogen Energy 34, 308 (2009).
4. **V.I. Arkhipenko, A.A. Kirillov, L.V. Simonchik et al.,** Open Chem. 13, 292 (2015).
5. **V.I. Arkhipenko, A.A. Kirillov, L.V. Simonchik et al.,** Int. J. Hydrogen Energy 41, 18320 (2016).
6. **V.I. Arkhipenko, A.A. Kirillov, T. Callegari et al.,** IEEE Trans. Plasma Sci. 37, 740 (2009).
7. **V.I. Arkhipenko, S.M. Zgirouski, A.G. Karoza et al.,** J. Appl. Spectrosc. 80, 99 (2013).
8. https://lweb.cfa.harvard.edu/HITRAN/.

# FEATURES OF DIELECTRIC BARRIER DISCHARGE IN MILLIMETER RANGE AIR DISCHARGE GAP

V. Parashchuk, V. Lyushkevich, S. Goncharik, I. Filatova

B. I. Stepanov Institute of Physics, National Academy of Sciences of Belarus,
68-2 Nezavisimosti Ave., 220072 Minsk, Belarus, Belarus, v_shchuka@rambler.ru

**Introduction**Non-thermal plasma at atmospheric pressure generated by dielectric barrier discharge (DBD) has been intensively investigated and widely used in various industrial applications due to its high efficiency and low operating costs /1, 2/. In general, DBD at atmospheric pressure manifests itself in a filamentary form which can leads to uneven treatment and local damage of treated surface /2/. This limits the prospects for DBD plasma application in new areas such as biomedicine and agriculture. This paper is devoted to optimize the conditions for DBD plasma obtaining with a homogeneous diffuse structure.

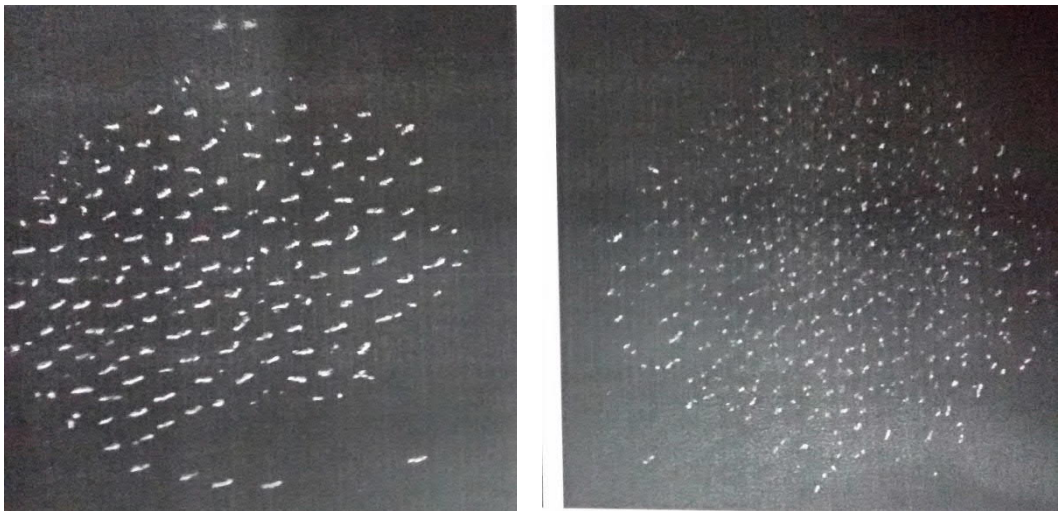
**Experimental part**

Dielectric barrier discharge is excited in a plane-parallel electrode configuration with diameter of 120 mm, one of which is mesh steel with a cell size about 1 mm, and the second is solid copper. The electrode distance was varied in the range of $d$ = 1–3 mm. A glass plate with a thickness of 1.5 mm was used as a dielectric. There were considered variants of DBDs with a dielectric coating of only one electrode, as well as the case of a dielectric coating of both electrodes. In some cases the surface of the copper electrode was subjected to mechanical cleaning. The applied voltage (peak-to-peak value) was up to $U$= 20 kV with the frequency of 1 kHz. The $U$ value was measured using a high-voltage capacitive compensated voltage divider. The electrical characteristics of the barrier discharge were studied using a GDS-72204E digital storage oscilloscope. Pictures of the discharge were obtained using a digital camera Canon PowerShot SX50HS in the direction normally to the plane of the electrodes. The average energy of the DBD for the period of the excitatory pulse ($E_{max}$) was measured by Lissageu's method /3/.

**Results and discussions**

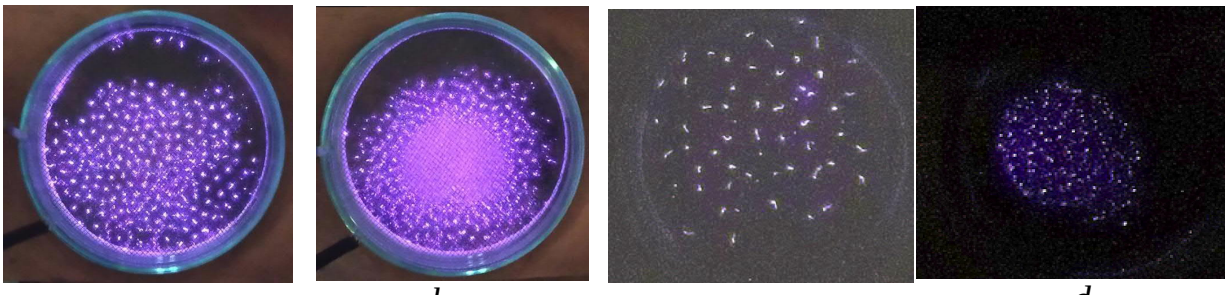
It was established that in the packet-pulse mode of DBD excitation at voltages $U \sim$ 15 – 16 kV for 3 mm discharge gap and non-cleaned copper electrode surface there is observed an increase in the total number of filamentary discharges within $t$ = 2 – 3 min after the onset of excitation (Fig. 1). And for cleaned electrode surface we observed "spatial compression" - narrowing of the discharges area (Fig. 2). For cleaned electrode surface, a partially diffuse discharge is also observed (Fig. 2b). Similar effects, but manifested in the DBD

area broadening accompanied by a change of modes (filamentary - diffuse and mixed discharges) was observed in /2/ were a sinusoidal excitatory pulse with a repetition frequency of $f \sim 10$ kHz was applied to the discharge with a small gap distance $d \sim 0.1 - 1.0$ mm. In our case, at such values of the discharge gap no discharge compression was obtained but we observed a transition over time to a homogeneous (diffuse) discharge over the entire area of the electrode (Fig. 3).



*a* *b*

Fig. 1. – The effect of increasing the density of filamentary discharges over time without changing the area of occurrence of filaments at non-cleaned copper electrode surface. $U \sim 15 - 16$ kV, $d = 3$ mm, $t = 0$ min (a), 10 min (*b*)



*a* *b* *c* *d*

Fig. 2. – The effect of increasing the density of filamentary discharges over time with a decrease in the area of occurrence of filaments; partial conversion to diffuse discharges at cleaned copper electrode surface (*b*); $U \sim 15 - 16$ kV, $d = 3$ mm, $t = 0$ min (*a, c)*, 10 min (*b, d*)

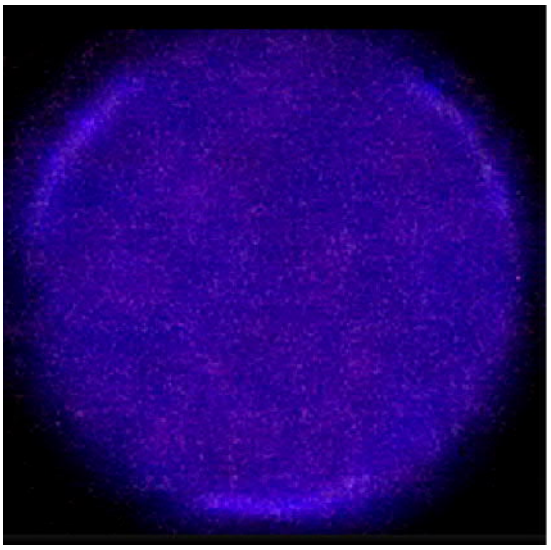


Fig. 3. – Excitation of homogeneous diffuse discharges; $U$ = 16 kV, $d$ = 1mm, $t$ = 10 min

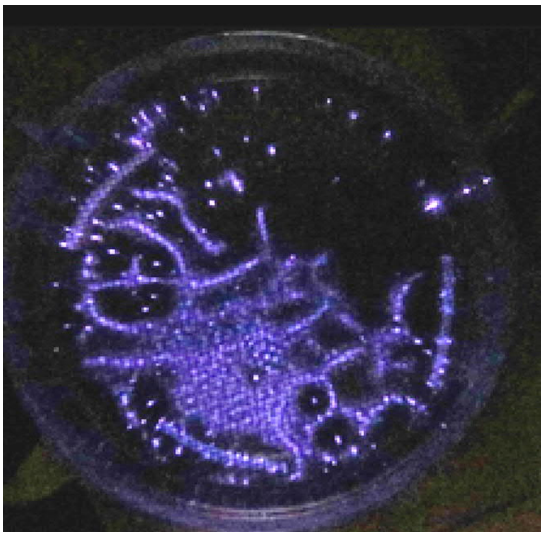


Fig. 4. – Formation of self-organized structures (case of using a reactor with two dielectrics); $U$ = 13 kV, $d$ = 3 mm, $t$ = 0 min

In the case of using a reactor with two dielectrics, a complex picture of filaments and diffuse discharges in the form of stationary and mobile chains of various shapes is observed (Fig. 4, cleaning copper), depending on the applied voltage and the magnitude of the discharge interval. Similar space-time structures have been observed previously (for example, /4, 5/), but the characteristic properties and conditions of excitation differ from those given. At the same time, for $d$ = 2 mm, there are more pronounced structures than in the case of $d$ = 3 mm. However after 2 – 3 min of the discharge burning the discharges behave approximately the same as in the case of one dielectric for a gap of 3 mm, they are concentrated, and the discharge pattern stabilized.

In order to optimize the conditions of excitation of DBD discharges, it was interesting to find out the dependence of the time pattern of discharges on the state of the surface of the lower electrode and the magnitude of the applied voltage. The comparison shows that with an untreated surface, unlike the case of treated and relatively low voltages $U \sim 5 – 7$ kV, filamentary discharges do not occur and surface (diffuse) ones develop. With a further increase in the applied voltage, the discharge pattern differs little for both cases. However, at $U$ = 16 kV, the area of "compressed" discharges close to the ring is larger and more homogeneous when cleaning the copper plate. In this area, the surface density of discharges is higher than at the initial moment.

The dependence of the average energy of the DBD for the period of the excitatory pulse ($E_{max}$) on its amplitude, exposure time ($t$) and other factors was studied. At the same time, Lissageu's energy measurements give values to $E_{max}$ =

6 – 10 mJ for $U$ = 12.5 kV and ~ 25 mJ for $U \geq$ 16 kV. Reducing the applied voltage from $U$ ~ 16 to 12.5 kV leads to a decrease in the time fluctuations of the $E_{max}$ value. At the same time, the discharge picture does not visually undergo significant changes over a long time $t \geq$ 30 min at a pulse packet repetition frequency $f$ = 1 kHz without breakdown phenomena, which indicates the stabilization and reproducibility of the operating mode. The above behavior of DBD discharges for the case of using two dielectrics in a discharge cell characterizes them as self-organized structures.

**Conclusions**

It is shown that in the packet-pulse mode of excitation of DBD for discharge gap of the millimeter range (~ 3 mm) in atmospheric air under certain conditions, a number of different plasma phenomena are possible such as the effects of increasing the density (total number) of filamentary discharges over time both unchanged and with a decrease in the area of filaments as well as the formation of complex space-time structures that can be explained by the processes of self-organization and should be a coupling of a discharge filamrnts pattern and charge pattern in a dielectric surface. Homogeneous diffuse discharges in electrode configuration with one dielectric were obtained for a gap distance of 1.0 mm. Some optimal conditions of DBD excitation for stabilization of its energy characteristics and obtaining the discharge with a homogeneous diffuse structure are determined.

**Acknowledgements**. This work was supported in part by the Belarusian Republican Foundation for Fundamental Research (grant No F21MC-016) and by the State Research Program “Convergence 2025. 2.2.02”, NIR 1. Development of the basis of the combined effect of plasma, electromagnetic fields and dichromatic laser radiation on materials and biological objects for use in new technologies”.

**References**

1. **Becker K. et al**. Non-Equilibrium Air Plasmas at Atmospheric Pressure. (2005) 700 pp.
2. **Fang Z. et al. J**. Phys. D: Appl. Phys. **40** (2007) 1401–1407.
3. **Brandenburg R**. Plasma Sources Sci. Technol. **26** (2017) 053001 29 pp.
4. **Dong L. et al**. Plasma Sources Science and Technology. **15** (2006) 840–844.
5. **Dong L. et al**. Physics of Plasmas. **18** (2011) 033506.

# PHYSICAL BASIS OF MATERIAL MODIFICATION BY RADIO-FREQUENCY DISCHARGE AT LOW PRESSURE

I. Abdullin[1], V. Zheltukhin[2], A. Shemakhin[3]

[1]Plasma-VST, LLC, Kurskaya St 27, 420081, Kazan, Russia, plasma.vst@gmail.com
[2]Kazan National Research Technological University, Karl Marx St 68, 420015, Kazan, Russia, vzheltukhin@gmail.com
[3]Kazan Federal University, Kremlyovskaya St 18, 420008, Kazan, Russia, shemakhin@gmail.com

The research results show that low-pressure (13.3-133 Pa) RF plasma allows processing organic and inorganic materials with different physical properties and structures. It can be used for deep cleaning and activation of the surface with the removal of defective layers, polishing, hardening, to coat and modify thin-film and multilayer coatings, modifying the hydrophilicity/hydrophobicity of polymers [1].

The variety of applications of low-pressure RF plasma is determined by some features that distinguish it from other discharges that are close in pressure range (glow discharge) or energy input method (inductively coupled RF discharge at atmospheric pressure).

The RF discharges properties were studied both in inert and in an argon/ molecular gas mixture in the range of gas flow rates from 0 to 0.2 g/s. The power in the discharge varied from 0.5 to 60 kW, the generator frequency varied from 1.76 to 30 MHz. Various types of RF discharges are implemented: both inductively coupled with a solenoidal inductor and capacitively coupled with ring and flat electrodes. The plasma properties were determined using a diagnostical suits.

As a result of comprehensive studies of low-pressure RF discharges, it was found that, unlike other types of gas discharges, they are characterized by the following distinctive features:

1) the plasma flowing from the discharge into the working chamber forms a plasma jet up to 0.5 m long, in which up to 50% of the total power deposited in the discharge is released. The electron density in the jet is several orders of magnitude higher than it should be in a decaying plasma, and, in addition, a significant electromagnetic field is detected;

2) near the surface of the specimen placed in the plasma jet, a layer of spatial positive charge (SPC) is formed. A thickness of SPC is from 0.1 to 5 mm depending on the plasma thermal nonequilibrium. The potential of the specimen relative to the plasma reaches values from 30 to 100 V;

3) due to the presence of SPC, plasma ions are accelerated to an energy of 30–100 eV. A low-intensity (0.3 - 25 $A/m^2$) flow of low-energy enters the

sample surface, which affects the properties of the surface layer of the material.

The accelerated ions collide with the specimen surface, recombine with electrons on it, and transfer both the kinetic and the recombination energy to the surface atoms. This is the main factor for the implementation of the processes of surface modifying.

A mathematical model has been developed that describes the processes in a quasi-neutral plasma, in a SPC, and in a double layer near the surface. As a result of the calculations, the dependences of the electromagnetic field, electron density, electron and gas temperatures, ion energy and density of the ion current on the sample surface on the setup parameters were established. It is shown that at ion energies up to 100 eV, the ion flux is focused on surface microroughness, which results in the selective nature of plasma treatment. The found effect is the basis for the implementation of the processes listed above and the main difference between this type of plasma-chemical treatment and others.

Studies of the interaction of low-pressure RF plasma with metals, dielectrics (organic and inorganic), and thin-film structures is carried out in order to develop a modification method that allows improving the functional and structural properties of engineering products.

It was found that in low-pressure RF discharge jet it is possible to implement the processes of formation of diffusion layers up to 200 μm with the simultaneous production of buried layers of atoms, including inert gas. The thickness of the buried layers reaches 20 nm.

As a result of treatment of a tungsten-cobalt alloy by a low-pressure RF jet discharge in a mixture of argon and propane-butane, a modified surface layer with a thickness of 70 to 420 nm is formed. The outer sublayer of ~10 nm by thickness contains carbon in the form of graphite; in the transition sublayer with a thickness of 10 nm to 70–420 nm, carbon is present in the composition of tungsten carbide, in a diamond-like state and in C–H and C–O–H bonds.

Nitrides, oxides and carbides of the metals are formed on the surface of titanium alloys, steels, when chemically reacting gases such as $N_2$, $O_2$, $CO_2$, $CH_4$, $C_3H_8/C_4H_{10}$ mixture are added to the plasma-forming gas. The lattice parameters of both *a* and *c* is increased. A tendency for surface hardness to increase after treatment in an oxygen-containing plasma has been found.

RF plasma treatment significantly accelerates diffusion processes, both from the gaseous medium into the surface layers of the material, and inside it. For example, the process of steel nitriding in low-pressure RF plasma proceeds 8 times faster than the “classical” furnace nitriding. RF plasma treatment also accelerates self-diffusion processes in steels. The consequence of this effect is the acceleration of tempering and recrystallization processes compared to conventional heat treatment.

The results of corrosion testing of steels and titanium alloys showed that a

general increase in corrosion resistance occurs after the RF plasma treatment. This effect is explained by the formation of a modified nanolayer on the surface.

Detailed studies using fractographic analysis after fatigue tests showed that sample destruction after plasma treatment begins on the one hand, fatigue strength and endurance limit increase by 25-35% with a simultaneous increase in microhardness by 10%, smooth diagrams of compressive residual stresses up to 200 μm deep is formed, and roughness is decreased on 2 classes.

Processing of both metals alloys and dielectrics allows efficient cleaning and activation before coating, which makes it possible to obtain high-quality coatings on silumin with an adhesive strength of about $10^9$ Pa at a temperature not exceeding 100ºC.

The principal difference between plasma polishing of metals, dielectrics, and semiconductors and other processing technique is the ability to remove cracked and relief layers simultaneously with polishing up to class 14 and above, which makes it possible to significantly increase fatigue strength and corrosion resistance.

The effect of low-pressure RF plasma jet on semiconductors reduces the reverse current density by 50%, the breakdown voltage of the p-n junction increases, and the packing density increases by 1-2 orders of magnitude.

The coating deposit using low-pressure RF discharge jet makes it possible to obtain films with improved parameters such as increased adhesive strength due to the formation of a diffuse transition layer. The film density is closed to the density of the bulk material; surface without impurity defects, micropores, and microcracks. Coatings can be applied both to products of complex configuration and to the inner surface of tubular products.

A process has been developed for volumetric processing of porous materials such as silica gel and various sorbents, which makes it possible to significantly improve their characteristics by increasing the specific porosity and equalizing the percentage of various pores.

Thus, the low-pressure RF plasma in gas blow mode is an unique method of different materials modifying to its property improvement.

**Acknowledgements**. This work was supported by the Russian Science Foundation (grant No. 19-71-10055).

## References

1. **Абдуллин И.Ш., Желтухин В.С., Кашапов Н.Ф.** Radio-frequency plasma-jet processing of materials at reduced pressures: theory and practice of application. Kazan: Kazan Univ. Press (2000).

| | Page |
|---|---|
| Abadias G. | 438 |
| Abdullin I.Sh. | 339 |
| Abdullin Kh.A. | 327 |
| Aberkane S. Messaoud | 181 |
| Abramov A.V. | 267 |
| Agabekov V. | 457 |
| Ageev S. | 382 |
| Aksiuchyts A. | 87 |
| Aksyuchits A.V. | 406, 410 |
| Altmark A. | 285, 289 |
| Andreev S. | 15, 239, 243 |
| Anishchenko S. | 414 |
| Anisovich A. | 165 |
| Anuchin S. | 374 |
| Anufrik S. | 263 |
| Apfelbaum E.M. | 149 |
| Ashkinazi E. | 335 |
| Astafiev A. | 285, 289 |
| Avdeeva K. | 457 |
| Avtaeva S. | 251 |
| Bagautdinova L.N. | 38 |
| Bahayeu S.I. | 342, 346 |
| Baryshnikov Yu.S. | 75 |
| Bashkircev O.E. | 132 |
| Batrak N.V. | 25, 480 |
| Batukaev T.S. | 67 |
| Bazhin P. | 58 |
| Beletskii E.V. | 472 |
| Belkov M.V. | 197, 277 |
| Belov M.M. | 217 |
| Bélteki Á. | 271 |
| Bernatskiy A.V. | 239, 243 |
| Bilera I.V. | 67 |
| Bogachev N. | 15 |
| Bokhanov A.F. | 42 |
| Boltnev R. | 116, 153 |
| Borisevich D.A. | 197 |
| Borodina V. | 273 |
| Bosak N.A. | 205, 229 |
| Bruhanova Yu. | 331 |
| Budaev V. | 169 |
| Buka A.V. | 205 |
| Butsen A. | 225 |
| Catsalap K.Yu. | 197, 277 |
| Chikiryaka A.V. | 75 |
| Chinnov V.F. | 366 |
| Chirtsov A. | 285, 289 |
| Chudják S. | 91 |
| Chumakov A.N. | 205, 221, 229, 382, 460 |
| Danilov P.A. | 177 |
| Demyanov A.V. | 247 |
| Doumaz D. Bennaceur | 185 |
| Draganov I. | 239 |
| Dudchik N. | 457 |
| Dyachkov L. | 124 |
| Dyatko N.A. | 243, 247 |
| Dyatlova E.M. | 205 |
| Dzlieva E. | 124, 132, 136, 142, 155 |
| Eldakli M. S.A. | 293 |
| Emlin R. | 29 |
| Epstein I. | 95 |
| Fedorovich S. | 169 |
| Filatova I.I. | 307, 311, 315, 327, 453, 492 |
| Fojtíková N. | 91 |
| Gabdullin M.T. | 327 |
| Gaisin Al. | 398, 402 |
| Gaković B. | 177 |

| | Page |
|---|---|
| Galbács G. | 271 |
| Galka A. | 259 |
| Gasilov M.A. | 155 |
| Gaysin Al.F. | 38 |
| Gaysin Az.F. | 38 |
| Gaysin F.M. | 38 |
| Gilmutdinov A.Kh. | 426, 430, 434 |
| Golubev M.S. | 155 |
| Golubev S.V. | 42 |
| Goncharik S.V. | 453, 492 |
| Goncharov V.K. | 319 |
| Gorbatov S. | 46, 50 |
| Gorbenko A. | 136 |
| Goroshko V.A. | 233 |
| Grigorian G.M. | 247 |
| Grigoryev E. | 382 |
| Grinchuk P.S. | 213 |
| Gurinovich A. | 414 |
| Gurnevich E. | 414 |
| Gusein-Zade N.G. | 442 |
| Heneral A. | 251 |
| Ionin A.A. | 177 |
| Islamov G. | 11 |
| Ivanov A.A. | 205 |
| Ivanov A.N. | 378 |
| Ivanov A.Yu. | 189, 193 |
| Ivanov I. | 46, 50, 209, 213, 217 |
| Ivanova P.A. | 378 |
| Ivković S.S. | 293 |
| Izotov I.V. | 42 |
| Jin K. | 209, 217 |
| Kalkozova Zh.K. | 327 |
| Kaplenko V.S. | 342 |
| Karasev V. | 124, 132, 136, 142, 155 |
| Karpov A. | 169 |
| Karpovich E.A. | 193 |
| Kavyrshin D.I. | 169, 366 |
| Kayumov R. | 402 |
| Kazak A.V. | 484, 488 |
| Kazantsev S.Y. | 442 |
| Kaziev A.V. | 62, 446 |
| Kellou A. | 181 |
| Kéri A. | 271 |
| Khafizov A.A. | 38 |
| Kharchenko E.F. | 339 |
| Kharkov M.M. | 446 |
| Khlyustova A. | 71, 394, 449 |
| Khmelnitsky R. | 335 |
| Khodasevich M.A. | 197 |
| Kholad V.M. | 213 |
| Khomich A. | 335 |
| Khrapak A. | 128 |
| Khudanov U. | 165 |
| Khvedchyn I. | 468 |
| Kirillov A.A. | 484, 488 |
| Kiris V.V. | 205, 277, 460 |
| Kiseleva E.M. | 42 |
| Kiyashko M.V. | 213 |
| Kladkov A. | 358, 362 |
| Kochetov I.V. | 239, 243, 247 |
| Kodirov T. | 165 |
| Kolodko D.V. | 62, 446 |
| Kolos V. | 422 |
| Konkov A. | 169 |
| Kononov E.A. | 3, 108, 110, 116, 120, 140 |
| Kopaleishvili N.G. | 25, 480 |
| Kormakov A.V. | 339 |
| Kornev V. | 201, 225, 464 |

| | Page |
|---|---|
| Koss X.G. | 140 |
| Kostrov A. | 112, 259 |
| Kotov D. | 87, 281, 406, 410, 418, 422 |
| Kovalchuk N. | 422 |
| Kozlov A.V. | 303 |
| Kozlov A.A. | 303 |
| Kozlovskiy A.L. | 209, 213, 217 |
| Krainov A.S. | 339 |
| Krashevskaya G.V. | 67 |
| Krčma F. | 91 |
| Kuchmizhak A.A. | 201 |
| Kudryashov S. | 79, 177 |
| Kukushkina M.S. | 446 |
| Kuputdinova A. | 402 |
| Kuraica M.M. | 484 |
| Kurakhmedov A.E. | 209, 217 |
| Kurakin R.O. | 75 |
| Kurian N. | 271, 374 |
| Kuryan N. | 263 |
| Kutyrev M.V. | 480 |
| Kuzenov V.V. | 25 |
| Kuzmanovic M. | 173 |
| Kuznechik O. | 382 |
| Kvaskov V. | 169 |
| Labutin T. | 271, 374 |
| Lapin R.L. | 42 |
| Lebedev Yu. A. | 67, 95 |
| Lellouche N. | 181 |
| Leonenko D. | 414 |
| Leonovich N. | 418, 422 |
| Leschinskaya N.M. | 453 |
| Leshchik A. | 79 |
| Lesiv A. | 285, 289 |
| Liavonchyk A. | 468 |
| Lipaev A. | 128 |
| Lisin E.A. | 120, 146 |
| Lisina I.I. | 140, 146 |
| Lobus N. | 271 |
| Logunov K. | 87 |
| Lomonosov G.S. | 446 |
| Lopaev D.V. | 390 |
| Lychkousky V.V. | 221, 229 |
| Lyushkevich V.A. | 307, 311, 315, 453, 492 |
| Makhsudov B. | 273 |
| Malyshev M. | 259 |
| Markevich M. | 165 |
| Maskevich S.A. | 307, 311, 315, 327 |
| Matasova E. | 335 |
| Matejčík Š. | 91 |
| Melezhenko D.E. | 390 |
| Melnikov A.D. | 21 |
| Menshakov A. | 331 |
| Miadzvetski A.V. | 307, 327 |
| Mikhalko A. | 457 |
| Mikhaylov D. | 273 |
| Milovanović D. | 177 |
| Mirkhanov D.N. | 398 |
| Mol'kov S. I. | 105 |
| Molchanov P. | 476 |
| Moravský L. | 91 |
| Morozov P. | 29 |
| Mukharaeva I. | 273 |
| Mustafaev A. | 273 |
| Myazin A.S. | 366 |
| Nagulin K.Yu. | 426, 430, 434 |
| Naumova I. | 394, 449 |
| Nedelko M. | 297, 460, 464, 472 |
| Nekrasov I.K. | 339 |

| | Page |
|---|---|
| Nescoromniy S. | 382 |
| Nevar A. | 297, 460, 464, 472 |
| Nikonchuk I. | 382 |
| Novikov L. | 124, 132, 142, 155 |
| Obradović B.M. | 293, 484 |
| Ochkin V.N. | 239, 243 |
| Orlov N.P. | 62 |
| Osipov A. | 87, 406 |
| Panarin V. | 99 |
| Pankratova E.A. | 267 |
| Parashchuk V. | 492 |
| Pavlov S. | 124, 132, 136, 142, 155 |
| Pechenitsin D. | 99 |
| Petrov O.F. | 3, 8, 108, 110, 116, 120, 128, 140, 146, 153 |
| Petrovskaya A. | 358, 362 |
| Petryakov S.Yu. | 398 |
| Platonov A. | 4 |
| Pobol I.L. | 342 |
| Podlesnikh S.V. | 442 |
| Polischuk V. | 136 |
| Polishchuk V.P. | 21, 303 |
| Polyakov A.V. | 42 |
| Poniaev S.A. | 75 |
| Prokhorova E. | 4 |
| Punanov I. | 29 |
| Pushkina N.V. | 453 |
| Puzyrev M.V. | 319 |
| Radomtsev A. | 225, 472 |
| Rafatov I. | 11, 54 |
| Ralchenko V. | 335 |
| Ramasanov T.S. | 327 |
| Rankovic D. | 173 |
| Rogachev A. | 457 |
| Rogozin K. | 169 |
| Rouba A. | 414, 476 |
| Rybkin V.V. | 378 |
| Ryskulov A.E. | 209, 217 |
| Safronov I.V. | 209 |
| Sakan N.M. | 255 |
| Saladukhin I.A. | 438 |
| Sametov E.A. | 120 |
| Sauchyn V. | 468 |
| Savastenko N.A. | 307, 311, 315, 327 |
| Savovic J. | 173 |
| Schitz D. | 99 |
| Sedov V. | 335 |
| Senoshenko R.V. | 108 |
| Shavelkina M.B. | 366 |
| Shcherbakov Ye | 29 |
| Shcherbovich A.A. | 307, 311, 315 |
| Shekelevski V. | 281 |
| Shevchenko M. | 335 |
| Shevchenok A.A. | 205 |
| Shishpanov A. | 58 |
| Shtykov A.S. | 105 |
| Shulgan N.I. | 319 |
| Shurupov A.V. | 303 |
| Shurupov M.A. | 303 |
| Shutov D.A. | 378 |
| Simić Z.J. | 255 |
| Simonchik L.V. | 484, 488 |
| Sirotkin N. | 71, 394, 449 |
| Sitkevich A.L. | 189, 193 |
| Skakun V. | 99 |
| Skalyga V.A. | 42 |
| Slyshov A. | 4 |
| Smirnova K.V. | 378 |
| Smolsky A.A. | 442 |

| | Page |
|---|---|
| Smyaglikov I.P. | 342, 346 |
| Sosnovskiy S. | 386 |
| Sovyk | 10 |
| Srećković V.A. | 255 |
| Sretenovich G.B. | 484 |
| Stepanjuk N.A. | 209 |
| Strizhakov E. | 382 |
| Suchkov A.N. | 233 |
| Sukhomlinov V. | 273 |
| Surov S. | 358, 362 |
| Sushkov N. | 271, 374 |
| Svetlov A.S. | 3 |
| Syrovatka R. | 128 |
| Tarasenka N. | 201, 225, 460, 464 |
| Tarasenko N. | 225, 297, 460, 464, 472 |
| Tarasov S.A. | 132 |
| Tarkovsky V.V. | 323 |
| Tatarinov A. | 95 |
| Tazmeev G. | 83 |
| Tazmeev Kh. | 83 |
| Terentiev A.A. | 430, 434 |
| Thoma M. | 128 |
| Tikhonov A. | 46, 50 |
| Tikhonov V. | 46, 50 |
| Timerkaev B. | 83 |
| Timofeev N. | 273 |
| Titov A. | 95 |
| Titov V. | 71, 394, 449 |
| Titovets P.A. | 442 |
| Tomkavich M.U. | 488 |
| Tovt P. | 418 |
| Tran V. | 169 |
| Trtica M. | 173 |
| Trukhachev F. | 8, 116 |
| Tsivilskiy I.V. | 426 |
| Tsyganov A. | 358, 362 |
| Tukmakov D. | 34 |
| Tumarkin V.A. | 62 |
| Turki M. | 185 |
| Tverdokhlebov K.V. | 75 |
| Uglov V.V. | 209, 213, 217, 233, 438 |
| Usachev A. | 128 |
| Usachonak M. | 15 |
| Usmanov R.A. | 21 |
| Valiev R.I. | 38 |
| Valko N.G. | 193 |
| Vasiliev M. | 116, 354, 370 |
| Vasiliev M.M. | 3, 8, 108, 110, 120, 140, 153 |
| Vasiliev S.V. | 189, 193 |
| Vasilieva T. | 350, 354, 370 |
| Vaulina O.S. | 146 |
| Vershinin I. | 259 |
| Vinogradov D. | 335 |
| Voronina E.N. | 390 |
| Vybin S.S. | 42 |
| Yahiaoui K. | 181 |
| Yanicin D.V. | 132 |
| Yartsev I.M. | 21 |
| Yashnov L. | 29 |
| Yesil C. | 11 |
| Zaletov V. | 58 |
| Zanka A. | 422 |
| Zanko A. | 418 |
| Zaparozhchanka Y.V. | 406, 410 |
| Zaytsev S. | 271, 374 |
| Zdorovets M.V. | 209, 213, 217 |
| Zheliaznova K.K. | 410 |
| Zhuk D.V. | 342 |

| | Page |
|---|---|
| Zhuravleva V. | 165 |
| Zissis G. | 273 |
| Zlotski S.V. | 209, 233, 438 |
| Zlotsky S.V. | 217 |
| Znosko K. | 161, 263, 323 |
| Zobnin A. | 128 |
| Zotovich A.I. | 390 |

Научное издание

The National Academy of Sciences of Belarus
B.I. Stepanov Institute of Physics of the National Academy of Sciences of Belarus Joint Institute for High Temperatures of the Russian Academy of Sciences

**X International Conference**

# PLASMA PHYSICS AND PLASMA TECHNOLOGY

**(PPPT-10)**

Minsk, Belarus
September 12 – 16, 2022

**CONTRIBUTED PAPERS**

Материалы докладов X Международной конференции «ФИЗИКА ПЛАЗМЫ И ПЛАЗМЕННЫЕ ТЕХНОЛОГИИ»
Минск, Беларусь, 12 – 16 сентября 2022 г.

На английском языке

Составители:
Тарасенко Николай Владимирович
Невар Елена Аркадьевна
Тарасенко Наталья Николаевна
Усачёнок Максим Сергеевич

Ответственность за авторство, достоверность опубликованной информации и цитирование источников несут авторы.

Подписано в печать 01.09.2022. Формат 60x84 1/16
Печать цифровая. Бумага офсетная.
Усл.печ.л. 30,2. Уч.-изд. л. 29. Тираж 130 экз. Заказ 821.

Отпечатано с готового оригинал-макета в ООО «Ковчег»
Свидетельство о ГРИИРПИ № 1/381 от 01.07.2014
Ул. Л. Беды, 11/1-205, 220040 г. Минск
Тел: (8017) 379 19 81. E-mail: kovcheg_info@mail.ru
Instagram: kovcheg_info, Facebook: infoKOVCHEG

ISBN 978-985-884-193-5

